eman ta zabal zazu

Universidad del País Vasco | **Euskal Herriko Unibertsitatea**

A METHODOLOGY FOR OPTIMIZING LPBF COMPONENTS DESIGN BASED ON CRYSTALLOGRAPHIC TEXTURE-INDUCED ANISOTROPY CONSIDERING POST-PROCESSING OPERATIONS BY MACHINING

José David Pérez Ruiz

Thesis submitted to the University of Basque country for the degree of Doctor

Department of Mechanical Engineering

Directed by
Dr. Luis Norberto López de Lacalle Marcaide
Dr. Gorka Urbikain Pelayo

January 2023, Bilbao

A METHODOLOGY FOR OPTIMIZING LPBF COMPONENTS DESIGN BASED ON CRYSTALLOGRAPHIC TEXTURE-INDUCED ANISOTROPY CONSIDERING POST-PROCESSING OPERATIONS BY MACHINING

José David Pérez Ruiz

Thesis submitted to the University of Basque country for the degree of Doctor

Department of Mechanical Engineering

Directed by

Dr. Luis Norberto López de Lacalle Marcaide
Dr. Gorka Urbikain Pelayo

January 2023, Bilbao

ii

Dedicated to my father, José, my mother, Elvira, my grandmother Graciela, my aunt Yaneth

and my daughters, Isabella Sofia, Katherin Daniela, and Melo. Thank you, GOD

Acknowledgments

First of all, thanks to GOD, the giver of life and health, who allowed me to fulfill becoming a Doctor in mechanical engineering and achieve it in such an important region as the Basque Country. It is undoubtedly a great privilege to meet such kind and helpful people as my thesis supervisors, Professor Luis Norberto López de la Calle and Professor Gorka Urbikain, who welcomed me, believed in my research project, and supported me from the beginning. Their support at this stage has undoubtedly enabled me to grow significantly as a Researcher. To Professor Aitzol Lamikiz for the advice and for allowing me to work in the Laser laboratory.

I want to thank my colleagues from the UPV/EHU and CFAA manufacturing group: Pablo Fernández, Haizea González, Gaizka Gómez, Felipe Marin, Ander del Olmo, Gonzalo Martínez de Pissón, Octavio Pereira, Cristian Pérez, Marta Ostolaza, Oihane Murua, Aizpea Urresti, Jon Iñaki Arrizubieta, and Sarvesh Mishra for their countless advice and time to discuss so many concepts, results and points of view, as well as the talks, get-togethers, and coffee time. I would also like to thank the workshop staff, Isaac Casas, Joxe Larrañaga, and Raul Cosgaya, for their patience and help in the handling and operation of the workshop equipment, and Dr. Mario Renderos for his help and guidance in deep topics of materials science, your extensive knowledge and experience were of great help. I am especially grateful to my colleagues and friends at Politecnico di Milano: professors Ali Gokhan Demir and Barbara Previtali, Researchers Francesco Galbusera and Leonardo Caprio, as well as SITEC colleagues Francesca Paradiso, Simone Maffia, Akshay Benni, Ali Aktas and Kenan Kaan Yetil for their valuable help during my stay in Milan, without any doubt, you are talented people. I would also like to thank Professors Jorge Bris, Jhovany Pacheco, Heriberto Maury, and Jaime Mesa from the Universidad del Norte (Colombia), Dr. Hugo Gonzalez, and Dr. Wilmer Velilla for their continuous advice and help.

I am deeply grateful to my family, especially to my father, José R Pérez, and my mother, Elvira Ruiz, for all their love and unconditional support, to my aunt Yaneth Ruiz and my grandmother Graciela Oviedo, to my siblings Carlos and Tatiana Pérez, to Cesar Osorio, Daniela montes, to my daughters Melany montes, Isabelita and katherincita for all their love, to Sofia Salazar and to many others that I cannot name. I want to thank Pastor Jesús Giraldo, his wife Esther, and the Romero family for all their help, teachings, and advice, and my friends Juan Pablo the "Vasco Zuluaga" and Cristina Giraldo for their great friendship and happiness. I cannot forget my childhood friends who encouraged me during this time: Fabian Robles, Denier Rocha, Paola Pereira, Evelio Mejia, Elias Romero, Juan Carlos Benavides, Tatiana Noriega, the Alvarez brothers, and yompli. Thank you, thank you ALL.

Summary

The LPBF manufacturing process allows components of high geometric complexity to be obtained and the crystallographic texture controlled through laser scanning strategies. At the same time, the crystallographic textures can reach different degrees of intensity depending on the laser manufacturing parameters. An essential aspect of the LPBF process is the development of crystalline patterns associated with each LPBF manufacturing configuration; in this way, it is possible to some extent to be sure of the primary crystalline orientations that will develop in the material relative to the reference system of the component. To this end, this Thesis considers the repeatability of the crystalline patterns associated with different LPBF fabrication configurations, showing that it is possible to obtain expected crystalline directions in an experimental range.

The proposed methodology looks to obtain the material's mechanical properties as a function of different orientations of the load vectors to improve the mechanical design of LPBF components by having the components fabricated in orientations where the principal strain vectors coincide mainly with the crystalline directions of the highest mechanical strength. Additionally, this thesis considers the pos-processing by machining and the ways to improve the machining stability and decrease the cutting shear strength. As the orientation that increases mechanical strength does not always coincide with the orientation that decreases cutting shear strength, it is necessary to consider multi-objective optimization as a tool to obtain manufacturing configurations that allow a balanced design solution to be obtained where component design priorities are established. Additionally, multi-objective optimization requires mathematical functions to quantify the effect of the LPBF manufacturing parameters on the mechanical properties, for which different mathematical models and methodologies are presented in this document.

In this thesis, different case studies are presented to evaluate the proposed models for the quantification of shear strength as a function of microstructure, for the increase of component stiffness by controlling anisotropy and temporal stiffeners, for the effect of beam shaping on the microstructure and to compare the effect of LPBF manufacturing configurations on physical parameters and mechanical properties among others.

Table of Contents

V. Vector-based model to characterize shear strength sensitive cutting force coefficient of LPBF anisotropic parts .. 151

VI. A holistic methodology for the design and manufacturing of LPBF functional parts considering post-processing operations 196

Figure index

Table index

Nomenclature

AM   Additive manufacturing

BD   Binder jetting

CNC   Computer numerical control

CAD   Computer-Aided Design

CAM   Computer-Aided Manufacturing

DED   Direct energy deposition

DOE   Design of experiments

EBM   Electron beam melting

EDM   Electro discharge machining

EBSD   Electron backscatter diffraction

HIP   Hot isostatic pressure

KAM   Kernel average misorientation

LAM   Laser-assisted machining

LMD   Laser Metal Deposition

LPBF   Laser powder bed fusion

LMD   Laser Metal Deposition

MIM   Metal injection moulding

MQL   Minimum quantity lubrication

ND   Non-destructive

PBF   Powder bed fusion

SEM   Scanning electron microscope

WAAM   Wire arc additive manufacturing

Chapter I. Introduction

I.   Introduction

This chapter presents the background of this work application considering the industrial environments and projections. Afterward, the main objectives for the proposed methodology are specified in detail, the document structure is described, and the purpose of each chapter is exposed.

I.1. General Introduction

Crystallographic texture to induce superior physical properties is a topic of great scientific interest today (Hagihara et al. 2021; 2017; Sun, Hagihara, and Nakano 2018a; Sprouster et al. 2021; Bittner, Thielsch, and Drossel 2021). However, its practical application in improving industrial parts has not yet been fully developed, which is one of the interests of this thesis.

This thesis presents the result of a methodology for manufacturing LPBF components considering post-processing by machining and the effect of crystallographic texture-induced anisotropy on the material's mechanical properties as a tool for component design optimization.

Nowadays, additive manufacturing, especially the LPBF technique, have progressed in developing parts with near-net shape, complex shapes, lightweighting through lattice structures, thin walls, and hollow shapes, among many other features. All these features have made the manufacturing of LPBF functional parts a reality today. However, the directionality of LPBF additive manufacturing means that LPBF materials have a significant level of anisotropy. Anisotropy is a phenomenon in most materials, as pure isotropy is quite rare. However, many materials are considered isotropic because the levels of anisotropy do not significantly affect the mechanical properties, yet they are not isotropic. Anisotropy is not related to volumetric properties such as density or specific heat (Hutchinson 2015) but to many orientation-dependency-sensitive properties due to the material's microstructure.

Anisotropy is not a new aspect of metallic materials used to manufacture functional parts, as processes such as lamination generate columnar grains and textured materials. There is also a perception among many manufacturers that anisotropy is something to be avoided, but it could be related to a lack of knowledge of how to take advantage of it or how to avoid it. An excellent example of this perception is the single crystal turbine blades developed by Pratt & Whitney in the 1960s. It is very curious to hear in the industrial sector that single-crystal material is the holy

grail of materials; however, many of those who use this expression do not consider that single-crystal materials also have the maximum level of anisotropy. It is noteworthy to consider that the manufacturers of single-crystal turbine blades know how to take advantage of the benefits of anisotropy when manufacturing the parts where the load to which the parts will be subjected will correspond to the crystallographic directions of greater stiffness and resistance to plastic deformation.

Figure I-1a shows a single crystal nickel alloy turbine blade obtained by the directional solidification method, which requires a meticulous solidification process to ensure that the thermal gradient of the unsolidified zones follows the preferred crystallographic orientation of the seed dendrites. On the other hand, Figure I-1b compares blades of different microstructural classifications: single crystal, directionally oriented grains, and equiaxed grains. The blades with equiaxed grains correspond to those developed with the most common casting techniques, while the directionally oriented grains correspond to more advanced casting techniques and are the precedent for obtaining the single crystal turbine blades. In these materials, the anisotropy is lower in equiaxed blades and maximum in single-crystal blades. However, single-crystal blades have advantages related to being grain boundary-less and having higher corrosion and fatigue resistance than equiaxed grains blades, which are polycrystalline. Based on the above, it is possible to say that the significant anisotropy advantages related to the reduction or elimination of grain boundaries make the design complexities caused by anisotropy take a second place.
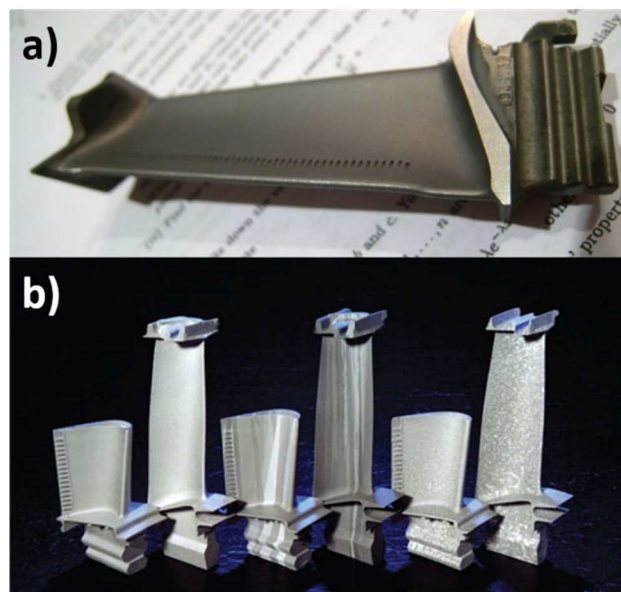
Figure I-1. Turbine blades. a). Single crystal blade (Make 2012) b). comparison of turbine blades from left to right: single crystal, directionally oriented, equiaxed (Langston 2015)

Other applications of anisotropy in designing components are related to increasing the magnetic properties. It is precisely the LPBF process currently used to develop new rotors for electrical machines, among other applications. Figure I-2a,b shows a Fe-Si-Cr-B rotor with high hardness (877 Hv), high electrical resistivity (178.2 μΩ), and a remarkable magnetic susceptibility (9.17) manufactured by LPBF. The researchers in charge of developing and fabricating the rotor reported a high correlation between induced-texture Anisotropy and magnetization response. In this line (Gargalis et al. 2020) compared the performance of a rotor manufactured by LPBF with a conventional rotor, finding similar power levels and efficiency but with greater scope for topological optimization to increase magnetic permeability. (see Figure I-2 c,d).
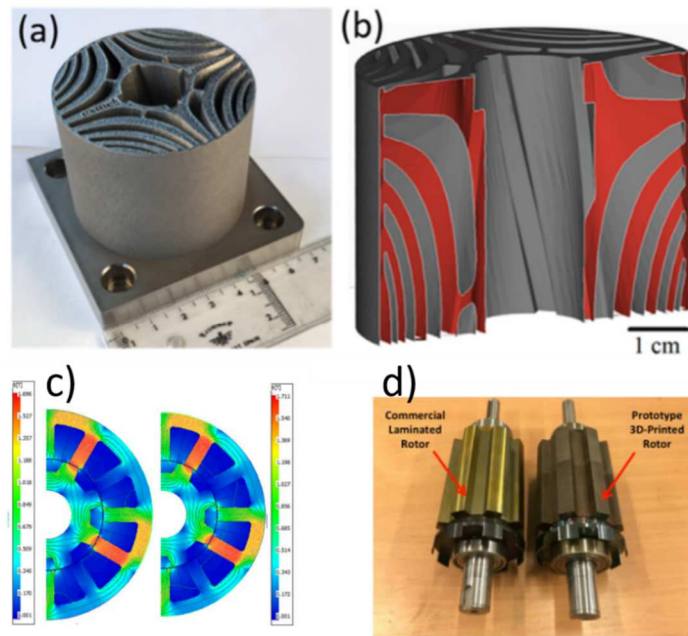
Figure I-2. Electric rotors manufactured by LPBF. a) Fe-si LPBF rotor topologically optimized. (Thorsson et al. 2022) b) detail of the rotor cross-section. (Thorsson et al. 2022) c) comparison of Flux density and magnetic field of conventional and LPBF rotors. (Gargalis et al. 2020) d) commercial laminated rotor and LPBF rotor benchmark.(Gargalis et al. 2020)

In addition, there are many other possibilities for using anisotropy to optimize the design of components to increase mechanical strength, stiffness, or electrical properties. Where mechanical properties, plastic strength, and stiffness can also be increased when the stress field to which the part is subjected is aligned with the stronger crystalline orientations. The increase in mechanical strength as a function of crystalline orientations depends on the material. Table I-1 summarizes Young's modulus value in the strong and weak orientation of some single crystal materials. It is observed that for some materials, the stiffness triples in the strong orientations

concerning the weak orientations. It is also important to note that the level of anisotropy is not the same for all materials, Nor is the crystalline orientation that is strong for one material necessarily strong for another.

Table I-1. Largest and smallest Young modulus in some single crystals. (Hutchinson 2015)

Material	Stiffest direction	Maximum Young's modulus, E_{max}	Least stiff direction	Minimum Young's modulus, E_{min}	Ratio E_{max}/E_{min}
Iron (bcc) steel	<111>	273	<100>	125	2.18
Stainless (fcc) steel	<111>	297	<100>	101	2.94
Copper (fcc)	<111>	190	<100>	67	2.84
Aluminium (fcc)	<111>	84	<100>	64	1.31
Molybdenum (bcc)	<100>	363	<111>	291	1.25
Titanium (hcp)	<0001>	146	< hki0>	104	1.40
Magnesium (hcp)	<0001>	50.8	< hki0>	45.5	1.12
Zinc (hcp)	< hki0>	124	<0001>	36.3	3.42

The purpose of this thesis is to present the methodologies and models necessary to use anisotropy as a design optimization tool in LPBF materials for the improvement of their mechanical properties and the improvement of machining stability, considering that the nature of this manufacturing process means that the manufactured parts will always have some degree of anisotropy. Since it will be present, it is more productive to take advantage of it. In the same way, this thesis presents primary indications of how to obtain materials in the range of polycrystals-like, textured polycrystals, or single-crystal likes from the configuration of the LPBF process and the different advantages and disadvantages of each crystalline classification.

The samples analyzed in this thesis are in an as-built state, so heat treatment is not included in the analysis. However, exploratory EBSD analysis of as-built IN718 LPBF samples and Heat treated IN718 LPBF samples by precipitation hardening were carried out. The results showed that the crystalline texture and anisotropy remained the same before and after the heat treatment.

I.2. Objectives

The methodology presented in this thesis has the following main objectives:

a) To present a methodology for manufacturing LPBF components that consider the crystalline patterns that each laser strategy leaves on the materials as a tool for predicting Young's modulus and Taylor factor maps as tools for optimizing the manufacturing orientation of the parts.

b) Show the interactions between LPBF configuration, physical parameters, physical properties, and machining post-processing.

c) To present a microplasticity model for quantifying the oblique cutting shear strength for the milling of LPBF materials as a function of the orientation density function(ODF).

d) To present a model for obtaining mechanistic coefficients sensitive to the shear strength of anisotropic materials.

e) To present a methodology based on multi-objective optimization to improve the stability of the machining without the detriment of the mechanical properties of the LPBF components.

f) To present a methodology for stiffening components that require surface quality improvement by machining through easily removable lateral supports that allow the set of printed parts to work as a temporary assembly.

I.3. Thesis organization

After contextualizing this thesis, its applications, and the present and future research fields, the document was organized by chapters as described below and summarised graphically in the diagram in Figure I-3.

In **Chapter II** it is presented the state of the art of evolution of the additive manufacturing process, the applications of the LPBF process and the drawbacks related to this process to increase its productivity, the material considerations related to the physical principles present in the process, the microstructural patterns present in LPBF materials, the typical defects and the evolution of hybrid manufacturing in the post-processing of this type of components, in particular by machining.

Chapter III comprehensively analyzes the interaction between LPBF parameters, physical parameters, and mechanical properties and the theories and models that allow the prediction of mechanical properties from the crystalline patterns and physical parameters associated with each studied LPBF configuration.

Chapter IV is dedicated to showing and quantifying the microstructural and physical origin of the variability of cutting forces as a function of the relative position of the tools to the workpiece, the tool geometry, and the crystalline arrangement of the material through a micro-plasticity model.

Chapter V presents a model to obtain mechanistic coefficients proportional to the shear strength in anisotropic metallic materials. The obtained model presents a vectorial approach to obtain instantaneous coefficients that are proportional to the instantaneous shear strength and that can be used in isotropic or anisotropic materials, as is the case of the materials obtained by LPBF.

Chapter VI presents a multiobjective optimization methodology that considers different objective functions to be optimized simultaneously according to the priorities defined in the component design. In this methodology, the objective functions to be optimized are related to the desired mechanical properties of the material and machining post-processing quality. So the multi-objective methodology is helpful to ensure that the process optimization not only improves the stability of the machining but also that the mechanical properties are maintained within the desired values. In this chapter, three case studies cover different aspects of the proposed methodology.

Finally, **Chapter VII** outlines the contributions and future directions associated with this thesis.
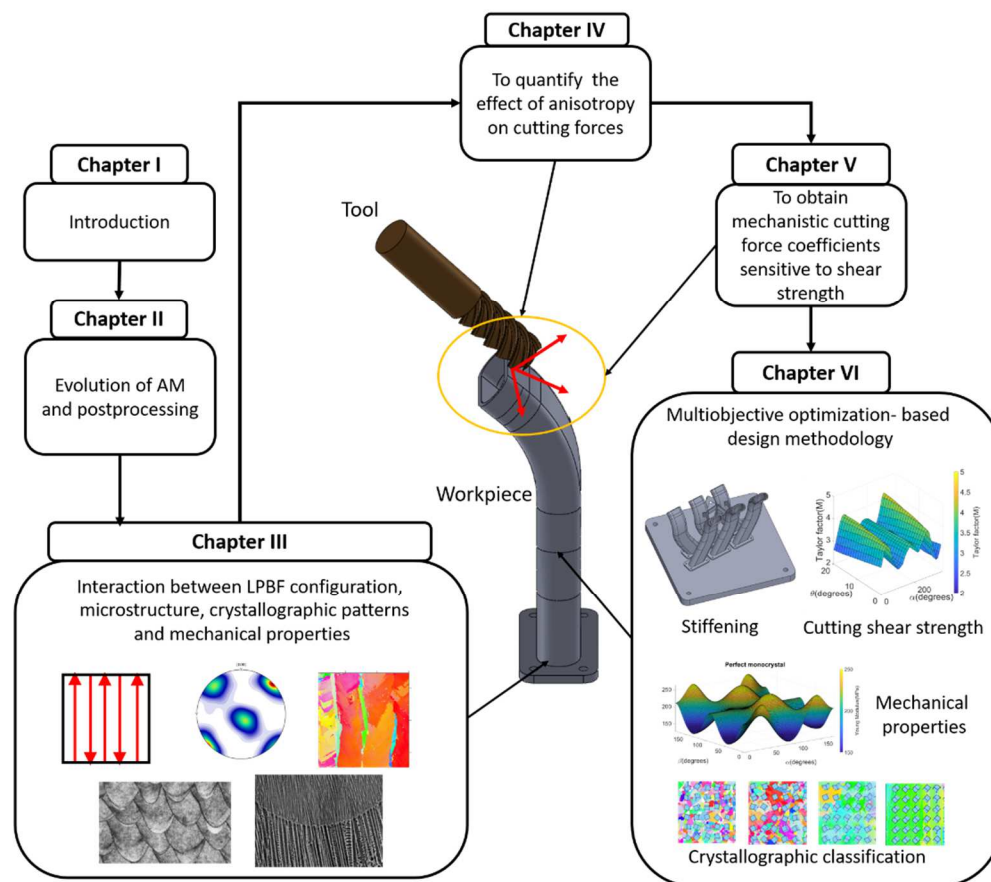
Figure I-3. Thesis organization Graphical abstract

Chapter II. Evolution of metal additive manufacturing and post-processing

II. Evolution of metal additive manufacturing and post-processing

This chapter presents a literature review of state of the art for the evolution of the additive manufacturing process, the drawbacks related to this process to increase its productivity, the implicit physical principles of the process, the microstructure of LPBF materials, manufacturing defects, and the hybrid manufacturing strategies in the post-processing of this type of components, in particular by machining.

II.1. Introduction

Metal printing has created a new segment in manufacturing geometrically complex parts. (Klahn, Leutenecker, and Meboldt 2015). Manufacturing techniques such as LPBF are being improved every day and open up the option of industrial production in small and medium batches.(Ford and Despeisse 2016; W. Gao et al. 2015). Aspects include direct translation from design to component manufacturing, hollow parts, parts with complex internal geometries, reduction in product development and manufacturing time, market insertion, and excellent scalability (Tofail et al. 2018; Thompson et al. 2016) are the potentialities of this new way of manufacturing.

As it is known, an advantage of AM technologies when compared to traditional manufacturing technologies, such as casting or forging, is the flexibility to manufacture much more complex parts that can include internal cavities with a low waste of material. However, some inherent limitations are associated with this technology, which is discussed in the next section.

Additive manufacturing is a key part of Industry 4.0, but there are questions about how it could be used in large-batch manufacturing environments. (Dilberoglu et al. 2017). This is why concepts such as a) group technologies (Mosier and Taube 1985), b) flexible manufacturing, and c) production cells become very important. From the quality and homogeneity of materials before and after the printing process to the dimensional and structural changes that parts undergo during the printing process, additive manufacturing has many challenges to overcome. (Kromm et al. 2018), in some cases, these anomalies are mitigated by optimizing manufacturing parameters or using supports. (Mishurova et al. 2018). Efforts have also been made to monitor the process and detect anomalies through image analysis techniques (Scime and Beuth 2018; Lott et al. 2011; Everton et al. 2016); despite the research effort, there is a need for further processing to ensure the desired dimensions and properties of the parts.

In addition to the implications in the manufacturing area, additive manufacturing must have economic, environmental, geopolitical, security, and intellectual property implications, among others. The number of patents for products and technologies related to additive manufacturing has grown exponentially in the last decade. Large manufacturers have started to include metal additive manufacturing in their new and traditional projects, thus replacing more traditional processes such as casting for many products (Campbell and Ivanova 2013).

II.2. Market of metallic additive manufacturing

The rapid growth of the additive manufacturing market explains the high industry interest in these new technologies. The metal AM market size was 2.4 Billion in 2019 and is projected to grow by nearly 30% between 2019 and 2024. The model calculations show that 3D printing can potentially reduce costs by 170-593 billion US$, the total primary energy supply by 2.54-9.30 EJ, and CO_2 emissions by 130.5-525.5 Mt by 2025 (Gebler, Schoot Uiterkamp, and Visser 2014). The most marketed technologies are currently PBF (LPBF and EBM), DED, and BJ, where the sale of inputs such as powders and wires is essential (Toyserkani et al. 2021).

The aerospace industry covers the largest share, followed by the medical sector. The aerospace industry profits from turbine, helicopter, jet-engine components, and new space applications such as rocket engines, attracting significant venture capital worldwide, especially in the United States. At the beginning of metal AM, Germany was the leading market region with its first movers in LB-PBF technology CONCEPT LASER (now GE), EOS, REALIZER (now DMG MORI), and SLM SOLUTIONS. Hence, many pioneering users were located in Germany and Europe. By now, however, the market share is more evenly distributed with suppliers and buyers from Europe, America, and Asia(AMPower 2021).

The aerospace additive manufacturing market is also one of the fastest growing. The radar systems sector alone is expected to grow to over USD 3 billion by 2027, with North America being the dominant region. (Marketresearchfuture 2022). Airbus has identified many parts considered non-critical that can be manufactured by additive manufacturing, including parts for the A380 aircraft. Other companies, such as Northrop Grumman, have defined that more than 1400 parts could be manufactured by additive manufacturing when the technology is mature enough to process all the required materials (Campbell and Ivanova 2013).

In this line, General electric recently celebrated that it has over 30,000 D-printed fuel nozzle tip for the leap engine (GE 2022) (see Figure II-1), proving that additive manufacturing can work for mass production, going from 20 parts that were previously welded together to a single part and achieving a 25% weight reduction as well.

Figure II-1. D-printed fuel nozzle tip (GE 2022)

SLM and Cellcore(ETMM 2019) collaborated to develop parts for a rocket propulsion engine by reducing the large number of individual parts for multifunctional and lightweight manufacturing thanks to lattice structures that cannot be obtained by traditional methods, thus reducing post-processing steps and manufacturing time.

Despite the above examples, metal additive manufacturing still has many challenges to overcome to make any product mass-producible. In this aspect (Barz, Buer, and Haasis 2016) developed a methodology to optimize the integration of additive manufacturing in the supply structure, considering supply nodes and production sites, among others, through computational simulations, where they evaluated the consequences of additive manufacturing on the supply chain, concluding that the design of the supply chain is critical to achieve greater dissemination of additive manufacturing in the market.

Aerospace brackets are another type of part widely manufactured by LPBF, such as the flap actuation bracket developed by Asco industries (see Figure II-2a), in which they managed to reduce the weight by 31% and eliminate the time required for assembly. In the same line (SHI et al. 2020; López-Castro et al. 2017) improved brackets design for aeronautical applications employing thermo-elastic topological optimization, significantly reducing the weight of these components (see Figure II-2 b,c).
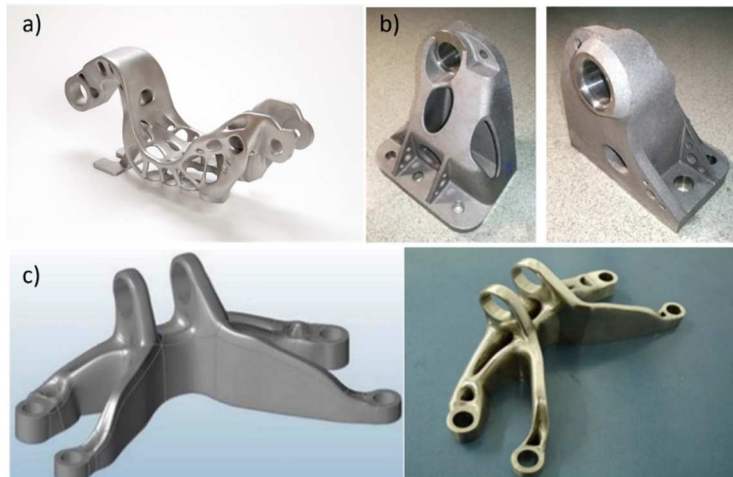
Figure II-2.Aerospace brackets a)Asco industries bracket(SLM 2022)b)aerospace bracket for aerospace application(SHI et al. 2020) c)Stainless steel optimized bracket(López-Castro et al. 2017)

Companies like Siemens are making significant efforts to manufacture combustion system components by additive manufacturing, such as the gas turbine burner front end (see Figure II-3a left). They obtained a one-piece burner with optimized cooling, the pilot gas feed integrated into the structure, a standard lead time of 3 weeks, and a weight of 3.5 Kg. 0n the other hand, the conventionally manufactured burner front(Figure II-3a right) has 13 machined parts, joined by 18 welds, with thermal barrier coating on front surface, external pilot gas feed, a standard lead time of 26 weeks, and a weight of 4.5 Kg.
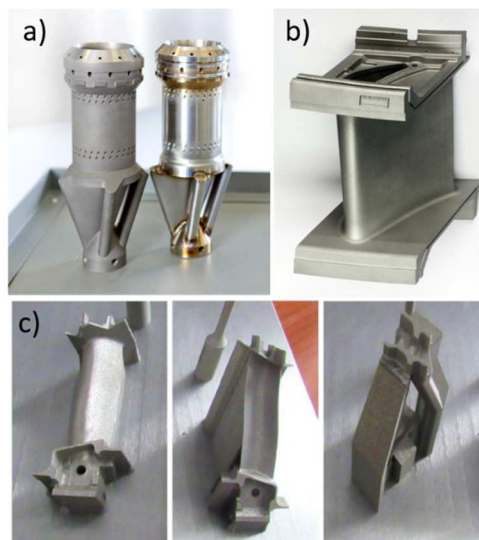
Figure II-3. Aerospace components manufactured by LPBF a) LPBF burner front (Finspång 2016) b) LPBF Siemens turbine blade (optics.org 2016) c) IN718 LPBF blades for anisotropy analysis (Caiazzo et al. 2017)

In turbine blade manufacturing, progress has also been made in producing turbine blades by LPBF. In this respect, Siemens and Fraunhofer ILT have developed blades and vanes for gas

turbines using a modular production process. (see Figure II-3b). In addition, other efforts have been made to manufacture this type of component, including the research carried out by (Caiazzo et al. 2017), where they evaluated the anisotropy of blades manufactured by LPBF as a function of slopping angle with the building plate, proposing recommendations for the use of supports and positioning of the blades to reduce geometric distortion (see Figure II-3c).

II.2.1 Applications and drawbacks of metal additive manufacturing

AM has established itself as one of the most disruptive manufacturing technologies; despite the difficulties of mass production by AM for many types of components, there are other aspects such as digital manufacturing, decentralization of manufacturing, flexibility in design editing, and others that make this technology very attractive and functional. (Toyserkani et al. 2021). Currently, many AM equipment manufacturers are looking to improve their processes by reducing manufacturing times and minimizing defects related to porosity, lack of fusion, and undesired variations in microstructure, among others. Additionally, there is a great interest in expanding the range of powder materials available for AM manufacturing to include highly reflective materials such as copper and aluminum in the catalog, which have comprehensive industrial projections, especially in the e-mobility sector.

Historically the weight reduction is a strong motivator of innovation in the aerospace industry, which looks for safety, performance, fuel efficiency, and range (Boyer et al. 2015). The most critical properties in the design of properties for the aeronautical industry are:

- Static strength: characterized by the tensile, compressive, and shear strength in which the structure is intended to remain in the elastic range.
- Durability: fatigue, environmental corrosion, damage tolerance. A high level of reliability is sought in metallic structures, and in case of damage, it must be possible to identify it before it becomes critical.
- Weight-to-cost ratio, where the aim is to reduce the weight within certain limits.

AM metallic materials require careful structural integrity assessment in terms of geometrical distortions, mechanical strength, porosity, corrosion resistance, delamination, residual stresses, and others; This is particularly important for components subjected to structural or cyclic loading. (Joshi and Sheikh 2015).

The strong relationship between process parameters, microstructure, and quality of materials obtained by additive manufacturing makes it essential to define appropriate process ranges to

increase the robustness of the process in terms of quality variability and mechanical properties (Russell et al. 2019). Some of these aspects to consider are:

- Feedstock attributes (purity, powder particle shape and size distribution, and chemistry).
- Processing conditions and controls (laser or electron beam power, hatch width, and scan rate).
- Thermal conditions during build (layer thickness and platform preheating).
- Build atmosphere and purity (shield gas or high vacuum).
- Post-processing [Hot Isostatic Pressing (HIP), heat treatment, and machining].

Some additional drawbacks of LPBF manufacturing are shown in Figure II-4, ranging from cracks, unmelted powder, variable roughness patterns depending on the laser scanning strategy, thermal distortions, and variations in the dimensions of the manufactured parts depending on the supports. All these aspects, plus those mentioned above, mean that additive manufacturing still has many hurdles to overcome to become a more robust process without sacrificing design flexibility.
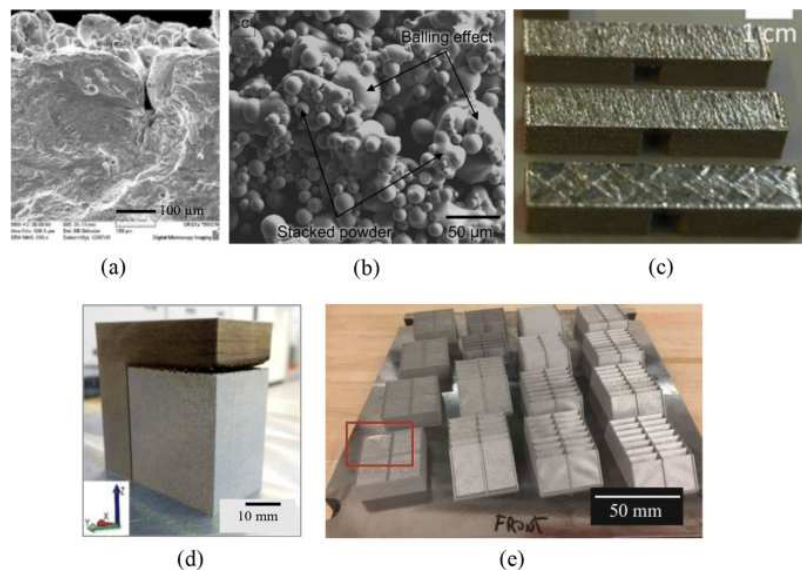
Figure II-4. Drawbacks of additive manufacturing. a) Crack formation, b) Unmelted powder, c) Variability on surface roughness by scanning strategy, d) Part distortion, e) Overhang tilt caused by thermal distortion (highlighted in red) (Jiménez et al. 2021a)

II.2.2 Additive manufacturing process classification

Additive manufacturing was initially intended to develop prototypes for marketing and design; over time, the number of applications increased, and functional applications became more and

more common. These functional applications were initially made from polymeric materials; however, recent breakthroughs in control, laser, monitoring, and advanced material characterization, among others, have allowed metal additive manufacturing to become a reality today under a wide range of techniques, materials, and technologies for the achievement of functional parts with industrial application. There are currently four main groups of metal fabrication under different physical principles and techniques (Jiménez et al. 2021a; ASTM 2022):

- Powder bed fusion(PBF) is one of the most successful and widely used techniques for manufacturing parts with high geometric complexity, hollow shapes, thin walls, and others (Razavykia et al. 2020; Yap et al. 2015). This technology is based on melting multiple layers of powder on a solid metal substrate with compatible weldability. Within this group are laser powder beam melting (LPBF), also known as selective laser melting (SLM), and electron beam melting (EBM). The main difference between LPBF and EBM is the nature of the heat source, which is a laser for LPBF and an electron beam for EBM (Dinda, Dasgupta, and Mazumder 2012).

- Direct energy deposition (DED) is a widely used process in 3D manufacturing. It is based on multiple heat sources (laser, electron beams, electric arc, plasma) acting on powder or metal wire fed through a nozzle. This group includes techniques such as LMD. (Herzog et al. 2016) among others.

- Binder jetting (BJ) technology consist of a printhead selectively depositing drops of binding liquid onto a thin layer of powder to glue particles together layer by layer (Gokuldoss, Kolla, and Eckert 2017). The binder content is consolidated by sintering. This technology is cheap; however, parts are not fully dense, and post-processing is required to reach low porosity levels.

- Material extrusion technology is based on metal powder extruded with thermoplastic filaments or rods. Afterward, the polymeric content is removed by chemical or thermal ways and consecutive sintering to increase the density of metallic parts (Goh et al. 2019).

II.3. Process and material considerations for LPBF

The mechanical properties of parts manufactured by AM exceed, in many cases, those of conventionally processed materials (casting, forging, etc.). However, not many publications report the variability in fatigue strength, impact, toughness, and microstructure, among others,

of parts, manufactured by AM due to machine, technique, and powder manufacturers' changes (Lewandowski and Seifi 2016). Additionally, the development of process-induced defects such as pores or lack of fusion or anisotropy limits the use of additive technologies in application-critical components. This is why all efforts related to identifying and predicting defects and controlling mechanical properties are welcome and can only be achieved through a thorough understanding of the physical fundamentals of process-microstructure relationships.

Standardizing additive manufacturing processes to current standards requires extensive experimentation and testing to develop statistically based quality assessment processes. This, in turn, can cost millions of euros and take years to complete, considering that parts obtained by AM have a high variability of their properties depending on the process parameters. This is why the quality assessment of an AM part through modeling may require fewer tests (Seifi et al. 2016). However, developing physics-based models with sufficient repeatability and reproducibility for AM processes can be very complex. Current qualification procedures such as AMS4999A are statistically based qualifications that come from large numbers of tests and make much sense for serial and mass-produced parts. However, this aspect can be a barrier for small and medium batch production, which makes holistic ICME (integrated computational materials engineering) qualification schemes that include pre-processing, processing, and post-processing more appropriate for this new way of manufacturing (NIST 2020).

Material standardization bodies usually consider that the critical mechanical properties for the quality of components manufactured by AM are tensile strength and fatigue resistance. Any change in geometry, number of parts per plate, or laser parameters, can significantly affect the thermal history, affecting the microstructure and defect type statistics, which in turn affects the mechanical properties (Seifi et al. 2017).

Laser strategy is one of the parameters that most affect the mechanical performance of AM components, causing anisotropic behavior in monotonic and fatigue cycles. Component orientation is a critical aspect of the directional dependence of mechanical properties, which makes the approach of using a single-part manufacturing orientation too conservative. The alternative to this is to use properties based on specific directions, but this can be a complex task considering that functional part designs contain a very high level of geometrical complexity, resulting in multi-axial stress states, which in turn makes fatigue strength prediction complex. Additionally, crack propagation analysis requires moving from the traditional planar crack growth model to the 3D crack growth model, which requires adjustments to conventional theories to ensure confidence levels in predicting the life cycle of fatigued parts (P. Li et al. 2016).

The fatigue strength of printed components can also be affected by the type of powder used, the microstructure, and roughness (Tang et al. 2015). Some defects can be eliminated through heat treatment; however, microstructural changes are more difficult to avoid or control. Additionally, roughness has adverse effects on fatigue strength, making improving surface quality through post-processing a key aspect (Spierings, Starr, and Wegener 2013).

II.3.1. Feedstock materials

The ease of transport, storage, feeding, and melting makes metal powders the main ally of additive manufacturing. Currently, there are several methods for obtaining metal powder; however, the high standards of additive manufacturing, especially the LPBF process, mean that the powders must have an exceptional level of quality. The quality of the parts manufactured by LPBF is directly proportional to the quality of the powder (X. Zhao et al. 2008; Karlsson et al. 2013) and their characteristics. These characteristics include powder size, chemical composition, size distribution, powder morphology, and flowability (Sames et al. 2016). Powder size ranges from 10-90 microns. Powder flowability is usually measured with the hall flow meter, powder morphology is measured with computed tomography or SEM, and powder distribution with laser diffraction (Santomaso, Lazzaro, and Canu 2003; Slotwinski et al. 2014).

Metal powders are manufactured by gas atomization, rotating plasma electrode, rotary atomization, and water atomization. Figure II-5a shows a gas atomizer, and Figure II-5b a schematic of the physical principle of the atomizer. In this process, the molten metal is atomized due to the high vacuum exerted by the flow of inert gases such as argon. Figure II-5c shows a powder distribution of Inconel 718 obtained by gas atomization.
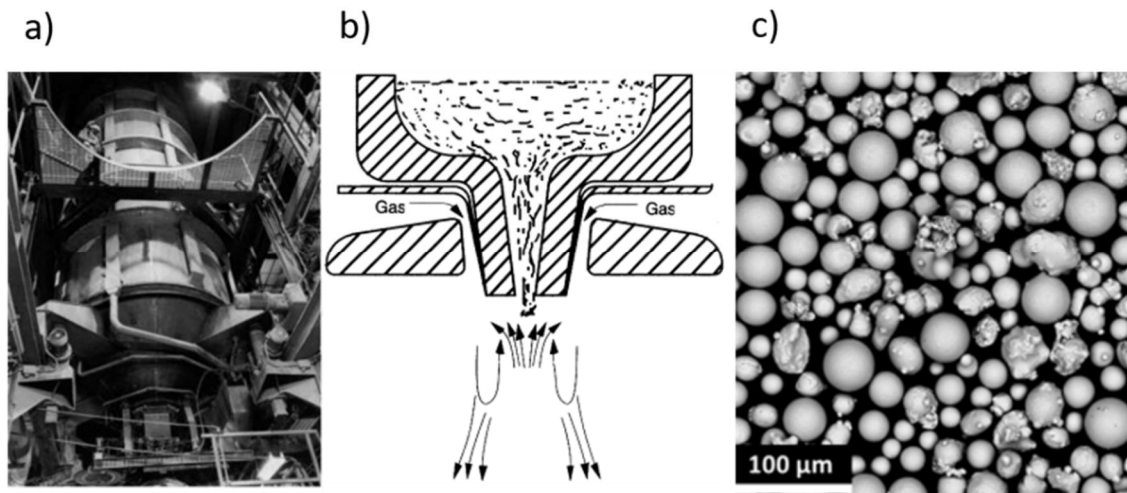
Figure II-5.Feedstock. a)Gas atomizer (Neikov 2009), b) gas atomizer principle scheme (Lawley 2001), c) IN718 powder distribution by SEM (Gruber et al. 2021)

Fine powder particles with uniform size distribution and smooth surfaces can provide uninterrupted flow through the feeder nozzles and promote a small pool size under the concentrated beam (DebRoy et al. 2018a)**;** This is one of the reasons why high-quality powders are expensive; however, they can be reused if they are sieved and appropriately stored.

II.3.2. Heat source characteristics

Some essential laser parameters in materials processing are spot size, wavelength, energy, and fluence. These parameters significantly influence the physical properties of the manufactured parts, which is why it is important to know the role of each of these parameters to determine the optimum process conditions. Other less common parameters can also be important for the process; one of these parameters is the laser beam shape, which is the distribution of light irradiance on the material of interest, in this case, the powder bed (Duocastella and Arnold 2012).

Gaussian beams (see Figure II-6a) are the most common beam shape in commercial equipment; however, there are laser systems that emit a multimode beam with a complex intensity distribution. Most lasers operate in the fundamental transverse electromagnetic mode and do not need additional elements to modify the beam shape. One property of gaussian beams is their low divergence, which makes it easier to obtain small, focused spots (Ion 2005).

Top hat beams (see Figure II-6b) are widely used too for laser material processing. In this category, optical elements are used, such as beam shaping when the output beam from the laser cavity is a Gaussian or homogenizer systems when the output is multimode. Compared to Gaussians, Top-hat beams have an M^2 value much higher than 10 where M^2 is a quality factor that indicates how close a real beam is to a perfect Gaussian beam ($M^2=1$). Thus, from Equation 1, it can be deduced that the minimum spot size will not be as small as with Gaussian beams and that the depth of field will not be as long. However, the improved spatial uniformity of Top-hat beams presents significant benefits for specific materials processing applications in comparison to Gaussian beams (Piqué et al. 2002).

$$d_f \approx 2 \frac{\lambda M^2}{\pi NA} \quad (\text{II}.1)$$

Where λ is the wavelength of the laser radiation, d_f diameter at the focus, and NA is the numerical aperture.

Despite the advantages of the Top-hat shape, one of the disadvantages of this method is that the shape is not maintained during the propagation of the laser beam, creating shape profile variability along the line of action of the laser, which can generate quality problems in the manufactured parts.
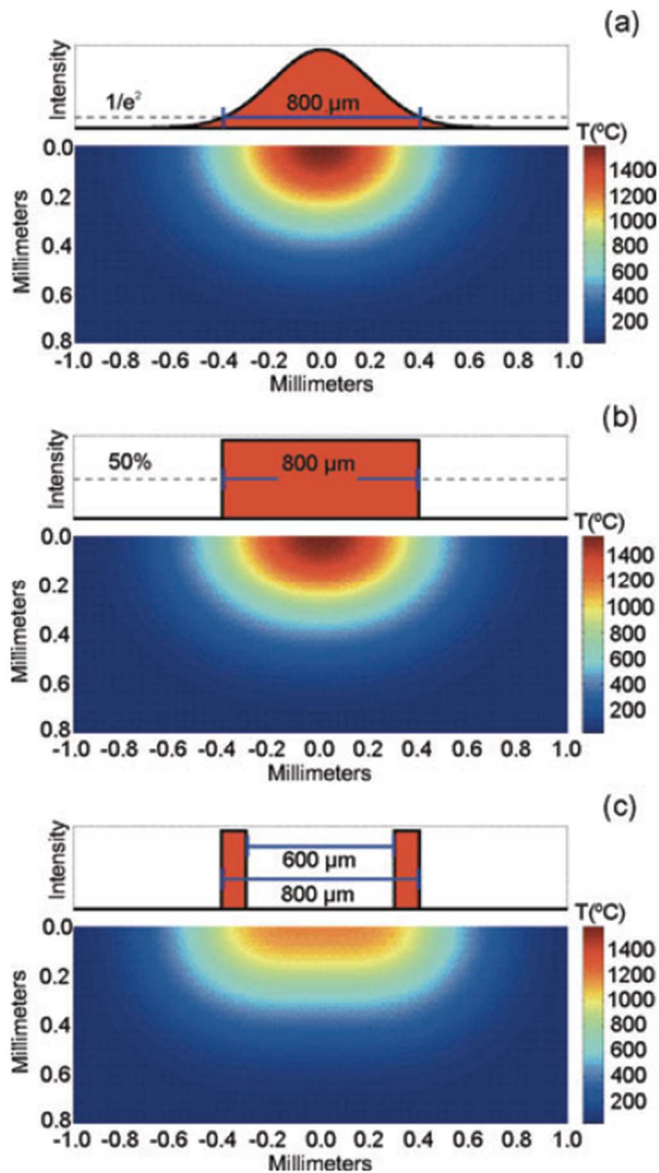
Figure II-6.Simulations of temperature profiles for different beam shaping modes. a) Gaussian beam, b)Top-hat beam, c) annular beam (Duocastella and Arnold 2012)

Laser beam shaping is not limited to the previously mentioned modes. Some unconventional beam shapes have worked in different applications, such as the Bessel beam, (Garcés-Chávez et al. 2002), or airy beams(Shvedov et al. 2010). These modes have made it possible to obtain functional characteristics that are not possible to obtain through Gaussian or top-hat modes. The use of annular beams (see Figure II-6c) joined with Gaussian beams has allowed the development of novel techniques even in image processing. Gaussian beams have advantages over the other modes in terms of the amount of energy available to modify experimental conditions; however, the way energy is distributed spatially and in time in other modes may be more appropriate for some applications or material types, which makes it desirable to have several fabrication modes in addition to the Gaussian mode (Duocastella and Arnold 2012). Figure II-6 shows some of the modes mentioned above and their associated temperature profiles.

II.3.3. Principles of laser powder bed fusion (LPBF)

In the LPBF process, the heat source energy is incident on the powder bed. When a fraction of the laser beam energy reaches a particle, a part of that energy is absorbed by the particle, and the rest of the energy is reflected in surrounding particles, the environment, or the substrate. The heat absorbed by the particles depends on the size of the particles, their density, and other physical properties such as absorptivity and reflectivity, among others.

For high energy densities, powder particles can be ejected, giving rise to spatter. In addition, there are other phenomena, such as pressure recoil (Mumtaz and Hopkinson 2010) due to local vaporization or the ejection of particles due to high electrostatic forces (Eschey, Lutzmann, and Zaeh 2009).

Interaction of the metallic powder with the heat source, progressive build-up of the layers, thermal cycles at selective zones as new layers are added on the previously deposited layers, and changes in the part shape are some of the features necessary for understanding AM.

The simulation of the transient temperature field in 3D is a complex task due to the large number of physical phenomena that are related and present in the melting and solidification processes (see Figure II-7). This is why most of the models in the literature resort to simplifications and modeling in 2 dimensions. Some of these simplifications involve the geometrical distribution of heat in the material or disregarding convective heat transfer, among others. Additionally, it is complex to consider the coupling of the phenomena of heat transfer, fluid motion, melting, and solidification, even with computational tools for the treatment of the powder bed. For this

reason, the powder bed surface is usually simplified as a flat surface, which has been shown not to affect the cooling rates and thermal gradients significantly. The transient temperature fields are usually obtained and simulated from the conservation of mass, momentum, and energy equations. See equations 2-4.

$$\frac{\partial(\rho u_i)}{\partial X_i} = 0 \quad (II.2)$$

$$\frac{\partial(\rho u_i)}{\partial t} + \frac{\partial(\rho u_j u_i)}{\partial X_i} = \frac{\partial}{\partial X_i}\left(\mu \frac{\partial u_i}{\partial X_i}\right) + S_j \quad (II.3)$$

$$\rho\frac{\partial h}{\partial t} + \frac{\partial(\rho u_i h)}{\partial X_i} = \frac{\partial}{\partial X_i}\left(\frac{k}{C_p}\frac{\partial h}{\partial X_i}\right) - \rho\frac{\partial\Delta H}{\partial t} - \rho\frac{\partial(u_i\Delta H)}{\partial X_i} \quad (II.4)$$

where ρ is the density, X_i the distance along i direction, u_i and u_j are the velocity components along i and j directions, t is the time, μ is the dynamic viscosity, S_j is a term associated with momentum, C_p is the specific heat, k is the thermal conductivity, h is the sensible heat, and ΔH is the latent heat content (Manvatkar, De, and DebRoy 2014; Manvatkar, De, and Debroy 2014).
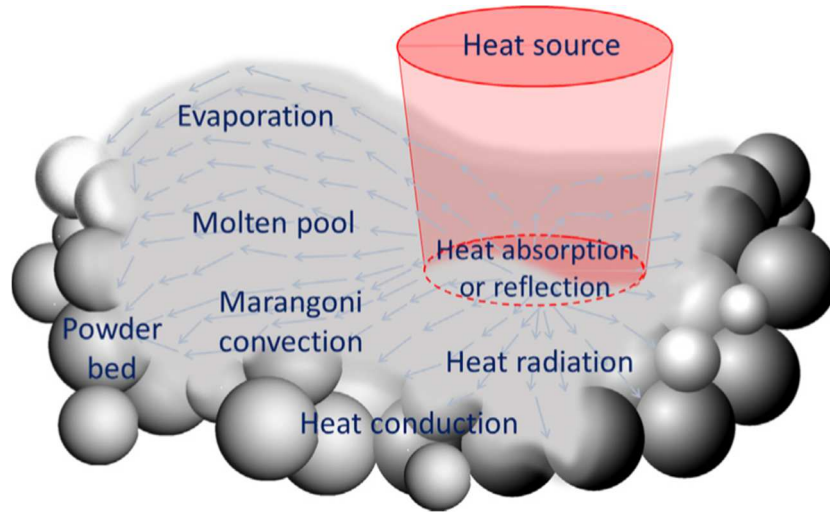
Figure II-7. Heat transfer and molten pool dynamic (DebRoy et al. 2018a)

Temperature control of the molten material is undoubtedly a crucial aspect of additive manufacturing (Qu et al. 2022). During the melting process, the temperature reaches different values along the melt pool, higher in the area closest to the laser heat source and lower in the areas further away. This spatial variation of the temperature is known as the thermal gradient,

which is why all efforts to predict its value are welcome. During the melting process, high-temperature zones are developed and sometimes exceed the boiling temperature, which means that keyhole pores could be developed for very high energy densities (King et al. 2014a). The keyhole is a rather deep and undesirable form of melt pool which will be discussed in more detail below.

The temperature distribution in a component manufactured by LPBF depends not only on the spatial location of a given area but also on the number of layers manufactured. When a part begins to be manufactured, a large amount of the heat generated by the laser source passes to the baseplate by conduction, which means that the temperatures reached do not reach very high values. However, when the manufacturing process has a considerable number of layers, the heat accumulates more in the area of incidence of the laser, and the temperature distribution along the part increases. This aspect makes it important to carefully consider the geometric design of the part to be manufactured and the changes in area of its cross-sections to avoid abrupt changes in the energy distribution that could generate geometric distortions or residual stresses. Additionally, the progressive increase in temperature of the part causes the microstructure to evolve along the manufacturing direction until it converges to a stable texture.

The configuration of the LPBF process for any given application is based on four laser parameters, see Figure II-8.
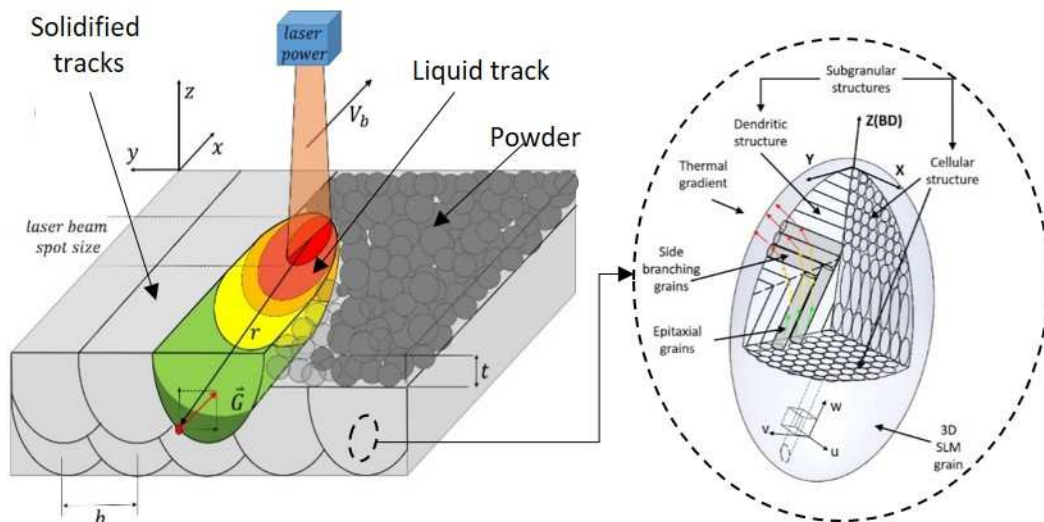
Figure II-8. LPBF parameters scheme (J D Pérez et al. 2021)

The laser power is determined by the power source, while the mechatronics of the laser head controls the laser speed and hatching space. On the other hand, the layer thickness is controlled by the mechatronics of the powder bed mechanism. The four parameters, in turn, define the amount of energy density, a macro-parameter of utmost importance for controlling product quality and microstructure (Dilip et al. 2017). See equation 5.

$$VED = \frac{P}{v_b * z * h} \quad (II.5)$$

Where VED is the volumetric energy density, P is the laser power, v_b is the laser speed, z is the layer thickness, and h is the hatching space.

II.3.4. Defects in the LPBF process

The large number of phenomena and physical parameters that are part of the LPBF process makes the development of defects a common occurrence (H Gong 2014; Di Wang et al. 2017; Cunningham et al. 2019; King et al. 2014a; Jinge Liu and Wen 2022; Karayagiz et al. 2018); however, many advances have been developed to control defectology and define optimal manufacturing conditions to minimize defects. These initiatives include real-time monitoring supported by statistics and machine learning (Q. Guo 2020; Cunningham et al. 2019; Leung et al. 2018). In addition, finite element modeling (Jean Willy et al. 2020; Olleak and Xi 2020) and analytical modeling (Coen, Goossens, and Hooreweder 2022; X. Ji, Wang, and Liang 2022) o experimentally based (Letenneur, Kreitcberg, and Brailovski 2019; Kuznetsov et al. 2022) have allowed predicting to some extent the boundaries of the process conditions necessary to reduce manufacturing defects. It is also important to note that eliminating defects in parts is a significant issue as defects such as pores, cracks etc. seriously affect the part's lifetime and reduce the range of possible applications of LPBF manufacturing (Yadollahi et al. 2018; X. Gao et al. 2022; Nafar Dastgerdi, Jaberi, and Remes 2022; Z. Wu et al. 2021).

Pores are the most common defects in additive manufacturing and must be eliminated or minimized due to their adverse effects on the material's mechanical properties (Carlton et al. 2016). porosity in AM parts originates from different mechanisms; one is related to the vaporization of the metal due to excess energy and poor control of the keyhole mode (King et al. 2014b). Pores can also be generated from gases trapped in the powder particles during the atomization process; however, this type of pore is much smaller in diameter than that caused by vaporization. Another way to generate porosity is from the entrapment of the shielding gas inside the molten pool.

Another widespread defect is the lack of fusion. This defect occurs when the molten pool of an upper layer does not penetrate sufficiently into the lower layers, resulting in areas filled with shielding gas. The lack of fusion zone is usually elongated and much larger than a pore, which makes it a much more critical defect. The poor penetration of the melt pool on the lower layers is usually associated with a poor selection of laser parameters that generate a low energy density or an inappropriate beam shaping mode that generates insufficient heat distribution in the central area of the melt pool (Kan et al. 2022; Shrestha and Chou 2022).

Figure II-9 shows optical micrographs of IN718 LPBF comparing the porosity defect and the lack of fusion defect in Figure II-9a a large number of pores caused by the keyhole mode can be seen. The pores are pretty spherical, which supports the idea that their origin is related to vaporized powder. In Figure II-9b, the lack of fusion defect can be seen; in this figure, the defects are horizontally elongated and larger than the pores generated by the keyhole. In Figure II-9c a sample with a high level of densification can be seen where only a few small pores are visible, perhaps caused by trapped gases in the powders during atomization.
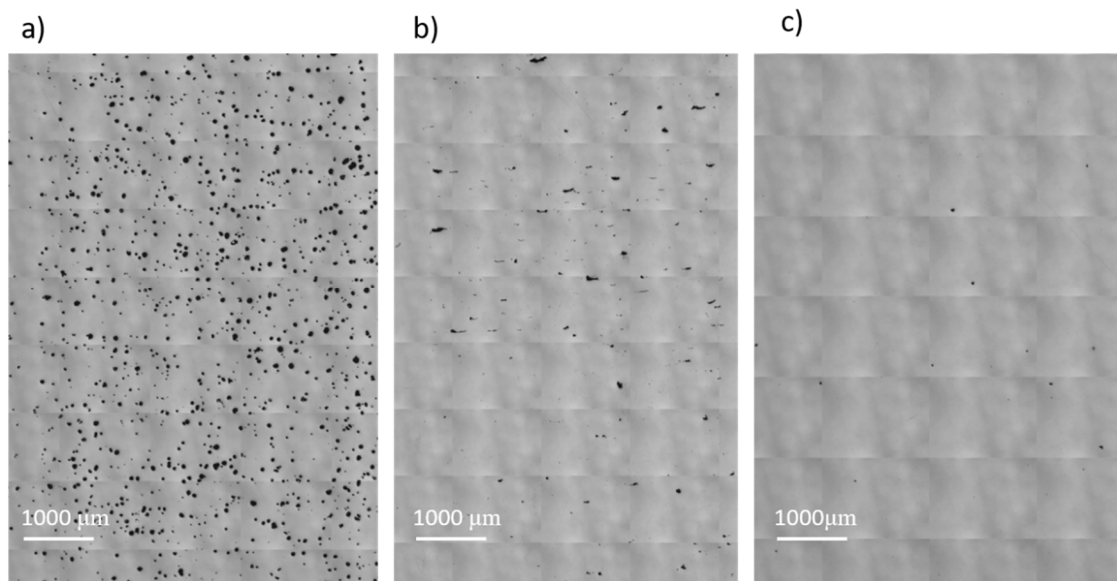
Figure II-9. common defects in LPBF IN718. a) Keyhole porosity, b) Lack of fusion porosity, c) Part with high densification.

Regarding the effect of defects on microstructure development, there are essential differences between pores and lack of fusion. In the case of pores, the microstructure surrounding the pore is usually not significantly affected by the presence of pores beyond the loss of mass continuity. It is shown in Figure II-10a, where a SEM micrograph of Inconel 718 LPBF shows that the dendrites surrounding the pore are practically the same, with only a slight dendrite refinement

of in the upper part of the pore. On the other hand, in Figure II-10b (IN718 LPBF), the lack of fusion has deeper implications on the microstructure. This can be seen in the fact that in the lower part of the lack of fusion, the columnar to equiaxial transition can be clearly observed, while in the upper part of the lack of fusion, the beginning of solidification from different nodes can be seen, giving rise to a high level of competitive growth of dendritic columnar grains.
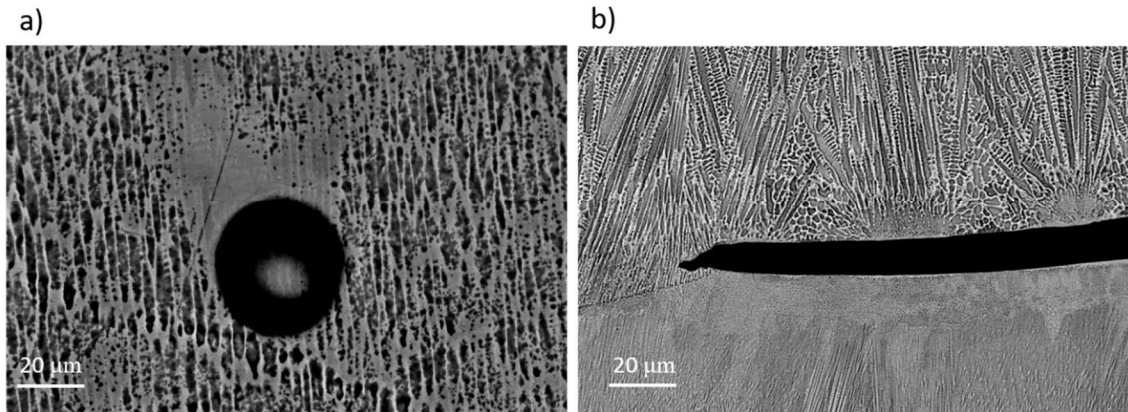
Figure II-10.SEM micrographs of defects and microstructure in IN718 LPBF. a) Effect of pores. b) Effect of lack of fusion.

Other defects in the AM process are associated with the stability of the process as it relates to the equilibrium that must exist between the solidification rate and the heat transfer rate. Process instabilities are often due to Kevin Helmholtz's hydrodynamic instability (Kan et al. 2022; Shrestha and Chou 2022) or plateau Raleigh capillary instability. In the first case, the solidification velocity is lower than the shielding gas velocity, which generates hydrodynamic instabilities on the surface of the molten metal. This effect is strongly related to the humping mode in which the melt pool starting zone is usually wider than later zones. In the case of plateau Raleigh capillary instability, high scanning speeds tend to form highly unstable narrow melt pools that separate into balls with uniform capillary pressure. This instability is strongly linked to the balling mode, which is detrimental to the quality of the parts obtained by LPBF.(Gusarov and Smurov 2010).

The development of cracks during additive manufacturing is another aspect to consider, as these cracks' impact on fatigue life is direct, and the safety implications for aeronautical components are critical. Because of that, the selection of optimized operating parameters for the material-geometry set is critical for controlling this type of defect. Figure II-11 shows this type of defect for some additive manufacturing applications.
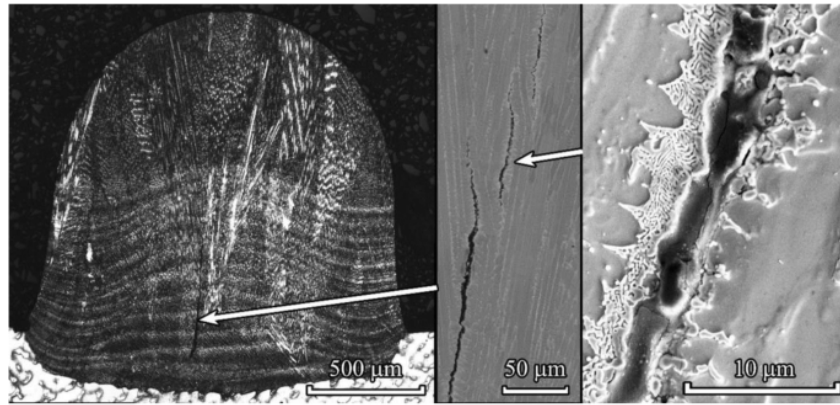
Figure II-11.Crack formation during the deposition step (Segerstark et al. 2018) (Jiménez et al. 2021b)

II.3.5. Residual stress and distortion

Residual stress is a phenomenon present in almost all metal manufacturing processes. The origin of this phenomenon for additive manufacturing is even more complex than for traditional processes such as welding or plastic deformation by rolling or forging. To understand how residual stress is developed in parts manufactured by LPBF, it is important to consider that the thermo-mechanical aspects such as plastic deformation, elastic deformation and thermal deformation, are insufficient to have a complete view of residual stresses. The anisotropy and columnar grain development must be considered to understand this phenomenon (Serrano-Munoz et al. 2021). That is why a more accurate view of the development of residual stresses must consider macroscopic aspects (thermo-mechanical coupling) and microscopic aspects (grains and crystals).

The macroscopic approach through analyzing thermo-mechanical deformations in metallic materials has been extensively studied for welding and other processes (J. C. Zhao and Westbrook 2003; Goldak and Akhlaghi 2005; Martukanitz et al. 2014), where fully coupled or sequentially coupled approaches usually solved by finite element packages are considered (Labudovic, Hu, and Kovacevic 2003; Smith et al. 2016; Lindgren 2001). In both cases, the residual stresses are firmly linked to the development of thermal deformations, which generate elastic and plastic deformations that go from compressive to tensile or vice versa depending on the heating or cooling stage. It is important to note that when a weld bead is applied, the molten zone reaches much higher temperatures than the base material, and the temperature gradient developed generates zones with a large thermal deformation that, in turn, generates plastic deformations by compression since the base material does not develop the same thermal

deformations. Then during the cooling stage, the decrease in thermal deformation generates an imbalance between the elastic and plastic deformation previously achieved, giving rise to the residual stresses.

Although the macroscopic approach has given good results in predicting residual stresses for processes such as welding, it is important to bear in mind that additive manufacturing has important differences with welding. This is mainly because in additive manufacturing (from several layers of filler layers), the material is applied on previously deposited beads and not on a base material all the time. Additionally, heat application in the LPBF process is selective, the fabricated walls do not represent large areas, and the area where the laser is applied is surrounded by powder. These aspects mean that the thermal deformations do not encounter the same level of resistance as they do in processes such as welding due to the limitation generated by the base material or substrate, as the area surrounding the molten zone reaches temperature levels that are not as far away from the molten zone as they are between the base material and the weld bead. This fact is not an aspect that should be considered as an absolute because some geometries manufactured by AM, some types of material, or abrupt changes in a section can develop zones with a wide temperature gradient, which can develop residual stresses that can be explained with the macroscopic approach.

The microscopic approach is indispensable for analyzing residual stresses in parts manufactured by LPBF as the microstructure and texture developed have different patterns from those developed by welding or other processes. One of the aspects that makes the most significant difference in the microstructure of LPBF parts compared to other processes is the laser scanning strategy. A deeper analysis of residual stresses is related to crystalline distortion analysis across the crystalline gradient. In this sense, many researchers have reported the effect of crystalline dispersion within the grains as evidence of plastic deformation and residual stress (Kamaya, Wilkinson, and Titchmarsh 2005). It is important to note that macroscopic analysis can predict, to some extent, the level of residual stresses. However, with microscopic analysis, it is possible to understand how grain formation and crystalline orientation interact with the level of residual stresses and their directional dependence. In this respect, Serrano-Muñoz et al (Serrano-Munoz et al. 2020a) have studied the effect of scanning strategies on the interaction between microstructure and residual stresses through ND techniques such as X-ray and advanced material analysis through SEM, EBSD, KAM, among others. Their findings show that the laser scanning strategy has profound effects on the distribution and level of residual stresses. In Figure II-12 The geometry of the sample analyzed, the laser scanning strategies used, and the microstructure of the samples can be seen. The IPF figures (Figure II-12e and Figure II-12f) show

a clear difference between the crystalline patterns of both samples, with a lamellar texture for the unidirectional strategy and a low texture for the rotational strategy (67°).
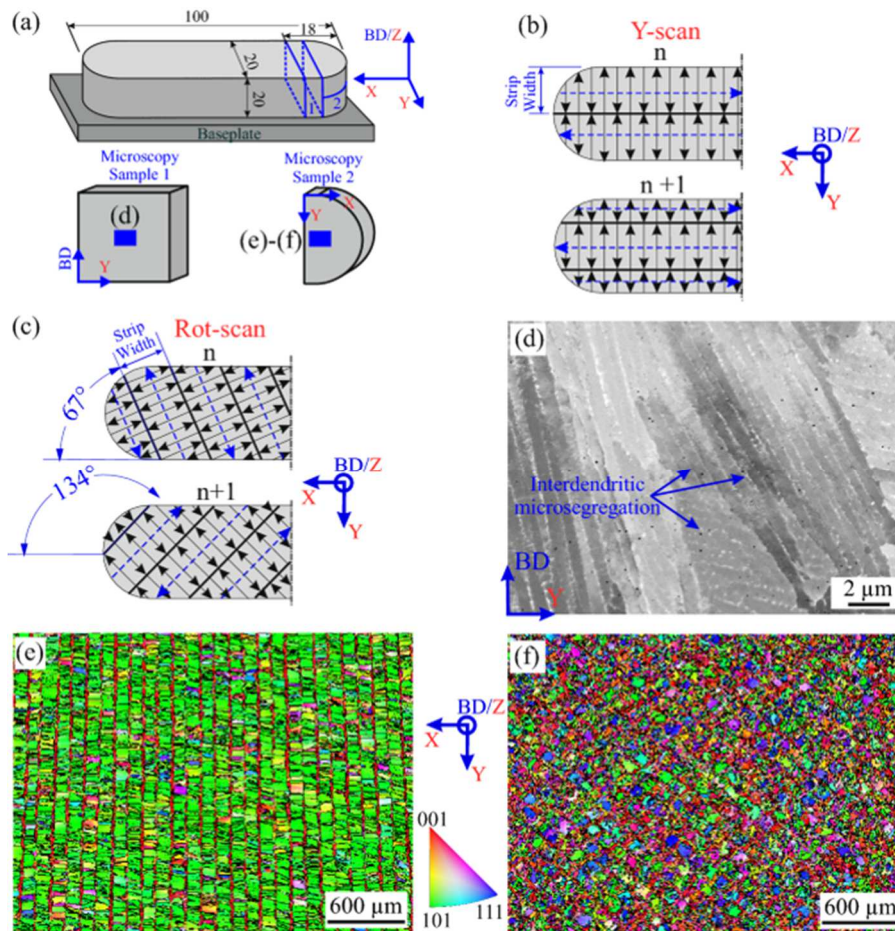
Figure II-12. IN718 samples for residual stress analysis with X-ray Energy Dispersive Diffraction (SXEDD). a) Sample geometry b) unidirectional laser scanning strategy. c) Rotational laser scanning strategy. d) SEM micrograph of AS-built dendritic cells. e) Unidirectional sample IPF figure f) Rotational sample IPF figure (Serrano-Munoz et al. 2020a)

Serrano-Muñoz et al. identified that the residual stresses in parts manufactured by LPBF of IN718 show significant differences depending on the orientation and laser scanning strategy. In this sense, they identified that the rotary scanning strategy (67°) generated lower stress levels in the X and Y axes, but higher in the Z axis compared to the unidirectional scanning strategy, see Figure II-13. The authors analyzed the KAM (kernel average misorientation) for the different strategies analyzed; however, they were not able to establish a clear explanation as to why the residual stresses in the direction of construction for the rotational strategy (67°) are higher than the residual stresses in the building direction of the other strategies. In addition, the authors were able to establish that columnar grains aligned with the direction of construction have a greater capacity to accumulate dislocations, which means that the prediction of residual stresses

for this type of material requires the analysis of the crystalline gradient in specific directions and the use of more advanced techniques for the evaluation of dislocations, crystalline distortion and grain boundaries in non-surface zones.
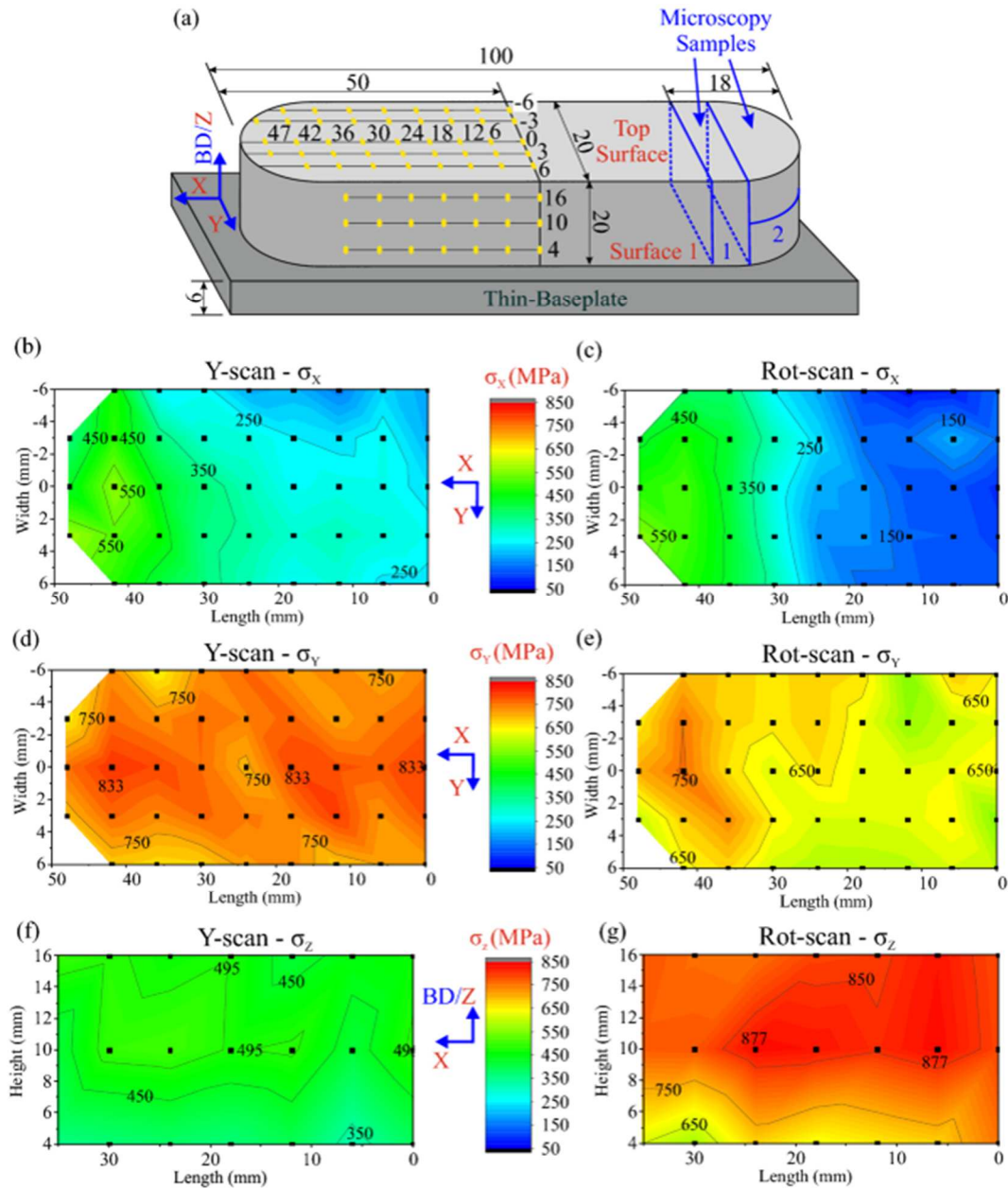
Figure II-13. Residual stress in X, Y, and Z axis with X-ray Energy Dispersive Diffraction (SXEDD). a) Sample geometry). b) X direction stress map for unidirectional sample. c)X direction stress map for rot sample. d) Y direction stress map for unidirectional sample. e) Y direction stress map for rot sample (Serrano-Munoz et al. 2020a)

II.4. Microstructure of LPBF components

The microstructure of LPBF parts often differs from the microstructure of parts obtained by traditional processes due to differences in melt pool size, rapid solidification, and the formation

of dendritic columnar structures, among others. The following sections expose the melt pool and dendrite growth characteristics of the LPBF process.

II.4.1. Melt pools

The laser scanning strategy has profound implications on how the melt pools of a layer interact with those of previously deposited layers so that each laser scanning strategy generates a pattern in the melt pools that has its characteristics. Figure II-14 shows the melt pools patterns of three strategies (rotation by 90º or R90, unidirectional or R0, and rotation by 67º or R67) in two different planes (XY, XZ) for IN718 manufactured with a RENISHAW AM400. The XY plane corresponds to the plane perpendicular to the direction of construction, and in the XZ plane, the vertical direction corresponds to the building direction.
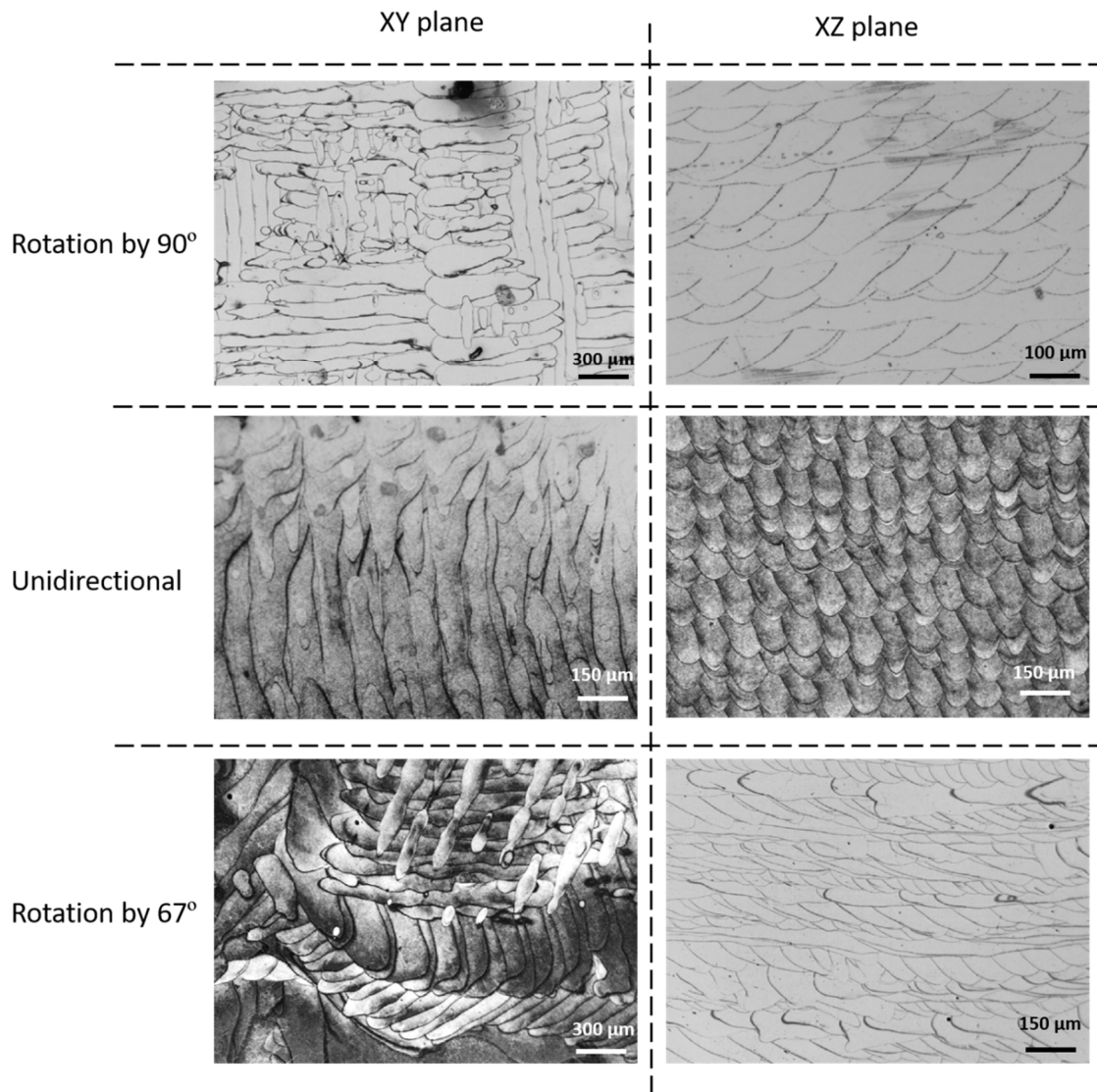
Figure II-14. Melt pool patterns by laser scanning strategy

The melt pools pattern for the R90 strategy is usually associated with a single crystal-like texture, while the unidirectional strategy usually develops two textures within a lamellar microstructure. On the other hand, the rotary strategy usually develops a ring crystalline-like texture.

There is currently much interest in relating melt pool morphology to the physical properties of LPBF materials. In this line (Großmann et al. 2019) developed dimensional analysis and energy balance to predict the size of the melt pools through numerous experiments with titanium Ti6Al4V, maraging Steel and aluminum, connecting the macroscopic dimensions of the melt pool with mesoscopic characteristics of the lattice structure. Other authors (Rahim Abadi et al. 2020; Matthews et al. 2020) have analyzed the influence of laser parameters and irradiance on the thermo-hydrodynamics in LPBF through three-dimensional characterization and novel process laser modifications to improve the properties and processability of LPBF materials, demonstrating a significant effect of melt pool ellipticity parameters on the development of the microstructure developed during solidification.

The shape of the melt pool is strongly linked to the energy distribution of the laser beam on the material (Manvatkar, De, and DebRoy 2014; Dilip et al. 2017; Matthews et al. 2020; K. H. Lee and Yun 2020). Gaussian sources usually generate melt pools with inverse Gaussian shapes; however, novel beam shape modes have developed large radius of curvature morphologies with non-Gaussian shapes with improved mechanical properties, reduced porosity, and increased process stability (Grigoriev et al. 2022; Tumkur et al. 2021).

One of the most critical aspects in the definition of the laser parameters of the LPBF process is the interaction of the shape of the melt pool with laser parameters such as hatching space and layer thickness. In this sense, it is important to differentiate that the laser parameters that influence the dimensions of the melt pool are mainly the power and speed of the laser beam, while the geometric parameters such as hatching space and layer thickness are more related to the microstructure pattern developed. At this point, it is essential to say that although laser power and speed influence the melt pool microstructure, it is the geometric parameters that define how the microstructures of the different melt pools fit together and therefore define the degree of competitive grain growth.

Figure II-15 shows the interaction between melt pools and the development of the subgranular microstructure for the steel. Figure II-15a and e show several melt pools stacked from a unidirectional strategy and a series of epitaxially growing dendrites identified by an arrow through several layers at the bottom of the melt pools. On the other hand, Figure II-15b, c, d, and g show how the dendrites grow in the direction of construction through side-branching.

Figure II-15e shows how the melt pool dendrites of a top layer grow from the dendrites formed in previous layers. These aspects will be discussed in more detail in chapter III.
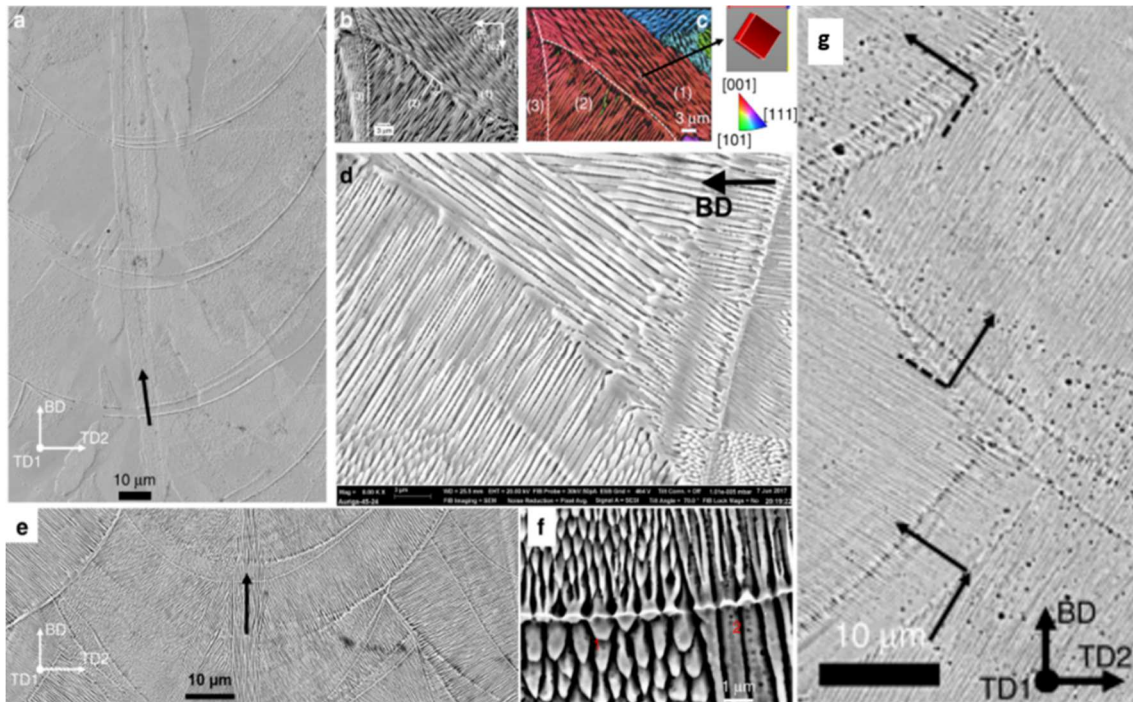
Figure II-15.Microstructure development due to side-branching in AM 316L. a, e) Epitaxial grain growth through several layers (highlighted by black arrows) along the centreline across melt pools. b–d) Side-branching at the sides of the melt pool. f) Dendrite growth from seed grains of previous melt pool g) zZig-zag side branching developed in bidirectional scanning strategy. (Pham et al. 2020b)

II.4.2. Dendrite and grain growth

Grain growth in additive manufacturing has unique and interesting characteristics. One of these characteristics is the dependence of the layer being added to the previously added layers, where the tip of dendrites from previous melt pools act as seed grain for the dendrites of the new melt pool, establishing the preferred crystallographic orientation (see Figure II-16). In this respect, it is essential to note that the rapid solidification makes the nucleation of new phases very difficult to develop due to the rapid development of epitaxial growth from the crystalline structure of the substrate (DuPont, Lippold, and Kiser 2011)**.**
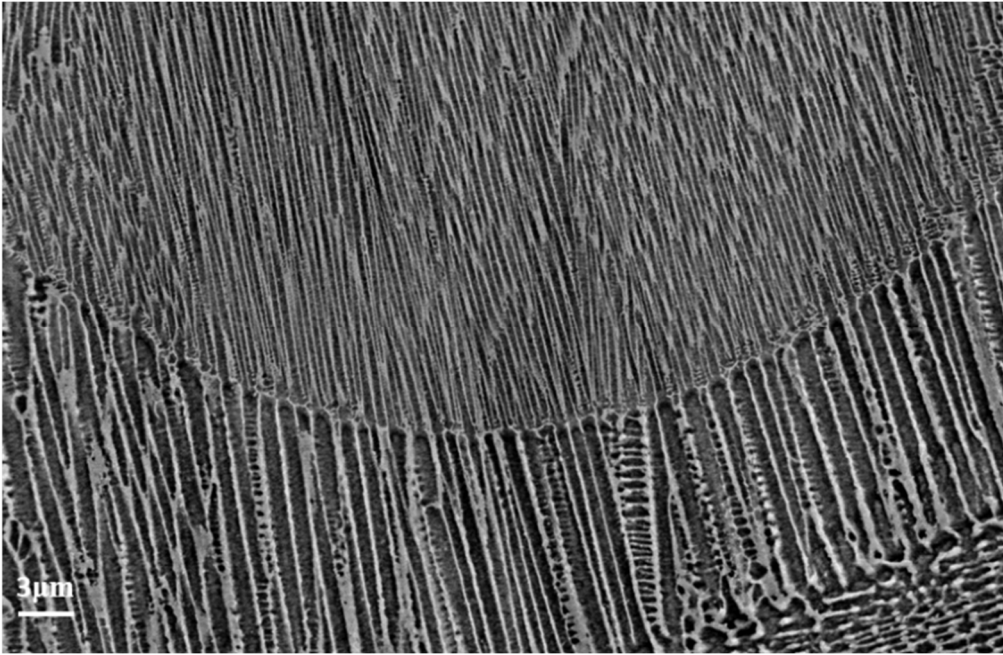
Figure II-16. Dendritic growth based on seed grain orientation from the previous melt pool IN718 LPBF

During the first deposited layers, the substrate greatly influences the microstructure of the LPBF part. This influence is noticeable in that the first layers are subject to a high grain growth competitiveness, mainly due to the isotropic and equiaxial nature of the substrate grains. The large number of crystalline orientations of the substrate causes many geometrically necessary dislocations to develop during solidification. This aspect causes a fraction of the grains in the transition zone to be equiaxial and others to be short columnar, giving rise to a slightly more intense texture than the substrate. On the other hand, the higher the number of layers, the dendritic growth reaches a balance between the thermal gradient orientation and the preferred crystallographic orientation of the seed grains (Rappaz and Gandin 1993; Z. Liu and Qi 2015b; 2015a), thus giving rise to more prominent grains and a more intense crystalline texture. These aspects can be observed in Figure II-17 where an IPF figure of the AM steel input on a steel substrate and the pole figures of each zone showing the texture's intensity level can be seen. In Figure II-17 three zones can be seen; the first zone corresponds to the substrate, which has a microstructure of equiaxial grains and a shallow level of texture intensity (1.2). The central zone corresponds to the transition zone; in this zone, the grains start out mainly equiaxial and gradually begin the transition to columnar. In this zone, the texture increases in intensity, reaching a maximum of 2.5, a third zone corresponds to the zone where the grains are already developed; in this zone, the grains increase in length and width, and the texture increases its maximum intensity to 3.
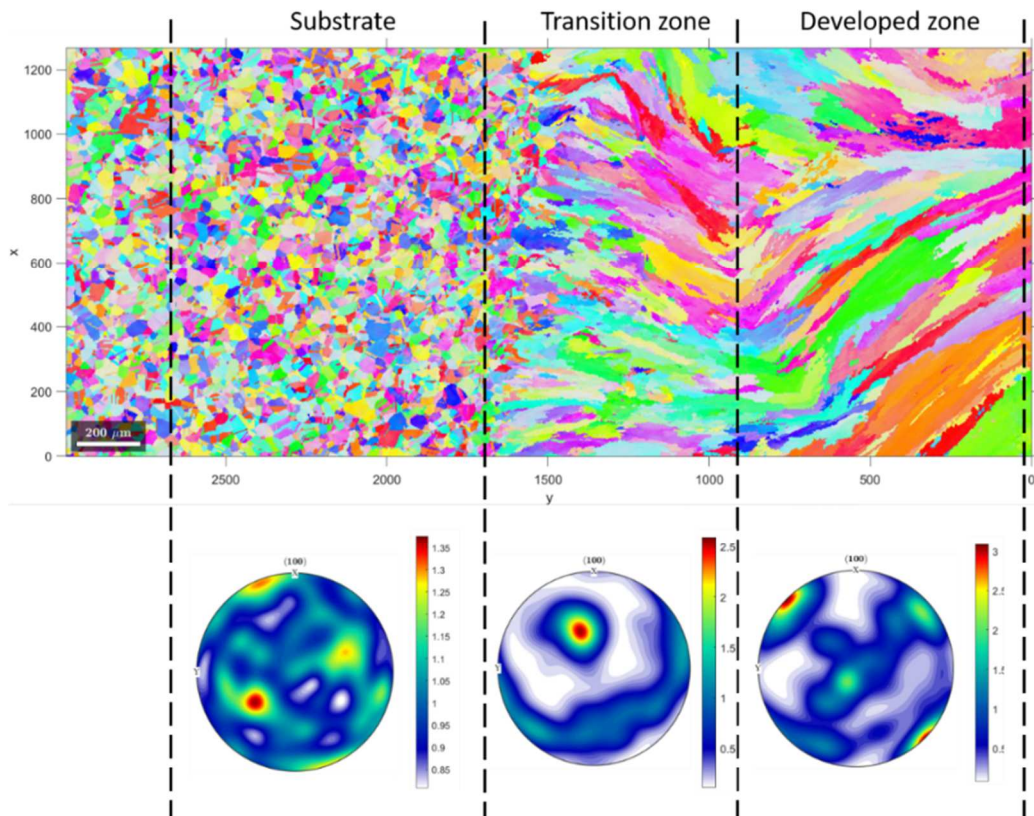
Figure II-17. Texture and grain growth evolution during the metal addition process

II.5. Hybrid manufacturing and postprocessing operations for AM metallic functional parts

The rapid adoption of AM metal components in multiple industrial applications has led to their post-processing being developed in conjunction with the need to ensure that the parts manufactured by AM meet the required surface quality and structural integrity targets. The need for assembly between functional parts means their dimensional tolerances are tight. In addition, surface roughness is one of the most critical aspects that decrease fatigue strength, making post-processing a necessary stage in planning LPBF part manufacture.

Some shortcomings of the LPBF process are related to the high cost of equipment and powder, low production rates compared with other technologies, variability in powder morphology, safety issues, etc. those aspects make it difficult to develop the LPBF for high production levels. Based on the above, there are many attempts to include hybrid operations in the chain process (see Figure II-18).
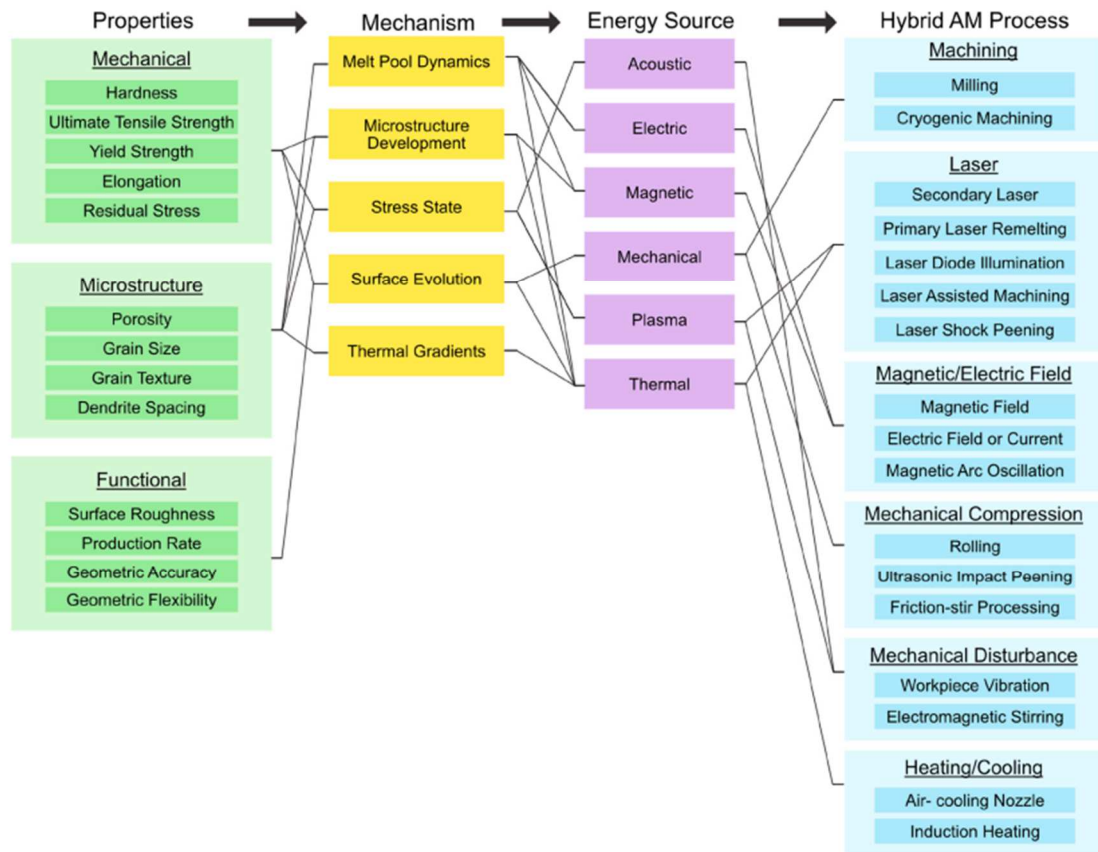
Figure II-18. Property – mechanism – energy source – hybrid-AM process (PMEH) framework for hybrid-AM classified by mechanism and energy source utilization. (Webster et al. 2021)

It is well known that the productivity of LPBF technology is much lower than the productivity of CNC subtractive technologies; therefore, the synergistic union of both technologies under hybridization strategies is generating much interest among researchers and the machine tool industry for the development of multi-axis equipment capable of achieving complex geometries, surface quality, and higher productivity. Machining such as milling or turning, heat treatments, shot peening, laser shot peening, and laser polishing are some post-processing operations being integrated into the new hybrid manufacturing technologies.

Hybrid manufacturing solutions have attracted the attention of many machine tool manufacturers in the last decade by developing modular hybrid solutions that, in some cases, can be integrated into existing subtractive or additive machines (Jiménez et al. 2021b). The CNC nature of additive and subtractive manufacturing equipment means that the two technologies are not mutually exclusive but complementary, which eases the production of parts with complex shapes, hollow areas, or thin walls with good surface finish. Additionally, hybrid manufacturing makes it possible to produce parts that cannot be produced alone by additive or

subtractive manufacturing. The combination of both technologies and their advantages can be seen in Figure II-19. It is clear that the synergic union of both technologies allows a broader field of action to be covered and functional parts to be manufactured that were previously impossible to manufacture, even by hand. The combination of both technologies allows for great flexibility in design and manufacturing, a reduction in material waste, less environmental impact, and in some cases, improvements in production times (Jiménez et al. 2021b).
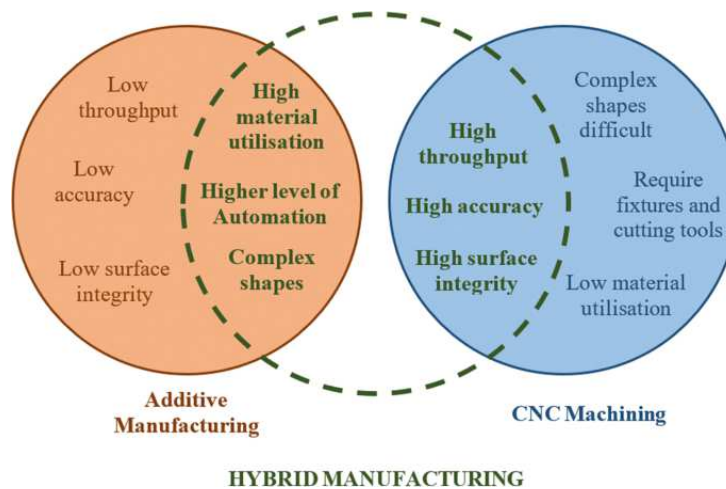
Figure II-19. Hybrid manufacturing scheme (Jiménez et al. 2021a)

It is noteworthy that, even when machining operations often improve the surface quality of LPBF parts, they cannot remove internal part defects, like porosity, structural variability, and residual stresses. Because of this, heat treatment and other operations, such as shot peening, are used as post-processing operations for many applications nowadays.

The early attempts to explore the development of strategies for hybridization are associated with component repair operations using additive techniques like LMD or welding and subsequent machining. In this regard (Liou et al. 2007) analyzed the feasibility of a hybrid production line process with an initial multi-axial LMD additive stage and a subsequent planning stage. The authors significantly reduced the dead time between the additive and subtractive stages due to the ease of incorporating both processes on a 5-axis machine. Another report (Karunakaran et al. 2010) presented a hybrid manufacturing process to obtain near-net shape parts from AM components named ArcHLM; the methodology is observed to be safe, feasible, and easy operation to produce complex parts from laser weld deposited components. Other non-conventional processes as EDM and ECM, have been used to reduce the roughness of AM parts. In this line (Hassanin et al. 2016) used EDM (Electro-Discharge Machining) as a strategy to reduce roughness on LPBF Ti6Al4V, however they reported that this process has productivity

constraints in terms of machining materials with low electrical conductivity, intricate surfaces and low material removal rates.

Many efforts have been made in the development of commercial equipment for the development of hybrid machines; in this line (Yamazaki 2016) developed for Mazak® a multi-tasking machine for the manufacture of small batches of complex geometry parts, for this purpose, the machine has an LMD additive manufacturing stage with complementary turning and milling functions. Mazak reported that the application of the hybridization strategy on the machine enabled significant advantages in quality, manufacturing time, and flexibility in achieving parts of high geometric complexity over conventional manufacturing strategies. Later (Foster et al. 2019) reported the development of a hybrid manufacturing methodology for remanufacturing tools and dies. For this purpose, the LMD process was used for material input on worn parts, machining for final sizing, and hot forging. For coating, they observed superior results using stellite 21 compared to the standard H13.

For the LPBF process, many advances in hybridization techniques and methodologies have recently been reported. In this line (Du, Bai, and Zhang 2016) developed a method for the hybrid manufacture of metal parts from LPBF and machining for the manufacture of steel moulds. Another report (Penchev et al. 2019) developed algorithms to analyze and simulate the feasibility of hybrid manufacturing of LPBF as a primary process and different post-processing stages. Simulation of different manufacturing scenarios established that implementing modular workpiece holding systems can enable additive manufacturing to be viable not only for small batches but also for medium and even large batches. In recent work (Mehmeti et al. 2020) developed a hybrid MIM/PBF mould manufacturing route where in the first stage, a metal preform is obtained by MIM (Metal Injection Moulding), on which the final shape is obtained by LPBF, which increases the manufacturing volume of these parts. The results of the mechanical tests showed that the mechanical properties of the parts obtained by the MIM/PBF route are similar and even better than those obtained only by MIM.

AM and subtractive machining chain has been intensely studied too. In this line (Ramoni et al. 2021) evaluated the capability of hybrid fabrication on LPBF Al-Si10-Mg alloy with MQL obtaining appropriate machinability levels (Teich, Maucher, and Möhring 2021) and reducing the hole-making time by including pre-built bores in the design of the LPBF manufactured part; in this way, drilling was eliminated from the process chain, and final hole sizing was achieved by reaming only. A similar work (J D Pérez et al. 2021) eliminated the drilling step for deep hole machining in IN718 LPBF by obtaining the holes by LPBF and finishing by reaming. Additionally

(Furumoto et al. 2021) developed a novel hybrid manufacturing process in which the LPBF and machining stages alternate. To this end, the authors succeeded in minimizing the geometric distortions caused during the material input stage by obtaining the optimum energy density and layer thickness conditions. For the correction of the remaining distortion and roughness, they used a two-step machining strategy.

Other hybrid manufacturing applications include improving prosthetics and other parts using concurrent design methodologies. In this sense (Ferchow et al. 2022) proposed a novel method for the use of sheet metal clamping within LPBF fabrication to facilitate milling operations in hard-to-reach areas for dental prostheses. The method showed that additional supports could be easily removed without generating clamping forces to the LPBF part facilitating the automation of the process chain. Additionally (de Oliveira and Del Conte 2021) carried out a concurrent design for the manufacture of maraging Steel parts in a 3-step process: LPBF-Heat treatment-Milling obtaining significant improvements in the reduction of roughness and residual stresses. Recent work (Mishra et al. 2022) analyzed the effectiveness of using internal lattice structures in milling hollow cylindrical geometries for weight reduction without sacrificing component stiffness. The results showed that the internal lattice structures could provide sufficient stiffness to the cylindrical structure without damage during machining, which is an example that concurrent structural design prior to the LPBF process is a good complement to hybrid manufacturing.

In this chapter, the literature related to post-processing operations by machining is covered with more emphasis, and, to a lesser extent, other technologies are also exposed.

II.5.1. Grinding and non-conventional finishing process

There are currently many techniques used for the post-processing of materials obtained by additive manufacturing apart from machining. One of these is grinding, which is widely documented in the literature for many materials; however, the use of this technique on additive materials is relatively recent. In this respect (Kirsch et al. 2021) evaluated the grindability of two AM AISI316L samples and compared them with conventional AISI316L and found that the operating parameters had to be significantly adjusted for the additive manufactured samples. Another work (Kadivar et al. 2021) analyzed the effect of workpiece orientation (LPBF TI6AL4V) on specific energy and found a 20% increase when machining in the plane perpendicularly to the building direction compared to the direction parallel to the building direction for less

aggressive rotational speeds. Surface quality was also superior for higher wheel rotation speeds, (see Figure II-20).
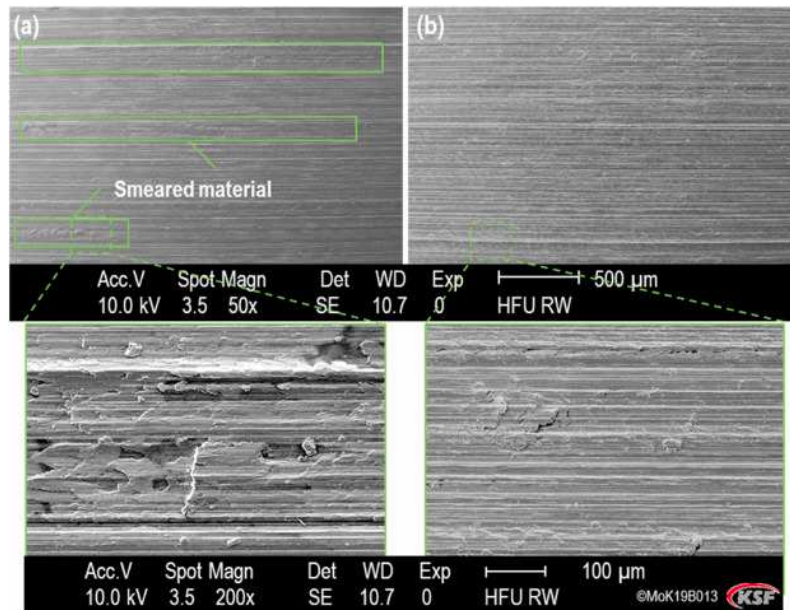
Figure II-20.SEM images of the ground surface obtained by grinding. a) *vw/ae* **= 5 × 104 mm/mm.min b)** *vw/ae* **= 11 × 104mm/min.min** (Kadivar et al. 2021)

Novel processes such as shape adaptive grinding (SAG) have been employed in reducing the surface roughness of additive manufacturing components due to the advantages of this technology in machining flexible or intricate geometry parts (Beaucamp, Namba, and Charlton 2015). This technology has been successfully used in the machining of EBM titanium alloys with geometrical transitions from convex to concave shapes with success (Jing et al. 2015).

One of the most differentiating aspects of LPBF technology compared to other methods is the ease of fabricating holes and internal cavities. In some cases, these cavities require special surface finishing. For this purpose, special techniques such as magnetic abrasive finishing (MAF) have been successfully used in the finishing of hollow tubes for LPBF IN718 (J. Guo et al. 2019). Another paper (P. Y. Wu and Yamaguchi 2018) implemented the use of large and small magnetic particles with the MAF technique to simultaneously remove different types of targets, successfully removing material from peaks and valleys with lower kurtosis than conventional abrasive methods. This technique has also been successfully applied to finishing LPBF 316L stainless steel, gradually removing defects from the additive process and reducing roughness by up to 75% (J. Zhang, Chaudhari, and Wang 2019). Other techniques implemented to finish cavities and holes in LPBF parts are ultrasonic cavitation abrasive finishing (UCAF) patented by Rolls-Royce and successfully implemented in internal channels of LPBF ALSi10mg (Nagalingam,

Yuvaraj, and Yeo 2020) and divergent fuel spray nozzles (LPBF IN625)(amirmahyar khorasani 2018), see Figure II-21.
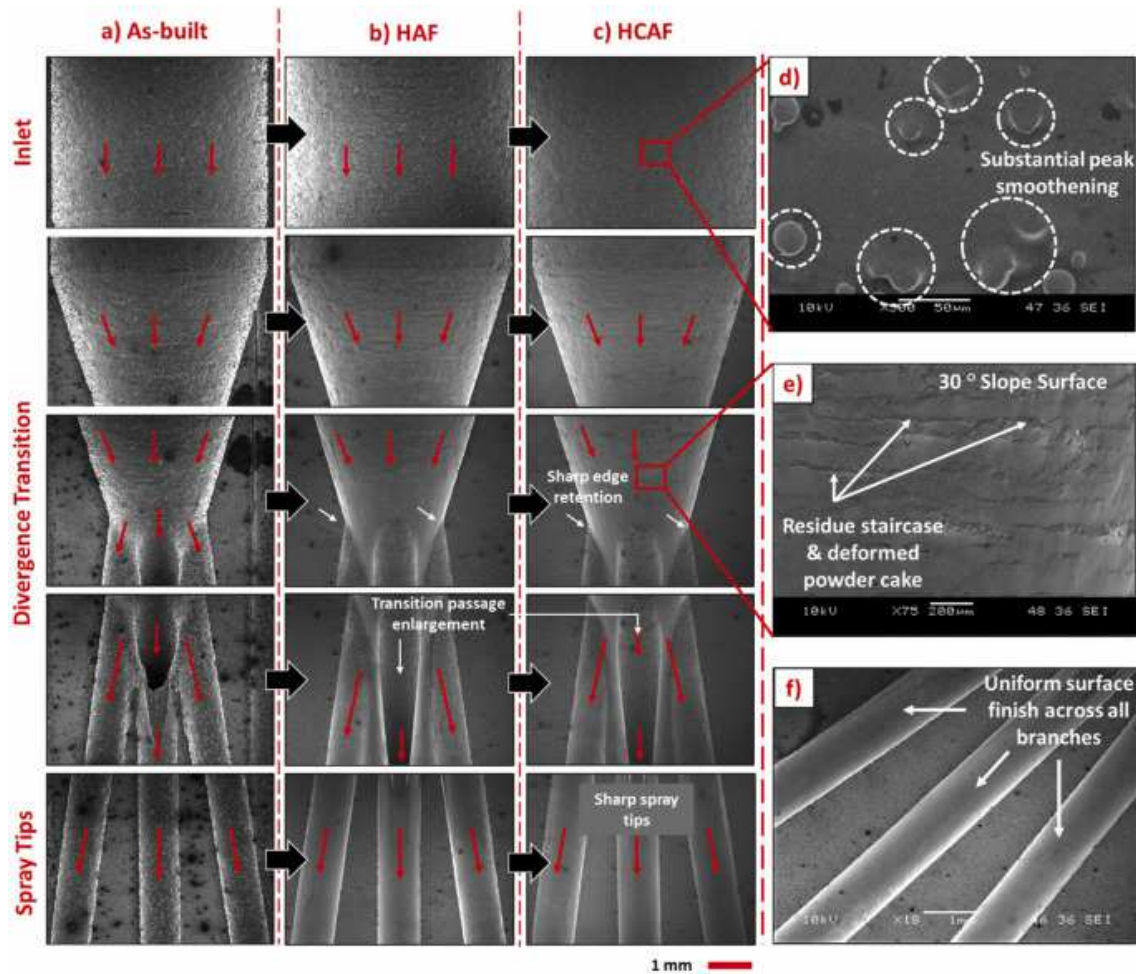
Figure II-21.The surface of the internal passage of the fuel nozzle improved by CAF (LPBF IN625)(amirmahyar khorasani 2018)

Other processes, such as electrochemical machining (ECM), allow the removal of material without contact with the part and without affecting the microstructural integrity of the parts through the mechanism of anodic electrochemical dissolution. This technique has been successfully used on LPBF 316L stainless steel (C. Zhao, Qu, and Tang 2021) and on Ti6AL4V (Hansal,W,Hansal,S.,Mann 2019) among others.

II.5.2. Machining of AM metallic alloys(not nickel alloys)

It is well known that additive manufacturing applications include the use of many metals; however, in this section, particular emphasis will be placed on work related to nickel alloys and other materials such as titanium and steel.

Titanium

One of the sectors where additive manufacturing has created a solid and developed niche is the biomedical implant manufacturing industry. For biomedical implants, the TI64ALV alloy has received particular attention concerning evaluating machinability, reducing tool wear, and improving the surface quality and structural integrity of implants and other parts of this material.

Much research has been developed to compare the Machinability of DED(directed energy deposition, LMD, and WAAM titanium parts with conventional titanium. This line (Bonaiti et al. 2017) evaluated the microstructure, hardness, porosity, and machinability of DED Ti6Al4V under three configurations of laser and standard Ti6Al4V parameters, reporting higher hardness in the AM titanium samples compared to the conventional alloy. On the other hand, standard titanium showed higher levels of roughness. Comparing the three samples manufactured by DED showed a decrease in porosity for the sample manufactured with higher laser power. In parallel (Shunmugavel et al. 2017) compared the machinability and mechanical properties of Ti6Al4V obtained by traditional methods and by additive manufacturing, finding higher levels of hardness, shear strength, and mechanical strength in LPBF Ti6Al4V and lower roughness and ductility. The authors considered this behavior related to the porosity and brittle nature of LPBF parts. Other research (Oyelola et al. 2018) observed that directed energy deposition (DED) Ti6Al4V exhibited high variability in surface quality after machining compared to wrought Ti6Al4V, which they attributed to the microstructural variability inherent to the DED process. DED Ti6Al4V samples were structurally homogenized by heat treatment to measure the effect of microstructure on the machinability of this material, and it was found that the heat-treated samples showed a 22% increase in compressive residual stresses and a 40% decrease in cutting forces. The authors attributed this difference to the grain coarsening generated by the heat treatment, which influences the decrease in grain boundary density. In another report (Woo et al. 2020) combined the fabrication of Ti6Al4V by directed energy deposition (DED) with post-processing by laser-assisted machining (LAM). The surface quality and cutting forces were compared with samples machined without preheating, and a significant reduction in cutting forces and roughness was found for the samples machined with laser preheating, and the tensile strength increased by 20% compared to samples machined by traditional means without preheating. Related to WAAM (Veiga et al. 2020) studied the feasibility of manufacturing Ti6Al4V parts from PAW-WAAM and milling, finding that the final quality of the parts is comparable to that obtained by traditional processes but that the mechanical properties of the parts obtained by PAW-WAAM were superior to those of traditional Ti6Al4V. Regarding the machining of this

material, the authors reported that the surface quality was similar in cutting forces for up-milling and down-milling, but the surface quality was superior for up-milling.

In the same way (Stefano Sartori et al. 2016) compared the turning of DMLS Ti6Al4V parts under dry cutting and cryogenic cooling, showing that although cryogenic cooling machining produced fewer surface defects and higher compressive residual stresses, the surface topography quality was worse than for dry cutting. Concerning the type of material, the authors report that DMLS Ti6Al4V presented better surface quality levels in relation to the increase of compressive residual stresses in the case of machining with cryogenic cooling. Another study (S. Sartori et al. 2017) studied tool wear during the turning of wrought Ti6Al4V, (DMLS) Ti6Al4V, and electron beam melting(EBM) Ti6Al4V under different cooling conditions. Their results showed that DMLS Ti6Al4V generated the highest tool wear through the cratering phenomenon due to the higher hardness and low thermal conductivity of this material compared to wrought or EBM Ti6Al4V. Of the materials analyzed, EBM Ti6Al4V showed the best machinability, and in all cases, the use of cryogenic cooling with Liquid Nitrogen (LN2) technology reduced the wear on the cutting edge and flank of the tools.

The effects of material anisotropy of titanium alloys on tool wear and cutting forces have been widely reported too. The work of (de Oliveira Campos et al. 2020) compares the machinability of micromachining Ti6Al4V LPBF for biocompatible applications, such as implants, with the traditional alloy. Their analysis showed an increase in the mechanical strength of the parts manufactured by LPBF; Additionally, the cutting forces were lower, with less burr formation and, therefore, better machinability. In the same line (Hojati et al. 2020) compared the micromachining of EBM Ti6Al4V with extruded Ti6Al4V and found that the cutting forces were 15% lower for EBM parts for chip thicknesses below 8 microns. Roughness was also lower for EBM Ti6Al4V. A deeper study (Lizzul et al. 2020) evaluated the effect of anisotropy induced in Ti6Al4V LPBF on wear on endmill tools. To this end, they performed measurements on parts in different orientations, measuring wear and chip morphology, reporting a 40% increase in tool wear when machining parts manufactured horizontally to those manufactured vertically, considering that the increase in wear was due to the interaction of the cutting angle of the tool with the angle of the melt pool boundaries. More recent work (Lizzul et al. 2021) analyzed the effect of TI6AL4V anisotropy on surface topography, surface defects, and machinability, determining a strong influence of tool edge orientation on the beta grain boundary density. In addition, the authors observed that parts manufactured horizontally showed better machinability compared to other orientations.

Additionally (Al-Rubaie et al. 2020) performed milling tests on Ti6Al4V LPBF and conventional Ti6Al4V. For the Ti6Al4V LPBF samples, they performed tests on As-built and stress-relief heat-treated samples. The test results showed that the lowest residual stresses were found in the conventional specimen, while the As-built specimen exhibited tensile residual stress, and the stress-relieved LPBF specimen exhibited high compressive residual stresses. Similarly, the lowest cutting force levels were found when machining the conventional alloy, and the highest was found when machining the LPBF sample with stress relief.

The machinability of EBM Titanium parts has been reported in several studies. In this sense (Bordin et al. 2014) reported a low machinability for EBM Ti6Al4V compared to wrought Ti6Al4V, which is contrary to the reported by (S. Sartori et al. 2017), who reported that tool wear was lower when machining EBM Ti6Al4V. The differences in the two studies may be related to using tools with different geometry, an indicator of microstructure's effect on machining post-processing. In another study (Bordin et al. 2017) conducted numerous tests to determine the suitability of cryogenic cooling processes in the machining of Ti6Al4V EBM, reporting that LN2 does not affect the quality of the machined surfaces even under the most severe cutting parameters, resulting in clean surfaces, low adhesion of the base material on the tool and higher chip breakability. On the other hand, dry and emulsion machining generated severe cratering on the tools. (Mallipeddi et al. 2020) studied the surface integrity of EBM Ti6Al4V after machining by turning and reported that contour setting significantly influences surface roughness. Additionally, they evaluated the surface quality of turned parts that received HIP; however, no significant differences were observed in the machinability of EBM Ti6Al4V as-built vs. HIPPed.

Another report (Milton et al. 2016) studied the structural integrity of Ti6Al4V LPBF after machining considering several manufacturing directions, cutting forces, roughness, and hardness, among others, and comparing the results with the same material obtained by hot rolling. This analysis showed that the samples obtained by LPBF presented higher work hardening behavior compared to conventional alloy and an increase of 22% of the cutting force in the axial direction compared to conventional alloy. In the same line (Milton et al. 2019) developed a hybrid approach to determine the heat flux and study the effect of temperature on the quality of the finish by milling Ti6Al4V EBM parts compared to conventional Ti6Al4V, finding that the heat flux generated when milling Ti6Al4V EBM parts is double that developed during the milling of the conventional alloy, attributing this difference to the difference in microstructure between the two samples. These results are supported by the fact that the tools used to machine Ti6Al4V EBM showed a tool life of 50% compared to those used to machine the

conventional alloy. The authors also reported a dependence of the frictional behavior on the adhesion mechanisms of the base material on the tool, which makes the selection of cutting parameters and cooling techniques critical for this type of material (Milton et al. 2021) performed an in-depth comparative analysis of the face milling machinability of Ti6Al4V obtained by LPBF and EBM, considering the effect of part manufacturing orientation and HIP treatment on the magnitude of the cutting forces and the interaction of these with the microstructure. The results of this study show a strong influence of the microstructure on the shear forces. For the parts manufactured by LPBF, little influence of the part manufacturing orientation on the cutting forces was observed. On the other hand, the parts obtained by EBM showed higher cutting forces when machining the face plane sample than cross-plane samples.

Steel

Steel alloys are a group of materials with significant industrial interest. The automotive and oil & gas industries invest significant resources in developing printed steel alloys for multiple applications. In this way (Alexeev, Balyakin, and Khaimovich 2017) developed experimental studies on the machinability of 316L LPBF concerning measurements of cutting forces, residual stresses, and hardness mainly. Their analysis evaluated the side milling of parts manufactured in a vertical and horizontal orientation and reported a 10% increase in cutting forces when machining parts in a horizontal orientation. Additionally, they reported an increase in residual stresses of parts manufactured in horizontal orientation relative to those manufactured in the vertical direction of 400 MPa vs. 750 MPa. They considered that melt pool boundaries act as effective barriers to dislocation flow. The surface quality, microstructure, and microhardness of 316L stainless steel LPBF parts after finish machining, vibratory surface finishing, and drag finishing post-processing operations were also evaluated by (Kaynak and Kitay 2019). They considered that finish machining operations are not recommended given the complex geometries of LPBF parts, so they recommended post-processing by drag-finishing and vibratory surface finishing. In other work (Y. Gong and Li 2019) studied the wear performance of milling cutters when machining LAM 316L stainless steel under different experimental conditions using the wear width of the blade as an indicator, reporting that the height of the manufactured parts has a strong relationship with the level of heat dissipation and the level of tool wear.

II.5.3. Machining of nickel alloys

This section presents the state of art in the machining of conventional and additively manufactured nickel alloys.

Machining of conventional nickel alloys

The global market for aeronautical products and aircraft engines(see Figure II-22 has been estimated at more than 80 billion by 2021. It is important to note that nickel alloys, including IN718, account for more than 50% of the volume or weight of aircraft engines. In addition, it is noteworthy that IN718 is the most widely used nickel superalloy on the market, accounting for 60% of the total volume of nickel superalloys, and its market is equivalent to some 4 billion dollars.
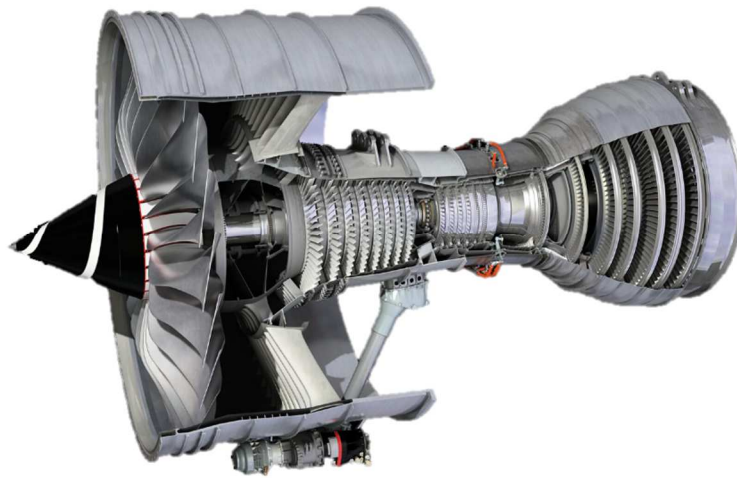
Figure II-22. Rolls Royce TRENT 1000 engine (Rolls-Royce 2022)

Inconel 718 obtained by traditional methods (casting, forging) usually receives precipitation-hardening heat treatments. The microstructural characteristics of this material and its physical properties allow it to withstand high working temperatures without suffering damage to its structural integrity due to thermal or mechanical fatigue. Some metallic elements that facilitate its strength are chromium, niobium, molybdenum, iron, titanium, etc. IN718 is an alloy with a nickel matrix (more than 50% of the alloy volume). This nickel matrix is usually referred to as γ. This matrix has an FCC-type crystalline structure (Jambor et al. 2017) which is key to the physical properties of this material in terms of elasticity and plasticity, as will be discussed further below.

One of the essential aspects in the microstructure of IN718 are the strengthening phases, such as the γ' and γ'' (see Figure II-23) which have FCC and BCT structures, respectively. phase γ'' which is composed of Ni3Nb, is a reinforcing phase that differentiates Inconel from other nickel alloys (Hong, Chen, and Wang 2001). Some authors like (R. Y. Zhang et al. 2020) even report that

the size differences between the crystalline cell of the phase γ'' with regard to the phase γ' is one of the reasons for the development of strain hardening in the IN718. This is considering that the phase γ'' is tetragonal and not cubic like the phase γ' and the matrix γ.

Another important aspect of IN718 is the compounds dissolved in the matrix and in the phases. These compounds or particles are usually NbC and TiC, which significantly increase this alloy's hardness and restrict plastic dislocations. A critical aspect of these particles is that they have different mechanical properties from each other (De Bartolomeis et al. 2021). An example of this is that TiC particles are more resistant to fracture than NbC particles. This significantly affects the shear strength of IN718, especially at low feeds and shear rates. This mechanical behavior is because NbC is more brittle and has lower mechanical strength than TiC, which makes TiC particles have more weight on the abrasive characteristics of IN718 (J. Zhou et al. 2011).
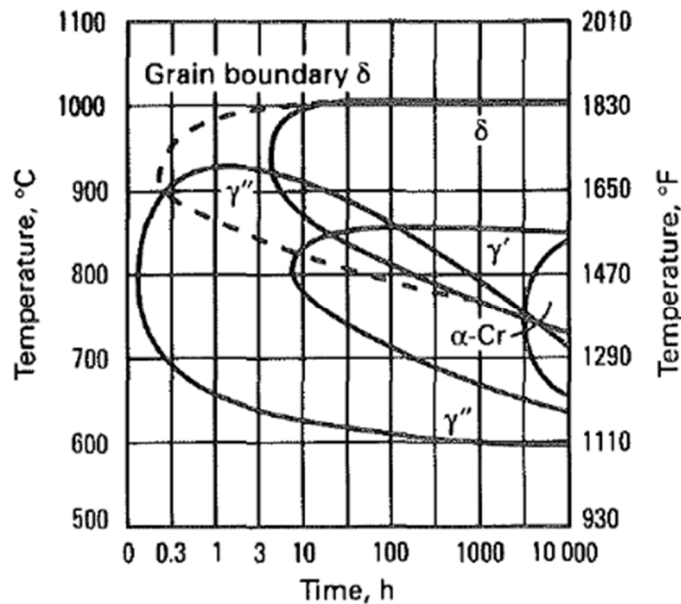
Figure II-23. TTT Phase diagram of IN718 (Jambor et al. 2017)

One of the most challenging aspects of machining any material is the development of high cutting forces and temperatures, and IN718 does not escape this difficulty. The low thermal conductivity of IN718 is another characteristic that makes this material complex to cut. This sum of effects makes finding the balance between productivity and surface quality a challenge for the machining of this superalloy. To overcome these challenges, many advances have been made in developing special cutting tool materials and geometries that facilitate the removal of chips and heat generated during cutting. However, the information available in some cases is limited for some geometries, and the uncertainty of the suitability of specific geometries and

materials for some process parameter ranges is often a significant drawback (Liang, Liu, and Wang 2019). In this sense, many studies have been carried out to identify common aspects in the machining of IN718 that allow the establishment of minimum conditions for predicting the process variables. In this line (Agmell et al. 2020) estimated the level of mechanical stresses developed during machining from finite element and experimental verification of the interaction between the cutting tool and the material interface, finding that peaks of 450 MPa and cutting temperatures above 1100º are possible. To counteract these effects, measures are usually conservative and are related to reducing cutting speeds and tool feed, which affects productivity (de Bartolomeis et al. 2021).

The machinability of nickel alloys is usually associated with the material's physical properties in terms of ductility, hardness, thermal conductivity, and abrasiveness, among others (Andersson and Ståhl 2007). The machinability of metals is a problematic aspect to quantify; however, most researchers, machinists, and technicians agree that at least four factors can be considered relevant in quantifying machinability: tool wear, cutting force, surface finish, and metal removal rate (Ståhl 2012). The machinability of alloys has been extensively analyzed for various materials concerning tool wear. In this respect, several works have been carried out for nickel alloys (Avdovic et al. 2010; Olovsjö et al. 2011), Steel (Xu et al. 2013), and other materials (Johansson et al. 2019) for industrial applications. Inconel 718 is recognized as a hard-to-cut alloy due to the short life of cutting tools and low productivity of machining operations, which has led to many studies being carried out to quantify the machinability of this material. In this sense, many analyzes with an experimental approach have been carried out to measure the machinability of IN718 in turning processes, considering different ranges of machining parameters (D. G. Thakur, Ramamoorthy, and Vijayaraghavan 2009b; Choudhury and El-Baradie 1999; D. G. Thakur, Ramamoorthy, and Vijayaraghavan 2009a; Rahman, Seah, and Teo 1997; Xavior et al. 2016). Also for cutting temperatures (Mahesh et al. 2021), tool geometries, and chemical agents (Yin et al. 2020), among others.

The thermal conductivity of nickel alloys during the cutting process is one of the most studied aspects that impact the quality of machining. The low thermal conductivity of IN718 makes this aspect critical for the correct production of components (see Figure II-24). Many methodologies, strategies, and practical recommendations have been developed for the correct machining of this alloy. However, process control through sensor-based monitoring is one of the most successful. Inconel 718 is known to be used in safety-critical applications, which means that the production of IN718-based components requires high structural integrity and high surface quality. Low structural integrity or poor surface quality represents component rejection during

manufacture or failure in service, which are negative aspects for different scales of severity (A. Thakur and Gangopadhyay 2016). This is why the machining process conditions of IN718 must be analyzed from a holistic perspective, considering not only surface aspects but also sub-surface and surface quality aspects beyond the dimensional one, meaning that aspects such as residual stresses and the microstructure of the material after machining are critical aspects to be considered.
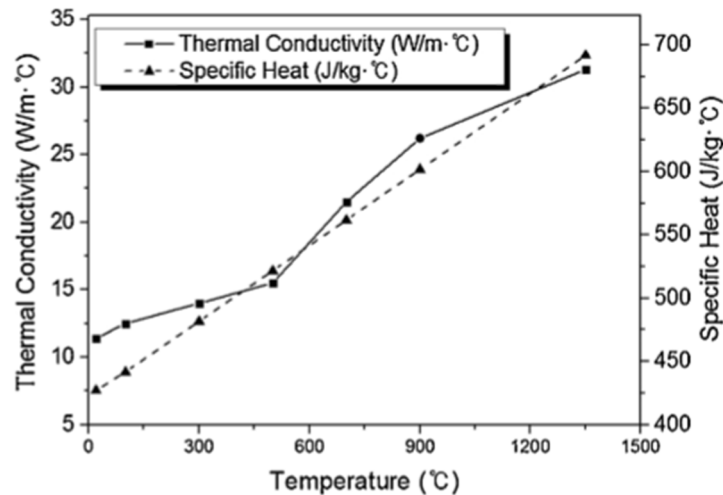
Figure II-24. Thermal conductivity and specific heat according to the temperature of IN718 (Baek, Woo, and Lee 2018)

Although there is much research on the machining of Inconel, it is essential to note that most of the literature is related to the turning process and a much smaller percentage of milling. Considering this aspect and the fact that not all tool geometries or materials have the same amount of research, we can say that the milling of Inconel 718 is a topic that still requires a lot of research and development. This and other aspects make it necessary to adjust cutting parameters in real-time in order to improve process control, tool life, and quality. Many control systems have been proposed in the last decades; some are based on closed-loop control, others based on experimental data, and others based on machine learning; however, in any of these systems, the key is real-time monitoring for early failure detection and adjustment of cutting parameters to new values of response variables. In this line (Subhas et al. 2000) reported that Inconel 718 suffers from dimensional instability after machining. Additionally, they noted that this behavior is not observed in other nickel-based alloys. They attributed this behavior to the presence of the γ'' phase and the residual stresses that develop after machining. These aspects added to the residual stresses formation, making it essential to monitor the process variables

such as temperature, cutting speed, depth of cut, vibration amplitude, cutting force, and others in real-time.

One of the most commonly used equipment in the machining of IN718 and other materials is the piezoelectric sensor dynamometer, where Kistler dynamometers stand out among these devices. Other equipments usually used for monitoring are accelerometers, thermocouples, and infrared sensors (Amrita and Kamesh 2021; Umbrello 2013; Fan et al. 2013; J. wei Ma et al. 2014).

Dynamometers require additional accessories such as signal amplifiers, data acquisition cards and software, and special cables. Although dynamometers represent the best option for monitoring shear forces, some authors have reported that monitoring the power consumed by the machine is an acceptable alternative (Ezugwu et al. 2005; C. W. Dai et al. 2018; E. J. Kim and Lee 2020; Khanna et al. 2020). However, consumption-based monitoring cannot provide helpful information for the dynamic analysis of cutting forces like a dynamometer.

(Segreto, Simeone, and Teti 2012) developed a multi-sensor monitoring system to evaluate tool wear using a dynamometer, acoustic emission, and accelerometers mounted on the tool holder when machining IN718. They used signal feature extraction with principal component analysis and neural networks to correlate the data from the sensors to tool wear by establishing pattern recognition for decision-making. This line (Axinte et al. 2004) used process monitoring to identify and characterize machined surface quality in broaching. Based on a Taguchi orthogonal array, the cutting speed, tool setting, coolant condition and tool wear were considered factors in an experimental design to produce machined surfaces of different quality. Similar work was done by (Mali, Telsang, and Gupta 2017), who measured cutting forces and vibrations for tool wear prediction. To this end, they relied on regression analysis and ANOVA to correlate the monitoring data with the tool wear level. Within their research, they noted that wear generated non-linear signals in the vibration and that direct prediction from the real-time data was tough to perform, requiring post-processing of the signals and additional programming. Other approaches in the same direction have been made for the early detection of severe faults based on dynamometer sensors with 3-axis sensors and acoustic signals (Balsamo et al. 2016) .in another work (B. Wang et al. 2020) developed an analytical and experimental approach to use the signals to monitor cutting energy consumption during high-speed machining processes for Inconel 718.

It is well known that milling is one of the most used machining processes in manufacturing components for aerospace applications (Cai et al. 2014). One of the characteristics of milling is

the interruption of the cuts between the teeth, which is increased in finishing processes where the teeth of the tool make impacts on the workpiece. These reciprocating movements generate intermittent thermal and mechanical stresses that influence the workpiece and the tool in terms of wear and micro-fractures (Çelik et al. 2017). Compared to turning, milling is a process where thermal damage is usually lower; however, the surface topography is usually affected by tooth pitch, which makes the feed rate a critical parameter for obtaining the super finish required for aeronautical application parts. This field (W. Li et al. 2014) reported that milling generates higher surface hardness levels than turning and other processes. In addition, they reported that milling is less likely to develop a white surface layer than turning due to the periodic cooling cycle of the milling process, which is non-existent in turning or grinding. In related work (C. Liu et al. 2015) observed four common types of defects during milling Inconel 718: (i) grooving, which is formed by parallel, slim and long scratches, (ii) tearing, which has a significant impact area but relatively shallow pit, (iii) cavities that are related with a deeper pit with small area and (iv) BUE which is the particle adhering to the milling surface. Additionally (Bouzid Saï, Ben Salah, and Lebrun 2001) noticed that small cutting speed values give poor surface quality due to forming a built-up edge, microhardness, and residual stress increasing too much with high feed and cutting speed.

Many studies have been done to evaluate the affected depth of residual stress after milling IN718. In this line, research on the effect of milling on slots was presented by (Holmberg et al. 2020a). They reported residual stress depth and distribution across the milled slot being affected by cutting tool material and the considerations about if the tool was new or worn and proposed an accurate methodology to measure the depth of such stresses. In addition, their results show that the residual stress was higher in the slots' center and gradually decreased toward the edges. Other research (Holmberg et al. 2020b) observed a high degree of deformation that differs for the up, center, and down milling. Based on their observations, they suggested using up milling for new inserts and switching to down milling due to a lower degree of deformation and residual stress when they are worn out. The milling tests were performed with new and worn ceramic carbide inserts. The residual stress was measured using X-ray diffraction, and microstructure analysis were EBSD based. Their strategy is to generate the lowest impact on residual stress and deformation.

The use of new cutting tool materials for machining nickel superalloys is a topic of continuous scientific and industrial development. In this line, ceramics are an exciting alternative to hard metal, considering this material's high thermal fatigue resistance. (Suzuki et al. 2014) reported that most cutting-edge wear in ceramic tools occurred at the beginning of machining. This led

to a dramatic modification of cutting geometry from sharp edge to round, resulting in the ploughing of the workpiece material. Additionally, they show that instantaneous tensile stress increase around the stagnation point might cause tensile failure in high-speed milling for ceramic inserts. This was confirmed by (Ucun, Aslantas, and Bedir 2013) and (Çelik et al. 2017), who observed that the tool wear mechanism was related to fatigue crack development due to the cyclical nature of milling. In this sense, the crack presence was higher on the cutting edges and extremes, which are related to low stiffness due to their shape. On the other hand, they found that abrasive wear mechanism was the most frequently observed, observing that the BUE (Built-up edge) formation during milling varied depending on the coating type (considering that DLC and TiALN+WC/C coatings showed a good performance). However, they also reported that much research is needed to avoid micro-chipping and fracture in the cutting edge of ceramic tools when milling IN718.

Another essential aspect in the machining of Inconel is lubrication and cooling. Many authors agree that lubrication can be more important than cooling, especially at low cutting speeds. In this respect (Liao, Liao, and Lin 2017) evaluated the effect of the water/oil percentage ratio when milling Inconel with MQL (Minimum Quantity Lubrication) and found that decreasing the oil percentage severely affects the increase of cutting forces and wear. Another study (Abdul Halim, Che Haron, and Abdul Ghani 2020) showed that tool life tripled when using MQL compared to CO_2 cooling. Despite these advantages of MQL in terms of its tribological advantages, MQL is often singled out as a less environmentally friendly technique due to the oil residues and odours associated with it.

Recently many strategies have been developed concerning using lubrication and cooling in IN718 machining (see Figure II-25). In this regard (Shokrani, Dhokia, and Newman 2017) proposed a hybrid cooling and lubrication technique by combining cryogenics with MQL, resulting in significant improvements in roughness levels and increased tool life. Their strategy was based primarily on externally focused cooling. In addition, they reported that this hybrid technique was more successful in turning than in milling, attributing this situation to the difficulties of keeping the nozzle over the cutting zone, considering the effect of a periodic tooth pitch. His results then showed that cryogenics is insufficient for correctly machining Inconel, especially for milling. These aspects have been improved through novel techniques for applying CO_2 and MQL blasting on the contact zone. In this line (O. Pereira et al. 2017) developed a technique in which a jet of CO_2 mixed with MQL passes through the inside of the tool and impacts much closer to the part-tool contact zone. The use of this technique compared with external cooling showed a 16% increase in tool life used for specific cutting parameters and a

reduction in CO2 consumption. This technology was compared with MQL, external cryoMQL, and wet machining. In more recent work (Octavio Pereira et al. 2020) reported a significant increase in the hardness of IN718 with the reduction of the cooling temperature. In their analysis, the use of wet machining reported the most extended tool life; however, wet machining is a technique increasingly avoided in industrial environments due to its high ecological impact, thus recommending the combination of CryoMQL as the best option for milling Inconel.
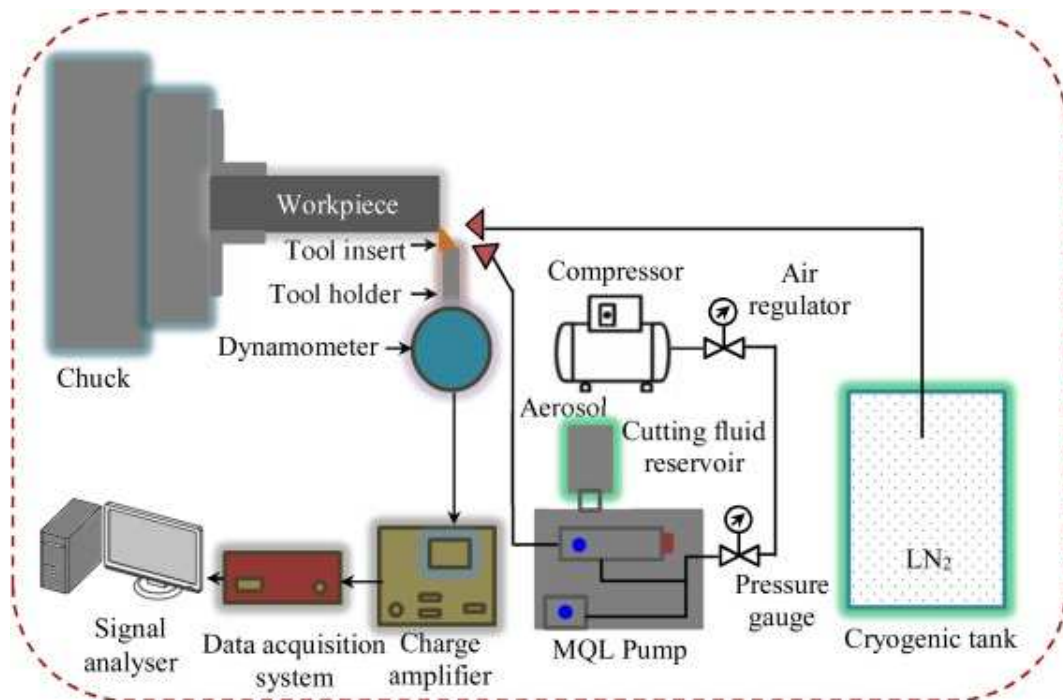
Figure II-25.Cryo-MQL experimental setup scheme(Gajrani 2020)

Machining of Additive manufactured nickel alloys

Aeronautic, oil&gas, and energy industries have dedicated significant resources to repair and manufacture AM IN718 functional components, where the surface quality and structural integrity are critical aspects. This fact can be observed in many research papers and patents where early and novel metallic AM technologies have received particular attention. In this line (Ostra et al. 2019) performed milling machining tests on IN718 parts manufactured by LMD and reported that the chips of the LMD-manufactured parts were much shorter and straighter than those of the forged IN718, while the mechanical properties were similar for both samples.

The heat treatment effect in LMD parts has been considered in several reports. In this line (Calleja et al. 2018) studied the machinability of IN718 obtained by LMD, finding that for both milling and turning, the cutting forces were higher for parts manufactured by LMD with heat treatment and for traditional IN718 compared to LMD IN718 as built recommending that machining operations on LMD IN718 be performed before heat treatment. Additionally (L. Chen et al. 2021) Compared the machinability of the wrought IN718 and the laser additively manufactured (LAM) IN718 by turning, showing that the AM IN718 exhibited irregular chip formation pattern, lower cutting force, lower hardness, and higher thermal conductivity than the wrought IN718. In more recent work (Careri et al. 2021) performed several machining tests on DED IN718 in as-built and heat-treated conditions showing that abrasive and adhesive wear mechanisms were present in both traditional IN718 and DED IN718, with higher wear in the tools that machined the heat-treated parts which are related to the precipitates developed in the heat treatment stage. The authors considered that, in general, the machinability of the heat-treated DED IN718 is similar to the machinability of the wrought IN718.

Post-processing by machining on LPBF and EBM IN718 has received much interest recently, too; (Kaynak and Tascioglu 2018) evaluated the use of post-processing by machining LPBF IN718 as a strategy for the reduction of surface roughness of this type of component and found a reduction in the roughness of more than 90% compared to the roughness of the as-built part. In addition, they reported a significant increase (16%) in the surface and sub-surface microhardness of the machined parts compared to the unmachined part due to work hardening.

Tool wear control and machinability optimization are relevant topics studied for AM IN718. In this way (D. M. Kim et al. 2018b) considered that the porosity and lack of fusion of the parts obtained by LPBF of Inconel lead to a low level of wear when machining the additive manufactured IN718 compared to IN718 wrought. The authors also observed the influence of the relative orientation of the tool concerning the workpiece on the variation of the cutting forces. On the other hand, they reported that the hardness presented similar levels in different zones of the additive manufactured part.

Additionally (Periane et al. 2020) developed a DOE to analyze the optimal face milling conditions for LPBF IN718 as built, with HIP and wrought, considering the minimum cutting energy, minimum tool wear, and minimum surface roughness as response variables. The authors reported that machining with emulsion presented lower energy consumption than dry machining and MQL. In recent work (Ducroux et al. 2021a) proposed a mechanistic model for the prediction of cutting forces by milling AM IN718 considering tool flank wear, run out, and

some microstructural aspects of the material. The study results show that the cutting coefficients obtained for AM IN718 are significantly lower than those of conventional IN718. A comparison of the effects of machining finish, drag finish (DF), and VSF (Vibratory Surface Finish) on the surface quality and machinability of LPBF IN718 has been presented by (Kaynak and Tascioglu 2020), who concluded that finishing by machining allowed the lowest roughness to be obtained. Regarding microstructure, the authors reported that all post-processing operations significantly affected microstructure, with the machining finish having a dominant role in this aspect. Regarding the hardness after post-processing, the authors reported that the machined sample generated higher hardness than DF and VSF.

Anisotropy and tool-workpiece orientation have recently received special attention too. The Work of (Patel et al. 2019) evaluated the effect of cutting direction and laser scanning strategy on cutting forces when milling LPBF IN625. The results showed that machining along the building direction generated higher cutting forces than in the other orientations. They also observed a significant effect of the laser scanning strategy on the magnitude of the cutting forces (Park et al. 2020) reported that the effect of tool orientation-building direction interaction on cutting forces when machining AM IN718 was superior to the effect of material hardness. In other work (L. Yang et al. 2020), the surface topography of machined parts made of LPBF IN625 was significantly affected by the relative orientation of the cutting tool related to the building direction, which allows machining processes for this type of material to be optimizable. A more recent work (Malakizadi et al. 2021) showed the effect of grain morphology, crystalline texture, precipitates, and degree of misorientation of EBM IN718 on cutting tool wear in turning operations by using advanced material characterization techniques such as SEM, EDS, and EBSD. The authors report that crystallographic texture and machining hardening play a significant role in the variation of cutting forces and heat generation for samples manufactured by EBM, which is related to the anisotropy of this type of material.

Chapter III.   Control of crystallographic texture through LPBF configuration and their interaction with physical parameters and mechanical properties

III. Control of crystallographic texture through LPBF configuration and their interaction with physical parameters and mechanical properties

This chapter aims to show the mechanisms of interaction between the LPBF process, the physical parameters, and the anisotropy of the elastic and plastic properties of the material. To this end, the basic concepts of elasticity and plasticity are presented, and how they are affected by the crystalline patterns generated during the LPBF process.

III.1. Introduction

Advances in additive manufacturing allow complex shapes and near-net shapes to be obtained, as well as crystallographic textures and microstructures, through the control of process parameters with unprecedented flexibility. Among the physical properties that can be modified are the mechanical properties (S. H. Lee, Hagihara, and Nakano 2012; Hagihara, Nakano, et al. 2016; Tane et al. 2008; Tekumalla et al. 2022), magnetism (X. Wang et al. 2022; Mao et al. 2007), and corrosion resistance (Hagihara, Okubo, et al. 2016).

In most studies, there is a pronounced interest in determining the mechanisms that govern texture variation as a function of material or process parameters. However, the focus of many studies is not to evaluate the repeatability in crystalline patterns, which is one of the objectives of this chapter. In this sense, Figure III-1 shows the crystalline pattern of two different materials manufactured with the same LPBF strategy (Gokcekaya et al. 2021; Marattukalam et al. 2020). Figure III-1a,b, and c show the detail of the lamellar microstructure, single crystal-like and polycrystal-like, respectively, of IN718 LPBF, manufactured with unidirectional strategy (R0) under different fabrication parameters, while Figure III-1a',b', and 'c' show the respective IPFs (Inverse Pole Figure) of each of the respective SEM scans of the above figures. On the other hand, Figure III-1d shows the detail of the pole figures{001} corresponding to 20 different laser speed and power combinations. It is interesting to observe that although the intensity of the poles increases in some combinations and decreases in others, the pattern is always the same, only observing that some secondary crystalline direction corresponding to the red grains are added in the lamellar sample (Figure III-1a'); in the same way in the polycrystal-like sample.

However, the predominant texture <011> remains in all the combinations. On the other hand, Figure III-1e,f shows the microstructure and crystalline pattern of 316 SS LPBF where the same crystalline pattern can be seen (see {001} pole figure in red dashed lines in Figure III-1 f) as for IN718 LPBF, being also the predominant texture <011> in this fabrication. Additionally, the IN718 LPBF samples were fabricated on an EOS M290 printer machine, while the 316 SS LPBF samples were fabricated on an EOS M100 machine by a different research group.
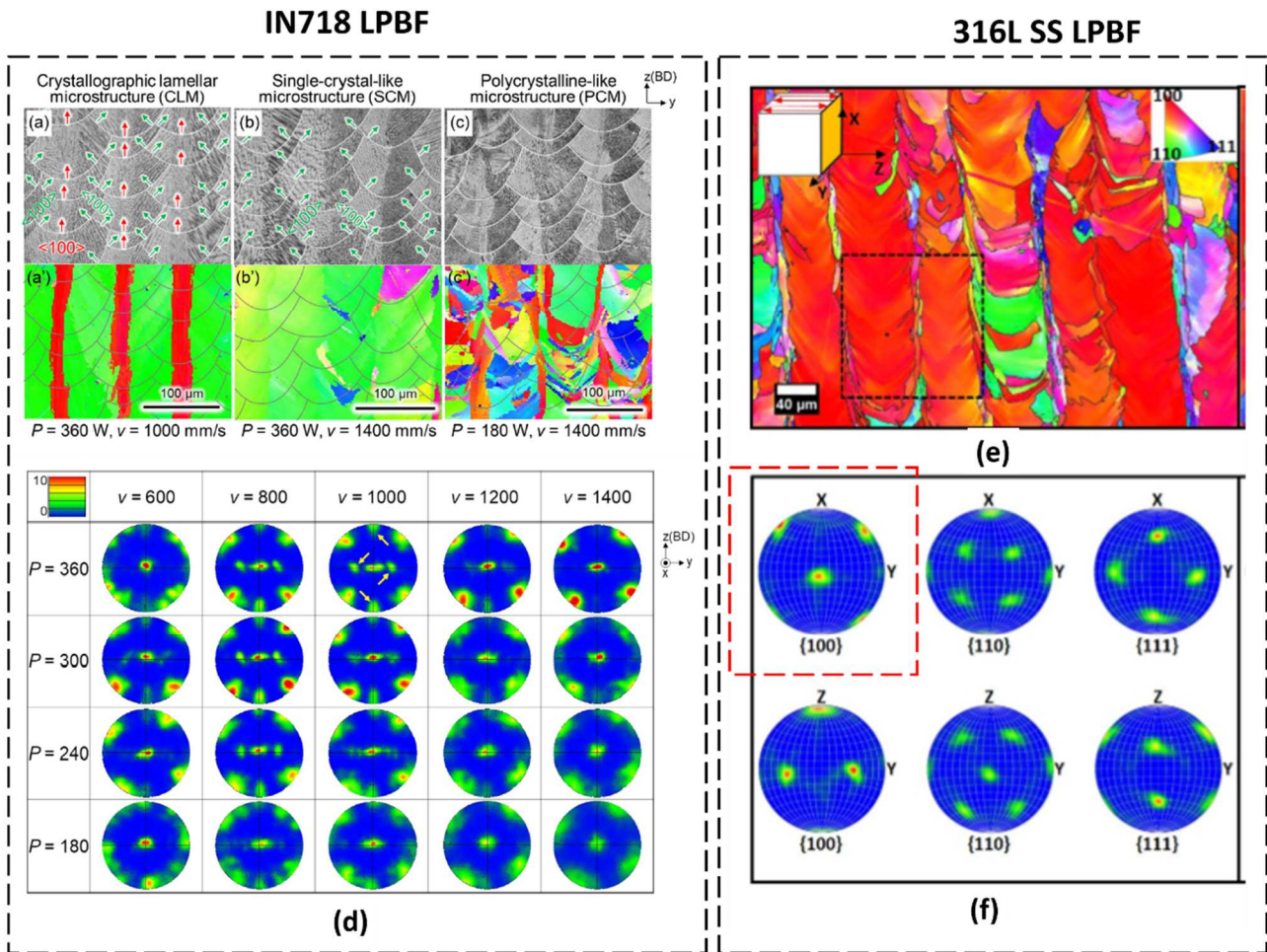
Figure III-1. Texture patterns for unidirectional strategy. a),b),c), a'), b'), c') Sem scans, IPF's and pole figures of IN718 LPBF samples (Gokcekaya et al. 2021) e),f) IPF and pole figures of 316L SS LPBF sample (Marattukalam et al. 2020)

Figure 2 shows the crystalline patterns for two samples fabricated with rotational strategy (R67) but from different materials and fabricated on different machines. Figure 2a,b shows the IPF and pole figure of a Ni-25Mo LPBF sample fabricated on an EOS M290 (Sun, Hagihara, and Nakano 2018a), while figure 1c,d shows the IPF and pole figures of a 316 SS LPBF sample manufactured on an EOS M100 (Marattukalam et al. 2020). In both cases, a fiber texture was developed, also known as: "Ring-like texture."
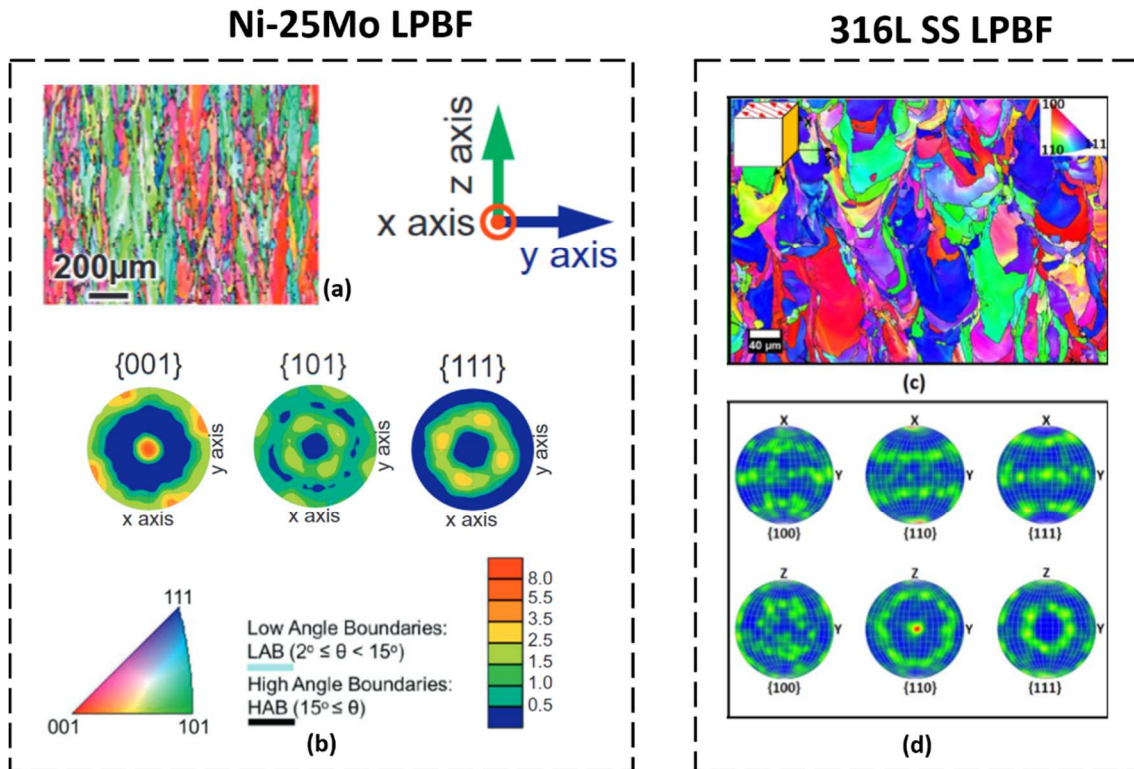
Figure III-2. Texture patterns for rotational strategy (R67). a),b IPF's and pole figures of Ni-25Mo LPBF samples (Sun, Hagihara, and Nakano 2018a) c),d) IPF and pole figures of 316L SS LPBF sample (Marattukalam et al. 2020)

In addition, many studies have reported the development of the same crystalline patterns for the RO and R67 strategies and other strategies. This is an essential aspect since, with repeatability in the crystalline patterns, it is possible to predict the mechanical properties of the components as a function of the crystallographic effect of the texture and to develop design methodologies. Although the development of crystalline patterns associated with each laser strategy has been demonstrated in the literature, it is necessary to assess the repeatability of the texture orientation, which will be presented in a subsequent section for a case study.

III.2. Microstructural design of LPBF parts

It is well known that the LPBF process allows manufacturing of parts with complex geometries. However, the flexibility of this process is much more comprehensive, and the correct control of the process parameters allows a wide range of mechanical properties and microstructural characteristics to be obtained. The scheme in Figure III-3 shows the effect of the LPBF process settings on the design of the material's microstructural and physical characteristics. The LPBF process configuration parameters (laser scanning strategy, LPBF parameters), main process-derived characteristics (competitive grain growth, melt pool morphology, volumetric energy

density), texture intensity, and crystalline classification of LPBF parts (single-crystal or polycrystal) are defined in this section. On the other hand, laser beam shaping and irradiance are defined in section II.3.2. This section will define the concepts related to each stage and their interactions.
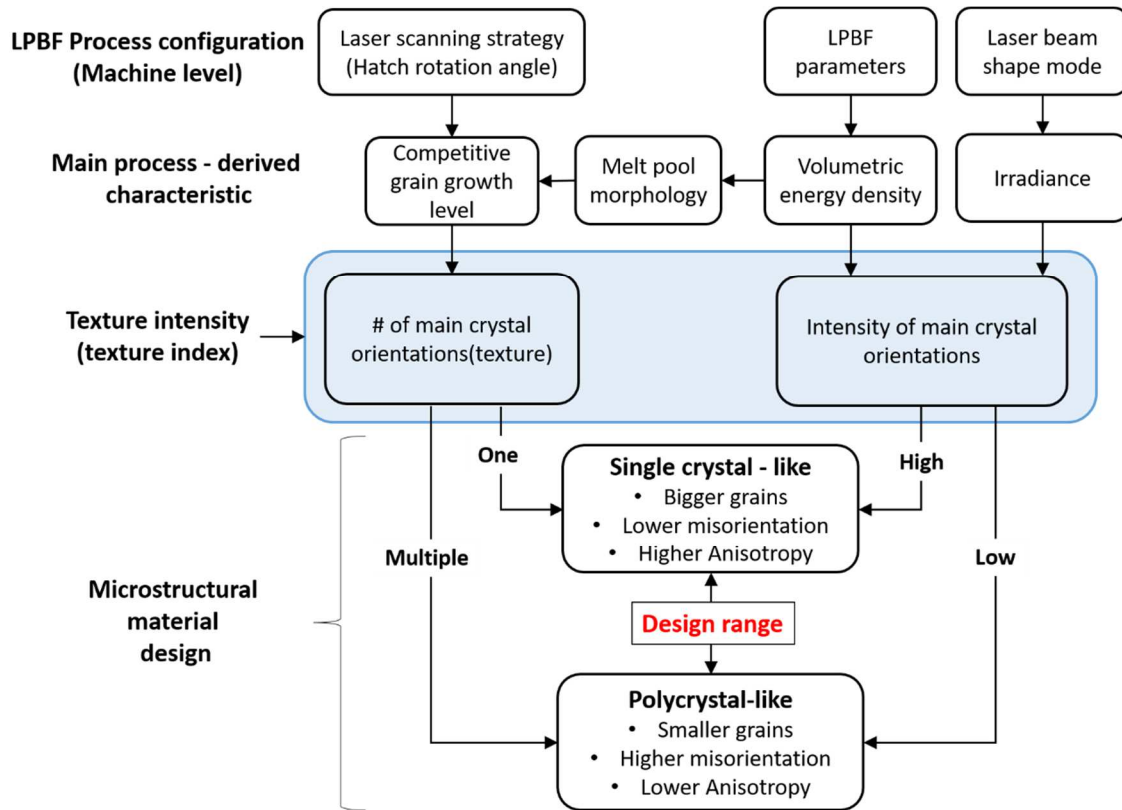
Figure III-3. Microstructural material design scheme

The microstructure of the LPBF-ed components depends on four main aspects: the solidification mode, laser scanning strategy (LSS), volumetric energy density (VED) (see Figure III-7), and laser beam shape mode. Moreover, these features depend on the following specific parameters: the laser power (P), layer thickness (t), hatching space (h) and laser speed (V_b).

The epitaxial growth of crystals is frequently reported in the literature (Pham et al. 2020b; Jian Liu and To 2017; Basak and Das 2016) as the most important phenomenon governing the columnar grain microstructure and causing it to appear in nearly all printed alloys, such as Inconel 718 (Parimi et al. 2014; Moussaoui et al. 2018). Several studies on the solidification of metals during LPBF, welding or casting processes agree that the thermal gradient ($\vec{G}$) and solidification rate (V_i) are the most significant factors that govern the columnar grain growth (Z.

Liu and Qi 2015c; Dinda, Dasgupta, and Mazumder 2012). In the case of Inconel 718, it can be concluded that grains are columnar at essentially any value of the solidification rate for a sufficiently high thermal gradient (Wei, Mukherjee, and DebRoy 2016).

Thus, the ratio $\frac{\vec{G}}{V_i}$ defines the solidification mode (columnar, mixed, equiaxed) while $V_i^{-m}G^{-n}$ corresponds to the scale or size of the microstructure (Pham et al. 2020b), where m and n are material constants. The solidification rate (V_i) can be calculated using the laser beam speed (V_b) and the angle (θ) formed between the laser beam speed vector and the vector normal to the isotherms of the liquid-solid interface. Figure III-4 shows the solidification map of IN718.
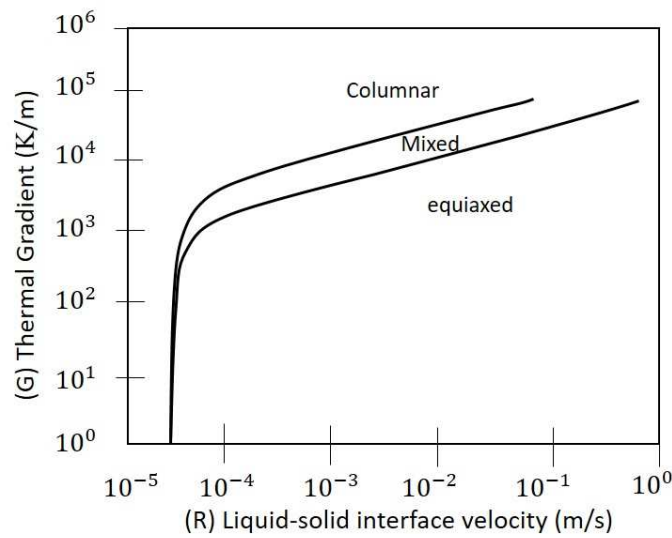
Figure III-4, IN718 solidification map adapted from(Wei, Mukherjee, and DebRoy 2016)

Inconel 718 has an FCC crystal structure (Bean et al. 2019a), which allows columnar grain growth in approximately the thermal gradient direction despite being a polycrystalline material (Gäumann et al. 1999; Kurz, Bezençon, and Gäumann 2001). In this manner, Rappaz (Rappaz et al. 1989) demonstrated that grain growth during solidification begins with a seed grain (see Figure III-6a) in the unmelted section of the liquid–solid border. The columnar grains formed during the new solidification then begin growing in this seed grain of the substrate, and the growth path approximately follows the direction of the closest thermal gradient G_i (Wei, Mazumder, and DebRoy 2015). The columnar growth of the grains from the seed grains and the significant influence of the thermal gradient on the direction of their growth are two main factors that allow us to infer the effect of crystallographic texture on the mechanical properties of LPBF-ed components. The literature (Jian Liu and To 2017; H. Y. Wan et al. 2018) showed that

process parameters significantly influence the crystallographic texture of materials printed using LPBF. This phenomenon enables the creation of extended columnar grains that cross multiple layers (Z. Chen et al. 2018). The solidification sequence functions quite well when specific scanning strategies (such as unidirectional ones) are applied (Dinda, Dasgupta, and Mazumder 2012) or in the absence of significant differences between the preferred growth direction and the thermal gradient vector. However, for more complex scanning strategies, the prediction of crystallographic texture is not straightforward. The columnar grain direction depends on multiple factors, among which the thermal gradient, preferred crystallographic direction of the seed grain, competitive grain growth, solidification rate, geometry of the melt pool, and layer thickness are prominent (Higashi and Ozaki 2020; Y. Wang, Shi, and Liu 2019).

Competitive grain growth frequently occurs in the LPBF process, which implies that the texture prediction is more complex and closely related to the manufacturing parameters, especially the energy density and laser scanning strategies. The latter and the former play leading roles in determining the texture type (Sun, Hagihara, and Nakano 2018b) and the texture intensity (Figure III-5), respectively. An essential aspect of columnar grain growth lies in the role of side branching, which develops when solidification occurs owing to the epitaxial growth of primary dendrites from the secondary ones of previous layers. These originate from the dendrites that grow perpendicular to the epitaxial direction.

Angles $\xi 1$ and $\xi 2$ correspond to the competitive grain growth mechanisms between the thermal gradient and the preferred grain orientation in the epitaxial and the side-branching directions (Figure III-6, melt pool 1), respectively. Studies conducted by Dinda (Dinda, Dasgupta, and Mazumder 2012) and Pham (Pham et al. 2020a) showed the significant effect of side branches on crystalline texture development for different scanning strategies, which, in some instances, produced a texture known as fishbone or chevrons (see Figure III-5).

The effect of the LSS on the texture is shown in Figure III-5, where the 67-degree rotation strategy is compared with the unidirectional one. When the latter is applied to cubic lattice materials (FCC, BCC), there exist two typical dendritic growth patterns: grain growth in the BD beginning at the bottom of the melt pools and spreading epitaxially through several layers, and oblique grain growth (45°) based on side branching, which occurs sideways to the melt pool. Growth in the BD and oblique grain growth (45°) are associated with the <001> and the <101> textures, respectively. However, the 67-degree rotation strategy is associated with a ring-like <001> texture. In both cases, the intensity of the <001> textures is higher at higher VED values (S. Y. Liu et al. 2020; Wei, Elmer, and Debroy 2016).
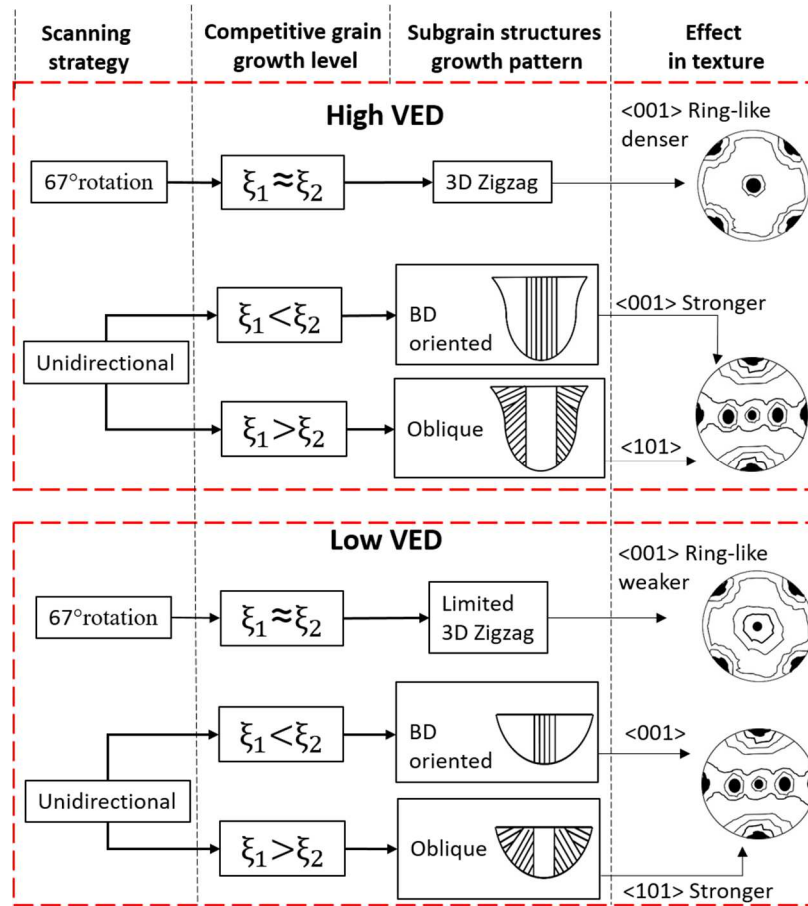
Figure III-5. Scanning strategy and VED interaction effect on texture (Pérez-Ruiz et al. 2021)

The 67-degree scanning direction strategy, wherein the change in the direction of the melt pools shortens the columnar grains, induces a high level of competitive grain growth. However, the grains adopt a zigzag growth pattern to advance along a direction as close as possible to the thermal gradient direction (see Figure III-6, melt pool 2). The growth of the surrounding dendrites also limits the zigzag growth of the grains. Additionally, the grain spreads across various melt pool boundaries; therefore, the grain size would be reduced for a low energy density (VED) because of the high cooling rates. Likewise, growth through secondary dendrites is limited, and nucleation of disoriented dendrites is possible during the first stage of the solidification of the track (Figure III-6 – melt pool 3). Afterward, columnar grains grow in a direction parallel to the thermal gradient when the thermal gradient is aligned with a preferred grain crystallographic orientation. The disoriented dendrites could correspond to crystalline gradients and dislocations (Moussa et al. 2017).
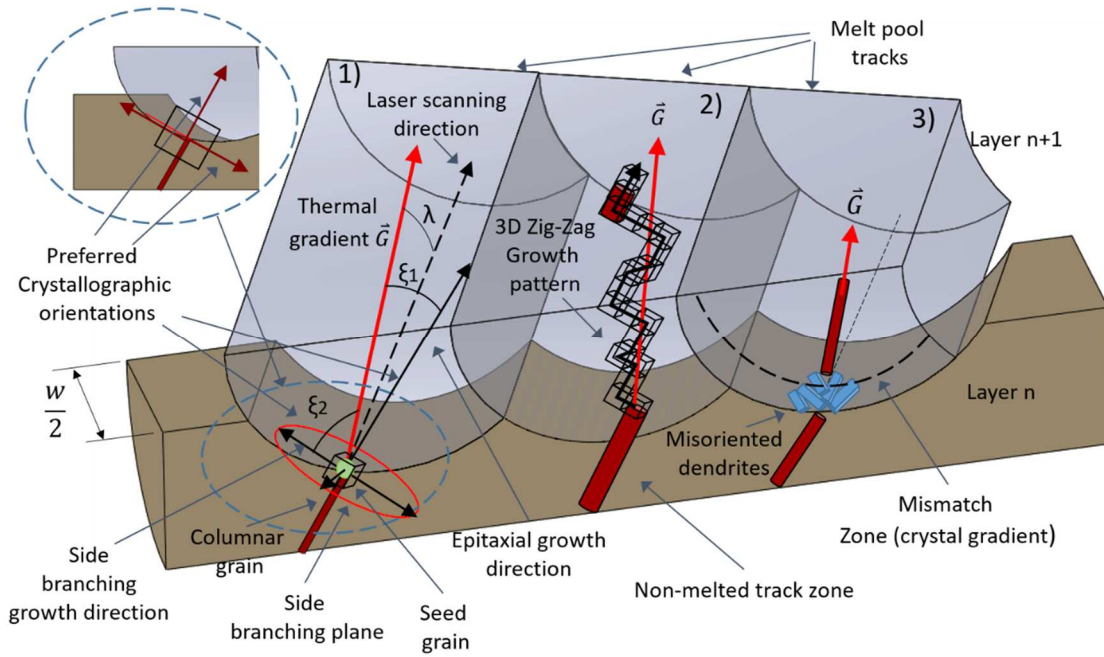
Figure III-6.Competitive grain scheme for a 67-degree rotation scanning strategy (Pérez-Ruiz et al. 2021)

The VED is a crucial LPBF parameter that describes the average applied energy per volume of material during powder bed fusion. It involves all the specific LPBF process parameters, such as laser power (P), scanning speed (V_b), hatching space (h) and layer thickness (z) (S. Y. Liu et al. 2020). The VED (H. Gong et al. 2014; Thijs et al. 2010) can be calculated using equation 1.

$$VED(\frac{J}{mm^3}) = \frac{P}{V_b h z} \qquad (III.1)$$

In literature, the effect of VED on grain size has been widely reported (DebRoy et al. 2018b). . (Zou et al. 2020) reported that the grain size grew from 2.3 to 4.9 µm when the energy density was increased by using a continuous or pulsed laser. The relationship between VED and grain size passes through two intermediate steps: the melt pool morphology (MPM) and the cooling rate. The relationship between VED and MPM has been widely reported in the literature, establishing a lack of fusion and balling mode for a low VED (Yi et al. 2019). However, in the presence of fusion, shallower or steeper melt pool shapes are produced with increasing energy density. However, for an excessive energy density, keyhole-mode melting occurs, and porosities may be produced (Yi et al. 2019; Lei et al. 2019; Criales et al. 2017a; Dilip et al. 2017; Scipioni Bertoli et al. 2017) (Figure III-7). Several studies affirm that the optimal level of energy density to be used in the process agrees with the conduction mode, where the melt pool presents a W/D ratio ≈2. Here, W is the melt pool width, and D is the depth of the track (Figure III-8). Lee

et al. proposed an analytical method to predict the melt pool morphology using a volumetric model with a Gaussian heat source (K. H. Lee and Yun 2020).

The relationship between the MPM and the grain size can be understood from the cooling rate. The classical theory of melting and solidification of metals states that the volume of melted material (MPM) increases with the energy density (VED), decreasing the cooling rate. This reduces the number of particles in the nucleation process; thus, the development of constitutional undercooling is affected, and the grain size increases (Easton and StJohn 2008; Mendoza et al. 2019; J. Dai et al. 2014). However, the study of the quantification of this relationship in LPBF is ongoing. Therefore, Ma et al. (M. Ma, Wang, and Zeng 2017) proposed a cubic relationship between the cooling rate and the grain size during LPBF.
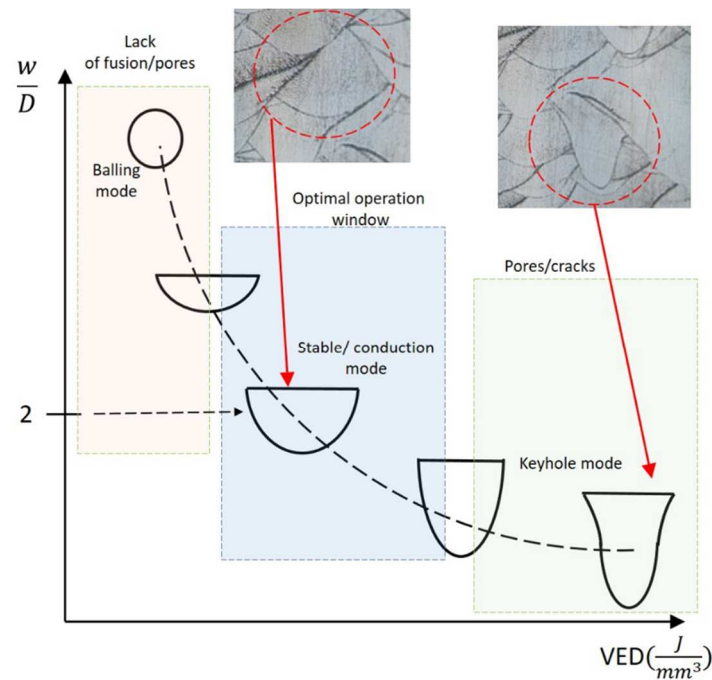
Figure III-7. Effect of VED on the melt pool morphology (MPM) by Gaussian mode (Pérez-Ruiz et al. 2021)

The MPM influences the volume of the grains parallel to the BD, corresponding to the volume of the grains with oblique directions (δ=45° or more). The high thermal gradient at the bottom of steeper melt pools causes increased grain growth in the BD. In contrast, the oblique grain growth is denser for shallower melt pools. A decrease in the layer thickness (t) and hatching space (h) favors a higher density of grains in the BD to the detriment of stray grains owing to their direct geometric relationship with the unmelted track zone geometry. This effect is more significant in steeper melt pools than in shallower ones.
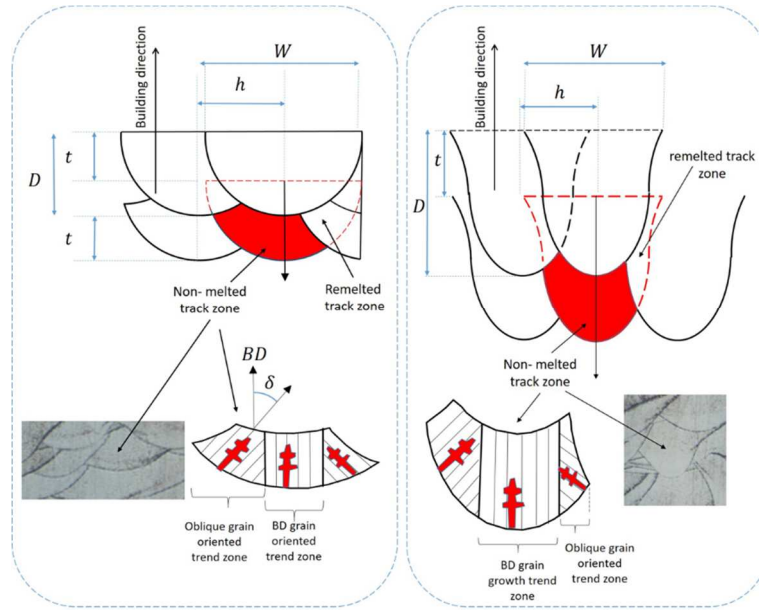
Figure III-8. Types of grain growth trend zones in a non-melted track zone (Pérez-Ruiz et al. 2021)

The crystalline range of the parts obtained by LPBF is quite broad, as polycrystalline parts with low anisotropy and single crystal-like parts with high anisotropy can be obtained, unlike traditional processes in which the crystalline range is more limited. Figure III-9 scheme compares the LPBF process and conventional processes. In conventional primary processes such as forging or casting, the materials obtained are mainly polycrystalline and isotropic, and the rolled can, to some extent, be textured polycrystals.
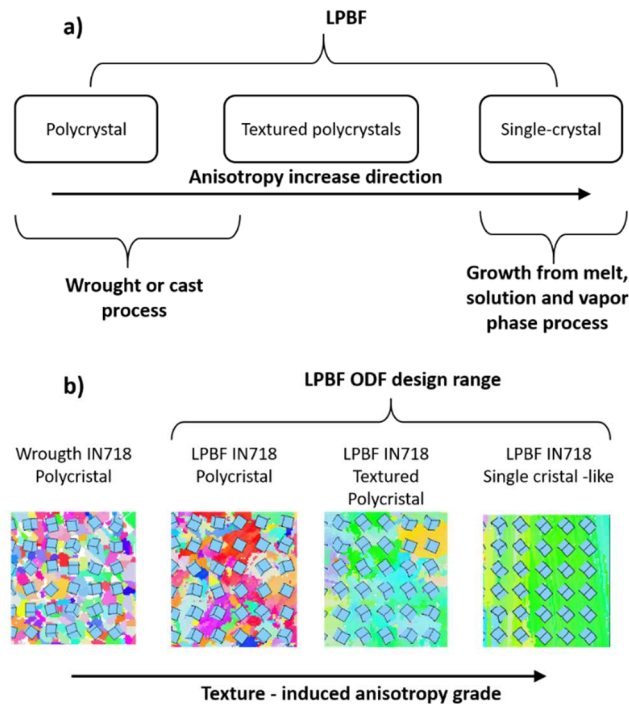
Figure III-9. Crystalline range comparative between LPBF and conventional process

On the other hand, single-crystal materials are conventionally manufactured under four process categories (growth from melt, solution and vapor phase, and epitaxy process). At this point, it is essential to note that in addition to the wide crystalline range that can be obtained with the LPBF process is the possibility of obtaining near-net complex shapes, which is not readily achievable with traditional methods. It is possible to establish then that the combination of flexibility of the crystalline range and complex geometrical shapes makes the LPBF process have vast possibilities for optimization of the components according to the mechanical and geometrical design requirements. To obtain the desired mechanical properties in a component, it is necessary to understand the effect of the physical parameters on these properties. The physical parameters of the material are crystalline texture, grain morphology, and composition phases. The crystalline texture is related to the orientation distribution function (ODF) in which the crystalline directions and their volume fraction are considered.On the other hand, grain morphology includes grain size, shape, and orientation. Each physical parameter is related to the material's mechanical properties. (see Figure III-10).
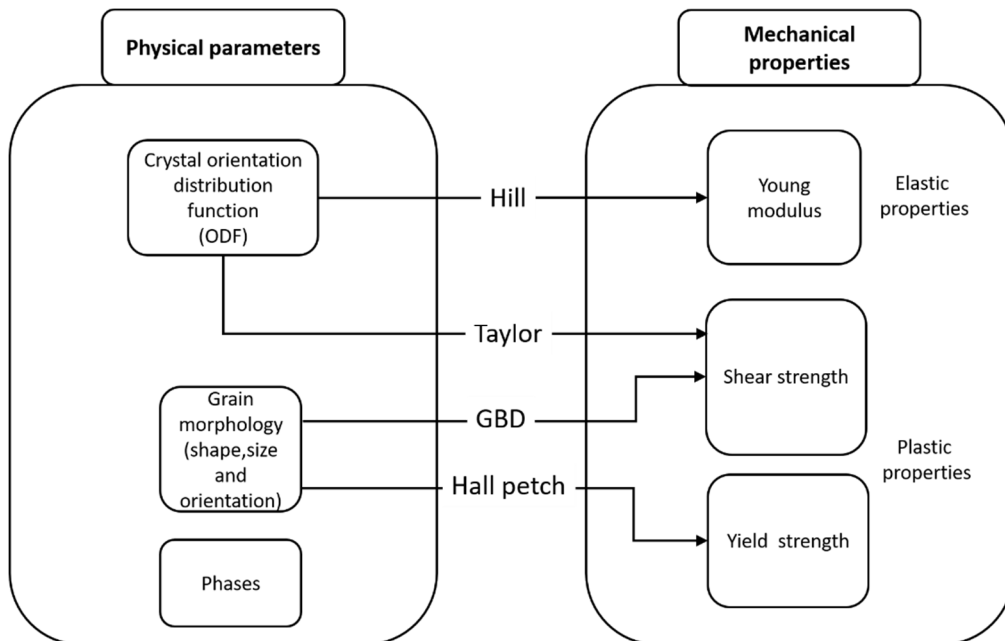
Figure III-10, Physical parameters and mechanical properties interaction

The following sections will present the theories that allow quantifying physical parameters' effect on mechanical properties. In this line, the Hill approximation will be used to obtain Young's modulus from the crystalline orientations present in the LPBF samples and their respective volume fractions. Similarly, Taylor's theory will be applied to quantify the shear strength and Hall Petch's law for yield strength, among others.

III.3. Physical parameters of LPBF parts

This section presents a brief description of the physical parameters of the material that have the most effect on the anisotropy of the mechanical properties. The crystalline information of the materials obtained by EBSD (Electron Backscattering Diffraction) and MTEX toolbox were used to calculate the physical parameters in this thesis.

III.3.1. Orientation distribution function (ODF)

The orientation distribution function (ODF) is a function that associates to each spacial orientation g the volume percent of crystals in a polycrystalline specimen in this specific orientation. This is expressed by equation III. 2

$$ODF(g) = \frac{1}{V}\frac{dV(g)}{dg} \quad \text{III. 2}$$

Figure III-11 shows small cubes representing the crystalline orientation of the crystals concerning the coordinate system of the sample.
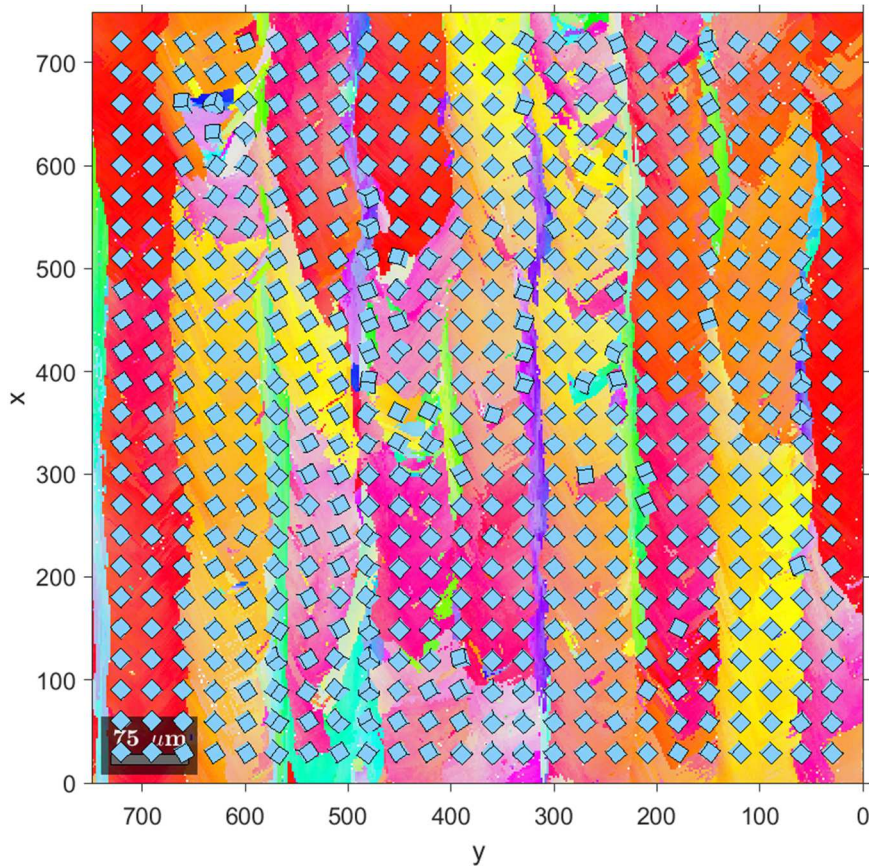
Figure III-11. crystalline grain orientations in an IN718 LPBF sample

It can be seen that the grains share a very similar crystalline orientation, which means that they have a low level of misorientation to their interior. The purpose of the ODF is then to statistically organize all the crystalline orientations into a function that allows knowing the most significant textures and, thus, correctly predicting the mechanical properties derived from each distribution.

With this in mind, it is critical to define that the ODF has two elements; the first is related to the existing crystalline directions, and the second is related to the density of each of these. The crystalline orientations are usually represented using Euler angles, and for this purpose, Figure III-12 represents the Euler angles of each of the crystalline orientations of the IN718 LPBF sample in Figure III-11.
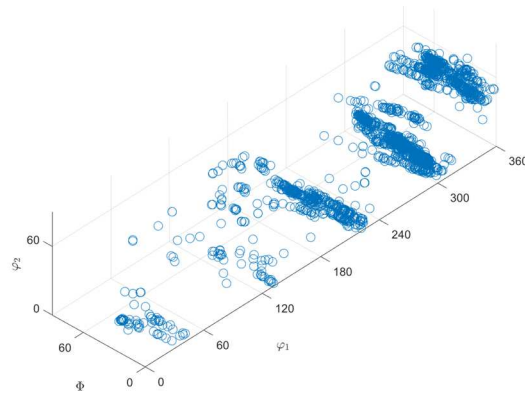
Figure III-12. Crystal orientations represented in Euler angles for LPBF sample

Where $\varphi_1, \phi, \varphi_2$ correspond to the Euler angles. Although Figure III-12 provides information about the crystalline orientations, the scope of the figure is limited as it does not include the density of each of these orientations. For this purpose, Figure III-13 is more complete as it represents by color the density of each of these orientations.
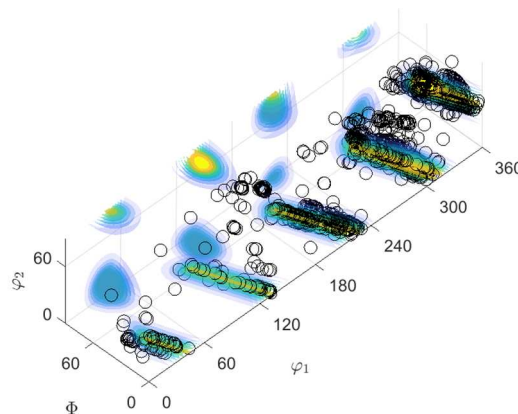
Figure III-13. orientation and density of crystal orientations represented in Euler angles for the LPBF sample

Currently, the most commonly used graphical representation of ODF is through pole figures. See Figure III-14.
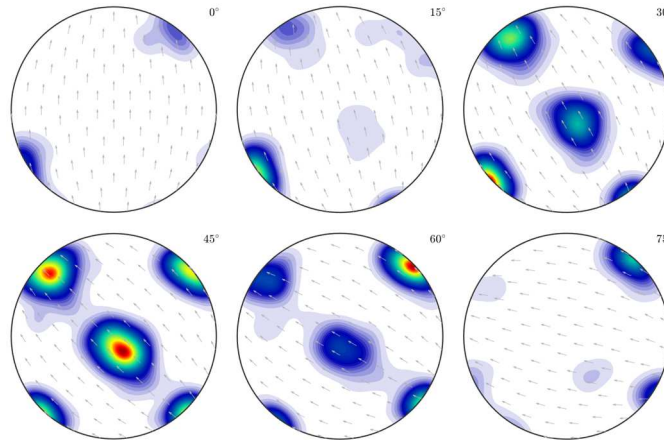
Figure III-14. ODF representation of LPBF sample in pole figures

Pole figures are a graphical representation of the crystalline orientation and are based on the stereographic projection of the crystalline orientation vectors in a spherical system onto the plane. Figure III-15a shows a crystalline cell in the workpiece(XYZ) coordinate system. In this figure, the normal vectors to the faces of the cube are observed. On the other hand, Figure III-15b shows the pole figure {001} corresponding to the crystalline orientation shown in Figure III-15a in the workpiece reference system. The poles in Figure III-15b correspond to the orientation of the normal vectors to the faces of the cube. The same logic is used for the pole figures {011} and {111}.
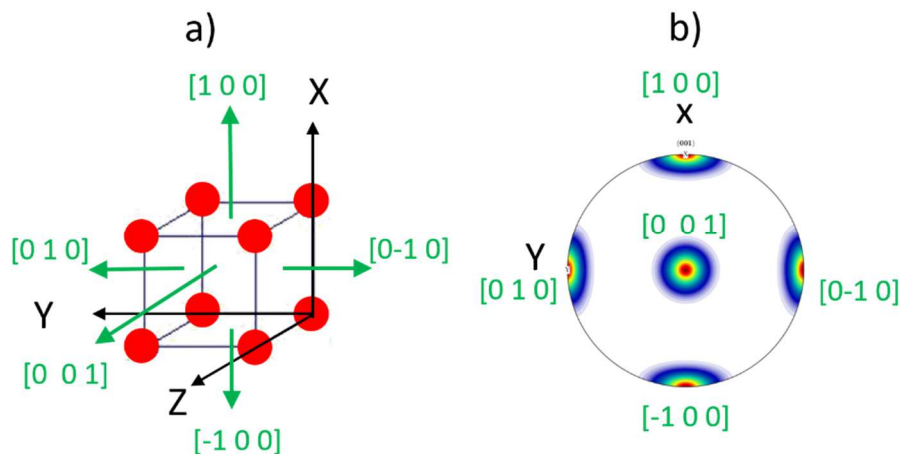
Figure III-15. Graphical representation of pole figure {001}. a)Cubic lattice with normal vectors to cubic face. B) Pole figure {001} that represents the crystal orientation

The EBSD (Electron Backscatter Diffraction) technique is usually used to obtain the crystalline directions. However, to obtain the density of crystalline directions, it is necessary to use advanced statistical techniques such as kernel density functions. Density estimation involves estimating density functions from sample data, the aim being to obtain approximate functions that best fit the empirical data.

The histogram is the easiest way to obtain a density function from a data sample; however, the histogram gives a constant step function which makes the data fitting for crystalline orientations inaccurate. A better option is estimation from kernel density functions. This application uses kernel smoothing to estimate the probability density and is based on kernels and weights. Considering that $(x_1, x_2, \ldots, x_n)$ are identical and independent distributed samples from univariate distributions with unknown density f, the kernel density is:

$$\hat{f}_h(x) = \frac{1}{n} \sum_{i-1}^{n} K_h(x - x_i) = \frac{1}{nh} \sum_{i-1}^{n} K\left(\frac{x - x_i}{h}\right) \text{ (III. 3)}$$

Where K is the kernel function and h is a smoothing parameter called bandwidth.

III.3.2. Texture index

The texture index J is an indicator of the severity of the texture or the sharpness of the texture (Bunge 1993) and is calculated with equation III.4.

$$J = \oint [f(g)]^2 dg \quad \text{(III. 4)}$$

where $f(g)$ is the orientation distribution function(ODF). Although equation III.4 looks simple, the calculation of the Texture index J is not a trivial aspect since the orientation distribution function $f(g)$ is the result of series expansions; therefore, a more accurate expression for the texture index J when considering the orthogonality of the generalized spherical harmonics is shown in equation III.5.

$$J = \sum_{l,\mu,\nu} \frac{1}{2l+1} |C_L^{u\nu}|^2 \quad \text{(III. 5)}$$

Where $C_L^{u\nu}$ are the coefficients of the series expansion in generalized spherical harmonics, the index ν is used to enumerate the number of linearly independent orthogonal solutions of the system of equations, μ represents the number of linearly independent solutions, l is the number

of calculations and L is the limit of l. The texture index J is helpful for crystalline classification, being J= 1 for polycrystals and J= ∞ for ideal single-crystals. Manufactured single crystals usually have values of J ≈10 -12.

III.3.3. Grain morphology and grain boundary density

Grain morphology comprises the geometrical aspects of the grains. For materials with equiaxial grains, it is usual to define the grain diameter as a sufficient parameter to quantify the grain size, however, for LPBF materials, the grains are mainly columnar, and the grain parameters are usually different. In this study, the ellipse will be used as a strategy for grain morphology. Within the ellipse, three parameters are considered: The major axis, the minor axis, and the angle of inclination δ. Figure a shows the grains of the LPBF sample previously shown, where the black lines represent the grain boundaries. On the other hand, figure B shows the ellipses corresponding to each grain for their respective size quantification.

There are other methodologies for measuring grain size; however, in the present thesis, the parameters previously defined for grain morphology will be used. Additionally, the grain and subgrain boundaries will be used to compare the different LPBF samples through the grain boundary density (GBD) analysis.
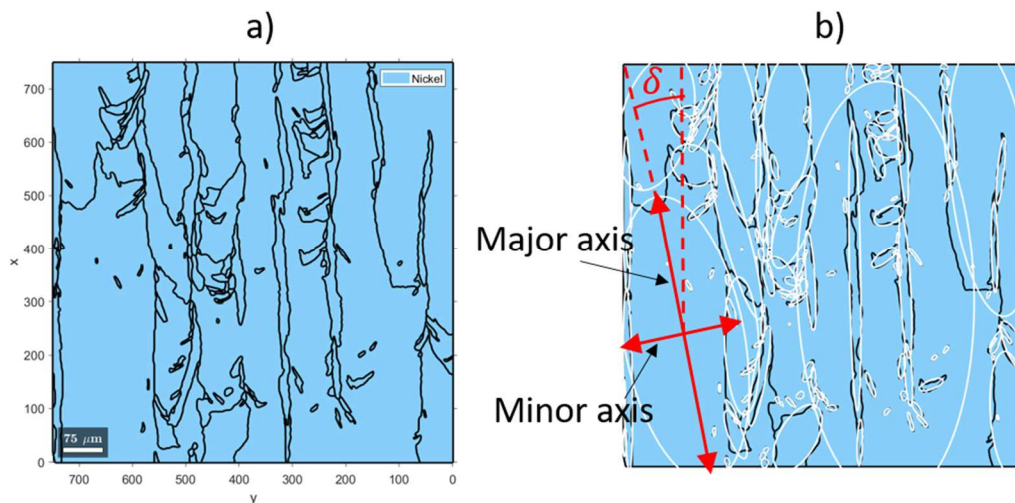
Figure III-16. Ellipse method for grain size quantification

The grain boundary density GBD is calculated according to equation III.6

$$GBD(\frac{1}{\mu m}) = \frac{GBP(\mu m)}{A_s(\mu m^2)} \quad (\text{III}.6)$$

where GBP is the perimeter of all grain boundaries present in the analyzed sample and A_s is the area of the analyzed sample.

III.3.4. Compositional phases

The compositional phases are the regions in an alloy where the physical properties are similar and uniform, and it is related not only to chemical composition but also to density and other physical properties.

Parts obtained by LPBF are usually homogeneous in their chemical composition. IN718 LPBF can be approximated to a single-phase material as the volume fraction of the phases γ and γ' exceeds 80% (Ferreri, Vogel, and Knezevic 2020). Furthermore, both phases have a cubic crystalline system. Figure III-17 shows a SEM scan of a sample of IN718 LPBF showing the dendritic cellular microstructure. The chemical composition of this sample was analyzed at four different points by EDX.
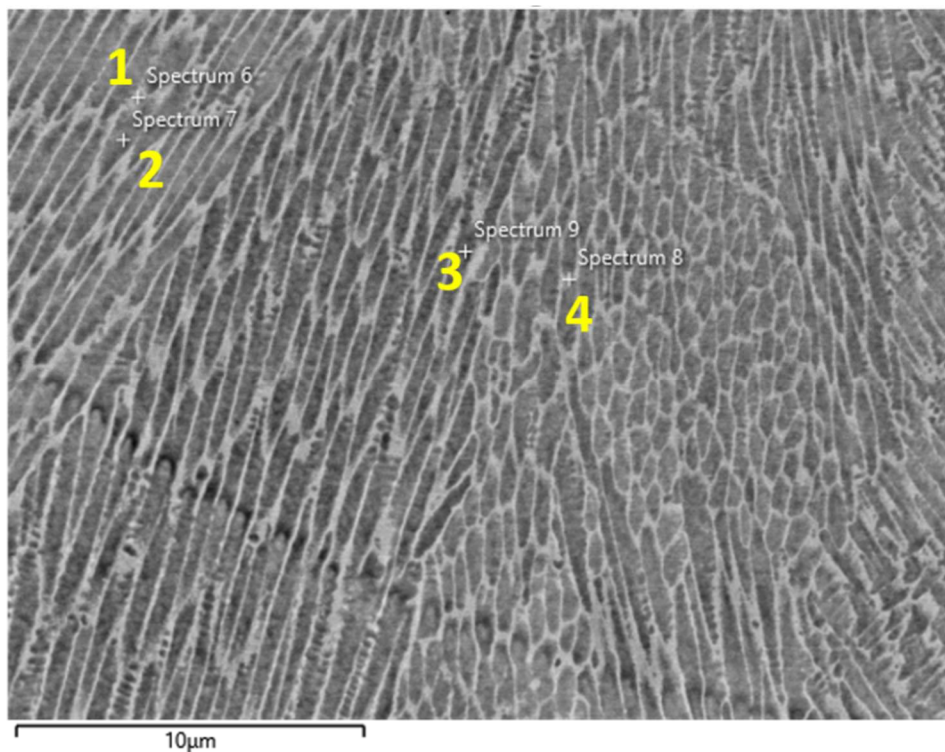
Figure III-17. SEM SCAN for EDX análisis in IN718 LPBF part

Figure III-18 shows the chemical composition spectra of the points indicated in Figure III-17. From the spectra analyzed, it is possible to establish that the variation in the chemical volume fractions of the analyzed zones is negligible, and likewise, the standard deviations of each composition.
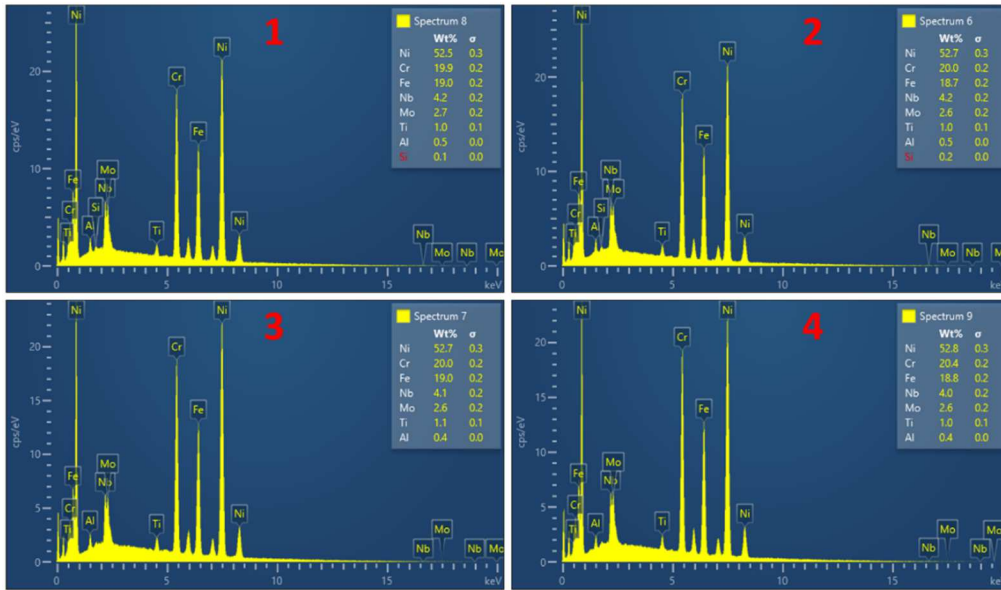
Figure III-18. Compositional spectrum of IN718 LPBF sample in four different zones

Additionally (see Figure III-19), a uniform distribution of the chemical elements in the sample analyzed by EDX is observed. Figure III-19a shows the inverse pole figure by EBSD, where the columnar shape of the grains of the sample is visible. However, in the SEM scan (Figure III-19d), no significant changes related to other phases in addition to the γ phase are apparent. This is confirmed by observing the uniform distribution of the chemical elements (Ni, Cr, Fe, Nb) throughout the sample in Figure III-19b,c,e,f.
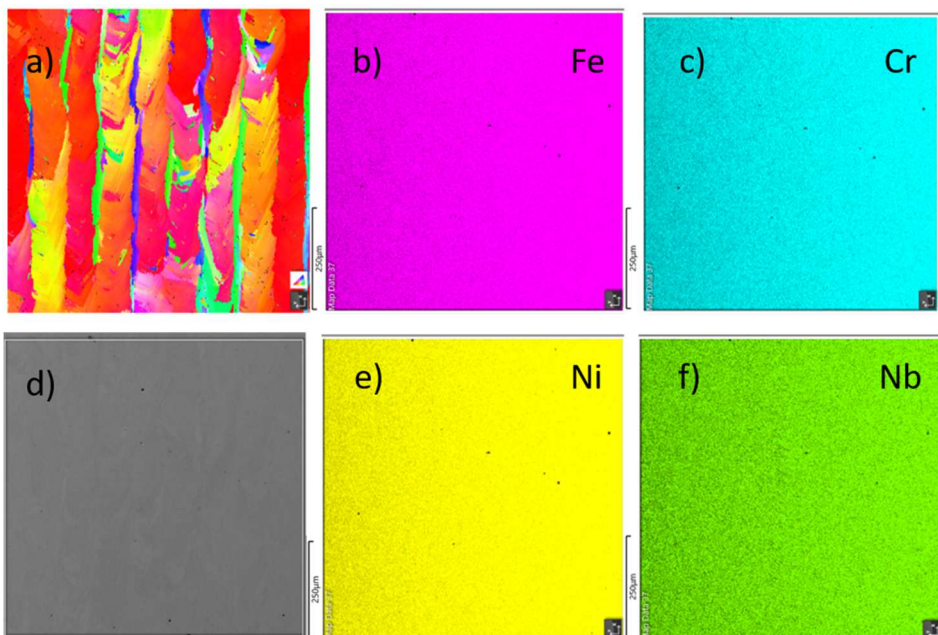
Figure III-19. EDX analysis of IN718 LPBF sample. a) IPF IN718 LPBF b) Fe distribution c) Cr distribution d) SEM Scan e) Ni distribution f) Nb distribution

Because of the above, the effects of the compositional phases on the mechanical properties will not be discussed further in this section, and it is possible to establish that the changes in mechanical properties in the IN718 LPBF are due to induced-texture anisotropy only.

III.4. Mechanical behavior of cubic lattice materials

This section presents some of the most accepted theories in the literature for predicting the mechanical properties of materials concerning elasticity and plasticity.

III.4.1. Elasticity in cubic crystals

Metallic components used in engineering are usually designed to remain in the elastic range since the plastic range represents undesirable deformations for most applications. For this reason, the mechanical properties related to elasticity are of utmost importance for the general analysis and design of components, structures, and machine parts. Hooke's law defines the elastic behavior of a solid. For isotropic materials, the strains caused by an external load are calculated by equation III.7

$$e_x = \frac{1}{E}\left[\sigma_x - \nu(\sigma_y + \sigma_z)\right]$$
$$e_y = \frac{1}{E}\left[\sigma_y - \nu(\sigma_z + \sigma_x)\right] \qquad (\text{III. 7})$$
$$e_z = \frac{1}{E}\left[\sigma_z - \nu(\sigma_x + \sigma_y)\right]$$

Where E is the Young modulus, ν is the Poisson ratio and e_x, e_y and e_z are the strains in the X, Y, and Z. axis

One characteristic of an isotropic crystalline material is that Young's modulus does not change with the orientation of the deformation vector, which means that the difference in stiffness between two components with the same functionality and made of the same isotropic material is only due to the geometric stiffness and not to the increase in Young's modulus. This is a crucial aspect of mechanical design, materials' strength, and topological optimization. However, for anisotropic materials, Young's modulus is not constant as a function of the deformation vector's orientation, which requires careful treatment.

For the case of generalized elasticity, the Hooke stiffness matrix considers all possible combinations of normal and shear deformations. Equation III. 8 shows the matrix of the 21 independent elastic compliances constants from which the different cases of anisotropy are derived according to the nature of the material $S_{ji} = S_{ij}$.

$$
\begin{bmatrix}
S_{11} & S_{12} & S_{13} & S_{14} & S_{15} & S_{16} \\
S_{12} & S_{22} & S_{23} & S_{24} & S_{25} & S_{26} \\
S_{13} & S_{23} & S_{33} & S_{34} & S_{35} & S_{36} \\
S_{14} & S_{24} & S_{34} & S_{44} & S_{45} & S_{46} \\
S_{15} & S_{25} & S_{35} & S_{45} & S_{55} & S_{56} \\
S_{16} & S_{26} & S_{36} & S_{46} & S_{56} & S_{66}
\end{bmatrix}
\qquad \text{(III. 8)}
$$

Equation 2 corresponds to the most general category of anisotropy, as is the case for triclinic (i.e., turquoise) materials; however, for FCC or BCC cubic materials, the constant elastic matrix is significantly simplified given the high symmetry of the cubic form. Equation III. 9 shows the constant elastic matrix for cubic crystalline materials.

$$
\begin{bmatrix}
S_{11} & S_{12} & S_{12} & 0 & 0 & 0 \\
S_{12} & S_{11} & S_{12} & 0 & 0 & 0 \\
S_{12} & S_{12} & S_{11} & 0 & 0 & 0 \\
0 & 0 & 0 & S_{44} & 0 & 0 \\
0 & 0 & 0 & 0 & S_{44} & 0 \\
0 & 0 & 0 & 0 & 0 & S_{44}
\end{bmatrix}
\qquad \text{(III. 9)}
$$

The elastic response of a crystal along any direction vector can be obtained from the stress state of the material in the crystal coordinate system from the elastic constant matrices. In the case of cubic crystalline materials, the Young modulus E_d for a direction d can be calculated from a tensile stress σ_d. The direction of the deformation vector d can be expressed from the cosines of the angles α, β, γ where directions 1, 2, and 3 correspond to the axes of the crystalline system, as shown in Figure III-20 (Hosford 1993).
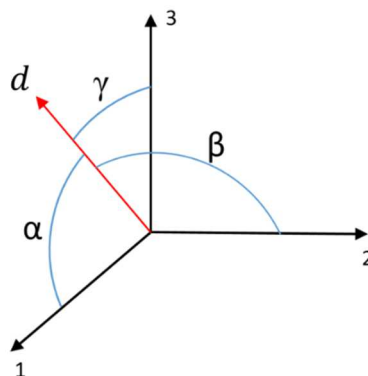
Figure III-20. Deformation vector in crystalline reference system adapted from (Hosford 1993)

The stresses in the crystalline system correspond to equations III. 10.

$$
\begin{array}{ll}
\sigma_1 = \alpha^2 \sigma_d & \sigma_{23} = \beta\gamma\sigma_d \\
\sigma_2 = \beta^2 \sigma_d & \sigma_{31} = \gamma\alpha\sigma_d \quad \text{(III. 10)} \\
\sigma_3 = \gamma^2 \sigma_d & \sigma_{12} = \alpha\beta\sigma_d
\end{array}
$$

Considering the matrix of elastic constants of equation III. 3, the corresponding deformations would be according to equation III. 11

$$
\begin{array}{ll}
\dfrac{e_1}{\sigma_d} = S_{11}\alpha^2 + S_{12}\beta^2 + S_{12}\gamma^2 & \dfrac{\gamma_{23}}{\sigma_d} = S_{44}\beta\gamma \\[2mm]
\dfrac{e_2}{\sigma_d} = S_{12}\alpha^2 + S_{11}\beta^2 + S_{12}\gamma^2 & \dfrac{\gamma_{31}}{\sigma_d} = S_{44}\gamma\alpha \quad \text{(III. 11)} \\[2mm]
\dfrac{e_3}{\sigma_d} = S_{12}\alpha^2 + S_{12}\beta^2 + S_{11}\gamma^2 & \dfrac{\gamma_{12}}{\sigma_d} = S_{44}\alpha\beta
\end{array}
$$

The resulting deformation for the direction d is calculated from equation III. 12

$$
\frac{e_d}{\sigma_d} = e_1\alpha^2 + e_2\beta^2 + e_3\gamma^2 + \beta\gamma\gamma_{23} + \gamma\alpha\gamma_{31} + \alpha\beta\gamma_{12} \quad \text{(III. 12)}
$$

Substituting equation III11 into equation III. 12 gives the expression for Young's modulus in the d -direction for a single crystalline material(see equation III. 13)

$$
\frac{1}{E_d} = \frac{e_d}{E_d} = S_{11} + (-2S_{11} + 2S_{12} + S_{44})(\beta^2\gamma^2 + \gamma^2\alpha^2 + \alpha^2\beta^2) \quad \text{(III. 13)}
$$

if d is expressed under the miller indices $[hkl]$ (see equation III. 14)

$$
\begin{aligned}
\alpha &= h/\sqrt{h^2 + k^2 + l^2} \\
\beta &= k/\sqrt{h^2 + k^2 + l^2} \quad \text{(III. 14)} \\
\gamma &= l/\sqrt{h^2 + k^2 + l^2}
\end{aligned}
$$

Equation III. 13 can be rewritten in the following way

$$
\frac{1}{E_d} = S_{11} + \frac{(2S_{12} - 2S_{11} + S_{44})(k^2l^2 + l^2h^2 + h^2k^2}{(h^2 + k^2 + l^2)} \quad \text{(III. 15)}
$$

The above equations correspond to the case of a monocrystalline material or the analysis of the particular grains of a polycrystalline material. For LPBF materials mainly belonging to the textured polycrystalline materials, obtaining Young's modulus as a function of any orientation d requires additional treatment. For this purpose, the most accepted approach is to obtain an average Young's modulus from Young's modulus of all the crystalline orientations present in the material, considering the volume fraction of each. For this, there are two approaches; the first approach is the Voigt approach, in which it is assumed that the local deformations are uniform and that Young's modulus is averaged for all orientations. This approach is shown in equation III. 16

$$E_v = \frac{(F - G + 3H)(F + 2G)}{2F + 3G + H} \quad \text{(III. 16)}$$

Where E_v is Young's modulus according to Voigt and F, G, H are obtained from equations III. 17.

$$
\begin{aligned}
F &= \frac{1}{3}(C_{11} + C_{22} + C_{33}) \\
G &= \frac{1}{3}(C_{12} + C_{23} + C_{13}) \quad \text{(III. 17)} \\
H &= \frac{1}{3}(C_{44} + C_{55} + C_{66})
\end{aligned}
$$

For cubic crystals, the equation of E_v is:

$$E_v = (C_{11} - C_{12} + 3C_{44})(C_{11} + 2C_{12})/(2C_{11} + 3C_{12} + C_{44}) \quad (III. 18)$$

On the other hand, the Reuss approach is the complete opposite as it assumes uniform local stress and is based on the average of the compliances for all orientations. Thus:

$$\frac{1}{E_R} = \frac{1}{5}(3F' + 2G' + H') \quad \text{(III. 19)}$$

Where

$$
\begin{aligned}
F' &= \frac{1}{3}(S_{11} + S_{22} + S_{33}) \\
G' &= \frac{1}{3}(S_{12} + S_{23} + S_{13}) \quad \text{(III. 20)} \\
H' &= \frac{1}{3}(S_{44} + S_{55} + S_{66})
\end{aligned}
$$

For cubic crystals, the equation of E_R is:

$$E_R^{-1} = \frac{1}{5}(3S_{11} + 2S_{12} + S_{44}) \quad (\text{III}.21)$$

Based on the above, Hill showed that the Voigt and Reuss averages correspond to the upper and lower limits of the true values of Young modulus, so he proposed that obtaining an average value between the two limits is a good approximation for polycrystalline materials.

III.4.2. Plasticity in cubic crystals

Plastic deformation in crystalline materials develops under different mechanisms. One of the most important is the slip mechanism, related to the shearing on crystallographic planes in the crystallographic orientations, known as slip systems. The slip mechanism occurs by the movement of the dislocations along the lattice, which is why the accumulation of dislocations left by the slip causes the work hardening. It is essential to clarify that the visible slip lines are the surface of a deformed metal and correspond to the displacement of thousands of atomic diameters occurring in planes relatively close to each other. On an atomic scale, slip displacements are small relative to grain size, so slip is often treated as a macroscopic homogeneous shearing process (Hosford 1993).

When a crystalline material is subjected to normal stress, the slip develops when the critically resolved shear stress (τ_c) is reached whereby the constant of proportionality between τ_c and the applied normal stress σ_a is known as the Schmid factor (m)(Sato et al. 1981; 1983; Fernandez-Zelaia et al. 2019), see equation III.22.

$$\sigma_a = \frac{\tau_{rss}}{m} \quad (\text{III}.22)$$

Equation III.22 allows us to infer that when the Schmid factor decreases, the applied stress must be greater to reach the resolved shear stress. Schmid factor (m) is obtained by equation III.23

$$m = \sin\chi\cos\lambda = \frac{\alpha l + \beta m + \gamma n}{\sqrt{\alpha^2 + \beta^2 + \gamma^2}} * \frac{\alpha h + \beta k + \gamma i}{\sqrt{h^2 + k^2 + i^2}} \quad (\text{III}.23)$$

Where χ and λ are angles made by the external force respectively with slip plane and slip direction, (l,m,n) is the slip plane vector, (h,k, i) is the slip direction vector, and $[\alpha, \beta, \gamma]$ is the direction of resultant cutting resistance vector. It is represented in Figure III-21 in the context of the machining process.
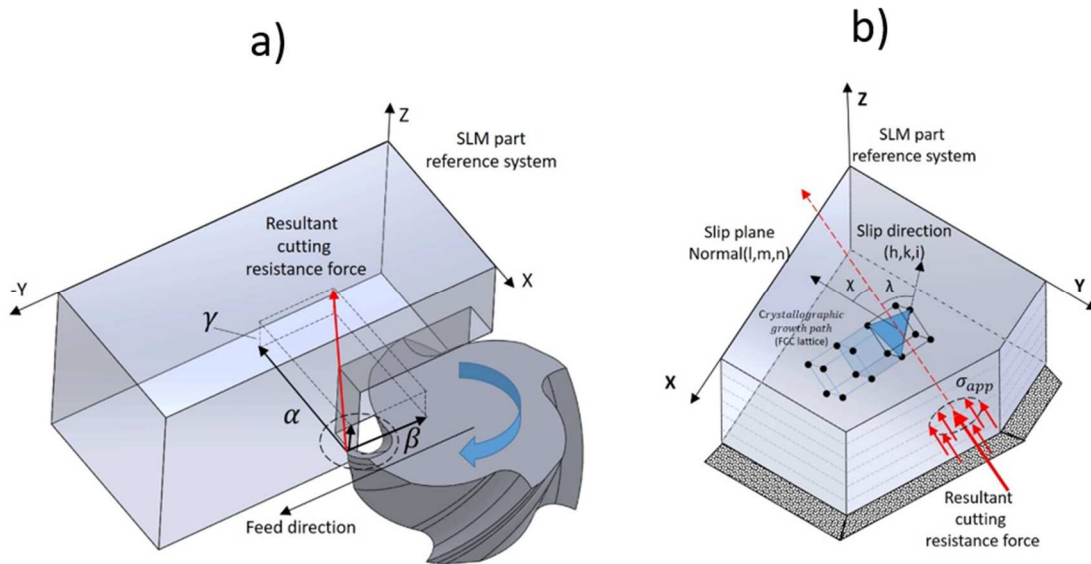
Figure III-21. Schmidt scheme. a) applied stress vector components b) applied vector in the crystal reference system

Although the Schmid factor helps compare the shear strength, its practical use is limited to single-crystalline materials under particular conditions. It is important to note that the deformation mechanisms of a polycrystalline material are similar to those of a single crystal. Therefore, many techniques used in quantifying the mechanical properties of single crystals can be used for polycrystals. Within this context, the Taylor factor is more appropriate for polycrystals. Taylor factor assumes that all grains subjected to the same loading undergo the same change in shape as the whole piece. Considering that, it is possible to establish the strain tensor components for a polycrystalline material subjected to uniaxial loading parallel to the direction x. See equation III. 18

$$d\varepsilon_y = d\varepsilon_z = -\frac{1}{2} d\varepsilon_x \quad and \quad d\gamma_{yz} = d\gamma_{zx} = d\gamma_{xy} = 0 \quad (\text{III. 24})$$

Where $d\varepsilon_x, d\varepsilon_y$ and $d\varepsilon_z$ correspond to the normal strain components and $d\gamma_{xy}, d\gamma_{yz}$ and $d\gamma_{zx}$ correspond to the shear strain components.

If it is considered that the work by volume dw is the required to deform all the slip systems in grain, then it is possible to relate the work done by the action of stress on a material to the crystalline characteristics of a grain. See equation III. 19

$$dw = \sum_i \tau d\gamma_i = \tau \sum_i |d\gamma_i| \qquad (III.25)$$

Where τ is the critical shear stress to develop the slip, which is assumed to be constant for all slip systems, and $d\gamma_i$ is the incremental slip of each slip system. If the term $\sum_i |d\gamma_i|$ is denoted as $d\gamma$ then dw can be obtained with equation III. 20.

$$dw = \tau d\gamma = \sigma_x d\varepsilon_x \quad (III.26)$$

This can also be expressed as:

$$\frac{\sigma_x}{\tau} = \frac{d\gamma}{d\varepsilon_x} = M \quad (III.27)$$

where M is the Taylor factor and depends on the crystalline orientation. Thus, it is possible to obtain the macroscopic Taylor factor of a polycrystalline material by calculating the average of the Taylor factor for all the crystalline orientations present in the material. This is expressed in equation III. 22:

$$\sigma_x = \bar{M}\tau \qquad and \qquad d\varepsilon_x = \frac{d\gamma}{\bar{M}} \quad (III.28)$$

To obtain the Taylor factor for a specific orientation, it is convenient to express the external strains $d\varepsilon_x, d\varepsilon_y, d\varepsilon_z, , d\gamma_{xy}$ in the coordinates of the crystalline system 1,2,3, obtaining the cubic strains $d\varepsilon_1, d\varepsilon_2, , , , , , d\gamma_{23}$ For this purpose, it is necessary to have the crystals' relative orientation (Euler angles) relative to the workpiece coordinates. Once the Euler angles of each crystal to the workpiece reference are available, it is possible to obtain the deformations in the crystalline axes from rotation matrices. Axes 1,2,3 of the cubic crystal can be seen in the figure. The next step consists of taking the deformations $d\varepsilon_1, d\varepsilon_2, , , , , , d\gamma_{23}$ to the sliding systems. For this purpose, it is essential to mention that the FCC materials have 12 slip systems (Table III-1). These systems originate from 4 slip planes (A,B,C,D) and the three slip directions (I,II, III) associated with the slip plane. Figure I-1 shows the Half of an octaedron that represents the FCC slip systems(Hosford 1993).

Table III-1. FCC slip systems

Slip Plane	(111)			$(\bar{1}\bar{1}1)$			$(\bar{1}11)$			$(1\bar{1}1)$		
Slip direction	$[01\bar{1}]$	$[\bar{1}01]$	$[1\bar{1}0]$	$[01\bar{1}]$	$[101]$	$[\bar{1}10]$	$[01\bar{1}]$	$[101]$	$[\bar{1}\bar{1}0]$	$[0\bar{1}\bar{1}]$	$[\bar{1}01]$	$[110]$
Slip system	I	II	III	I	II	III	I	II	III	I	II	III
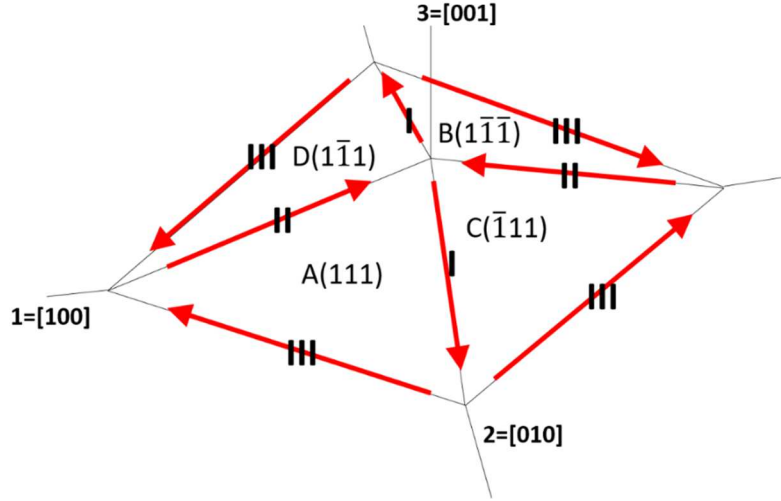
Figure III-22. FCC slip systems scheme adapted from (Hosford 1993)

Between each slip element and cube axes, a direction cosine represents the degree of difficulty of generating the slip deformation under external load. Together, these differences represent the level of mechanical resistance that a cubic material will exert in the face of a plastic deformation process. Because of that, the strains relative to the cube axes can be expressed according to equation III. 23:

$$
\begin{aligned}
d\varepsilon_1 &= (-d\gamma_{AII} + d\gamma_{AIII} - d\gamma_{BII} + d\gamma_{BIII} - d\gamma_{CII} + d\gamma_{CIII} - d\gamma_{DII} + d\gamma_{DIII})/\sqrt{6} \\
d\varepsilon_2 &= (+d\gamma_{AI} - d\gamma_{AIII} + d\gamma_{BI} - d\gamma_{BIII} + d\gamma_{CI} - d\gamma_{CIII} + d\gamma_{DI} - d\gamma_{DIII})/\sqrt{6} \\
d\varepsilon_3 &= (-d\gamma_{AI} + d\gamma_{AII} - d\gamma_{BI} + d\gamma_{BII} - d\gamma_{CI} + d\gamma_{CII} - d\gamma_{DI} + d\gamma_{DII})/\sqrt{6} \\
d\gamma_{23} &= (+d\gamma_{AII} - d\gamma_{AIII} - d\gamma_{BII} - d\gamma_{BIII} + d\gamma_{CII} - d\gamma_{CIII} - d\gamma_{DII} + d\gamma_{DIII})/\sqrt{6} \\
d\gamma_{31} &= (-d\gamma_{AI} + d\gamma_{AIII} + d\gamma_{BI} - d\gamma_{BIII} + d\gamma_{CI} - d\gamma_{CIII} - d\gamma_{DI} + d\gamma_{DIII})/\sqrt{6} \\
d\gamma_{12} &= (+d\gamma_{AI} - d\gamma_{AII} + d\gamma_{BI} + d\gamma_{BII} - d\gamma_{CI} + d\gamma_{CII} - d\gamma_{DI} + d\gamma_{DII})/\sqrt{6}
\end{aligned}
\tag{III.29}
$$

It is noteworthy that if a material is considered incompressible (such as the metals obtained by LPBF), the first three equations are not independent and, therefore $d\varepsilon_1 + d\varepsilon_2 + d\varepsilon_3 = 0$, which implies that there are only five independent expressions of the equation. On this basis, Taylor assumed that the deformation exerted on the grains occurs when the minimum energy necessary to develop the deformation is reached $\sum_i \tau d\gamma_i$, for this purpose, he considered that

the critical stress for slip τ is the same for all active slip systems with the same work hardening rate. In this way, he proposed an optimization to obtain the independent slip directions that generate the minimum value of $d\gamma/d\varepsilon_x = M$. In this way, the Taylor value for a combination of stress orientation concerning crystalline distribution represents the minimum resistance necessary to generate the deformation process. This makes the Taylor factor a practical and effective tool in assessing the anisotropy of material to define the orientations in which the material generates the most resistance to being plastically deformed by shear or tensile loads.

III.5. Interaction between VED, laser scanning strategies, and beam shaping on density, melt pool shape, and microstructure

This section presents the interactions of laser scanning strategies, VED, and beam shaping and the effect of these interactions on the microstructural and crystallographic aspects of the parts manufactured by LPBF. To this end, three laser scanning strategies will be analyzed, and the microstructural details of each strategy will be presented. Finally, a case study analyzes the interaction between beam shaping, VED, and the three laser strategies mentioned above.

III.5.1. Unidirectional strategy (R0)

In the unidirectional strategy, also known as R0, the tracks of one layer are deposited successively on top of the tracks of the previous layer without changing the angle of orientation of one layer to the other, as shown in Figure III-23. Usually, the tracks within the same layer are deposited alternating the direction of the tracks; however, there are fabrications where the tracks are deposited without alternating, all having the same direction. For this research, the alternation in the direction of the tracks was used.
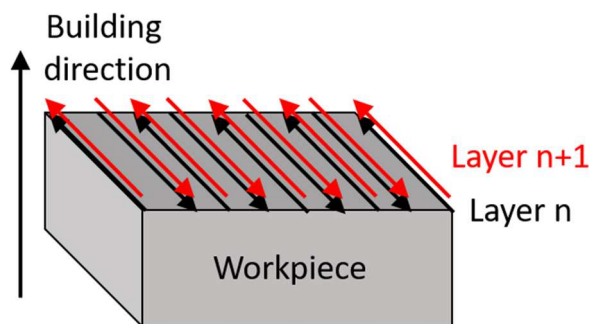
Figure III-23. Unidirectional strategy scheme(Hatch rotation angle = 0º)

Figure III-24 shows the appearance of the melt pools when using the unidirectional strategy. Figure III-21a shows the melt pools in the XZ plane; it shows how the tracks are interlaced vertically to guarantee the correct bonding between layers and horizontally to guarantee the bonding between tracks of the same layer. This is achieved by correctly selecting the layer thickness and hatching space parameters. On the other hand, figure III-21b shows the configuration of the tracks in the XY plane. It is critical to define that when the areas in the XY plane are relatively large, the beads are not thrown continuously along the whole length of the fabricated area, thus generating zones of longitudinal cross-linking of the tracks.
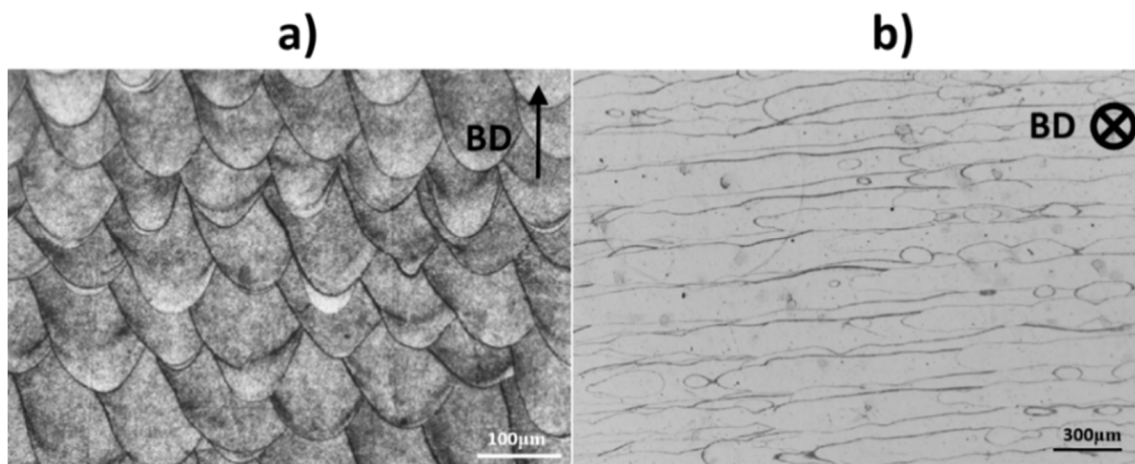
Figure III-24. IN718 LPBF Melt pools for unidirectional strategy. a) melt pools in the XZ plane, b) melt pools in XY plane

Figure III-25 shows the lamellar microstructure, typical in many fabrications obtained by the R0 strategy. This microstructure consists of two clearly defined textures: the central or epitaxial texture and the lateral texture by side branching. In the case of the central or epitaxial texture, also known as the <001> texture, the dendrites grow through the layers in the melt pool bottom zone, as shown by the red arrows. The union of these dendrites creates thin, elongated columnar grains. The crystalline orientation of these grains is sometimes parallel to the building direction but generally follows a (101) or (111) orientation depending on the characteristics of the thermal gradient and the cooling ratio. On the other hand, the lateral texture or <101> develops from the 90-degree zig-zag growth between dendrites (see yellow arrows) through the side branching mechanism, which is a characteristic of the cubic nature of the FCC lattice.
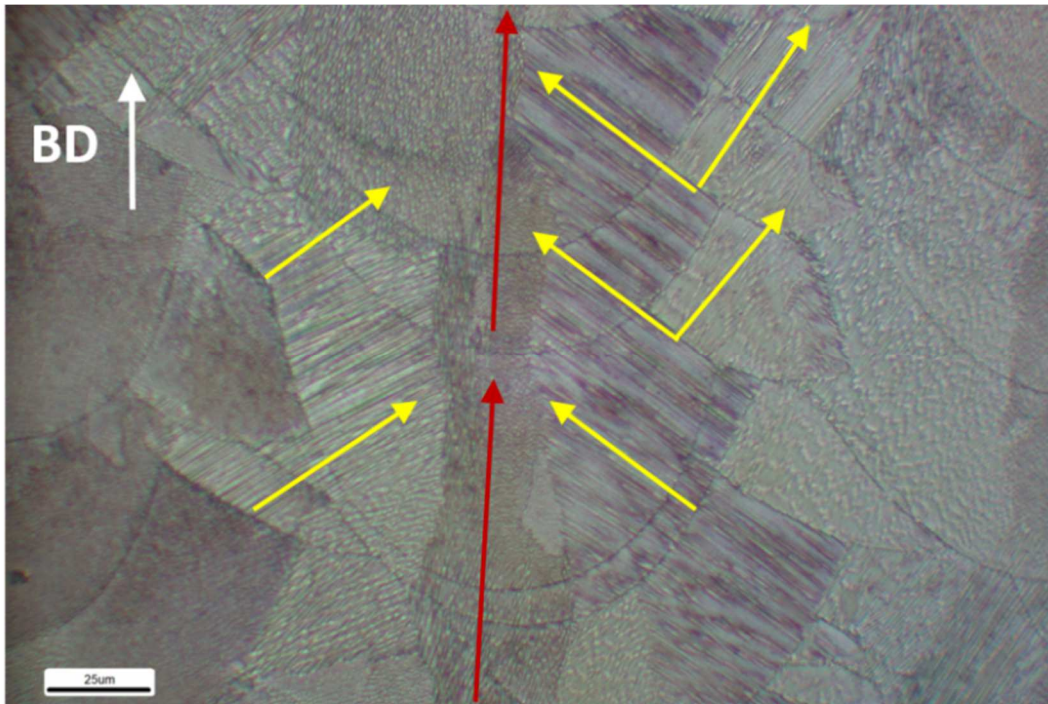
Figure III-25. IN718 LPBF Lamellar microstructure obtained through unidirectional strategy

Figure III-26 shows the crystalline details of the lamellar microstructure generated by the unidirectional strategy. For this purpose, Figure III-26a shows five zones in the sample. Zones 1, 3, and 5 correspond to side-branching growth zones, while zones 2 and 4 correspond to epitaxial growth zones. It is also possible to observe that zones 2 and 3 have darker coloring than the surrounding zones and that zones 2 and 4 are aligned with the melt pool bottom through the layers. On the other hand, Figure III-26b shows the IPF (Inverse Pole Figure) of the sample in Figure III-26a. In this case, it can be seen that each zone has its coloring, which allows us to establish that each zone corresponds to a grain with particular characteristics. Figure III-26c shows the crystalline orientation of the sample analyzed, where it can be seen that the crystals of the grains corresponding to zones 1, 2, and 3 have very similar orientations, observing a slight misorientation in the grain of zone 3 with respect to zones 1 and 5, which causes the coloring to be more orange in contrast to the reddish coloring of the grains of zones 1 and 2. However, this misorientation can be considered minimal and does not give rise to a considerable difference within the context of HAGB (High angle grain boundaries).
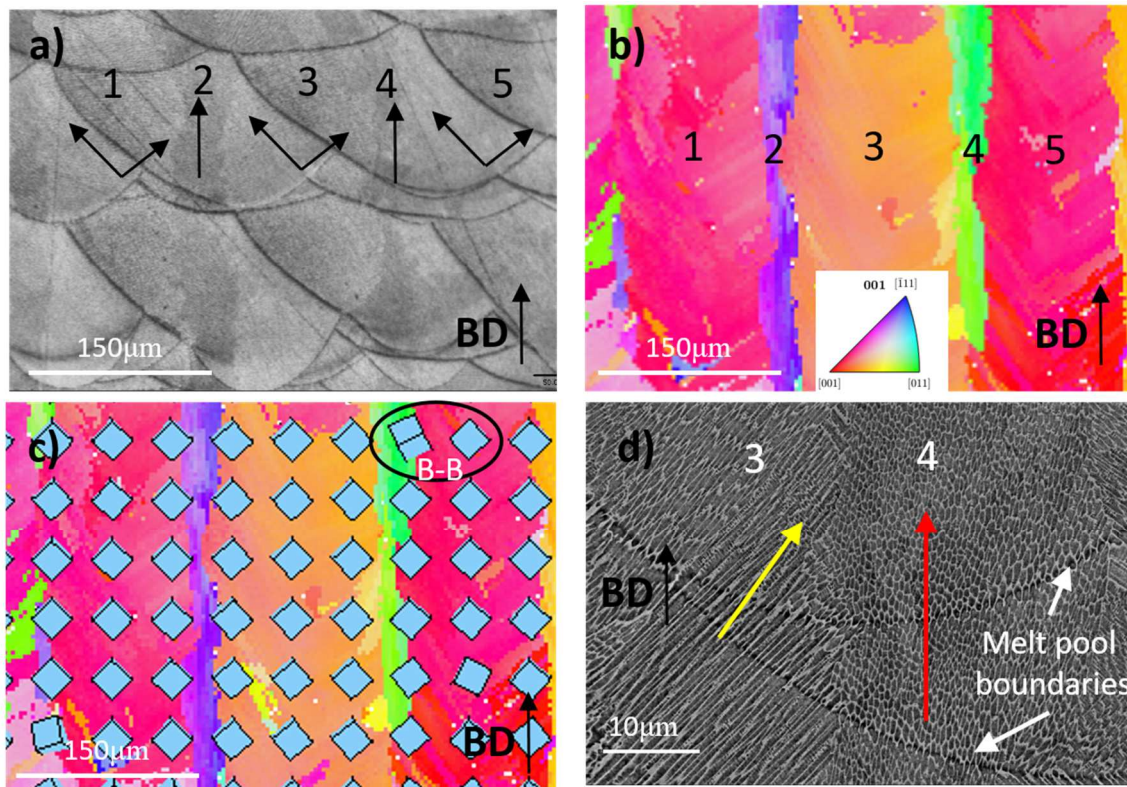
Figure III-26. IN718 LPBF lamellar microstructure zones through unidirectional strategy. a) zones in lamellar microstructure, b) IPF of lamellar microstructure, c) crystalline orientations of lamellar zones, d) SEM scan magnification of a typical R0 melt pool.

On the other hand, when observing the two cubes of the region demarcated by the oval B-B in Figure III-26c, it is possible to observe that the orientation of the left cube is significantly different from the orientation of the right cube. This is because the left cube represents the crystalline orientation of the grain corresponding to region 4, which has an epitaxial origin, while the right cube represents the crystalline orientation of region 5 based on the <011> texture created by side-branching. Figure III-26d shows the detail of dendritic growth patterns associated with each texture.

The lamellar microstructure is not the only microstructure that can be obtained from the unidirectional strategy. Figure III-27 corresponds to the second case, showing a single crystal-like structure from the unidirectional strategy with a novel beam-shape mode. Figure III-27a shows the melt pools and the AA box. the detail of the microstructure of the AA box can be seen in Figure III-27c, where it can be seen that the dendrites are joined at a 90° angle through side branching, disappearing the epitaxial texture <001>. on the other hand, Figure III-27b shows uniformity in the crystalline orientation of the sample, which confirms that it is possible to obtain single crystal-like parts from the LPBF process.
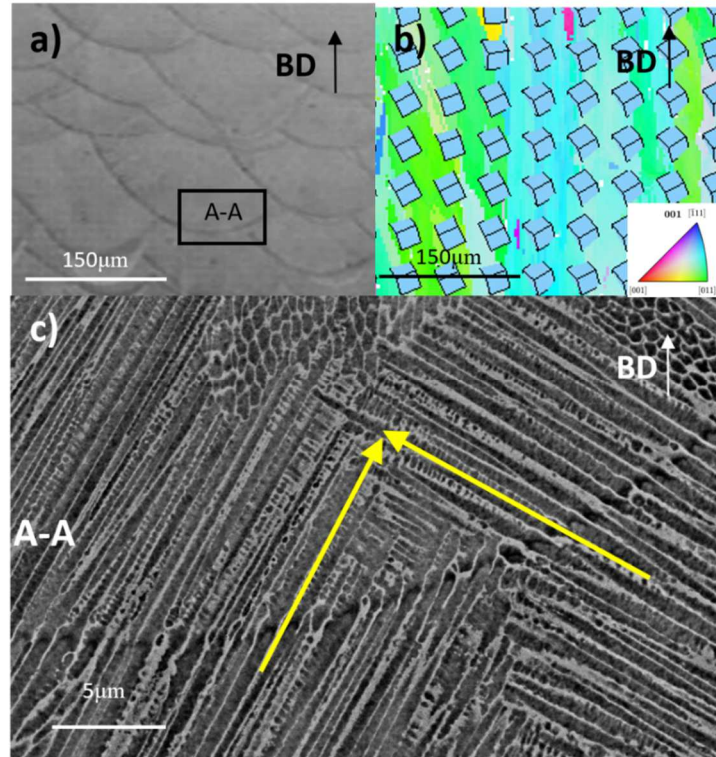
Figure III-27. IN718 LPBF single crystal-like microstructure obtained with unidirectional strategy through Gaussian mode a)melt pools by unidirectional strategy b) Crystalline orientation of single crystal-like microstructure by side-branching. c) side branching growth as the basis of single crystal-like microstructure through Gaussian mode

In addition to the Gaussian distribution, other laser beam shape modes allow the single crystal-like microstructure to be obtained. The modification of the laser energy distribution on the working surface is called irradiance (see Figure III-3) and is an alternative to VED to modify the melt pool morphology and the microstructure. These aspects are observed in Figure III-28, whereas differences and similarities can be observed related to Figure III-27. Figure III-28a shows that the melt pools obtained are shallower than the previous ones; however, Figure III-28b shows that the crystalline distribution is also uniform, allowing it to be categorized as single crystal-like. On the other hand, Figure III-28c shows that the dendritic growth is mainly epitaxial, not only in the melt pool bottom area but also along the whole melt pool perimeter, which is the main difference between the sample obtained with beam shaping and the sample obtained by Gaussian distribution (see Figure III-27). This microstructural difference is related to the fact that the beam shaping mode used for the fabrication of this sample allowed the heat distribution to have 80% of the power directed to the ring of the laser optical fiber and 20% to the core of the laser fiber. Section III.5.4 will elaborate on these topics in more detail.
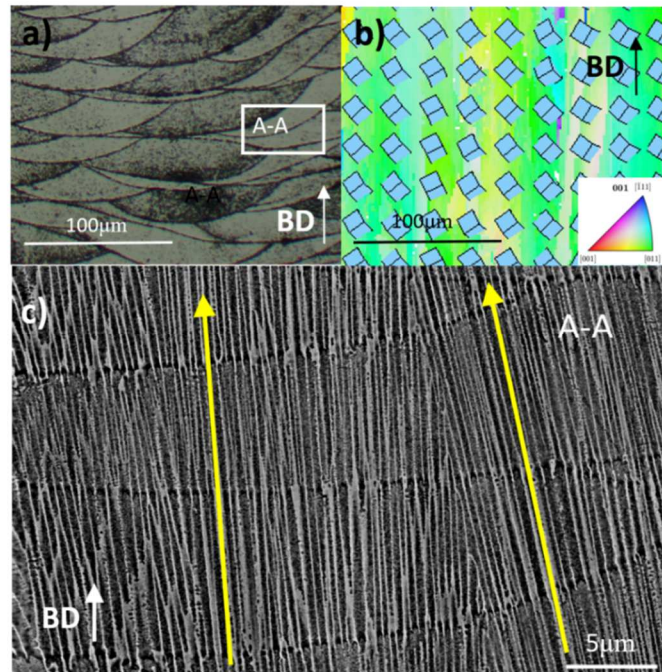
Figure III-28. IN718 LPBF Single crystal-like microstructure obtained with unidirectional strategy through beam shaping. a) melt pools by unidirectional strategy with beam shaping, b) Crystalline orientation of single crystal-like microstructure by epitaxial growth, c) Epitaxial growth as the basis of single crystal-like microstructure through beam shaping

III.5.2. Bidirectional strategy (R90)

In the bidirectional strategy R90, the tracks of one layer are deposited successively on top of the tracks of the previous layer but changing the angle of orientation of one layer with respect to the other by 90º (hatch rotation angle), as shown in Figure III-29. the tracks within the same layer are deposited alternating their directions.
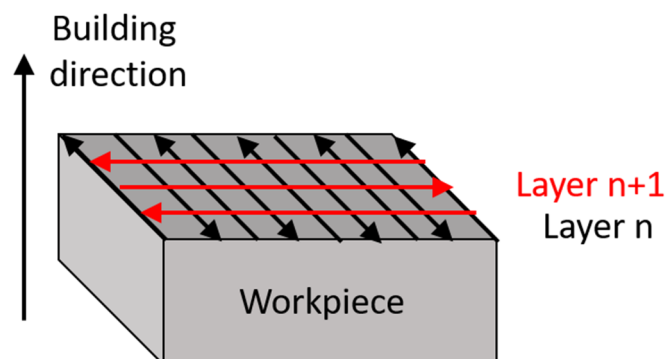
Figure III-29. Bidirectional strategy scheme(Hatch rotation angle = 90º)

The 90-degree rotation between layers is visible in Figure III-30a for the XZ plane and Figure III-30b for the XY plane.
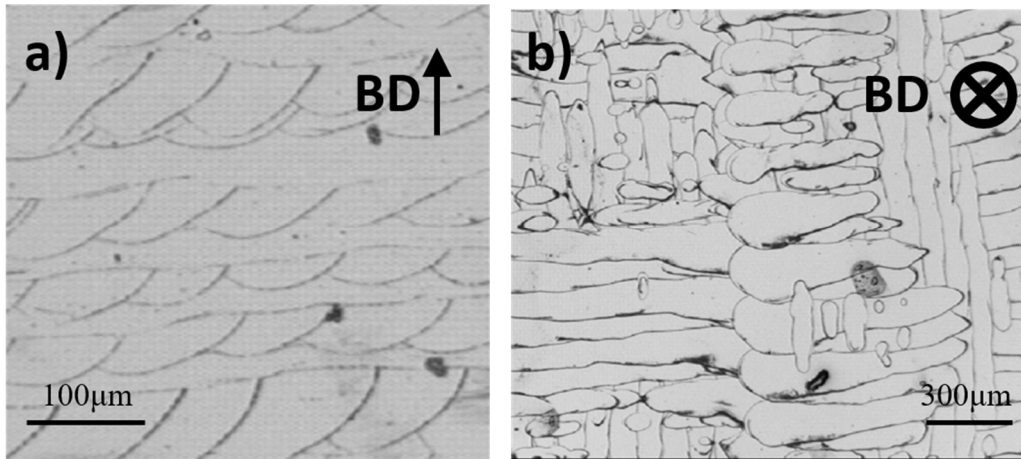
Figure III-30. IN718 LPBF melt pools for bidirectional strategy. a) melt pools in the XZ plane, b) melt pools in the XY plane

In most cases, the bidirectional strategy obtains a <001> texture (see Figure III-32). Figure III-31a shows the melt pools of an R90 sample manufactured with a non-gaussian beam shape. It can be seen that the crystalline arrangement obtained with the bidirectional strategy is uniform (single crystal) with a low misorientation angle (Figure III-31b), which indicates that the bidirectional strategy is another option to obtain the single crystal-like microstructure. These aspects are best understood by looking at the ODF of the analyzed sample in Figure III-32, where a single crystal texture with well-defined poles can be seen, indicating a significant level of texture intensity.
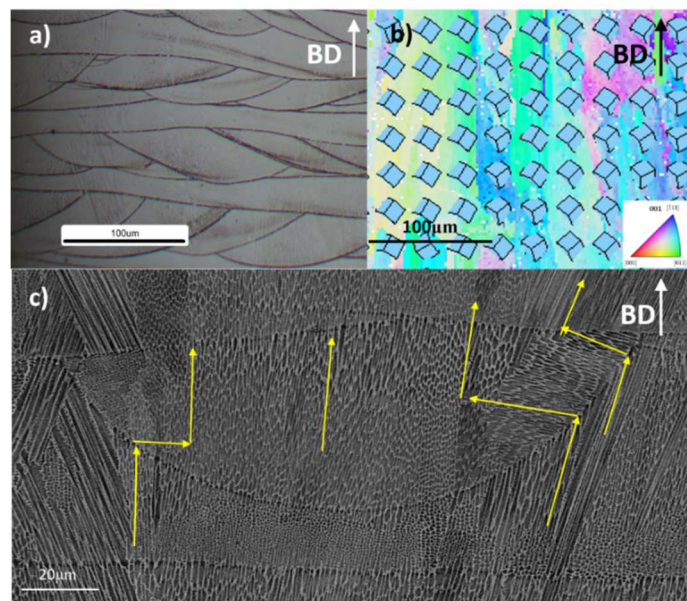
Figure III-31. IN718 LPBF Single crystal-like microstructure obtained with Bidirectional strategy. a) melt pools by Bidirectional strategy, b) crystalline orientation of single crystal-like microstructure by side-branching, c) side branching and epitaxial growth as the basis of a single crystal-like microstructure

To understand why the bidirectional strategy yields a uniform crystalline arrangement, it is vital to understand the characteristics of dendritic growth. These characteristics can be seen in Figure III-31c where it can be seen that there are two groups of dendrites. The dendrites in the central zone maintain epitaxial growth through several layers, and the dendrites in the lateral zones that initially grow vertically, then grow horizontally by side branching and then vertically again using side branching, which can be considered a double 90° zigzag.
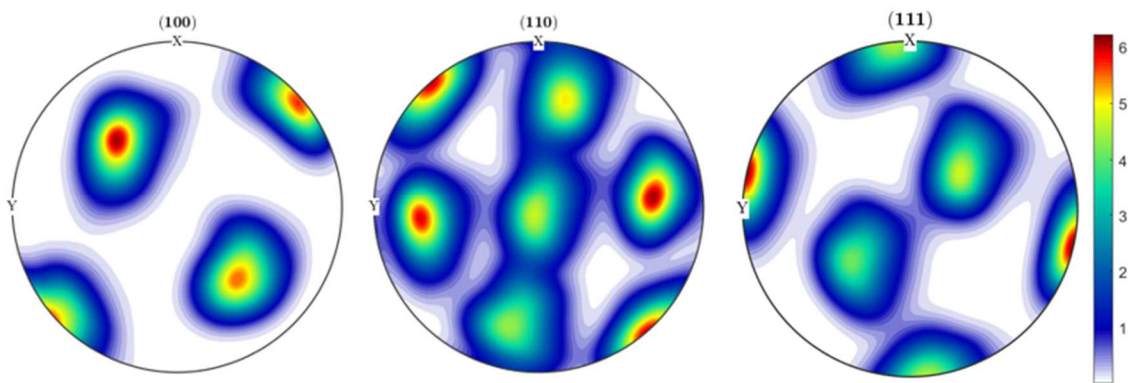
Figure III-32. ODF pole figure of IN718 LPBF sample obtained with bidirectional strategy R90

The diagram in Figure III-33 provides a better understanding of how the dendrites of an n-layer melt pool interconnect with the dendrites of the n+1 layer (Marattukalam et al. 2020). In Figure III-33a, the dendrites are represented as blue arrows for layer n. In these, it can be seen that the dendrites in the central zone are vertically oriented (epitaxial), while the dendrites in the lateral zones are horizontally oriented until they reach the central zone. This arrangement means that when the track of layer n+1 is fused (see Figure III-33b), the dendrites of layer n (blue arrows) function as seed grains for the dendrites of layer n+1 (red arrows). In this way, the blue dendrites in the central zone continue to grow epitaxially, while the blue lateral dendrites become new lateral dendrites for the new melt pool (but rotated by 90) or vertical dendrites, depending on their location through side branching in both cases.
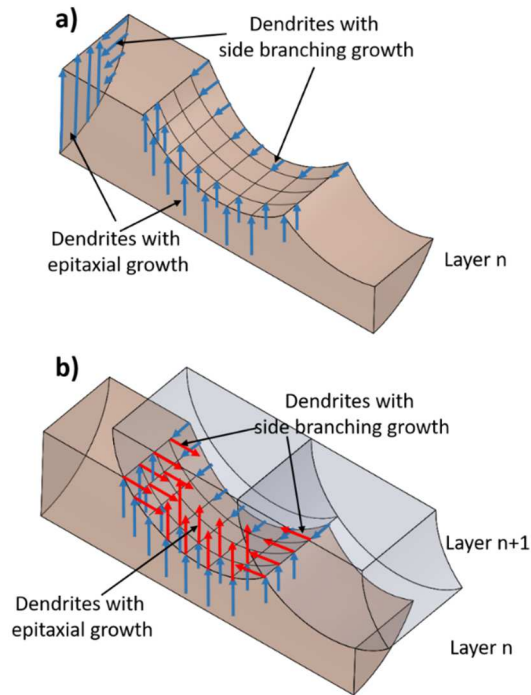
Figure III-33. Dendritic growth pattern for bidirectional strategy scheme. a) dendrites orientation for layer n, b) dendritic growth in layer n+1 from seed dendrites of layer n

Based on the above, it is possible to theorize that the bidirectional strategy creates dendritic columnar growth zones at the intersections of tracks, as shown in Figure III-34. These intersections give rise to nuclei that retain similarities in crystalline orientation and allow the single-crystal texture to be obtained.
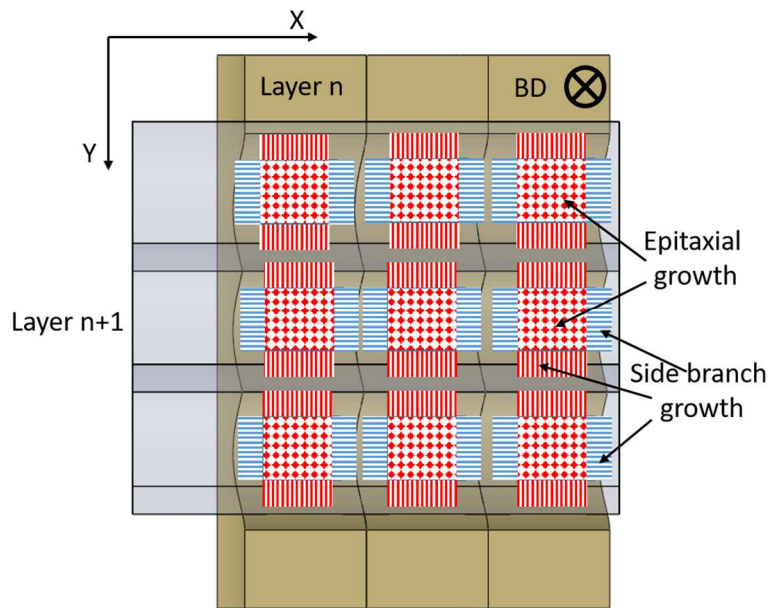
Figure III-34. epitaxial and side branching growth cores in the track's intersections for an R90 strategy scheme

III.5.3. Rotational strategy (R67)

In the rotational strategy, the tracks of one layer are deposited successively on top of the tracks of the previous layer, changing the layer's tracks orientation angle by 67° (hatch rotation angle) related to the previous layer, as shown in Figure III-35. The tracks within the same layer are deposited alternating directions.
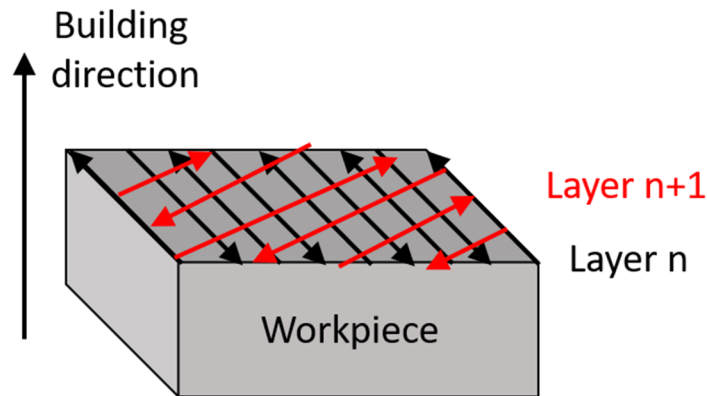
Figure III-35. Rotational strategy R67 scheme (hatch rotation angle = 67°)

Figure III-36 shows the melt pool pattern when using the rotational strategy. It can be seen that the shape and size of the melt pools change layer by layer as a result of the changes in section size due to the hatch rotation angle.
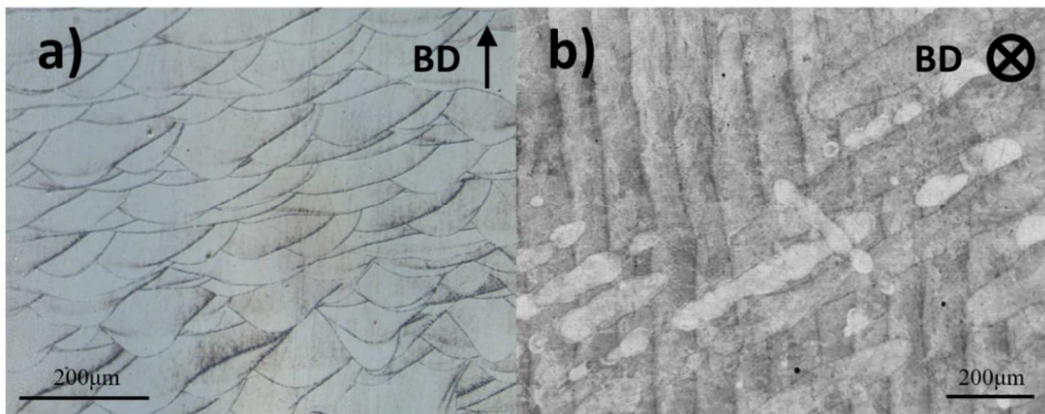
Figure III-36. IN718 LPBF melt pools for Rotational strategy. a) melt pools in the XZ plane, b) melt pools in the XY plane

The microstructure of the parts obtained by the R67 strategy presents a high number of primary crystalline orientations due to the rotation of the tracks layer by layer. The number of crystalline orientations can be higher or lower depending on the volumetric energy density or the

irradiance level. For the case of parts fabricated with high VED, it is prevalent to observe the spread of epitaxial dendritic growth(see red arrows) across several layers, as seen in Figure III-37a.
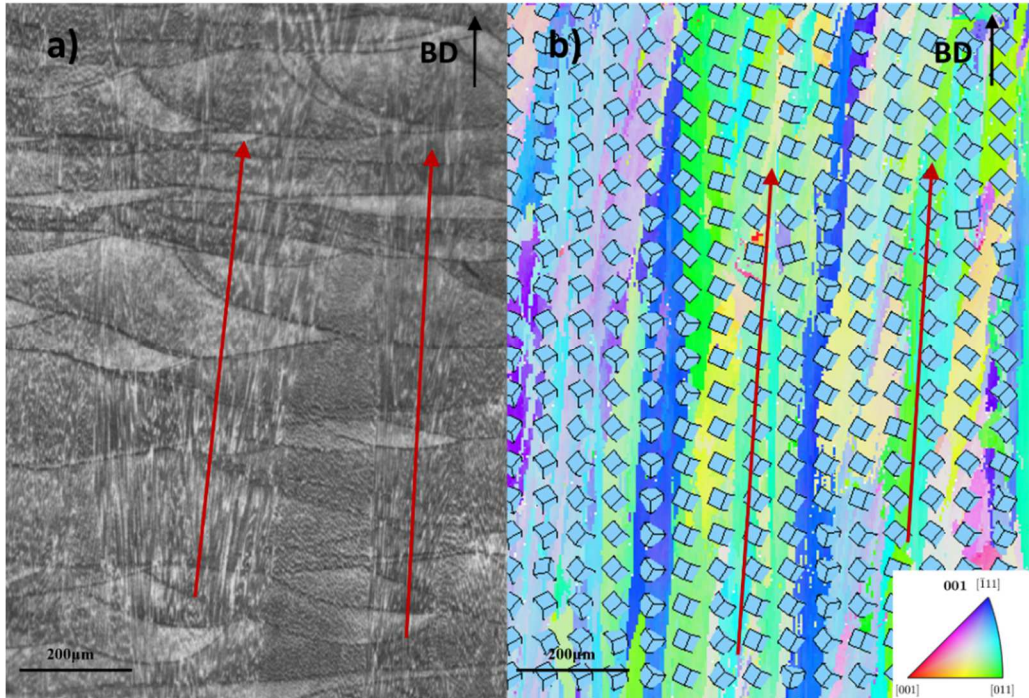
Figure III-37. IN718 LPBF Dendritic epitaxial growth spread across several layers when using rotational strategy and high VED

These dendrites form grains with crystalline homogeneity, as shown in Figure III-37b, which allows us to infer that the connection of the dendrites layer by layer not only influences the formation of columnar grains but also the crystalline homogeneity in the sense of grain growth.

The rotational strategy is strongly associated with a ring-like texture. The diagram in Figure III-38 eases the understanding of the mechanism that gives rise to this type of texture. For this purpose, the first row of the diagram shows four regions of the complete sample (IPF). In turn, each region belongs to different columnar grains of the sample. The second row of the diagram shows the ODF (pole figures) of each of the four regions mentioned above. Each ODF has small rotations with respect to the others but with a common pole. By overlaying the ODF's of the four regions previously mentioned, it can be seen that together they form a ring that rotates around the main pole, which resembles the ring-like texture of the complete sample that can be seen at the bottom.
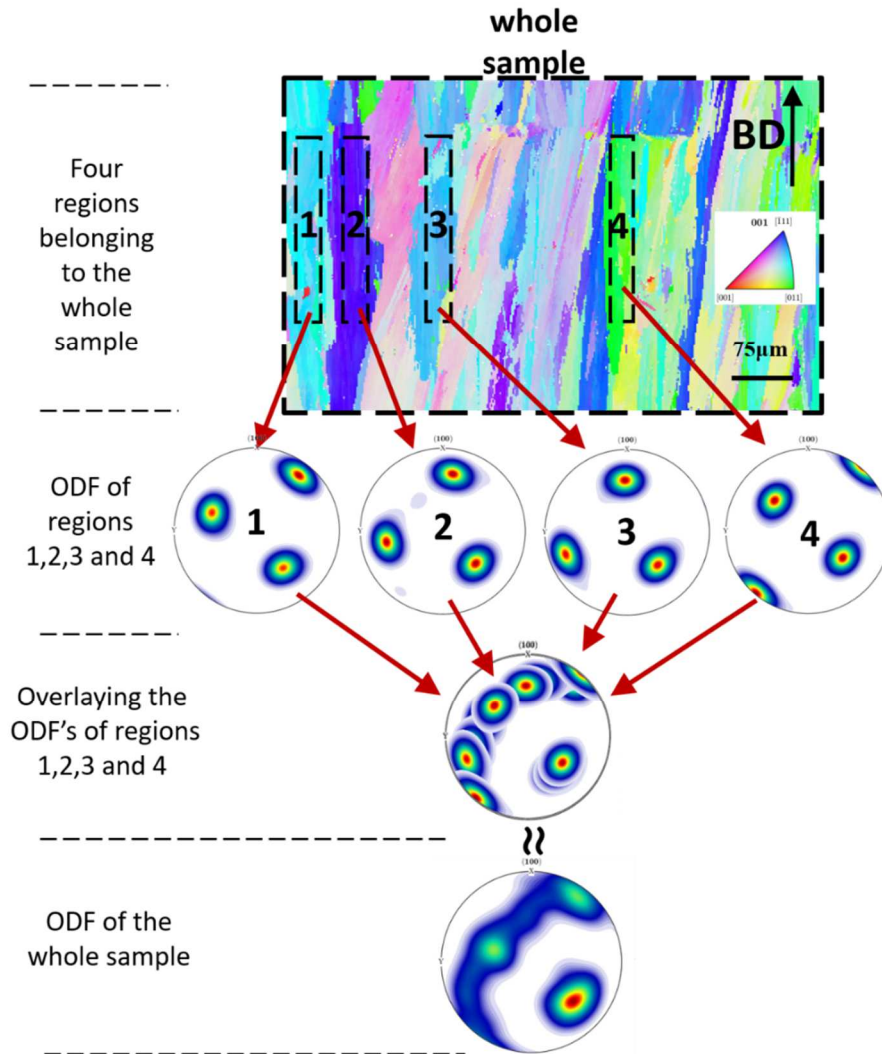
Figure III-38. Ring-like texture obtained with rotational strategy and high VED scheme

It is clear then that the ring-like texture typical of rotational strategy arises from the formation of columnar grains with a clearly defined pattern of crystalline rotation between them. Although the rotational orientation of the tracks layer by layer is made so that the material is polycrystalline and isotropic, the formation of the columnar (crystalline homogeneous) grains makes the material not completely isotropic but only transversely isotropic. This fact allows the material's mechanical properties to be very different between the direction parallel to the building direction and the directions perpendicular to the building direction.

Figure III-39 shows three melt pools corresponding to different layers and rotated at 67° to each other. In the center of the intersection of the melt pools, there is a common core in which the epitaxial dendritic growth develops, giving rise to the columnar grains mentioned in Figure III-37 and Figure III-38.
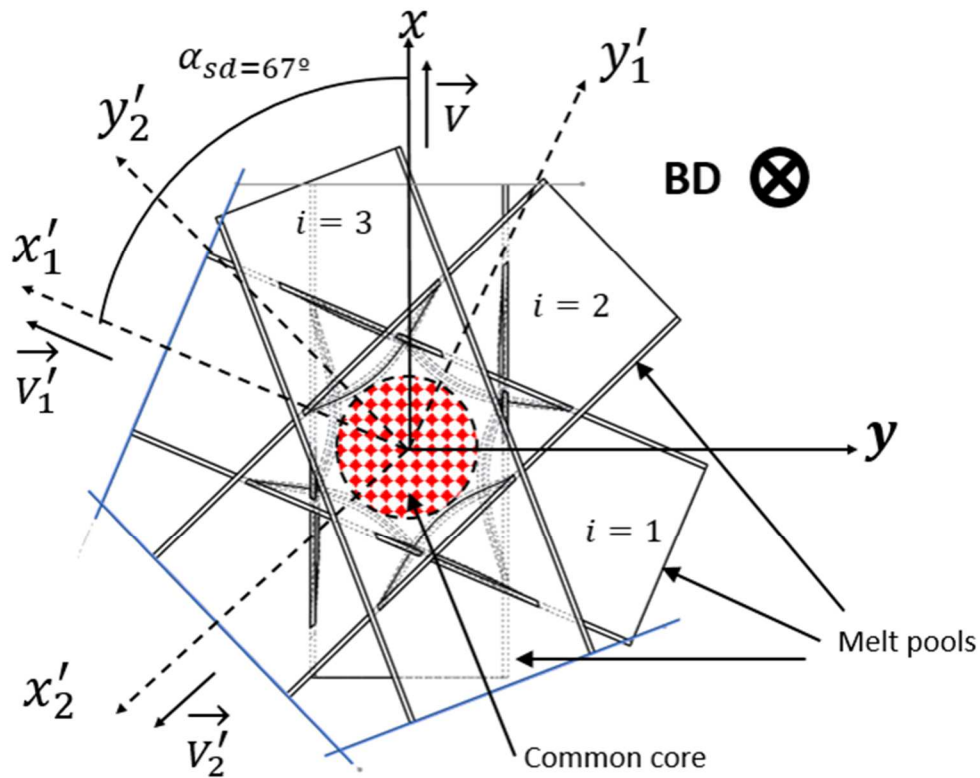
Figure III-39. Common core for epitaxial growth in rotational strategy

Notably, the common core shown in Figure III-39 only occurs under certain operating conditions. As mentioned in the previous section, these operating conditions are usually related to high VED or beam shape modes that facilitate epitaxial growth. However, the pattern of columnar grains rotated in relation to each other allows an understanding of the nature of the ring-crystal texture.

For low VED R67 manufactured parts, the crystalline dispersion is much higher and, therefore, the grain refinement because the higher cooling ratio allows the dendrites to grow faster, significantly increasing the level of competitive grain growth and thus increasing the density of the geometrically necessary dislocations (GND's) see Figure III-40. The multiple crystalline orientations observed in Figure III-40a correspond to the dispersion of the dendritic growth observed in Figure III-40b, represented by the yellow arrows. Figure III-40C shows the ODF of this sample which has low texture intensity, indicating that the low VED R67 strategy allows for obtaining polycrystalline-like materials. These, in turn, have a lower level of anisotropy compared to lamellar or single crystal-like microstructures.
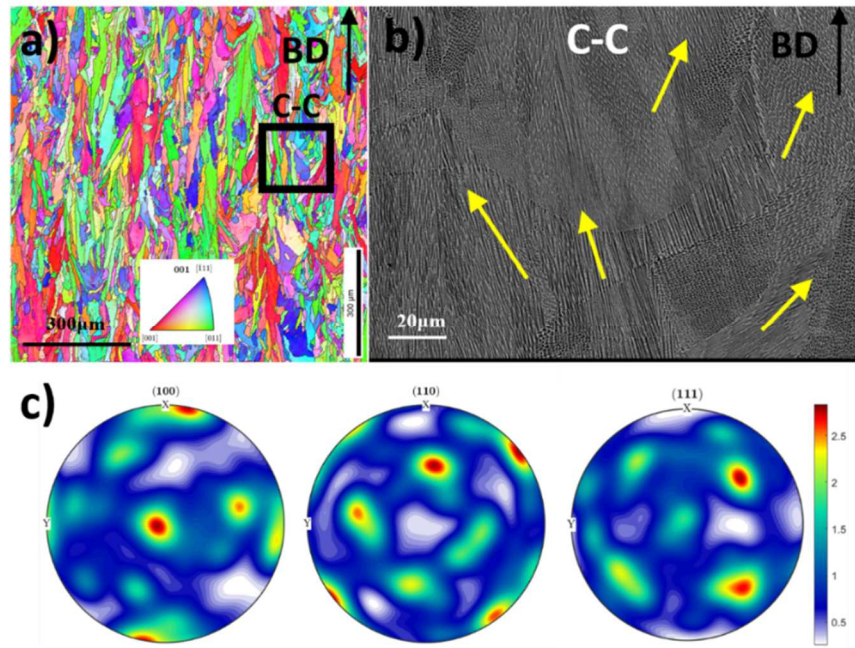
Figure III-40. IN718 LPBF low VED sample. a) Inverse pole figure for IN718 LPBF low VED sample, b) IN718 LPBF SEM scan for low VED sample characterization, C) IN718 LPBF ODF pole figure for low VED sample

III.5.4. Beam shaping effect on density(porosity) and melt pool shape of IN718 LPBF

Sixty samples (see Figure III-41a) were manufactured for microstructural characterization using three laser scanning strategies, four beam shaping modes, and five levels of laser speed. The details of the beam shape modes used are shown in Figure III-41b.
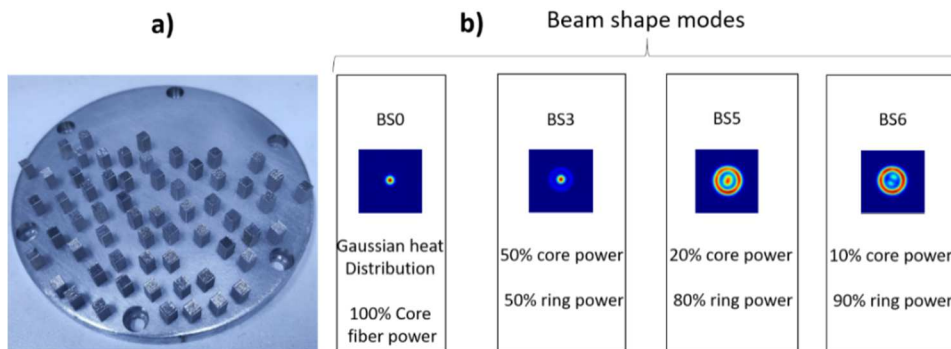
Figure III-41. manufactured samples by beam shaping. a) sixty samples manufactured in a 3D NT machine with different beam shape modes, b) beam shape modes scheme

The samples were fabricated on a 3DNT multi-mode machine capable of generating seven beam-shape modes. The fixed and variable parameters of the LPBF process are detailed in table 2.

Table III-2. LPBF parameters for IN718 sample manufacturing

Fixed parameters	
Material	IN718
Hatch distance(µm)	70
Layer thickness(µm)	30
Laser power(W)	200
Replicates n	1
Varied parameters	
Hatch rotation angle(º)	0, 67,90
Scan speed(mm/s)	500,750,1000,1250,1500
Beam shape BS(-)	0,3,5,6

Figure III-42 shows the density of the 60 samples analyzed under the evaluated beam shaping modes. In the BS0 (Gaussian) mode, a significant influence of the laser speed on the density is observed. It can also be seen that the density levels are acceptable only for values higher than 1000 mm/s. On the other hand, it can be seen that the BS3, BS5, and BS6 modes (which correspond to power distribution between the core and the ring, as shown in Figure III-41a) achieve high-density levels for all speed levels and all laser scanning strategies.
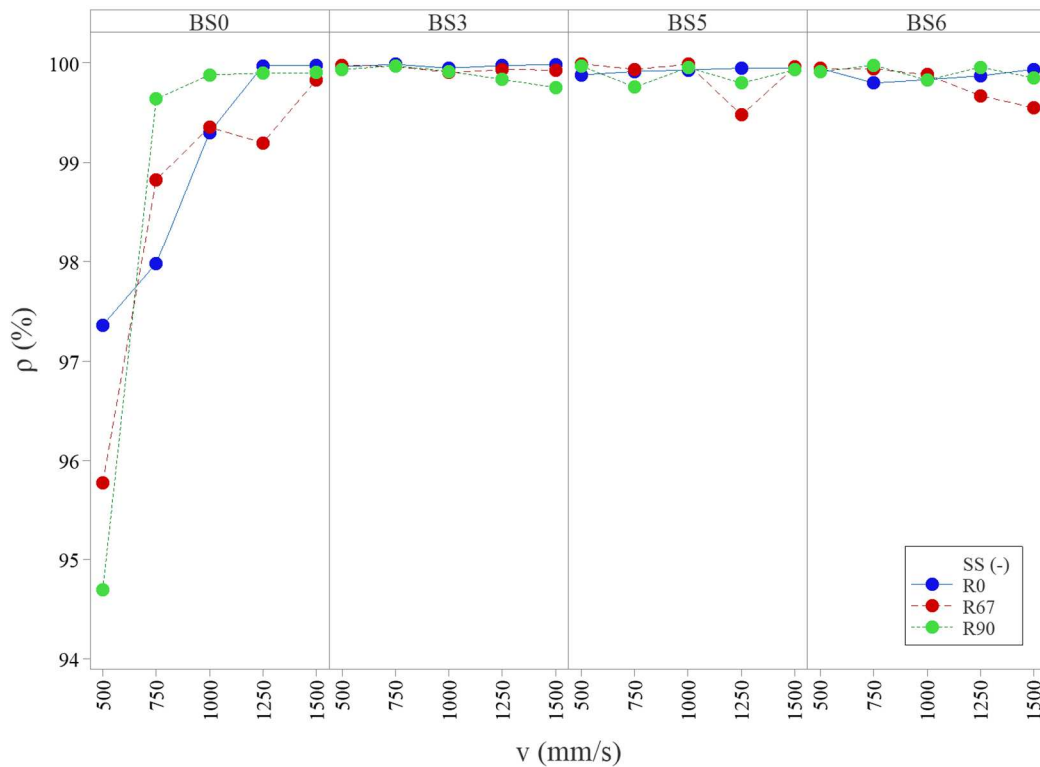
Figure III-42: Densification for manufactured samples

For the melt pool dimensions analysis, measurements were made on the samples manufactured with the R0 strategy, considering that this strategy allows for measuring the dimensions more reliably. For this purpose, measurements were taken of the melt pool in terms of height h and width w and measurements of the non-remelted area in terms of height c, width b, and the radius of curvature of the melt pool bottom (see Table III-3). The parameter c/b is related to the remaining microstructure, as will be discussed later. The parameter 2*r/w is introduced to differentiate the conduction mode from the conduction-keyhole transition mode, considering that it is possible to obtain a h/w ≈0.5 for conduction melt pools and conduction-keyhole transition; however, only a pure conduction melt pool has a 2*r/w ≈ 1. The samples fabricated with the BS0 (Gaussian) mode presented a conduction-keyhole transition mode mainly and a lower percentage of keyhole-like melt pools. On the other hand, the samples fabricated with the BS3, BS5, and BS6 modes presented conduction and low conduction modes. Table III-3 shows a schematic of some melt pool shape patterns and the non-remelted area for the R0 strategy observed in the samples of this report.

Table III-3. Melt pool shape patterns and non-remelted area patterns.
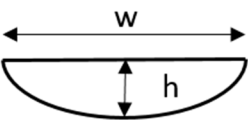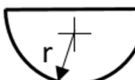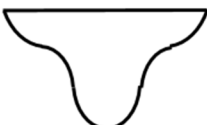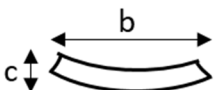
	Low conduction	Conduction	Conduction- key hole transition	Keyhole-like
Melt pool Shape patterns				
Non remelted área shape patterns				
Geometric shape Parameters relations	2*r/w>>1 h≈z h/w <<0,5 c/b<<1	r/w ≈ 1 h>z h/w ≈ 0,5 c/b ≈ 1	2*r/w<<1 h>z h/w ≈ 0,5 c/b ≈ 1	2*r/w < 1 h>>z h/w >>0,5 c/b > 1

Figure III-43 shows the effect of the beam shape mode on the h/w parameter. For the Gaussian mode (BS0), there is a reduction in the h/w parameter as v increases from h/w values > 0.5 for v=500-750 mm/s to values close to h/w ≈ 0.4 for v=1000-1500 mm/s. For h/w > 0.5, the development of the keyhole mode is observed, which is consistent with the low-density levels observed for v=500-750 mm/s (fig 1). For v=1000-1500 mm/s, the melt pool developed the transition mode from conduction to the keyhole. This fact can be verified by evaluating the parameter 2*r/w, where r is the bottom radius of the melt pool. Figure III-44 shows that for the Gaussian mode, the parameter 2*r/w remains almost constant around 0.4, which implies that, even if the h/w parameter reaches values lower than 0.5, the melt pool profile cannot be considered circular. This aspect is essential and affects the microstructure.
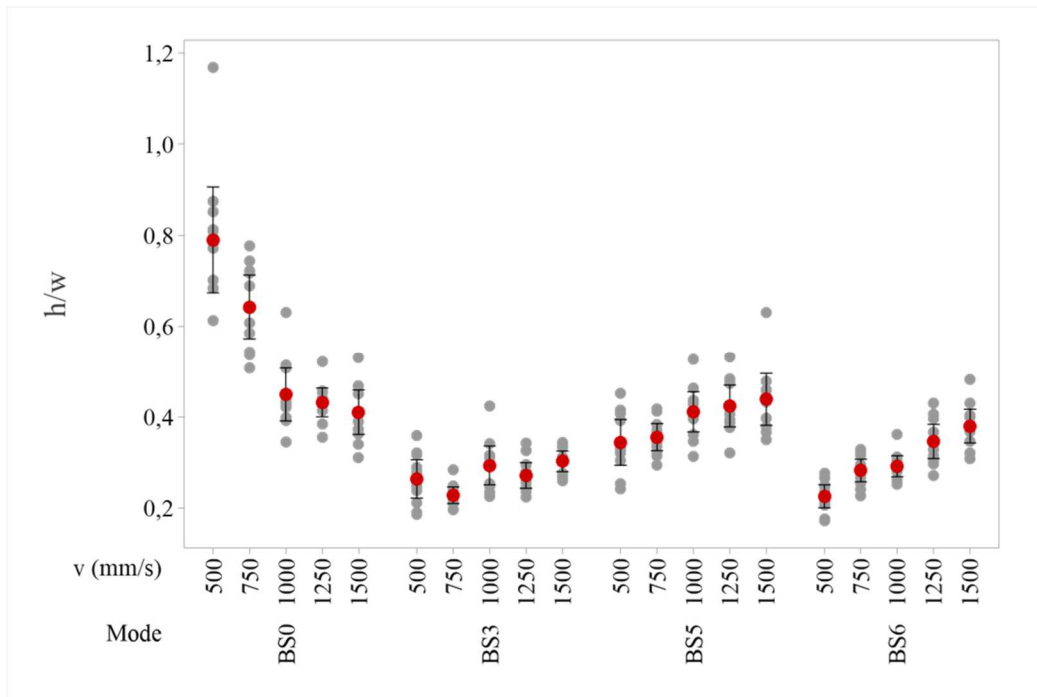
Figure III-43. h/w parameter comparison.

The BS3, BS5, and BS6 modes show an opposite trend to the Gaussian in the effect of v(mm/s) on the h/w parameter. In the BS3 mode, a trend transition is seen, where the increase of h/w concerning v (mm/s) is irregular. On the other hand, BS5 and BS6 modes have a clear trend of increasing h/w as a function of increasing v (mm/s). It is essential to note that the h/w values of BS5 are slightly higher than those of BS6, which is related to the higher percentage of power in the ring for this mode compared to the other modes. For the BS5 and BS6 modes, the parameter 2*r/w decreases as v (mm/s) increases towards values close to 1, which shows the transition from low conduction to conduction mode (see Figure III-44).
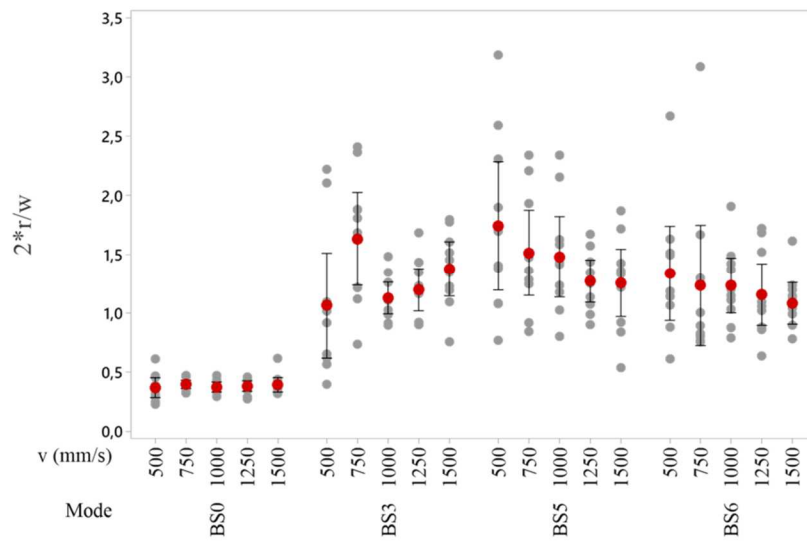
Figure III-44: 2r/w non-remelted area parameter.

Figure III-45 hows the c/b parameter for the experimental configurations studied. It can be seen that the trend is similar to that of the h/w parameter but shallower. It is interesting to note that in the BS3, BS5, and BS6 modes, the velocity has little effect on c/b, observing that the levels between the different modes are similar, especially between BS5 and BS6 modes. This implies that the beam shape mode affects the non-remelted shape area more than the laser velocity.
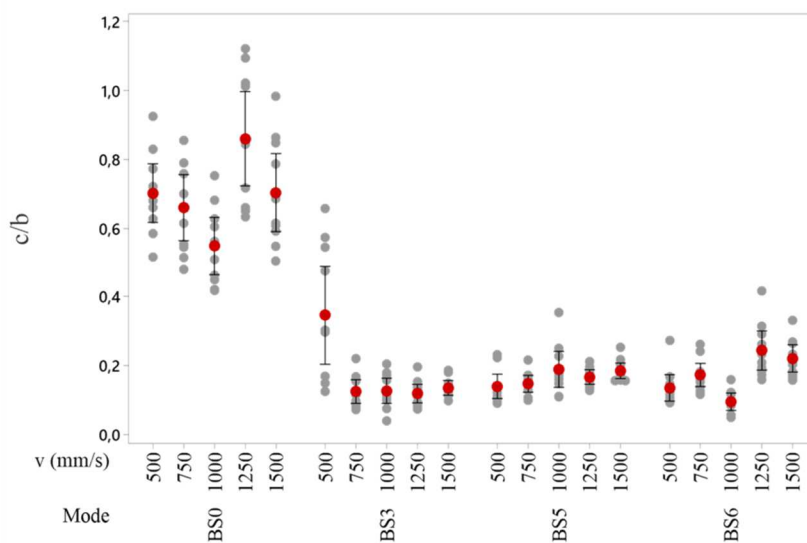
Figure III-45. c/b non-remelted area parameter.

III.5.5. Beam shaping effect on the microstructure of IN718 LPBF

The effect of volumetric energy density under the Gaussian mode on dendritic growth patterns is widely reported in the literature. However, the effect of the interaction of irradiance and volumetric energy density on dendritic growth patterns has not been sufficiently reported yet. Figure III-46 shows a comparative scheme of the effect of the evaluated modes on the dendritic growth patterns for the R0 strategy, considering that the dendritic growth path through several layers is best observed for this strategy. The first column corresponds to the Gaussian mode (BS0) at a v=1000 mm/s. the second column corresponds to the BS3 mode with v=1000 mm/s, and the third column corresponds to the BS5(v=1000 mm/s) and BS6(v=1500 mm/s) modes. BS6 mode is presented with v= 1500 mm/s instead of v=1000mm/s because, at that laser speed, a dendritic pattern similar to the BS5 mode is observed. This aspect will be discussed in more detail later.

The first row shows the icons of the irradiance modes (beam shape modes) evaluated and the laser speed for each case. The second and third rows show melt pool diagrams in the top and front view, with arrows representing the orientation of the dendrite growth, which is closely related to the orientation of the thermal gradient for each case and the preferred crystallographic orientation of the seed grain. The fourth row shows the detail of the grain and sub-grain boundaries; grain boundaries HAGB's (10 degrees of misorientation) in black and the LAGB's (1 degree of misorientation) subgrain boundaries in blue. And the fifth-row show SEM micrographs for each sample.

The samples manufactured under the Gaussian mode developed mainly a lamellar-type microstructure characterized by alternating two texture types. A <011> texture is developed in the melt pool lateral fringes under the side branching growth mechanism (green arrows), and a <001> texture (red arrows) is associated with the bottom of the melt pool. For <011> texture, the subgrain boundaries are oriented at 45 degrees related to BD (chevron pattern). On the other hand, texture {001}, represented by the elongated grains arising from the bottom of the melt pools, has mainly epitaxial dendritic growth. The SEM micrograph shows that the <001> texture is primarily cellular for this cross-section, confirmed by the higher subgrain boundary density of these grains, represented by the blueish color.

In the BS3 mode (central column), the level of competitive growth is higher than in the Gaussian mode. It is observed that the dendritic growth mechanism is mainly epitaxial; however, the dendrites do not have a defined orientation, as dendrite orientations have a range of about 30 degrees around the BD direction (see SEM micrograph). It is also observed that a good percentage of the dendrites grow normal to the surface of the melt pools, which is indicative of the influence of the melt pool curvature as related to the interaction of the thermal gradient and the preferred crystallographic direction. The effect of dendrite orientation growth variation is observed in the orientation of the subgrain boundary (blue lines). It can be seen that although the grains have a columnar shape and orientation quite close to the BD direction, they are formed by subgranular structures and boundaries mostly tilted to the BD direction.
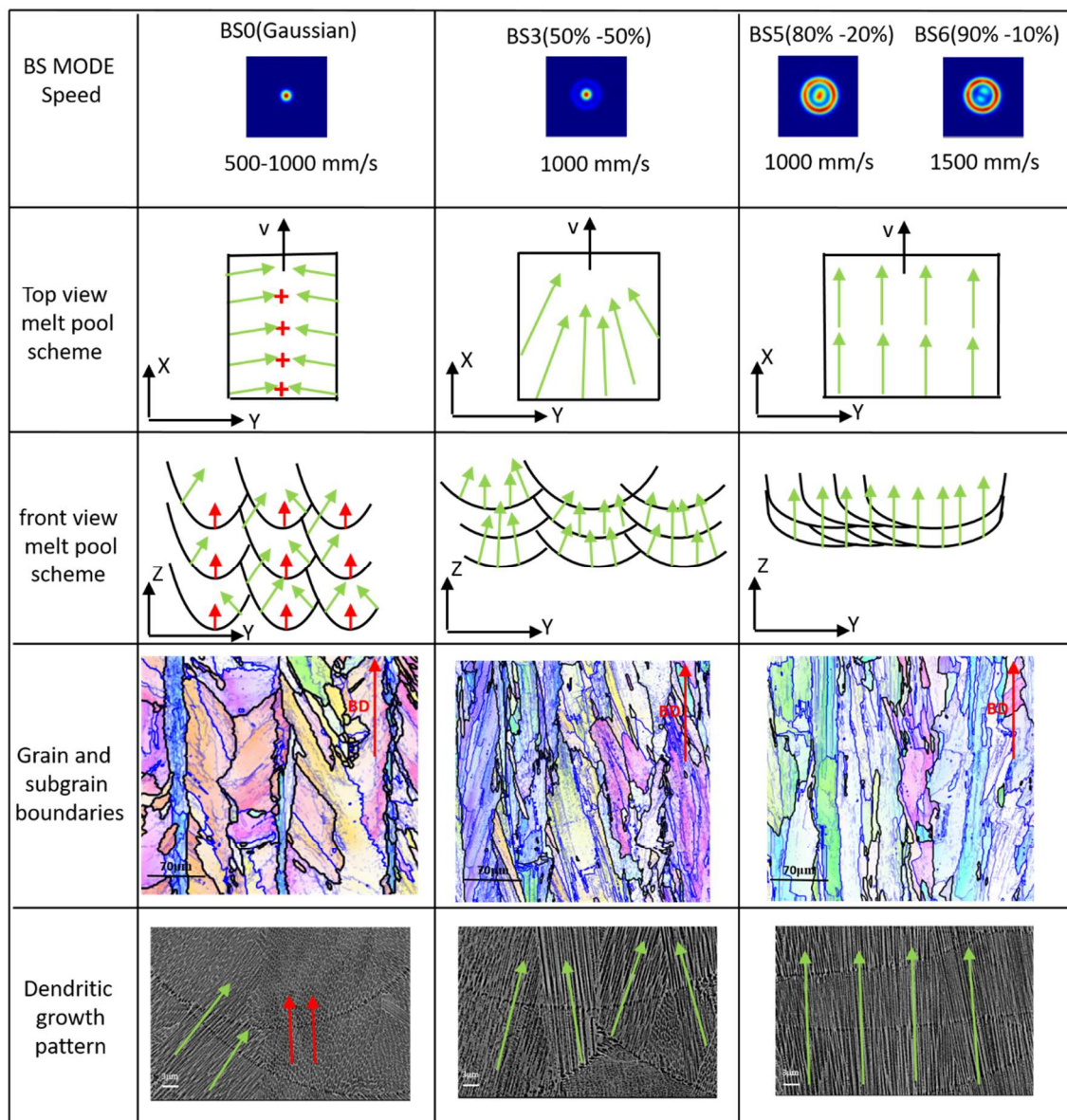
Figure III-46: Effect of beam shape mode on grain growth mechanism and developed textures

On the other hand, modes BS5 and BS6 presented a unique melt pool morphology, which consists of a flatter melt pool bottom and a dendritic growth more aligned with the building direction, as shown in the SEM micrograph. It is also observed that the level of competitive grain growth is lower than BS0 and BS3 modes, evidenced by a lower density of subgranular boundaries (light blueish color). The subgranular boundaries are more aligned with the BD, and the major grain axis size is larger than for the other modes. The dendritic growth mechanism is mainly epitaxial, spreading across several melt pool layers.

Figure III-47 shows a quantitative comparison of the grain boundary density for two scenarios. The first scenario is presented in Figure III-47a; it shows the effect of the interaction between the beam shape mode and the scanning strategy on grain boundary density at a laser velocity of v=1000 m/s. This figure shows that the effect of irradiance is significant on grain size. For the BS3, BS5, and BS6 modes, the grain boundary density is lower than the Gaussian mode (BS0) for most cases, especially for the R0 and R90 strategies.

In the second scenario (Figure III-47b), the effect of the interaction between the irradiance (mode) and the laser velocity v on grain boundary density is exposed. It can be seen that interactions for each mode-laser speed group result in a different response of the grain boundary density. The BS0 mode presents very similar density values for the first two levels and decreases for the third speed level. On the other hand, the BS3 mode has a progressive increase in grain boundary density versus laser speed. The BS5 mode reaches similar values for levels 2 and 3, and the BS4 mode presents similarities between levels 1 and 3 and a high grain boundary density for level 2 (v=1000 mm/s). The BS5 reached the lowest levels of grain boundary density for all the laser speed levels, which is also reflected in the larger grain size for the BS5 mode samples.
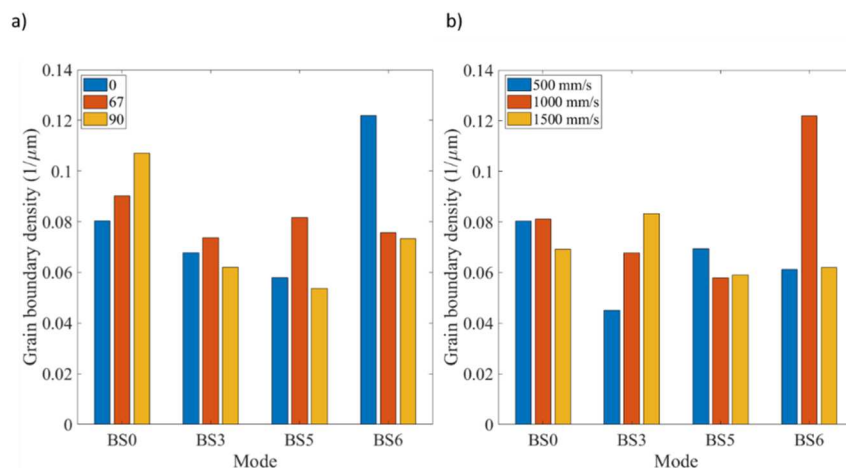
Figure III-47: Grain boundary density by mode. a) mode vs. laser strategy, b) mode vs. laser speed

The difference in grain size for the BS0 and BS5 mode samples can be seen in Figure III-48, where the grain boundaries are formed by the black lines (considering a misorientation angle of 10 degrees for both samples). Both figures correspond to samples manufactured with laser speed v=1000 mm/s and R0 strategy, considering that Figure III-48a corresponds to the BS0 (Gaussian) mode and Figure III-48b to the BS5 mode. BS0 sample shows a lamellar microstructure and a maximum grain width of 140 µm, while the BS5 sample shows a more significant thickening and elongation of the grains with widths reaching 300 µm.
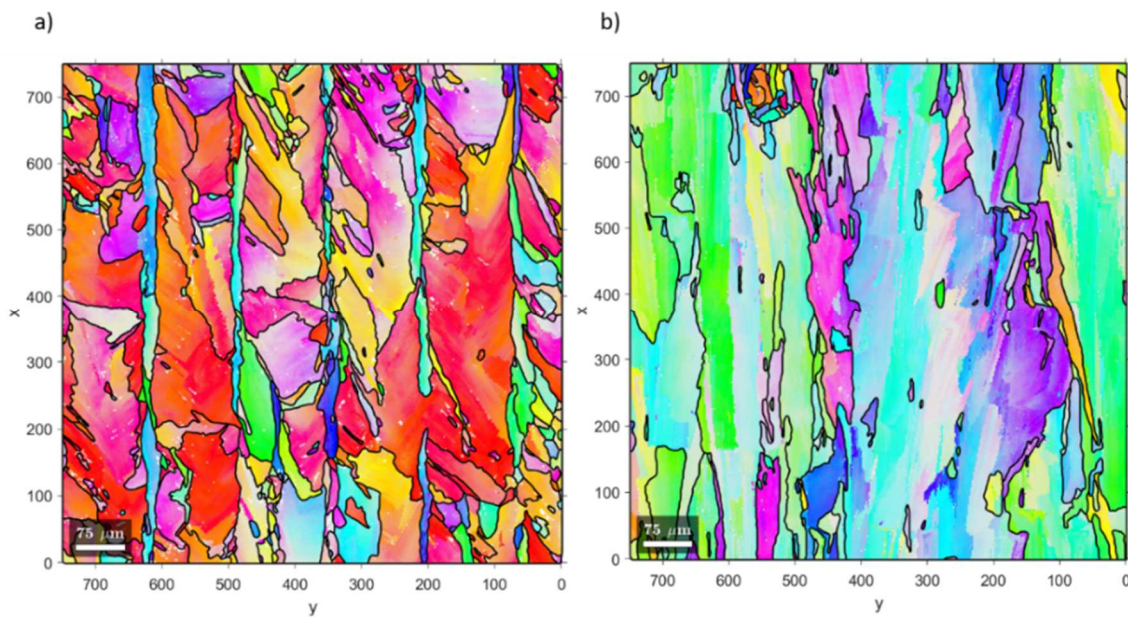
Figure III-48: Grain morphology comparison for R0 at v=1000 mm/s. a) BS0 mode, b) BS5 mode

Figure III-49 shows the {001} pole figures for different combinations of beam shape mode, laser strategies, and laser velocities. Figure III-49a shows the beam shape mode and the laser strategy interaction for a fixed laser velocity (v=1000 mm/s). The first column corresponds to the R0 strategy; in this strategy, the two previously mentioned textures (011 and 001) can be seen for the Gaussian mode (BS0). Although the intensity of the poles corresponding to texture 011 is relatively high, the overall texture index of the sample is low since a significant volumetric fraction of the crystals is part of texture <001>.
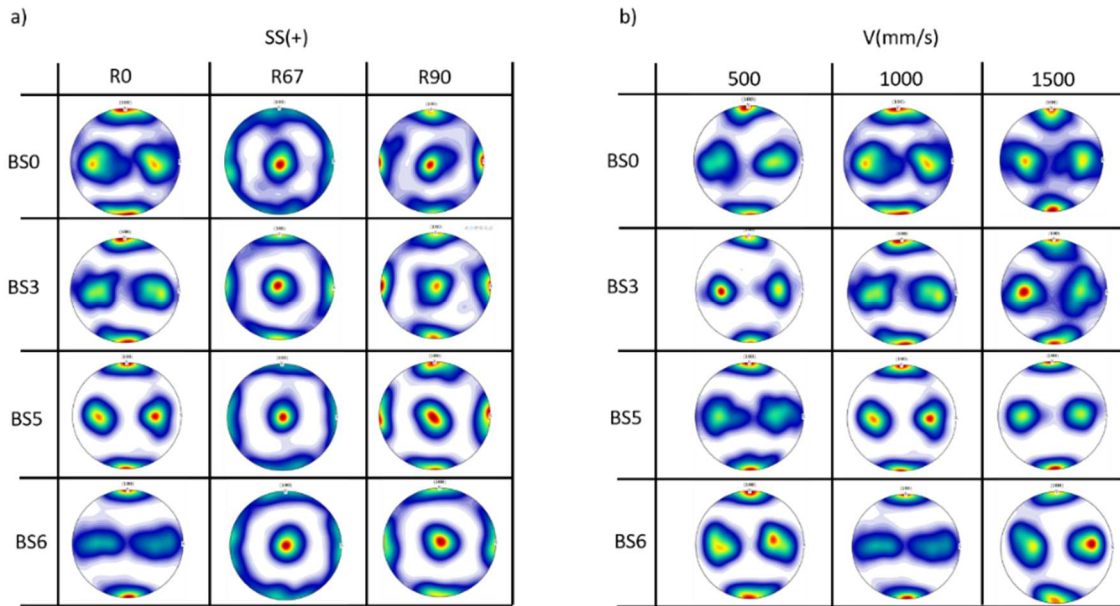
Figure III-49. 001 Pole figures comparison. a) beam shaping mode Vs Scanning strategy for v=1000 mm/s, b) beam shaping mode Vs laser speed for R0 strategy

For BS3, BS5, and BS6, only <011> texture is observed; however, the texture intensity is low for BS3 and BS6, indicating a significant crystalline distortion in these modes. On the other hand, the BS5 mode presents the highest texture intensity, which can be considered single crystal-like, while the BS6 mode presents the lowest level of texture intensity.

For beam shape mode samples with the R67 strategy, a reduction in the continuity of the ring-like texture is observed. It is important to note that the rotational strategy for the 001 pole figure under the Gaussian mode is associated with a ring-like texture or ring distribution (Pérez-Ruiz et al. 2021). However, for the BS3 and BS5 modes, the ring distribution of the poles tends to weaken in the 110 directions. In the BS6 mode, the crystalline ring distribution becomes stronger again, but unlike the Gaussian mode, the intensity of the main poles is higher. For the R90 strategy, it can be observed that the texture intensity for the Gaussian mode sample is also low, reaching a higher level for the BS5 mode with a single crystal-like texture and medium intensity levels for the BS3 and BS6 modes.

Figure III-49b shows the effect of the interaction between the beam shape mode and the laser speed on the texture intensity for the samples manufactured with the R0 strategy. For Gaussian mode BS0, the texture intensity is almost the same for all laser speed levels, while for BS3, BS5, and BS6 modes, the laser speed effect is significant. For BS3, the highest texture intensity occurs when v=500mm/s, for BS5 when v=1000 mm/s, and for BS6 when v= 1500 mm/s. This interaction between beam shape mode and laser speed may be related to the fact that all 3 cases developed melt pools with low conduction mode, as shown in Figure III-44a.

III.6. Repeatability analysis of primary crystalline orientations in IN718 LPBF samples

This section analyzes the repeatability of the crystalline array orientation relative to the reference system of the LPBF workpiece for different strategies, beam shape modes, LPBF parameters, and different LPBF machines. The {001} pole figures presented ahead show the crystalline orientation in the workpiece reference frame. Additionally, the workpiece reference frame relative to the base plate reference frame, as well as the orientation of the laser tracks of each laser strategy relative to the workpiece reference frame, are presented in Figure III-50.
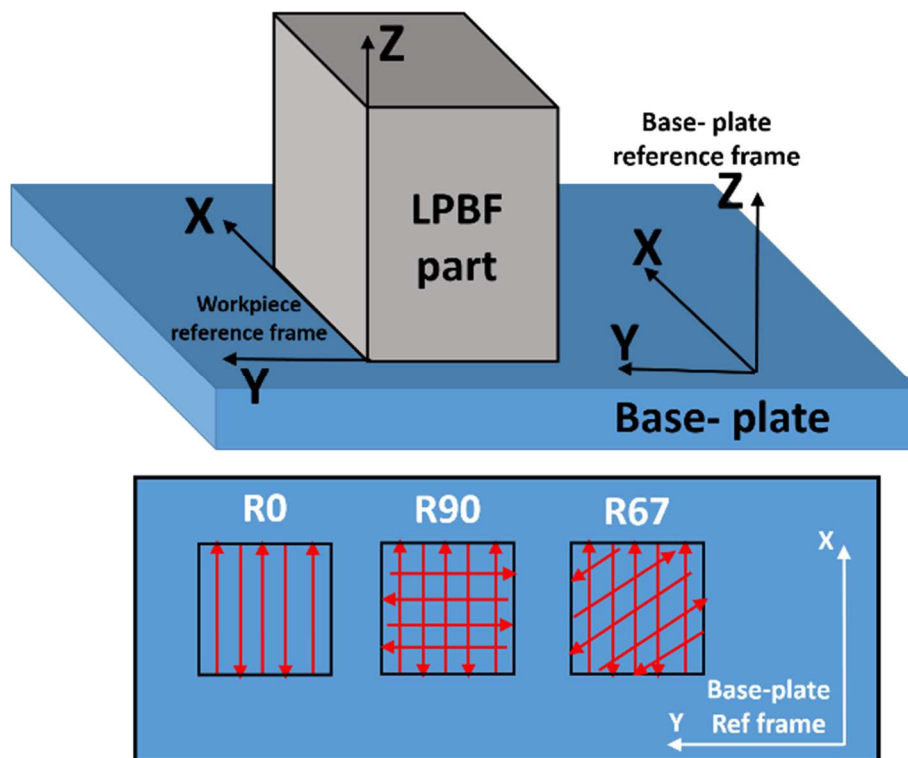
Figure III-50. Laser tracks orientation relative to the LPBF reference system

III.6.1. Primary crystalline orientations for unidirectional strategy (R0)

This section shows the crystalline patterns (ODF) for the R0 strategy under different configurations (machine, beam shape mode, LPBF parameters) to determine the discrete ODF and assign an orientation in Euler angles (Bunge notation). Figure III-51 compares the ODF obtained using a 3DNT (multi-mode) machine and a Renishaw AM400 (Gaussian mode) for BS0 mode (gaussian) only.
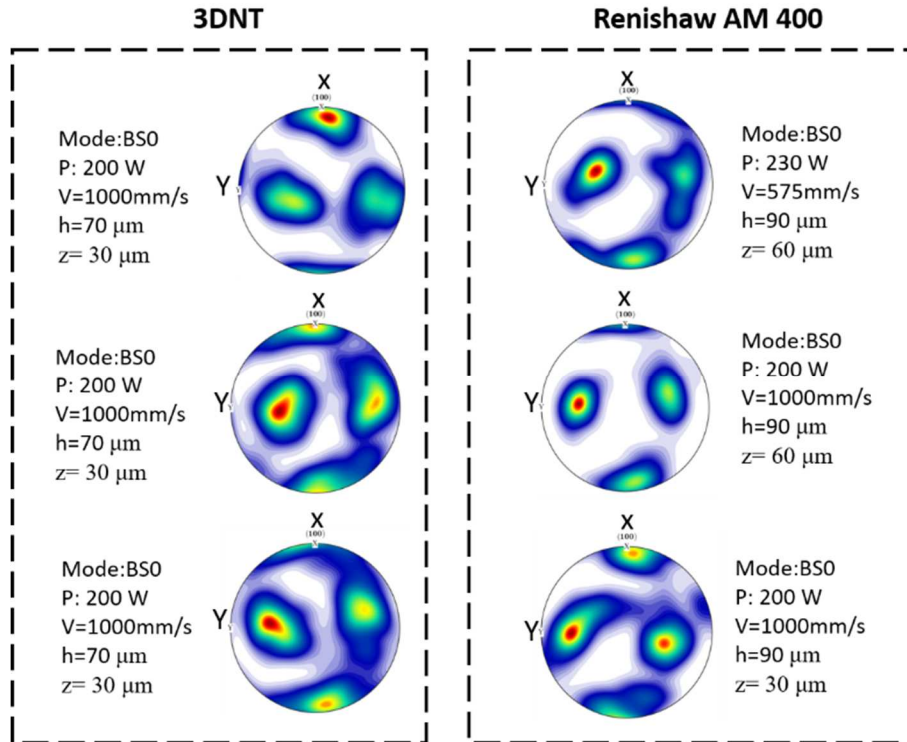
Figure III-51. ODF patterns for R0 strategy and BS0 mode (Gaussian) under different LPBF parameters and machines

Interestingly, all the ODF's compared present the crystalline orientation g(0,45,0) as the main orientation independently of the machine or LPBF parameters. It is noteworthy to say that the g(0,45,0) orientation is equivalent to the <011> texture previously mentioned for the lamellar microstructure. However, from now on, the Euler angle orientation (Bunge notation) will be considered as it can be used in the models discussed in chapter VI. Additionally, it is essential to note that the ODFs present minor variations that make the orientation g(0,45,0) not exact for all the ODFs presented; however, the orientation g(0,45,0) is the most representative of all the samples evaluated, and the one that is also the most reported in the literature. On the other hand, other secondary crystalline orientations are observed, but with much lower density, so they will not be considered in this section.

The other modes analyzed in this section are BS3, BS5 and BS6. For these modes, samples were obtained on the 3DNT machine, as the Renishaw AM400 only has the BS0 (Gaussian) mode. Figure 48 shows the ODFs corresponding to the R0 strategy and the BS3, BS5, and BS6 modes at different laser speeds (500 mm/s, 1000 mm/s, and 1500 mm/s).
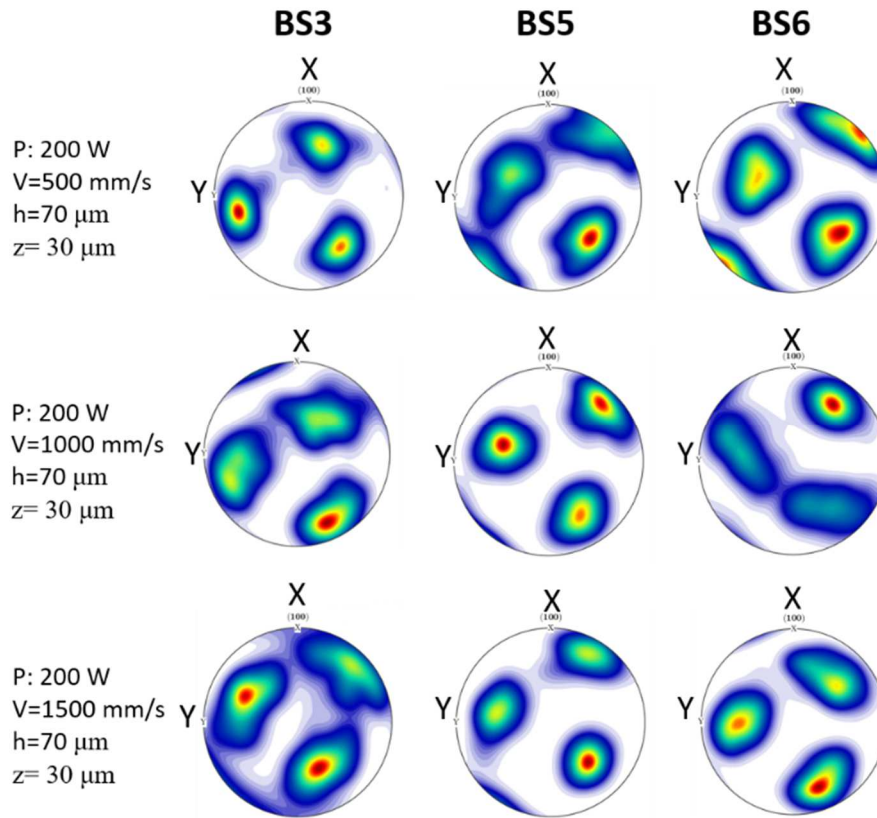
Figure III-52. ODF patterns of RO strategy and BS3, BS5, and BS6 modes for different LPBF parameters manufactured in a 3DNT machine

For the BS3 mode, the laser speed has a relatively significant effect on the primary crystalline orientation since it varies between g(20,-60,45) and g(-20,-60,45), while Beam shape modes BS5 and BS6 alternate between g(-135,90,45) and g(-135,110,45), which is equivalent to g(-135,100,45) with a misorientation of +/-10°.

On this basis, it is possible to establish that the repeatability of the primary crystal orientation g(0,45,0) for the BS0 (Gaussian) mode is sufficiently robust, as the results obtained in the present analysis agree with those reported by many authors in the literature. However, for novel beam shape modes such as BS3, BS5, and BS6 with R0 strategy, it is still too early to establish a dominant crystalline direction per beam shape mode since these modes are just starting to be reported in the literature, and there is not yet enough empirical evidence to establish these patterns as repetitive. However, it is possible to establish that the crystalline patterns depend on the mode used, so much more research is needed on non-Gaussian modes for the R0 strategy.

III.6.2. Primary crystalline orientations for bidirectional strategy (R90)

Figure 49 illustrates the ODFs corresponding to the samples fabricated with the R90 strategy for different beam shape modes, LPBF parameters, and machines. A dominant crystalline orientation in the g(-135,110,45) +/-15° direction is observed for all samples irrespective of the machine, LPBF parameters, and beam shape modes, which is an indicator that this orientation can be considered robust to establish it as the crystalline pattern of the R90 strategy. However, in the literature, some studies show the g(0,0,0) direction for a keyhole-like melt pool shape as the primary orientation. Nevertheless, it is possible to establish that within the range of experimental configurations evaluated, the orientation g(-135,110,45) can be considered as the primary crystal orientation for the R90 strategy, considering that the melt pools were developed in conduction mode and with a high density, which is difficult with keyhole-like mode.
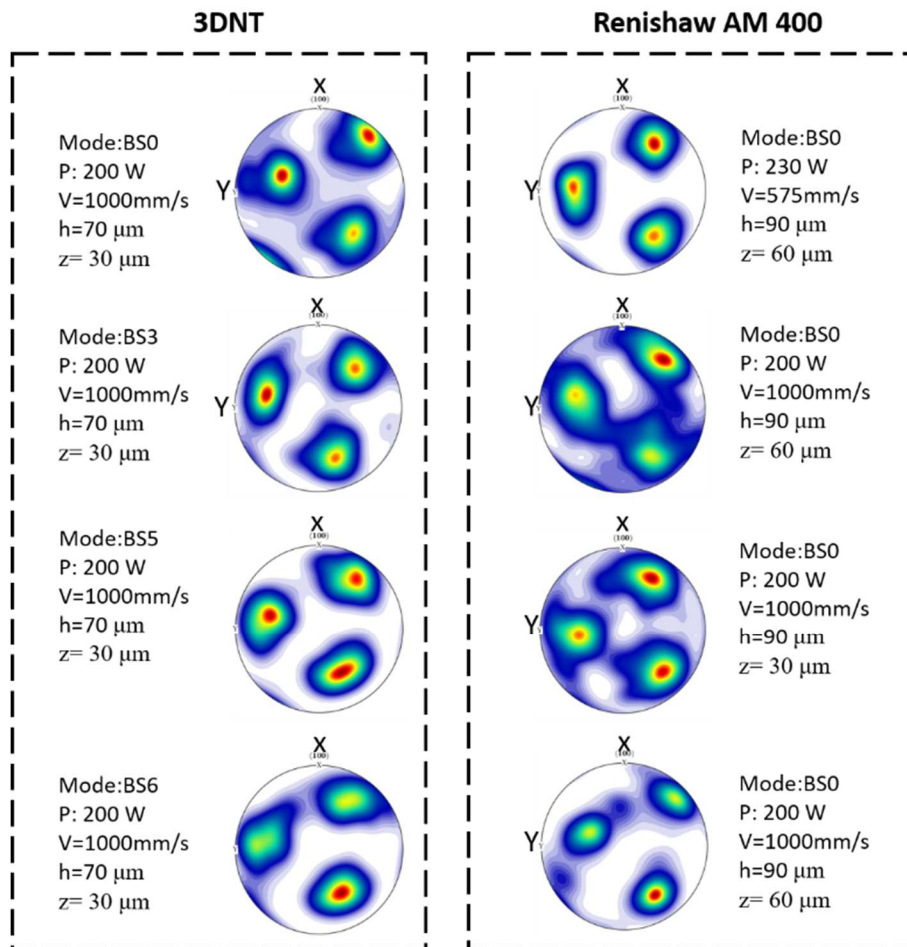
Figure III-53. ODF patterns for R90 strategy and BS0, BS3, BS5, and BS6 modes for different LPBF parameters and machines.

III.6.3. Primary crystalline orientations for rotational strategy (R67)

As in the previous sections, Figure III-54 illustrates the ODF's corresponding to the samples fabricated with the R67 strategy for different beam shape modes, LPBF parameters, and machines. In all the ODFs analyzed, the fiber texture, also known as ring-crystal-like texture, is observed. As mentioned in section III.5.3, this texture usually has a central pole and different crystalline orientations around the central pole. For the experimental conditions of the present study, the central pole has an orientation at miller angles <-2 -2 1> and multiple crystalline orientations around this pole. Despite having multiple crystalline orientations, it is possible to discretize these orientations into three main crystalline orientations with equal volume fractions as in Figure III-38, which are g(-45,60,0), g(-45,60,30) and g(-45,60,60).
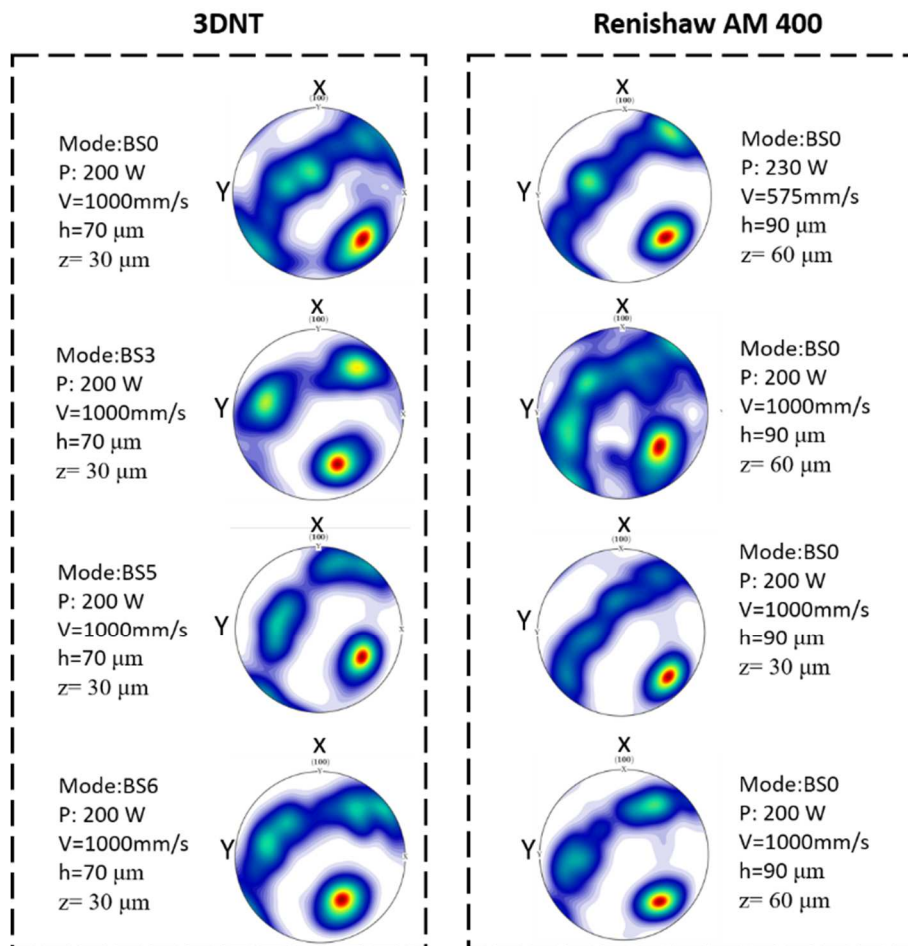
Figure III-54. ODF patterns for R67 strategy and BS0, BS3, BS5, and BS6 modes for different LPBF parameters and machines.

III.7. Conclusions

This chapter discusses the effects of the process parameters at the machine level with the physical parameters and, subsequently, the relationship of the physical parameters with the mechanical properties. The main aspects are as follows:

- The physical principles governing the interaction between scanning strategy, VED, and beam shaping and their effect on dendritic and crystalline patterns associated were exposed.

- The effect of beam shaping on samples' density and melt pool shape was evaluated, finding high-density levels for all the beam shaping modes analyzed, regardless of the laser speed or the laser strategy.

- It was observed that BS5 and BS6 modes developed shallow melt pool shapes with conduction or low-conduction modes.

- The beam shape modes BS5 and BS6 developed epitaxial dendritic growth in most of the melt pool volume, unlike the Gaussian mode, in which dendritic growth is mainly based on side-branching.

- The repeatability of the primary crystalline orientations for the different strategies analyzed with the Gaussian mode was demonstrated.

- It is observed that samples fabricated with non-Gaussian modes can have crystalline patterns different from the Gaussian mode for the R0 strategy; however, little variability of the crystalline patterns was observed for samples fabricated with the R90 and R67 strategies at different modes.

Chapter IV. Physical relationships between LPBF material anisotropy and cutting forces

IV. Physical relationships between LPBF material anisotropy and cutting forces

This chapter presents a microplasticity model based on Taylor's theory to quantify the shear strength of textured LPBF materials as a function of tool geometry, tool position, and crystalline orientation distribution function. Additionally, the effect of grain boundary density is considered, and the interactions between microstructure and orientation dependency of milling cutting forces are explained.

This chapter is based on the paper entitled: "On the relationship between cutting forces and anisotropy features in the milling of LPBF Inconel 718 for near net shape parts" https://doi.org/10.1016/j.ijmachtools.2021.103801

IV.1. Introduction

Presently, combining additive and subtractive processes into a hybrid manufacturing method is of scientific and industrial interest (Flynn et al. 2016). Metallic additive manufacturing (AM) is an effective method for obtaining fully functional components (Dilberoglu et al. 2017; Thompson et al. 2016). Processes such as Laser Powder Bed Fusion (LPBF) provide sufficient flexibility for manufacturing complex morphologies that, in some instances, cannot be produced by subtractive methods. Therefore, LPBF is of particular interest in manufacturing complex shapes and thin walls, such as ducts for aeronautical engines, vanes, and other power system components. Components produced by metallic AM can be classified as having near-net shapes; therefore, machining requirements are finishing ones. Additionally, the assembly of the posterior printed parts along with other components necessitates a milling operation. Milling such parts frequently involves small chip sizes and highly interrupted machining; therefore, models are essential in predicting the cutting forces to ensure the final surface quality.

The additive/subtractive hybrid manufacturing method requires multidisciplinary efforts ranging from a) design methodologies to b) evaluating the elastic and plastic anisotropic natures of the AM testpieces. These efforts include fixture design, methodologies for interaction control between the initial and final shapes, overstock requirements and finish machining allowance, surface integrity control (la Monaca et al. 2021), CAM utilities (Guhaprasanna Manogharan 2014; Niechen Chen, Barnawal, and Frank 2018) and the effects of the LPBF parameters, laser scanning strategies, and heat treatment on the mechanical properties and anisotropy (S. Y. Liu et al. 2020; Nadammal et al. 2017; D. Zhang et al. 2015; Chlebus et al. 2015; Hosseini and Popovich 2019). These were also reported for LPBF-ed Inconel 718 (Sanchez et al. 2021; Xia et

al. 2016; Criales et al. 2017b). In this regard, Mang et al. (M. Ni et al. 2017a) investigated the effects of microstructure and fiber textures on the anisotropy and mechanical properties of LPBF-ed Inconel 718 through a tensile test, which was supported by Schmid's law. Chen et al. (Z. Chen et al. 2018) evaluated the anisotropic mechanical behavior of an LPBF-processed Ni-based superalloy K418 printed using two laser scanning strategies. Other researchers studied the microstructural characteristics of LPBF-printed parts concerning surface quality after machining (Yuying Yang et al. 2018; Brown et al. 2018a). (Du, Bai, and Zhang 2017)performed a directional independence analysis of the hardness, cutting forces, and surface quality of the printed parts of LPBF-ed 18Ni-300 maraging steel and 6511 martensitic stainless steel. They obtained higher cutting forces in the machined LPBF samples, caused by the grain refining effect, compared to the wrought samples.

Anisotropy and microstructural heterogeneity are commonly regarded as two of the primary drawbacks to be rectified in metal AM processes (Kok et al. 2018). Although one solution is typically linked to recrystallization processes, it cannot be employed, in many cases, on thin-walled parts or complex shapes. In machining, anisotropy significantly impacts the stiffness of the parts (and, therefore, associated with vibrations) and the cutting forces. Thus, understanding the interactions between the LPBF parameters, microstructural-crystallographic characteristics and machining parameters, tool geometry, and tool position is essential for reducing the variability in the cutting forces and improving the surface quality. In this manner, Ni et al. (C. Ni et al. 2020) conducted a micro-hardness-based anisotropy analysis on AM-ed Ti-6Al-4V , considering both the microstructure of alloys and the surface quality . In addition, Bai et al. (Yuchao Bai, Cuiling Zhao, Yu Zhang, Jie Chen 2021) evaluated the machinability of AM-ed CuCrZr by orthogonal cutting, considering the surface quality, chip morphology, and mechanical properties. The theoretical quantification of the anisotropy effect on the cutting forces was mainly investigated for single-crystal metals (Sato et al. 1981; 1983) by orthogonal cutting. For example, Lee et al. (W. B. Lee and Zhou 1993; W. B. Lee et al. 2003; W. B. Lee, Cheung, and To 2002) demonstrated, through Taylor's microplasticity theory, the dependence of cutting forces on the feed direction relative to the crystalline orientation for orthogonal cutting. However, there are few studies regarding the anisotropy effect on the cutting forces for oblique cutting in polycrystalline materials, considering that LPBF materials are also regarded as textured and polycrystalline (Bean et al. 2019b; Thijs et al. 2013). With this reasoning, Fernandez-Zelaia et al. (Fernandez-Zelaia et al. 2019) analyzed the crystallographic effect of AM-ed CoCrMo on the average cutting forces in slot milling. They obtained moderate deviations when the feed direction for machining ran parallel to the building direction (BD) in samples with a dominant

<001> texture. Hence, Fei (Fei et al. 2019) performed face milling operations on LPBF-ed nickel alloy 625 pieces, obtaining significant differences in the cutting force levels; the reasons for which were not explained. Regarding AM-ed Inconel 718, Ji et al. (Hansong ji,Munish kumar gupta, quinghua song,wentong cai, tao zheng,youle zhao,zhanquian liu 2021) explored the influence of the microstructure on the machinability of the parts, either printed or heat-treated. They considered peripheral milling and analyzed the surface quality and microstructure using an empirical approach. In contrast to the above-mentioned studies, this one presents the influence of the crystallographic effect and grain morphology (size and orientation) on the directional cutting force response dependency when oblique cutting was applied to LPBF workpieces, considering tool position and geometry.

This study investigates the effect of the LPBF process parameters on the anisotropy of printed alloys as well as on the cutting forces in the peripheral milling of LPBF-ed Inconel 718. Therefore, the crystallographic and grain morphology effects were studied and quantified. A model based on Taylor's microplasticity theory is proposed for peripheral milling in order to obtain the Taylor factor as a shear strength indicator for the AM parts. AM scanning strategies generate specific patterns in the crystallographic distribution; therefore, the fluctuation in the shear strength along the crystalline distribution can correspond to the laser scanning strategy (LSS). Thus, it is possible to quantify the effect of the LPBF process configuration on the subsequent machining operations. To correlate the effect of the grain morphology on the cutting forces, the grain boundary density was quantified. Therefore, LPBF samples were initially manufactured and their microstructural and crystallographic features were subsequently extracted. Lastly, experimental milling tests were performed. The model exhibited a good correlation between the Taylor factor distribution and the measured cutting forces trend.

IV.2. Interaction between LPBF parameters and machining issues

Cutting force prediction in the machining of AM parts is challenging owing to the nonlinearities of the LPBF process. However, additive (LPBF process) and subtractive (machining) domains share a mutual interaction with key aspects, a few of which include grain size, grain orientation and crystallographic texture. The numerous variables are summarised in Figure IV-1.
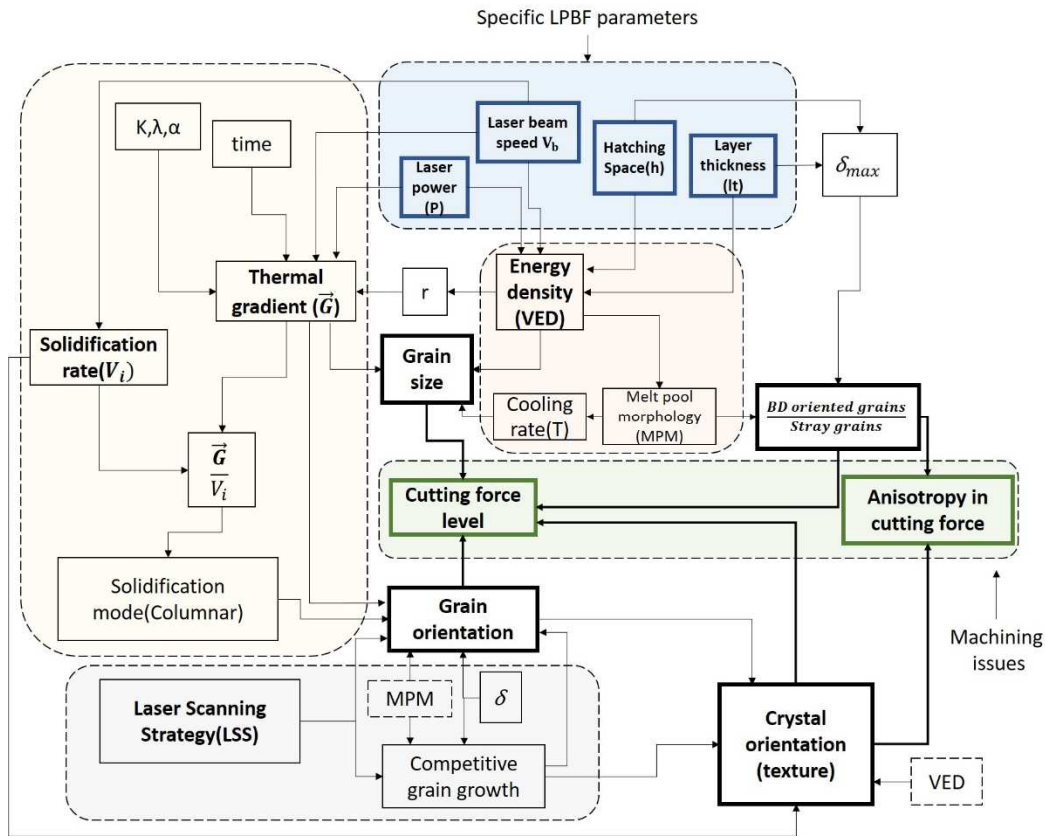
Figure IV-1. Interactions between LPBF-microstructure-machining.

IV.3. Effect of material anisotropy on cutting forces

To evaluate the effect of material anisotropy on the cutting forces, considering the plastic deformation of the cutting process in the slip mode is essential. At the macroscopic level, the cutting area is usually simplified as a plane. At the microscopic level, however, the shear zone is comprised of multiple slip directions, which form what is usually referred to as the plane of the shear band when combined. However, the macroscopic assessment of the cutting process is insufficient to explain the differences in the cutting forces for different positions of the tool concerning the workpiece, this is because it is necessary to evaluate the resistance to dislocations along the direction of the plane of the shear band. An important difference between LPBF and other manufacturing processes is the abundance of columnar grains. Unlike equiaxial grains, they cannot be simplified through an equivalent diameter (d) as it is necessary to size them at least by a major (d1) and a minor axis (d2). Additionally, columnar grains are more associated with a predominant crystalline orientation.

To assess the resistance to shear action, it is necessary to consider the resistances offered by the grain boundaries (Komatsu et al. 2012; xian Wu, Liang li, Chengjiao Yao 2016) and by the grain. The Hall–Petch theory and the Zerilli–Armstrong model (Zerilli and Armstrong 1987; 2008) can explain the increase in yield and flow stresses with decreasing grain size. Based on this, it can be inferred that the increase in the grain boundary density is proportional to that in the cutting forces. To evaluate this effect, an analysis of the grain boundary densities for different configurations is presented in Section 6.2. Regarding the resistance to dislocation within the grain, it is necessary to consider the crystalline structure of the material and the interaction between the direction of the strain tensor and the slip systems. Therefore, a model based on Taylor's microplasticity theory was developed in order to evaluate the resistance to dislocation by crystal orientation (Section 3.1).

IV.4. Oblique cutting shear strength prediction model

The proposed model is focused on textured polycrystalline materials and is based on the work of Lee et al. on single crystals (W. B. Lee and Zhou 1993). This model allows the quantification of the shear strength due to the crystallographic effect in any shear plane. This is the result of oblique cutting by end milling through transforming the macroscopic strain tensor from the workpiece reference frame to the crystal reference frame in three steps: firstly, the tool orientation is changed to the workpiece reference frame; secondly, the plane of the shear band is changed from the tool reference frame to the workpiece one; and thirdly, the macroscopic strain tensor can be changed to the crystal reference system once it is in the workpiece reference system. The orientation of a tool corresponding to the workpiece reference system can be fully defined using Euler angles with the Bunge notation (ZYZ). This is defined using Equation IV.1 and is represented in Figure IV-2a.

$$G = \{\varphi 1^T, \varphi^T, \varphi 2^T \} \text{ (IV.1)}$$

The rotation matrix spanning the reference system of the tool and that of the material is obtained from the aforementioned Euler angles (see Equation IV.2).

$$R_O(G) = \begin{bmatrix} [\cos(\varphi 1^T)\cos(\varphi^T)\cos(\varphi 2^T) - \sin(\varphi 1^T)\sin(\varphi 2^T)] & [-\cos(\varphi 1^T)\cos(\varphi^T)\sin(\varphi 2^T) - \sin(\varphi 1^T)\cos(\varphi 2^T)] & \cos(\varphi 1^T)\sin(\varphi^T) \\ [\sin(\varphi 1^T)\cos(\varphi^T)\cos(\varphi 2^T) + \cos(\varphi 1^T)\sin(\varphi 2^T)] & [\sin(\varphi 1^T)\cos(\varphi^T)\sin(\varphi 2^T) + \cos(\varphi 1^T)\cos(\varphi 2^T)] & \sin(\varphi 1^T)\sin(\varphi^T) \\ -\sin(\varphi^T)\cos(\varphi 2^T) & -\sin(\varphi^T)\sin(\varphi 2^T) & \cos(\varphi^T) \end{bmatrix} \text{ (IV.2)}$$
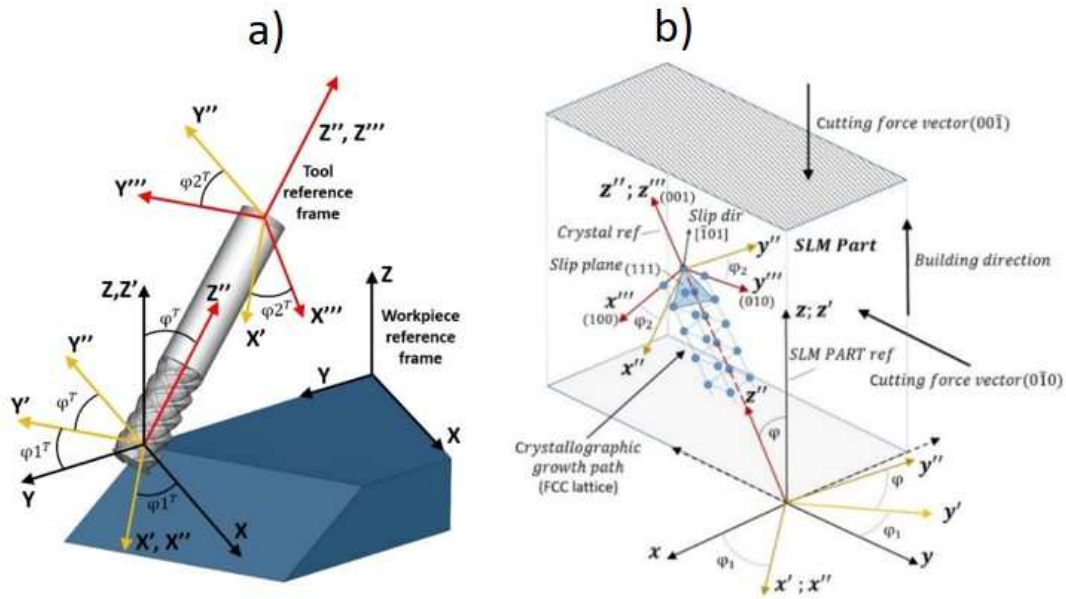
Figure IV-2 a) Euler angles in the tool reference frame with respect to the workpiece reference frame, b) Euler angles in the workpiece reference frame with respect to the crystal reference frame

Regarding the second step, the plane of the shear band concerning the workpiece reference system is defined by the shear angle ϕ_c, the helix angle β and the relative engagement angle α (see Figure IV-3). R_ϕ is the transformation matrix defined by the shear band reference frame (x''', y''', z'') and the equivalent tool reference frame (x'', y'', z'') prescribed by the rotation of ϕ_c. R_Z is the transformation matrix defined by the equivalent tool reference frame (x'', y'', z'') and the trochoidal position reference frame (x', y', z') prescribed by the rotation of β. Lastly, R_α is the transformation matrix defined by the trochoidal position reference frame (x', y', z') and the workpiece reference frame (x, y, z) prescribed by the rotation of α (see Equation IV.3 and Figure IV-3).
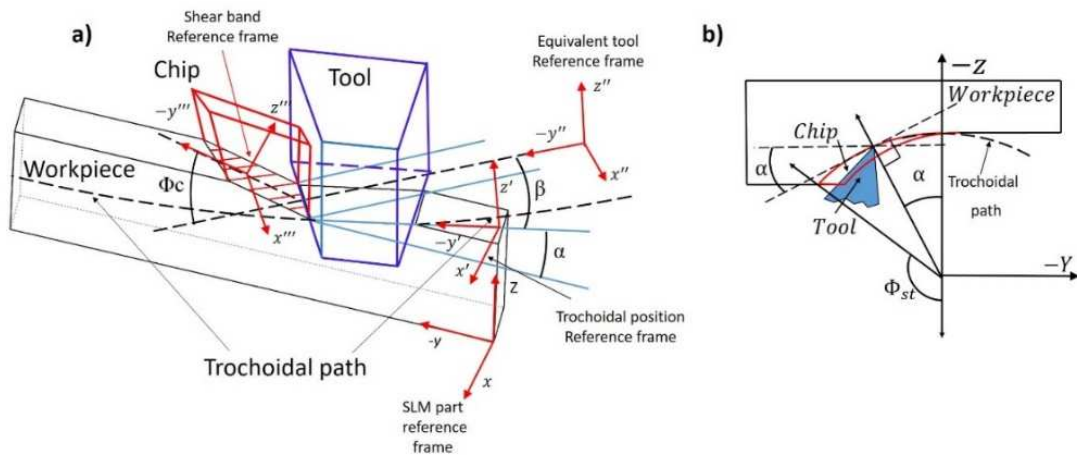
Figure IV-3. a) cutting and shear band geometry, b) details of engagement by the angle α

$$R_\phi R_Z R_\alpha = \begin{bmatrix} 1 & 0 & 0 \\ 0 & \cos(\phi_c) & -\sin(\phi_c) \\ 0 & \sin(\phi_c) & \cos(\phi_c) \end{bmatrix} * \begin{bmatrix} \cos(\beta) & \sin(\beta) & 0 \\ -\sin(\beta) & \cos(\beta) & 0 \\ 0 & 0 & 1 \end{bmatrix} * \begin{bmatrix} 1 & 0 & 0 \\ 0 & \cos(\alpha) & \sin(\alpha) \\ 0 & -\sin(\alpha) & \cos(\alpha) \end{bmatrix} \quad \text{(IV.3)}$$

The incremental work during a plastic deformation caused by end milling can be defined by

$$dW = \sigma d\varepsilon_w(G, \alpha, \beta, \phi_c), \quad \text{(IV.4)}$$

where σ is the equivalent stress and $d\varepsilon_w$ is the macroscopic effective strain tensor in the shear band caused by the cutting process.

The equation for the virtual work done in deforming a single crystal (W. B. Lee, Cheung, and To 2002) can be written as

$$\sigma d\varepsilon_w = \tau_c \, d\Gamma \; ; \; \frac{\sigma}{\tau_c} = \frac{d\Gamma}{d\varepsilon_w} = M \quad \text{(IV.5)}$$

where $d\Gamma$ is the total dislocation shear strain accumulated in the crystal, σ is the equivalent stress and τ_c is the critical resolved shear stress. M is the Taylor factor, which is the ratio between the microscopic shear strain and the macroscopic strain. Alternatively, it is the ratio between the equivalent normal and shear stresses, implying that higher values of the Taylor factor lead to higher equivalent stresses.

The Taylor factor for oblique cutting in a physically distinctive crystal orientation (g_i) can be defined as:

$$M(g_i, G, \alpha, \beta, \phi_c) = \frac{d\Gamma}{d\varepsilon_w(G, \alpha, \beta, \phi_c)} = \frac{\sigma}{\tau_c} = \frac{dW}{\tau_c \varepsilon_c^i(g_i, G, \alpha, \beta, \phi_c)} \quad i=1, 2\ldots N, \text{ (IV.6)}$$

where N is the number of crystalline orientations evaluated and ε_c is the imposed strain in the crystal.

Equation IV.7 is the expression proposed to obtain the strain tensor in the shear band for oblique cutting during end milling for any tool position in the workpiece reference frame.

$$\varepsilon_w(G, \alpha, \beta, \phi_c) = R_0^T(G) R_\alpha^T R_Z^T R_\phi^T E_S R_\phi R_Z R_\alpha R_0(G), \quad \text{(IV.7)}$$

$$E_S = d\Omega/2 \begin{bmatrix} 0 & 0 & 0 \\ 0 & 0 & -1 \\ 0 & -1 & 0 \end{bmatrix}, \quad \text{(IV.8)}$$

where E_S is the displacement gradient and $d\Omega$ is the shear strain in the shear band.

The imposed strain in the crystal ε_c^i is obtained using equation IV.9.

$$\varepsilon_c^i(g_i, G, \alpha, \beta, \phi_c) = C_i(g_i) \varepsilon_w(G, \alpha, \beta, \phi_c) C_i^T(g_i), \text{ (IV.9)}$$

where C_i is the transformation matrix (Equation IV.10) defined by the workpiece reference frame and the crystal reference frame, prescribed by the rotation of $g_i = \{\varphi 1_i^c, \varphi_i^c, \varphi 2_i^c\}$ (Bunge notation; see Figure IV-2b).

$$C_i(g_i) = \begin{bmatrix} [\cos(\varphi 1_i^c)\cos(\varphi_i^c)\cos(\varphi 2_i^c) - \sin(\varphi 1_i^c)\sin(\varphi 2_i^c)] & [-\cos(\varphi 1_i^c)\cos(\varphi_i^c)\sin(\varphi 2_i^c) - \sin(\varphi 1_i^c)\cos(\varphi 2_i^c)] & \cos(\varphi 1_i^c)\sin(\varphi_i^c) \\ [\sin(\varphi 1_i^c)\cos(\varphi_i^c)\cos(\varphi 2_i^c) + \cos(\varphi 1_i^c)\sin(\varphi 2_i^c)] & [\sin(\varphi 1_i^c)\cos(\varphi_i^c)\sin(\varphi 2_i^c) + \cos(\varphi 1_i^c)\cos(\varphi 2_i^c)] & \sin(\varphi 1_i^c)\sin(\varphi_i^c) \\ -\sin(\varphi_i^c)\cos(\varphi 2_i^c) & -\sin(\varphi_i^c)\sin(\varphi 2_i^c) & \cos(\varphi_i^c) \end{bmatrix} \text{ (IV.10)}$$

According to Taylor's minimum work principle, five independent slip systems are required to develop a plastic strain, considering the incompressibility condition of solids. This implies that an optimization process must be executed to obtain the combination of the five slip systems that minimises the work due to an imposed strain (C.N 1973).

The shear required to develop a strain by five independent slip systems is given in Equations IV.11 and IV.12, with the former being the compact form of the detailed equation in Equation IV.12 .

$$[\varepsilon_c^i] = [E] [\gamma_i] \quad \text{or} \quad [\gamma_i] = [E^{-1}] [\varepsilon_c^i], \quad \text{(IV.11)}$$

$$
\begin{pmatrix} \varepsilon_{c22}^i \\ \varepsilon_{c33}^i \\ \varepsilon_{c23}^i \\ \varepsilon_{c13}^i \\ \varepsilon_{c12}^i \end{pmatrix} =
\begin{bmatrix}
(n_2^1 b_2^1) & (n_2^2 b_2^2) & (n_2^3 b_2^3) & (n_2^4 b_2^4) & (n_2^5 b_2^5) \\
(n_3^1 b_3^1) & (n_3^2 b_3^2) & (n_3^3 b_3^3) & (n_3^4 b_3^4) & (n_3^5 b_3^5) \\
(n_2^1 b_3^1 + n_3^1 b_2^1) & (n_2^2 b_3^2 + n_3^2 b_2^2) & (n_2^3 b_3^3 + n_3^3 b_2^3) & (n_2^1 b_2^1 + n_1^1 b_2^1) & (n_2^1 b_2^1 + n_1^1 b_2^1) \\
(n_1^1 b_3^1 + n_3^1 b_1^1) & (n_1^2 b_3^2 + n_3^2 b_1^2) & (n_1^3 b_3^3 + n_3^3 b_1^3) & (n_2^1 b_2^1 + n_1^1 b_2^1) & (n_2^1 b_2^1 + n_1^1 b_2^1) \\
(n_1^1 b_2^1 + n_2^1 b_1^1) & (n_1^2 b_2^2 + n_2^2 b_1^2) & (n_1^3 b_2^3 + n_2^3 b_1^3) & (n_1^4 b_4^4 + n_2^4 b_1^4) & (n_1^5 b_5^5 + n_2^5 b_1^5)
\end{bmatrix}
\begin{pmatrix} \gamma_{1i} \\ \gamma_{2i} \\ \gamma_{3i} \\ \gamma_{4i} \\ \gamma_{5i} \end{pmatrix} \text{(IV.12)}
$$

Where $[E]$ is the direction cosine of any combination of the five slip systems, $[\gamma_i]$ is the corresponding shear related to the crystal orientation i, n is the slip plane, b is the slip direction, and the superscript corresponds to the slip system. Table IV-1 lists the slip systems for the FCC lattice.

Table IV-1. Slip systems for the FCC lattice in the crystal reference frame

Slip plane(n)	(111)			($\bar{1}\bar{1}1$)			($\bar{1}11$)			($1\bar{1}1$)		
Slip direction(b)	[$01\bar{1}$]	[$\bar{1}01$]	[$1\bar{1}0$]	[$01\bar{1}$]	[101]	[$\bar{1}10$]	[$01\bar{1}$]	[101]	[$\bar{1}\bar{1}0$]	[$0\bar{1}\bar{1}$]	[$\bar{1}01$]	[110]
Slip system	1	2	3	4	5	6	7	8	9	10	11	12

Once the optimization process is complete and the five-slip system set is defined, the increment in the plastic work (dW) can be obtained (Equation IV.13), and the Taylor factor for oblique cutting in a physically distinctive crystal orientation (g_i) is calculated (Equation 6). The macroscopic or sample Taylor factor for any combination of G, α, β and ϕ_c can be attained from the previously obtained single-crystal Taylor factors (Equation IV.6) using the following equation (Przybyla 2005).

$$\overline{M(G, \alpha, \beta, \phi_c)} = \int \int \int M(g_i, G, \alpha, \beta, \phi_c) f(g) dg \quad \text{(IV.13)}$$

Considering that $f(g)$ is the orientation distribution function ODF (see Equation IV.14),

$$f(g) = ODF(g) = \frac{1}{V} \frac{dV(g)}{dg}, \quad \text{(IV.14)}$$

where dV is the volume fraction corresponding to a crystalline direction, dg is the differential of the crystalline orientation, and V is the total volume of the Eulerian space (see Equation IV.15).

$$V = \int dg = \int d\varphi 1 \sin\varphi \, d\varphi 2 = \frac{1}{8\pi^2} \text{ (IV.15)}$$

The macroscopic (polycrystalline) Taylor factor can then be expressed as a function of the volume fractions using Equation IV.16.

$$\overline{M(G, \alpha, \beta, \phi_c)} = \int \int \int M(g_i, G, \alpha, \beta, \phi_c) \frac{dV(g)}{V} \text{ (IV.16)}$$
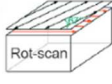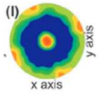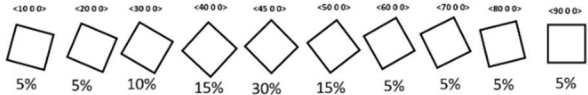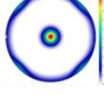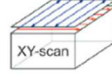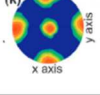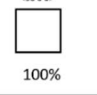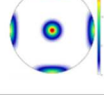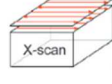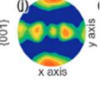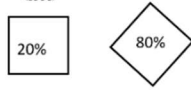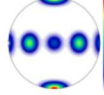
Obtaining the macroscopic Taylor factor in a shear plane from the crystalline orientations with the highest volume fraction is an approximate but practical solution when machining staff do not possess the experimental information (i.e. EBSD) regarding the crystalline ODF. Considering that laser rotation strategies are evidently associated with the crystalline texture patterns observed in the pole figures, which is widely reported in the literature, it is, therefore, possible to obtain the crystalline orientations with the highest volume fractions from the pole figure of an experimentally obtained crystalline texture (see Table IV-2). This represents a discretization of the crystalline distribution, which can be a useful approach to analysing the trend of the shear strength of a range of tool positions with respect to the workpiece reference system or when a defined tool orientation and geometry are analyzed. The accuracy depends on the number of crystalline orientations considered and the size of the increment in the Euler angles: $g = \{\varphi 1_i^c, \varphi_i^c, \varphi 2_i^c\}$. For rigorous evaluation, using the experimental ODF is recommended.

The volume fraction of a particular orientation can be obtained by multiplying its density by the increment of each Euler angle (Cho, Rollett, and Oh 2004) (see Equation IV.17).

$$1 = \frac{1}{8\pi^2} \sum_{\varphi 1} \sum_{\phi} \sum_{\varphi 2} f\left(\varphi 1, \varphi_j, \varphi 2\right) \Delta\varphi 1 \Delta\varphi 2 [\cos\left(\varphi_j - \frac{\Delta\varphi}{2}\right) - \cos\left(\varphi_j + \frac{\Delta\varphi}{2}\right)] \text{ (IV.17)}$$

Table IV-2 depicts the use of this technique in the context of LPBF, where discretization of the crystallographic orientation is obtained from the patterns of the pole figures of the textures associated with various laser scanning strategies. The simulated pole figures based on the volumetric fractions and discretized crystalline directions are shown on the right. The patterns of the pole figures reported and the simulated ones are quite similar in the different cases, indicating that the crystalline directions obtained are similar to those of the experimental sample.

Table IV-2. Discretization of the crystalline orientation distribution from experimental texture pole figures

From a discrete ODF (DODF) that can be associated with an LSS, the macroscopic (polycrystalline) Taylor factor for any tool orientation can be approximated using Equation IV.18.

$$\left[\overline{M(G, \alpha, \beta, \phi_c)} \right]^{LSS} \approx \left[\sum_{i=1}^{N} M(G, \alpha, \beta, \phi_c) \frac{dV(g_i)}{V} \right]^{LSS} \quad \text{(IV.18)}$$

Owing to the Taylor factor being a good shear strength indicator, the effect of the laser rotation strategy on the shear strength under certain tool positions can be calculated using the proposed model and observed using Taylor maps for different combinations of tool positions (G), shear angles (ϕ_c) relative engagement angles (α), helix angles (β) and laser rotation strategies. Figure IV-4 shows six Taylor maps that consider the interaction of two LSSs (rotation by 67°and 90°) with three milling configurations (G(0 0 0), G(0 45 0), G(0 90 0) for $\beta = 30°$, an α range from 0° to 32° and a ϕ_c range from 0° to 90°).
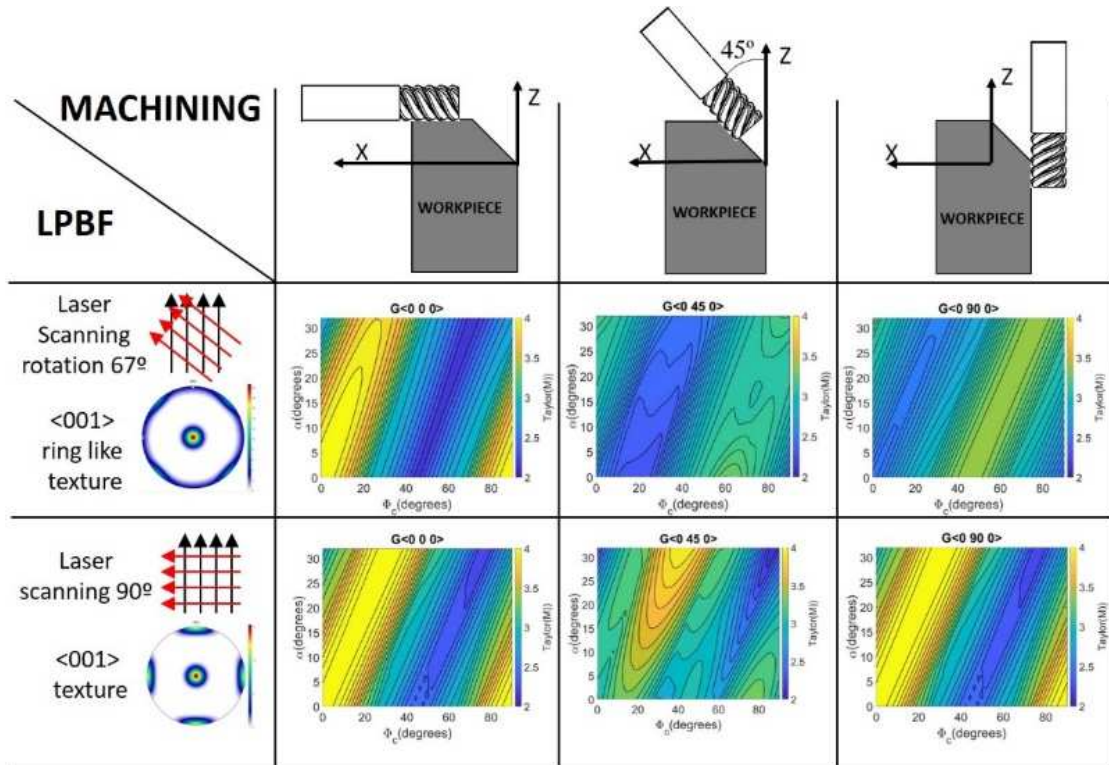
Figure IV-4. LPBF and machining process interaction by ODF patterns

To quantify the material crystallographic effect on the shear strength (or cutting forces) when the cutting tool changed position, it is necessary to determine the variation in the Taylor factor with the tool positions. Therefore, it is necessary to extract a Taylor factor value that represents the shear strength for each tool position. With regards to peripheral milling, there exist different relative engagement angles (α) and shear resistance values associated with each one. The shear angle for each relative engagement angle (α) can be predicted (ϕ_c^p) through the effective Taylor factor M' (W. B. Lee and Zhou 1993), which is based on the principle of maximum stress. It is calculated as M/cos (2ψ), where ψ is the angle of deviation of the shear angle (ϕ_c) corresponding to an angle of 45°, because the shear strain increases by an order of 1 / cos (2ψ) to maintain the macroscopic strain.

Once the shear strength profile (expressed by the Taylor factor) along the tool engagement path is obtained (see Figure IV-5), a representative value of the shear strength can be extracted. Considering that the maximum cutting force is usually associated with the maximum chip thickness, which usually occurs in the initial moments of the engagement between the tool and the part, the Taylor factor corresponding to Φ_{st} can be considered a significant value. Likewise, the mean value can be representative when the variations in the Taylor factor throughout the engagement are not very large.

Figure IV-5 shows the variation in the Taylor factor as a function of the engagement angle (α) for down milling for G (0 90 0) and g (45 0 0) with β = 30° (see Figure IV-24 in the appendix). The white line in Figure IV-5b corresponds to the predicted shear angle values (ϕ_c^p) for each α value based on the specific tool position and crystal orientation. Considering that ϕ = 180 - α, it is then possible to obtain the shear strength profile during engagement using the Taylor factor as a function of the engagement angle (ϕ) (Figure IV-5c).
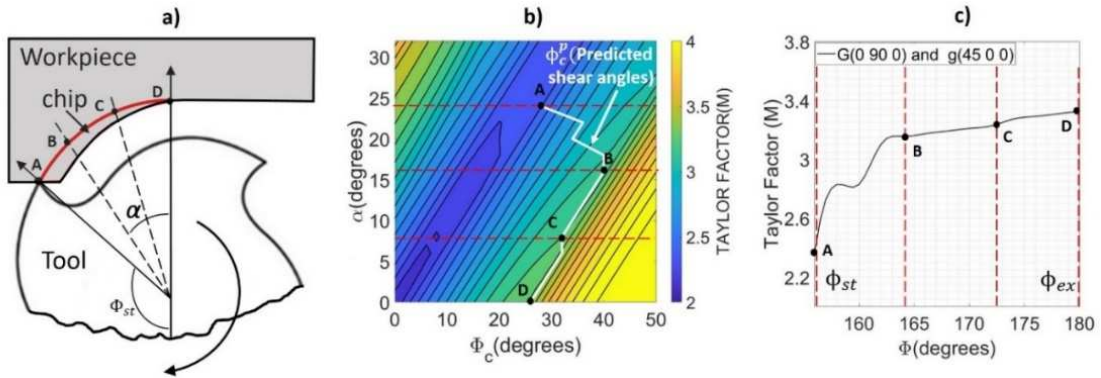
Figure IV-5.a) details of tool engagement, b) predicted shear angle with respect to the effective Taylor factor, c) Taylor factor in the function of the engagement angle

IV.5. Methodology and experimental procedure

Four prismatic samples of Inconel 718 were manufactured simultaneously using a Renishaw AM 400 machine to characterise the cutting forces using end milling. The sample geometry was a 4×4×8 cm L-cube, as shown in Figure IV-6b, having two zones with different layer thicknesses (30 and 60 μm). Layers of 60 μm are used to minimise the processing time, while those of 30 μm are used when precision was required. Layer thicknesses smaller than 30 μm are inconsistent with the feed powder size, and layers larger than 60 μm on Inconel 718 produce excessive internal porosity.

The 30 μm zone (zone 1) was printed first, and the 60 μm zone (zone 2) was added on top. This L-cube shape simplifies machining. A laser rotation strategy of 67° per layer was used (Figure IV-6a), which is considered useful for reducing residual stress (Dianzheng Wang et al. 2017). The scanning direction was on the XY plane, and the BD was along the Z-axis.
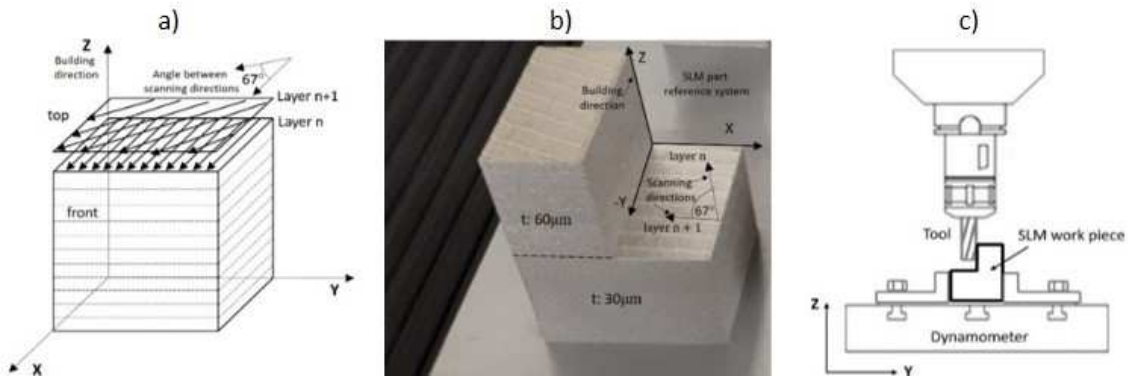
Figure IV-6. a) 67-degree rotation scanning direction strategy, b) LPBF-ed Inconel 718 component for characterization, c) milling setup

To observe the effect of material anisotropy on oblique cutting forces on LPBF-ed Inconel 718, a factorial experiment design $3^3 2^1$ was adopted. Peripheral milling experiments were performed on a Kondia A6 milling centre with a Fagor 8070 CNC. The milling forces were measured using a Kistler 9255B dynamometer (16384 Hz). Figure IV-6c shows a schematic diagram of the setup used for measuring the cutting force. The tool cutting edge quality was controlled to ensure accuracy of the measurements. A 5 mm axial depth of cut was selected in accordance with the tool diameter; it avoids cutting with the same tooth at two different heights. The selected radial depth of cut range corresponds to the usual stock of material to be removed from a printed piece (in the range of 0.1 to 0.2 mm). Depending on the orientation of the manufactured parts on the printing plates, these overstocks can be slightly larger. The selected feed range corresponds to one-tenth of the radial depths of cut evaluated, which is in accordance with a superfinishing and low roughness process.
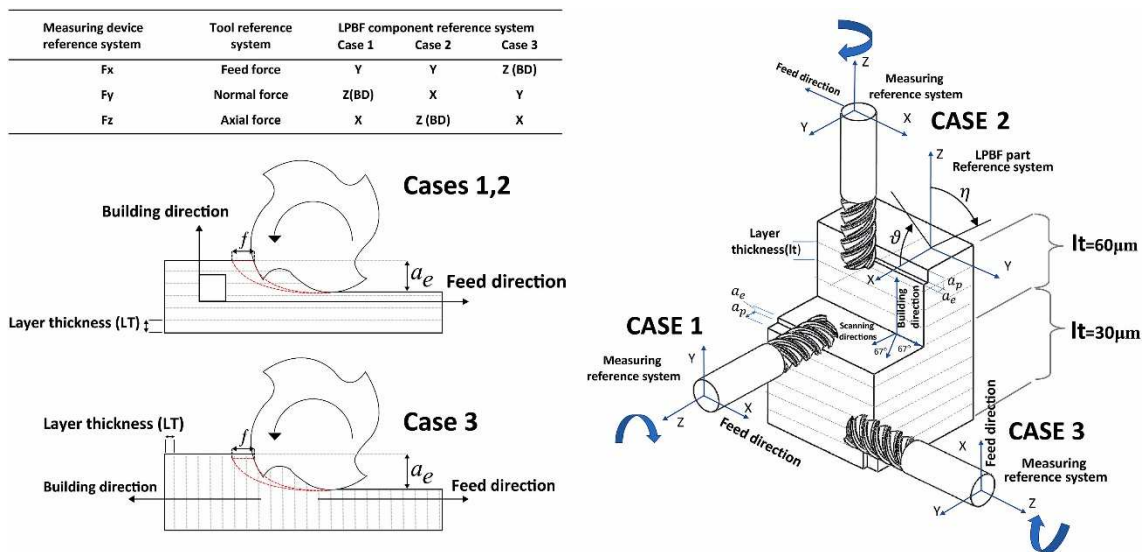
Figure IV-7. Conventions for cutting forces in different reference systems by milling cases

The LPBF parameters, cutting parameters, tool information and experimental factors are listed in Table III-1. Additionally, three milling configurations (hereinafter referred to as 'milling cases') were analyzed to consider the directional dependence of machinability for LPBF-ed Inconel 718 components; these were the three climb milling types. The end mill tool orientation relative to the LPBF component and the equivalence of the measured cutting forces in the tool and LPBF component reference frames are shown in Figure IV-7.

Table IV-3. LPBF parameters, cutting parameters, and experimental factors

LPBF Parameters			Milling experimental factors and levels			
	Zone 1	Zone 2	Factor	Low	Middle	High
Power (W)	200	200	Feed-f (mm/rev·z)	0.03	0.04	0.05
Speed (mm/s)	1000	1000	a_e (mm)	0.1	0.3	0.5
Hatch spacing (mm)	0.09	0.09	Milling case $(\overrightarrow{a_p}\ \overrightarrow{a_e}\ \overrightarrow{f})$	Case 1 (XZY)	Case 2 (ZXY)	Case 3 (XYZ)
Layer thickness (µm)	30	60	Layer thickness (µm)	30	-	60
Laser beam spot size (µm)	70	70	**Cutting parameters and tool information (HM end mill-4 flutes)**			
			Cutting speed V_c (m/min)	60	Tool diameter (mm)	10
			Axial depth (a_p) (mm)	5	Helix angle β (°)	30

The study of grain features, subgrain structures, and crystalline textures was aided by electron microscopic observations using scanning electron microscopy SEM and electron backscatter diffraction (EBSD). Furthermore, the MPM was studied using an optical microscope. Inverse figures, pole figures, and Taylor maps were obtained using MTEX. Therefore, two samples of 30 and 60 µm were analyzed, as described in the subsequent sections, named as lt30 and lt60, respectively. A mapping area of 1000 µm x1000 µm and a step size of 2 µm were used for EBSD mapping. Additionally, a 12° misorientation angle was used to distinguish different grain boundaries.

IV.6. Results

The results are presented in two steps. Firstly, the effect of LPBF on the microstructure and texture of LPBF-ed Inconel 718 samples is presented in Section 5.1. Secondly, an analysis and characterizations of the cutting force features and machining parameters are presented in Section 5.2.

IV.6.1. Microstructural and crystallographic characterization

The characterisation of the material was developed in four stages. Firstly, the MPM was evaluated. Secondly, the microstructural characterisation was obtained using EBSD. Thirdly, the

grain morphology was characterised. Lastly, the crystallographic textures of the samples evaluated were compared. Hardness was compared using the Rockwell C scale for both samples with mean values of 36.4 Rc and 32 Rc for the lt30 and lt60 samples, respectively. This implies that hardness did not appear to be the best criterion to explain the influence of anisotropy on oblique cutting forces for this type of material.

Melt pool shapes and dimensions

The melt pool shapes for the lt30 and lt60 samples are displayed in Figure IV-8, with the contours of certain melt pool boundaries outlined for better comprehension. The differences in the shapes and sizes between the melt pools are significant, and the width and depth of the melt pool are observed to be more prominent in the lt30 sample. This is due to a greater VED during the manufacturing process, which produces steeper melt pools in certain cases closer to the keyhole-mode (Figure IV-8a). However, the shape of the melt pool was shallower in the lt60 sample (Figure IV-8b).
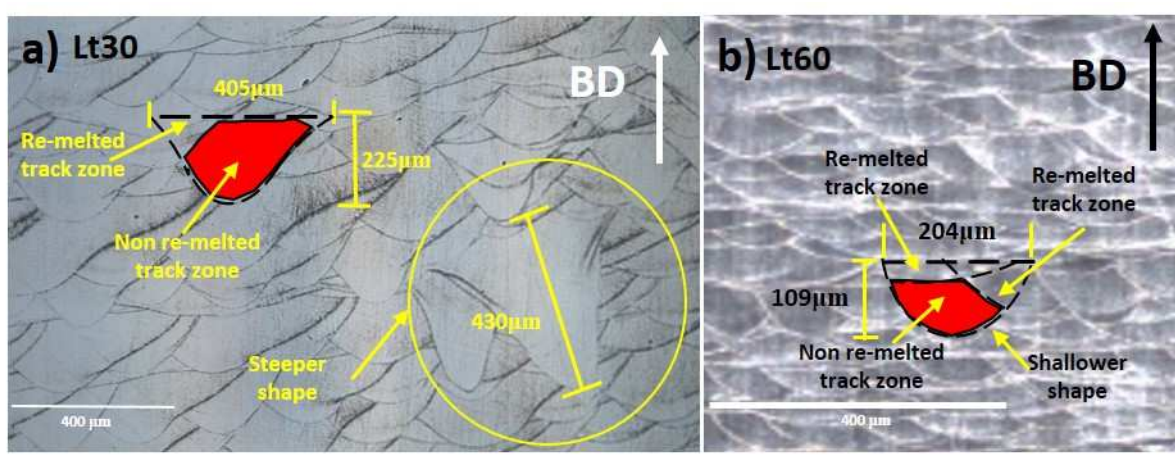
Figure IV-8. Melt pool shape characterization. a) melt pools corresponding to the lt30 sample, b) melt pools corresponding to the lt60 sample

EBSD grain characterization

EBSD and SEM were performed on the lt30 and lt60 samples. Figure IV-9a and Figure IV-9g correspond to the YZ planes, while Figure IV-9c and Figure IV-9j represent the XY planes (upper view) of 30 μm and 60 μm, respectively. Pole figures and inverse pole figures are displayed with <uvw> directions parallel to the BD.
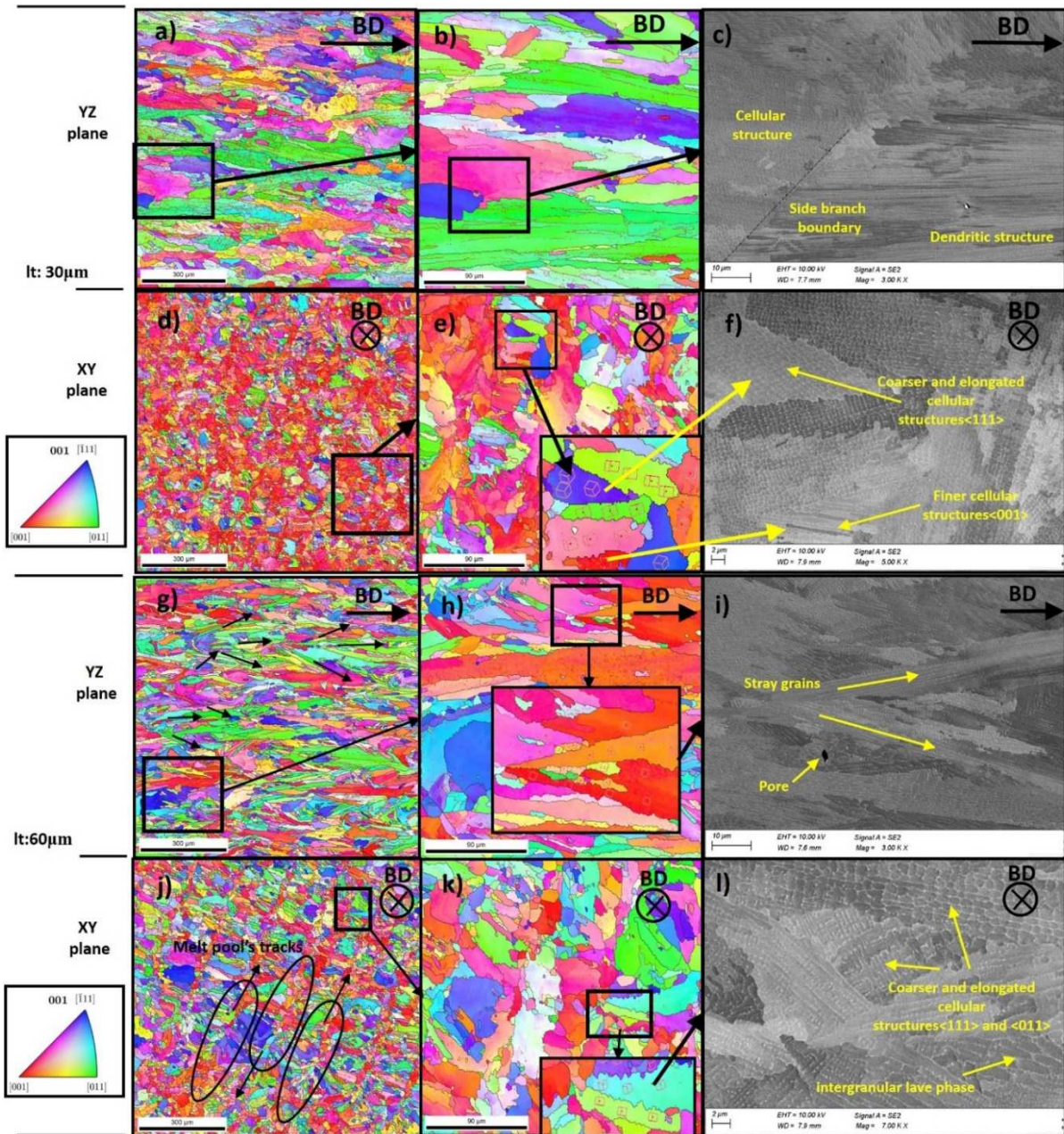
Figure IV-9.Figure 11. EBSD and SEM scans of the samples. a) EBSD of lt30 in the YZ plane, b) and c) SEM scan of lt30 in the YZ plane, d) and e) EBSD of the lt30 sample in the XY plane, f) SEM scan of the lt30 sample in the XY plane, g) and h) EBSD of lt60 in the YZ plane; i) SEM scan of the lt60 sample in the XY plane

Strong epitaxial growth was observed in both samples in the red <001> and green <011> columnar grains. Notably, a few grains crossed over 20 layers; these grains were frequently localised at the bottom of the melt pools where the thermal gradient is stronger and oriented along the BD. Figure IV-9d shows a grain equiaxial arrangement of the lt30 sample, representing the cross-section of the columnar grains (XY plane). This equiaxial arrangement indicates a greater proportion of grains aligned with the BD <001>, represented by the colour red. However, Figure IV-9j shows that the grains present rows of small equiaxial grains (reddish) and rows of

larger columnar grains with different orientations. The former arise from the bottom of the melt pool tracks and are aligned with the BD, while the latter correspond to the lateral zones of the melt pools having oblique orientations. The high directionality in the lt30 sample is caused by the higher input values of energy densities, leading to lower cooling rates than in the lt60 sample. However, the predominant epitaxial orientation of the grains in the lt30 sample can be corroborated in Figure IV-9b and Figure IV-9c, which show a predominant epitaxial growth pattern in the columnar dendritic grains. The epitaxial grain growth pattern can also be observed in the cellular structure depicted in Figure IV-9f. This is because the grains have a dendritic cellular subgrain structure, which is the cellular structure pattern observed mainly on the XY plane (Figure IV-9f) and the dendritic structure pattern observed on the YZ plane (Figure IV-9c). In Figure IV-9c, a few columnar grains in the dendritic epitaxial structure can be observed to be crossing several manufacturing layers, reaching lengths along the BD of over 200 μm, which is equivalent to seven layers or more. This indicates that the strategy of laser rotation at 67° does not prevent epitaxial growth of the grains through the layers at higher energy densities. This behaviour could be explained using the concept of competitive grain growth, which becomes tangible within the observed 3D zigzag grain growth patterns (see Figure III-6b and Figure IV-10); it is key to understanding how the grains can cross multiple layers despite the 67-degree laser-rotation strategy. The zigzags formed by columnar grains follow the thermal gradient vector, which is the mechanism used when Inconel 718 crystals grow as close as possible to the thermal gradient direction (see Figure III-6b). The zigzag reflects the alternation between epitaxial and side-branching grain growth along the BD (see Figure IV-10).
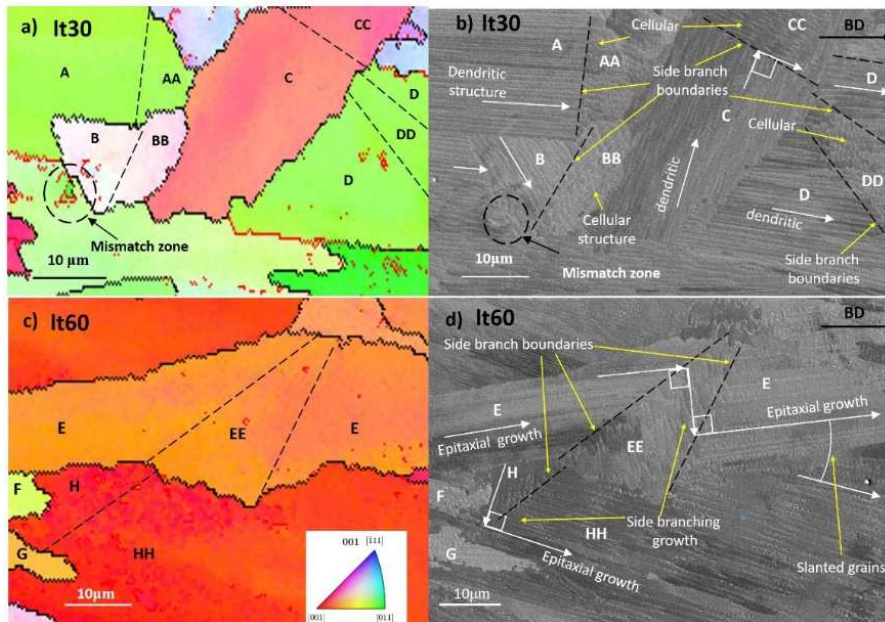
Figure IV-10. 3D zigzag subgrain growth pattern in the lt30 and lt60 samples

Figure IV-10a and Figure IV-10c show the EBSD maps of the SEM shots displayed in Figure IV-10b and Figure IV-10d, respectively (lt30 and lt60). In Figure IV-10b, zones A, B, C and D represent the sections of grains with dendritic subgrain structures. However, the AA, BB, CC and DD zones represent the sections of the grains with cellular subgrain structures. Notably, A and AA represent sections of the same grain, which can be verified in Figure IV-10a, wherein zones A and AA are both in green, which implies that both grain sections share the same crystalline orientation <011>. Therefore, it can be concluded that side branching is the primary cause for the change from dendritic to cellular subgrain structures in these cases. The same reasoning can be applied when comparing zones B-BB, C-CC and D-DD. This behaviour is also present in the 60 µm sample, which can be observed in Figure IV-10c and Figure IV-10d in sections E-EE and H-HH. Both subgrain structures are dendritic but rotated 90° to each other, which is also caused by the side branching and zig-zag subgrain growth patterns.

It is essential to mention that the interaction of the grain growth mechanism with a low cooling rate eases the development of coarse columnar grains. For High volumetric energy density, the larger grains below the newly added layer have enough time(by the lower cooling rates) to swallow the smaller grains or select the grains with a preferred crystallographic orientation (Y. Ji, Chen, and Chen 2018) similar to the seed grain orientations to follow growing(grain coarsening) in the building direction(epitaxially grain spreading across various layers) and laterally through side branching (zig-zag grain growth mechanism). In the same way, the grain coarsening promotes that crystallographic texture intensity increases because the developed crystallographic orientations get larger volumetric fractions. Then by considering the strong influence of texture intensity in material anisotropy, it is possible to infer the indirect effect of subgrain growth behavior on the directional dependency of milling force response.

Grain morphology characterization

The grain sizes and orientations of the lt30 and lt60 samples were quantified on the YZ plane. As shown in Figure IV-11a, an oval profile was used to simplify the shape of the grains to measure their major and minor axes, while the grain equivalent diameter method was applied in Figure IV-11d. In both cases, the grain size was more prominent in the lt30 samples than in the lt60ones.

The cumulative distribution of the grain sizes is displayed in Figure IV-11a, wherein, in the lt30 sample, nearly 30 % of the grains have major axis lengths exceeding 30 µm (Fig 13 point a) and 12 % exceeded 60 µm (Figure IV-11 point c). In contrast, the grains in the lt60 sample are shorter and thinner than in the lt30 sample, with 19 % and 6 % of grains exceeding 30 and 60 µm,

130

respectively (Figure IV-11 points b and d). Figure IV-11b shows the grain aspect ratio, and it can be inferred that the lt60 grains are slenderer than the lt30 ones; this is evident when comparing Figure IV-9a and Figure IV-9g.

The grain orientation is represented by δ (see Figure IV-11c). Notably, for 80 % of the grains, δ lies between 0° and 20° in the lt30 sample and between 0° and 38° in the lt60 one. Therefore, it can be verified that increasing VED slows the cooling rate, thereby promoting the broadening and growth of grains through several layers. Likewise, steeper melt pool shapes favour epitaxial growth along the BD owing to higher thermal gradient values at the bottom of the melt pool.
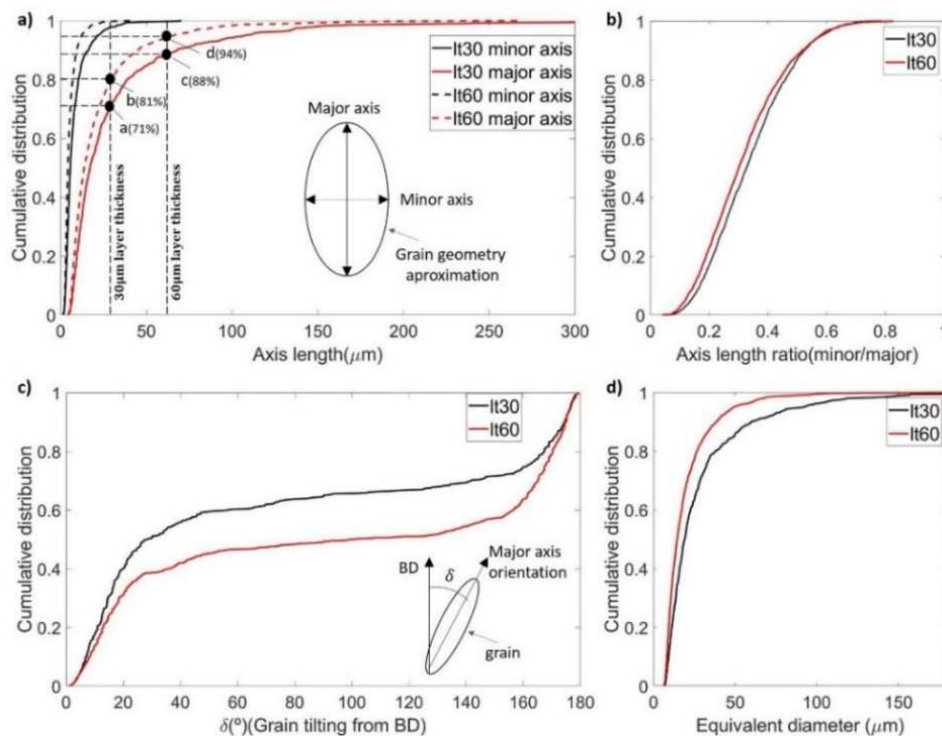
Figure IV-11. Grain characterization

Figure IV-11d shows that the lt30 sample has a larger equivalent grain diameter distribution than the lt60 sample, which directly affects the cutting forces. The grain boundaries act as obstacles to the dislocation flow. When an LPBF-ed component is subjected to stress, dislocations originate within the active slip systems of the textured grain zone with a higher resolved shear stress. When the dislocations reach a grain boundary, they accumulate, and a local stress state is developed.

Crystallographic texture

The crystallographic textures of the evaluated samples are depicted in Figure IV-12. The lt30 sample has a strong ring-like <001> texture with a maximum probability density of 6.5. The lt60 sample also exhibits a ring-like <001> texture, but it appears less dense (3.4 maximum probability). In the lt30 sample, it can be inferred that φ (Bunge notation) ranges from approximately 0° to 15°, indicating a high density of crystalline arrangements aligned along the BD. However, the lt60 sample exhibits <111> and <011> textures on a minor scale. In both samples, the ring-like effect in the texture was caused by the laser rotation strategy.
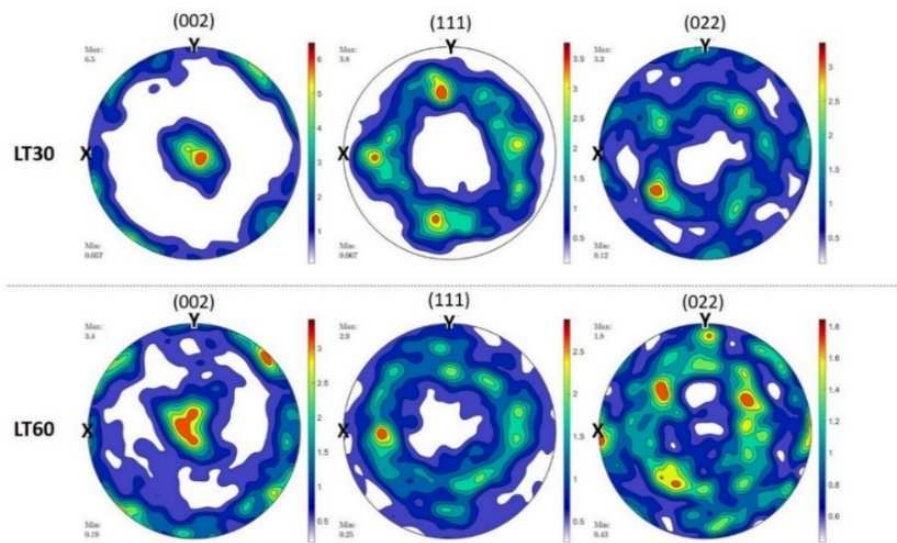
Figure IV-12.Crystallographic textures pole figures (lt30 and lt60 samples)

From Figure IV-12, for both samples, most of the crystals are observed to be rotated 45°to the Z-axis (φ_1). A second group of crystals with a lower density was rotated 70° and 5°to the Z-axis in the lt30 and lt60 samples, respectively.

The strong correlation between the crystalline and grain orientations is an indicator of the effect of the VED on the growth of the subgrain structure. In the lt30 sample, the lower cooling rates allow a steadier growth of the grains in length and width through the zigzag growth mechanism. The influence of the melt pool on the texture is also significant; the shallower melt pools of the lt60 sample developed BD-oriented oblique grains in similar proportions to <001> and <011> textures.

IV.6.2. Cutting force characterization

In this section, the measured cutting force components are compared in milling cases (Figure IV-7). Additionally, the specific tangential and radial cutting force coefficients for the 54 experimental conditions are presented. The analysis of homoscedasticity through Bartlett's test, the uncut chip thickness, radial depth of cut, and the interaction effects of the feed rates on the variability of coefficients are also presented. Thus, the effect of the tool direction on the resultant cutting force is presented as the percent increase in the cutting force ΔF(%) when changing from one milling case to another under the same machining parameters. The same method is used to evaluate the increase in the cutting force due to the layer thickness (lt30 to lt60). Additionally, the variability in the specific cutting force coefficients ΔKt (%) and ΔKr (%) are obtained considering the percentage increase from the minimum to the maximum values of the coefficients under the same experimental conditions (layer thickness, feed rate, radial depth of cut), with the milling case being the only varying parameter. Lastly, the tangential coefficient $\overline{Kt}$ is presented as the average of the three coefficients of the milling cases under the same experimental condition. In Section 6, the microstructural and crystallographic aspects of materials and their relationship with the cutting force variability are discussed. Appendix A (Table IV-4,Table IV-5,Table IV-6) presents the details of the components of the average and maximum forces (X, Y, Z) under each experimental condition evaluated.

Figure IV-13 shows the differences between the average cutting force components by milling case. More pronounced differences and higher force levels were observed in the lt60 sample. Notably, milling cases 1 and 2 generated the highest and lowest cutting forces, respectively.
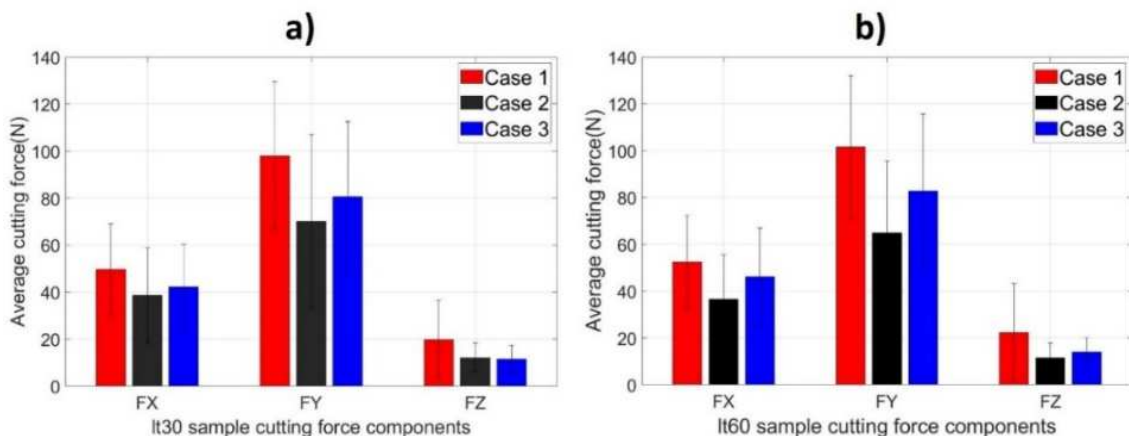
Figure IV-13. Average cutting force components. a) lt30 sample, b) lt60 sample

Figure IV-14a and Figure IV-14b show $\Delta F(\%)$ when the tool direction changes, according to the aforementioned cases, from cases 2 to 1, 3 to 1 and 2 to 3, respectively, for different radial depth values. The results reveal that the material anisotropy effect on the measured cutting forces is more significant when the radial cutting depth (a_e) is small, reaching values over 150 % in certain cases, and it decreases as a_e increases. For a_e values of 0.5 mm, the anisotropy effect on the cutting forces decreases to a range between 5 and 25 % for the lt30 sample and between 18 and 48 % for the lt60 sample. The significant increase in $\Delta F(\%)$ as the radial cutting depth decreases can be related to intrinsic(grain size) and extrinsic(depth of cut) size effects, which are widely reported in literature as root causes of specific cutting force variability(Fu and Wang 2021; Ni Chen et al. 2021). However, the difference between the 2to1, 3to1, and 2to3 curves means that the increased ΔF (%) values were not homogeneous. the largest difference was observed while changing from cases 2 to 1 in all scenarios and the change from cases 3 to 1 exhibited the smallest difference. It suggests that material anisotropy plays an important role in maximizing or minimizing these size effects.

The energy criterion was used to compare the effects of anisotropy on the cutting forces in both samples, suggesting that the lt60 sample requires 37% more cutting energy than the lt30 sample (this topic is discussed extensively in Section 6.2).
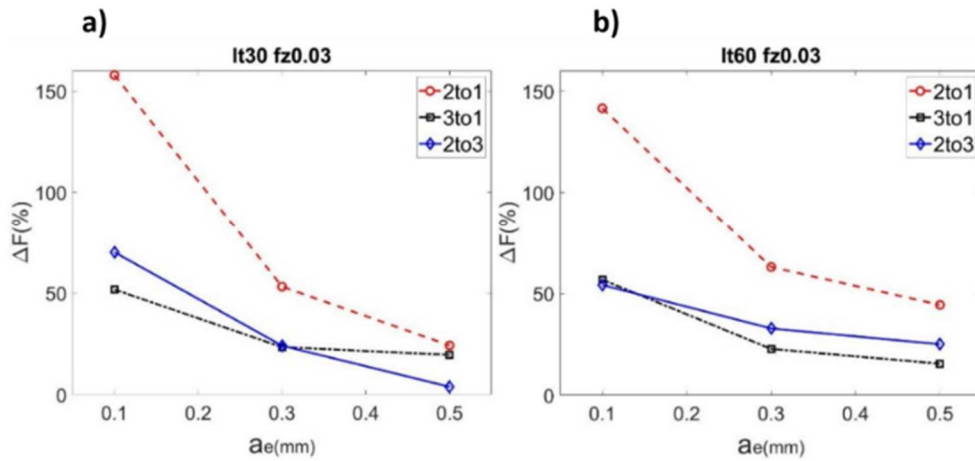
Figure IV-14. Cutting force anisotropy patterns: a) lt30 sample; b) lt60 sample

Figure IV-15 shows the tangential (Kt) and radial (Kr) cutting force coefficients for the lt30 and lt60 samples as functions of the average uncut chip thickness under the 54 experimental conditions evaluated. Each figure comprises three groups of nine coefficients corresponding to different a_e values (0.1, 0.3 and 0.5 mm). Within each group, the coefficients are further grouped according

to the corresponding feed rates (0.03, 0.04 and 0.05 mm/rev). Lastly, each feed rate group is formed by the coefficients corresponding to each milling case.
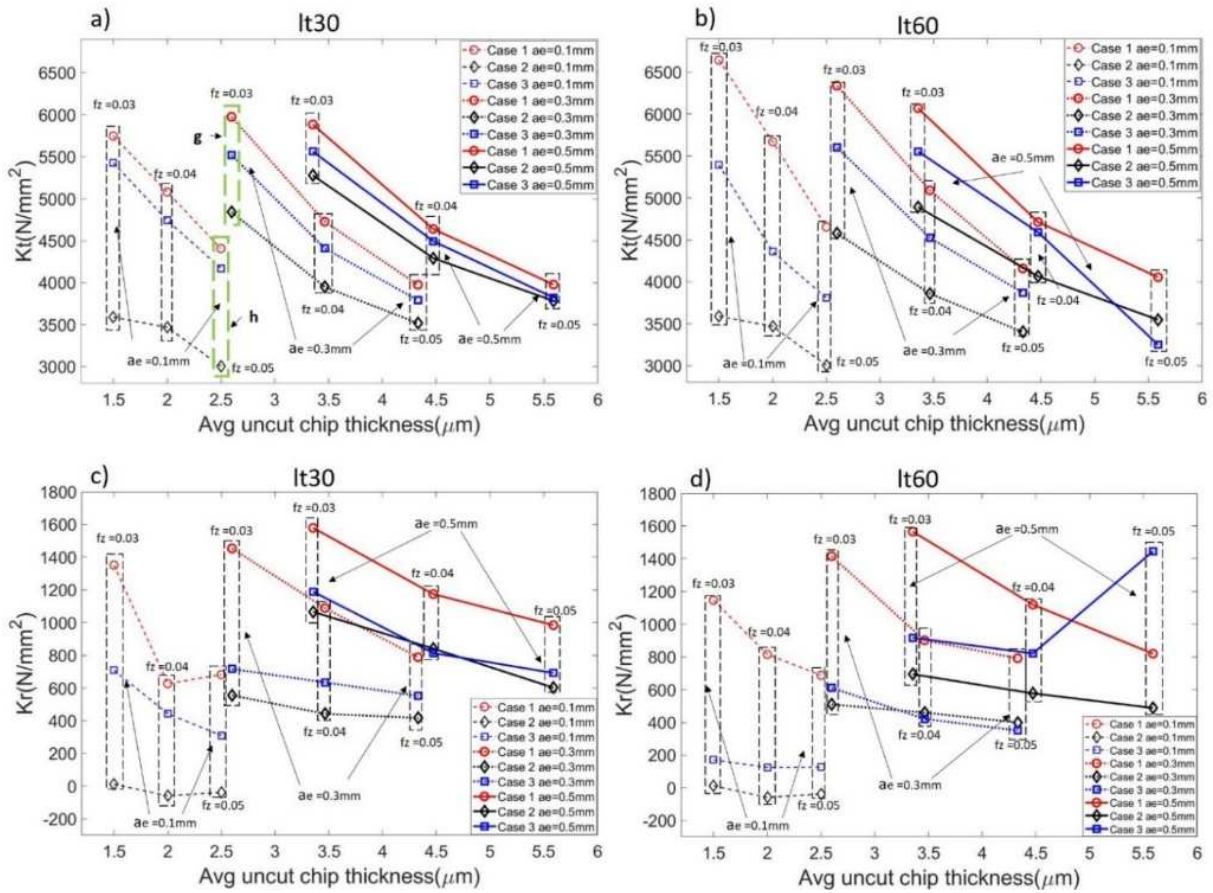
Figure IV-15. Tangential and radial cutting force coefficients as functions of the average uncut chip thickness. a) Kt for the lt30 sample, b) Kt for the lt60 sample, c) Kr for the lt30 sample, d) Kr for the lt60 sample

Notably, at lower average uncut chip thicknesses, the variability of the tangential coefficients increased significantly. However, this effect was more pronounced in the lt60 sample than in the lt30 one (Figure IV-15a and Figure IV-15b). The effect of the average uncut chip thickness on the dispersion of Kr is much smaller; however, the variability of Kr within the feed rate group coefficients is larger than that of the Kt coefficients for all uncut chip thickness levels. Some cutting force coefficients for traditionally produced Inconel 718 (cast and forged) are compared with LPBF cutting force coefficients from this research in appendix A, Table IV-7.

From Figure IV-15a, it is evident that the difference between the coefficients of cases 1 and 3 remains nearly constant for all the evaluated levels. However, milling case 2 was more sensitive to reductions in the uncut chip thickness, which can be observed by a decrease in the coefficients. On the other hand, for the lt60 sample, the decrease in chip thickness can be observed to affect the dispersion of the tangential coefficients Kt for the three milling cases in a similar ratio.Figure

IV-16 corresponds to the Bartlett's test conducted to evaluate the variances of the Kt and Kr coefficients with respect to the average uncut chip thickness. Box-whisker plots for Kt and Kr are shown in Figure IV-16a and Figure IV-16b, respectively. Figure IV-16c shows the details of the statistical analysis using Bartlett's test, where P-values of 0.0128 and 0.25 for Kt and Kr, respectively, were observed. This indicates that the Kt coefficients do not correspond to a normal distribution having significant differences between the variances of each level. While the Kr coefficients adhere to the assumption of normality related to homoscedasticity, consequently, the level of anisotropy observed in the tangential coefficients is very sensitive to the uncut chip thickness. In contrast, the levels of anisotropy in the radial coefficients were similar at all uncut chip thickness levels.
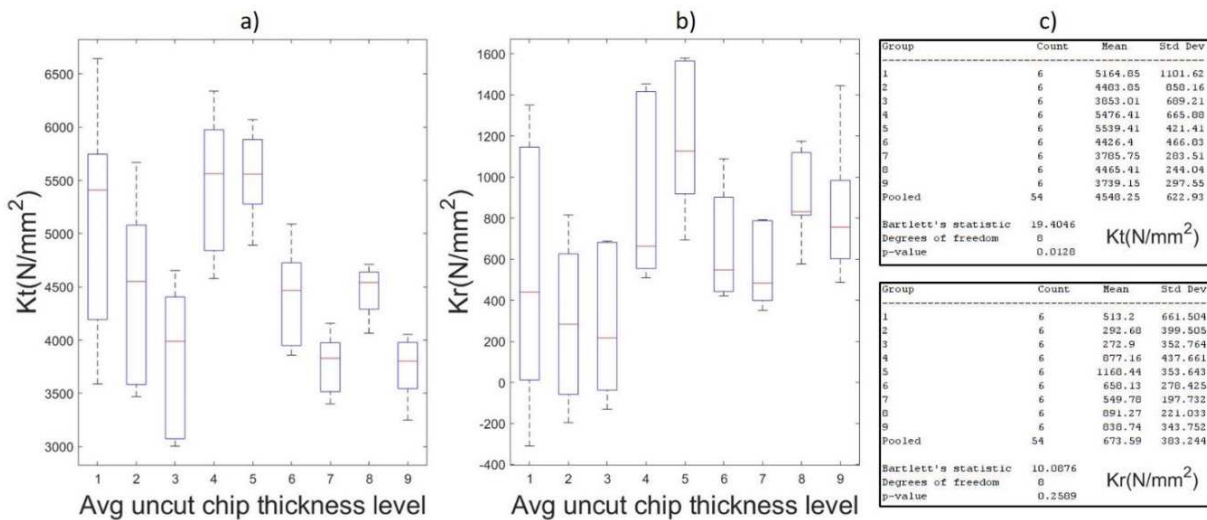
Figure IV-16. Kt and Kr Bartlett's test analysis. a) box-whisker plot for Kt, b) box-whisker plot for Kr, c) statistical details regarding Bartlett's test

Figure IV-17a and Figure IV-17b show the distribution of ΔKt (%) and ΔKr (%) with respect to the uncut chip thickness. From Figure IV-17a, it is possible to infer a relationship between the decrease in ΔKt (%) and the increasing average uncut chip thickness for both samples. Considering a 10% variation in the coefficients as a control value for evaluating the significance of material anisotropy in the milling process and also that ΔKt (%) is an indicator of material anisotropy, it can be concluded that, for the lt30 sample, the anisotropy is significant for values equal to or less than a 4 μm average uncut chip thickness. However, for the lt60 sample, the anisotropy levels were significant at all uncut chip thickness levels evaluated. This value is hereafter referred to as the *critical average uncut chip thickness* to facilitate further analysis.

It is essential to consider the direct relationship between the average uncut chip thickness, shear angle and average shear length $\overline{Ls}$. For the lt30 sample, it can be established that the critical

average uncut chip thickness (4 μm) corresponds to $\overline{Ls}$ = 7.5 μm (See vertical red dashed line in Figure IV-17a), considering ϕ_c= 33 °according to the analysis of the effective Taylor factor. Similarly, the value of $\overline{Ls}$ = 7.5 μm is hereinafter referred to as the critical average shear length ($\overline{CLs}$) for case 2 in the lt30 sample.

The alignment of columnar grain growth with the BD allows the correlation of the grain dimensions (major and minor axes) with certain milling parameters. For milling case 2, a relationship between the major axis length of the grain $d1$ and a_p can be established because both magnitudes are oriented on the Z-axis (BD). In a complementary manner, the minor axis length of the grain $d2$ could be related to $\overline{Ls}$ (Figure IV-17e). Analysing the grain dimensions of the lt30 sample demonstrates a correlation between the average length of the minor axis of the grain (7.8 μm, see Figure IV-17c) and $\overline{CLs}$ (7.5 μm, see Figure IV-17a, Figure IV-17c, Figure IV-17d and Figure IV-17e). This suggests that the difference between the tangential coefficients of milling cases 1 and 2 may be significant when $\overline{Ls} \lesssim d2$.
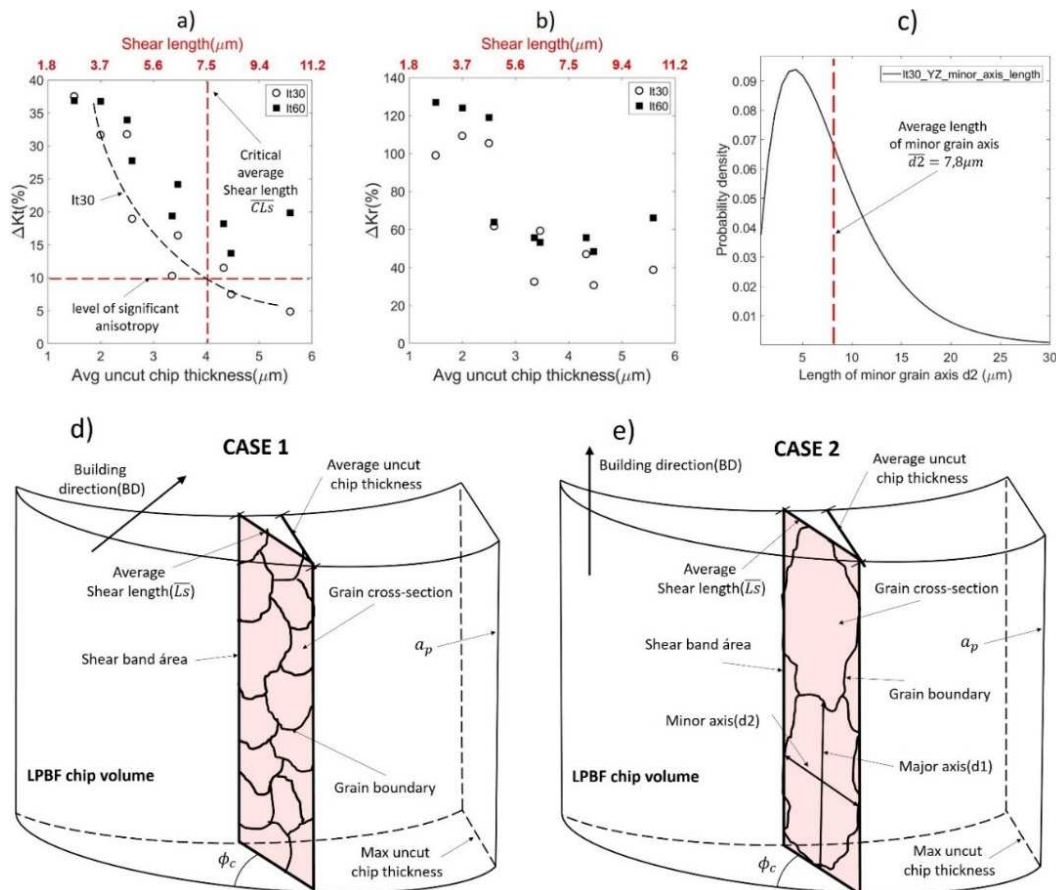
Figure IV-17.Correlation between (CLs) and d2. a) ΔKt (%), b) ΔKr (%), c) Length of minor axis of the grain for the lt30 sample in the YZ plane, d), e) Details of the grain cross-section scheme in the shear band area for cases 1 and 2

Figure IV-17b shows significant levels of anisotropy in the radial coefficients for all uncut chip thickness levels. However, notably, there are two groups of ΔKr (%) values: the first group with

values higher than 100% and chip thicknesses between 1.5 and 2.5 μm corresponding to the tests with lower radial depths of cut ($a_e = 0.1\ mm$) and the second group with ΔKr(%) values ranging from 30 to 65% under the remaining experimental conditions evaluated. In both cases, the ΔKr(%) values were similar, which agrees with Bartlett's test.

The feed rate plays an important role in determining the value of the cutting force coefficients (radial and tangential) beyond its direct relationship with the uncut chip thickness. From Figure IV-15, it is observed that there are groups of different feed rates with very similar uncut chip thicknesses (i.e. points h and g, Figure IV-15a outlined by dashed green lines), but with significant differences in their coefficients. In all instances, the groups with higher feed rates can be observed to have lower coefficient values. In this regard, Figure IV-18a shows the effect of the interaction between f_z and a_e on ΔKt (%). It is observed that for all levels of a_e and both samples (lt30 and lt60), f_z has no significant effect on ΔKt (%). However, from Figure IV-18b, it can be seen that f_z plays a significant role in determining the mean value of the tangential coefficients ($\overline{Kt}$) while a_e is irrelevant. Thus, it can be concluded that the relationship between the uncut chip thickness and the ΔKt (%) variability is mainly due to a_e, while the variation in ($\overline{Kt}$) is mainly due to the feed rate.
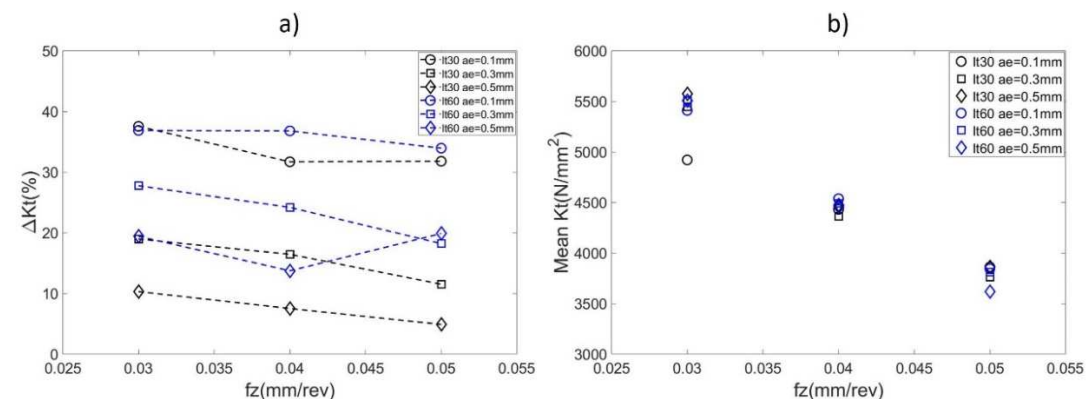
Figure IV-18. f_z and a_e interaction effects on Kt. a) effect on ΔKt (%), b) effect on $\overline{Kt}$

IV.7. Discussion

From Section IV.6, three main issues can be established. The first is related to the variability (anisotropy) in the radial and tangential coefficients due to the change in tool position (milling cases) for each combination of f_z and a_e. The anisotropy is observed under all the experimental configurations analyzed, and it is significant for Kt over the entire range of the average uncut chip thicknesses considered for the lt60 sample and for values equal to or lower than 4 μm for

the lt30 sample under the established control parameters. In the case of Kr, the anisotropy was significant under all the experimental conditions evaluated. The second issue is related to the relationship between the level of anisotropy [ΔKt (%) and ΔKr(%)] and the average uncut chip thickness, where an inversely proportional relationship between anisotropy and the uncut chip thickness was observed for the tangential coefficients. The third issue pertains to the effect of f_z on $\overline{Kt}$, where it can be observed that increasing the feed rate decreases Kt for any value of a_e in both samples. This aspect, however, is not related to the anisotropy of the material, as shown in Figure IV-18a. This behaviour (third issue) can be explained using the effect of the increase in f_z on the increase in the cutting temperature, which, in turn, decreases the plastic flow stress $\acute{\sigma}_y$ (temperature softening). Consequently, a decrease in $\acute{\sigma}_y$ leads to a decrease in the values of the cutting forces. Although it is present in the experimental results, the third issue will not be discussed further in this section because it is not relevant to the analysis of the effect of material anisotropy on the cutting forces.

The observed correlation between the significantly high anisotropy control level, the average critical shear length and the average minor axis length of the grain indicates that the directional dependency of the cutting forces in the shear band may partially depend on how large the fraction of the cutting force resulting from the crystal shear strength $R_{Crystal}$ (slip within the grain) is compared to that resulting from the grain boundary strength $R_{Boundary}$ (slip across grain boundaries). This process of restricting dislocation movement across grain boundaries forms the basis of the grain boundary strength effect (Mouritz 2012).

Namely, the development of significant levels of anisotropy (i.e. the cutting force variation between cases 2 and 1 when $\overline{Ls} \lesssim d2$) is related to the interactions of both tool positions with the microstructure. In this regard, the corresponding tool position in case 2 favours a fraction of the cutting force due to the crystal shear strength that is considerably higher than that due to the grain boundary strength ($R_{Crystal} \gg R_{Boundary}$); i.e., the slip deformation mode mainly develops inside the grains and at a much lower level across the grain boundaries. However for the tool position in case 1, $R_{Crystal} \approx R_{Boundary}$ (because the XY plane has a more extensive fraction of the equiaxed grain structure owing to the columnar grain cross-section compared to the YZ plane). This implies that for $\overline{Ls} \lesssim d2$, milling case 2 resembles the milling of single-crystalline materials, where the grain boundary density is much lower than those of polycrystalline materials (Polák 2016). However, milling case 1 resembles the milling of a polycrystalline material.Based on the discussion above, the directional dependency of the

measured milling forces and their variabilities are analyzed in terms of the crystallographic and grain morphology effects with the Taylor factor and grain boundary density, respectively.

Anisotropy in shear strength by the crystallographic effect

The high level of the <001> ring-like texture intensity observed in Figure IV-12 indicates the necessity to consider the crystallographic effect as a cause of anisotropy concerning the cutting forces related to the machining cases. Therefore, the distribution of the Taylor factor was calculated using the measured ODF, obtained using EBSD, and the DODF from the orientations with the highest volumetric fraction. The tool geometry, tool positions and the pole figure pattern were considered, and the model proposed in Equations 2 to 19 was employed.
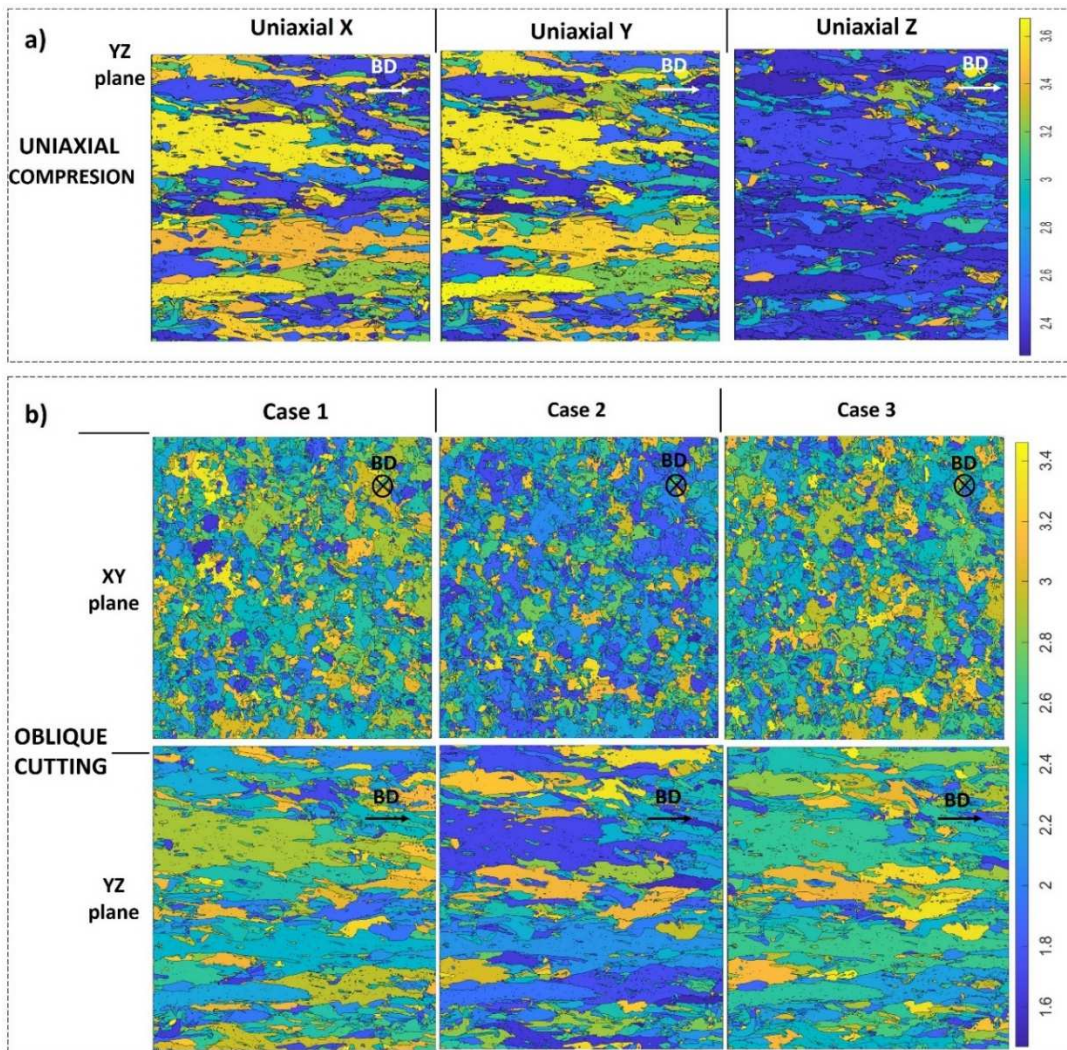
Figure IV-19. a) uniaxial compression Taylor factor by grains–lt30 sample, b) oblique cutting Taylor factor by grains

Figure IV-19 shows the Taylor factor for uniaxial compression and oblique cutting. For this purpose, the statistical distribution of the Taylor factor in each crystal orientation of the grains was calculated using the model proposed in Equations 2–19 for oblique cutting (Figure IV-19b). Figure IV-19a shows the Taylor maps under three uniaxial compressive loads for the lt30 sample, and although the X- and Y-axes show similar distributions, the one along the Z-axis is significantly different. The lower Taylor values of the Z-axis imply lower shear strengths of the material by uniaxial Z load related to the X or Y directions. The observed ring-like textures resulting from the rotation scanning strategy can explain the similarity between the uniaxial Taylor factors in the X and Y directions. Meanwhile, the low shear strength across the Z-axis indicates that the epitaxial growth along the BD is not completely prevented with a laser rotation strategy. The similarity between the uniaxial X and Y Taylor values implies that this material can be classified as transversely isotropic in many cases.

Figure IV-19b shows a comparison between the Taylor factors in each grain under oblique loads for each milling case in the lt30 sample when a_e=0.5, β=30° and ϕ_c=35° (instant of the first contact between the tool and workpiece). The blueish colour of the case 2 maps (XY and YZ) indicates that the lower shear strength for peripheral milling occurs when milling case 2 is applied; this is corroborated by the experimental cutting forces. A comparison between the Taylor's cumulative distribution for different milling cases for the lt30 and lt60 samples is displayed in the appendix (Figure IV-24).

Figure IV-20a shows the macroscopic Taylor factor for each milling case and engagement angles ranging from 154° to 180° (see Figure IV-5) for the lt30 sample. Figure IV-20b, Figure IV-20c, and Figure IV-20d represent the statistical distribution of the Taylor factor corresponding to the crystalline orientation of each grain present in the sample. The value of the macroscopic Taylor factor is observed to be similar to the mean value of the distributions in Figure IV-20b, Figure IV-20c, and Figure IV-20d. This is an important aspect when considering that the machining process is a macroscopic one, and a representative magnitude of the crystalline distribution is required for comparing the resistance to cutting owing to the tool position. Figure IV-20a shows a significant difference in the level of case 2 with respect to cases 1 and 3. However, as the engagement of the tool with the material progresses, the level of resistance to cutting can be observed to decrease for cases 1 and 3 and increase for case 2. The differences between the Taylor factor in cases 2 and 1 are noticeable; however, the levels for cases 1 and 3 are similar. The overall mean Taylor factor obtained was the highest for case 1, followed by case 3, and case 2 exhibited the lowest one. This agrees well with the measured cutting force levels.
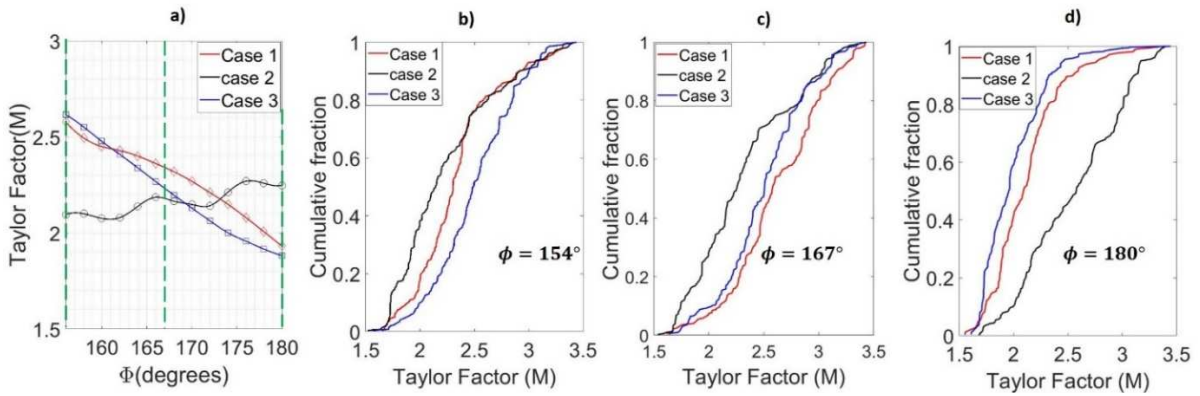
Figure IV-20. a) macroscopic Taylor factor obtained from the DODF in the function of the engagement angle ϕ, b), c), d) single-crystal Taylor factor distributions by ODF when ϕ=154°, 167° and 180°, respectively

Figure IV-21 shows the variation in the macroscopic Taylor factor (polycrystalline) for different tool positions according to its rotation on the Y- (ϑ angle; Figure IV-21a) and X-axes (η $angle$; Figure IV-21b) (for details regarding ϑ and η, see Figure IV-7) compared to the tangential cutting force coefficient (Kt). The trend in the Taylor factor is observed to be similar to the one in the Kt (the same was observed for the average cutting forces). Fluctuations in the Taylor factor are associated with changes in the alignment of the strain tensor to the crystalline slip systems, considering that the vast majority of grains have a crystalline orientation aligned with the manufacturing direction (BD).
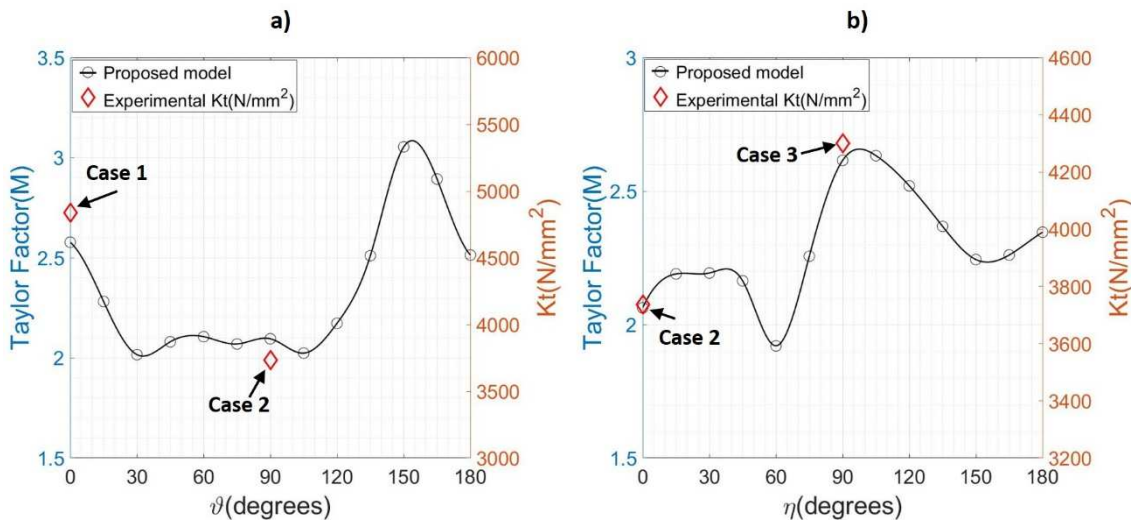
Figure IV-21. a), b) fluctuations in the macroscopic Taylor factor prescribed by rotations of the tool by ϑ and η , respectively, obtained from the proposed model and compared with the experimental Kt for each milling case

Effect of grain size and grain morphology on cutting forces

It is well known that the cutting forces depend on the mechanical properties of the material, and the yield stress is a relevant parameter. During plastic deformation, dislocations move through the crystalline arrangement within alloy grains until they reach a grain boundary. At this point, the large atomic mismatch between the different grains creates resistance to dislocation. Reduction in the grain size leads to a higher grain boundary density (ρ), creating further resistance to the dislocation movement and, in turn, strengthening the material. The Hall–Petch law outlines the effect of the grain size on the yield strength (see Equation IV.19).

$$\sigma_y = \sigma_0 + \frac{k_y}{\sqrt{d}} \quad \text{(IV.19)}$$

where σ_y is the yield stress, d is the equivalent grain diameter, and σ_0 and k_y are material constants. Thus, k_y represents the Hall–Petch slope of the yield stress function with respect to the grain orientation (δ). The Hall–Petch slope is generally higher in <100> textured materials than in <110> ones. This could be the consequence of a low density of dislocation sources combined with a lower density of high disorientation angle of grain boundaries (HAGBs) and the difficulty of activating the grain boundary shearing process (Godon et al. 2010).
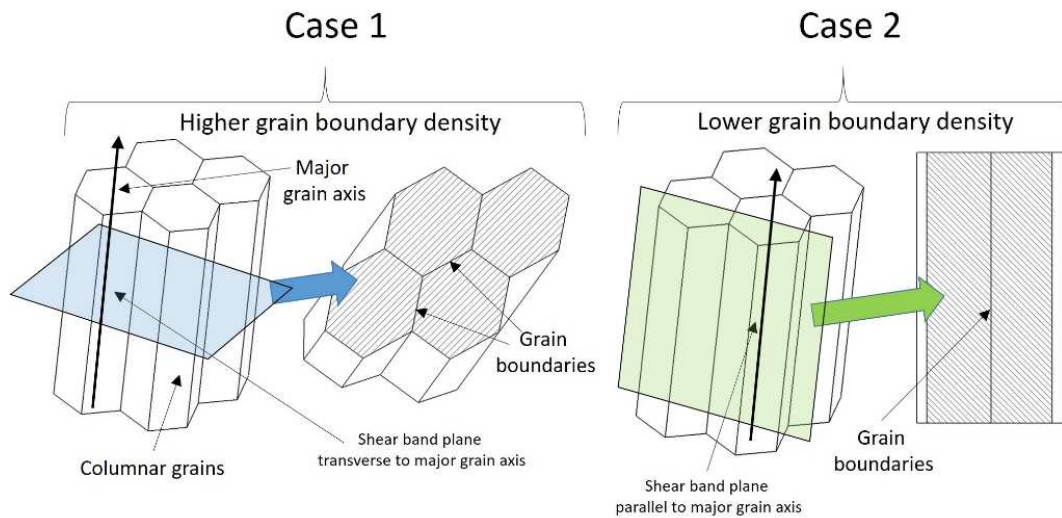
Figure IV-22. Effect of the shear band orientation on the grain boundary density scheme

The grain dimensions shown in Section 5.1 indicate a predominant columnar morphology. Therefore, this shape implies that grain diameter is not the most appropriate concept to consider. Considering that the grain boundary density is defined as the total perimeter of the grain boundaries divided by the evaluated area (Dere et al. 2013) and that the cutting action is

developed from the theory of the plane of a shear band, the grain orientation relative to this plane produces variations in the effective grain boundary density when changing the tool position (see Figure IV-22).

Figure V-23a, Figure V-23b and Figure V-23c represent the grain orientation relative to the chip zone for each milling case. Evidently, case 1 implies that grains are mainly cut transversely, while case 2 represents a shear plane that is more aligned with the grain orientation. Case 3 represents an axial cut at the beginning and a transverse cut at the end of the engagement. These aspects are crucial to understanding the effects of grain morphology on the cutting forces.
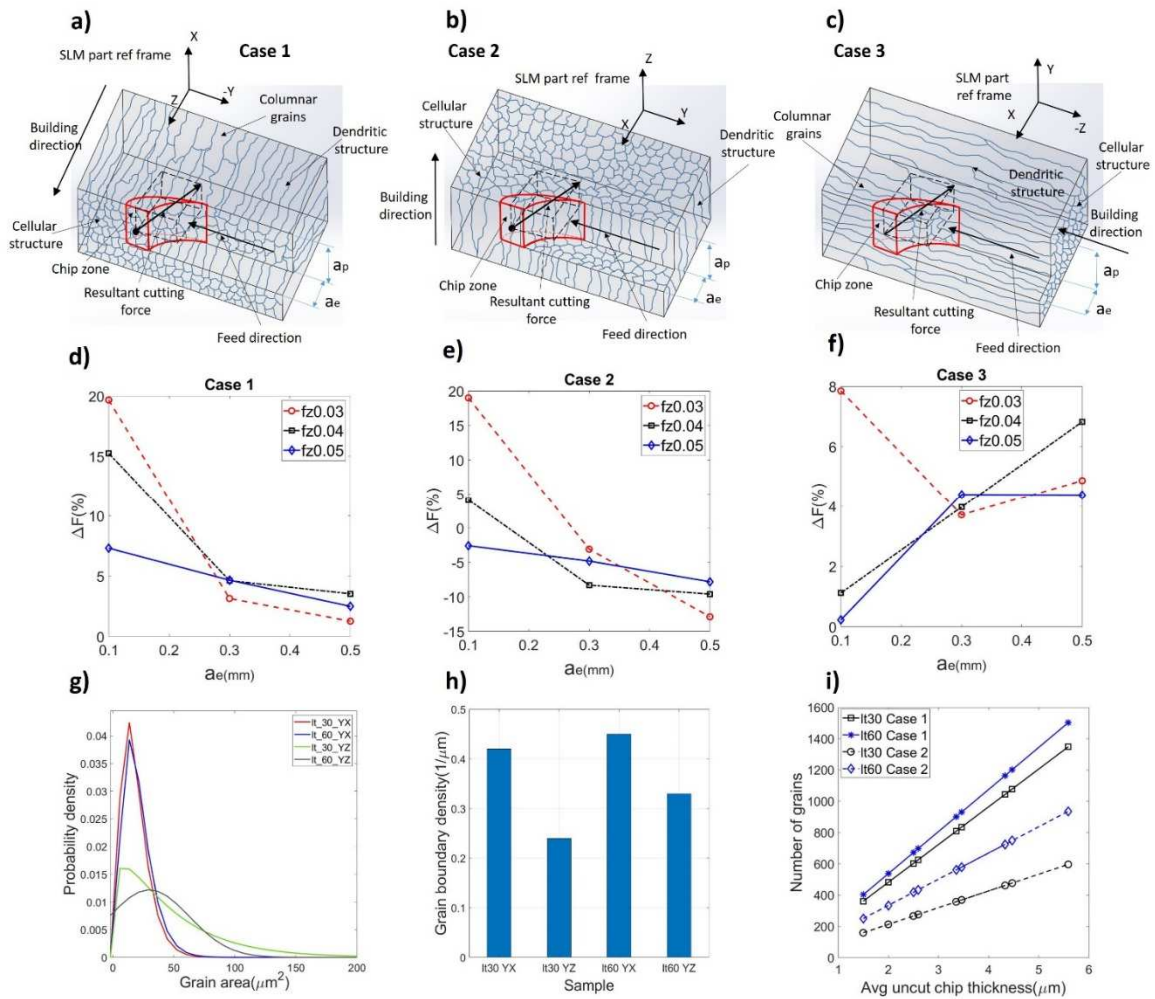
Figure IV-23. a), b), c) representation of the milling cases, d), e), f) percent increment in cutting force by grain refining, g) grain area distribution by sample, h) Grain boundary density (GBD) by sample, i) Number of grains in the function of average uncut chip thickness.

Figure V-23d, 25e, and 25f show the percentage increase in the cutting forces $\Delta F(\%)$ when milling the lt60 sample compared to when milling the lt30 sample under the same machining parameters; each graph corresponds to a milling case representing an increase in the cutting

force in most cases. This increase is small because the radial depth of cut and feed increase for case 1, but the pattern is different for cases 2 and 3.

Figure V-23g shows the grain area distribution, considering an ellipsoid shape for the YZ and XY sample planes (based on the d1 and d2 distributions). The average grain areas for the lt30 sample are 46.81 μm^2 and 20.73 μm^2 for the YZ and YX planes, respectively, while those for the lt60 sample are 29.8 μm^2 and 18.6 μm^2 for the YZ and YX planes, respectively. Figure V-23h shows the grain boundary densities for the YZ and XY planes in lt30 (0.42 μm^{-1} in the XY plane and 0.23 μm^{-1} in the YZ one) and lt60 (0.45 μm^{-1} in the XY plane and 0.34 μm^{-1} in the YZ one). Considering the decreased average grain area and the increased grain boundary in both planes in the lt60 sample compared to those in the lt30 one, the increased development of grain refining in the lt60 sample compared to that in the lt30 sample can be confirmed. The observed increment in the grain boundary density of the lt60 sample correlates with the increase in the cutting force for milling cases 1 and 3 under all experimental conditions; this increment is more pronounced in milling case 1. Figure V-23i depicts the number of grains in the plane of the shear band as a function of the average uncut chip thickness considering the average grain area values from Figure V-23g. the number of grains per uncut chip thickness in both samples evidently increases to a greater extent for case 1 than for case 2.

In case 2, grain refining produced an effect contrary to that expected because the cutting forces decreased under most experimental conditions. This phenomenon had been reported by Papanikolau et al. (Papanikolaou and Salonitis 2021), who concluded that grain boundary sliding is the root cause. To understand this unique behaviour, it is important to consider two conditions: the first is that for case 2, the major axis of the grain is nearly parallel to the milling tool axis (Figure V-23b), and the cutting edge encounters parallel grains with smaller grain sizes. Furthermore, such an encounter could promote an increase in the grain boundary sliding strain mode to the detriment of the slip strain mode compared to cases 1 and 3. Considering that grain boundary sliding mainly develops when the grain size is less than 10 μm (Nieh et al. 1998), which is the case for the lt60 sample. the lack of intragranular shear of larger grains (by slip strain mode), as in cases 1 or 3, could constitute one of the reasons for the lower milling forces in case 2 when milling the lt60 sample.

Based on the above discussion, it is possible to define the cause of the increased anisotropy in cutting forces when machining the lt60 sample compared to when machining the lt30 one based on the differentiated effect that grain refinement has on cases 1 and 2. This is because grain refinement increases the level of cutting force in case 1 owing to an increased grain boundary

density (where the slip strain mode occurs by intragranular shear). However, in case 2, grain refinement decreased the cutting force because the tool position with respect to the grain orientation favours the development of the grain boundary sliding mode.

IV.8. Conclusions

This study analyzes the effect of LPBF process parameters on the anisotropy of AM-ed parts as well as on cutting forces during the milling of such parts. The main relationships between LPBF, microstructure and machining were explained through the analysis and characterisation of the alloy microstructure and texture. A model that considers the crystalline orientation distribution function, texture pole figure patterns (associated with LSSs), tool position, and tool geometry was proposed to calculate the Taylor factor in LPBF components under oblique cutting conditions. The model demonstrated a good correlation between the Taylor factor distribution and the measured cutting forces.

The main results are summarized as follows:

- The directional dependency of the milling force is closely related to the interaction between the orientation of the plane of the shear band (due to the relative tool position with respect to the workpiece), predominant crystalline textures, and orientation and size of the LPBF-printed columnar grains.

- The effect of material anisotropy on the variation of cutting forces as a function of tool position can be explained and quantified through the crystallographic and grain morphology effects. High-VED manufactured parts are associated with steeper melt pools, columnar grains closely aligned with the BD and dense crystallographic textures. For which, quantification of the crystalline effect on the shear strength through the Taylor factor enables a good prediction of the trend in the cutting force fluctuation at various tool positions. However, low-VED manufactured parts are associated with multiple crystalline orientations, implying that the crystallographic effect on the cutting force is smaller, rendering the grain morphology effect more relevant. The proposed model could be expanded to accommodate different cutting tool geometries and/or BCC lattice materials with the necessary modifications.

- A relationship was observed between the uncut chip thickness and the variability in the tangential cutting force coefficients with respect to the tool position. In the case of the high-VED sample, significant levels of anisotropy were observed to occur under

experimental conditions with an average shear length equal to or less than the length of the minor axis of the columnar grains.

- The effect of grain morphology (grain size, grain shape and orientation) on the cutting force was evaluated using grain boundary density analysis, which allows the evaluation of the effects of material anisotropy on the cutting forces when the crystallographic effect is weak. Indeed, a correlation was obtained with the measured cutting force levels for both the low-and high-VED printed parts.

- The low-VED manufacturing conditions increase the grain boundary density. Considering the possible development of the grain boundary sliding mode for small grains (<10 μm), cutting forces were lower when the tool axis was parallel to the columnar grain major axis (or BD). Conversely, the highest cutting forces occurred when the tool position generated planes of the shear bands transverse to the major axis of the columnar grains.

IV.9. Appendix: cutting forces by experimental conditions, predicted shear angles, and single crystal Taylor distributions

Table IV-4. Data on the measured cutting forces and experimental conditions of milling case 1

ae(mm)	t(μm)	fz(mm/rev)	FX_mean(N)	FY_mean(N)	FZmedia(N)	FX_MAX(N)	FY_MAX(N)	FZ_MAX(N)	h(μm)	Kt(N/mm^2)	KR(N/mm^2)
0,1	30	0,03	21,71	50,5	4,8	92,75	149,8	24	0,0015	5745,75	1351,45565
0,1	30	0,04	27,31	57,55	9,499	125,3	160,6	43	0,002	5079,50707	627,165441
0,1	30	0,05	32,55	61,74	9,741	131	179	47,8	0,0025	4406,14814	682,242292
0,3	30	0,03	45,73	97,95	13,66	163,6	268,8	61,6	0,002598	5974,51888	1453,5601
0,3	30	0,04	52,96	99,97	14,19	175,5	280,6	62	0,0034641	4726,48832	1089,13379
0,3	30	0,05	52,04	119,3	19,4	192,2	287,3	68	0,0043301	3975,18289	788,404365
0,5	30	0,03	63,56	125,8	17,61	199	345	66	0,0033541	5883,23021	1578,95517
0,5	30	0,04	70,88	132,9	21,1	213,6	358,4	72,3	0,0044721	4639,53264	1174,48309
0,5	30	0,05	79,6	137	24,05	230,7	382,4	81,1	0,0055901	3978,31813	984,359583
0,1	60	0,03	24,88	61,56	7,84	116	164,4	39	0,0015	6642,38676	1146,54607
0,1	60	0,04	30,41	67,16	8,636	136,6	182,5	50,2	0,002	5669,36238	815,49274
0,1	60	0,05	31,13	68,21	9,895	139,5	187,9	57	0,0025	4653,46097	687,927645
0,3	60	0,03	49,41	99,93	14,29	178,1	280,6	62,6	0,0025980	6337,90891	1416,2539
0,3	60	0,04	55,83	104,2	7,6	202,1	289,1	46	0,0034641	5090,22377	901,566506
0,3	60	0,05	62,16	107,6	17,23	203,1	298,6	70,4	0,0043301	4159,22681	791,720472
0,5	60	0,03	64,08	127,3	19,46	208,2	353	74,2	0,0033541	6069,2441	1565,97745
0,5	60	0,04	74,28	137	22,61	221,5	359,5	84,9	0,0044721	4712,53228	1119,32781
0,5	60	0,05	80,08	141,2	25,14	249,3	375,6	90,3	0,0055901	4054,88664	819,54262

Table IV-5. Data on the measured cutting forces and experimental conditions of milling case 2

ae(mm)	t(μm)	fz(mm/rev)	FX_mean(N)	FY_mean(N)	FZmedia(N)	FX_MAX(N)	FY_MAX(N)	FZ_MAX(N)	h(μm)	Kt(N/mm^2)	KR(N/mm^2)
0,1	30	0,03	10,98	17,26	4	75,5	76	30	0,0015	3588,878	11,8444842
0,1	30	0,04	15,93	27,08	6,298	99,3	95,99	41,54	0,002	3469,66399	-58,8078643
0,1	30	0,05	19,43	34,71	7,114	107,05	104,4	46,54	0,0025	3005,41943	-37,6654599
0,3	30	0,03	30,24	63,16	9	155,1	195,3	49,03	0,0025988	4841,51577	555,44787
0,3	30	0,04	39,97	75	12,48	169,2	211,9	57,17	0,0034641	3949,27581	442,492986
0,3	30	0,05	43,67	79,25	14,22	186,95	237,3	62,12	0,0043301	3517,14566	417,414929
0,5	30	0,03	49,15	101,8	14,76	194,75	293,25	66,36	0,0033541	5277,60357	1065,254
0,5	30	0,04	57,23	111,5	19	212,65	316,4	68,75	0,0044724	4291,16214	841,523622
0,5	30	0,05	73,32	119,6	22,03	245,15	337,95	82,85	0,0055901	3783,65243	602,165915
0,1	60	0,03	13,5	22,57	4,84	95,05	81,975	31,6	0,0015	4193,53965	-309,733263
0,1	60	0,04	17,63	27,68	5,623	106,35	95,35	41,625	0,002	3583,54871	-195,43399
0,1	60	0,05	19,16	33,23	6	112,75	103,55	42,5	0,0025	3074,35433	-130,763106
0,3	60	0,03	27,55	62,66	7	147,25	184,15	50	0,0025980	4578,99065	509,851403
0,3	60	0,04	32,54	70,46	9,53	164,05	208,4	57,5	0,0034641	3859,6373	459,591661

ae(mm)	t(µm)	fz(mm/rev)	FY_mean(N)	FZmedia(N)	FX_MAX(N)	FY_MAX(N)	FZ_MAX(N)	h(µm)	Kt(N/mm^2)	KR(N/mm^2)
0,3	60	0,05	44,29	79,98	13,85	181,1	229,25	60,75	0,0043301	3401,91095	399,176343
0,5	60	0,03	47,23	84,65	15,39	194,05	258,25	66,27	0,0033541	4891,51659	694,307682
0,5	60	0,04	57,13	97,67	18,7	215,05	286,2	73,83	0,0044721	4065,67437	577,102706
0,5	60	0,05	68,83	109,3	22,36	235,7	310,9	67,98	0,0055901	3546,80915	487,962035

Table IV-6. Data on the measured cutting forces and experimental conditions of milling case 3

ae(mm)	t(µm)	fz(mm/rev)	FY_mean(N)	FZmedia(N)	FX_MAX(N)	FY_MAX(N)	FZ_MAX(N)	h(µm)	Kt(N/mm^2)	KR(N/mm^2)
0,1	30	0,03	30,47	4,83	99,59	129,5	29,9	0,0015	5426,9057	708,537047
0,1	30	0,04	43,58	7	121	145,95	42	0,002	4742,8276	443,279823
0,1	30	0,05	50,04	7,184	135,85	157,65	45,35	0,0025	4171,62735	309,851708
0,3	30	0,03	79,27	10,63	173,9	225,75	51,135	0,0025980	5522,00849	716,417216
0,3	30	0,04	82,64	12,63	182,05	243,3	55,175	0,0034641	4407,83119	634,723546
0,3	30	0,05	87,66	15,56	195,4	261,95	68,3	0,0043301	3791,55349	551,71725
0,5	30	0,03	107,6	9	202,15	312,05	70	0,0033541	5560,95032	1188,54228
0,5	30	0,04	115,9	12	226,85	327,2	93	0,0044721	4493,93892	813,945981
0,5	30	0,05	123,6	24,12	241,15	347,85	90,6	0,0055901	3821,93668	692,361025
0,1	60	0,03	37,48	5,85	110,2	117,4	26,8	0,0015	5391,60923	170,560573
0,1	60	0,04	44,08	7,1	119,15	126,15	38,05	0,002	4358,17798	124,367085
0,1	60	0,05	48,89	8,656	129,5	138,35	48,63	0,0025	3807,05413	125,788423
0,3	60	0,03	80,35	11,58	180,65	224,9	55,27	0,0025980	5603,52945	611,407171
0,3	60	0,04	85,05	13,52	198	238,65	60	0,0034641	4524,93121	421,249178
0,3	60	0,05	92,07	15,6	212,25	254,5	69,375	0,0043301	3869,48199	350,263769
0,5	60	0,03	107,5	16,82	214,35	299,2	67,165	0,0033541	5553,92072	917,632506
0,5	60	0,04	117,8	20,27	232,3	333,55	79,355	0,0044721	4589,64956	821,245944
0,5	60	0,05	127,7	24,19	138,95	361,8	92,54	0,0055901	3249,29507	1446,04175

Table IV-7. Traditional produced Inconel 718 cutting force coefficients Vs Inconel 718 LPBF-ed cutting coefficients

IN718 type	ae(mm)	Vc(m/min)	Fz(mm/rev)	Kt(N/mm^2)	Kr(N/mm^2)
Solution-treated and aged(Lin et al. 2021)	1.2	56.5	0.06	4372	
Solution-treated and aged (Moufki, Le Coz, and Dudzinski 2017)	1	60	0.07	4100	
wrought(Z. Zhang et al. 2021)	2.5	50	0.1	1042	302.8
wrought(Tsai et al. 2018)	--	30	0.05	5800	
LPBF lt30(this research) Case 1	0.3	60	0.04	4726	1089
LPBF lt30 (this research) Case 2	0.3	60	0.04	3949	442
LPBF lt30 (this research) Case 3	0.3	60	0.04	4407	334
LPBF lt60(this research) Case 1	0.3	60	0.04	5090	901
LPBF lt60 (this research) Case 2	0.3	60	0.04	3859	459
LPBF lt60 (this research) Case 3	0.3	60	0.04	4524	421
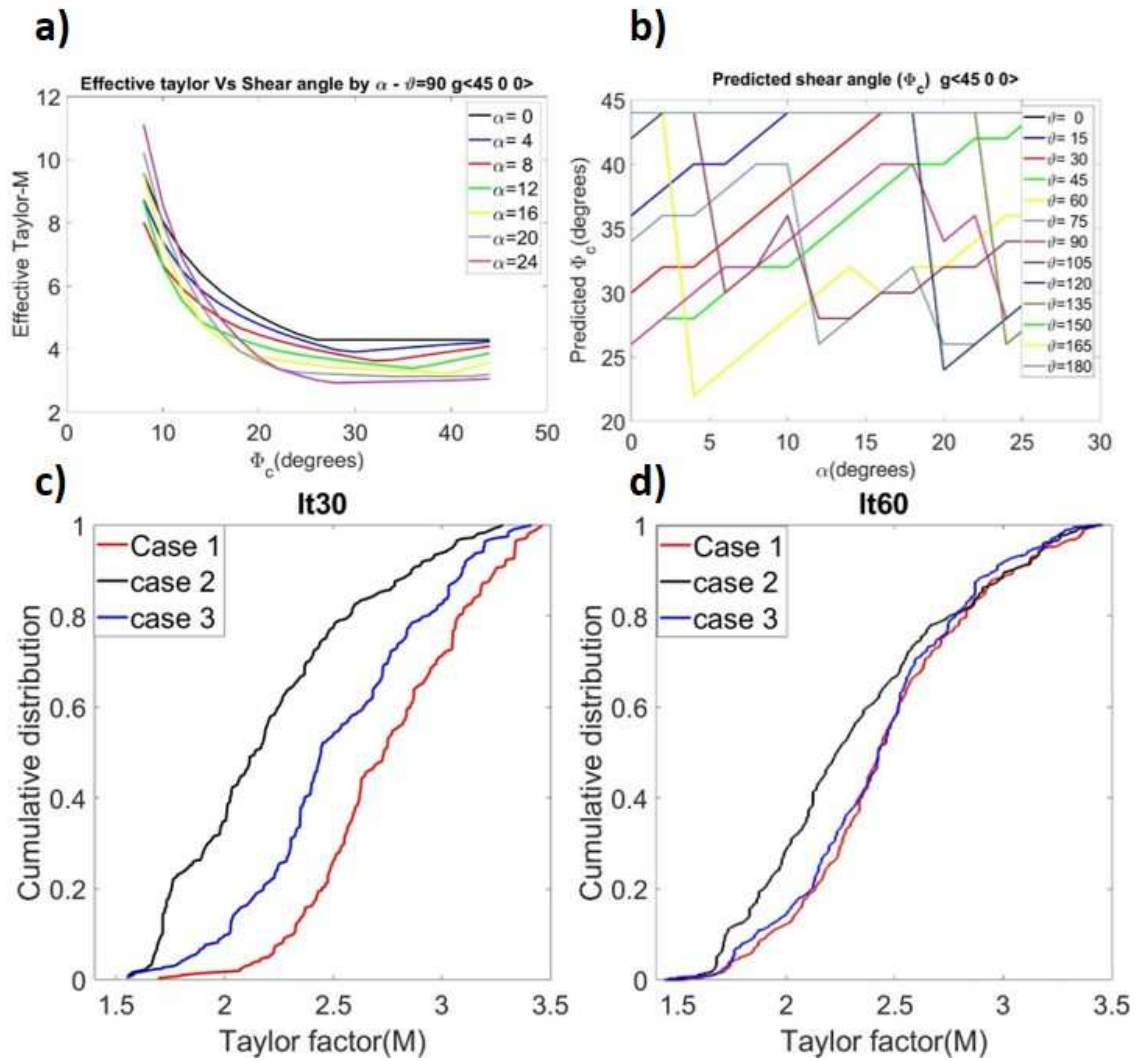
Figure IV-24. a) predicted shear angle by effective Taylor factor, b) predicted shear angle by tool position and relative engagement angle, c), d) comparison between the single crystal Taylor factor distributions for the lt30 and lt60 samples

Chapter V. Vector based model to characterize and predict shear strength sensitive cutting force coefficients of LPBF anisotropic parts

V. Vector-based model to characterize shear strength sensitive cutting force coefficient of LPBF anisotropic parts

This chapter presents a vector-based model to characterize physically meaningful cutting coefficients that can be integrated into microstructure-based models.

V.1. Introduction

Additive manufacturing (AM) has made it easier to obtain components with complex shapes, hollow and lattice-like structures, parts with better magnetic properties for electro-mobility applications(Bittner, Thielsch, and Drossel 2021), or even with improved mechanical damping (Scott-Emuakpor et al. 2018). However, industrial applications of these components usually require high surface quality for assembly operations and fatigue control. In this aspect, many techniques are used to obtain the surface finish of the parts manufactured by AM, including finishing by machining, non-conventional techniques such as SAG (Beaucamp, Namba, and Charlton 2015), electro discharge machining (EDM)(Hassanin et al. 2016), Electrochemical machining (ECM) (C. Zhao, Qu, and Tang 2021) or ultrasonic cavitation abrasive finishing (UCAF) (amirmahyar khorasani 2018), among others. In this aspect, it is noteworthy to establish that finishing by machining is one of the most successful techniques, given the higher productivity it provides and the rapid integration of both processes in the CNC system and modular workpiece holding systems, among others (Jiménez et al. 2021a; Webster et al. 2021). One of the most studied aspects of machining components manufactured by AM is machinability, which includes tools wear, cutting forces, and residual stresses (Bonaiti et al. 2017; de Oliveira Campos et al. 2020). Within this field, there are significant efforts to characterize the magnitudes of the cutting forces for milling and turning of AM components (Kaynak and Tascioglu 2018; Ducroux et al. 2021b), being the cutting force prediction a key factor for the planning of the hybrid(AM+machining) process chain.

The modeling of the cutting process has been widely studied and reported in the literature. In this respect, Ehmann et al. (Ehmann et al. 1997) classified the models into three main groups: analytical, experimental, and mechanistic. Among the basic analytical models stand out the works of Merchant (Merchant 1944), who, based on the principle of minimum energy, established the equations to

determine the shear angle, and Tobias and Fishwick (Tobias and Fishwick 1958), who considered the effect of varying chip thickness on cutting forces and gave rise to stability analysis. A more recent work (D. W. Wu and Liu 1985) included the effects of friction and elastic properties of the material within the analytical model. Works such as Oxley (P. L. B. (Peter L. B. Oxley 1989), (Young, Mathew, and Oxley 1994) and li (X. P. Li et al. 1999) are benchmarks for simulating cutting forces by incorporating high rates of deformation, stress flow, and material properties, among others, considering plasticity models such as Johnson-cook (JOHNSON et al., n.d.), that favor computational analysis thanks to its relative simplicity compared to other more exhaustive models. Other studies, such as that of Oxley (P. L. B. Oxley 1961),(Kegg 1965), and Altintaş (Altintaş and Budak 1995), increased the accuracy of analytical models by considering process non-linearities related to ploughing. Despite improvements in analytical modeling, the high complexity of analytical models, the complexities of modern materials, and the geometrical evolution of tools have limited the use of analytical models. (Layegh K and Lazoglu 2014).

On the other hand, the experimental models are intended mainly to determine the dynamic cutting force coefficients under different approaches; those are the static approach (Das and Tobias 1967), dynamic approach (Peters, Vanherck, and Van Brussel 1971),(Goel 1976), and time series approach (Ahn, Eman, and Wu 1985). Empirical models, in many cases, allow a good prediction of experimental results. However, the lack of understanding of some physical phenomena involved in machining processes and the large number of parameters that are part of these models make the derived mathematical expressions too complex and impractical for industrial applications.

The first breakthroughs in developing mechanistic models came from (Koenigsberger and Sabberwal 1961)and (Sabberwal 1962), where basic concepts, such as chip thickness and workpiece tool contact area, were established. In this topic, Budak et al. (E. Budak, Altintaş, and Armarego 1996) obtained cutting force coefficients from the oblique shear theory of Armarego. With the classical orthogonal shear database, the cutting force prediction was compared with a calibrated mechanical model and Experimental results. However, finding that it is an entirely viable technique requires a reliable and updated materials and tools database, making mechanistic models more recommendable for new materials and applications, such as the metals printed by LPBF. Mechanistic models have recently been developed and established as the most widely used in the industry due to the ease of integrating these models with computer simulation of cutting processes through tools widely used in as CAD-CAM packages, among others. These models include process effects such as

runout, tool wear, and others. Along this line, Altintas et al. (Y. Altintas, Spence, and Tlusty 1991) and (Yücesan and Altintaş 1994) developed a methodology for predicting forces by peripheral milling in a linear path. The linear model of Altintas has been widely used and is the basis of most of the current mechanistic models(Gonzalo et al. 2010a). On the other hand, Shin and Waters (Shin and Waters 1997) developed an alternative mechanistic method for calculating cutting forces in peripheral milling through an iterative component.

In another paper, Wang (M. Wan et al. 2007) developed geometric models that include the tool runout into the linear model to reasonably predict the difference in cutting force peaks per tooth in peripheral milling. Other Works, such as that of (Yoon and Kim 2004) based on the mechanical model of Altintas, show that the force prediction is inaccurate for small chip section values. More recent work (Gonzalo et al. (Gonzalo et al. 2010b) proposed an inverse model to determine the shear and edge coefficients from the instantaneous cutting force. For this purpose, they proposed an optimization solution to solve the simulated instantaneous force values equation with the experimental values. The results show the advantages of the instantaneous force model over the average force model. A related topic (Adetoro and Wen 2010) developed a hybrid methodology of two steps, Firstly, by FEM, the cutting force coefficients are calculated, and in the second step, the mechanistic model predicts the cutting forces. Additionally, there are many mechanistic models for chatter mitigation (F. J. Campa et al. 2007; Francisco Javier Campa et al. 2011; Olvera et al. 2016), machining on complex surfaces (Lamikiz et al. 2005; 2004; Subrahmanyam et al. 2010), and curved and circular trajectories that incorporate the effect of run-out and differences in the thickness of chip during cutting due to differences in feed rate by the effect of curvature(Yun Yang, Zhang, and Wan 2011; B. Wu et al. 2013), ball-end milling (Layegh K and Lazoglu 2014), dynamic milling force prediction in inclined operations, serrated end-mills (Urbikain Pelayo and Olvera Trejo 2020; Pelayo 2019) among others.

The prediction of cutting forces by milling in anisotropic materials is a topic that has been studied mainly in wood derivatives (Goli et al. 2010)(Dippon et al. 1999) and composite materials (Song and Jin 2020; Gordon and Hillery 2003; Mullin et al. 2020); In this line, the cutting forces used to be represented as periodic functions depending on the fiber cutting angle. However, Metallic materials obtained by additive manufacturing require special treatment in terms of obtaining cutting force coefficients since, for finishing processes, the magnitude of the cutting forces changes significantly when the tool-workpiece orientation changes (Pérez-Ruiz et al. 2021; Fernandez-Zelaia et al. 2019;

Malakizadi et al. 2021). It is noteworthy that isotropic metallic materials usually have equiaxial grains with multiple crystalline orientations, and the shear resistance does not change significantly with the tool orientation relative to the workpiece; therefore, the current mechanistic models can work correctly for any position of the tool to the workpiece. However, for single-crystals or textured polycrystal materials such as those obtained by additive manufacturing (especially the LPBF type), the grains are primarily columnar, and the crystalline orientation tends to have clearly defined patterns (crystalline texture). Figure V-1 compares the shear strength (through the Taylor factor) of two Inconel 718 samples. In the first row is shown isotropic Inconel obtained by forging, and in the second row is the anisotropic Inconel obtained by LPBF. The first column corresponds to each sample's inverse pole figures (IPF), where great differences in grain morphology can be observed, mainly equiaxial grains for the isotropic Inconel sample and columnar grains for the LPBF Inconel sample. It is noteworthy that wrought Inconel sample grains have multiple crystal orientations, while for the LPBF Inconel sample, a predominant <001> crystal texture is observed. The middle and right columns allow comparing the Taylor factor of both samples for two orthogonal directions (X and Y axis). It is observed that the plastic strength variation for the wrought Inconel sample is negligible (same average Taylor factor ≈ 3), which is observed by the similarity in the coloring of the grains for both orientations. In contrast, for the LPBF Inconel sample, the difference in shear strength is significant between both orientations (average Taylor factor from 2.2 to 3.6), which is observed in the big differences in the coloring of the grains (from yellow to blue). These aspects then cause the grain boundary density and crystal orientation to change significantly as a function of the shear plane induced by the tool orientation, which is why the current mechanistic models are not recommended for anisotropic metallic materials.
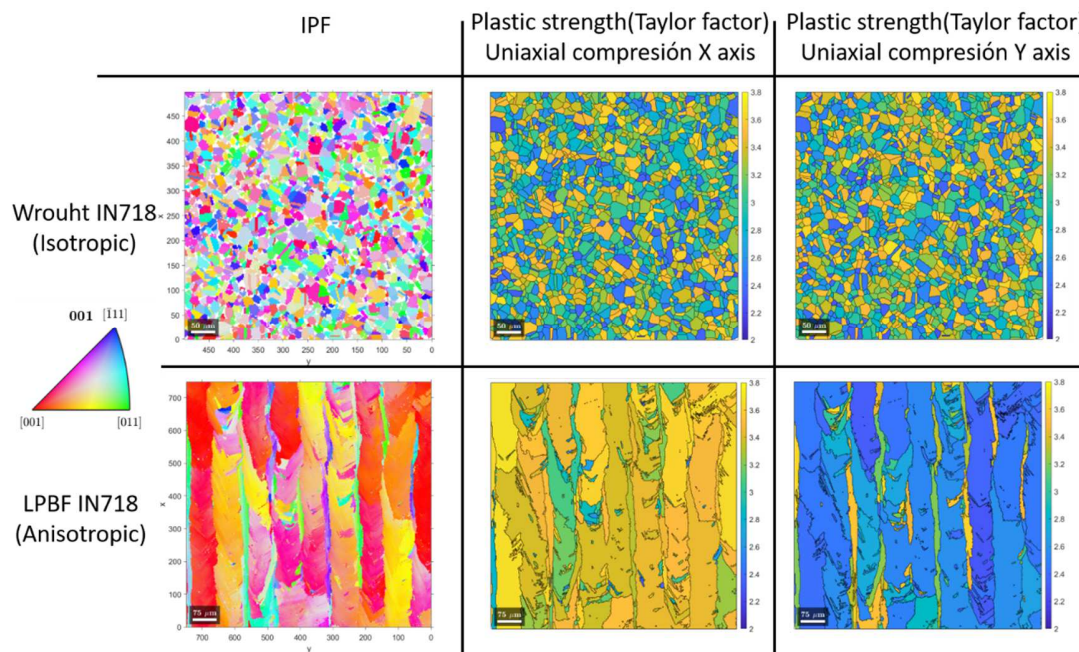
Figure V-1. Plastic strength and grain morphology differences between Isotropic and anisotropic Inconel 718

The cutting force prediction for LPBF materials is a topic that has not been studied in deep yet. Most of the studies for AM materials are conducted to assess machinability and are related to tool wear and surface quality. In this line, Brown et al. (Brown et al. 2018b) have studied the surface characterization of the printed and machined Inconel 718, finding that the microhardness varies according to the building direction, which is a characteristic of this anisotropic materials family. In other recent research, Grove et al. (Grove et al. 2018) conducted a machinability and surface quality analysis for Ti 5553. They compared the Ti 5553 LPBF with the Ti 5553 forged, finding interesting differences in surface quality. However, they observed a strong building direction influence on tool wear and residual stresses. Kim et al. (D. M. Kim et al. 2018a) compared the wear on cylindrical milling cutters when machining Inconel 718 forged versus Inconel 718 SLMed, finding that although Inconel LPBF is harder than forging, tool wear levels are higher when machining Inconel 718 forged attributing the causes to the presence of porosities and cavities in the Inconel 718 SLMed.

Current inverse mechanistic models (the linear model, e.g.) for determining linear or exponential coefficients allow the cutting forces to be simulated acceptably; however, their calculation is closely linked to linear regression or non-linear optimization processes, which in many cases do not allow

the obtaining of physically meaningful coefficients. This aspect means that obtaining the LPBF-type mechanistic coefficients by linear regression methods makes it necessary to carry out tests in all possible tool orientations due to the directional dependency of the cutting forces, which is very demanding and not recommendable. However, In recent work, the interactions between the microstructure of Inconel 718 LPBF, the tool position, and the cutting forces were shown (Pérez-Ruiz et al. 2021), and an oblique shear microplasticity model was presented to obtain the Taylor factor on the oblique shear planes generated by a helical endmill cutter. Based on the proportionality between cutting force coefficients and the Taylor factor (Sato et al. 1983; W. B. Lee and Zhou 1993; Pérez-Ruiz et al. 2021), it is then possible to establish a quantitative relationship between the experimentally obtained coefficients and the Taylor factor for any tool position which works as a reference to predict the cutting coefficients for other tool orientations related to the workpiece and avoiding multiple experimental tests for any other direction. The coefficients obtained in the proposed model are proportional to the average cutting forces, and the shear cutting forces are proportional to the Taylor factor; for this reason, the shear cutting force coefficients obtained with the proposed model for a specific tool orientation $Ks(ref)$ could be used as a reference to obtain the coefficients for any other tool orientation.This is clearly seen in expressions I and II.

$$c = \frac{Ks(ref)}{M(ref)} \quad (I)$$

$$Ks(x) = c * M(x) \quad (II)$$

Where c is the proportionally constant between experimental shear cutting force coefficient $Ks(ref)$and Taylor factor $M(ref)$ for a reference tool-workpiece orientation, $Ks(x)$ is the predicted shear cutting force coefficient for a x tool-workpiece orientation and $M(x)$ is the Taylor factor(or any other physical parameter sensitive to the directional dependency) for a x tool-workpiece orientation.

The aspects discussed above can be better understood in the schematic in figure 2, where the proposed inverse model is compared with the linear inverse model. The proposed inverse model uses a vector approach based on the instantaneous real contact area and the instantaneous normal vector of this area. The vector approach allows the obtained shear coefficients to be proportional to the material's cutting strength, making the obtained coefficients physically meaningful. On the other hand, the coefficients obtained by the conventional linear inverse model are not related to

the shear strength variability of anisotropic materials, which limits their use to isotropic materials. In the proposed model, instantaneous coefficients are obtained as a function of the engagement angle, and a methodology for obtaining the six single-value coefficients ($Ktc, Kte, Krc, Kre, Kac, Kae$) required by the direct model (for cutting force simulation) is presented.
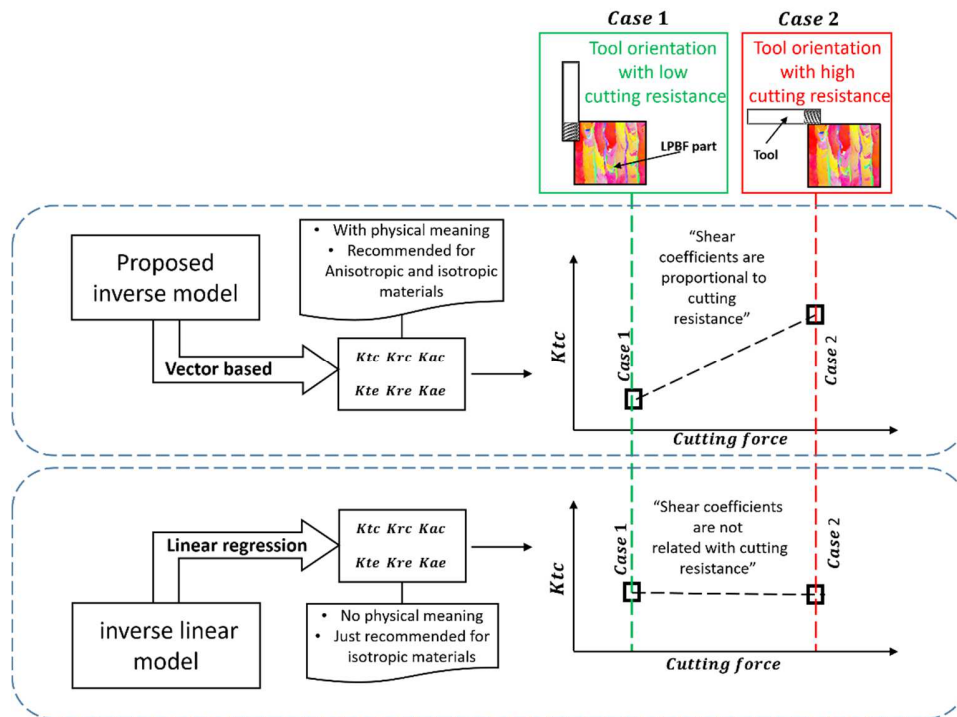
Figure V-2. Proposed inverse model vs. inverse linear model Scheme

At this point, it is essential to clarify that the experimentally obtained coefficients $Ks(ref)$ must be proportional to the average cutting force and be related to the real contact area and shear force vectors. The above is because the Taylor model considers the shear strength is related to the slip deformation mode(plasticity). Therefore, the experimentally obtained coefficients must differentiate which cutting resistance fraction is due to shear and which fraction is related to the tool edge or flank friction (ploughing). This study aims to differentiate how much of the cutting forces measured by the dynamometer corresponds to the shearing process and how much fraction is related to ploughing by comparing the instantaneous normal vectors of the rake area with the instantaneous measured resultant vectors(Dynamometer). For this reason, the cutting force

coefficients $Ks(ref)$ obtained with the proposed model can be integrated into microstructure-based cutting force prediction models (recommended for anisotropic metallic materials such as LPBFed).

In this line, the paper is split into three sections. Firstly the expressions to obtain the real contact area and $Ks(ref)$ coefficients are displayed. Secondly, a case study is presented, and the instantaneous coefficients graphs are displayed. Finally, the proposed model is verified.

V.2. End-mill instantaneous real contact area model

As a first approach, the tool-workpiece contact area sections are defined—secondly, the mathematical expressions for the rake face profile are introduced. The expressions to extract the shear and ploughing force fractions from dynamometer data are presented. Finally, the expressions for calculating the rake-face mesh points coordinates, their normal vectors, and instantaneous and accumulated contact area are presented for down and up milling in Appendix A.

V.2.1. Definition of tool-workpiece area

The methodology of the proposed model is based on developing three contact area combinations considering the unmachined zone and the machined zone. Figure V-3 shows a sequence of positions of the tool in relation to the workpiece. Figure V-3a shows when the tool cuts the flat area (unmachined area). The contact area between the tool and the unmachined area has a triangular appearance, as shown in the figure. Figure V-3b shows the instant when the tool cuts simultaneously on the flat (unmachined) and the curved area (previously machined). In this figure, the boundary contact lines on the rake face due to both surfaces (curved and flat) are clearly visible. The area between these lines and the outer helix forms the instantaneous contact area. Figure V-3c shows an instant where the tool only has contact with the curved area (previously machined).
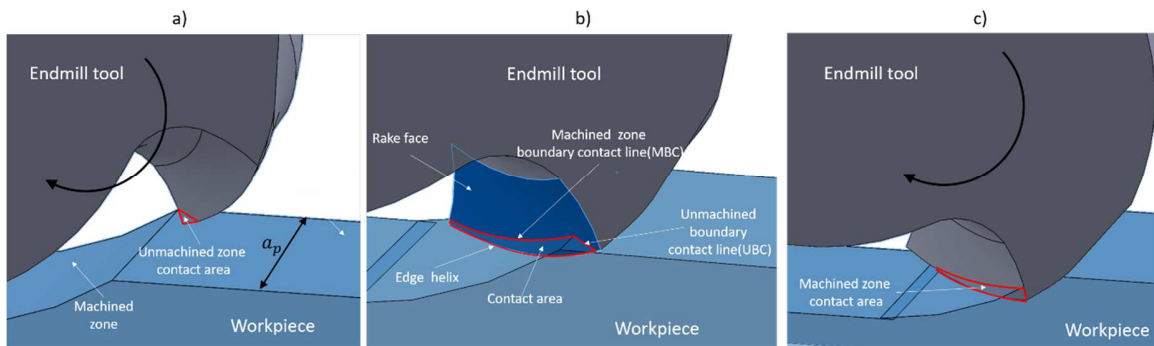
Figure V-3. Contact area zones

The first step is to calculate the contact area, their centroid, and the resultant normal vector for each engagement angle value, as shown in Figure V-4. Figure V-4a shows the instant when the tool has wholly reached the flat surface contact area. Figure V-4b shows an instant when the tool cuts both areas simultaneously but has not yet reached the maximum contact area. Figure V-4c shows the maximum contact area. The three figures show the change in the centroid position and normal vector magnitude as the engagement angle increases. Determining these three variables is the central aspect of the first stage of the present model.
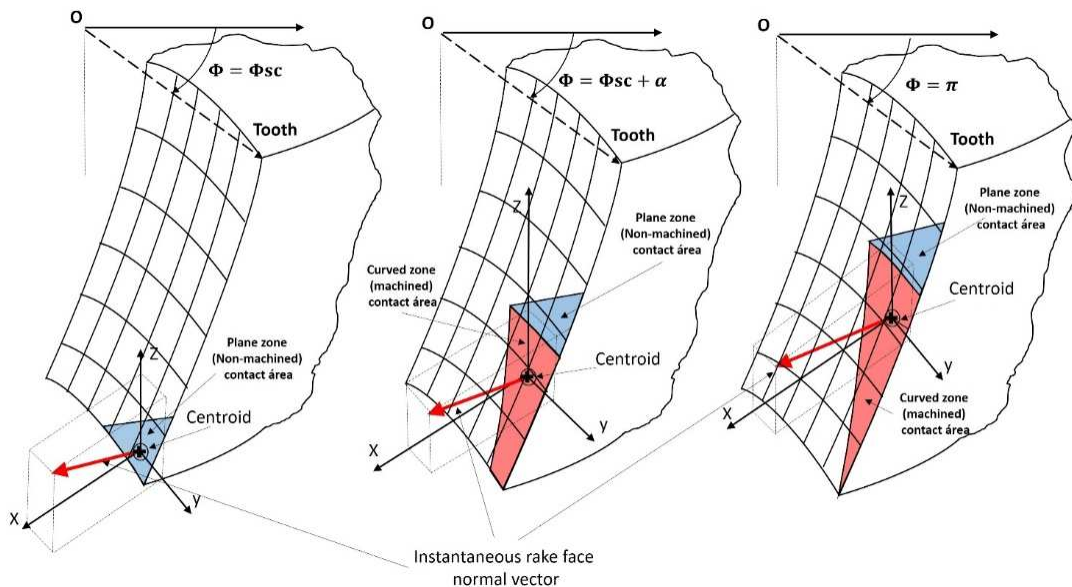
Figure V-4. Engagement-driven growth of the contact zone

The proposed model seeks to obtain the points that make up the mesh corresponding to the discretization of the tool rake face that gets in contact with the workpiece (see Figure V-5) as a function of the engagement angle. Once the coordinates of the points are obtained, it is possible to calculate the instantaneous contact area, instantaneous centroid, and instantaneous resultant normal vector. The development of the equations for obtaining the mesh points as a function of tooth engagement angle and the other variables associated with them is presented in Appendix A.
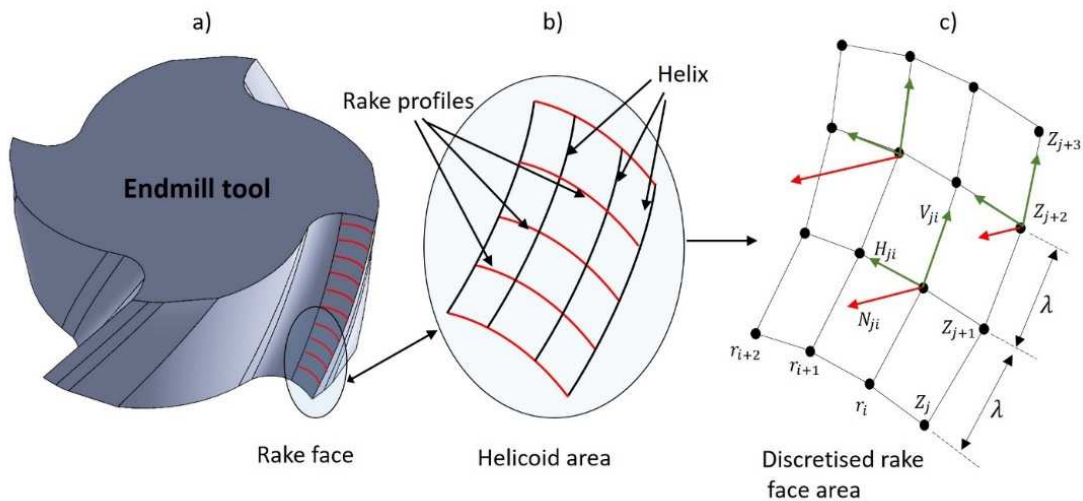
Figure V-5. Rake face discretization

Rake face profile

Most endmills with constant helix angle and pitch have a constant rake face profile along the tool axial axis. It is essential to define that the rake profile is referred to the profile of a tooth in a plane normal to the longitudinal axis (XY plane), as shown in Figure V-6. In the literature, many authors consider the rake angles; however, in this work, the rake angles are included in the geometrical modeling of the rake face.

Figure V-6b shows the detail of the rake face profile and the geometric parameters related to it. In the present model, the geometry of the rake face profile is modeled using a circular function associated with a radius of curvature R_f.
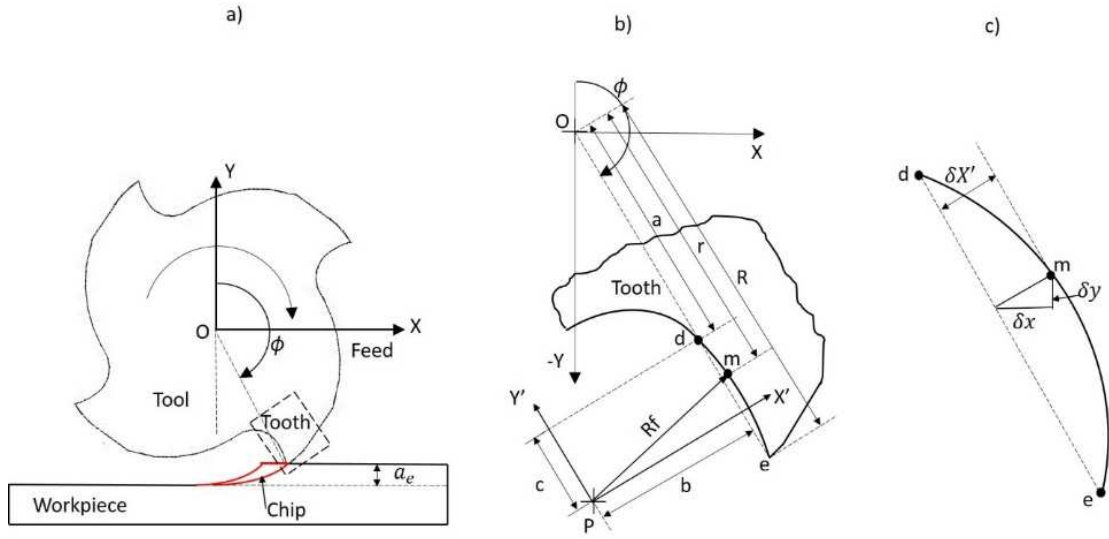
Figure V-6. Geometric parameters of the rake profile

From Figure V-6a, it can be seen that O is the tool rotation center, ϕ is the engagement angle and a_e the radial cutting depth. Figure V-6b shows the detail of the parameters set to model the rake face arc, from now on named the rake profile, with P being the center of curvature of the arc formed between d and e. d and e points are formed by the intersection of the straight line between O and the point e. In turn, the m points correspond to the points that are part of the arc. d e. It is noteworthy to mention that the model is proper when the straight distance $d - e$ is bigger than a_e.

The coordinates of the m points(points of the $d - e$ arc or rake profile) for the X, Y coordinate system are determined by equations V.1-V.4.

For down-milling:

$$m_x = r * sin(\pi - \phi) + \delta x' * cos(\pi - \phi) \quad \text{(V.1)}$$
$$m_y = r * cos(\pi - \phi) + \delta x' * sin(\pi - \phi) \quad \text{(V.2)}$$

For up-milling:

$$m_x = -r * sin(\phi - \pi) + \delta x' * cos(\phi - \pi) \quad \text{(V.3)}$$
$$m_y = r * cos(\phi - \pi) + \delta x' * sin(\phi - \pi) \quad \text{(V.4)}$$

where

$$\delta x' = x' - b \quad \text{(V.5)}$$

$$x' = \sqrt{R_f^2 - y'^2} \quad \text{(V.6)}$$

$$y' = c - \Delta a \quad \text{(V.7)}$$

161

$$\Delta a = r - a \quad \text{(V.8)}$$

$a, b \text{ and } c$ are geometrical parameters associated with the curvature of the rake profile (See Figure V-6b).

Replacing equations 5-8 in equations 1 - 4, we obtain explicit expressions for the calculation of m_x and m_y See equations 9-12.

For down-milling:

$$m_x = r * sin(\pi - \phi) + \left[\sqrt{R_f{}^2 - (c + a - r)^2} - b \right] * cos(\pi - \phi) \quad \text{(V.9)}$$

$$m_y = r * cos(\pi - \phi) - \left[\sqrt{R_f{}^2 - (c + a - r)^2} - b \right] * sin(\pi - \phi) \quad \text{(V.10)}$$

For up-milling

$$m_x = -r * sin(\phi - \pi) + \left[\sqrt{R_f{}^2 - (c + a - r)^2} - b \right] * cos(\phi - \pi) \quad \text{(V.11)}$$

$$m_y = r * cos(\phi - \pi) + \left[\sqrt{R_f{}^2 - (c + a - r)^2} - b \right] * sin(\phi - \pi) \quad \text{(V.12)}$$

$m_x \text{ and } m_y$ points represent the basis for calculating the X, Y, and Z coordinates of the mesh points of the contact zone between the tooth and the workpiece. These aspects are discussed in more detail in Appendix A.

Contact area sequence

The contact area stages can be developed under several cases. The characteristics of each case are displayed in Table V-1, while ξ and α_{st} are obtained from equation 13.

Table V-1 Contact área cases

Case	Condition	Characteristic
1	$\alpha_{st} < \xi$	The flat zone contact area disappears entirely or partially before $\phi = \pi$
2	$\alpha_{st} = \xi$	$\gamma = 0$ and there is no stage C(see Figure V-7)

| 3 | $\alpha_{st} < \xi$ and $\xi + \alpha_{st} < \dfrac{\pi}{N}$ | The stages A, B, C, D, and E are developed according to Figure V-7, and only a tooth is cutting |
| 4 | $\alpha_{st} < \xi$ and $\xi + \alpha_{st} > \dfrac{\pi}{N}$ | The stages A, B, C, D, and E are developed according to Figure V-3, and two or more tooths could cut simultaneously |

$$\xi = \frac{a_p * 180 * tan^{-1}(\beta)}{\pi * R}; \quad \alpha_{st} = \pi - \phi_{st} \quad (V.13)$$

Where ξ is the tool rotation angle from the first contact of the flute with the workpiece until it reaches a_p, N is the number of tool flutes, ϕ_{st} is the engagement angle related to the first tool-workpiece contact, and β is the hélix angle.

The development of the contact area sequence for case 3 is shown in Figure V-7. The three contact area combinations shown in Figure V-3 are developed in 5 stages to consider how the contact area increases, remains constant, and decreases. Figure V-7 shows the five stages: A, B, C, D, and E. For the down-milling, the contact area starts when the engagement angle reaches the value of ϕ_{st}. The contact area with the flat surface (stage A) is developed in a tool rotation interval corresponding to η. once this interval has been covered, the engagement angle ϕ_{sc} is reached. The angle ϕ_{sc} corresponds to the angle where the tool first reaches the curved surface (previously machined). Stage B corresponds to the tool–curved surface contact zone. In this section, the contact area with the curved surface increases while the area of contact with the flat surface remains at the maximum value. Section B ends when the engagement angle reaches a value equal to π. During stage C, the contact area remains constant and is displaced in the Z-axis direction. This stage occurs during a rotation interval corresponding to the angle γ, bearing in mind that $\gamma = \psi - \alpha_{st}$. Subsequently, during stage D, the contact area with the flat zone starts to decrease, which develops during the interval η. Once stage D is completed, stage E begins with the reduction of the contact area with the curved zone during the rotation of the angle α_{sc} bearing in mind that $\alpha_{sc} = \pi - \phi_{sc}$ and $\eta = \phi_{sc} - \phi_{st}$ For up-milling, the five stages are reversed, as shown in Figure V-7.
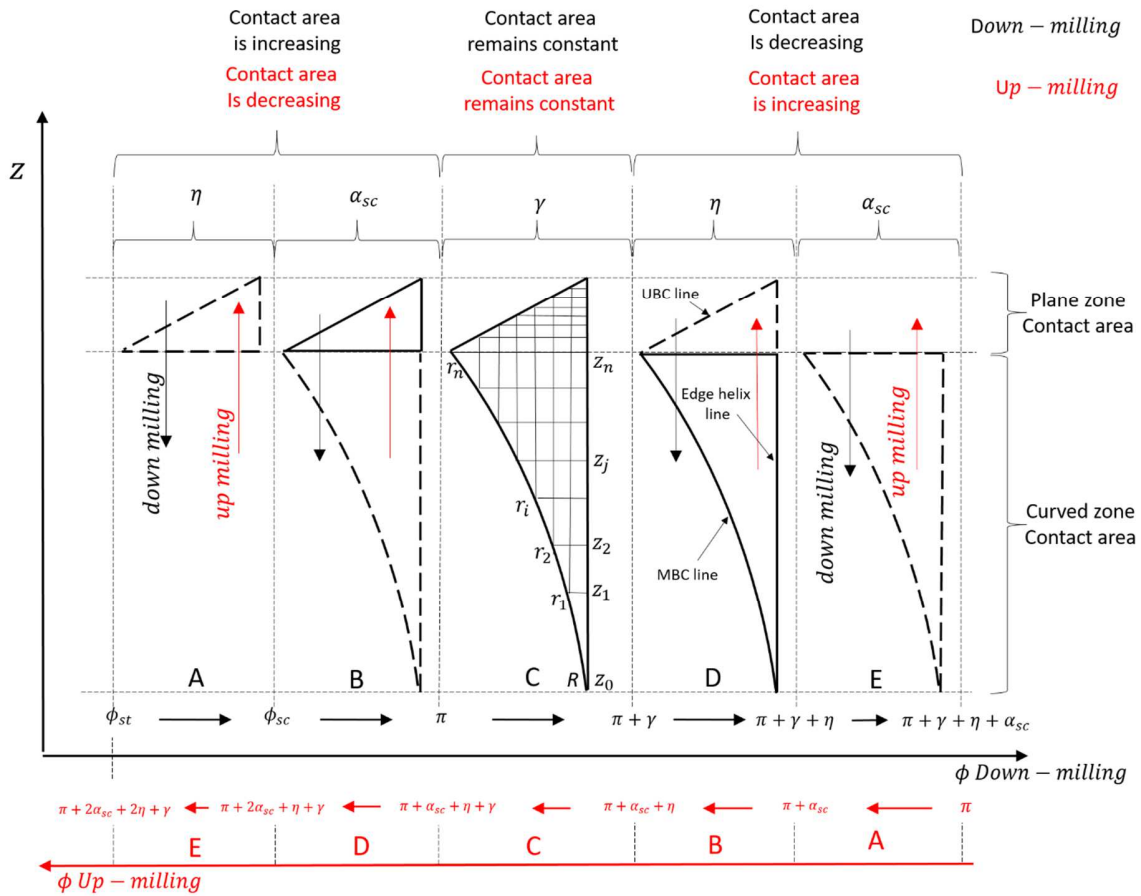
Figure V-7. The sequence of development of the contact area for Down-milling and Up-milling

The diagrams and equations for calculating the instantaneous contact area and the instantaneous normal vector during the tooth engagement can be found in Appendix A.

V.3. Extracting shear and ploughing forces components from measured data

This section shows how to extract the cutting force fractions caused by shear and ploughing from the dynamometer data using a vector approach (see Figure V-8) and how to obtain the instantaneous cutting force coefficients.
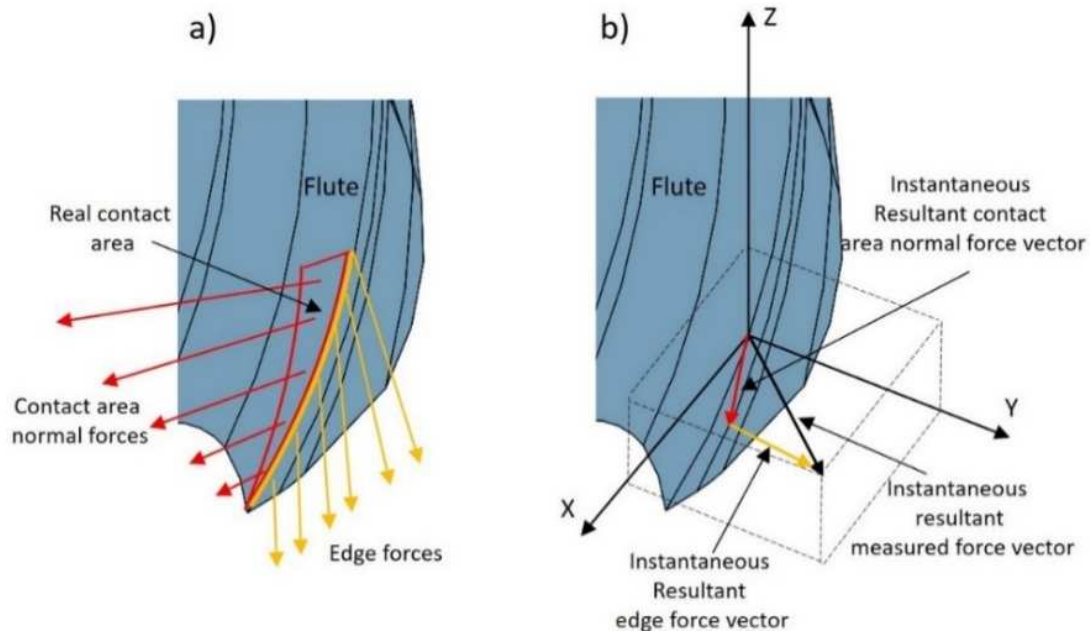
Figure V-8. Shear and ploughing force components scheme

The accumulated normal vector Na_k (see Table V-6 in Appendix A) allows us to know the orientation of the normal component force related to shear; however, to know the magnitude of this force in addition to the orientation, it is necessary to know at least the value of one of its components in the Cartesian system.

Figure V-9a and Figure V-9b represents the normal stress σ and friction stress τ exerted by the material on the tool at any instant. On the other hand, Figure V-9c shows the resultant stress δ exerted on a differential element of the tool. If δ is assumed uniform in the rake face area and the cutting edge radius, it is possible to extract the force fraction in Z related to the rake face and the cutting edge by comparing the ratio of both Z projected areas. The ploughing effect on the Z-force component could be significant, considering that the fraction of the cutting edge curvature may have a significant area projection in the direction of the Z-axis related to the rake area projection in the Z-axis for small feed advance or minimal rake face contact areas.
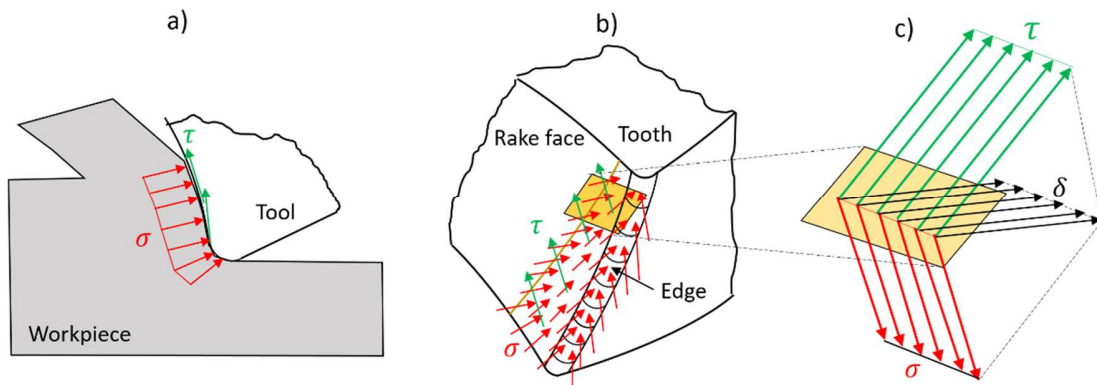
Figure V-9. Rake face contact area and edge area

Considering a differential force element dF_Z as the measured force(dynamometer) corresponding to a differential band area, it is possible to infer that dF_Z is the sum of the Z force fraction caused by the edge dFz_e plus the Z force fraction caused by the rake face dFz_r (see equation 14).

$$dF_Z = dFz_e + dFz_r \text{ (V.14)}$$

Considering that l_r is the horizontal length(XY plane) of the differential contact area of the rake face (dashed red line in Figure V-10) and that l_e is the perimeter of the cutting edge radius (solid red line in Figure V-10), that q is the fraction of l_e that has effect on the edge Z force component, that β is the helix angle, and dz the differential element of length along the Z-axis, it is possible to define dF_Z according to equations 15-17.
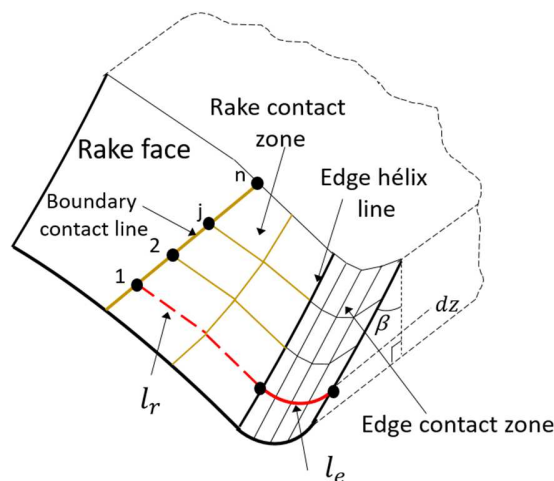
Figure V-10. l_e and l_r schem

$$dFz = \delta * q * l_e * dz * tan\beta + \delta * l_r * dz * tan\beta \ (V.15)$$

$$l = q * l_e + l_r \ (V.16)$$

$$dFz = \delta * dz * tan\beta (q * l_e + l_r) = \delta * dz * tan\beta * l \ (V.17)$$

denoting ρ as the ratio between l_r and $(q * l_e)$ (Eq 18) it is possible to obtain the ratio between l_e and the total perimeter length l (see equation 19). It is noteworthy that the total length l is related to the measured force in Z.

$$\rho = \frac{l_r}{q*l_e} \ (V.18)$$

$$q * l_e = \frac{l}{(1+\rho)} \ (V.19)$$

Equation 20 is obtained by replacing equations 18 and 19 in equation 17. it can be seen that the left-hand side of this equation corresponds to the fraction of the edge Z force component and the right-hand side of the equation corresponds to the measured Z force (dynamometer) divided over $(1 + \rho)$. In this way, it is then possible to know the fraction of the Z-measured force caused by the edge (Equation 21) and the fraction caused by the rake face (Equation 22).

$$\delta * dz * tan\beta * q * l_e = \frac{\delta*dz*tan\beta*l}{(1+\rho)} \ (V.20)$$

$$dFz_e = \frac{dFz}{(1+\rho)} \ (V.21)$$

$$dFz_r = dFz - dFz_e = dFz * (1 - \frac{1}{1+\rho}) \ (V.22)$$

The next step is to obtain the force components related to the rake face and the cutting edge from the instantaneous forces measured by a dynamometer. For this purpose, it is necessary to obtain the time signal corresponding to the passage of a tooth or a period. The Z force component related to the rake face $\vec{F}z_{r,k}$ is obtained by equation 23.

$$\vec{F}z_{r,k} = \vec{F}z_k * (1 - \frac{1}{1+\rho_k}) \ (V.23)$$

Where $\rho_k = \frac{Aa_k}{k*q*l_e*\lambda}$; Aa_k is expressed in Table V-6(Appendix A) and $\vec{F}z_k$ is the instantaneous Z-force measured by a dynamometer corresponding to the passage of a tooth or a tool revolution.

To obtain the force components $\vec{F}x_{r,k}$ and $\vec{F}y_{r,k}$ which correspond to the X and Y components caused by the rake face, respectively; it is necessary to know the ratios of both components (X and Y) concerning the Z component. $\vec{F}x_{r,k}$ and $\vec{F}y_{r,k}$ components are calculated according to equations 24 and 25.

$$\vec{F}x_{r,k} = \vec{F}z_{r,k} * \frac{Nax_k}{Naz_k} \text{ (V.24)}$$

$$\vec{F}y_{r,k} = \vec{F}z_{r,k} * \frac{Nay_k}{Naz_k} \text{ (V.25)}$$

where Nax_k , Nay_k and Naz_k are the components of the accumulated normal vector Na_k(see equation in Table V-6 of Appendix A) up to the position k in X, Y, and Z coordinates.

The force fractions corresponding to the cutting edge are obtained according to equations 26-28.

$$\vec{F}x_{e,k} = \vec{F}x_k - \vec{F}x_{r,k} \text{ (V.26)}$$

$$\vec{F}y_{e,k} = \vec{F}y_k - \vec{F}y_{r,k} \text{ (V.27)}$$

$$\vec{F}z_{e,k} = \vec{F}z_k - \vec{F}z_{r,k} \text{ (V.28)}$$

The instantaneous shear coefficients(Ktc_k, Krc_k, Kac_k) and instantaneous edge coefficients (Kte_k, Kre_k, Kae_k) as a function of k are obtained from equations 29-34.

$$Ktc_k = \frac{\vec{F}x_{r,k} * \cos(\Omega_k) + \vec{F}y_{r,k} * \sin(\Omega_k)}{Aa_k} \text{ (V.29)}$$

$$Krc_k = \frac{\vec{F}x_{r,k} * \sin(\Omega_k) + \vec{F}y_{r,k} * \cos(\Omega_k)}{Aa_k} \text{ (V.30)}$$

$$Kac_k = \frac{\vec{F}z_{r,k}}{Aa_k} \text{ (V.31)}$$

$$Kte_k = \frac{\vec{F}x_{e,k} * \cos(\Omega_k) + \vec{F}y_{e,k} * \sin(\Omega_k)}{Ld_k} \text{ (V.32)}$$

$$Kre_k = \frac{\vec{F}x_{e,k} * \sin(\Omega_k) + \vec{F}y_{e,k} * \cos(\Omega_k)}{Ld_k} \text{ (V.33)}$$

$$Kae_k = \frac{\vec{FZe_k}}{Ld_k} \quad (V.34)$$

where Ω_k is the centroid angle of the mesh points for the position k(see Figure V-11) and is obtained with equation 35. while Ld_k is the edge length in contact with the workpiece for a k value and is obtained by equation 36.

$$\Omega_k = Tan^{-1}\left(\frac{\overline{X_k}}{\overline{Y_k}}\right) \quad (V.35)$$

$$Ld_k = \lambda * k \quad (V.36)$$

where $\overline{X_k}$ and $\overline{Y_k}$ are the mean values of $X_{p^{i,j,k}}$ and $Y_{p^{i,j,k}}$ mesh point coordinates(see Table V-4 in Appendix A and Figure V-11) for a k position.
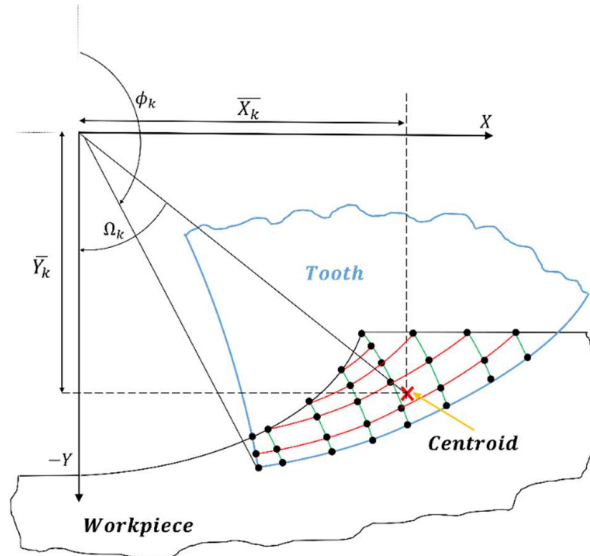
Figure V-11. Instantaneous centroid scheme

V.4. Methodology and experimental procedure

Prismatic samples of IN718 LPBF were manufactured (See Figure V-12a) using a Renishaw AM400 machine to obtain the end milling cutting force coefficients using the proposed model. The sample geometry is a 4x4x8 cm L-cube for 30 μm of layer thickness, as shown in Figure V-12a. The samples were manufactured using a 67° rotational laser scanning strategy on the XY plane, and the building direction was along the Z axis. The peripheral milling experiments were performed under three down-milling cases to measure the directional dependency of the cutting force coefficients in a KONDIA A6 milling centre with a Fagor 8070 CNC. The cutting forces were measured with a Kistler 9225B dynamometer (16384Hz). Figure V-12b shows a schematic diagram

of the three milling cases performed in this research. The tool edge quality was controlled to ensure the accuracy of the measurements. The radial and axial depths were selected according to the usual stock of material to be removed. The selected feed range is according to the superfinishing process.
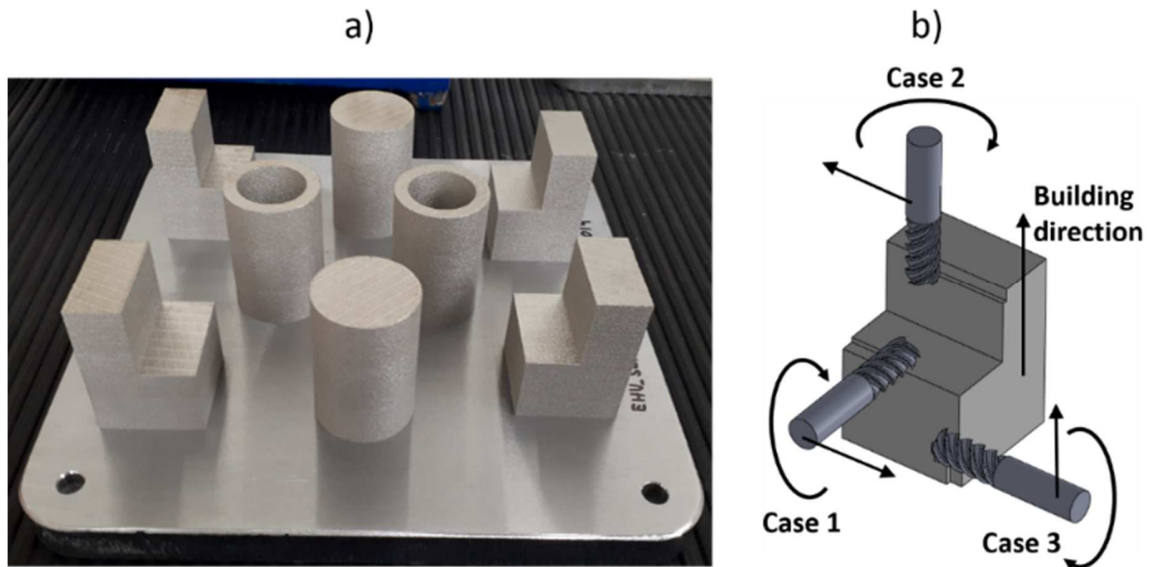
Figure V-12. LPBF samples. a) prismatic samples manufactured by LPBF, b) tool orientation cases for cutting force coefficient evaluation

Table V-2 shows the machining parameters, tool information, experimental factors and levels, and the LPBF parameters used to manufacture the samples.

Table V-2. Milling parameters, Milling experimental factors, and LPBF parameters

Milling experimental factors and levels			
Factor	**Low**	**Middle**	**High**
Feed-f (mm/rev·z)	0.03	0.04	0.05
Milling case	Case 1	Case 2	Case 3
Cutting parameters and tool information (HM end mill)			
Cutting speed V_c (m/min)	60	Tool diameter (mm)	10
Axial depth (a_p) (mm)	5	Helix angle β (°)	30
a_e (mm)	0.3	Flutes	4
LPBF parameters			
Laser power (W)	200	Layer thickness(μm)	30
Scan speed (mm/s)	1000	Spot size(μm)	70
Hatch distance (μm)	90	Hatch rotation angle(°)	67

V.5. Material anisotropy verification, tool edge, and rake profile characterization

The material's microstructure was characterized to confirm the material's anisotropy significance. Figure V-12a shows the inverse pole figure corresponding to the XY plane of the piece(perpendicular to the building direction), where a high directionality of the crystals oriented in the building direction (mainly reddish area) is observed. The sample shows a single-crystal <001> crystalline texture associated with the 67-degree hatch rotation strategy. This directionality is confirmed in the SEM scan (Figure V-12b), where it can be seen that the microstructure is mainly dendritic cellular. Additionally, Figure V-12c, Figure V-12d, and Figure V-12e present the uniaxial compression Taylor maps for the X, Y, and Z directions, respectively, where it is evident that the mechanical strength is much lower when compressive stresses are exerted in the Z direction (bluish color), which is an indication that the anisotropy of the material in the plastic range is significant. The average Taylor factor value for the X-axis direction is 3.2; for the Y-axis direction is 3.1; for the Z-axis direction is 2.4, indicating a significant variation between the plastic compressive strength between the building direction(Z-axis) and the axes of the XY plane.
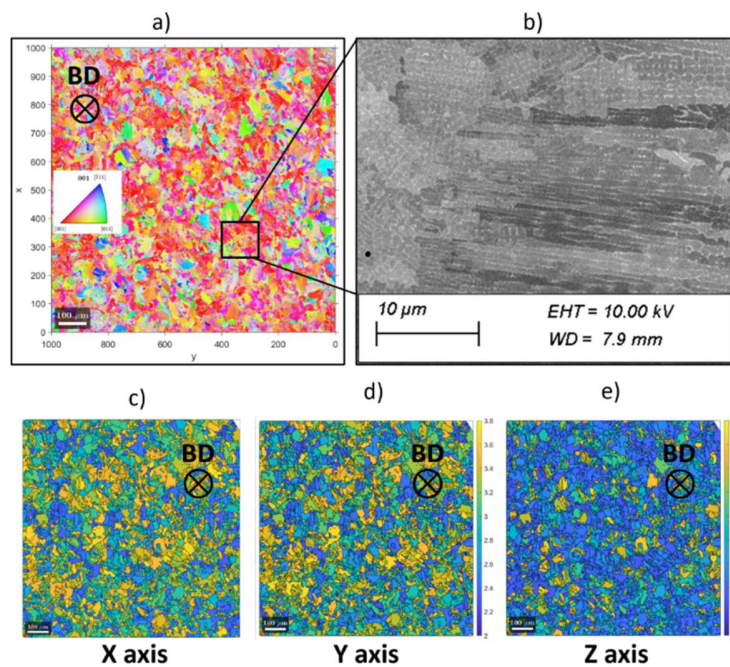
Figure V-13. Sample microstructure characterization. a) inverse pole figure(XY plane), b) SEM scan for XY plane, c) uniaxial compression Taylor map X direction, d) uniaxial compression Taylor map Y direction, e) uniaxial compression Taylor map Z direction

The tool's rake surface and clearance surface were scanned with an Alikona infinite Focus G5 (see Figure V-14a) to obtain the cutting-edge radius *r* and the a,b, and c parameters related to the rake profile (see Figure V-6b). The rake profile geometry and the previously mentioned parameters are shown in Figure V-14b.

a)   b)
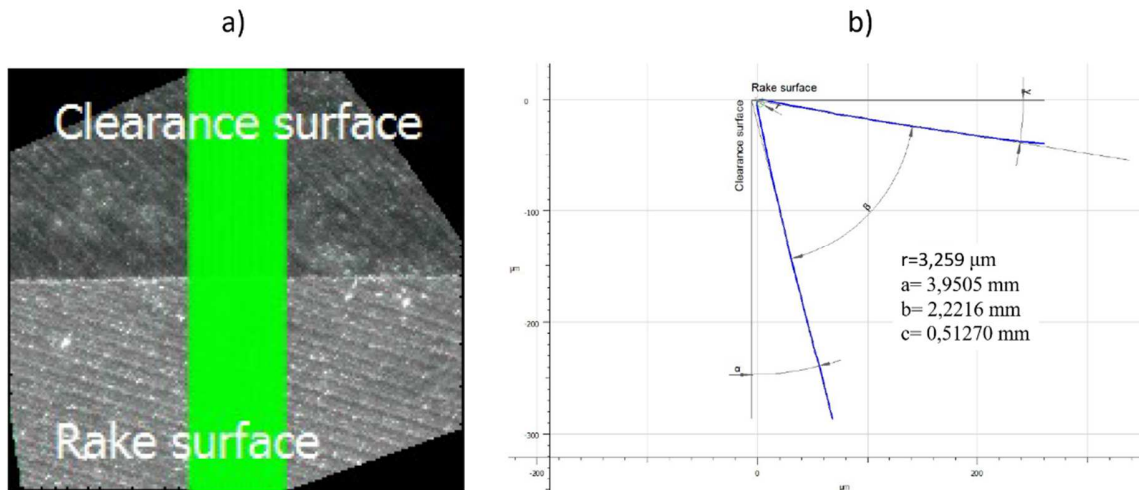
Figure V-14. Rake profile parameters obtained by scanning

V.6. Results and discussion

This section presents the instantaneous mechanistic coefficients obtained through the proposed model in section 2 for the three milling cases, the methodology to establish the six single-value coefficients, and the model verification. Figure V-15 shows a comparison of the average cutting forces in the X, Y, and Z coordinates for the three cases evaluated when $fz = 0.05$mm/rev . where it can be observed that the highest levels of cutting forces are developed for case 1 while the lowest for case 2. one of the purposes of the proposed model is to obtain mechanistic coefficients that are proportional to the cutting resistance. For instance, the obtained mechanistic coefficients have physical meaning if the case 1 shear coefficients are greater than case 2 coefficients; if that is fulfilled, the obtained coefficients can be used as reference coefficients $Ks(ref)$ for force prediction models based on physical or microstructural parameters as the Taylor factor $M(x)$.
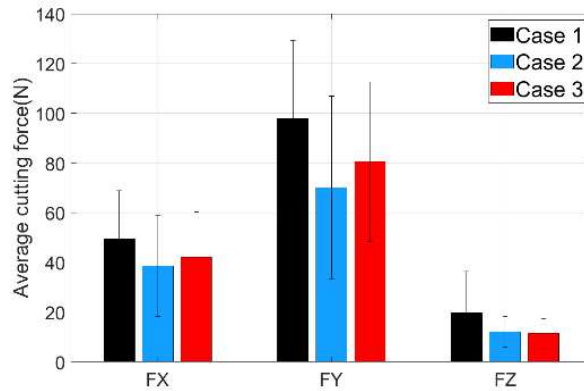
Figure V-15. Average cutting force components by milling case

Figure V-16 a shows the maximum real contact area in 3D for the geometry of the tool used in this study for fz=0.03mm/rev. It can be seen how the contact area is higher in the highest zone and gradually decreases as Z decreases. On the other hand, Figure V-16b compares the accumulated contact areas as a function of the engagement angle obtained through the proposed model vs. the linear model. Although both graphs are similar, it is essential to highlight that the difference between them becomes more noticeable for higher feeds since the linear model does not correctly consider the contact area with the non-machined zone. Additionally, it is important to establish that the primary motivation of the present study is to use the instantaneous accumulated contact area to obtain the instantaneous normal vectors and not only to obtain the accumulated area.
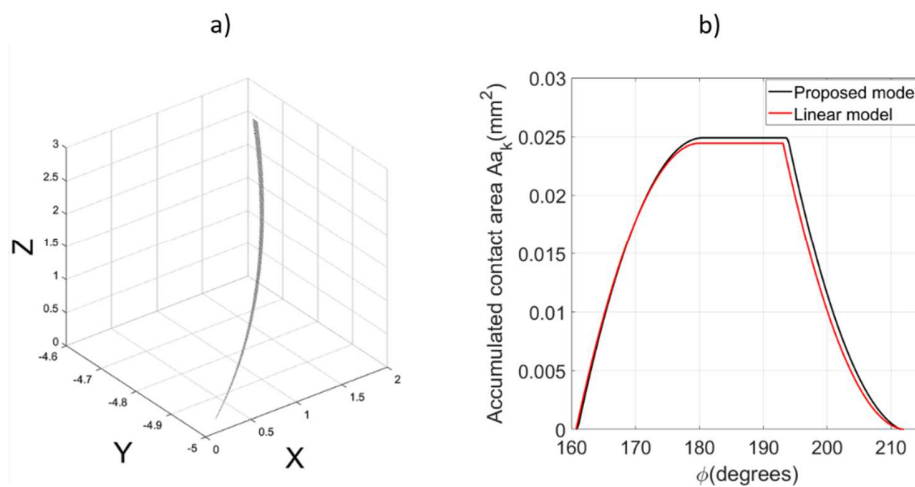
Figure V-16. Contact area graph. a) 3D real rake contact surface, b) accumulated contact area

Figure V-17 shows the instantaneous cutting force coefficients for a complete tool revolution, where the four zones corresponding to each tooth's engagement are observed, and the zones where the coefficients have a value of zero correspond to the moments when the tool does not cut the material. It can be seen that the patterns of each tooth and their average values are similar to each other. The peaks at the beginning of each tooth engagement are related to the impact phenomena. At that moment, the theoretical contact area is still minimal, which means that the values of the coefficients are much higher than those of the middle zone of each sector, which are more related to the cutting process. Similarly, the peaks at the end of each sector may be related to remaining frictional forces and minimal values of the theoretical contact area for that instant. These aspects are essential to correctly extract the single-value coefficients from the instantaneous coefficient curves.
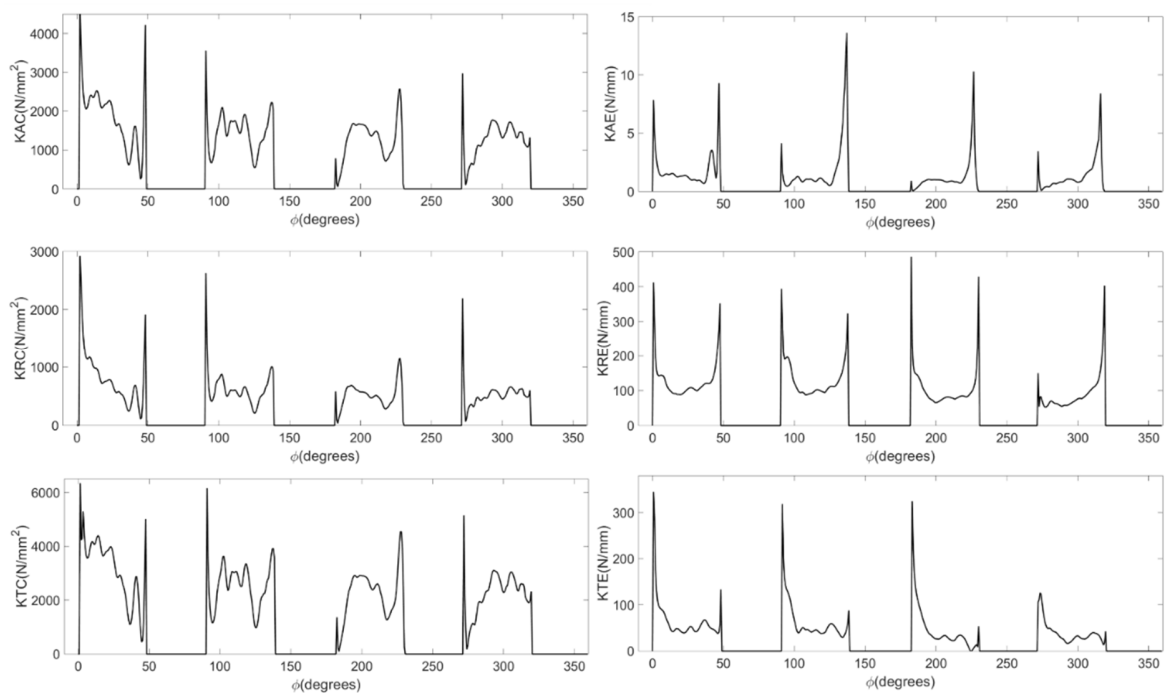
Figure V-17. Instantaneous cutting force coefficients for a tool period ($a_e = 0.3mm$; $f_z = 0.05mm/rev$)

Figure V-18 shows a set of curves corresponding to the instantaneous shear coefficients as a function of the engagement angle ϕ_k, considering the three milling cases evaluated at different feed advances. The graphs represent the cutting interval of a single tooth. The graphs show that each of the evaluated cases has a different curve shape pattern, with cases 2 and 3 more similar to each

other and notable differences for case 1. Additionally, when comparing the graphs of the same case at different feed advances, it can be observed that the pattern of the curves is similar but tends to increase for lower feed advances, which may be related to the size factor. Additionally, it can be observed that the coefficients corresponding to case 1 are much higher than those of case 2, while the values of cases 2 and 3 are more similar to each other, which is in accordance with the values observed in the levels of the mean forces in Figure V-17. The high coefficient values at the beginning of the tooth engagement are related to the initial impact of the tooth when it touches the workpiece, as was exposed above.
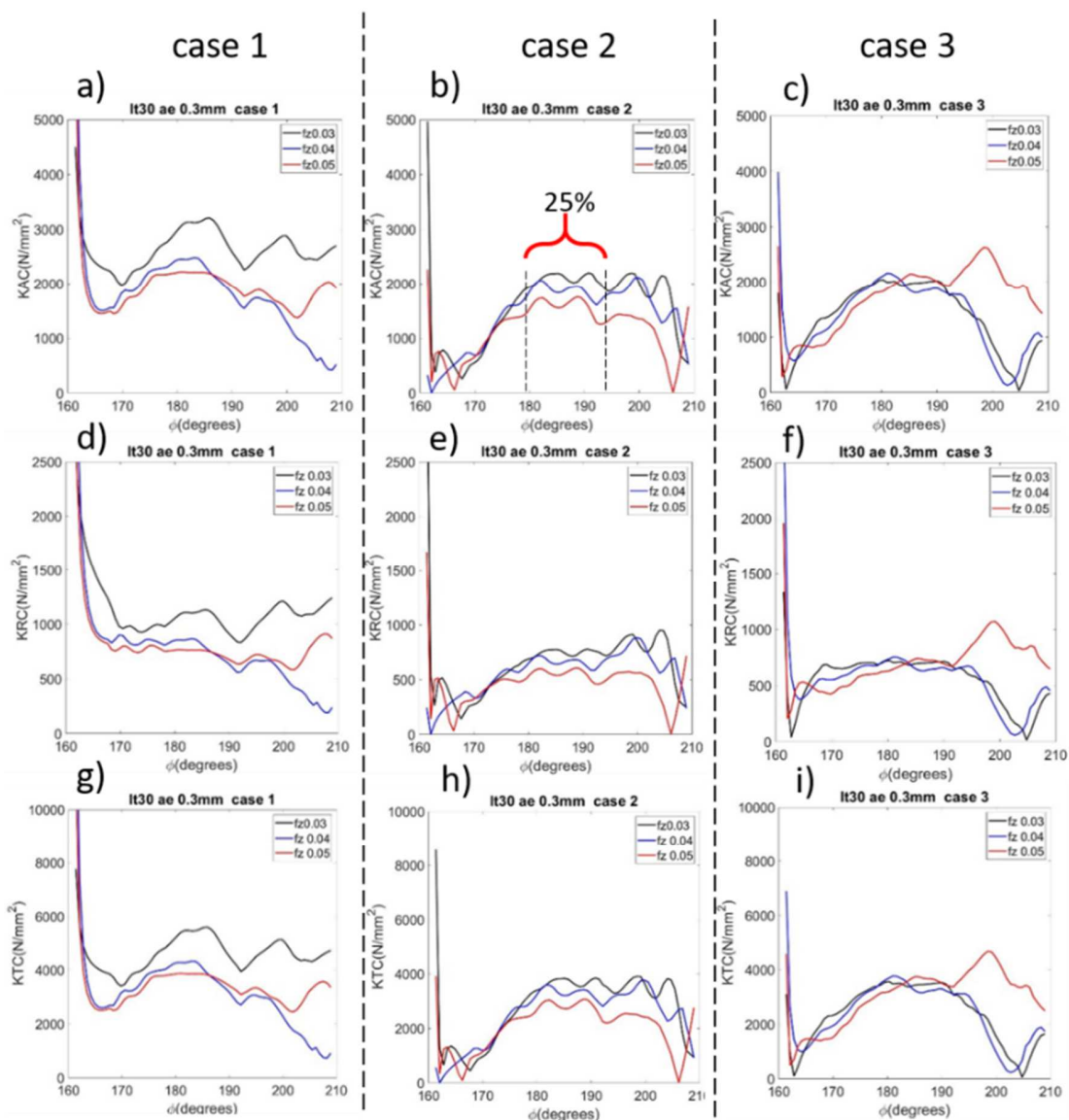
Figure V-18. Instantaneous shear coefficients. a-c) Kac coefficients, d-e) Krc coefficients, g-i) Ktc coefficients

Similarly, Figure V-19 shows the edge coefficients as a function of the engagement angle. An interesting aspect of the observed patterns in this graph is the similarity of the curve patterns for all milling cases. Additionally, the tool orientation (milling case) does not significantly affect the average cutting-edge coefficients, which makes physical sense. Notably, the directional dependency of the cutting forces is related to the changes in the crystalline slip resistance and boundary density as functions of the shear plane orientation, while the tribological nature of the ploughing processes generated at the cutting edge is not significantly affected by the material.
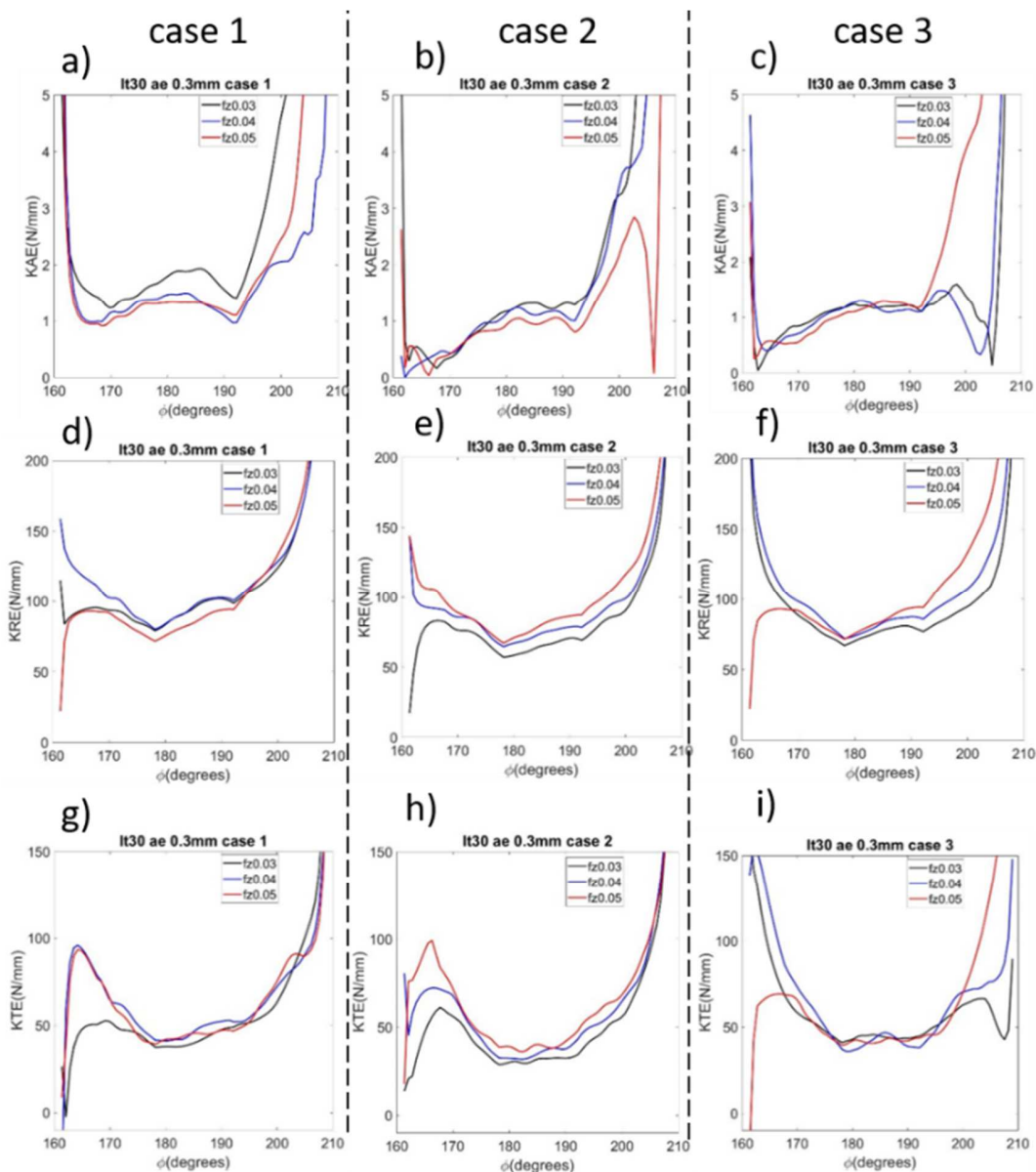
Figure V-19. Instantaneous edge coefficients. a-c) Kae coefficients. d-e) Kre coefficients. g-i) Kte coefficients

Additionally, it is observed that the effect of feed advance on the cutting-edge coefficients is also not significant. Figure V-20 shows the shear coefficients as a function of the cumulative instantaneous contact area. Figure V-20 a,b, and c show the evolution of the coefficients as a function of the contact area for case 1. These graphs show that for stage C (when the contact area remains constant), the coefficients have a certain level of variability that decreases as the feed rate increases. When comparing the mean values of the stage C coefficients for each feed rate, it can be seen that they increase exponentially as the feed rate decreases, which the size effect can explain. It is important to note that during stage C, the highest stability of the shear regime is reached, so it could be the best area to compare the instantaneous shear coefficients related to feed advances or milling cases. Figure V-20a shows the trend of the instantaneous coefficients related to the contact area for stage B when *fz*=0.03 mm/tooth. In this stage, it can be seen that although the area is small, the coefficients are large, possibly due to the tooth impact at the beginning of the tooth engagement.
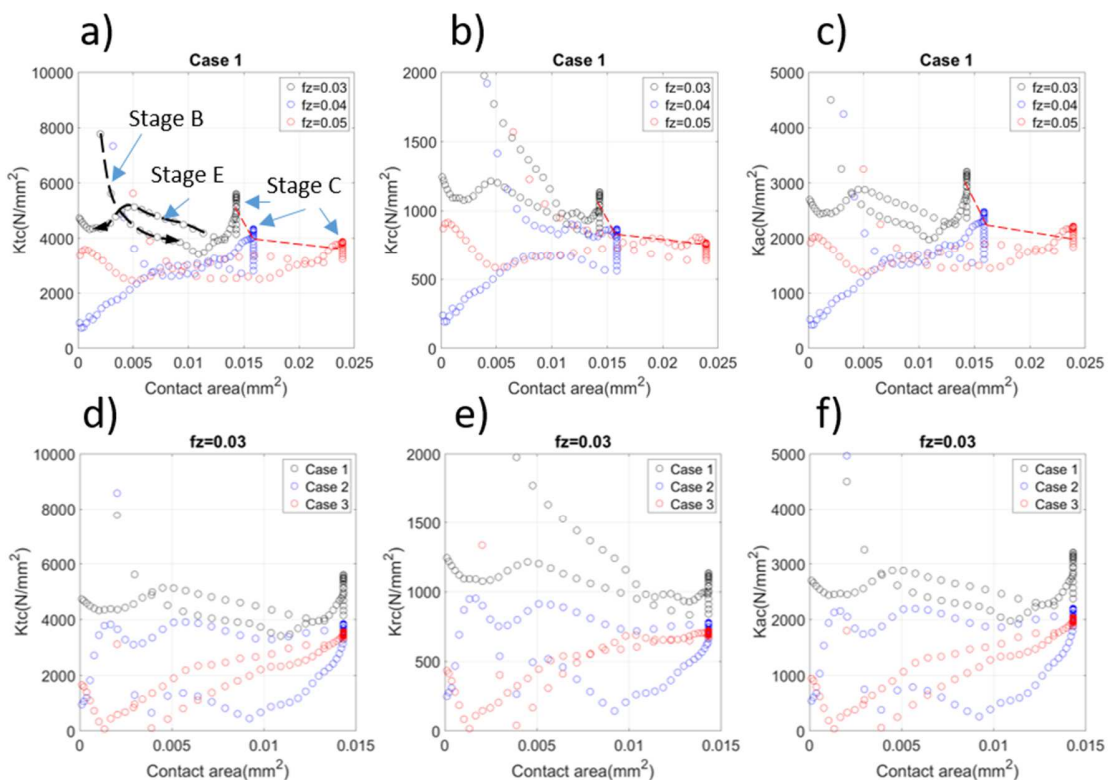
Figure V-20. Instantaneous shear cutting coefficients vs. contact area

On the other hand, during stage E, the area decreases progressively, but the coefficients maintain relatively constant values. Similar behavior is observed for f_z= 0.04 and 0.05 mm/tooth. Additionally, in Figure V-20 d,e, and f, the trend of instantaneous coefficients as a function of the contact area is compared for the 3 cases analyzed when f_z= 0.03 mm/tooth in these figures, it is possible to appreciate the effect of the anisotropy in shear coefficients when comparing the milling cases. It is seen that the coefficients of case 1 are significantly higher than those of the other cases for all stages of the contact area.

Although instantaneous cutting coefficients provide interesting information about the machining process, the practical application of instantaneous coefficients to the industrial or simulation environment is limited, which makes single-value coefficients more proper to use and implement in chatter prediction or other models. Therefore, the next step is to define which single-value coefficients match better in predicting the cutting forces. For this purpose, the average forces predicted with the direct linear model were calculated using four groups of coefficients. The first group was extracted from the mean and median of 25% of the instantaneous data (Figure V-18 and Figure V-19). It is important to note that the data is taken symmetrically from the midpoint of the curve, as shown in Figure V-18b. The second group is based on 50% of the data, the third group on 75%, and the fourth group is based on 100%. The predicted mean and median forces were compared with the experimental mean force values, and the results of fitting the predicted mean and median forces about the experimentally measured forces are shown in figure 20. It is noteworthy that for the Fx force, the best fitting is obtained when 50% of the data is used, while for the Fy force, the fitting improves as the percentage of used data decreases. for Fz, the opposite is true as the best fitting is obtained when all the data is used. The lower fitting error ranges from 9% for Fx to 22% for Fy and Fz when using the single value coefficients from the mean value of 25% of instantaneous data, as shown in Figure V-21. It is possible to infer that the lower fitting error when using 25% of the data could be related to the stability of the shear regime achieved during stage C (the contact area remains constant).

Based on the above results, the proposed model was verified by predicting the cutting forces by introducing the coefficients obtained with the proposed inverse model in the direct linear end-mill mechanistic model (Yusuf Altintas 2011). For this purpose, the coefficients were obtained from the average of 25% of the instantaneous curve data (See Figure V-18b). The verification was carried out for five experimental conditions different from those used to obtain the coefficients. Ver Figure

V-22. The results show a good prediction of the cutting forces for all tests performed, even for tests with a_e= 0.2 mm and a_e= 0.5 mm, which are different from the one used for calculating the coefficients (a_e= 0.3 mm). the verification test information is exposed in Table V-3. The experimental cutting force signals used for verification in Figure V-22 are unfiltered.
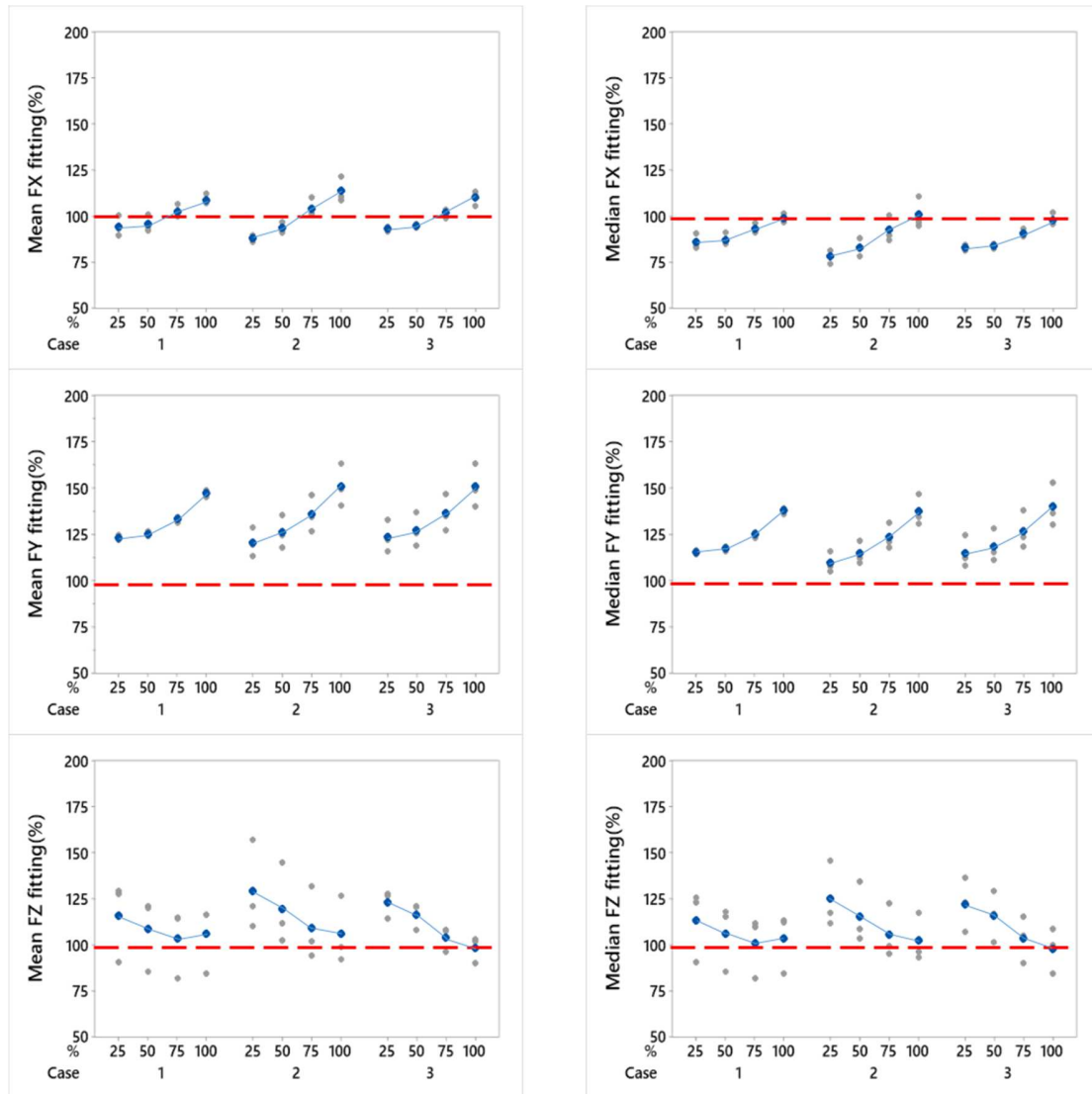
Figure V-21. Mean and median cutting force fitting(%)

Table V-3. Verification test information

Verification Tests	$a_e(mm)$	$f_z(mm/rev)$
1	0.2	0.035

2	0.2	0.04
3	0.3	0.035
4	0.3	0.045
5	0.5	0.03
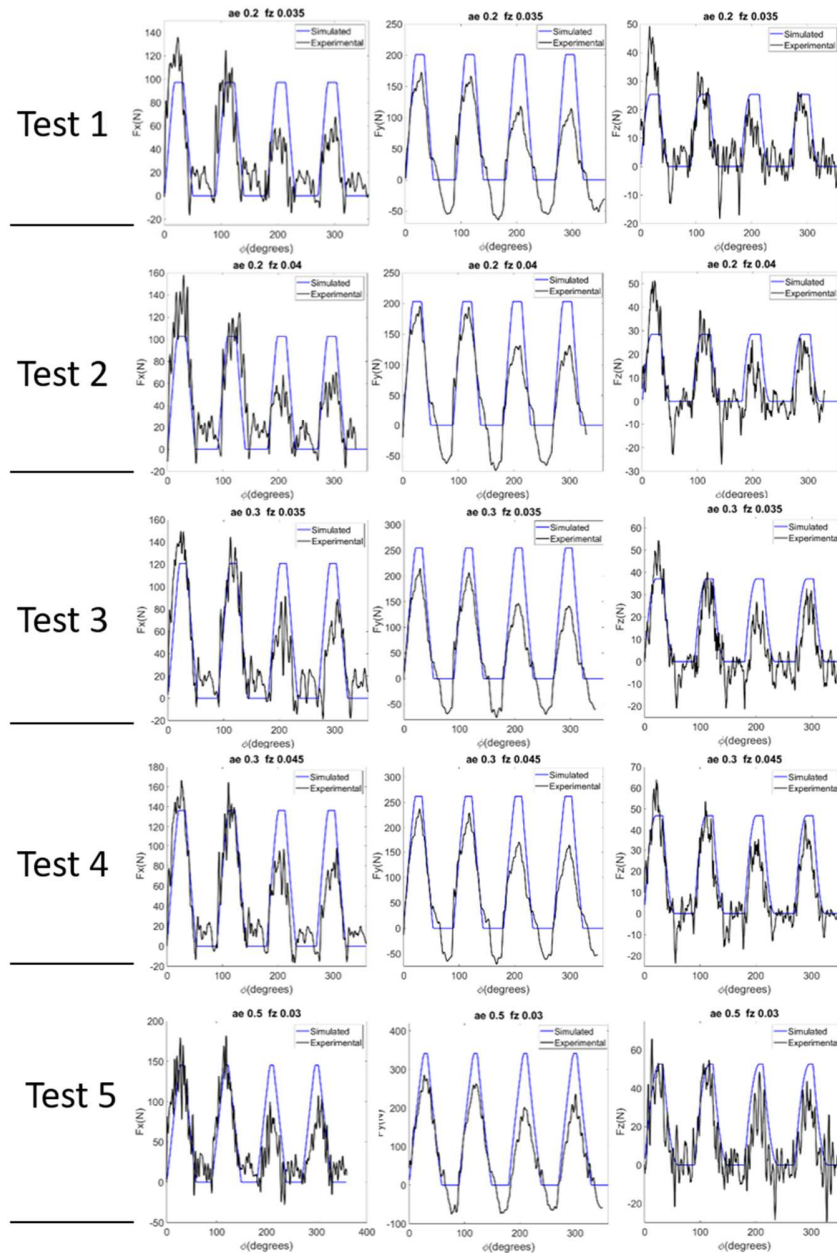
Figure V-22. Simulated cutting forces vs. unfiltered experimental cutting forces

The first two teeth show similar or slightly higher force levels than the simulated force, while teeth 3 and 4 show lower force levels due to the tool run out. However, the excess in maximum value in one tooth matches with the decrease in the other, and the run-out was around 7-9 microns. The

forces in X and Z present more noise in the signal in comparison with the force in Y, which may be related to the fact that the force in Y is more correlated with the tool edge length than with the rake face contact area of the rake face, which makes its value more linear. Additionally, negative values are observed in the Y force in the interval corresponding to the moment the teeth do not cut, which is due to the intrinsic flexibility of the system. Figure V-23 compares the correlation between the cutting force module (the resultant of the average force components $\sqrt{F_X^2 + F_Y^2 + F_Z^2}$.) and shear cutting coefficients $Ktc\ and\ Krc$ obtained by the linear model and the proposed model.
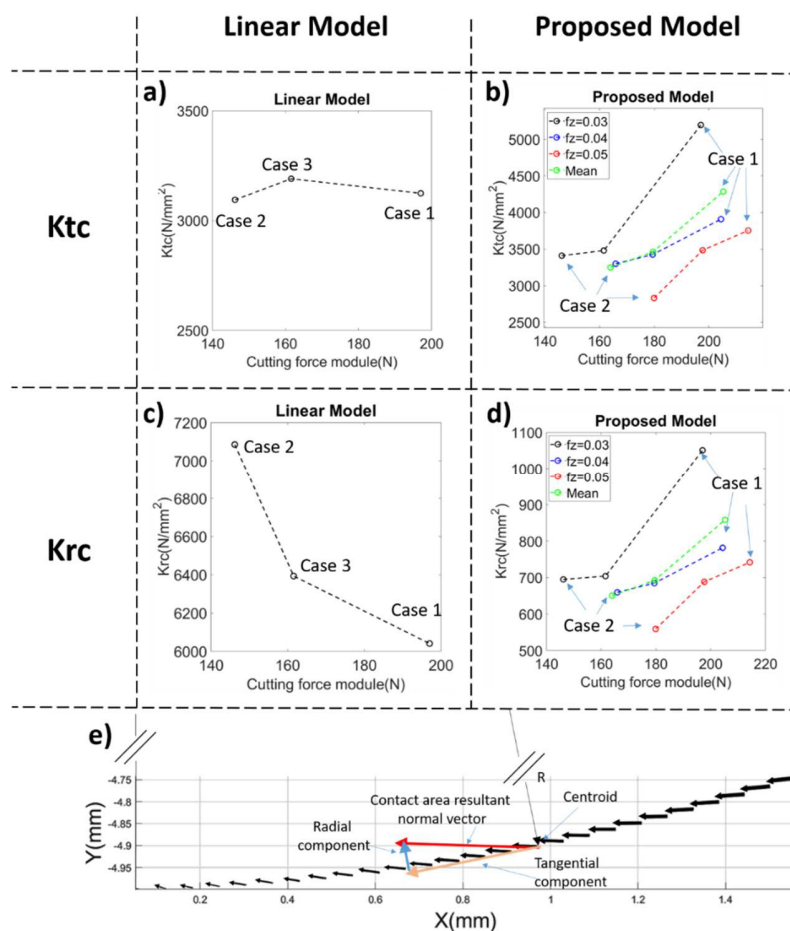
Figure V-23. Correlation between cutting force module and shear coefficients, a) Ktc by linear model, b) Ktc by proposed model, c) Krc by linear model, d) Krc by proposed model, e) Normal vector of rake face contact area

A high correlation is observed for the proposed model, as shown in Figure V-23b and Figure V-23d for the evaluated feed advances. On the other hand, the coefficients obtained by the linear inverse model do not correlate with the cutting force module, and their trend is not predictable. In Figure

V-23e, the rake face normal vectors and the resultant one in the XY plane are observed for different area segments when the contact area is maximum. The tool's geometry causes the tangential component of the normal vector to be significantly higher than the radial one along the tooth engagement. This aspect is essential to understand why the tangential coefficients Ktc are larger than the radial ones Krc when using the proposed model. On the other hand, the opposite is observed in the linear model where Krc is signifficantly higher than Ktc, which reinforces the fact that the coefficients obtained by the linear model are physically meaningless.

This aspect is relevant, considering that the mechanistic coefficients necessary for the cutting force prediction in anisotropic materials must correlate with the cutting forces and indirectly with the Taylor factor. In this line, it is possible to establish that the obtained shear coefficients with the proposed model can work as reference coefficients $Ks(ref)$ and can be used to predict the shear coefficients for other tool positions $Ks(x)$ through the correlation between cutting force and physical and microstructural parameters (e.g., Taylor's factor $M(x)$).

V.7. Conclusions

This study presents an inverse model for obtaining the mechanistic cutting force coefficients from the instantaneous real tool-workpiece contact area and the instantaneous normal vector of that area. A vector-based approach was used to ensure that the shear coefficients obtained by the model were proportional to the material's shear strength since the experimental force vector is split into the sum of the normal surface vector and the complementary vector. In this way, the normal surface vector is used to calculate the shear coefficients, and the complementary vector is used to absorb all ploughing-related effects. The model was tested on IN718 LPBF for three tool positions to observe the correlation between cutting force and shear coefficients when changing the tool position. The results show a high correlation between the magnitude of the cutting forces and the coefficients obtained for the cases evaluated. While the coefficients obtained by the linear inverse model do not correlate with the cutting forces levels.

The present study also presents a methodology to obtain the single-value coefficients from the instantaneous coefficient curve values; in this way, it is possible to integrate the coefficients of the proposed model with the widely used direct linear model. Verification tests were also performed where the six coefficients extracted from the instantaneous curves were applied to the direct linear

model for cutting force simulation. The simulated forces were compared with the unfiltered experimental force signals, and a high similarity between the magnitude of the experimental force and the simulated force was observed, especially for the teeth with low run out.

Based on the above, it is possible to establish that the mechanistic coefficients obtained from the proposed vector-based approach have enough physical sense and are recommendable to be integrated into microstructure-based predicting cutting forces models, making the proposed model especially significant for anisotropic metallic materials such as the materials obtained from LPBF.

V.8. Appendix: Expressions to obtain the instantaneous contact area and instantaneous normal vector for down-milling and Up-milling

Down-Milling

This section presents the expressions to obtain the coordinates of the contact zone mesh points, the discretized cells area, and the normal vectors associated with each mesh point for down-milling. Figure V-24 shows some parameters for the down-milling mode. ϕ_{st} is the engagement angle related to the first tool-workpiece contact (See Figure V-24a). It is noteworthy to state that the initial contact of the rake profile with the workpiece is on the flat surface (Unmachined area). On the other hand, Figure V-24b shows the engagement angle of the first contact between the rake face profile and the curved zone(machined area) ϕ_{sc} , in other words, it is the engagement angle when the rake face profile reaches the V point. The zone which corresponds to the interval between ϕ_{st} y ϕ_{sc} is defined in this model as the unmachined area, while the zone between ϕ_{sc} and π corresponds to the machined zone. It is important to differentiate both zones considering that the line resulting from the intersection of the rake face with the curved surface (machined zone), from now on, referred to as machined boundary contact line (MBC line), is different from the line resulting from the intersection of the rake face with the flat surface (unmachined zone), from now on referred to as unmachined boundary contact line (UBC line). This discrimination could be negligible for minimal feed advances; however, it is included in the model to make it more generic.
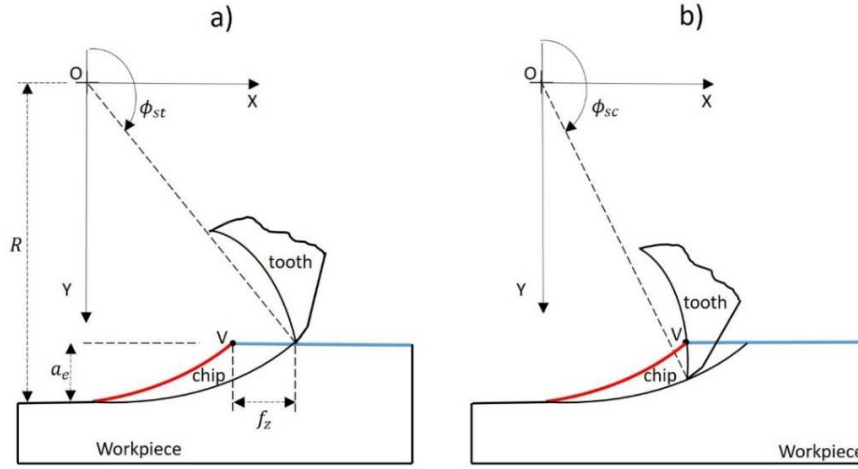
Figure V-24. Down milling geometry, a) tool contact with unmachined zone, b) tool contact with the machined zone

ϕ_{st} is obtained from equation 37.

$$\phi_{st} = \pi - \text{acos}[\,(R - a_e)/R]\quad \text{(V.37)}$$

To obtain ϕ_{sc} the equations 9 and 10 must be solved as a non-linear system to obtain the ϕ value where $m_x = V_x$ and $m_y = V_y$. the V_x y V_y values are obtained from equations 38 and 39.

$$V_x = R * \sin(\pi - \phi_{st}) - fz\quad \text{(V.38)}$$

$$V_y = R - a_e\quad \text{(V.39)}$$

Where R is the tool radius, fz is the feed per tooth and a_e the radial depth of cutting.

Determination of area and normal vector associated with mesh points

This section develops the mathematical expressions for the calculation of the contact mesh points and other associated variables in the range between ϕ_{st} and ϕ_{sc} for the unmachined zone and between ϕ_{sc} and π for the machined zone. Three indices will be used for this purpose. The index k corresponds to the tool's engagement angle position; the index j corresponds to the XY plane lines forming the rake face profiles. It is essential to state that all the points that make up the j lines are at the same Z-axis height. In addition, the index i refers to the helical lines on the rake face. Figure V-25a shows the configuration for the machined zone, while Figure V-25b shows the configuration for the machined zone.
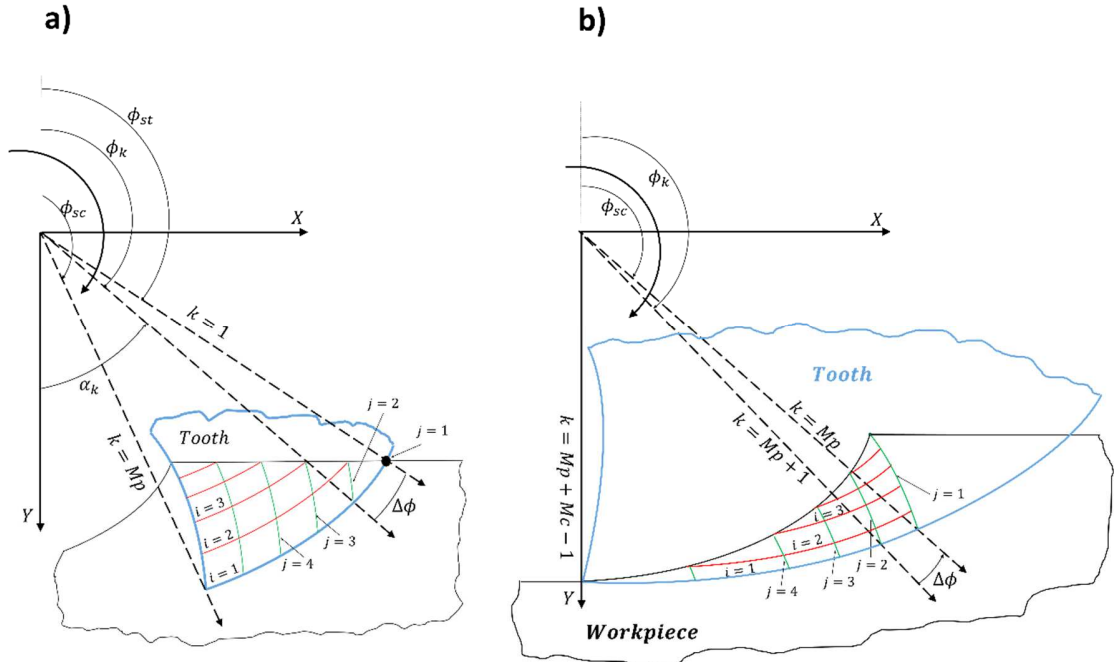
Figure V-25. Down milling zones. a) unmachined zone scheme, b) machined zone scheme

The logical index structure is:

- Each engagement angle position has an index k assigned value.

- The number of $i\ and\ j$ instant lines corresponds to the index k value of the evaluated instant.

- The intersections points between $i\ and\ j$ lines form the rake face mesh points.

- The number of points on each i line corresponds to the j value of the corresponding j line

the ϕ_k discretized values as a function of k are obtained from equations 40-45:

Unmachined zone:

$$np_k = \frac{\phi_k - \phi_{st}}{\Delta\phi} \ (V.\,40)$$

$$Mp = \frac{\phi_{sc} - \phi_{st}}{\Delta\phi} + 1 \ (V.\,41)$$

$$\phi_k = \phi_{st} + (k-1)*\Delta\phi = \{\phi_{st}, \phi_{st} + \Delta\phi, \phi_{st} + 2*\Delta\phi,,,,\phi_{sc}\} \ \text{for k = 1,2,3,,,,} Mp \ (V.42)$$

Machined zone:

$$nc_k = \frac{\phi_k - \phi_{sc}}{\Delta\phi} \quad (V.43)$$

$$Mc = \frac{\pi - \phi_{sc}}{\Delta\phi} + 1 \quad (V.44)$$

$$\phi_k = \phi_{st} + (k-1)*\Delta\phi = \{\phi_{sc}, \phi_{sc} + \Delta\phi, \phi_{sc} + 2*\Delta\phi, ,, \pi\} \text{ for } k = Mp, Mp+1, \dots, Mp+$$
$$Mc\text{-}1 \quad (V.45)$$

where $\Delta\phi$ is the step value to discretize the engagement angle.

The points that make up the UBC and MBC lines are obtained for each k value. The radial dimensions of those points (corresponding to the radial lengths from the longitudinal axis of the tool to the UBC and MBC lines) are denoted as rp_k and are calculated with equations 46 and 47(see Figure V-26 and Figure V-27). The rp_k values represent the basis for obtaining the other points of the rake face mesh.

For unmachined zone:

$$rp_k * cos(\pi - \phi_k) - \left[\sqrt{R_f^2 - (c+a-rp_k)^2} - b\right] * sin(\pi - \phi_k) = R - a_e \quad (V.46)$$
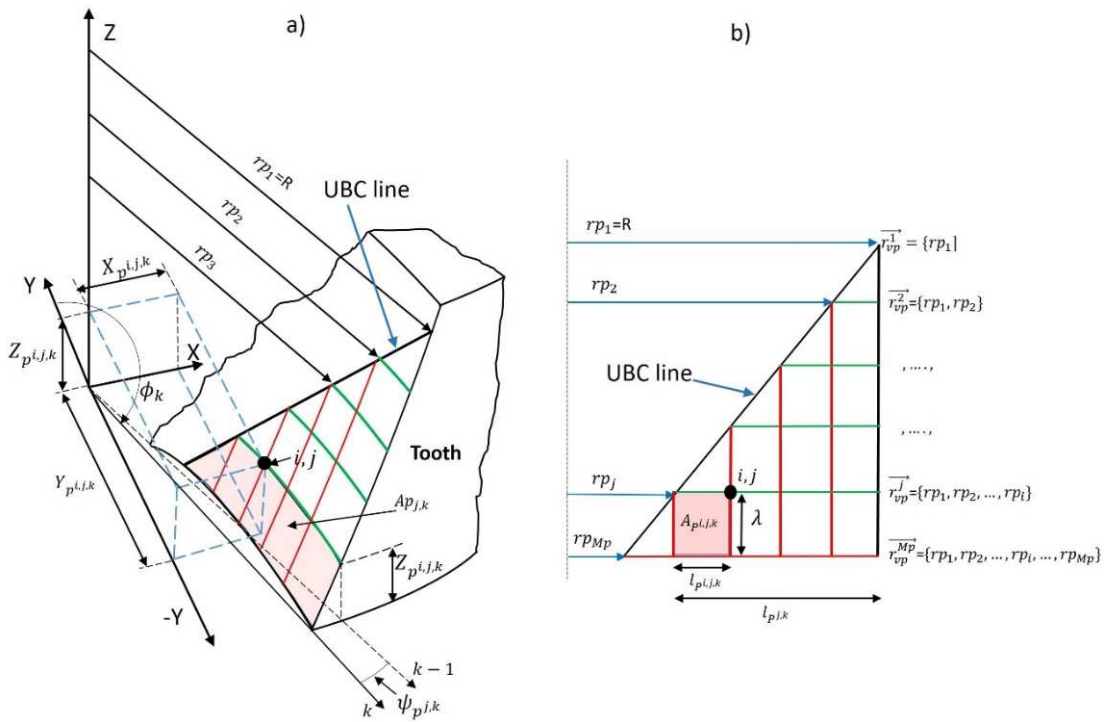
Figure V-26. Unmachined contact zone. a) contact zone scheme, b) detail of unmachined zone mesh points parameters

For machined zone:

$$\left(rp_k * sin(\pi - \phi_k) + \left[\sqrt{R_f^2 - (c + a - rp_k)^2} - b\right] * cos(\pi - \phi_k) + fz\right)^2 + \left(rp_k * cos(\pi - \phi_k) - \left[\sqrt{R_f^2 - (c + a - rp_k)^2} - b\right] * sin(\pi - \phi_k)\right)^2 = R^2 \quad (V.47)$$
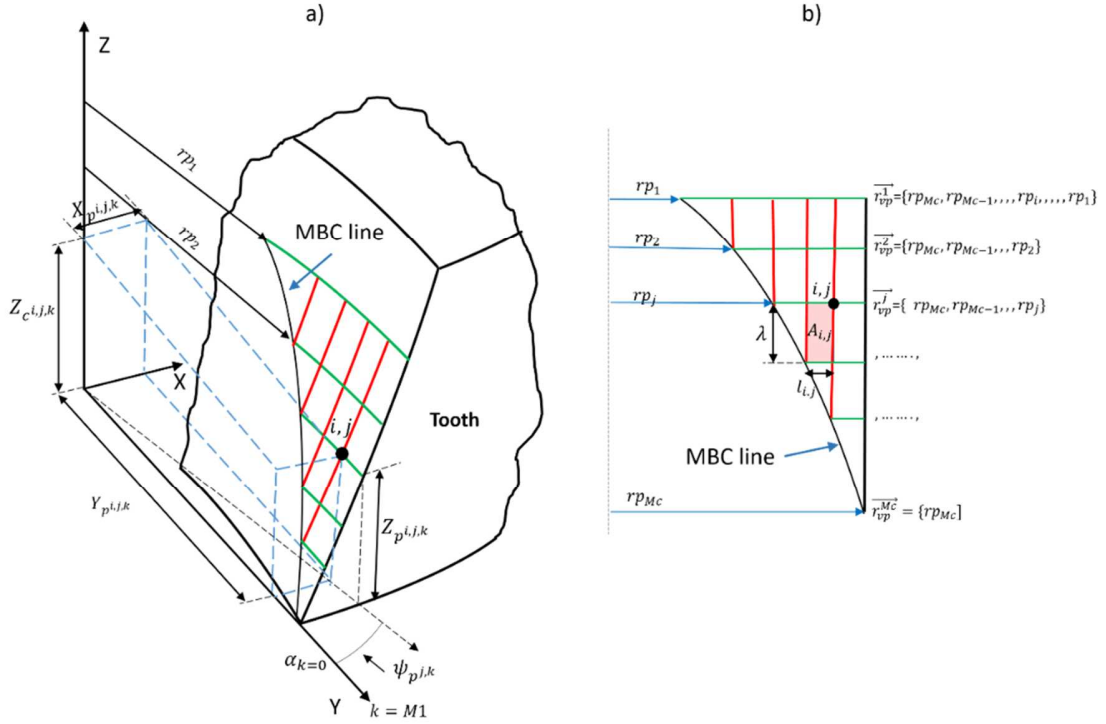
Figure V-27. Machined contact zone. a) contact zone scheme, b) mesh points parameters of the Unmachined zone

The r_{vp^j} vectors (equations 48 and 51) contain the radial length of the mesh points between the UBC or MBC lines with the helix line of the cutting edge that share the same height j (see Figure V-26b and Figure V-27b). moreover, i represents the position of each point within the vectors, and its maximum value is a function of j value.

The number of contact points grows as the engagement angle ϕ_k increases. The rp_k values can be arranged in a three-dimensional array $R_{p^{i,j,k}}$ (see equations 49 and 52). It means that, for a value of k, the points are arranged in a 2D matrix with i rows and j columns; however, for a new value of k, the number of contact points in the mesh increases, and it becomes necessary to store them in a new 2D matrix. The irregular shape of the contact area causes the number of elements in each row

187

to increase as a function of j . It is the reason why the mesh points form a three-dimensional array($R_{p^{i,j,k}}$) of 2D different-sized matrices. Some examples are shown in equation 50.

For unmachined zone:

$$i \ = \ 1,2.,,.j \ ; \ j \ = \ 1,2,,,,k; \ k = Mp, \ Mp+1, \dots, Mp$$

$$r_{vp^j} \ = \ \{rp_1, rp_2.,,.rp_i\}^{\ j} \quad (V.48)$$

$$R_{p^{i,j,k}} = \begin{bmatrix} r_{I^1} \\ r_{vp^2} \\ r_{vp^j} \\ r_{vp^{Mp}} \end{bmatrix}^K = \begin{bmatrix} rp_1 \\ rp_1, rp_2 \\ , \dots \dots \dots, \\ rp_1, rp_2, , , rp_j \\ , \dots \dots \dots, \\ rp_1, rp_2, , , , , rp_i, \dots., , rp_{Mp} \end{bmatrix}^K \quad (V.49)$$

$$R_{p^{i,j,2}} = \begin{bmatrix} r_{vp^1} \\ r_{vp^2} \end{bmatrix}^2 = \begin{bmatrix} rp_1 \\ rp_1, rp_2 \end{bmatrix}^2 ; \qquad R_{p^{i,j,4}} = \begin{bmatrix} r_{vp^1} \\ r_{vp^2} \\ r_{vp^3} \\ r_{vp^4} \end{bmatrix}^4 = \begin{bmatrix} rp_1 \\ rp_1, rp_2 \\ rp_1, rp_2, rp_3 \\ rp_1, rp_2, rp_3, rp_4 \end{bmatrix}^4 \quad (V.50)$$

For machined zone:

$$i \ = \ 1,2.,,. Mc - j + 1 \ ; \ j \ = \ 1,2,,,,k - M_p + 1; \ k = Mp, \ Mp+1, \dots, Mp+Mc-1$$

$$r_{vp^j} \ = \{rp_{Mc}, rp_{Mc-1}, rp_{Mc-2}, , , , , rp_j\} \ (V.51)$$

$$R_{p^{i,j,k}} = \begin{bmatrix} r_{vp^1} \\ r_{vp^2} \\ r_{vp^j} \\ r_{vp^{Mc}} \end{bmatrix}^K = \begin{bmatrix} rp_{Mc}, rp_{Mc-1}, , , , rp_i, , , , , rp_1 \\ rp_{Mc}, rp_{Mc-1}, , , rp_2 \\ , , , , , , , , , , , , , , , , \\ rp_{Mc}, rp_{Mc-1}, , , rp_j \\ , , , \\ rp_{Mc} \end{bmatrix}^K \quad (V.52)$$

UP MILLING

This section presents the steps to determine the contact area and the normal vector for up-milling. Moreover, the development of the equations is similar to the previous section, with the necessary geometrical changes. Figure V-28 shows the main parameters for the up-milling. In Figure V-28a,

the angle ϕ_{ec} is shown, which is the engagement angle related to the instant when the rake profile reaches the V point. Figure V-28b shows the angle ϕ_{ex} which corresponds to the angle of the engagement when the rake profile no longer touches the unmachined zone of the material. The angle ϕ_{ex} is obtained from equation 53.

$$\phi_{ex} = \pi + acos[(R - a_e)/R] \quad \text{(V.53)}$$

To obtain the angle ϕ_{ec} equations 11 and 12 must be solved as a non-linear system to obtain the angle ϕ when $m_x = V_x$ and $m_y = V_y$. where V_x and V_y are calculated from equations 54 and 55.

$$V_x = -R * \sin(\phi_{ex} - \pi) + fz \quad \text{(V.54)}$$
$$V_y = R - a_e \quad \text{(V.55)}$$
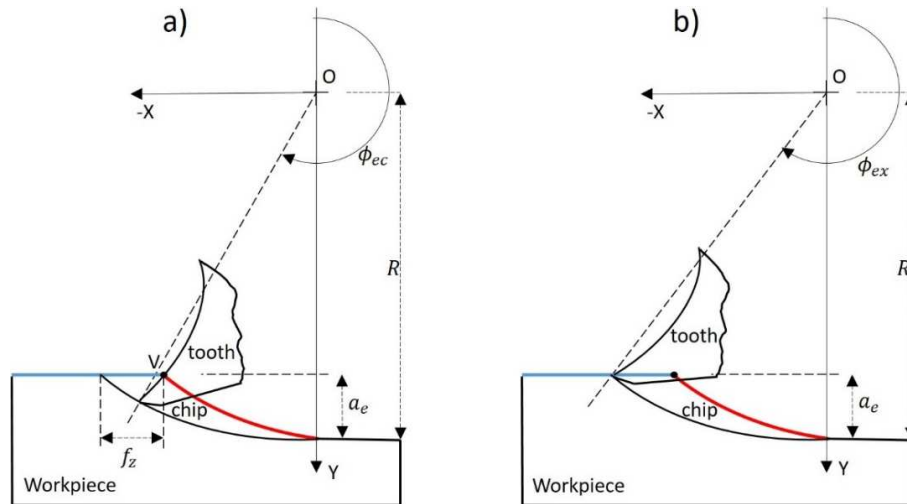
Figure V-28.Up milling geometry. a) Tool contact with unmachined zone, b) Tool contact with the machined zone

The equations for calculating the variables of interest are developed according to the logic of the previous sections. In this section, the number of points of each line j increases as the engagement angle increases (see Figure V-29).

The engagement angle values ϕ_k discretized as a function of the k-index are calculated from equations 56-61.

Machined zone

$$nc_k = \frac{\phi_k - \pi}{\Delta\phi} \text{ (V.56)}$$

$$Mc = \frac{\phi_{ec} - \pi}{\Delta\phi} + 1 \text{ (V.57)}$$

$$\phi_k = \pi + (k-1) * \Delta\phi = \{\pi, \pi + \Delta\phi, \pi + 2 * \Delta\phi, , , \phi_{ec}\} \text{ for k = 1,2,3,,,,} Mc \text{ (V.58)}$$

Unmachined zone

$$np_k = \frac{\phi_k - \phi_{ec}}{\Delta\phi} \text{ (V.59)}$$

$$Mp = \frac{\phi_{ex} - \phi_{ec}}{\Delta\phi} + 1 \text{ (V.60)}$$

$$\phi_k = \phi_{ec} + (k-1) * \Delta\phi = \{\phi_{ec}, \phi_{ec} + \Delta\phi, \phi_{sc} + 2 * \Delta\phi, , , \phi_{ex}\} \text{ for k = } Mc, Mc + 1, \dots, Mc + Mp -$$
$$1 \text{ (V.61)}$$

Radial lengths rp_k are obtained from equations 62 and 63. See Figure V-26 and Figure V-27.
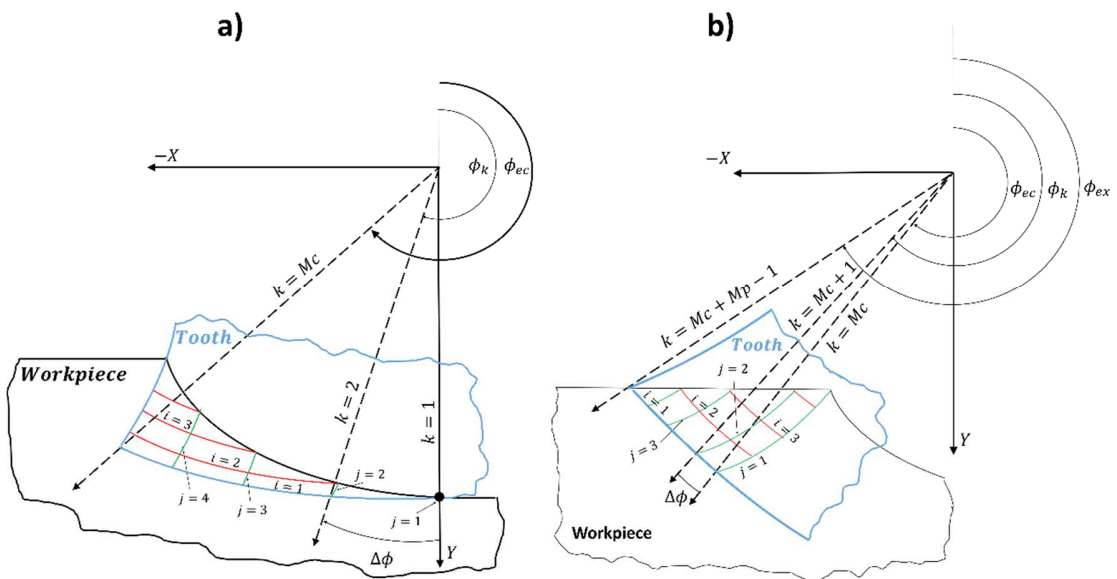
Figure V-29. Up-milling zones. a) unmachined zone scheme, b) machined zone scheme

Machined zone

$$\left(rp_k * \sin\left(\phi_k - \pi\right) + \left[\sqrt{R_f{}^2 - (c + a - rp_k)^2} - b\right] * \cos\left(\phi_k - \pi\right) + fz\right)^2 + \left(rp_k * \cos\left(\phi_k - \pi\right) - \left[\sqrt{R_f{}^2 - (c + a - rp_k)^2} - b\right] *$$

$$\sin\left(\phi_k - \pi\right)\right)^2 = R^2 \text{ (V.62)}$$

Unmachined zone

$$rp_k * \cos\left(\phi_k - \pi\right) - \left[\sqrt{R_f{}^2 - (c + a - rp_k)^2} - b\right] * \sin\left(\phi_k - \pi\right) = R - a_e \quad \text{(V.63)}$$

The three-dimensional array($R_{p^{i,j,k}}$) is calculated from equations 64-67.

Machined zone

$$i = 1,2.,,.j \, ; \, j = 1,2,,,,k; \quad k = 1,\, 2, \dots, Mc$$

$$r_{vp^j} = \{rp_1, rp_2.,,.rp_i\}^j \quad \text{(V.64)}$$

$$R_{p^{i,j,k}} = \begin{bmatrix} r_{vp^1} \\ r_{vp^2} \\ , \\ r_{vp^j} \\ , \\ r_{vp^{Mc}} \end{bmatrix}^K = \begin{bmatrix} rp_1 \\ rp_1, rp_2 \\ , \dots \dots \dots, \\ rp_1, rp_2,,, rp_j \\ , \dots \dots \dots, \\ rp_1, rp_2,,,,, rp_i, \dots.,, rp_{Mc} \end{bmatrix}^K \quad \text{(V. 65)}$$

Unmachined zone

$$i = 1,2.,,.Mp - j + 1 \, ; \, j = 1,2,,,,k - M_c + 1; \, k = Mc, \, Mc + 1, \dots, Mc + Mp - 1$$

$$r_{vp^j} = \{rp_{Mp}, rp_{Mp-1}, rp_{Mp-2},,,,, rp_j\} \text{ (V.66)}$$

$$R_{p^{i,j,k}} = \begin{bmatrix} r_{vp^1} \\ r_{vp^2} \\ , \\ r_{vp^j} \\ , \\ r_{vp^{Mp}} \end{bmatrix}^K = \begin{bmatrix} rp_{Mp}, rp_{Mp-1},,,, rp_i,,,,, rp_1 \\ rp_{Mp}, rp_{Mp-1},,, rp_2 \\ ,,,,,,,,,,,,,, \\ rp_{Mp}, rp_{Mp-1},,, rp_j \\ ,,, \\ rp_{Mp} \end{bmatrix}^K \quad \text{(V. 67)}$$

The mesh points coordinates ($X_{p^{i,j,k}}$, $Y_{p^{i,j,k}}$, $Z_{p^{i,j,k}}$),the discretized segment length ($l_{p^{i,j,k}}$), the discretized band area ($Ap_{j,k}$) and the terms related to the normal vector ($H_{p^{i,j}}$, $V_{p^{i,j}}$, $N_{p^{i,j,k}}$, Np_j) are calculated with the expressions stored in Table V-4.

Where $l_{p^{i,j,k}}$ is the discretized segment length formed by the straight line between two adjacent points that share the same j value. $A_{p^{i,j,k}}$ is the area of a discretized cell (see Figure V-26b), $Ap_{j,k}$ is

the area of all discretized cells that shares the same j value from now on named as discretized band area (see Figure V-26a), $H_{pi,j}$ and $V_{pi,j}$ are the horizontal and vertical vectors needed to perform the cross product (See Figure V-3), $N_{pi,j,k}$ is the normal vector associated with each mesh point and $Np_{j,k}$ is the resultant normal vector of a line corresponding to the height j. additionally $\psi_{j,k}$ is the lag angle of the mesh points corresponding to line j for tool position k concerning the angle ϕ_k (see Figure V-26a) and λ is the straight length between two successive points of the discretized cutting edge helix (see Figure V-5).

Table V-4. Mathematical expressions for mesh points

	Down-milling equations	Unmachined zone	Machined zone
Mesh points coordinates	$X_{p^{i,j,k}} = R_{p^{i,j,k}} * \sin(\pi - \phi_k + \psi_{j,k}) + \left[\sqrt{R_f^2 - (c + a - R_{p^{i,j,k}})^2} - b\right] * \cos(\pi - \phi_k + \psi_{j,k})$ $Y_{p^{i,j,k}} = R_{p^{i,j,k}} * \cos(\pi - \phi_k + \psi_{j,k}) - \left[\sqrt{R_f^2 - (c + a - R_{p^{i,j,k}})^2} - b\right] * \sin(\pi - \phi_k + \psi_{j,k})$ $Z_{kp^{jk}} = \frac{\pi * R * \psi_{j,k}}{180 * \tan(\beta)}$	$\psi_{j,k} = (np_k + 1 - j) * \Delta\phi$ $i = 1,2,,,j;$ $j = 1,2,,,,k;$ $k = 1,2,,,,Mp$	$\psi_{j,k} = (nc_k + 1 - j) * \Delta\phi$ $i = 1,2,,,Mc - j + 1;$ $j = 1,2,,,k - Mp + 1;$ $k = Mp, Mp + 1, ..., Mp + Mc - 1$
Discretized segment length	$l_{p^{i,j,k}} = \left[\left(X_{p^{i+1,j,k}} - X_{p^{i,j,k}}\right)^2 + \left(Y_{p^{i+1,j,k}} - Y_{p^{i,j,k}}\right)^2\right]^{1/2}$	$for\ i = 1,2,,,j - 1;$ $j = 2,3,,,k;$ $k = 1,2,,,Mp$	$for\ i = 1,2,,,Mc - j;$ $j = 1,2,,,k - Mp;$ $k = Mp, Mp + 1, ..., Mp + Mc - 1$
Discretized cell area	$A_{p^{i,j,k}} = l_{p^{i,j,k}} * \lambda;\ \lambda = \frac{\Delta\phi * \pi * R}{180 * \sin(\beta)}$	$for\ i = 1,2,,,j - 1;$ $j = 2,3,,,k - 1;$ $k = 1,2,,,Mp$	$for\ i = 1,2,,,Mc - j;$ $j = 1,2,,,k - Mp - 1;$ $k = Mp, Mp + 1, ..., Mp + Mc - 1$
Discretized band area	$Ap_{j,k} = \frac{(l_{pj,j+1,k}) * \lambda}{2} + \sum_{i=1}^{a} l_{p^{i,j,k}} * \lambda;$	$for\ j = 2,3,,,k - 1;$ $k = 1,2,,,Mp$ $a = j - 1$	$for\ j = 1,2,,,k - M_p - 1$ $k = M_p, M_p + 1, ..., M_p + M_c - 1$ $a = Mc - j$
Normal vector expresions	$H_{p^{i,j,k}} = \left\{\left(X_{p^{i+1,j,k}} - X_{p^{i,j,k}}\right), \left(Y_{p^{i+1,j,k}} - X_{p^{i,j,k}}\right), \left(Z_{p^{i+1,j,k}} - Z_{p^{i,j,k}}\right)\right\}$ $V_{p^{i,j,k}} = \left\{\left(X_{p^{i,j+1,k}} - X_{p^{i,j,k}}\right), \left(Y_{p^{i,j+1,k}} - X_{p^{i,j,k}}\right), \left(Z_{p^{i,j+1,k}} - Z_{p^{i,j,k}}\right)\right\}$ $N_{p^{i,j,k}} = H_{p^{i,j,k}} \times V_{p^{i,j,k}}$ $N_{p^{j,k}} = \sum_{i=1}^{j-1} N_{p^{i,j,k}}$	$for\ i = 1,2,,j - 1;$ $j = 2,3,,k - 1;$ $k = 1,2,,Mp$	$for\ i = 1,2,,Mc - j;$ $j = 1,2,3,,,k - Mp$ $k = Mp, Mp + 1, ..., Mp + Mc - 1$

	Up-milling equations	Machined zone	Unmachined zone
Mesh points coordinates	$X_{p^{i,j,k}} = R_{p^{i,j,k}} * \sin(\phi_k - \pi - \psi_{j,k}) + \left[\sqrt{R_f^2 - (c + a - R_{p^{i,j,k}})^2} - b\right] * \cos(\phi_k - \pi - \psi_{j,k})$ $Y_{p^{i,j,k}} = R_{p^{i,j,k}} * \cos(\phi_k - \pi - \psi_{j,k}) - \left[\sqrt{R_f^2 - (c + a - R_{p^{i,j,k}})^2} - b\right] * \sin(\phi_k - \pi - \psi_{j,k})$ $Z_{kp^{jk}} = \frac{\pi * R * \psi_{j,k}}{180 * \tan(\beta)}$	$\psi_{j,k} = (nc_k + 1 - j) * \Delta\phi$ $i = 1,2,,,j;$ $j = 1,2,,,,k;$ $k = 1,2,,,,Mc$	$\psi_{j,k} = (np_k + 1 - j) * \Delta\phi$ $i = 1,2,,,Mp - j + 1;$ $j = 1,2,,,k - Mc + 1;$ $k = Mc, Mc + 1, ..., Mc + Mp - 1$
Discretized segment length	$l_{p^{i,j,k}} = \left[\left(X_{p^{i+1,j,k}} - X_{p^{i,j,k}}\right)^2 + \left(Y_{p^{i+1,j,k}} - Y_{p^{i,j,k}}\right)^2\right]^{1/2}$	$for\ i = 1,2,,,j - 1;$ $j = 2,3,,,k;$ $k = 1,2,,,Mc$	$for\ i = 1,2,,,Mp - j;$ $j = 1,2,,,k - Mc;$ $k = Mc, Mc + 1, ..., Mc + Mp - 1$
Discretized cell area	$A_{p^{i,j,k}} = l_{p^{i,j,k}} * \lambda;\ \lambda = \frac{\Delta\phi * \pi * R}{180 * \sin(\beta)}$	$for\ i = 1,2,,,j - 1;$ $j = 2,3,,,k - 1;$ $k = 1,2,,,Mc$	$for\ i = 1,2,,,Mp - j;$ $j = 1,2,,,k - Mc - 1;$ $k = Mc, Mc + 1, ..., Mc + Mp - 1$
Discretized band area	$Ap_{j,k} = \frac{(l_{pj,j+1,k}) * \lambda}{2} + \sum_{i=1}^{a} l_{p^{i,j,k}} * \lambda;$	$for\ j = 2,3,,,k - 1;$ $k = 1,2,,,Mc$ $a = j - 1$	$for\ j = 1,2,,,k - M_c - 1;$ $k = M_c, M_c + 1, ..., M_c + M_p - 1$ $a = Mp - j$
Normal vector expresions	$H_{p^{i,j,k}} = \left\{\left(X_{p^{i+1,j,k}} - X_{p^{i,j,k}}\right), \left(Y_{p^{i+1,j,k}} - X_{p^{i,j,k}}\right), \left(Z_{p^{i+1,j,k}} - Z_{p^{i,j,k}}\right)\right\}$ $V_{p^{i,j,k}} = \left\{\left(X_{p^{i,j+1,k}} - X_{p^{i,j,k}}\right), \left(Y_{p^{i,j+1,k}} - X_{p^{i,j,k}}\right), \left(Z_{p^{i,j+1,k}} - Z_{p^{i,j,k}}\right)\right\}$ $N_{p^{i,j,k}} = H_{p^{i,j,k}} \otimes V_{p^{i,j,k}}$ $N_{p^{j,k}} = \sum_{i=1}^{j-1} N_{p^{i,j,k}}$	$for\ i = 1,2,,j - 1;$ $j = 2,3,,k - 1;$ $k = 1,2,,Mc$	$for\ i = 1,2,,,Mp - j;$ $j = 1,2,3,,,k - Mc;$ $k = Mc, Mc + 1, ..., Mc + Mp - 1$

The parameters $M1, M2, M3 \ and \ M4$ are the limits of the k index for the previously mentioned stages and are obtained according to Table V-5 and $Mg = \frac{\gamma}{\Delta\phi}$ The equations for calculating the cumulative contact area Aa_k, and the instantaneous cumulative normal vector Na_k for each of the previously mentioned stages are exposed in Table V-6.

Table V-5. k Index limits

Down-milling	Up-milling
$M1 = Mp + Mc - 1$	$M1 = Mc + Mp - 1$
$M2 = Mp + Mc + Mg = M1 + Mg$	$M2 = Mc + Mp + Mg = M1 + Mg$
$M3 = 2*Mp + Mc + Mg = M2 + Mp - 1$	$M3 = 2*Mc + Mp + Mg = M2 + Mc - 1$
$M4 = 2*Mp + 2*Mc + Mg = M3 + Mc - 1$	$M4 = 2*Mc + 2*Mp + Mg = M3 + Mc - 1$

Table V-6. Accumulated contact area and normal vector equations

DOWN MILLING					
	STAGE A	**STAGE B**	**STAGE C**	**STAGE D**	**STAGE E**
Index range	For $k = 1, 2, \dots, Mp$	For $k = Mp, Mp + 1.,,,,,.M1$	for $k = M1, M1 + 1, M1 + 2,,,,,.M2$	for $k = M2, M2 + 1, M2 + 2.,,,,.M3$	for $k = M3, M3 + 1, M3 + 2.,,,,.M4$
Accumulated contact area	$Aa_k = \sum_{j=2}^{k-1} Ap_{j,k}$ $Aa_k = Aa$ when $k = Mp$ ($Ap_{j,k}$ is according to unmachined zone)	$Aa_k = Aa + \sum_{j=1}^{k-Mp-1} Ap_{j,k}$ $Aa_k = Amax$ when $k = M1$ ($Ap_{j,k}$ is according to machined zone)	$Aa_k = Amax$	$Aa_k = Amax - \sum_{j=2}^{k-M2} Ap_{j,k}$ ($Ap_{j,k}$ is according to unmachined zone)	$Aa_k = Amax - Aa - \sum_{j=1}^{k-M3-1} Ap_{j,k}$ ($Ap_{j,k}$ is according to machined zone)
Accumulated normal vector	$Na_k = \left(\sum_{j=2}^{k-1} \frac{Np_{j,k}}{\|Np_{j,k}\|_j} \right) * \sum_{j=2}^{k-1} Ap_{j,k}$ $Na_k = Na$ when $k = Mp$ ($Np_{j,k}$ and $Ap_{j,k}$ are according to unmachined zone)	$Na_k = Na + \left(\sum_{j=1}^{k-Mp-1} \frac{Np_{j,k}}{\|Np_{j,k}\|_j} \right) * \sum_{j=1}^{k-Mp-1} Ap_{j,k}$ $Na_k = N_T$ when $k = M1$ ($Np_{j,k}$ and $Ap_{j,k}$ are according to machined zone)	$Na_k = N_T$	$Na_k = N_T - \left(\sum_{j=2}^{k-M2} \frac{Np_{j,k}}{\|Np_{j,k}\|_j} \right) * \sum_{j=2}^{k-M2} Ap_{j,k}$ ($Np_{j,k}$ and $Ap_{j,k}$ are according to unmachined zone)	$Na_k = N_T - Na - \left(\sum_{j=1}^{k-M3-1} \frac{Np_{j,k}}{\|Np_{j,k}\|_j} \right) * \sum_{j=1}^{k-M3-1} Ap_{j,k}$ ($Np_{j,k}$ and $Ap_{j,k}$ are according to machined zone)
UP MILLING					
	STAGE A	**STAGE B**	**STAGE C**	**STAGE D**	**STAGE E**
Index range	For $k = 1, 2, \dots, Mc$	For $k = Mc, Mc + 1.,,,,,.M1$	for $k = M1, M1 + 1, M1 + 2,,,,,.M2$	for $k = M2, M2 + 1, M2 + 2.,,,,.M3$	for $k = M3, M3 + 1, M3 + 2.,,,,.M4$
Accumulated contact area	$Aa_k = \sum_{j=2}^{k-1} Ap_{j,k}$ $Aa_k = Aa$ when $k = Mc$ ($Ap_{j,k}$ is according to machined zone)	$Aa_k = Aa + \sum_{j=1}^{k-Mc-1} Ap_{j,k}$ $Aa_k = Amax$ when $k = M1$ ($Ap_{j,k}$ is according to unmachined zone)	$Aa_k = Amax$	$Aa_k = Amax - \sum_{j=2}^{k-M2} Ap_{j,k}$ ($Ap_{j,k}$ is according to machined zone)	$Aa_k = Amax - Aa - \sum_{j=1}^{k-M3-1} Ap_{j,k}$
Accumulated normal vector	$Na_k = \left(\sum_{j=2}^{k-1} \frac{Np_{j,k}}{\|Np_{j,k}\|_j} \right) * \sum_{j=2}^{k-1} Ap_{j,k}$ $Na_k = Na$ when $k = Mc$ ($Np_{j,k}$ and $Ap_{j,k}$ are according to machined zone)	$Na_k = Na + \left(\sum_{j=1}^{k-Mc-1} \frac{Np_{j,k}}{\|Np_{j,k}\|_j} \right) * \sum_{j=1}^{k-Mc-1} Ap_{j,k}$ $Na_k = N_T$ when $k = M1$ ($Np_{j,k}$ and $Ap_{j,k}$ are according to unmachined zone)	$Na_k = N_T$	$Na_k = N_T - \left(\sum_{j=2}^{k-M2} \frac{Np_{j,k}}{\|Np_{j,k}\|_j} \right) * \sum_{j=2}^{k-M2} Ap_{j,k}$ ($Np_{j,k}$ and $Ap_{j,k}$ are according to machined zone)	$Na_k = N_T - Na - \left(\sum_{j=1}^{k-M3-1} \frac{Np_{j,k}}{\|Np_{j,k}\|_j} \right) * \sum_{j=1}^{k-M3-2} Ap_{j,k}$ ($Np_{j,k}$ and $Ap_{j,k}$ are according to unmachined zone)

Chapter VI. A holistic methodology for the design and manufacturing of LPBF components considering post-processing operations by machining

VI. A holistic methodology for the design and manufacturing of LPBF functional parts considering post-processing operations

This chapter presents a methodology to optimize the mechanical properties of LPBF components by controlling anisotropy. To this end, the interactions between the process and the physical parameters, the effect of the LPBF configuration on the crystalline classification, and the methodology based on multi-objective optimization to balance the process design variables and manufacture components that allow machining stability and optimal mechanical properties are presented.

VI.1. Introduction

Crystalline texture control is a topic of great interest recently in the scientific and industrial community, which is beginning to be implemented for the microstructural design of metallic materials fabricated by LPBF. Furthermore, the LPBF process allows much flexibility to exercise this control, given the multiple combinations that can be obtained between scanning laser strategies, LPBF parameters, and beam shape modes. The components manufactured by LPBF are anisotropic, and there are many efforts in the scientific community to decrease the anisotropy of these materials without much success. However, anisotropy can be used as a valuable tool for component design if the knowledge barriers on how to quantify and understand it are overcome.

Additive manufacturing has created a new segment in the manufacturing of complex-shaped metallic parts (Klahn, Leutenecker, and Meboldt 2015). These processes have been studied for industrial applications in medium and small-batch lots (Ford and Despeisse 2016; W. Gao et al. 2015). Certain aspects, such as the smooth integration between the 3D model and the manufacturer, excellent scalability, low design limitations with internal shapes, and lattice structures, render additive manufacturing a better option than other manufacturing techniques (Tofail et al. 2018; Thompson et al. 2016). However, although in the context of Industry 4.0, additive manufacturing plays a key role, specific concerns regarding its application in large batch manufacturing exist (Dilberoglu et al. 2017). Consequently, group technology and production cells are essential to overcome this issue (Mosier and Taube 1985). Additive manufacturing processes are of particular interest in the segment of thin-walled, hollow, and slender parts; nevertheless, post-processing, machining, is necessary to guarantee the dimensional and

surface quality of functional parts. Currently, combining additive and subtractive processes into a hybrid manufacturing method (Flynn et al. 2016; Guhaprasanna Manogharan 2014) has enabled the manufacture of functional parts for aeronautical engine parts, turbines, biomedical implants, and many other applications.

Recently, several studies have been conducted on the machining of LPBF-printed parts. Many of these studies have focused on analysing the surface quality, machinability, and microstructural characteristics of the material (Yuchao Bai, Cuiling Zhao, Yu Zhang, Jie Chen 2021; Hansong ji,Munish kumar gupta, quinghua song,wentong cai, tao zheng,youle zhao,zhanquian liu 2021). However, the surface quality of the as-printed LPBF components is not sufficient for functional applications, and post-processing by milling or a similar process is often needed (Jiménez et al. 2021a). Further, support fixtures are essential to ensure the stability of the milling process, affecting the surface and deflection of the workpiece (Hintze et al. 2020). However, milling complex LPBF parts is a challenge because of the necessity of support for manufacturing, affecting the stiffness of the part and resulting in vibrational problems that amplify the cutting instability, particularly for flexible structures. Consequently, certain industrial solutions have been provided for specific geometries through the use of special supportive workholding during finish machining (Saunders 2017). Most recent studies have been based on machining prismatic or cylindrical workpieces with sufficient stiffness. Few studies focusing on the machining of near-net-shape parts for functional applications have been conducted (Didier et al. 2021), wherein thin walls and complex and slender shapes represent a machining challenge owing to the low stiffness of these components and the difficulties of implementing conventional fixture supports. The use of base-plate sacrificial supports for clamping and positioning AM workpieces to ensure fixation during the machining process has also been evaluated (Guha Manogharan, Wysk, and Harrysson 2015); however, its optimization is complex and not well known. Therefore, developing robust hybrid manufacturing methodologies (Perez Ruiz et al. 2020) that include aspects related to the LPBF manufacturing process, machining parameters, part design, and microstructural characteristics of the material is essential.

The flexibility of the LPBF process is dependent on both the several complex shapes that can be manufactured and the improvement of the mechanical properties of the workpiece. This is because of the possibility of changing the distribution of the crystalline orientation in the material through the configuration of the laser power, laser speed, layer thickness, hatching space, and laser rotation strategy (Tucho et al. 2017). In this regard, Karimi et al. (Karimi et al. 2018) established relationships between volumetric energy density, hardness level, and

porosity, and Liu et al. (S. Y. Liu et al. 2020) reported the interaction between LPBF parameters and anisotropy in mechanical properties through variations in the Taylor factor for different sample orientations. The different combinations of LPBF parameters allow different values of volumetric energy density and different solidification modes to be obtained, which translates into the control of the size and orientation of the grains and modification of the crystalline texture. Considering this, Lei et al. (Lei et al. 2019) analyzed the effect of hatching space and laser speed on grain refinement, roughness, and microhardness, and concluded that volumetric energy density played a major role in these variables. Further, Yi et al. (Yi et al. 2019) explored the effect of linear energy density on yield strength. Components manufactured via LPBF are considered to be textured, rendering them anisotropic. Many authors consider that the primary cause of the anisotropy in mechanical properties is related to the development of ultrafine columnar grains that grow epitaxially along the building direction and preferred crystalline orientations (Z. Chen et al. 2018; Suwas and Ray 2014; Dinda, Dasgupta, and Mazumder 2012; Pham et al. 2020b). The anisotropy in the Young's modulus of LPBF printed components indicates that the material exhibits much higher stiffness values for specific directions and shallow values in certain directions, which has been widely reported in the literature for the evaluation of as-printed LPBF (Z. Liu and Qi 2015c) and heat-treated samples (M. Ni et al. 2017b), and their interaction with the cutting process (Pérez-Ruiz et al. 2021; M. Zhou and Ngoi 2001). An essential factor in increasing the stiffness of a component from the design (CAD) and LPBF printing stages is the orientation of the printed parts. In addition, the mechanical properties of LPBF components can change even at the same energy density(de Souza et al. 2019).

The high thermal gradient, fast cooling rates, and development of columnar grains in the LPBF process are the leading causes of crystalline gradients, residual stresses, and geometric distortions. In certain cases, the residual stresses and distortions can be minimised by optimising the manufacturing parameters or using fixture supports (Mishurova et al. 2018). Further, real-time monitoring can reduce the cost of non-quality, specifically in the case of premature failures. Certain works relate techniques that process monitoring through image analysis and detect anomalies to take action (Scime and Beuth 2018; Lott et al. 2011; Everton et al. 2016). However, in certain cases, achieving the required mechanical properties is not possible using the LPBF process. This limitation can be overcome through the use of appropriate heat treatments to homogenise and increase the mechanical properties. Additive manufacturing processes cannot produce finished parts with narrow tolerances and optimal surface quality, even with optimized parameters. Therefore, post-processing using machining is often required.

This chapter connects the different concepts and models presented throughout this thesis through a methodology. For this purpose, it is explained step by step by means of diagrams, figures, and equations how the LPBF manufacturing configuration affects the microstructure, mechanical properties, and post-processing. Three case studies covering most aspects of the methodology are also presented.

VI.2 Methodology

This section presents a methodology to manufacture LPBF parts considering the design of some mechanical properties and post-processing by machining. For this purpose, the effects of the LPBF process parameters on the physical parameters and their subsequent effect on the mechanical properties are considered. The interaction of the mechanical properties with the machining stability is also considered. The schematic in Figure VI-1 represents the interactions between the LPBF process, the physical parameters, and some mechanical properties. Likewise, the connection of the mechanical properties with the stability during the machining process. It is noteworthy remind that the LPBF parameters, the physical parameters, and the interactions between them are extensively presented in chapter III.
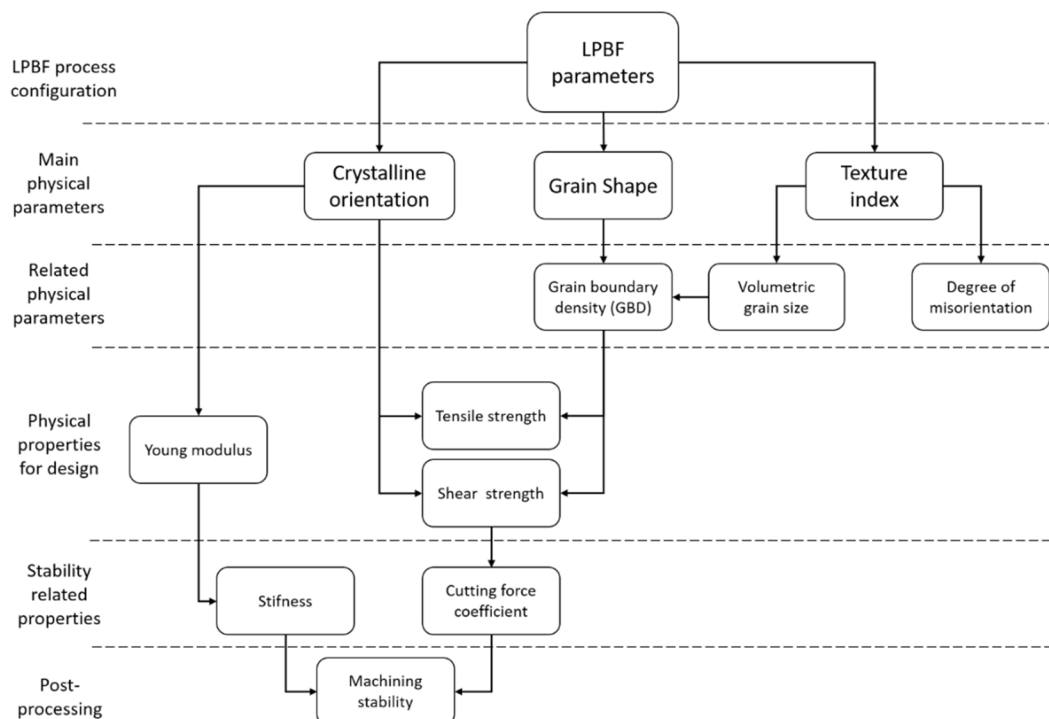
Figure VI-1. Flow chart of the interaction of the LPBF process with physical parameters and mechanical properties for material design and post-processing by machining

The scheme in Figure VI-1 is the leading guide of the present methodology as it gives an overview of which physical parameters are related to the mechanical properties. This research considers three main physical parameters: the primary crystalline orientation, the grain shape, and the texture index. These parameters are related, but their effects on mechanical properties differ, so treating them separately is better.

In addition to the main physical parameters, secondary physical parameters are derived from the main ones, such as the misorientation level, which affects the crystal lattice's disorder and corrosion resistance. Other secondary physical parameters are the volumetric grain size on which it depends and the grain boundary density, considering that the grain boundary density depends on the interaction between the volumetric grain size, the grain shape, and the shear plane in which it is to be determined. It is essential to clarify that grain boundary density (GBD) is a parameter that depends on the orientation in which it is measured.

Figure VI-2 shows the theories used to relate physical parameters to mechanical properties and the relationship between mechanical properties and the stability of the machining process. The theories of hill's elasticity, Taylor's plasticity, and hall petch's law are extensively discussed in chapter III.
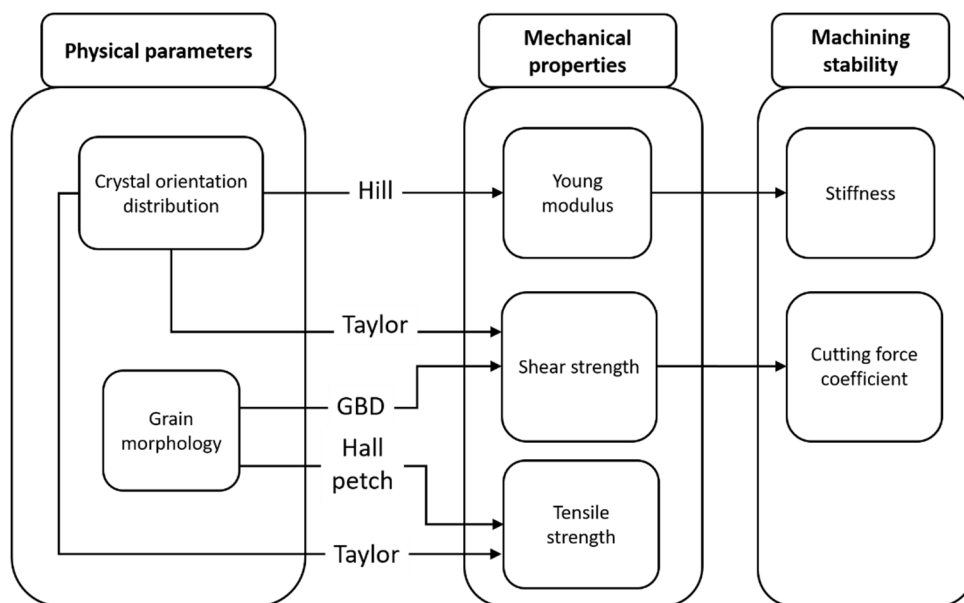
Figure VI-2. Theories and models used to predict the mechanical properties from the physical parameters

Figure VI-2 shows that Young's modulus depends on the crystalline distribution, and its value is not affected by grain size or grain boundary density. This is because no dislocation flow develops during elastic deformation, so Young's modulus only depends on the resultant of the atomic forces as a function of the tensile or compressive load vector. On the other hand, the shear and tensile strength related to the plastic strain of the material depend on at least three factors, which are the resistance of the crystalline grain formation to slip deformation, the dislocation density of the material, and the grain boundary density.

The Taylor factor is used to quantify the resistance of crystals to plastic deformation due to the action of a deformation tensor. The deformations can be in uniaxial orientations or shear directions. The present study used the Taylor factor to quantify the resistance to plastic deformation under uniaxial tension-compression and pure shear deformation loading. The resistance to uniaxial loading deformation is directly related to the yield stress and ultimate tensile strength. On the other hand, the resistance to shear deformation is directly related to the magnitude of the shear coefficients, as shown in chapter IV. It is important to note that the Taylor factor only quantifies the effect of crystalline texture on the resistance to deformation by uniaxial or shear loading; however, the effect of grain boundaries is also essential. Unfortunately, there are currently no theories to reliably calculate the grain boundary density as a function of the direction of a shear plane. However, in the present study, some guidelines are given to predict the trend of increasing or decreasing grain boundary density as a function of the manufacturing parameters and the orientation of the external loads. Based on the above, it is important to establish that the effect of crystallographic texture through the Taylor factor will be used throughout this chapter under a theoretical and experimental approach. In contrast, the effect of grain boundary density or hall petch on mechanical properties will be shown only experimentally in Section VI.4.4.

The variation of Young's modulus as a function of the crystalline distribution and its effects on the stiffness of the manufactured parts will be presented in sections VI.4.4 and VI.4.5. On the other hand, the correlation between the shear strength and the cutting forces will be made through the Taylor factor maps for oblique shear action for different positions of the tool. It will be presented in section VI.5.

VI.2.1. Texture index effect

The texture index is undoubtedly one of the material's most important physical parameters, as it characterizes whether a material is polycrystalline, textured polycrystalline, or single-crystal.

The details for the calculation of the texture index are explained in more detail in chapter III. This section will show how the LPBF fabrication parameters and the texture index interact in more detail.

Figure VI-3 shows three levels of crystalline classification of the materials fabricated by LPBF. The first column shows the polycrystal-like types in which the combination of the R67 strategy with low VED energy density allows a non-hierarchical dendritic subgranular dendritic structure and a high level of different crystalline orientations (in chapter III, these aspects are deepened). This, in turn, allows the texture index to be low (between 1 and 2) and the degree of anisotropy to be shallow. Additionally, the average grain size is smaller, which leads to an increase in the grain boundary density. From the hall petch law, grain refinement increases the yield stress, so the parts manufactured this way would have a higher mechanical strength due to the hall petch strengthening. However, the grain refinement of polycrystalline parts has disadvantages related to the increase of crystalline dislocations that are largely related to corrosion tendency and lower fatigue resistance compared to single-crystal components. Likewise, the texture strengthening is not intense in this type of material.

The second column shows the category of textured polycrystals. This is the category where most of the fabrications made by LPBF are found. In the textured polycrystals, the texture index reaches values between 3 to 6, which can be obtained from different strategies. The present study presents only R0, R67, and R90, but other strategies can produce textured polycrystals. One of the characteristics of this type of material is that despite being polycrystalline, the intensity of the texture in these materials is relatively significant and its effect on the mechanical properties is also significant. This, in turn, makes the level of anisotropy in these materials significant.

Similarly, the grain size in textured polycrystals is larger than in polycrystal-like materials but smaller than single crystal-like, which makes them a more balanced choice between mechanical strength and level of crystalline misorientation. Within this classification, levels depend on the strategy; for example, the R67 strategy with high VED allows obtaining textured polycrystals with an intermediate texture index and anisotropy level. In this configuration, the grains tend to be columnar and quite elongated (see chapter III). A large number of grains means that the mechanical strength due to the grain boundary density (hall petch strengthening) is relatively high. Additionally, a medium texture index level means that the strength due to the texture effect is also high, which means that for specific orientations, the strength of materials manufactured with R67 and high VED allows a good balance between mechanical strength due

to grain boundary density and due to the texture effect. However, unlike polycrystal-like materials, the higher level of anisotropy present in textured polycrystals means that the orientation in which the parts are manufactured must be done with care so that the external load vectors generate elastic deformations that coincide as closely as possible with the crystalline orientations that offer greater resistance to elastic and plastic deformations. This aspect will be discussed further in section VI.4.6.
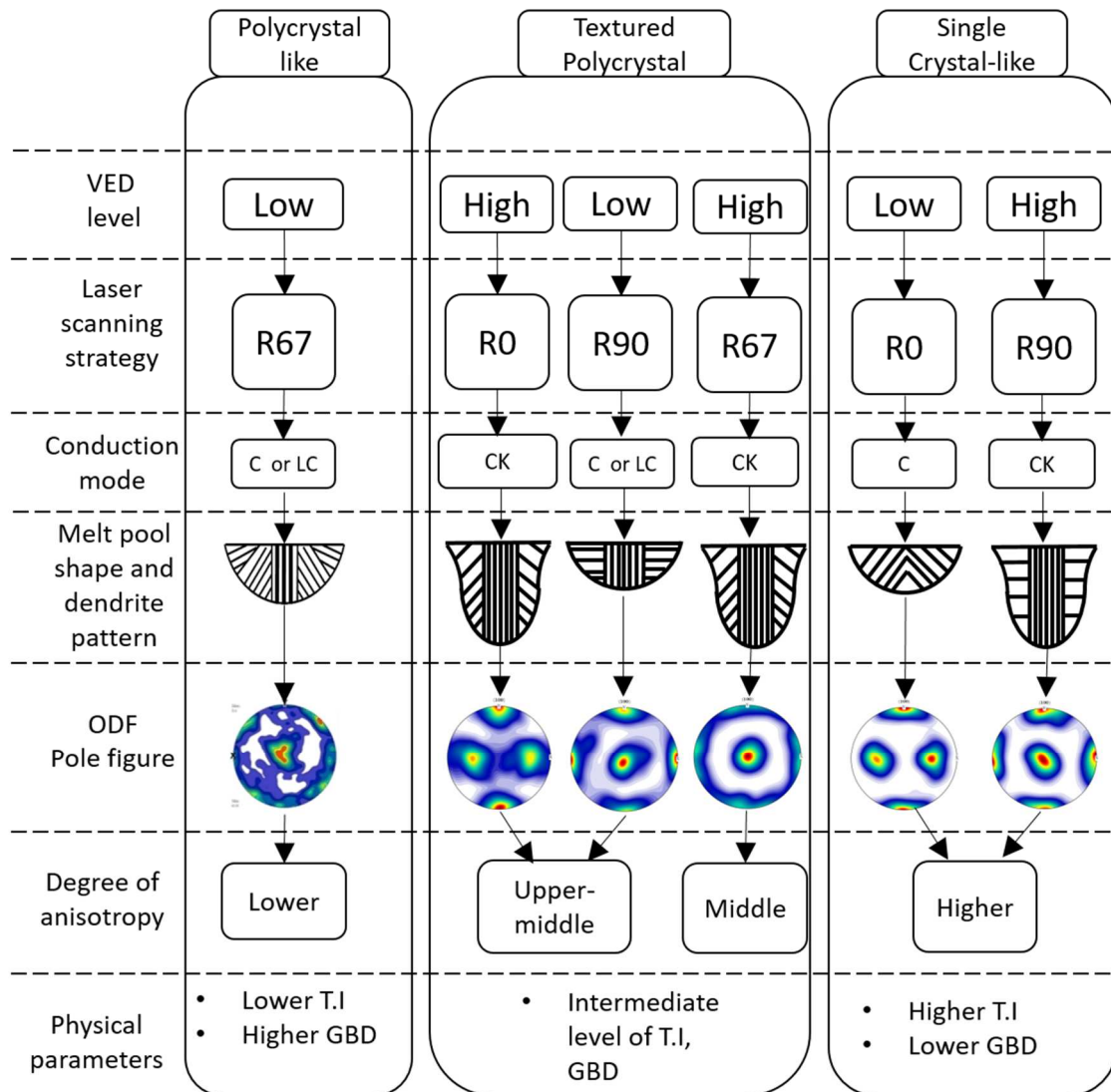
Figure VI-3. VED and laser scanning strategy interaction effect on Texture index(T.I) and grain boundary density(GBD)

Additionally, the R0 and R90 strategies with Low and High VED values allow the production of textured polycrystal materials. The materials fabricated with these configurations have a higher texture index level than the materials fabricated with the R67 High VED; however, the texture

index is not high enough to be considered at least as single-crystal-like. Using these configurations allows the development of hierarchical dendritic microstructures in a higher percentage than in the previously mentioned configurations. The configuration formed by the R0 strategy and High VED allows the formation of steeper melt pools under the conduction-keyhole (CK) mode. In this configuration, the lamellar microstructure causes at least two main crystalline directions to exist, which makes the texture index reach intermediate or intermediate-high levels (see chapter III). On the other hand, the R90 Low VED configuration allows the formation of steeper melt pools under conduction mode (C) or low-conduction mode(LC). In this configuration, only one main crystalline direction is obtained, but with low texture intensity, so they do not reach the single crystal-like level.

Finally, the third column shows the configurations to obtain single crystal-like materials. In this type of material, the texture index is between 6 and 9. These materials cannot be called single-crystals because although the degree of misorientation is much lower than in the previous configurations, there are still some grains and sub-granular structures with a certain level of misorientation. Despite this, the level of organization of the crystalline arrangement is significantly higher thanks to the development of hierarchical dendritic subgranular dendritic structures, which is achieved through a balance between the preferred crystallographic orientation of the seed grains and the orientations of the thermal gradient during solidification. For the case of the R0 Low VED configuration, it is possible to develop a conduction mode in the melt pools. This mode, together with a suitable hatching space, can facilitate that the dendritic growth be only by side-branching, disappearing the epitaxial growth in the melt pool bottom, which makes the secondary (epitaxial) crystalline direction present in the lamellar microstructure of the R0 High VED configuration disappears and therefore the texture index increases.

On the other hand, with the R90 High VED configuration, single crystal-like parts can also be obtained; however, the solidification mechanism and the pattern of hierarchical dendritic structures is different. In this configuration (R90 High VED), the dendritic growth mechanism is also by side-branching, but unlike in the R0 Low VED configuration, the side branching is at 90 degrees concerning the building direction, while in the R0 Low VED configuration, the side branching connections are at 45 degrees about the building direction. In most cases, the texture indices employing both strategies are usually relatively high, as observed in the literature and in the tests carried out in this study.

As with polycrystal-like and textured polycrystals, single-crystal-like materials have advantages and disadvantages. Among the advantages is the lower grain boundary density due to lower levels of crystalline misorientation, which means that corrosion resistance in these materials can be superior to the other categories. The same applies to fatigue resistance. However, these topics still need to be studied and verified experimentally. Additionally, the high texture index of single crystal-like samples makes the anisotropy in mechanical properties higher than in textured polycrystal or polycrystal-like samples. This aspect can be considered a disadvantage if there is a lack of knowledge about controlling and manipulating the anisotropy. However, it can be advantageous if there is knowledge about how to design the workpiece to align the load vectors with the strong crystalline orientations, which is the objective of the methodology presented in this chapter.

VI.2.2. Grain shape effect

Grain morphology is of vital importance in the anisotropy of a material. Isotropic materials usually have equiaxial grains and multiple crystalline orientations, so regardless of the orientation in which an isotropic metallic material is plastically deformed, the flow of dislocations will find the same resistance regardless of the direction of the load vector causing the deformation. In the case of columnar grains, the mechanical behavior of the material under loading is very different since the density of grain boundaries changes significantly as a function of the shear plane evaluated. On the other hand, the volumetric size of the grains is insufficient to define the density of grain boundaries since an elongated columnar grain can have the same volume as a less elongated but wider columnar grain. All these aspects make it necessary to consider grain morphology as an additional physical parameter.

Taking into account the crystalline classification of the materials manufactured by LPBF, it is possible to establish that the volumetric size of the grains is smaller when the texture index is lower so that the polycrystal-like materials obtained by the R67 Low VED configuration will have a much smaller grain size than other configurations with a higher texture index. In the case of single-crystal-like materials, it is possible to establish that the grain size obtained will be the largest possible, considering that an ideal single-crystal material is theoretically composed of a single grain. However, in the case of textured polycrystals, the classification is less intuitive and depends on the configuration used.

Figure VI-4 scheme compares the typical grain shape obtained with the R0 High VED and R67 High VED configurations. As already mentioned in the previous section and chapter III, the

typical lamellar microstructure of parts fabricated with the R0 High VED configuration comprises large crystalline-oriented grains <011> (green) alternating with smaller crystalline-oriented grains <001> or <101> (red). Both grain types could be elongated, with shortening by zones with higher levels of misorientation; however, the lamellar microstructure, once developed, is quite hierarchical and remains in the piece, so the development of this alternation makes the level of grain boundary density lower compared to other strategies as is the case of the R67 High VED shown in the right column. In the case of the R67 High VED strategy, the grains are also columnar but narrower than the <011> grains of the lamellar microstructure of the R0 High VED configuration. Details of this microstructure are given in chapter III.
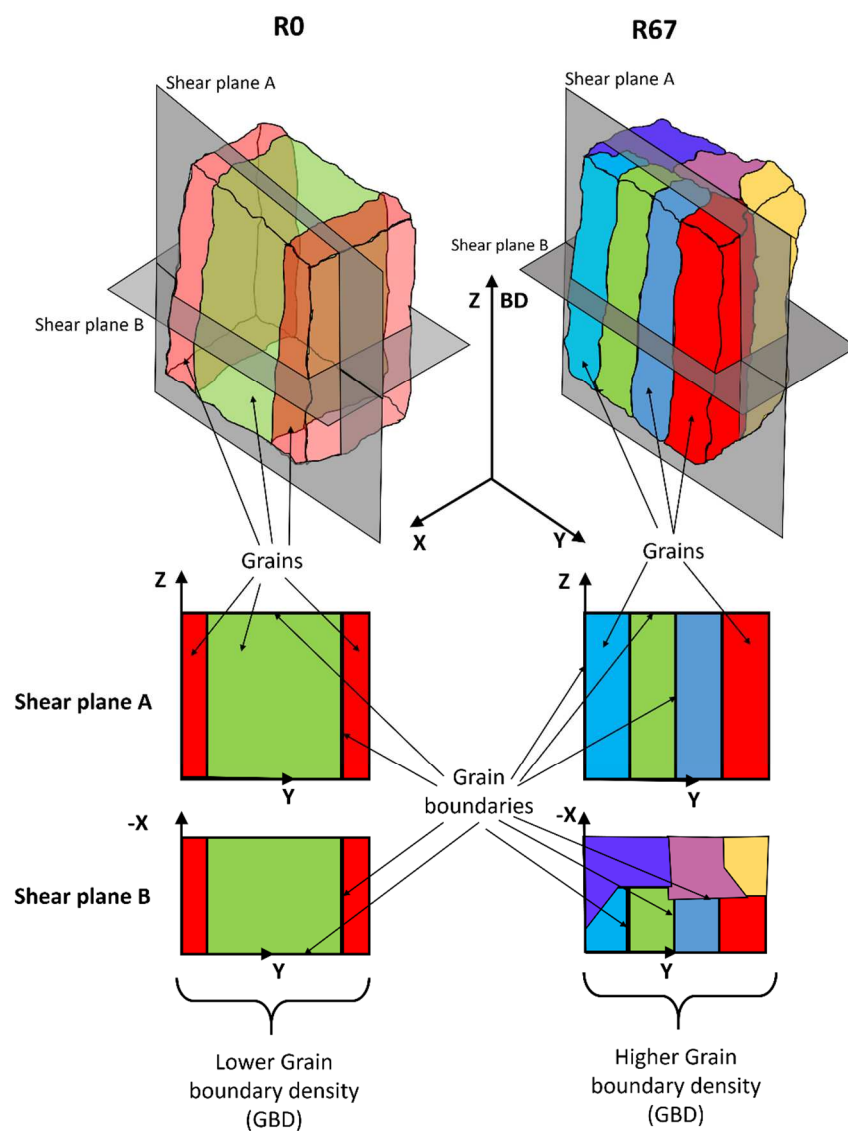
Figure VI-4. Grain shape effect on grain boundary density scheme

When comparing the cuts made in shear planes A and B on both materials, it is observed that there is an increase in the grain boundary density for the R67 low VED material, both in plane A and plane B, which leads to considering that although both fabrications are textured polycrystals, the level of grain boundary density from one to the other changes significantly. These aspects will be measured and presented experimentally for various fabrication configurations in the following sections.

VI.2.3. Primary crystalline orientation effect

Considering that laser strategies are associated with primary crystalline orientations (as demonstrated in section III.6), it is then possible to categorize the main crystalline directions according to the laser strategy used and the crystalline classification of the part.

The scheme in Figure VI-5 shows the main crystalline directions for the different crystalline strategies and classifications analyzed in this study under Gaussian mode (BS0). Euler angles with Bunge's notation represent the main crystal orientations. These angles represent the crystals' orientation relative to the workpiece's reference system.
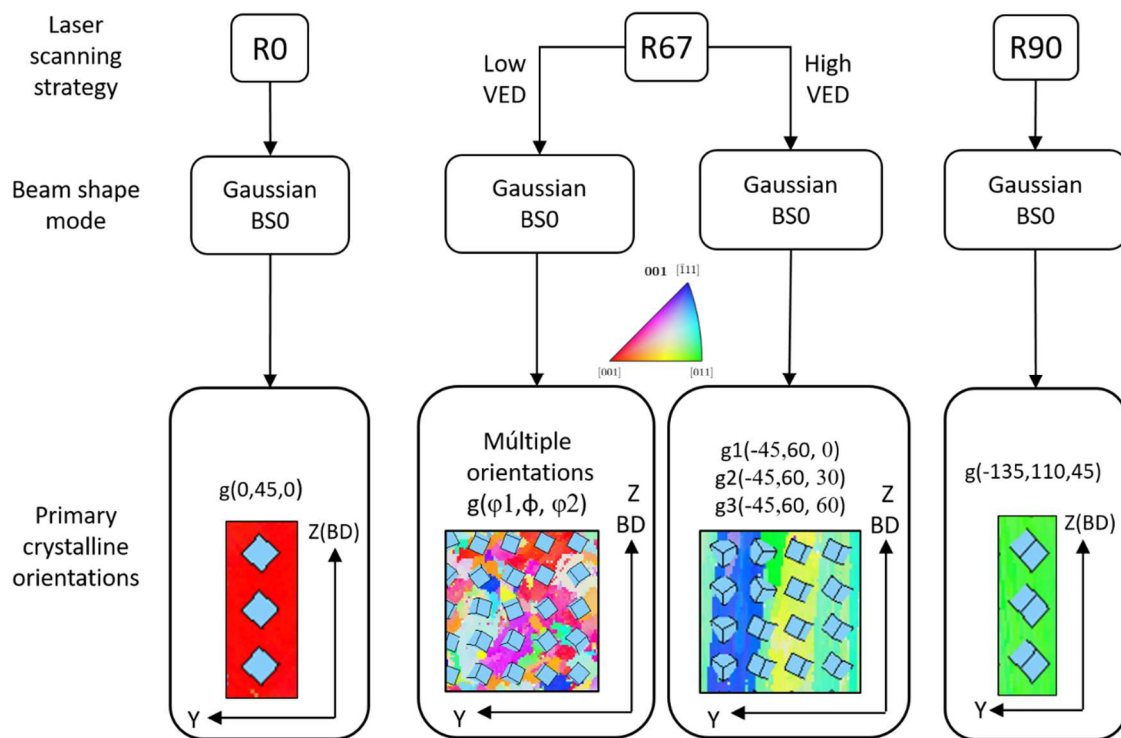
Figure VI-5. Primary crystalline orientations by laser scanning strategies

It is interesting to note that for low VED R67 Polcrystal-like strategy, it is impossible to establish primary crystal directions as there are multiple crystal orientations, which means that in this type of fabrication, the crystal directions can be considered as random (polycrystalline-like). However, in the case of the high VED R67 configuration, the ODF can be discretized into three primary crystalline orientations, as detailed in section III.6.3.

Considering that the anisotropy of the parts manufactured by LPBF means that the mechanical properties depend on the orientation of the load vectors, it is, therefore, necessary to express the direction of the load vectors as a function of only two variables in order to be able to construct maps in which the third variable (Z-axis) be the desired mechanical property. For this purpose, the azimuthal-elevation angle system was used. In this system, the azimuthal angle (α) is the angle formed from the X-axis of the part in a counterclockwise direction, as shown in Figure VI-6, and the path of this angle will always be on the XY plane. On the other hand, the elevation angle(β) starts from the XY plane, and the position vector of the azimuthal angle is in a counterclockwise direction, as shown in Figure VI-6.
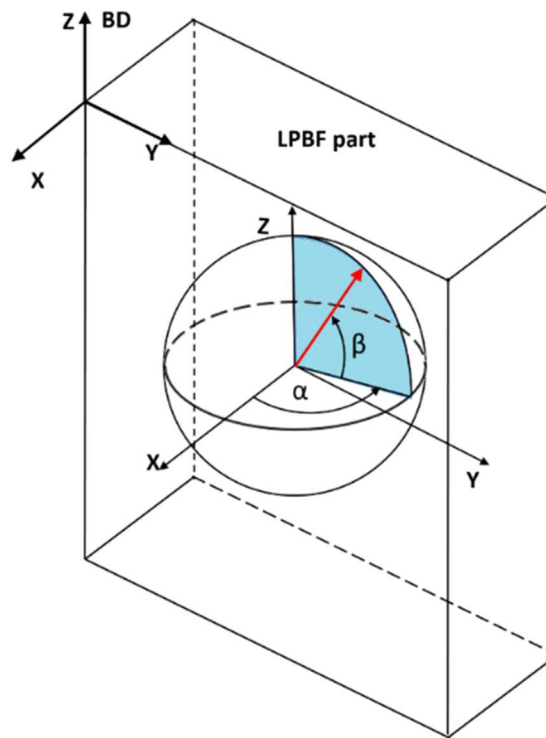
Figure VI-6. Azimuthal and elevation angle reference system

Once the reference system for quantifying the orientation of the load vectors has been defined, it is possible to obtain Young's modulus and Taylor factor maps for the different crystalline patterns associated with each laser strategy.

Figure VI-7 shows the map of the uniaxial tensile Taylor factor for the three strategies used in this study (RO, R90, R67) as a function of azimuthal angle (α) and elevation (β) for discrete ODF and real ODF. Discrete ODF represents the simulated pole figures from the primary crystalline orientations identified in Figure VI-5. At the same time, the real ODF represents all crystalline orientations obtained from EBSD of an authentic sample. The purpose of Figure VI-7 and Figure VI-8 is to show that the patterns in the Taylor factor as a function of the angles α and β are significantly affected by the primary crystalline orientations and that the changes in the maps by adding crystalline orientations with low volumetric fraction only affects the amplitude but does not change the pattern of the physical property. This can be observed mainly for the R67 strategy. Based on this, it is possible to say that once the Taylor maps are known, it is possible to know in which direction (combination of angles α and β) the material is more resistant by the texture effect to plastic deformations due to tensile, compressive, or shear loads. In the same way, it is possible to know through Young's modulus maps in which directions of the load vector the material offers greater resistance to elastic deformation, which is directly related to the stiffness.
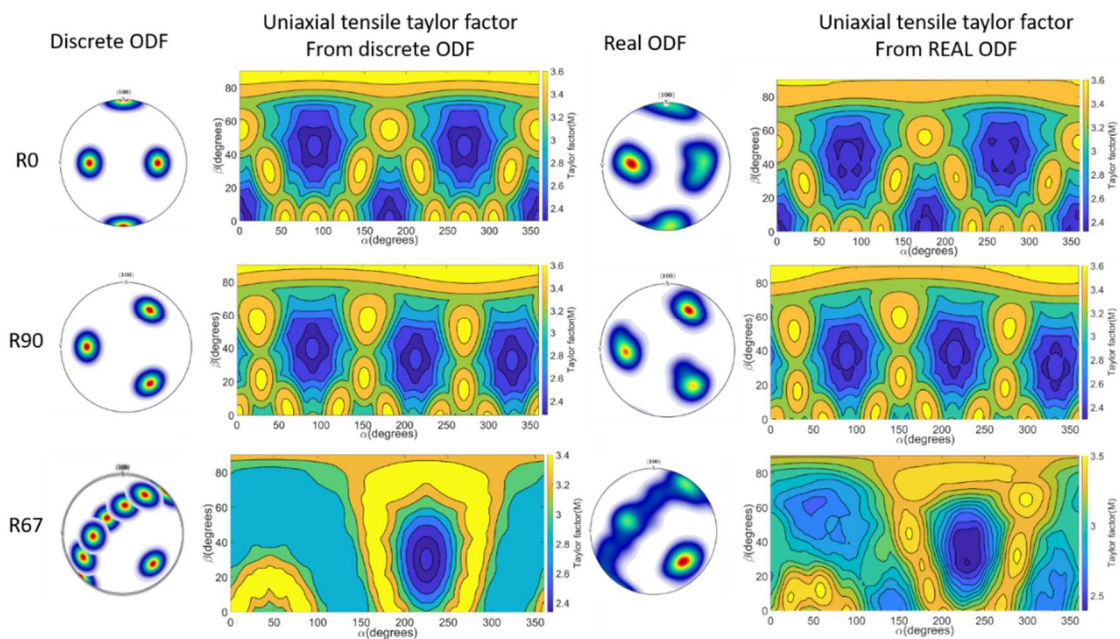
Figure VI-7. Comparison of discrete ODF and real ODF on uniaxial tensile Taylor factor

Figure VI-8 represents the oblique shear Taylor factor for a helix angle of 30 degrees and a shear angle of 30 degrees. In this map, unlike Figure VI-7, the azimuthal angle (α) and elevation angle (β) represents the tool orientation, not the tensile load vector orientation. Therefore, combining the azimuthal and elevation angles with the model described in chapter IV is necessary to know the shear plane's orientation.
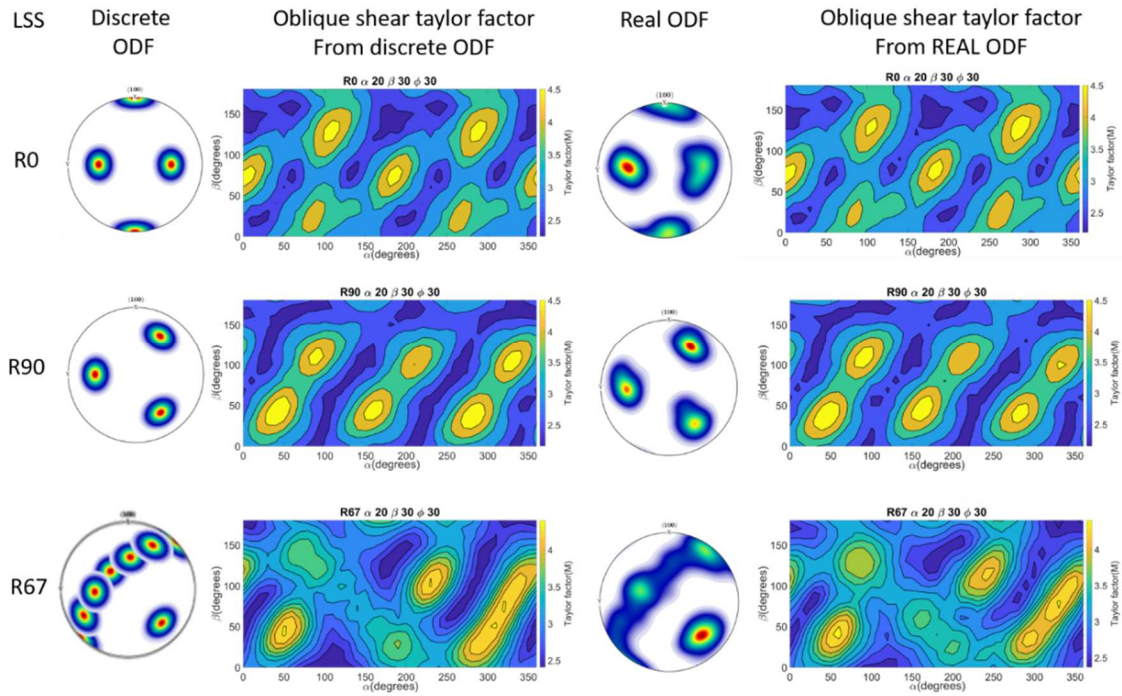
Figure VI-8. comparison of discrete ODF and real ODF on oblique shear Taylor factor

As in Figure VI-7, it is observed that the variations in the oblique shear Taylor factor maps obtained from the discrete ODF vs. the real ODF are small, and the patterns in both cases are conserved. It confirms that the primary crystalline orientations generated by each strategy are the basis for the mechanical design of the LPBF components and allow us to know the weak and strong points of each manufacturing configuration; This, in turn, means that anisotropy can be used as an optimization tool to take advantage of the manufacturing configurations allowing the best mechanical properties to be obtained depending on the orientation of the loads to which the part will be subjected.

VI.2.4.General multi-objective optimization(MOO)

Considering the concepts of the previous section, it is important to establish that the manufacturing configuration can be optimized to make the material single-crystalline or stiffer, but not necessarily easier to cut in a specific direction. Similarly, a manufacturing configuration can be selected that makes the material less resistant to cutting in a specific direction at the expense of sacrificing mechanical strength or misorientation level. In order to achieve that the manufactured part is balanced in terms of mechanical properties and stability during post-processing by machining, multiobjective optimization is necessary, where the variables to control are the crystalline orientation relative to the workpiece reference frame, the geometry of the tool and tool orientation. It is also necessary to know the orientation of the critical loads to which the part will be subjected and the direction of the strain vector field generated by these loads, either by tension, compression, or tool-cutting action.

Before carrying out the optimization process, it is essential to establish the limits of the laser manufacturing parameters and part orientation, as the LPBF process, like any other process, has its limitations. To this end, the diagram in Figure VI-9 illustrates the basic concepts to be considered prior to the mechanical design stage. The first basic concept relates to the LPBF design rules (Gaikwad n.d.; Mani, Jee, and Witherell 2017). This topic considers fundamental aspects, such as the maximum inclination at which a part can be manufactured without the need for supports or the need to place supports in areas where there are abrupt section changes to reduce the development of excessive geometric distortions and residual stresses, among others.

The other basic concept that limits the design window is the range of LPBF (power, speed, layer thickness, hatching space) parameters that allow low levels of porosity to be obtained. Chapter III shows that beam shaping mode fabrication can extend the range of LPBF parameters in which low porosity levels are obtained compared to the Gaussian mode, which makes the use of beam shaping in the LPBF process a powerful tool to extend the possibilities in the design.
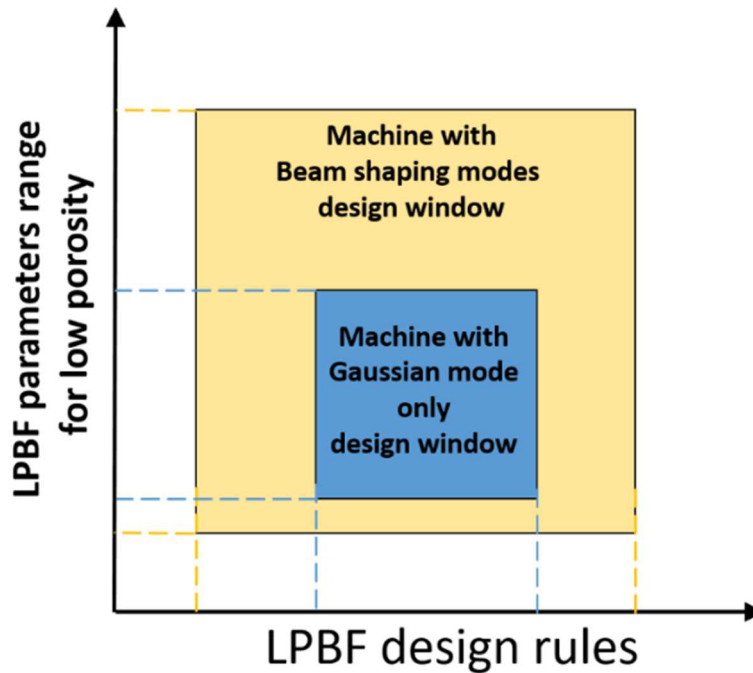
Figure VI-9. Design window based on LPBF and design rules limits for Gaussian and beam shaping modes

Once the limits of the LPBF parameters and the part's positioning concerning the base plate have been defined, it is possible to begin the iterative optimization process. In this line, the diagram in Figure VI-10 shows the elements that make up the iterative design process by multivariable optimization. In this process, the design variables to be controlled are the LPBF manufacturing configuration (related to the combination of laser scanning strategy and VED), the part orientation, the tool geometry, and the tool orientation. Also part of the design process are the physical parameters that have already been exposed in previous sections, the load orientations, and the mechanical properties maps. All these elements feed the multivariable optimization function that allows determining the values of the design variables that best suit the design requirements in terms of crystalline classification, grain size, and mechanical properties that allow the material to have acceptable strength levels and at the same time an improvement in stability during machining and good surface quality. The physical parameters and mechanical properties maps have been extensively explained in chapter III and sections VI.2.1, VI.2.2, and VI.2.3. The following sections will explain the design variables and load orientation details in more detail.
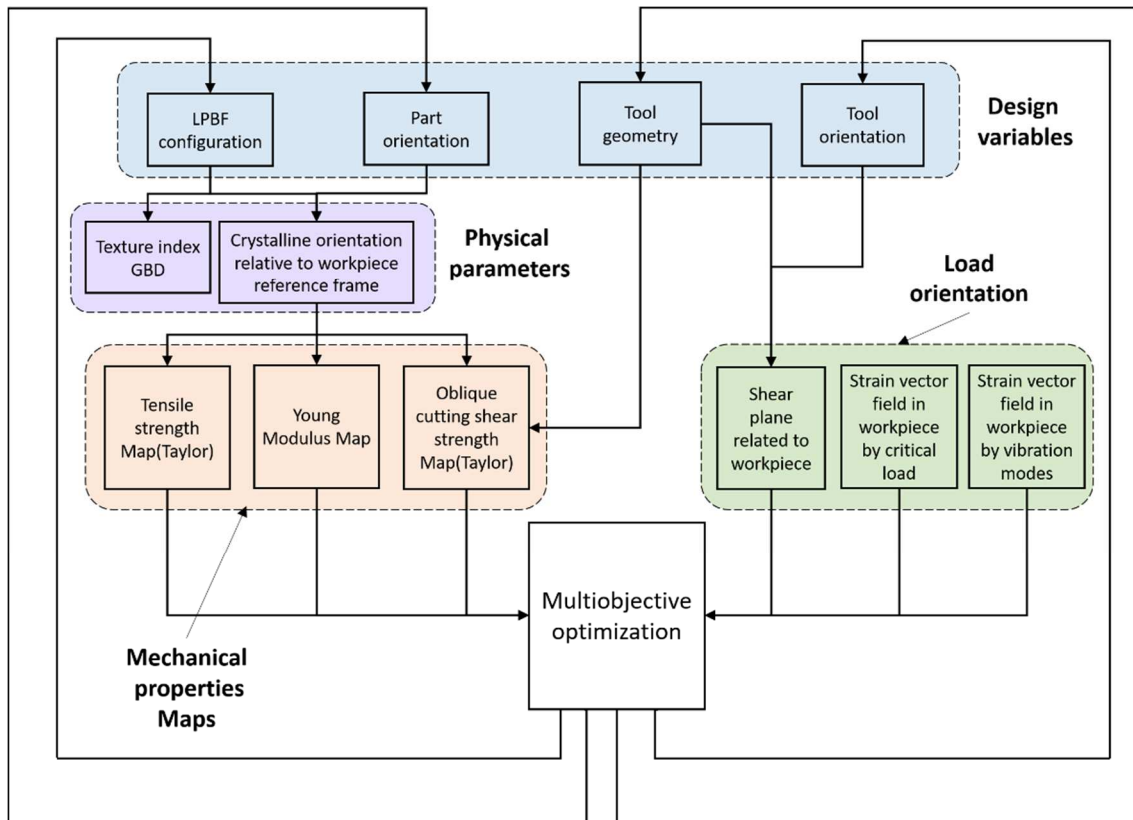
Figure VI-10. Flow chart of multiobjective optimization as a tool for manufacturing and designing LPBF parts.

Design variables

This section presents some variables that are considered relevant in the process of optimizing the mechanical design of the components and the machining stability.

Part orientation

The part orientation variable refers to how the part to be manufactured is oriented about the melt pool track's direction and the workpiece tilting to the base plate. These aspects can be better understood in Figure VI-11 by analyzing the 3 cases stipulated there. The first case compares two parts (A and B), where both parts are manufactured with the R0 strategy. Although the parts have different orientations to the base plate, the orientation of the melt pools concerning the workpiece is the same, which makes the crystalline orientation of the parts the same to the workpiece coordinate system. This indicates that both parts would have the same orientation-dependency of mechanical properties despite being manufactured in different orientations.

Case 2 shows two parts also manufactured with the R0 strategy where the parts' reference system coincides with the base plate's reference system. However, in part C, the melt pool tracks are aligned with the X axis, while in part D, the melt pool tracks are aligned with the Y axis. This change of orientation of the melt pool tracks generates a significant change in the orientation of the crystals concerning the coordinate system of the workpiece, which also has significant effects on the change of the mechanical properties.

In case 3, the R0 strategy is used, changing the orientation of part F with part E; however, the orientation of the melt pool tracks is the same. In this case, it is interesting to note that the crystalline orientation remains the same in both parts to the base-plate coordinate system but changes relative to the coordinate system of the workpiece.
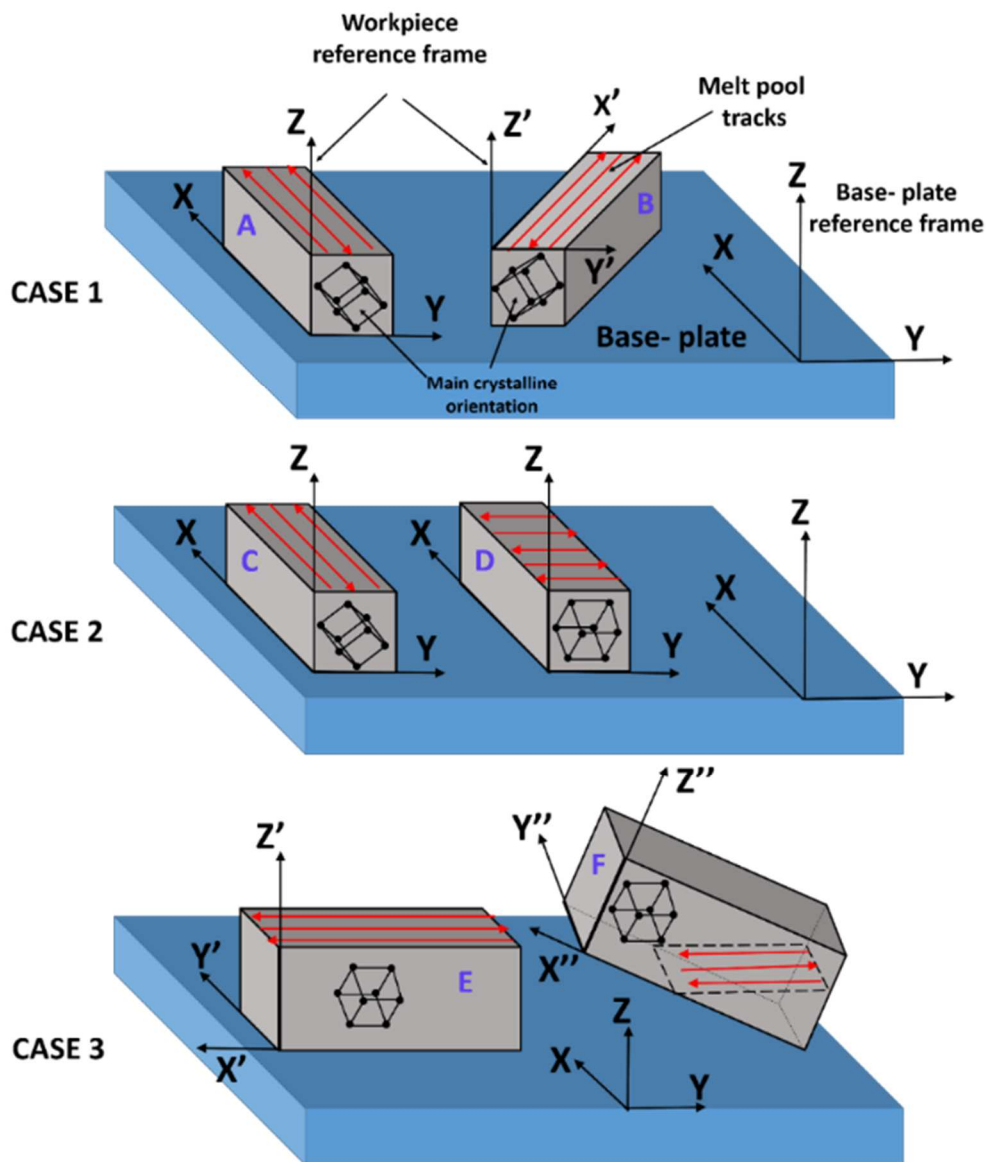
Figure VI-11. Effect of the interaction between part orientation and melt pool track orientation scheme

Considering the abovementioned cases, it is possible to generate strategies where the parts are oriented so that the load vectors coincide with the strong crystalline orientations, thus increasing mechanical strength or stiffness. Alternatively, also, by changing the orientation of laser tracks without changing the part orientation, the same goal is achieved.

The orientation of the part relative to a reference position or the base-plate reference system can be quantified through Euler angles in Bunge notation (ZXZ). For this purpose, the orientation of the part can be defined as $G_P(\varphi1_P, \phi_P, \varphi2_P)$ where $\varphi1_P$ is the angle of rotation of the part around the Z-axis, ϕ_P is the angle of rotation of the part around the new X-axis, and $\varphi2_P$ is the angle of rotation around the new Z-axis.
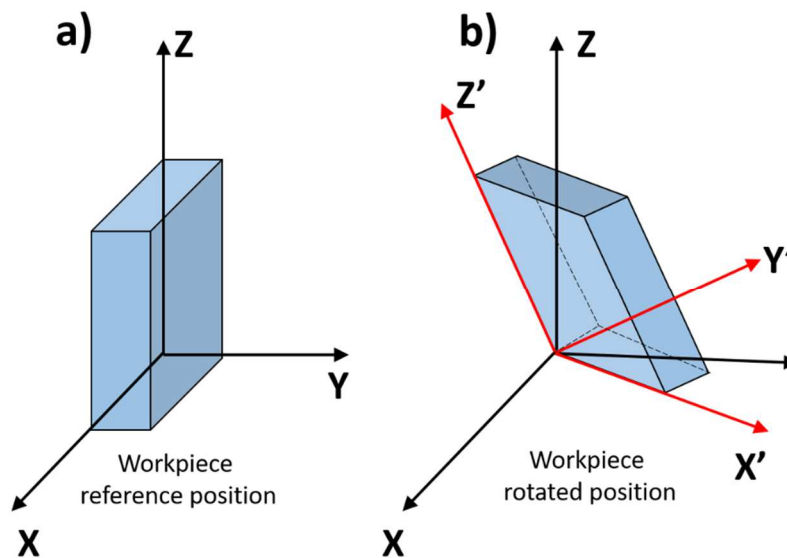
LPBF configuration

LPBF configuration is another design variable that can be used to change the crystalline orientation relative to the coordinate system of the workpiece; however, the implications of this variable are more profound than those of part orientation, since, in addition to changing the crystalline orientation, the texture index and therefore the crystalline classification can also be changed. This means the part can be polycrystal-like, textured polycrystal-like, or single-crystal-like. The effect of the LPBF configuration on the crystalline orientations concerning the workpiece coordinates has been extensively discussed in chapter III and section VI.2.3.

Tool geometry and Tool orientation.

The tool's geometry and tool's orientation relative to the workpiece are other variables that can be used in the iteration of the design process, especially when the part requires an improved

surface finish and machining is the best option. This is because changing the helix angle also changes the shear-cutting plane orientation. Similarly, if the rake face angles are changed, there are changes in the orientation of the shear-cutting plane. It is important to note that the effect of the crystalline texture on the shear strength is related to the interaction of the shear planes with the slip systems of the crystal lattice, which for Inconel 718 is mainly the FCC. The details of those design variables and obtaining the slip planes as a function of tool position and geometry by calculating the Taylor factor as a function of crystalline orientation are extensively discussed in chapter IV.

Load orientation

In this section, some types of loads are presented, which represent the critical component application. The Load orientation is divided into several groups.

Shear deformation tensors

The first group corresponds to the shear deformation tensors that are generated during the engagement of a cutting tool in the material. During the rotation of the tool, different shear plane orientations are generated, which in turn interact with the slip systems of the material. The calculation of the tool action deformation tensors, the generated shear planes, and the effect of the tool geometry is extensively dealt with in chapters IV and V.

Strain vector field by critical loads

The second type of load is related to the workpiece function. At this point, it is essential to note that the proposed methodology only covers design for resistance to low cycle loads. Therefore, fatigue design is not covered and is a topic that can be integrated in the future depending on the development and reliability of fracture toughness prediction models for multi-axial cyclic loads in LPBF materials. In this line, the loads considered in this methodology are axial deformation loads, bending loads, pressure loads, or all those in which the load can generate plastic deformation of the material. Also, in this category, there are loads that do not generate plastic strain but do generate elastic strain. At this point, it is essential to consider that the mechanical design of the part has usually been done before using this methodology, and the dimensions of the part are usually selected considering that the material is isotropic. Therefore, this methodology aims to ensure that the texture's effect on the material's strength is exploited to the maximum to compensate as far as possible for the reduction in mechanical strength that a possible increase in grain size could generate. The best option is to use finite elements to obtain the strain vector field generated by loads.

Strain vector field by vibration modes

The third group is related to the strain vector field produced by the vibration modes when the part is subjected to machining. For this purpose, the vibration modes and the strain vector field associated with each vibration mode are obtained by finite elements. A case study where this item is treated in more detail is presented in section VI.5.

Objective functions

Once the desired crystalline classification of the workpiece and the loads to which it will be subjected have been defined, it is possible to perform multi-objective optimization. The purpose of multi-objective optimization is to find a combination of design variables that allows an acceptable level of mechanical properties to be obtained in the target material and, at the same time to increase machining stability by reducing the shear strength and increasing the stiffness of the workpiece for the machining process. It is important to note that a design configuration that increases part stiffness under machining loads may also increase cutting forces or vice versa, so the possibility of conflicting objectives or conflicting optimization directions makes multi-objective optimization a good technique. To this end, it is necessary to consider the dominance between the solutions, which leads to the need to prioritize the objectives. The general form of multi-objective optimization (MOO) is given in equation 1.

$$\begin{aligned}maximize \quad &F(X) = [F_1(X), F_2(X), F_3(X), .., F_k(X)]^T\\subject\ to: &H_j(X) \le a; \quad j = 1,2 \dots., m\end{aligned} \qquad (VI.1)$$

where $F(X)$ is the vector of objective functions, $F_1(X)$ Is the objective function # 1, k is the number of objective functions, m is the number of inequality constraints, and X is the vector of design variables.

When considering filtering the interests(to establish dominance) from the point of view of the designer, manufacturer, or subsequent machining process manager, the use of decision-making tools using objective weights or AHP (Analytical Hierarchy Process) through the validation of different scenarios for decision-making from 2x2 matrices considering an inconsistency of less than 10%, is advised. These tools also allow the robustness of the selection of manufacturing alternatives to be established by changing the initial weights through sensitivity analysis. Some applications software for this are Expert Choice, Zingtree, or Yonix.

The objective functions in this methodology depend on the desired scope of the design. For a general scenery, four objective functions are considered; however, other parameters or objective functions could be included.

Objective function # 1. $F_1(X)$

The first objective function $F_1(X)$ is according to equation 2.

$$F_1(X) = \sigma = \varepsilon * E(h,k,l) \qquad (VI.\,2)$$

Equation 2 represents the implicit objective function $F_1(X)$ related to the stiffness at critical load. In this equation σ is the mean value of the distribution of tensile or compressive stresses in the workpiece under critical load, ε is the vector field of strains generated by the critical load and $E(h,k,l)$ is the modulus of Young as a function of any angle orientation in the Miller index system (h,k,l). This equation is implicit as it is not directly expressed as a function of the design variables. For this purpose, equations 3, 4, and 5 allow correlating equation 2 with the design variables.

Equation 3 shows how to calculate Young's modulus $E(hkl)$ as a function of the compliances constants of the stiffness matrix S_{12}, S_{11} and S_{44} and the orientation of the load vector under the miller index system. $E(\alpha,\beta)$ y $E(hkl)$ are equivalent once the miller index reference system is converted to the azimuthal system. for more details about Young's modulus equation from the miller indices, see chapter III.

$$E(hkl) = \cfrac{1}{S_{11} + \cfrac{(2S_{12} - 2S_{11} + S_{44})(k^2l^2 + l^2h^2 + h^2k^2)}{(h^2 + k^2 + l^2)}} \qquad (VI.\,3)$$

The compliance elastic constants S_{12}, S_{11} and S_{44} are obtained from elastic compliance tensor S_{ijkl} which is calculated employing the Hill approximation (see equation 4).

$$S_{ijkl} = \cfrac{1}{\frac{1}{2}\left(\sum_{n=1}^{N} f(g_n)T(g_n) + [\sum_{n=1}^{N} f(g_n)T^{-1}(g_n)]^{-1}\right)} \qquad (VI.\,4)$$

where $f(g_n)$ is the volumetric fraction of a crystal orientation g_n, $T(g_n)$ is the individual tensors with crystal orientation g_n, and N is the number of orientations present in the material. It is important to note that the orientation density function ODF also corresponds to the volume fractions of the crystalline orientations g_n as expressed in equation 5.

$$f(g_n) = ODF(g_n) = \frac{1}{V}\frac{dV(g_n)}{dg_n} \qquad (VI.\,5)$$

Section VI.2.4 defines the main crystalline orientations for each LPBF configuration. In this way, equation 1 can be re-written as a function of the design variables (ODF_{LSS} and G). See equation 6.

$$F_1(X) = \sigma = \varepsilon * E\left(ODF_{LSS}, G(\varphi1, \varphi, \varphi2)\right) \text{ (VI. 6)}$$

Where ODF_{LSS} is the discrete ODF associated with each LPBF configuration (see section VI.2.3 and chapter III), and G is the part orientation relative to the base plate reference system in Euler angles. The design variable G is extensively explained in the design variable section. It is essential to clarify that the primary crystalline orientations of the ODF_{LSS} Shown in section VI.2.3 and chapter III are relative to the base-plate reference frame.

Objective function # 2. $F_2(X)$

The objective function $F_2(X)$ is similar to $F_1(X)$ with the difference that the origin of the strains does not come from the critical load but from the vibration modes generated by the machining. In this way, the stress generated is calculated from equation 7.

$$F_2(X) = \sigma1 + \sigma2 + \sigma3 = \varepsilon_1 * E(ODF_{LSS}, G) + \varepsilon_2 * E(ODF_{LSS}, G) + \varepsilon_3 * E(ODF_{LSS}, G) \text{ (VI. 7)}$$

where $\varepsilon_1, \varepsilon_2$ and ε_3 are the strain vector fields associated with each vibration mode, and $E(ODF_{LSS}, G)$ is obtained in the same way as for $F_1(X)$.

Objective function # 3. $F_3(X)$

The objective function $F_3(X)$ is related to the resistance to plastic deformation in tension or compression by texture effect, where the Taylor factor is used to quantify this resistance. For this purpose, the uniaxial tension-compression Taylor factor is calculated according to equations 8 to 13, similar to the oblique shear cutting Taylor factor obtained in section IV.4.

$$F_3(X) = \overline{M(\alpha,\beta)} = \varepsilon * \int \int \int M(g_n)f(g_n)dg_n = \overline{M(ODF_{LSS}, G)} \text{ (VI. 8)}$$

$$M(g_n) = \frac{d\Gamma}{d\varepsilon_w(\alpha,\beta)} = \frac{\sigma}{\tau_c} = \frac{dW}{\tau_c\varepsilon_c^n(\alpha,\beta)} \quad n=1, 2\dots N, \text{ (VI.9)}$$

$$\varepsilon_w(\alpha,\beta) = R_\beta^T R_\alpha^T E_S R_\alpha R_\beta \quad \text{(VI.10)}$$

$$E_s = d\Omega/2 \begin{bmatrix} 1 & 0 & 0 \\ 0 & -0.5 & 0 \\ 0 & 0 & -0.5 \end{bmatrix} \text{ (VI. 11)}$$

$$\varepsilon_c^i(\alpha,\beta) = C_n(g_n)\varepsilon_w(\alpha,\beta)C_n^T(g_n) \text{ (VI. 12)}$$

$$C_n(g_n) = \begin{bmatrix} [\cos(\varphi1_n^c)\cos(\varphi_n^c)\cos(\varphi2_n^c) - \sin(\varphi1_n^c)\sin(\varphi2_n^c)] & [-\cos(\varphi1_n^c)\cos(\varphi_n^c)\sin(\varphi2_n^c) - \sin(\varphi1_n^c)\cos(\varphi2_n^c)] & \cos(\varphi1_n^c)\sin(\varphi_n^c) \\ [\sin(\varphi1_n^c)\cos(\varphi_n^c)\cos(\varphi2_n^c) + \cos(\varphi1_n^c)\sin(\varphi2_n^c)] & [\sin(\varphi1_n^c)\cos(\varphi_n^c)\sin(\varphi2_n^c) + \cos(\varphi1_n^c)\cos(\varphi2_n^c)] & \sin(\varphi1_n^c)\sin(\varphi_n^c) \\ -\sin(\varphi_n^c)\cos(\varphi2_n^c) & -\sin(\varphi_n^c)\sin(\varphi2_n^c) & \cos(\varphi_i^c) \end{bmatrix}$$

$$(VI.13)$$

where ε is the strain vector field generated by the critical load, N is the number of main crystalline orientations present in the material, ε_c is the imposed strain in the crystal, $\varepsilon_w(\alpha, \beta)$ is the strain tensor as a function of $\alpha \ and \ \beta$. And E_s is the displacement tensor. Additionally C_n is the transformation matrix (Equation 14) defined by the workpiece reference frame and the crystal reference frame, prescribed by the rotation of $g_n = \{\varphi1_n^c, \varphi_n^c, \varphi2_n^c\}$ (Bunge notation).

Objective function # 4. $F_4(X)$

The objective function $F_4(X)$ (see equation 14) is related to the shear strength due to the effect of crystallographic texture and is also quantified from the Taylor factor. The development of the equations for this function is extensively presented in section IV.3.

$$F_4(X) = \left[\overline{M(G, \alpha, \beta, \phi_c)}\right]^{LSS} \approx \left[\sum_{i=1}^{N} M(G, \alpha, \beta, \phi_c)\frac{dV(g_i)}{V}\right]^{LSS} \quad (VI.14)$$

Constraint functions. $H_j(X)$

The constraint functions $H_j(X)$ are more related to LPBF design rules and depend on each particular case. Therefore, there is no general rule to define them. Section VI.5 exposes some constraints for the evaluated case study.

VI.2.5. methodology for additional stiffening when low-stiffness parts must be machined

Since the manufacturing priority is to ensure structural integrity, high density, and mechanical properties, obtaining a design configuration that improves machining stability by increasing part stiffness is a priority, and even if these conditions are improved, it is possible that the part cannot be machined without additional stiffening. To this end, this section presents the steps necessary to increase the part's stiffness by using easily removable lateral stiffeners. An advantage of the use of stiffeners is the possibility of increasing the stiffness of the workpiece without the need to change the crystalline orientation of the material.

This section proposes a methodology to improve the manufacturing process of low-stiffness LPBF parts using an iterative design process based on deformation boundary conditions. An

initial configuration was proposed for positioning the components, which in turn were joined together by lateral stiffeners to achieve the required surface and dimensional quality. The methodology is divided into five phases: i) preliminary machining analysis, ii) enhancement of Young's modulus, iii) stiffness enhancement with lateral stiffeners, iv) manufacturing and verification, and v) analysis and improvement of the current stiffening configuration. Figure VI-12 shows the general flow chart of the proposed methodology, and Figure VI-13 shows the detailed steps within each stage and the specific interactions between stages.
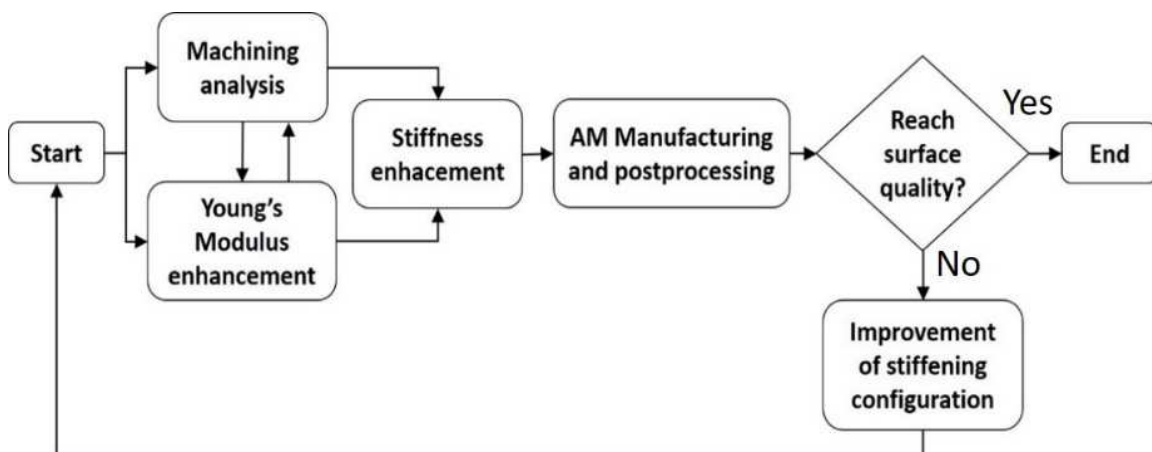
Figure VI-12. Simplified LPBF functional part stiffening methodology scheme

In the preliminary machining analysis, an initial evaluation of cutting conditions, cutting forces, machining operations, tool geometry, and excitation frequencies were performed to detect whether the initial machining conditions required the use of conventional support systems or if the lateral stiffener method was a feasible option. If the cutting force levels are manageable, and the excitation frequencies are significantly lower than the natural frequency and chatter frequency, it is recommended to proceed to the second stage, that is, enhancement of Young's modulus. In the second stage, anisotropy is exploited to enhance Young's modulus and improve the stiffness of the component owing to the anisotropic nature of the materials obtained through the LPBF process. For this purpose, it is recommended that it be started with a couple of parameter settings to obtain the stiffness tensor and Young's modulus distribution. On obtaining the Young's modulus, it is possible to compare the LPBF parameters and strategies that maximize Young's modulus concerning the workpiece geometry and load state. Consequently, if Young's modulus increases or anisotropy decreases, it is recommended to advance to the third stage, that is, stiffness enhancement with lateral stiffeners. The third stage

assesses whether the improvement in Young's modulus (second stage) is sufficient to achieve minimum stiffness.
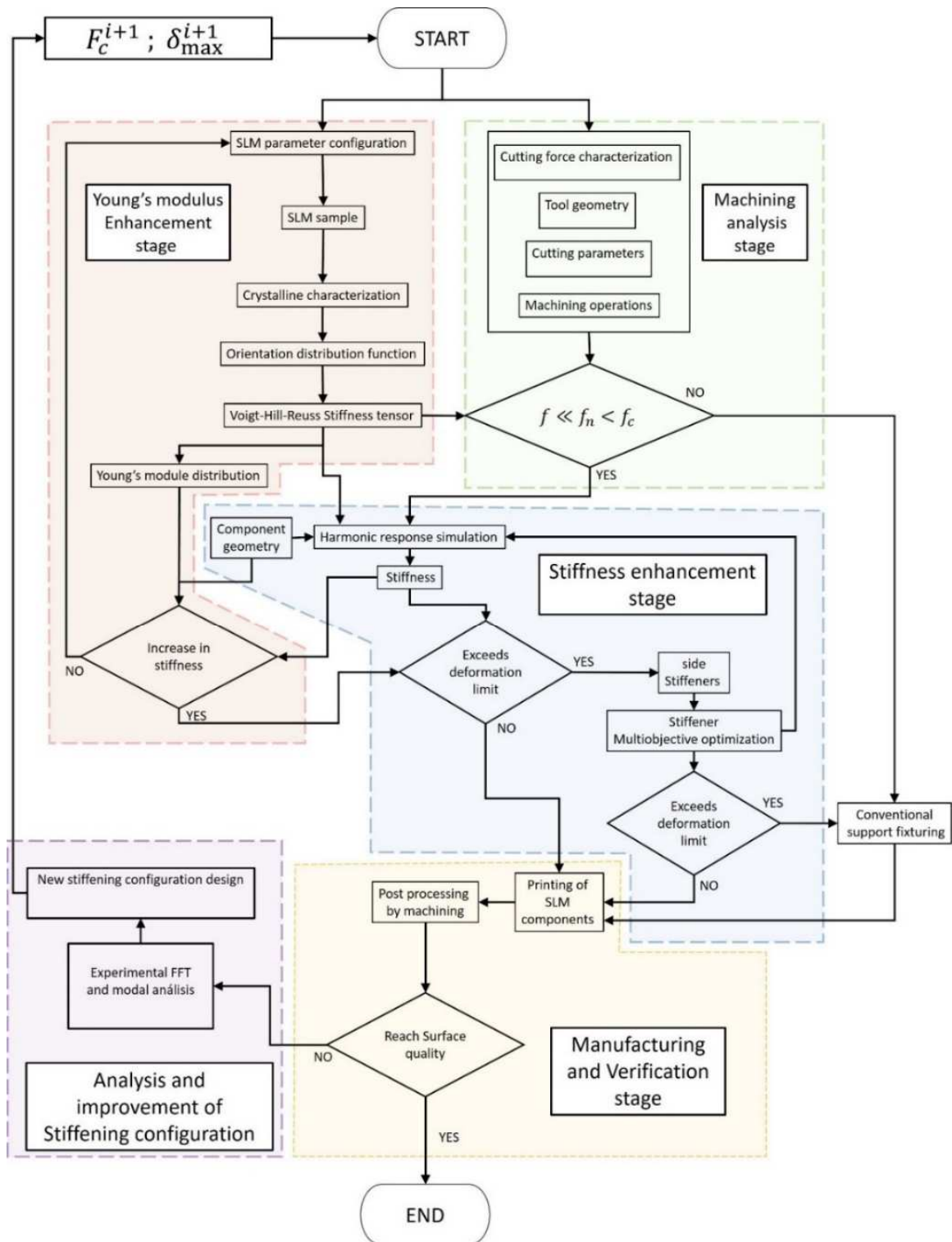
Figure VI-13. Detailed Iterative LPBF stiffness enhancement component methodology flow scheme

The evaluation begins by establishing a boundary deformation (δ_{max}) for the first iteration. If the workpiece stiffness is sufficient (the deformation caused by the cutting forces is lower than δ_{max}), it is possible to manufacture the part. However, if the stiffness is insufficient, but the sum of two or more stiffnesses of the workpiece surpasses the minimum stiffness, the lateral stiffeners may be an option. The unknown shape, size, and location of the temporary lateral stiffeners are necessary to design these elements. Once the stiffness enhancement reaches the objective, the manufacturing and verification stages can occur. The workpiece is manufactured in the manufacturing and verification stages according to the stiffening configuration that provides the best balance between the stiffener volume and deformation level. It is recommended that dimensional control of the LPBF component manufactured be exercised using lateral stiffeners to adjust the CAM program before the machining operations. Once the machining process finishes and the quality level is sufficient, the design can be considered appropriate. However, if the surface and dimensional quality are not achieved, it is recommended to decrease the value of boundary deformation (δ_{max}) and proceed to a new iteration in the design of the stiffening elements or increase Young's modulus. In addition, conventional or special fixture support is recommended if the desired workpiece quality is not reached after certain iterations.

VI.3 Case study 1

In this section, a case study is presented to validate the proposed methodology of section VI.2.5. following the established steps. Including the multi-objective optimization to obtain the geometry of the stiffeners. This study proposes a methodology for increasing the stiffness of the components by increasing Young's modulus and using temporary lateral stiffeners, which allows the printed components to behave as a temporary assembly, thereby decreasing the cutting forces and roughness levels. The methodology is based on an iterative design process, wherein the harmonic response of the component is analyzed, considering the initial boundary deformation values, by testing different configurations and geometries for the lateral supports and evaluating the response of each configuration on the maximum amplitude of the displacement in the area of application of the cutting force. The methodology was evaluated through its application to a case study wherein temporary lateral stiffeners were introduced to increase the stiffness of Inconel 718 LPBF-angled ducts to improve the surface quality of the peripheral milling in the extreme zone of the ducts. The results for the first design iteration showed a significant improvement in the surface quality relative to the duct without stiffening.

VI.3.1. Preliminary machining analyisis

The quantification of the cutting forces for various machining conditions is critical for a preliminary analysis. Thus, two samples of Inconel 718 LPBF were manufactured using a 67° laser scanning strategy. The samples have two zones, each with different layer thicknesses. The lower zone was manufactured with a 30 μm layer while the upper zone with a 60 μm layer. (See Table VI-1). The lower 30 μm zone is hereafter referred to as lt30, and the upper 60 μm zone as lt60. The purpose of these samples was to perform peripheral milling operations with radial cutting depths in the range of 0.1 to 0.5 mm at different feed rates. The milling operations were performed on the XZ plane of the specimens and the feed rate in the X-axis direction. The LPBF parameters used in manufacturing the samples, machining parameters, and tool geometry are listed in Table VI-1.

The layer thickness values used in the research were considered as boundary limits (considering the other selected LPBF parameters, see Table VI-1), considering the structural and quality issues needed in AM workpieces. Layers of 60 μm are often used to minimise the processing time, while those of 30 μm are used when precision is required. However, layer thicknesses smaller than 30 μm are inconsistent with the feed powder size, and those greater than 60 μm on Inconel 718 are not recommended owing to the production of excessive internal porosity. In both cases (lt30 and lt60), the energy density was within the operating limits, avoiding the lack of fusion or balling effect.

The nature of the LPBF process causes melting and solidification to occur almost simultaneously in each track and layer, and the laser heat-affected volume is in low proportion with respect to the overall workpiece volume, which reduces the possibility of significant geometric distortions due to residual stress. Consequently, a laser rotation strategy of 67° per layer was used, which is considered helpful in reducing the residual stress (Serrano-Munoz et al. 2020b; Dianzheng Wang et al. 2017).

The LPBF samples and workpiece were manufactured using a Renishaw AM-400 machine and machining operations were performed in an Ibarmia ZV-25/U600 machining centre. Further, the cutting forces were measured using a dynamometer (Kistler 9225 B) and an OROS data acquisition system.

Table VI-1. LPBF parameters, Cutting parameters, tool geometry, and LPBF sample geometry

LPBF parameters		
	Zone 1	**Zone 2**
	(lt30)	**(lt60)**
Power (W)	200	200
Speed (mm/s)	1000	1000
Hatch spacing (mm)	0.09	0.09
Layer thickness (µm)	30	60
Laser beam spot size (µm)	70	70

Cutting parameters and tool geometry	
Cutting speed V_c (m/min)	60
Axial depth a_p (mm)	5
Tool diameter (mm)	10
Helix angle β (°)	30
Flutes (z)	4
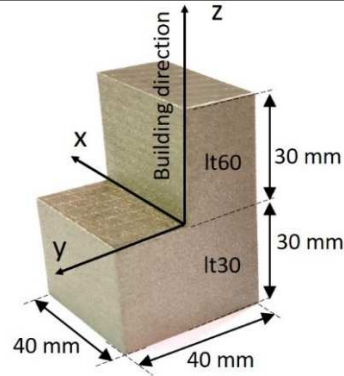
The mean cutting forces corresponding to the parameters mentioned in table 1 with feed rates f_z of 0.03, 0.04 and 0.05 mm/min and radial cutting depths a_e of 0.1, 0.3, and 0.5 mm, respectively, are listed in Table VI-2.

Table VI-2. Measured cutting forces by peripheral milling

Layer thickness	a_e	$\overline{F_t}(N)$ f_z (0.03)	f_z (0.04)	f_z (0.05)	$\overline{F_r}(N)$ f_z (0.03)	f_z (0.04)	f_z (0.05)	$\overline{F_a}(N)$ f_z (0.03)	f_z (0.04)	f_z (0.05)
	0.1	12.2	16.0	19.4	19.4	27.5	34.4	3.7	6.2	7.0
Lt30	0.3	30.6	40.2	44.4	63.4	74.1	80.3	9.6	12.5	14.4
	0.5	49.3	57.3	73.1	102.1	111.6	118.2	14.7	19.1	21.8
	0.1	13.6	17.5	19.2	23.5	28.3	33.6	5.0	5.71	6.5
Lt60	0.3	27.7	32.7	44.6	62.7	70.2	74.8	7.5	10.0	27.9
	0.5	47.8	57.2	68.8	86.1	97.6	107.7	15.0	18.8	22.36

Another relevant aspect of this section is to define whether the excitation frequency due to the tooth passing frequency f is significantly lower than the natural frequency f_n of the workpiece and the chatter frequency f_c. This aspect can be evaluated by analyzing the directional dynamic milling coefficient α_{yy}, which can be calculated using equation 14 (Erhan Budak 1994).

$$\alpha_{yy} = \frac{1}{2}[-\cos 2\theta - 2K_r\theta - K_r \sin 2\theta]_{\phi_{st}}^{\phi_{ex}} \quad \text{(VI.14)}$$

where θ is the engagement angle, K_r is the radial force coefficient, and ϕ_{ex} and ϕ_{st} are the exit angle and start angle, respectively. Considering that the axial depth limit a_{lim} is always a positive value, it is suggested that the chatter frequency will be higher or lower than the natural frequency depending on the sign of the directional milling coefficient α_{yy} (see Equation 15).

$$a_{lim} = \frac{1}{\frac{\Omega}{2\pi}\alpha_{yy}K_t Re[G_y(if_c)]} \quad \text{(VI.15)}$$

where Ω is the spindle speed, K_t is the tangential force coefficient, and $Re[G_y(if_c)]$ is the real component of the transfer function of the workpiece in the Y-direction.

Further, several hammer tests were developed in the X and Y directions to obtain the experimental modal parameters (damping ratios and natural frequencies) (see Figure VI-14a).

The transfer function of the workpiece in the Y-direction G_y, indicates the relationship between the natural frequency, chatter frequency, and modal parameters, and is expressed as Eq. (16).

$$G_y(if_c) = \frac{\frac{f_{ny}^2}{k_y}}{f_{ny}^2 - f_c^2 + 2\xi_y f_{ny} f_c i} \quad \text{(VI.16)}$$

where k_y, ξ_y and f_{ny} are the stiffness, damping ratio, and undamped natural frequency, respectively, in the Y direction. Therefore, it can be defined that the chatter frequency f_c will be higher than the natural frequency f_n when coefficient α_{yy} has a negative sign. This is the case for down-milling. Figure VI-14b shows α_{yy} related to the start angle ϕ_{st} when down-milling for K_r = 4.45 and 6.06, based on the cutting forces and axial depths in Table VI-2. The duct geometry is shown in Figure VI-14c.

Considering that the excitation frequency f is 127 Hz (where $f = \frac{z*\Omega}{60}$, and z is the number of flutes in the tool), the natural frequencies are f_{ny} = 935 Hz, and f_{nx} = 983.7 Hz, and that the chatter frequency f_c is higher than the natural frequency (considering that α_{yy} has a negative sign, see Figure VI-14b); therefore, $f << f_n < f_c$.

Consequently, it is possible to establish that the excitation frequency is significantly lower than the resonance and chatter frequencies, and that the harmonics of the excitation frequency do not match the resonance frequency. The fulfilment of this condition allows the establishment of the geometrical characteristics of the workpiece and the improvement of the stiffness through

the increase of the Young's modulus and the use of lateral stiffeners (following sections) would decrease the possibility of exciting resonance or chatter frequencies.
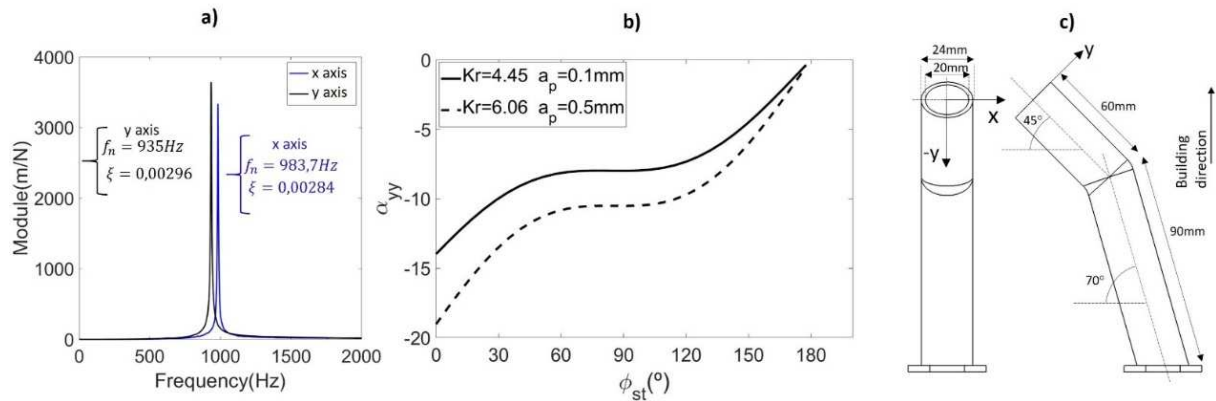
Figure VI-14. Preliminary analysis. a) hammer test results, b) directional dynamic milling coefficient α_{yy}, c) angled duct geometry

VI.3.2. Young modulus enhancement

Elastic anisotropy is an extended characteristic of LPBF components. This is mainly caused by the formation of columnar grains closely aligned in the building direction (BD) owing to the fast solidification of the melt pool tracks. Figure VI-15 shows the SEM scans of the lt30 and lt60 samples and a comparison of the microstructures. The columnar dendritic grains in the lt30 sample are aligned with the building direction.

In contrast, the columnar grains in the lt60 sample present a broader range of orientations and a lower density of grains aligned in the building direction, which is related to the lower elastic anisotropy of the lt30 sample. Moreover, the lower volumetric energy density (VED) of the lt60 sample is the leading cause of stray grain development in this sample.
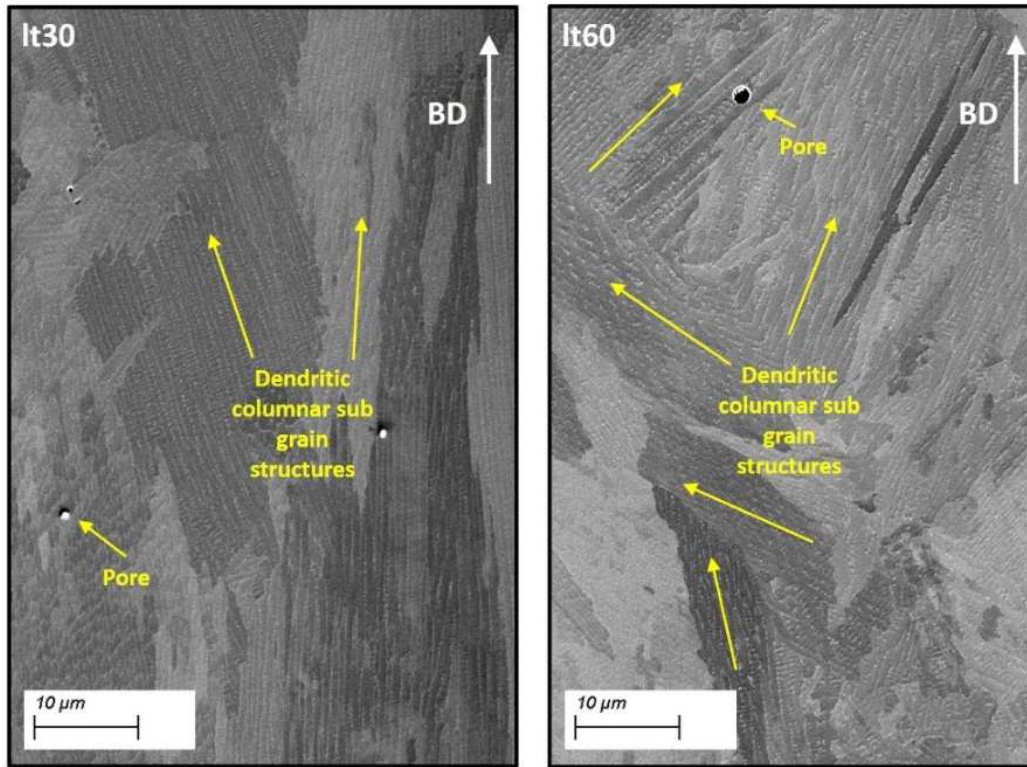
Figure VI-15. SEM scans in lt30 and lt60 samples

Additive manufacturing of metallic components is typically associated with anisotropy. Anisotropic mechanical properties counteract the application-specific advantages offered by the LPBF process. Initial investigations were conducted to evaluate the directional elastic modulus with varying layer thickness during the LPBF process. Based on these observations, the part was designed for the final milling operation.

Elastic anisotropy is often considered a drawback for LPBF manufacturing, and currently research has been focused on ensuring its reduction (Kok et al. 2018). However, careful tailoring of the elastic anisotropy must be exploited during the design of additive manufacturing. If a specific direction of higher mechanical properties (yield strength, elastic modulus, etc.) of an LPBF component coincides with the longitudinal direction of the fabricated parts (critical stress direction), it may lower the milling force-induced deformation and vibration signatures. A primary advantage of the LPBF process is its flexibility in modifying the mechanical properties (Young's modulus) of the manufactured components according to the laser scanning strategy and manufacturing parameters. Further, obtaining sufficient stiffness in the LPBF workpiece is a significant aspect when avoiding poor surface quality due to excessive vibration, considering the significant effect of Young's modulus on stiffness.

The geometry of the angled ducts facilitates the easy optimization of the Young's modulus without affecting other design considerations because these components are usually associated with tensile and compressive stresses (José David Pérez et al. 2020) (by longitudinal loads or bending) in the longitudinal direction of the ducts (where Young's modulus has been optimized). However, for intricate shapes, the optimization of Young's modulus by managing the anisotropic aspects must be carefully investigated.

The elastic stiffness matrix C_{ijkl} expressed as Eq. (17) relates the stress and strain tensors, based on which the elastic mechanical properties, including Young's modulus, are derived.

$$\sigma_{ij} = C_{ijkl}\varepsilon_{kl} \ \ (VI.17)$$

One approach to obtaining the stiffness matrix C_{ijkl} in polycrystalline materials as LPBF workpieces is using the Hill tensor $\langle T \rangle^{Hill}$ (Eq. 5), which corresponds to the average of the Voigt $\langle T \rangle^{Voigt}$ and Reuss $\langle T \rangle^{Reuss}$ tensors (Eqs. (6) and (7)). The Hill tensor has been extensively used in the literature and has proven to be quite effective in obtaining the stiffness matrix from the crystal orientation density function (ODF).

The Voigt average specimen effective tensor $\langle T \rangle^{Voigt}$ is defined by the volume average of the individual tensors $T(g_m^c)$ with crystal orientation g_m^c and volume fraction V_m assuming that the strain field is constant. In contrast, the Reuss average effective tensor $\langle T \rangle^{Reuss}$ is defined by assuming that the applied tensor field is constant, which implies that the stress field is considered constant.

$$\langle T \rangle^{Hill} = \frac{1}{2}\left(\langle T \rangle^{Voigt} + \langle T \rangle^{Reuss}\right) = C_{ijkl} \ \ (VI.18)$$

$$\langle T \rangle^{Voigt} = \sum_{m=1}^{M} V_m T(g_m^c) \ \ (VI.19)$$

$$\langle T \rangle^{Reuss} = \left[\sum_{m=1}^{M} V_m T^{-1}(g_m^c)\right]^{-1} \ \ (VI.20)$$

In Voigt notation Young's modulus $E(x)$ is expressed as Eq. (21)

$$E(x) = (S_{ijkl}x_i x_j x_k x_l)^{-1} \ \ (VI.21)$$

where x is the direction of Young's modulus, and S_{ijkl} is the elastic compliance tensor, which is expressed as Eq. (22):

$$S_{ijkl} = \frac{1}{C_{ijkl}} \ (VI. 22)$$

Samples lt30 and lt60 were analyzed via EBSD to obtain the orientation density function (ODF) and elastic stiffness matrix C_{ijkl}. Figure VI-16a, c shows the inverse pole figures (IPF) obtained from EBSD scans of lt30 and lt60 samples in the YX plane. In addition, Figure VI-16b, d show the texture pole figures for the lt30 and lt60 samples, respectively. Both samples showed a ring-like <001> texture. Further, the lt30 sample was significantly intense, with a maximum probability density of 5. Moreover, in both samples, the ring-like effect in the texture was caused by the laser rotation strategy. Pole figures and IPF figures were obtained using MTEX from lt30 and lt60 ODF data.

Laser scanning strategies are associated with the crystalline texture patterns observed in pole figures (Pérez-Ruiz et al. 2021). Subsequently, the ODF represented in the texture pole figures can be related to Young's modulus spatial distribution patterns (Geiger, Kunze, and Etter 2016), rendering the proposed methodology repeatable.

The spatial distribution of Young's modulus for both samples is shown in Figure VI-16e, f, g, and h, where a higher degree of anisotropy is evident in sample lt30. In a similar manner, it is observed that in both samples, Young's modulus is minimum in the Z direction (150 and 175 GPa) and maximum in the XZ (230 and 220 GPa) and YZ (225 and 212 GPa) directions. Considering that section A of the duct (Figure 3b) has an orientation of 70° in the YZ plane, it can be inferred from Figure 5e that the lt60 sample has a higher Young's modulus (190 GPa) compared to the lt30 sample (175 GPa) for the orientation previously mentioned.
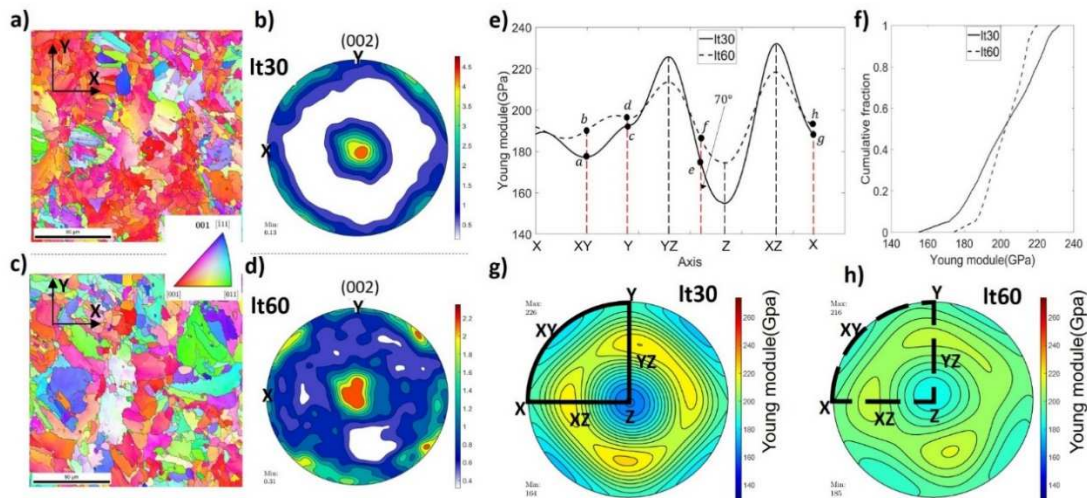
Figure VI-16. a) c) Inverse pole figures for lt30 and lt60 samples, b), d) pole figures of crystallographic texture in lt30 and lt60 samples, e), f), g), h). Spatial Young's modulus distribution in lt30 and lt60 samples

Table VI-3 presents the Voigt-Reuss-Hill elastic stiffness tensor for the lt30 and lt60 samples obtained from the ODF data. The lower elastic anisotropy of the lt60 sample and its higher Young's modulus, owing to its geometry, render it a better choice for the manufacture of the angled duct; therefore, a layer thickness of 60 μm was used to manufacture the case study workpiece and evaluate the stiffness-based methodology proposed in this work.

Table VI-3. Voigt-Reuss-Hill Elastic stiffness tensor for lt30 and lt60 samples.

Lt30							Lt60						
$C_{ij}(GPa)$	1	2	3	4	5	6	$C_{ij}(GPa)$	1	2	3	4	5	6
1	285.3						1	283.4					
2	127.0	283.2					2	129.0	285.0				
3	141.3	143.4	268.9				3	141.2	139.5	272.8			
4	-0.63	-2.37	3	89.06			4	1.14	2.09	-3.23	84.08		
5	0.13	-1.33	1.2	-0.99	86.		5	2.4	0.58	-2.98	-0.5	86.08	
6	1.21	-0.41	-0.8	-1.37	-0.71	70.43	6	-1.61	2.10	-0.49	0.65	1.27	72.49

VI.3.3. Stiffness enhancement with lateral stiffeners

This stage aims to propose decision criteria to evaluate the initial stiffness of the part with the previously improved Young's modulus and determine whether the part has sufficient stiffness to proceed to the manufacturing stage (case 1). If the stiffness of the workpiece is insufficient, additional lateral stiffening is necessary (case 2). In contrast, if the additional lateral stiffness is insufficient, it is necessary to stiffen the part using specific or conventional support fixtures (case 3) and remove the printed part from the base plate to perform the machining operations.

The following decision criterion is proposed using Eq. (23-25).

$$\begin{cases} if \quad K^i_{wx\_b} < K^i_{wx} \quad then \quad case \, 1 \quad (VI.23) \\ if \quad K^i_{wx\_b} > K^i_{wx} \, and \, K^i_{wx\_b} < nK^i_{wx} \quad then \, case \, 2 \quad (VI.24) \\ if \quad K^i_{wx\_b} > nK^i_{wx} \, then \, case \, 3 \quad (VI.25) \end{cases}$$

where $K^i_{wx\_b}$ is the boundary stiffness of the workpiece for iteration (i) in x direction, K_{wx} is the actual stiffness of the workpiece in x direction, n is the number of parts that fit on the base plate. and $K^i_{wx\_b}$ is obtained according to Eq. (26)

$$K^i_{wx\_b} = \frac{F^i_c}{\delta^i_{b\_x}} \quad \text{(VI.26)}$$

where $\delta^i_{b\_x}$ is the boundary deformation and F^i_c is the resultant cutting force obtained from the tangential, radial, and axial force components, as defined in Eqs. (10-13), applicable for x, y, z in the workpiece reference frame.

Considering that the milling of flexible elements implies an increase in the cutting force related to the characterized forces (Table VI-2), it is recommended that the selected cutting forces F^i_t, F^i_r, F^i_a be adjusted by a coefficient, as expressed in (27).

$$F^i_t = \overline{F}_t S_i; \; F^i_r = \overline{F}_r S_i; \; F^i_a = \overline{F}_a S_i \quad \text{(VI.27)}$$

where $\overline{F}_t, \overline{F}_r, \overline{F}_a$ are the average forces measured for the selected cutting conditions (from Table VI-2), and S_i is the selected safety factor for iteration i.

The parameters established for the iteration $i = 1$ in the case study are summarised in Table VI-4.

Table VI-4. Parameters for iteration 1.

Parameters for $i = 1$	
$\delta^1_{b\_x,y,z}(mm)$	0.1
Tooth passing freq (Hz)	127
$a_e(mm)$	0.1
$\overline{F}_t(N)$	19.4
$\overline{F}_r(N)$	34.4
$\overline{F}_a(N)$	7
S_1	6

For the case study, the resulting cutting force F^1_c, and the boundary stiffness $K^1_{b\_min}$ were $240.6\ N$ and $2406 N/mm$, respectively. Based on this, the criteria defined in Eqs. (10-14) can be evaluated.

The analysis of the harmonic response was conducted in ANSYS® for a frequency ranging from 0 to 300 Hz, angle **α** from 0° to 90°, and a damping ratio of 0.003, where **α** represents the angular position of the tool relative to the workpiece, as shown in Figure VI-17. Force-induced deformation and stiffness of the ducts were obtained across an **α** range of 90 °. Harmonic response simulations for the lt30 and lt60 samples are shown in Figure VI-18a. Simulations were

conducted using the elastic properties obtained using the Voigt-Reuss-Hill elastic stiffness tensors, as shown in Table VI-3.

Based on the results of the first simulation (Figure VI-18a), it is worth noting that the lt60 sample has a greater stiffness (1560 N/mm) at 127 Hz (tooth passing frequency) than the lt30 sample; however, it does not exceed the boundary stiffness; therefore,

$$K^1_{w\_lt30} < K^1_{w\_lt60} < K^1_{w\_b} \quad (VI.28)$$

The evaluation of Eq. 28 implies that Case 1 is not fulfilled, and Case 2 must be assessed.

To evaluate whether case 2 was fulfilled, harmonic response simulations were developed under six configurations with different lateral stiffening positions. Figure VI-18b shows the scheme of the evaluated configurations and the deformations δ^1_x and δ^1_y under the previously mentioned excitation conditions. Figure VI-18b shows that configurations 4 and 6 satisfy the criteria of Case 2. In addition, to advance the investigation, configuration six was selected because it maximises productivity and fits in the base plate of the LPBF machine.
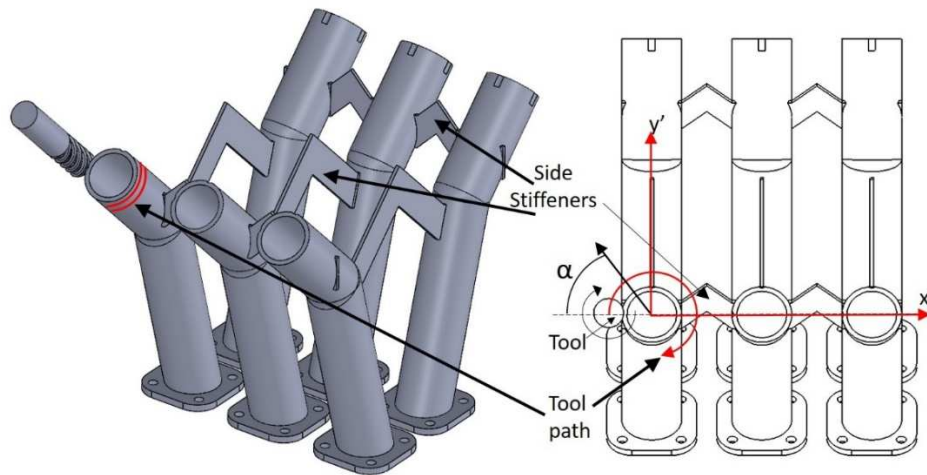
Figure VI-17. Workpiece geometry with lateral stiffeners

Because lateral stiffening is feasible, the next step is to define the location, geometry, and size of the temporary stiffeners. For this purpose, new harmonic simulations using different stiffener dimensions were performed with configuration 6. Two aspects were considered for the shape of the temporary stiffeners: first, vertical supports were not added, and second, the direction of maximum Young's modulus. Consequently, the stiffener angle relative to the base plate was fixed at 45°. Figure VI-18c shows the maximum deformation for different values of width W and

thickness t of the temporary lateral stiffeners for frequencies in the range of 0–2000 Hz. In a complementary manner, the Pareto front was obtained from a multi-objective optimization, as shown in Figure VI-18d.

The multi-objective optimization was conducted between the duct deformation function and the stiffener volume function, determining the minimum stiffener volume to obtain the minimum duct force-induced deformation and waste of material, considering that the lateral stiffeners were temporary elements that must be removed after machining. The results obtained allowed the establishment of width ($W = 12 \, mm$) and thickness ($t = 1 \, mm$) values for iteration i =1. Further, to realise multi-objective optimization, a genetic algorithm function (MATLAB) was applied, considering a double vector population type, a population size of 100, the lower and upper bounds according to volumetric restrictions, 100 generations, 100 stall generations, a function tolerance of 1e^{-4}, and a constraint tolerance of 1e^{-3}.
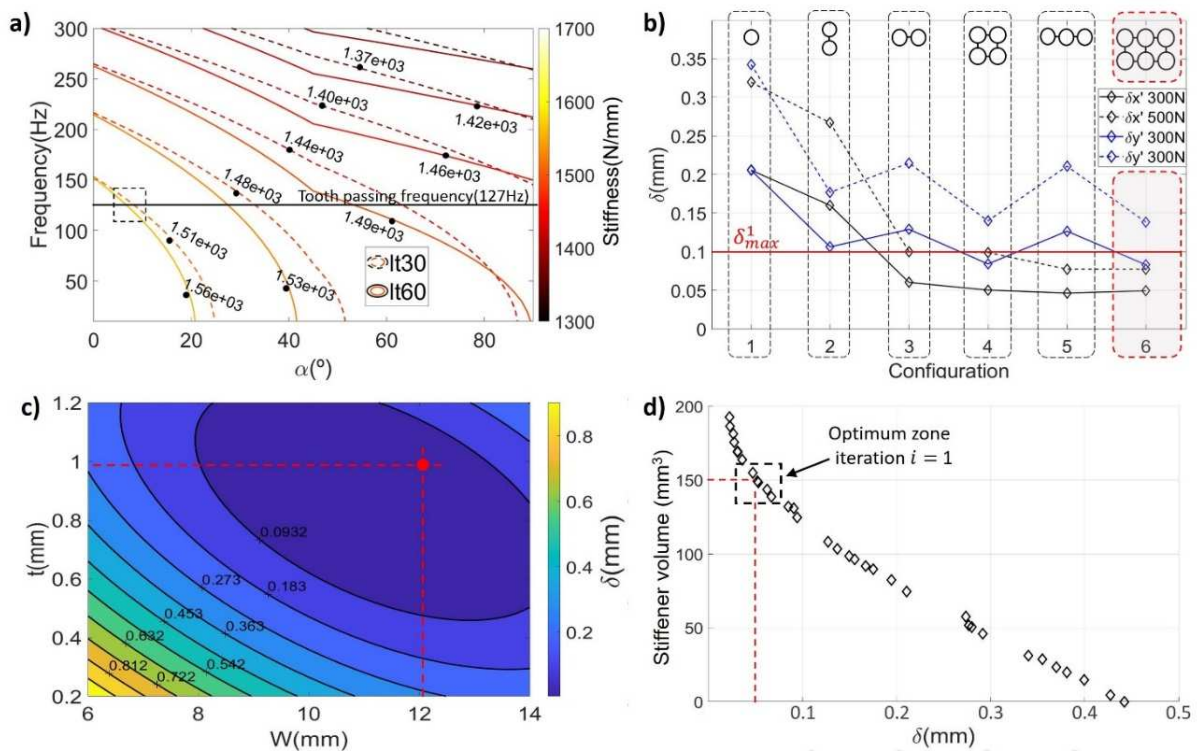
Figure VI-18. Stiffener design phase. a) stiffness by α and frequency for lt30 and lt60 samples, b) elastic deformation by configuration, c) elastic deformation by t and W with configuration six, d) Pareto front for multiobjective optimization

VI.3.4. Manufacturing and verification

Once the simulation and design phases of the lateral stiffeners were completed, six laterally stiffened ducts with a layer thickness of 60 μm were fabricated according to Configuration 6. The stiffeners are located in a machining-free zone close to the duct extreme to increase stiffness, and an easily removable design was chosen (Figure VI-19b). The steady-state stiffness was verified for Configurations 1 and 4; the experimental values were observed to be quite similar to the values simulated using ANSYS, as shown in Figure VI-19c.
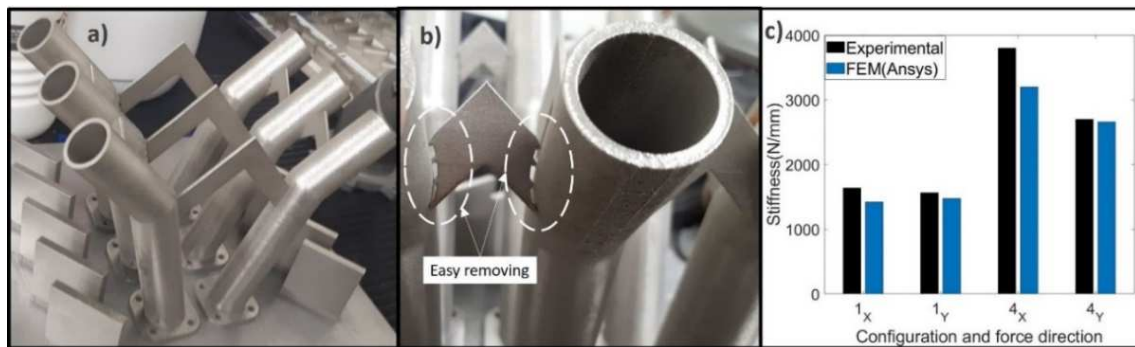
Figure VI-19. LPBF Workpiece. a) as printed, b) lateral stiffener with easy removal, c) Measured vs. FEM stiffness

Before conducting any milling process, the geometric distortion of the manufactured part was verified using computed tomography.(see Figure VI-20).
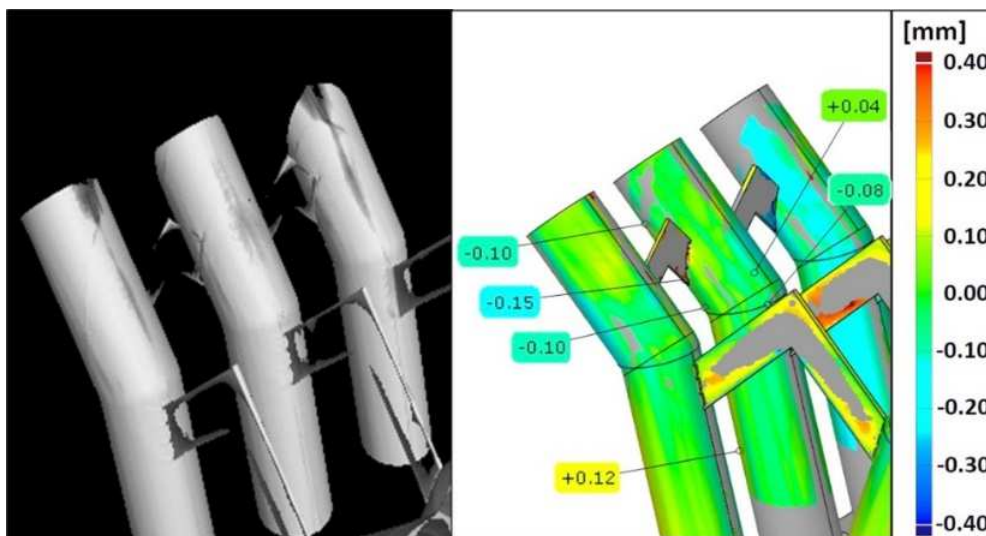
Figure VI-20. Geometric distortion analysis. a) computed tomography scan of LPBF workpiece, b) dimensional control or LPBF workpiece.

The analysis was conducted in a GE SEIFERT X-CUBE compact 195 KV with a minimum voxel size of 90 µm, and the data were evaluated using GOM Inspect 2019 software. Figure VI-20 shows that the dimensional deviation in the area to be machined is in the order of 0.1 to 0.2 mm.

Once the level of geometric distortion was evaluated and the tool path was adjusted in the CAM program, peripheral milling was performed at the duct extreme for Configuration 4 (with lateral stiffeners) and Configuration 1 (without any lateral stiffeners). The cutting parameters were as follows: radial depth of cut $a_e = 0.1\ mm$, axial depth of cut $a_p = 5\ mm$, cutting speed $V_C = 60\ m/min$ feed rate per tooth $f_z = 0.05\ m/min$.

Figure VI-21 compares the surface quality after peripheral milling of the stiffened duct (left) and unstiffened duct (right). Visually, the unstiffened duct exhibited inferior surface quality, with visible tool marks. The effect of stiffness of the set tool-workpiece was also observed by analysing the surface topography and roughness profile.
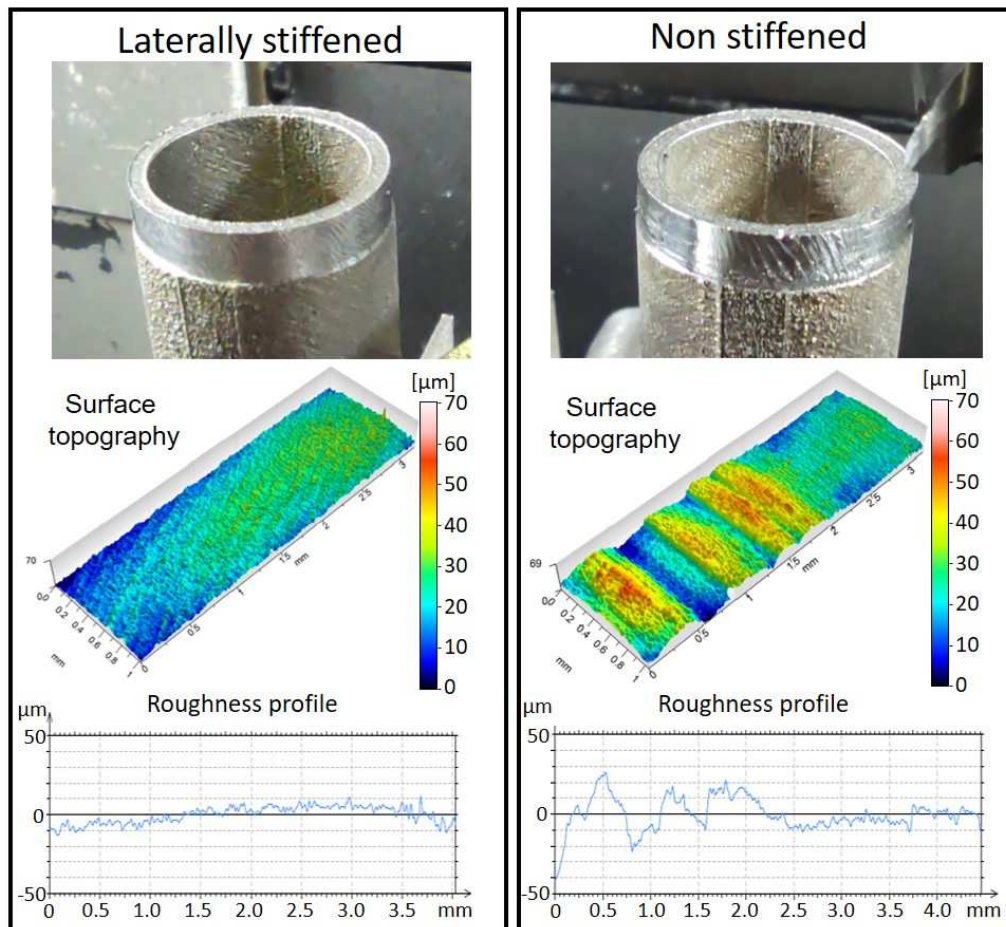
Figure VI-21. Surface quality and roughness comparison between stiffened and unstiffened ducts after the milling process

The stiffened duct presented a smoother and constant deviation along with the manufactured profile, with an apparent magnification of the deviation in the region manufactured by the tool's extreme. However, in the non-stiffened duct, the magnification due to the tool load cannot be identified because of the severe oscillations of the tool and the marks left. In addition, without the use of stiffeners, the roughness profile surpasses the target limits recommended for finishing.

Figure VI-22 shows the FFT frequency spectra of the force signal according to the angular position θ during the peripheral milling of the duct. In addition, a dephased of 45° concerning the X'-axis (Figure VI-24) was used to ensure good engagement of the tool-workpiece. Figure VI-22a (unstiffened duct), it can be observed that the force amplitude reached significant peaks of force amplitude for the tooth passing frequency and for the first mode of vibration (natural frequency), indicating that during the machining of the unstiffened duct, the resonance and chatter frequencies were excited. Further, in the case of the stiffened duct (Figure VI-22b), the FFT analysis of the force signal exhibits lower amplitude levels for the tooth passing frequency; however, significant peaks were observed at angular positions of 90° and 270°. In these regions, through the modal analysis (CAE), a correlation with the sixth vibration mode (1418 Hz) was observed, indicating the direction to improve the design of the stiffeners in a subsequent iteration. This aspect is further discussed in Section VI.3.5.
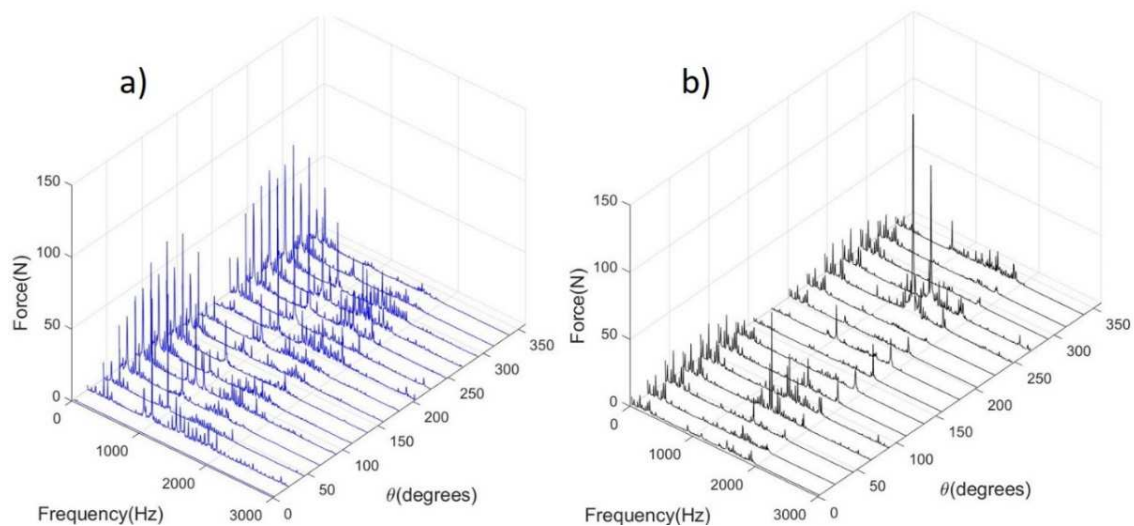
Figure VI-22. FFT Cutting force-frequency spectra as a function of θ. a) unstiffened duct, b) stiffened duct.

The roughness Ra (Figure VI-23a) and Rz (Figure VI-23b) are shown as functions of θ for both stiffened and unstiffened ducts. It is evident that the roughness levels for the unstiffened duct

across all θ ranges were almost double that of the stiffened duct. Furthermore, the stiffened duct roughness exhibits low fluctuations across the θ range, whereas, for the unstiffened duct, the increase in Ra is significant between θ values of 90° (2 μm) and 270° (3.6 μm).

Figure VI-23c shows the instantaneous cutting force as a function of θ during the machining of both ducts. In the case of the stiffened duct, it is observed that the resultant forces fluctuate between 10 and 20 N, whereas for the unstiffened duct, the forces fluctuate between 20 and 70 N, that is, five times more. Further, a sudden increase in the resultant force is observed when θ is equal to 50° and 180° for the unstiffened duct, which increased the instability of the process and magnified the roughness in the surrounding mechanized areas, as shown in Figure VI-23a and Figure VI-23b.
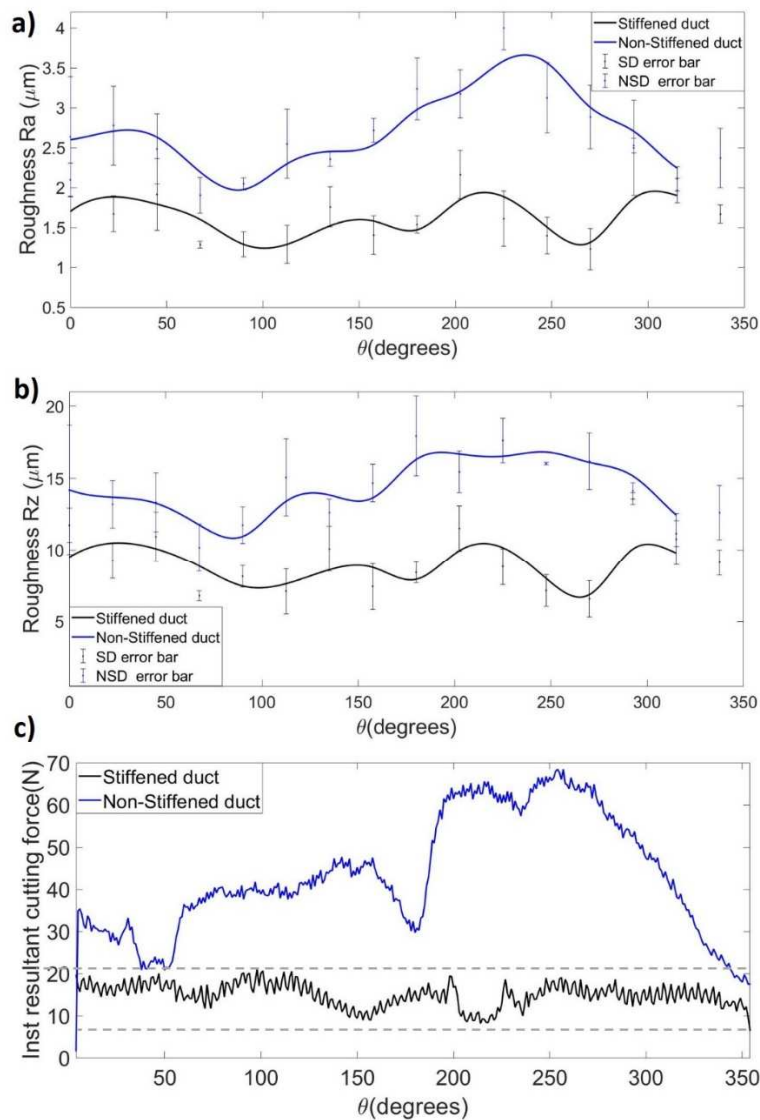
Figure VI-23. Roughness and cutting force as a function of θ. a) Ra, b) Rz, c) Instantaneous resultant cutting force

In a similar manner, it is evident that the reduction of the resultant cutting force did not instantaneously improve the roughness, resulting in a delay in stabilization. A more stable milling process is achieved using lateral stiffeners, with a significant decrease in roughness and cutting forces; therefore, stiffeners represent a valuable and economical alternative for controlling surface quality in LPBF parts that require finish machining operations. In addition, it is possible to infer that the current stiffener shapes, dimensions, and locations represent a good initial approximation for the complete design of the temporary assembly, which can be improved during subsequent stages of optimization of the LPBF parameters and stiffener design

VI.3.5. Analysis and improvement of current stiffening configuration

The observed peaks in the cutting force at frequencies corresponding to the sixth mode of vibration (1418 Hz) for values of θ equal to 90° and 270° during the machining of the stiffened duct (see Figure VI-22b) resulted in the performing of a new analysis of the stiffening design to improve the performance of the manufacturing processes. In Figure VI-24, the x' axis is aligned with the direction of the main stiffener, and the Y' axis with the secondary stiffener. The vector field shows the resultant cutting force in the plane of the feed direction as a function of θ. Point A corresponds to the initial position of the tool, which advances clockwise. Further, the regions at the outer perimeter of the duct were marked by B, C, E, F, H, I, K, and L to represent the machined areas where the surface topography was evaluated.

From Figure VI-24, it is evident that the resultant cutting force vectors at points D (θ=90°) and J (θ=270°) are oriented in the direction of the main stiffener (X' axis). In addition, it is evident that the sixth vibration mode direction was excited at the angular positions between D, E, K, and J (Figure VI-25c). However, the resultant vector of the resultant cutting force near region G (Figure VI-24) aligned with the secondary stiffener (Y' axis) and the direction of the third mode of vibration (Figure VI-25b). Consequently, it is possible to establish a relationship between the orientation of the resultant cutting force vector, the position of the stiffeners, and the maximum amplitudes of the cutting force as a function of the angle θ. Furthermore, when θ is equal to 180°, the cutting force peak reaches its highest amplitude for the third mode of vibration (1033 Hz), and the same is observed for θ values of 90 °and 270 °for the sixth mode of vibration (1418 Hz).

Based on the above, it can be inferred that the largest cutting force amplitudes occur when the resultant cutting force vectors are aligned with the position of the stiffeners. In turn, the observed peak cutting force amplitude is proportional to the stiffener capacity, which is evident

when comparing the low peak in Figure VI-25b (when the resultant force vector is aligned with the secondary stiffener) with higher peaks in Figure VI-25c (when the resultant force vector is aligned with the main stiffener). In addition, it is observed that the surface quality in the machined areas (see Figure VI-24) at angles after the force peaks were lower than those observed before the force peaks. For example, the quality at C was better than that at E. This is also true when comparing F with H and I with K, implying that to improve the surface quality and decrease the variability of cutting force peaks, the stiffener design and its position must ensure sufficient duct stiffness homogeneity across all θ ranges, which should be considered in the configuration and design of the stiffeners for subsequent iterations.
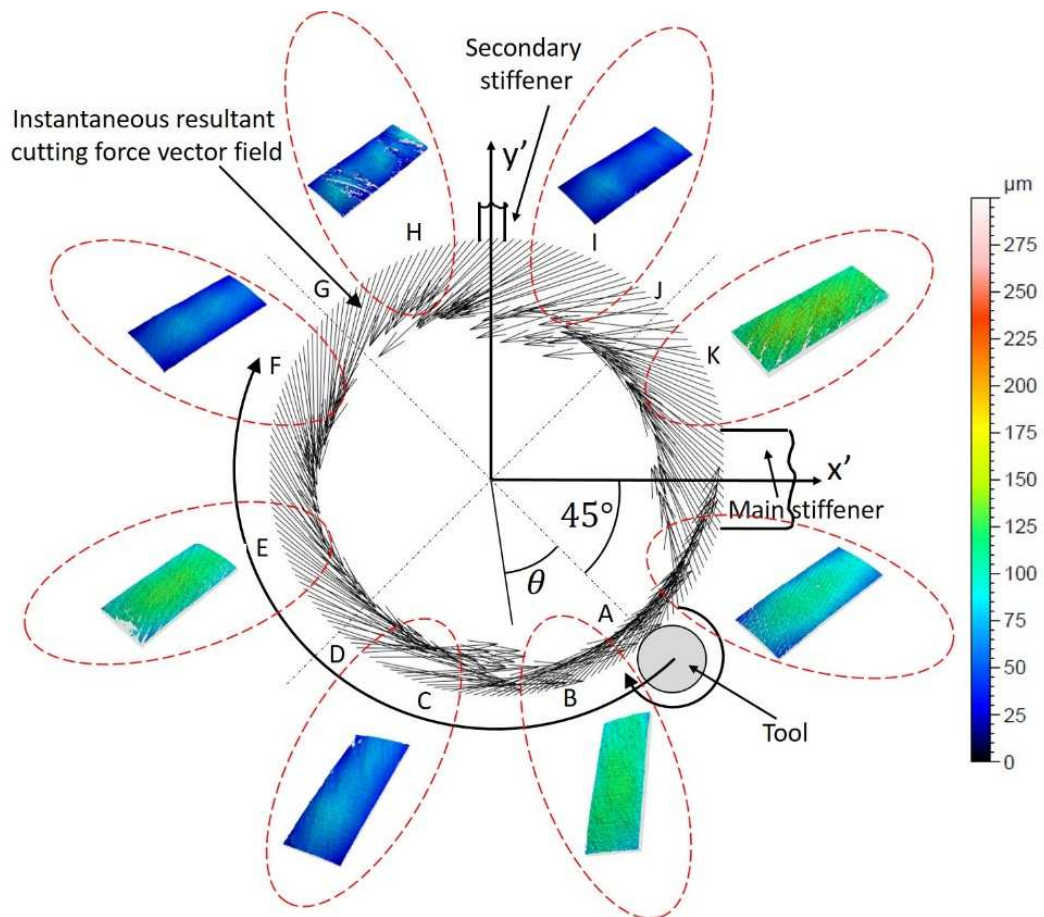
Figure VI-24. Instantaneous resultant cutting force vector field and surface topography as a function of θ
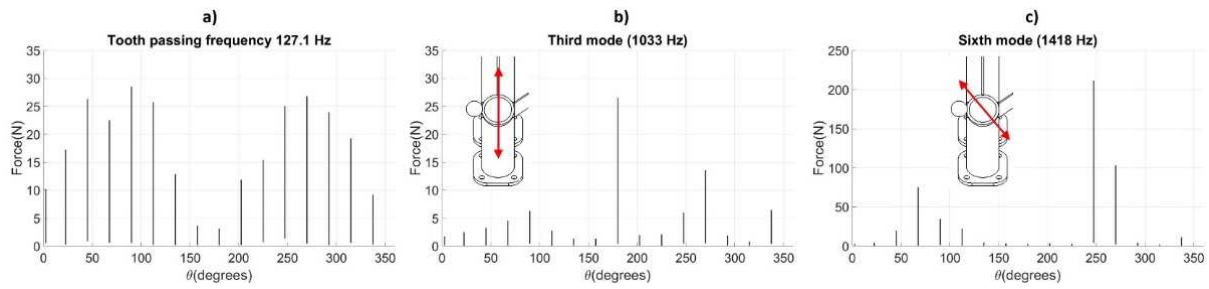
Figure VI-25. Cutting force amplitude as a function of θ for tooth passing freq, the third mode, and sixth mode in stiffened duct

Figure VI-26 compares the current configuration of the stiffeners (IT 1) with the proposed configuration for the next iteration (IT 2). Three aspects of the proposed configuration (IT 2) were considered based on the analysis. Primarily, there is a reduction in the distance between the ducts to improve stiffness, which has been obtained on rotating ducts by 45° to the base plate, ensuring the vertical orientation of the duct extreme (Figure VI-26b). Further, three stiffeners per duct have been proposed, consisting of two main stiffeners peripherally 90° to each other with 45° inclination to the duct extreme orientation. The inclination from the duct extreme (45°) provided maximum support to the duct perimeter. The third stiffener was oriented vertically between the two main stiffeners to counteract the chances of diagonal deformation. Finally, a lower stiffener volume fraction ρ (%) was proposed for IT 2 (3.52 %) than IT 1 (5.66 %), as shown in Eq. 28.

$$\rho(\%) = \frac{Stifeners\ volume(mm^3)}{Ducts\ volume(mm^3)} x100 \quad (VI.28)$$
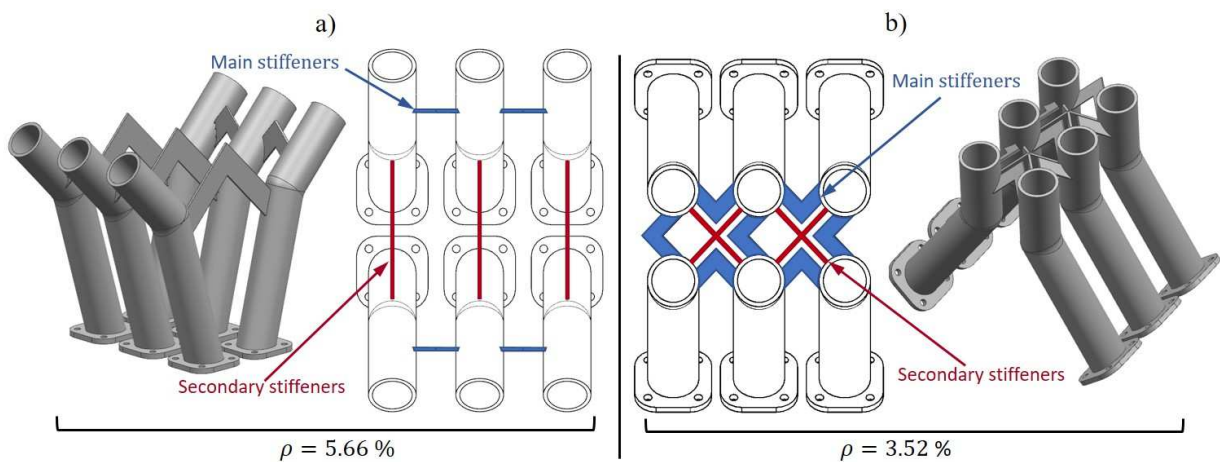
Figure VI-26. a) current stiffening configuration, b) the proposed stiffening configuration for a second iteration

VI.4. Case study II

In this section, a case study is presented to validate the proposed methodology of section VI.2 about the effect of the LPBF process on the physical parameters and the successive effect of the physical parameters on mechanical properties. The study was carried out in two stages. In the first stage, the microstructural characterization of six samples of Inconel 718 LPBF is presented. In the second stage, the mechanical properties evaluation is carried out. Finally, the measurement of static stiffness and frequency response function of plate samples is exposed.

VI.4.2. Materials and procedure

In order to evaluate the effect of the process parameters on the physical parameters and mechanical properties, samples with two different configurations (low VED and high VED) were manufactured on a Renishaw AM400 for microstructural characterization and mechanical properties verification (see Table VI-5 for low VED samples and High VED samples). In each set, samples were produced with three laser scanning strategies (three hatch rotation angles) and two-part orientation related to the building direction to observe the mechanical properties' orientation dependency.

Table VI-5. LPBF Parameters for low VED and High VED samples

Fixed parameters	Set # 1 (Low VED)	Set # 2 (High VED)
Material	IN718	IN718
Hatch distance(μm)	90	90
Layer thickness(µm)	60	60
Laser power(W)	200	230
Scan speed(mm/s)	1000	575
Replicates n	1	1
Varied parameters	**Low VED**	**High VED**
Hatch rotation angle(º)	0, 67,90	0, 67,90
Part orientation(º)	50,9	50,9

Figure VI-27 shows the previously mentioned sets of parts. In Figure VI-27a, samples of the low VED set are presented, and in Figure VI-27b, the specimens of the High VED set are presented. In both sets, there are specimens for the tension tests, plates for the stiffness tests, and cubes for the cutting force tests in the vertical direction parallel to the building direction (90º) and

inclined (50°). The dimensions of the plates are 85x60x3 mm, and the dimensions of the cubes are 50x40x40 mm.

a)   b)
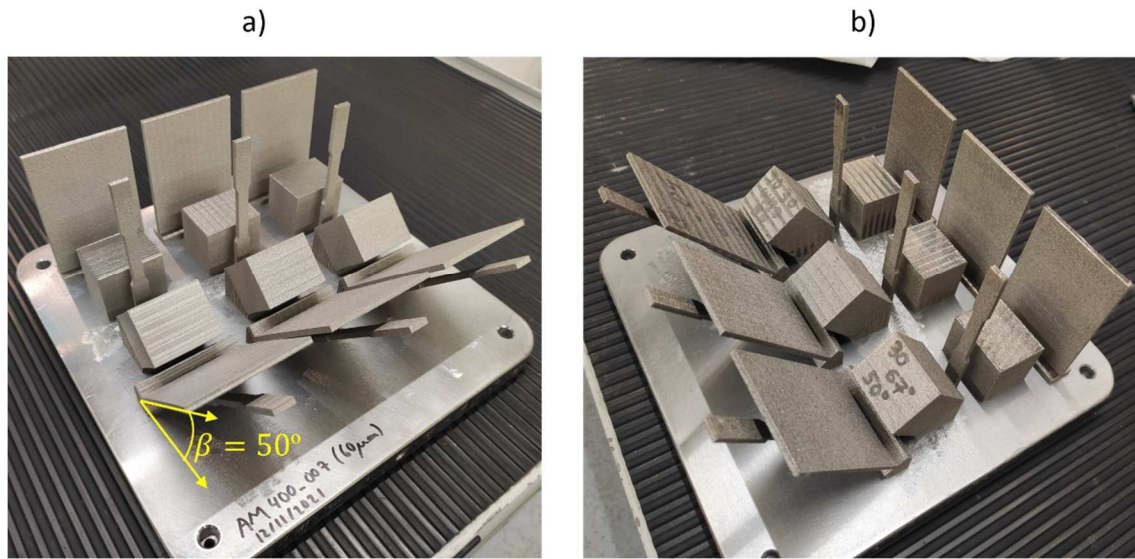
Figure VI-27. IN718 LPBF sample sets. a) low VED samples. b) high-VED samples

VI.4.3. Microstructural characterization

This section presents the microstructural characterization of six samples, their physical parameters, and the effect of the physical parameters on the mechanical properties (shear strength is analyzed in chapters IV and V). The samples are compared under the parameters established in sections III.2, III.3, and III.4 to show the correlation between the process parameters and the mechanical properties. (see Figure III-3), which is the core of the proposed methodology in this chapter for the microstructural design of parts from the LPBF process.

In order to observe the correlation between the physical parameters and the mechanical properties of the fabricated specimens, microstructural characterization by SEM and EBSD was performed. The specimens fabricated with a unidirectional strategy are referred to as R0. Those fabricated with rotational strategy are referred to as R67, and those fabricated with bidirectional strategy are referred to as R90. The physical parameters obtained from the microstructure are the ODF and the grain boundary density; likewise, the mechanical properties predicted from the physical parameters are Young's modulus and the tensile strength. The Young's modulus was obtained from the ODF using the HILL approximation (see section III.4). Similarly, to measure the level of tensile strength, the Taylor factor was used, which is obtained from the ODF (see section III.4) and the grain boundary density GBD (see section III.4).

Figure VI-28 and Figure VI-29 show the ODF of high VED and low VED samples, respectively. The first column shows the appearance of the grains from an IPF figure; the second column shows the ODF employing a pole figure, and the third column shows the ODF in crystal representation. Similarly, each row corresponds to the previously mentioned R0, R67, and R90 strategies.

In Figure VI-28 (High VED samples), The three samples developed columnar grains; however, the number of main crystalline directions changes from one sample to another. Strategy R0 presents two main crystalline orientations and an intermediate texture index. In contrast, strategy R90 presents one primary orientation and a high texture index, which indicates that the sample has a low level of misorientation and is close to being single crystal-like. In the case of strategy R67, a ring crystal-like texture is clearly seen. Although strategy R67 has many crystalline orientations, it is essential to note that the central crystalline pole is quite intense, which shows that the grains are columnar, quite extended along the layers and that the level of anisotropy of this sample is significant.
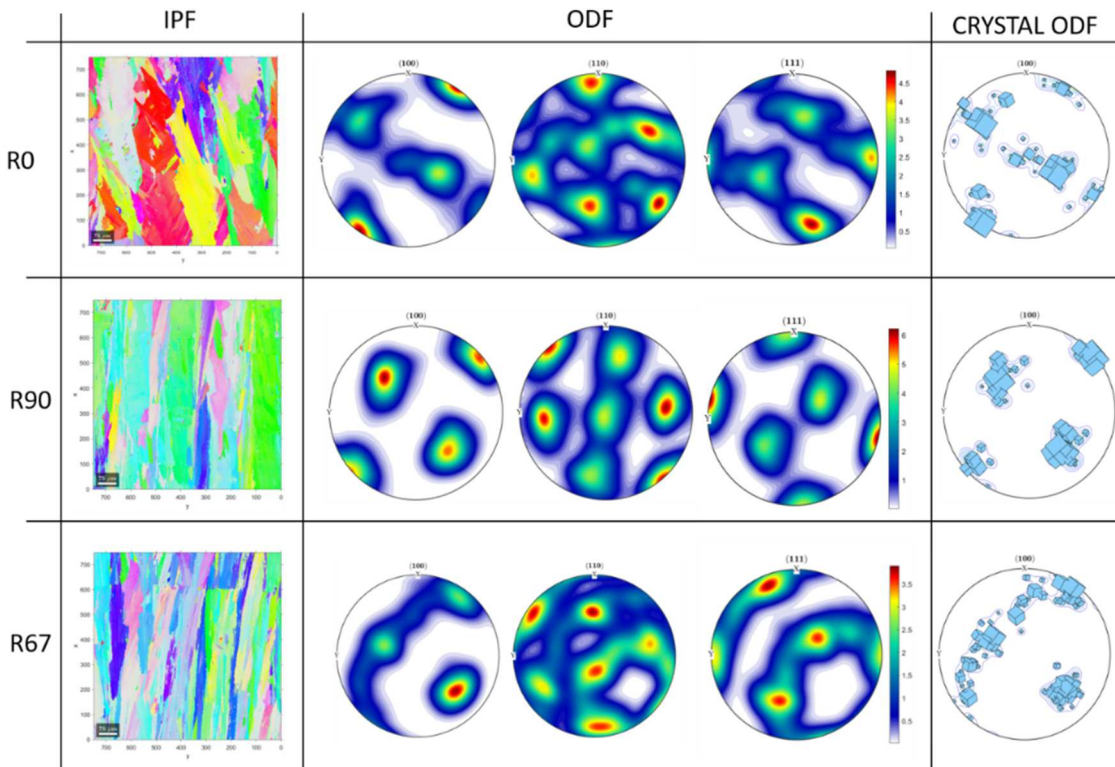
Figure VI-28. Crystallographic texture and ODF`s characterization of High VED samples

Figure VI-29 (Low VED samples) shows that the R0 strategy developed a lamellar microstructure with a main crystalline direction. Likewise, this sample shows a high texture index. In the case of samples R90 and R67, clear grain refinement and multiple crystalline orientations are

observed in comparison to the high VED samples. The low texture index of sample R67 makes this sample be considered polycrystal-like. Sample R90 has a slightly higher texture index than sample R67, meaning it could be categorized as low textured polycrystal.
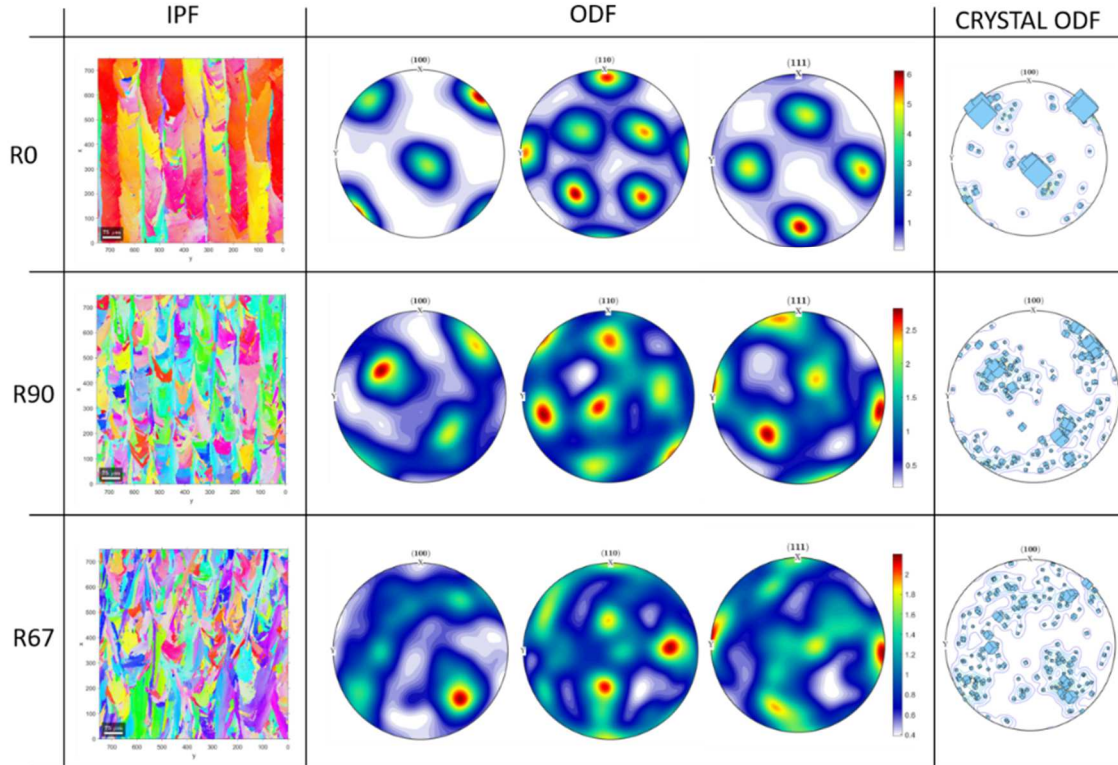
Figure VI-29.Crystallographic texture and ODF`s characterization of LOW VED samples

The comparative of texture index can be seen in Figure VI-30. It can be seen that the highest texture intensity was found in the R0 low VED sample, followed by the R90 High VED sample. It is important to note that there is only one primary crystalline orientation for both samples, and their texture is close to being single crystal-like. The lowest texture indices were obtained for samples R67 and R90 with low VED. At first sight, it could be said that at higher energy density, higher texture index were developed, and therefore at lower energy density, lower texture index; however, this was only present for the R67 and R90 strategies, where the steeper melt pool shape caused by high VED facilitates the epitaxial growth of the dendrites through the layers in the common nuclei (see Figure III-39 in sección III.5). On the other hand, the fact that the R0 low VED has obtained the highest texture index can be explained by the fact that the thermal conduction mode was developed for this strategy, which allows obtaining a radius of curvature and profile of the melt pool that facilitates the development of a high texture index. To understand this, it is essential to consider that the melt pool curvature is associated with the orientation of the thermal gradient, and for certain levels of melt pool curvature, a significant alignment is achieved between the preferred crystallographic direction of the seed grains and

the direction of the thermal gradient which will facilitate crystalline uniformity through dendritic growth by side branching. On the other hand, the R67 and R90 strategies, having rotation between their melt pools, generate a higher level of competitive grain growth, which makes the increase in the texture index of these strategies very dependent on the melt pool having steeper shapes.
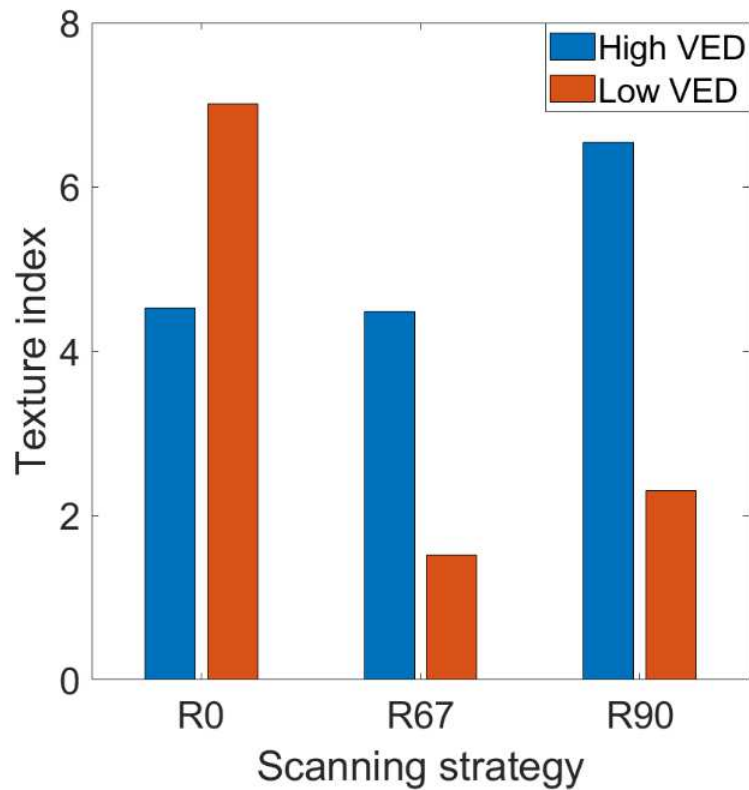
Figure VI-30. Texture index of samples

Figure VI-31 shows the grain boundary density (GBD) and sub-grain boundary density (SGBD)for each of the samples analyzed in the ZY and XY planes. The grain boundary density was selected instead of grain diameter as it is considered a more reliable measure of grain size as it considers the perimeter of all grain boundaries in the sample.

It is important to note that the highest GBD was obtained with the R67 strategy, second place with the R90 strategy, and lowest levels with the R0 strategy. On the other hand, the SGBD presents similar levels in all the samples for the ZY plane but much higher for the R0 low VED sample in the XY plane.
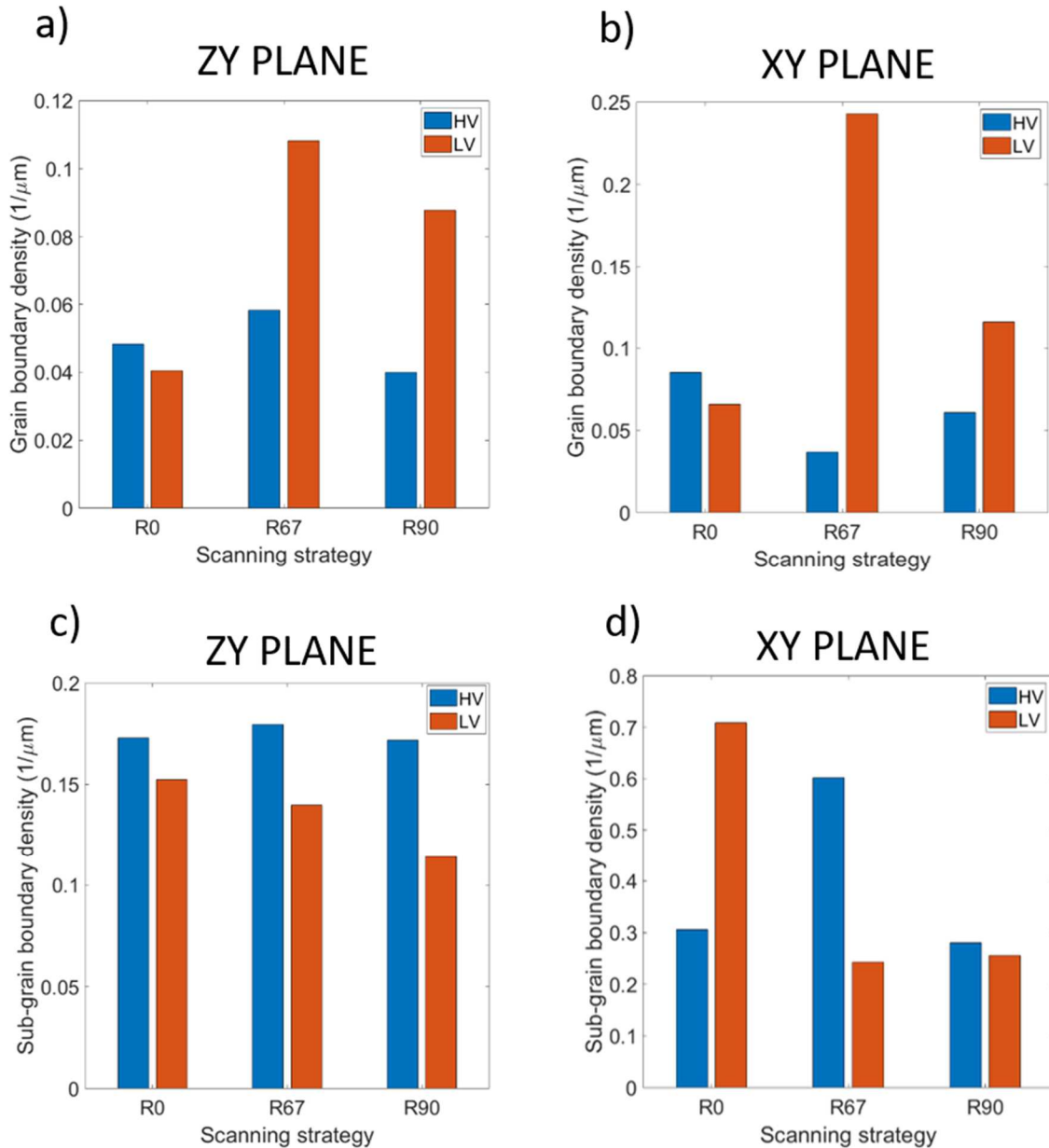
Figure VI-31. Grain boundary density of samples

In general, it is possible to observe an inversely proportional relationship between the samples with higher texture index and higher GBD for the ZY plane, which makes sense. This fact is better appreciated in Figure VI-32, where the inverse correlation between both physical parameters is seen, where for both planes (ZY, XY), the increase in the texture index generated a decrease in the GBD density. To understand this correlation, it is essential to consider that a higher texture index represents a lower number of main crystalline orientations and that the intensity of these crystalline orientations is high.

In the case of the single crystal-like texture, there is only one primary crystal orientation, and the dispersion of crystals around this main orientation is low (low degree of misorientation). Since grain boundaries develop when the degree of misorientation between two regions is significant, it is clear that the single crystal-like sample has a lower grain boundary density.

Interestingly, the samples R0 low VED and R90 High VED share all three aspects, as they both have single crystal-like texture, high texture index, and low GBD. This implies that achieving a high texture index is not an exclusive aspect of one strategy but that the careful configuration of the parameters of different strategies can allow obtaining this type of result.
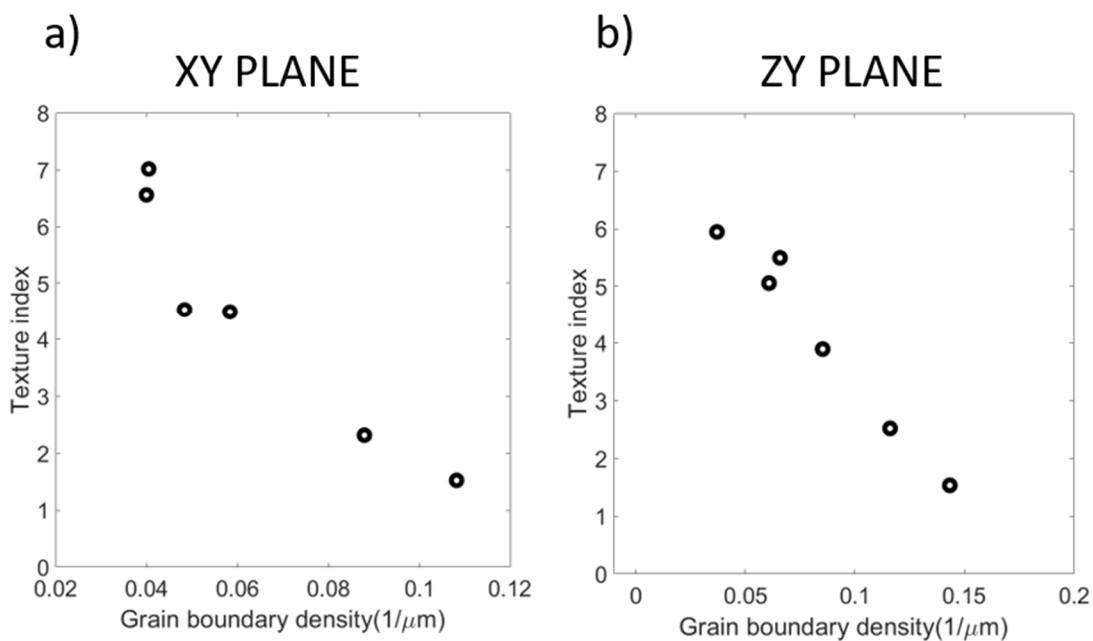
Figure VI-32. Grain boundary density and texture index correlation. a) in XY plane b) in ZY plane

The correlation between texture index and GBD represents an essential tool in the mechanical design of LPBF components since GBD has a significant effect on the plastic properties of the material, as will be observed in the next section.

VI.4.4. Mechanical properties verification

Figure VI-33 shows the set-up where mechanical stiffness and dynamic stiffness tests were carried out with the plates. To evaluate the static stiffness, the plates were installed on a Kistler dynamometer to measure the force; on the other hand, an inductive sensor was used to measure the displacement of the plate in the center, as shown in Figure VI-33a.

a)   **b)**
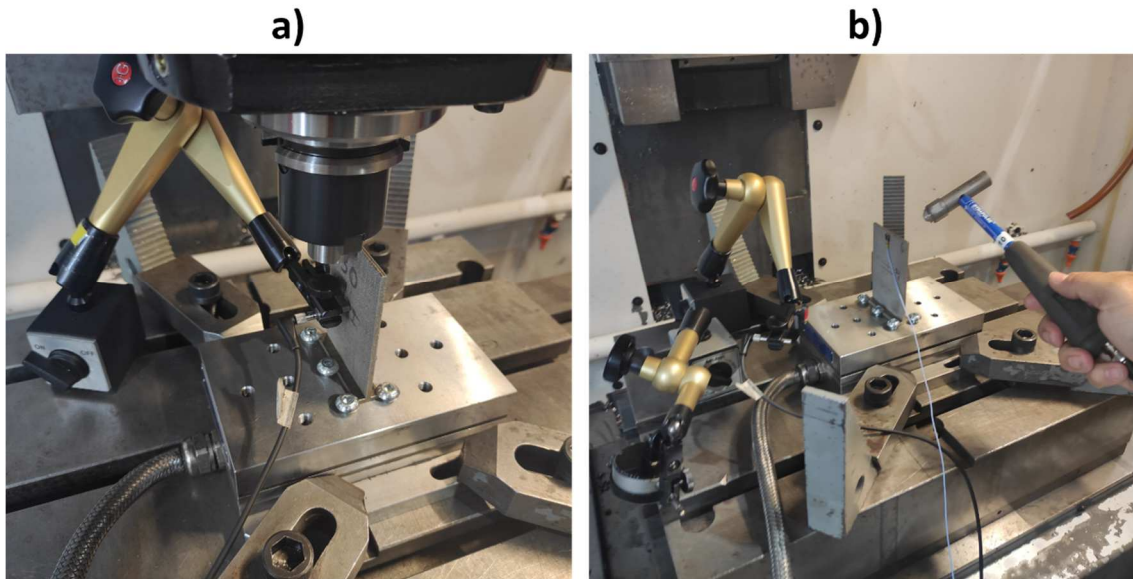
Figure VI-33. Set-up for plate stiffness measurement. a) static stiffness measurement set-up, b) dynamic stiffness measurement set-up

To measure the modal parameters and dynamic stiffness, a piezoelectric hammer and accelerometer were used in addition to the Kistler dynamometer to record the acceleration signals as a function of the force to determine the FRF (frequency response function), as shown in Figure VI-33b.

To obtain the experimental Young modulus and plastic properties of the manufactured specimens, tensile tests according to ASTM E8M were carried out. Table VI-6 shows the results obtained for the Young modulus, yield stress, and ultimate tensile strength of each of the samples analyzed. The results show a clear increase in the Young's modulus and plastic properties for the specimens fabricated with an angle of orientation $\beta=50^\circ$ (see Figure VI-27) compared to the specimens fabricated in the vertical orientation ($\beta=90^\circ$).

Table VI-6. Mechanical properties of samples

Test	Hatching rotation angle	Beta(°)Sample orientation	VED level	Young modulus E (GPa)	Yield stress(MPa)	Ultimate tensile strength(MPa)
1	0	90	HIGH	173.22	625.3	816.3
2	0	50	HIGH	243.18	650.1	898.3
3	67	90	HIGH	180.84	640.2	885.9
4	67	50	HIGH	235.36	655.1	878.4
5	90	90	HIGH	188.3	602.5	833.7
6	90	50	HIGH	234.1	637.2	818.8
7	0	90	LOW	153.76	633.8	780.9

8	0	50	LOW	231.20	776.7	1027.8
9	67	90	LOW	192.1	702.8	926.1
10	67	50	LOW	235.9	746.9	984.6
11	90	90	LOW	167.9	704.7	903.2
12	90	50	LOW	222.54	724.56	967.3

The results presented in Table VI-6 show a strong correlation between the grain boundary density (GBD) and the plastic properties, as shown in Figure VI-34. A clear proportionality is observed between the grain boundary density GBD, yield strength, and UTS. Additionally, it is observed that the samples with β=50° orientation presented better mechanical properties than those manufactured in the vertical orientation (β=50°).
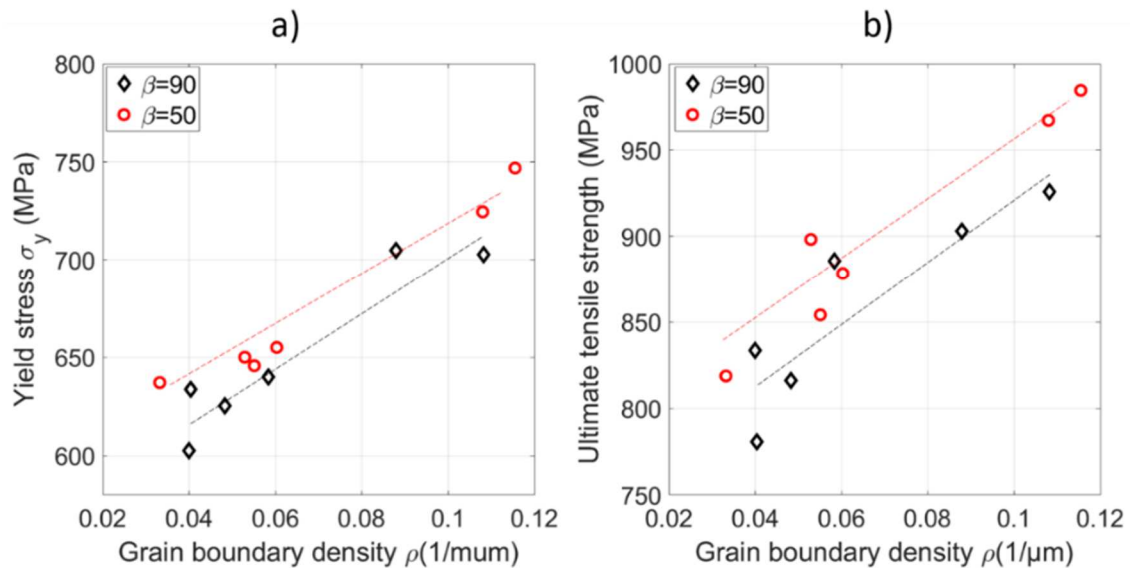
Figure VI-34. Correlation between grain boundary density and mechanical properties. a) correlation between GBD and Yield stress, b) correlation between GBD and ultimate tensile stress

Considering the correlation between GBD and texture index, as seen in Figure VI-32, an inverse proportionality is expected between the texture index and the mechanical properties, as seen in Figure VI-35. It is also noted that the samples manufactured with β=50° show higher levels of mechanical strength.
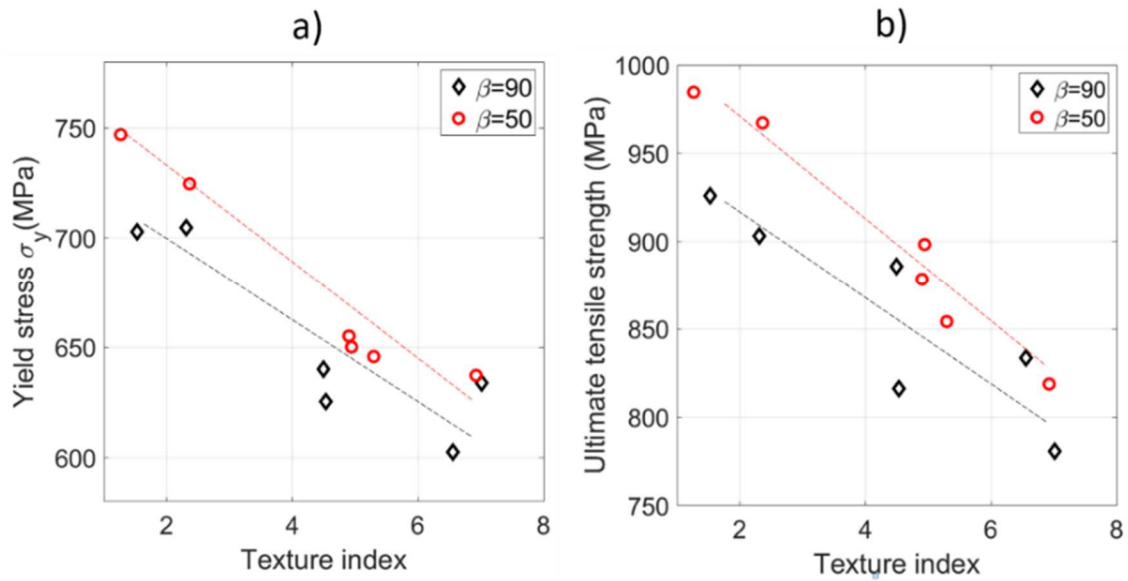
Figure VI-35. Correlation between texture index (TI) and mechanical properties. a) correlation between TI and σ_y, b) correlation between TI and UTS

Hall Petch's law explains the increase in mechanical strength of parts as a function of increasing GBD. As the number of grain boundaries increases, the material's resistance to the movement of dislocations also increases since each grain boundary functions as an accumulator of pile-up dislocations when a deformation process is in progress. It should be noted that the mechanical strength of parts manufactured in inclined orientation (β=50°) is higher than that of vertical parts (β=90°) even at similar GBD levels or TI values, which leads to the conclusion that the effect of grain boundaries is not the only one to be taken into account.

Figure VI-36 shows the effect of the triple interaction between scanning strategy, sample orientation, and VED on GBD.
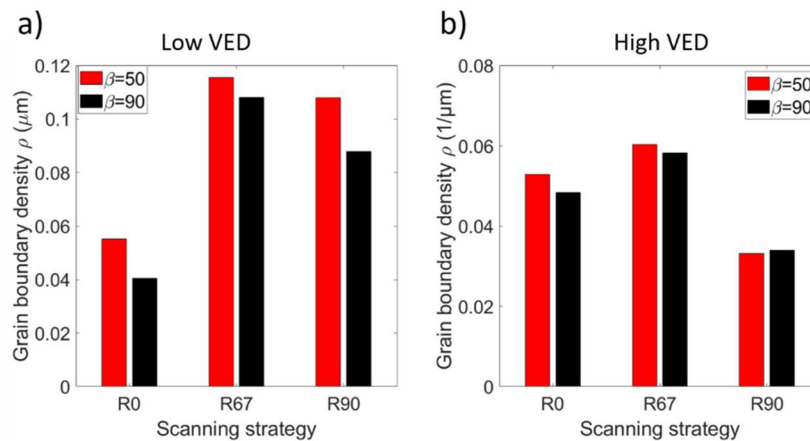
Figure VI-36. Effect of VED, Scanning strategy, and sample orientation on grain boundary density a) Low VED samples. b) High VED samples.

It is important to note that for almost all combinations of strategy and VED, the GBD was higher when β=50°. To better understand this aspect, it is essential to consider that columnar grains (present in all samples) increase the GBD in diagonal cross-sections, which is the case for inclined samples. Additionally, it is observed that the rotational strategy for both VED levels generates the highest GBD levels due to the large number of crystalline orientations generated by this strategy. On the other hand, the increase of GBD for low VED is because, at lower energy density levels, the cooling ratio is higher, producing grain refining.

Although the GBD of the samples manufactured with β=50° has higher GBD than those with β=90°, it is interesting to note that there are samples with similar GBD values but different levels of mechanical properties. This is because, in addition to the hall petch strengthening effect, there is an increase in strength due to the texture effect. The Taylor factor is used to quantify the effect of crystalline orientation on plastic deformation strength under tensile or shear loads. In Figure VI-37 the Taylor factor under tensile load is exposed for high VED samples.
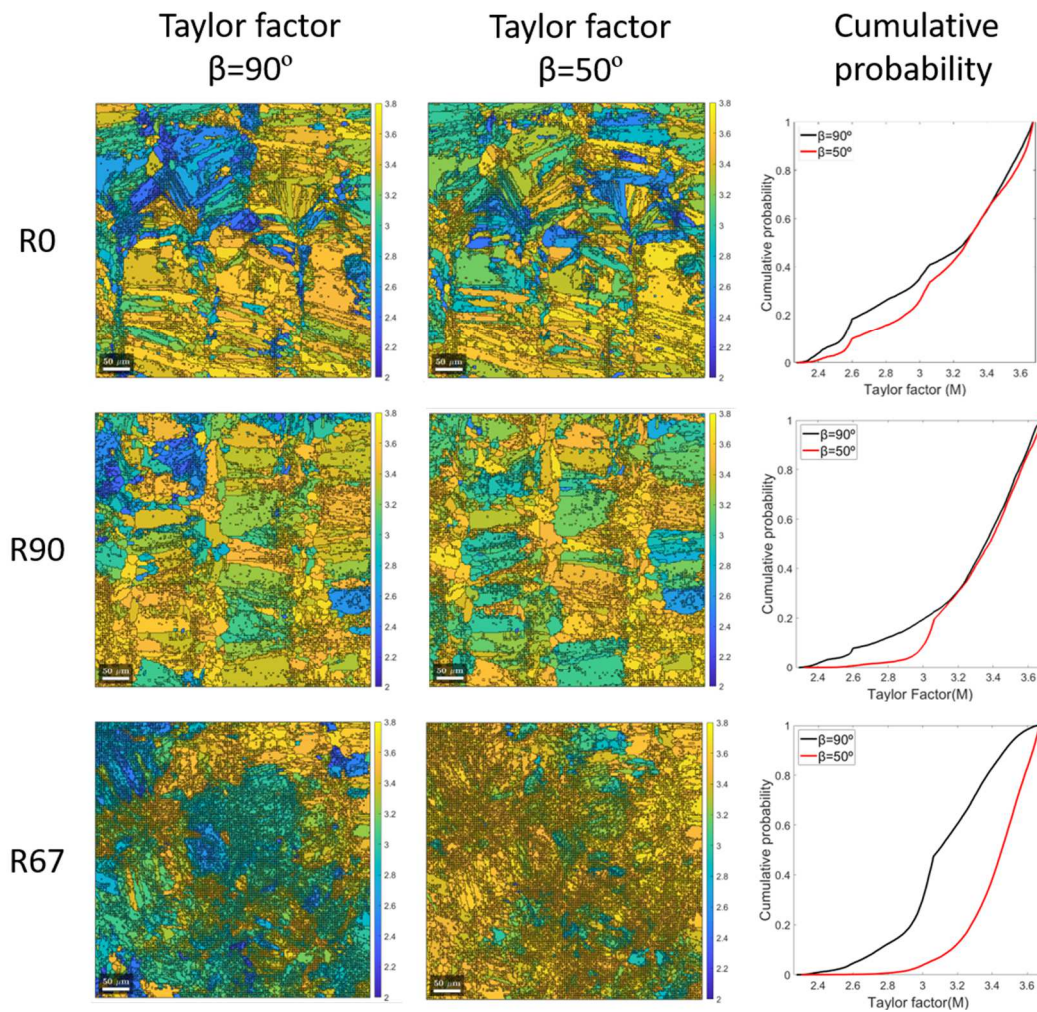
Figure VI-37. Tensile Taylor factor by strategy and sample orientation for high VED samples

Similarly, Figure VI-38 shows the Taylor factor under tensile load for low VED samples.
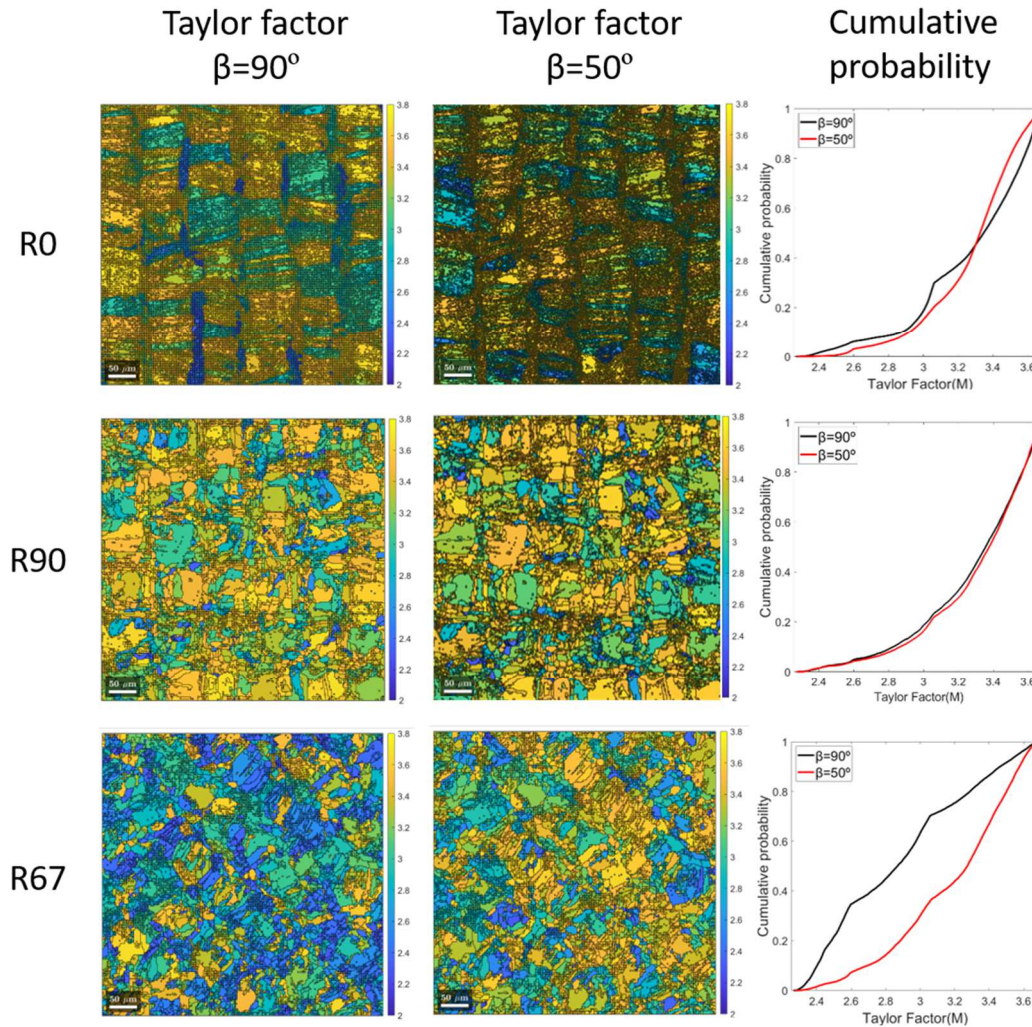
Figure VI-38. Tensile Taylor factor by strategy and sample orientation for low VED samples

In general, it is observed that the Taylor factor is higher for the samples with β=50°; however, in some cases, the average Taylor factor is practically the same for both orientations except for the high VED samples and R67 scanning strategy because high VED samples present higher levels of texturization which increase the influence of crystallographic effect on plastic strength. However, when the texture is lower, the crystallographic effect is weak, and the effect of the GBD on the mechanical strength is more significant. In the case of strategy R67.

VI.4.5. Evaluation of static stiffness and modal parameters

The static stiffness measurements on the plates agree with the Young's modulus levels of the tensile test samples, as seen in Figure VI-39. plates fabricated at β= 50º are 35 to 50% stiffer than plates in the vertical orientation. At this point, it is important to note that the elastic properties depend more on the crystalline orientation than the grain boundary density, as no dislocation flow develops in the elastic range.
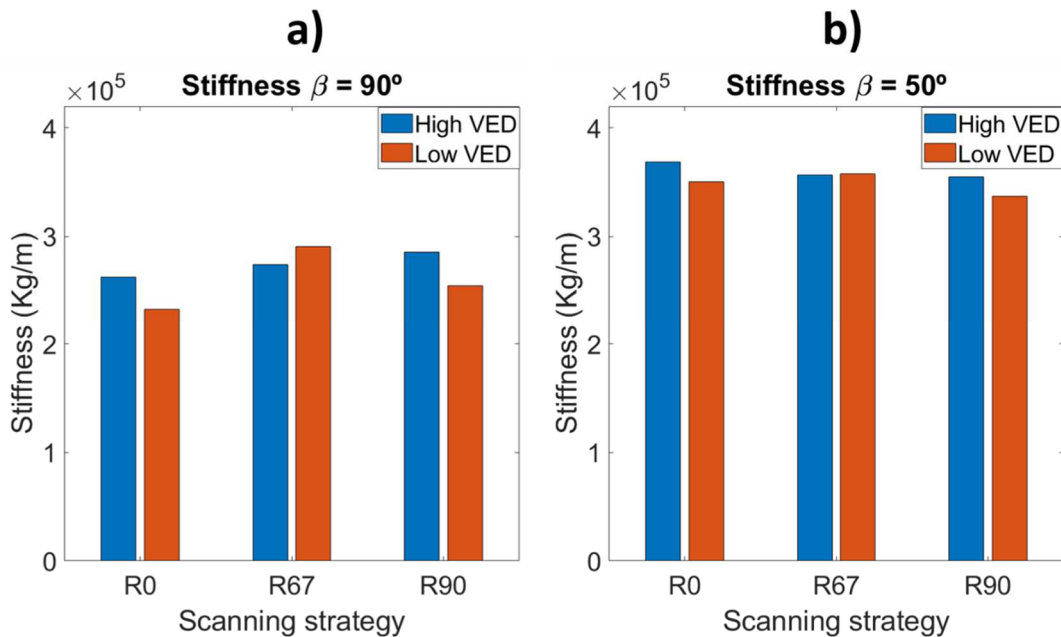
Figure VI-39. Static stiffness for low and High VED. a) static stiffness of samples with β=90º b) static stiffness of samples with β=50º

The increase of static stiffness is helpful from a mechanical design approach, as plastic or elastic deformations are usually not welcome in the functional parts of machines. On the other hand, the stiffness of LPBF parts is beneficial for reducing vibration during the cutting process. Therefore, increases in the stiffness of LPBF parts make the post-processing by machining more efficient and higher surface quality.

Figure VI-40 and Figure VI-41 show the frequency response function(FRF) of low and high VED samples. The bending mode was excited for hammer impact in the center, as seen in the first column. On the other hand, when hammer impact was applied on the corner, the torsional and bending modes were excited. It is interesting to note that for samples produced with β=50º, the

bending mode frequency is significantly higher than for vertically produced samples, which means that the anisotropy of the material can be exploited to increase the bending mode excitation frequency if the parts are correctly oriented, improving surface quality.
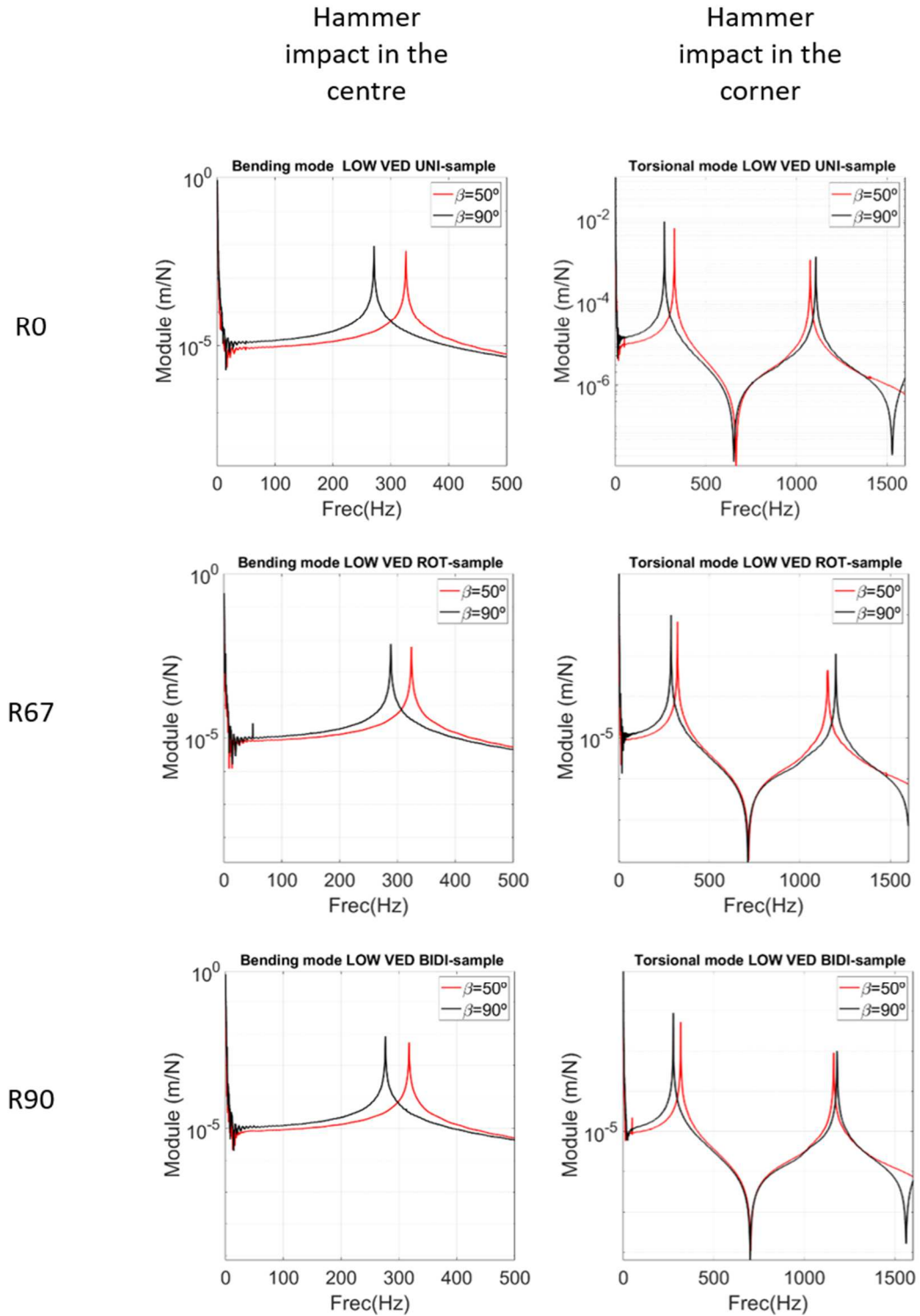
Figure VI-40.Semi-logarithmic scale FRF of low VED samples by centre and corner hammer impacts

On the other hand, the torsional mode frequencies of vertically fabricated samples showed higher dynamic stiffness and excitation frequencies than those fabricated at β=50°.
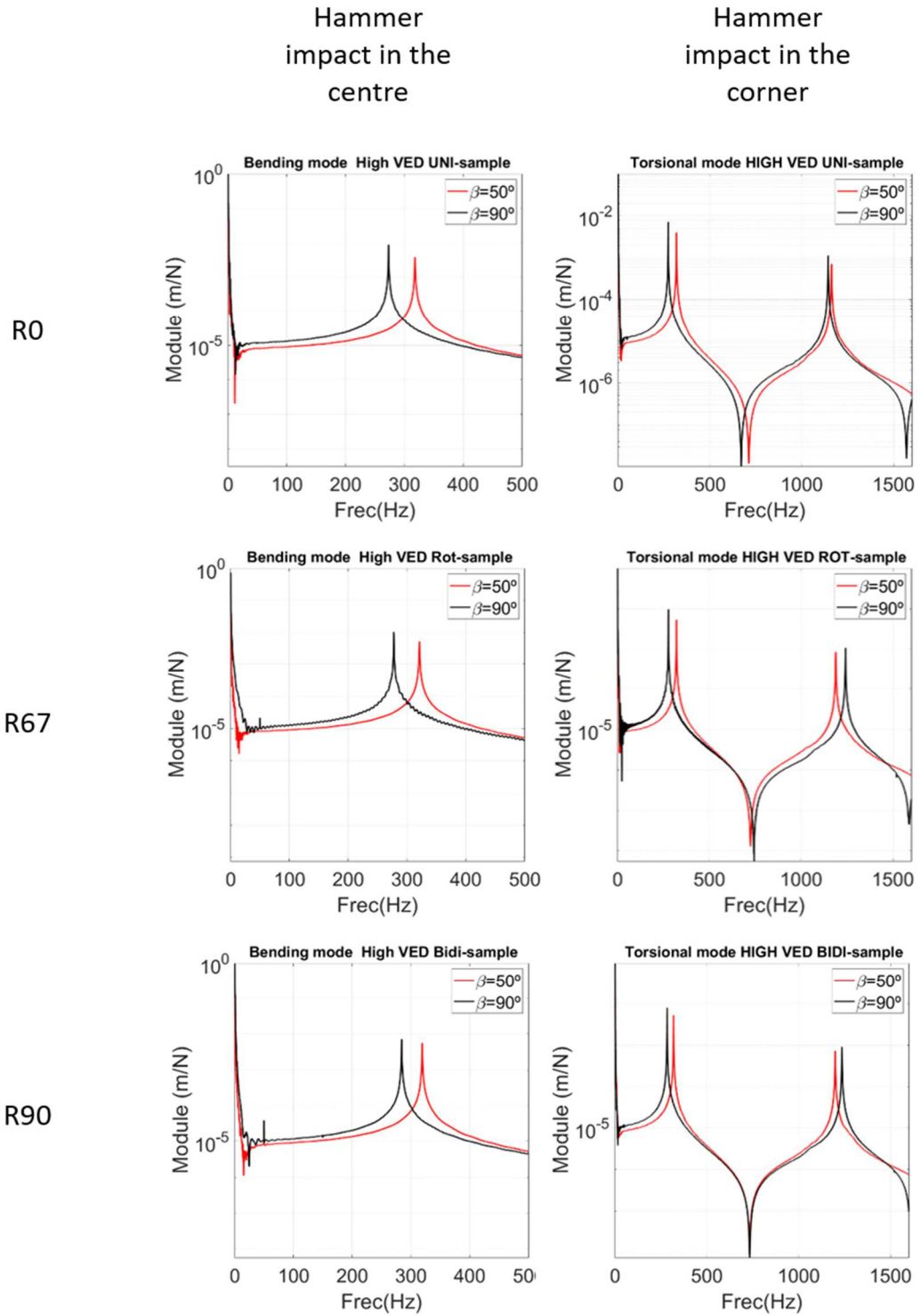
Figure VI-41. Semi-logarithmic scale FRF of high VED samples by centre and corner hammer impacts

VI.5. Case study III

This section considers the part's design requirements, the LPBF limitations, and some design rules to evaluate the methodology proposed in the previous sections. It is essential to establish that the strategies used in manufacturing the parts are the same as those used in case study II in section VI.4, so the microstructural characterization obtained in section VI.4 parts will be used in this section as well.

VI.5.1. Design Process

Table VI-7 shows the geometry dimensions of the part to be manufactured, the manufacturing constraints, design variables, and objective functions. The part is an Inconel 718 duct with a rounded rectangular cross-section and a wall thickness of 1.3 mm, which requires finishing by machining at the upper end for assembly with other parts (see red area). As far as manufacturing constraints are concerned, a fast production speed without the use of supports is required, which implies that the part must be manufactured without tilting relative to the XZ plane of the base plate. In addition, good surface quality is required at the end of the part, implying that objective machining functions should be included in the optimization. The part is not subjected to significant structural loads, so it is not necessary to include in the design functions F1(X) and F3(X) objective functions, and it is only necessary to consider those that improve the stability of the machining (F2(X) and F4(X)). Higher mechanical properties are desired(then higher GBD).

Table VI-7. Part geometry, manufacturing constraints, and objective functions

Manufacturing constraints	Requirement
Production speed	Fast
Supports	No
Critical loads	No
Surface quality	Yes

Design variables	Range value considering constraints
VED	Low
LSS	R0-R67-R90
Part orientation	$G_p(\varphi 1_p, 0,0)$ $\varphi 1_p$=0-360°
Tool orientation	$G_T(90\ \text{-}45\ 0)$
Tool geometry (helix angle)	30

Objective functions	Optimization direction
F1(X)Stiffness for critical load	N/A
F2(X)Stiffness for machining stability	Maximize
F3(X)Tensile/compresión strength under critical load	N/A
F4(X)Shear cutting resistance	Minimize

Objective functions	Expression
F1(X)	$\sigma = \varepsilon * E(ODF_{LSS}, G_p)$
F2(X)	$\sigma = \varepsilon_1 * E(ODF_{LSS}, G_p) + \varepsilon_2 * E(ODF_{LSS}, G_p) + \varepsilon_3 * E(ODF_{LSS}, G_p)$
F3(X)	$\overline{M(\alpha,\beta)} = \varepsilon * \int \int \int M(g_n)f(g_n)dg_n = \varepsilon * \overline{M(ODF_{LSS}, G_p)}$
F4(X)	$\left[\overline{M(G_T,\alpha,\beta,\phi_c)}\right]^{LSS} \approx \left[\sum_{i=1}^{N} M(G_T,\alpha,\beta,\phi_c)\frac{dV(g_i)}{V}\right]^{LSS}$

Machined zone — 22 mm — 13 mm — 102 mm — 67 mm

The manufacturing constraints limit the range of design variables in which the objective functions can be evaluated. For this reason, the range of VED that can be used is LOW, considering that the HIGH level can generate higher spatter and porosity. The available strategies are R0, R67, and R90. Regarding the part orientation $G_P(\varphi 1_P, \phi_P, \varphi 2_P)$ the restriction of not using supports means that the part can only be rotated around the Z-axis, which means that the only Euler angle that can be changed is $\varphi 1_P$ in the range of 0-360º. Concerning tool orientation, the area requiring machining means that the tool position can only be as indicated in Figure VI-46, which in Euler angles is equivalent to $G_T(90, -45, 0)$. Additionally, the tool geometry is fixed and is limited to an endmill with a helix angle of 30 degrees.

The multi-objective optimization process requires evaluating objective functions and determining Pareto limits where the combinations of design variables that satisfy the scope of the design objectives are found. In this section, a graphical approach to optimization will be used to present the practical use of objective functions and manufacturing constraints in a simple way. The texture index should be considered a design objective as it is helpful to compare the grain boundary density (GBD) of different samples(as higher the texture index as lower the grain boundary density). Since there is no objective function to predict the texture index (J) from design variables, the values obtained experimentally during the characterization of the samples in section VI.4 will be used.

Considering the manufacturing constraints, the analysis of this section will be carried out only to minimize the cutting resistance and increase the part's stiffness as far as possible while respecting the hierarchy of the highest priority objective functions. Therefore, only the effects of changing the laser strategy and part rotation on part stiffness and cutting resistance will be analyzed, and a configuration will be selected to increase stability during machining according to the priority established in the objective functions.

Stiffness optimization for machining stability F2(X)

This section will show step by step how to optimize the stiffness of the part when the strain vector field is caused by the vibration modes generated by the machining. For this purpose, the strain vector fields $(\varepsilon_1, \varepsilon_2, \varepsilon_3)$ associated with each mode of vibration are calculated using modal analysis and harmonic response by finite elements with ANSYS. The strain vector fields obtained by FEM are obtained in Euler angles $\varepsilon_1(\varphi 1, \varphi, \varphi 2), \varepsilon_2(\varphi 1, \varphi, \varphi 2)$ and $\varepsilon_3(\varphi 1, \varphi, \varphi 2)$ to be converted to the azimuthal system $(\varepsilon_1(\alpha, \beta), \varepsilon_2(\alpha, \beta)$ and $\varepsilon_3(\alpha, \beta))$ in order to multiply them by the Young modulus values assigned to each orientation in the Young modulus map. $E(\alpha, \beta)$ and, in this way, obtain the stress distributions $\sigma 1, \sigma 2$ and $\sigma 3$ required to generate the

deformation of each mode. In the simulation with ANSYS, the material must be configured as isotropic so that the orientation of the deformations follows the course in which the part is deformed without alterations due to anisotropy since the effect of anisotropy will be included by multiplying the deformation vector field by Young's modulus map $E(\alpha, \beta)$ which consider all the variations of Young's modulus depending on the orientation. An alternative to this method is to obtain the stiffness matrix corresponding to each crystalline configuration and each part orientation through Hill's theory and to simulate in finite elements the strains of the part for each stiffness matrix; however, it is cumbersome. For this reason, the method proposed here allows an easier understanding of the optimization process thanks to the practical and graphical approach.

The above concepts are better understood by employing the following example. For this purpose, Figure VI-42a shows the strain vector field associated with vibration mode 1 in the workpiece. Figure VI-42b shows the details of each mesh node's principal strain vectors. Figure VI-42c shows the distribution of the strains of each of the nodes of the part in azimuthal system coordinates, where it can be seen that although there are deformations in many directions, and the larger deformations have more effect on the displacement at the end of the part, which is where the machining will be carried out.
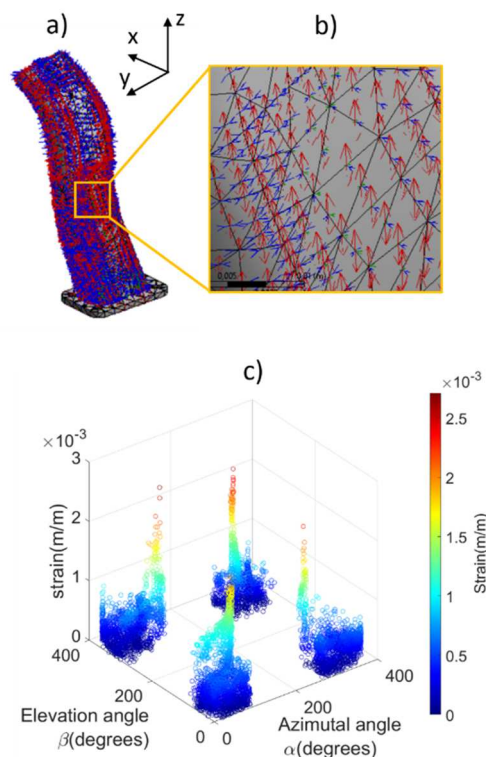
Figure VI-42. Strain vectorial field. a) strain vectorial field in workpiece caused by vibration mode 1. b)detail of some strain vectors in workpiece wall. c) Strain vector field in the azimuthal system

The schematic in Figure VI-43 shows that the superposition of the strain's vector field map $\varepsilon_1(\alpha, \beta)$ with the the Young's modulus map $E(\alpha, \beta)$ gives a quick idea of whether the orientations of the deformation vectors coincide with areas of low or high Young modulus. This makes both maps a graphical and easy way to perform a preliminary optimization. As mentioned before, in a comprehensive way, the computation of each strain with each value of Young's modulus allows to obtain the stress distribution, and the mean of the stress distribution is the function that the multi-objective optimization process seeks to maximize. In this section, however, to explain the process step by step, the graphs will be used to support the decision-making to select the design variables values that maximize or minimize the objective functions. It is essential to establish that currently the FEM software only allows the inclusion of the elastic constants of the material when there is anisotropy but does not include the change in elastic constants when the relative position of the crystals is rotated relative to the coordinates of the piece. However, the proposed Young's modulus maps $E(\alpha, \beta)$ presented in this research allow to know the areas of higher or lower modulus of Young quickly depending on the rotation or inclination of the piece. Additionally, the maps proposed here can be used as a database, and through programming algorithms in FEM sub-routines, the real stress distribution can be obtained by multiplying the deformation of each node by the value of Young's modulus in $E(\alpha, \beta)$ assigned to the strain direction α, β of each node.
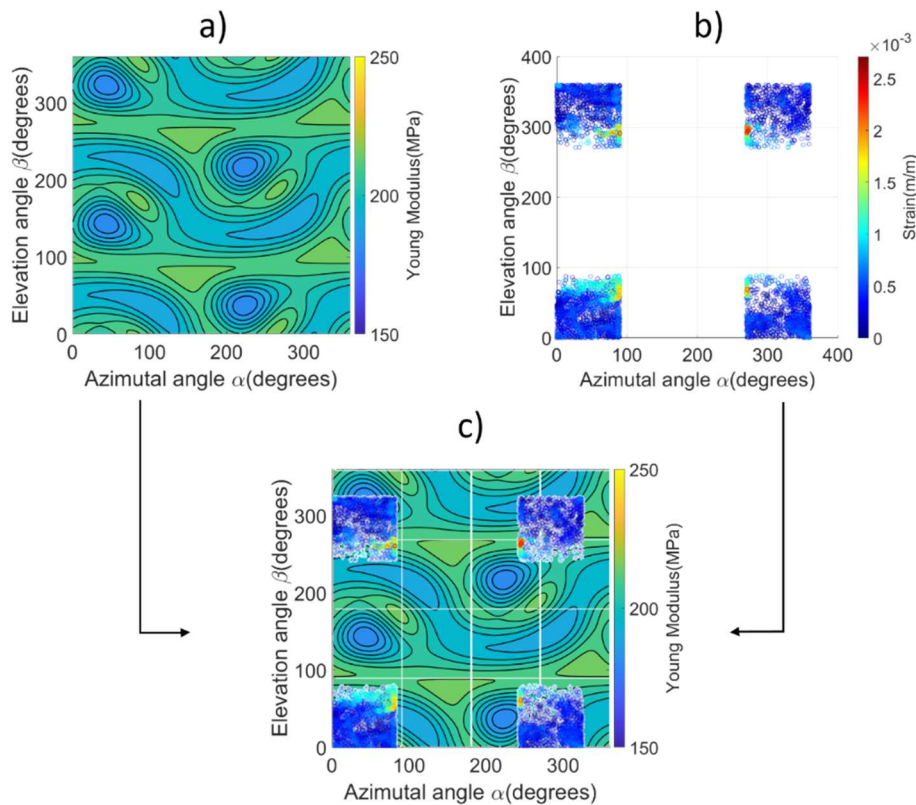
Figure VI-43. Interaction between Young's modulus map and strain map

Based on the methodology described above, the vector strain fields $\varepsilon_1(\alpha, \beta)$, $\varepsilon_2(\alpha, \beta)$ and $\varepsilon_3(\alpha, \beta)$ were obtained, as shown in Figure VI-44. In the present study, only the first three vibration modes were considered as they are the ones that contribute the most weight to the displacement of the part, although more modes can be included if a more exhaustive analysis is required. Figure VI-44d shows the direction of the deformation caused by the modes in the parts through the red arrows, considering that the part is clamped at its base.
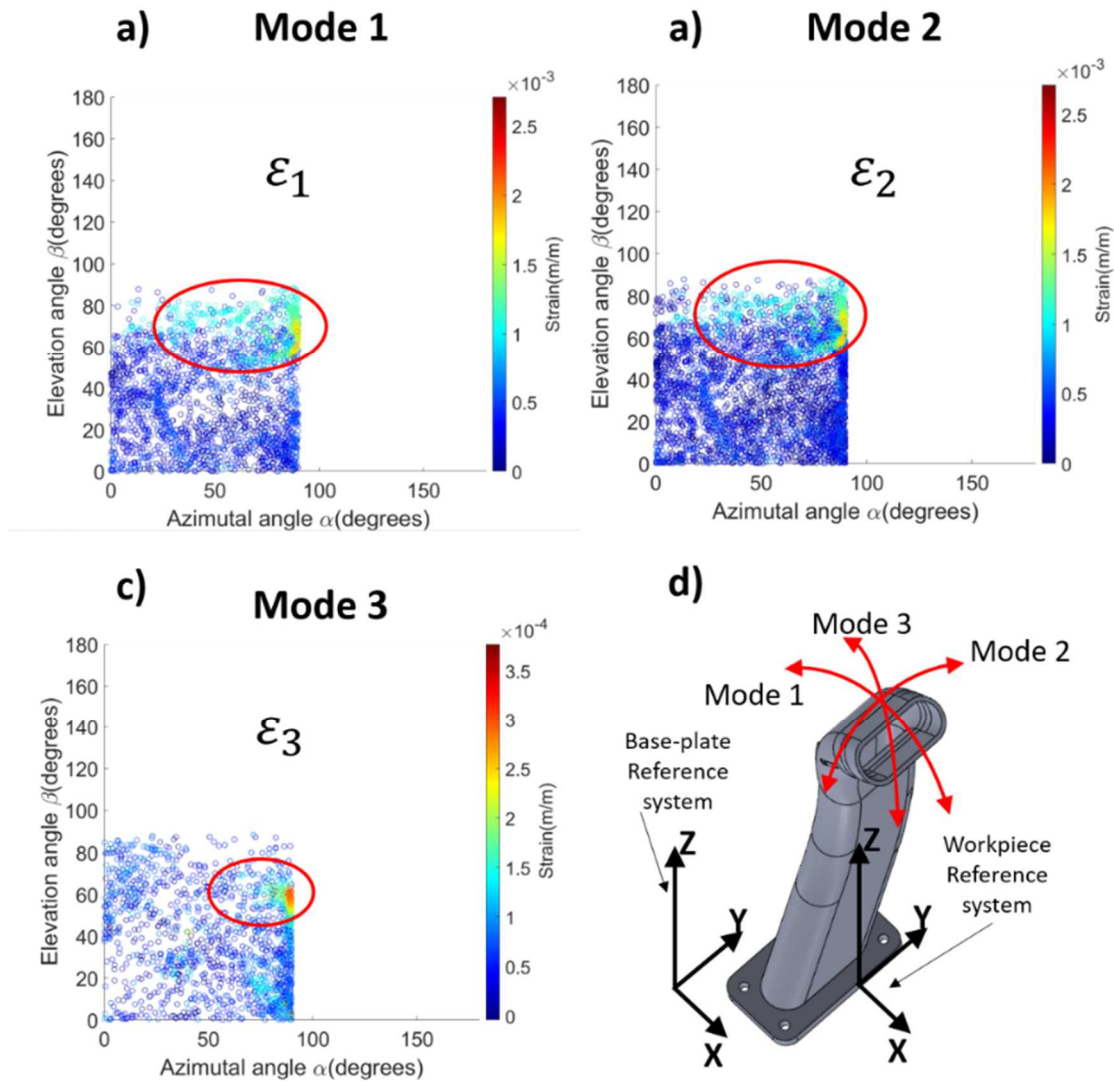
Figure VI-44. Strain vector fields for vibration modes 1,2 and 3

From Figure VI-44 a, b, and c, it can be seen that the strain vectors with the highest magnitude are found in the areas enclosed by a red ellipse, which corresponds to a range of α = 50° to 90° and β = 60° to 90° Aprox. Figure VI-45 shows the Young maps for the R0, R90, and R67 strategies when the laser tracks are in the orientation indicated for each figure.
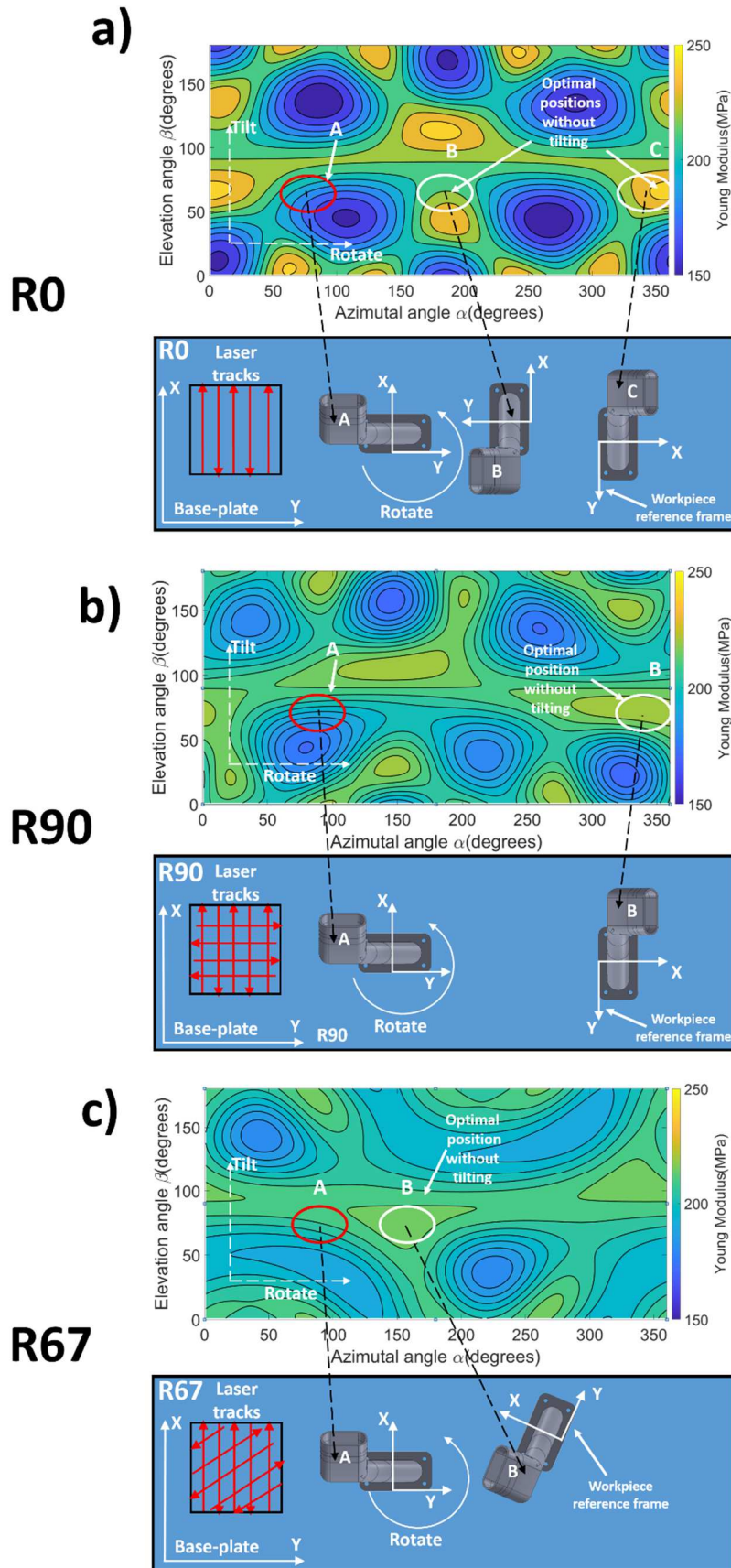
Figure VI-45. optimization of part stiffness as a function of part rotation for the strategies studied. a) R0 strategy, b) R90 strategy, c) R67 strategy

Additionally, the orientations of the significant strain vectors (red ellipses in From Figure VI-44) have been placed on the maps for each strategy in Figure VI-45 a,b, and c. At this point, it is vital to clarify that the orientations of the strain vectors were calculated for the part in question when it is oriented related to the base-plate reference system, as shown in Figure VI-44d. Therefore, the orientations of the vectors that are inside the red ellipses in Figure VI-45a, b, and c correspond to a workpiece whose reference axis is aligned with the reference axis of the base plate, as can be seen in the ducts with the letter A.

When analyzing the parts located in the A zones (red ellipse), it is observed that they are not optimal locations to obtain a high Young modulus, finding that there are zones with a higher Young modulus (optimal), such as positions B or C. Considering that one of the manufacturing constraints is that the parts must not be manufactured inclined relative to the XY plane of the base plate, the optimal location can only be done by changing the rotation of the parts around the Z axis, which means moving in the Young modulus map $E(\alpha, \beta)$ only along the azimuthal angle α maintaining the same angle of elevation β. Based on this, it is possible to establish that the optimum orientations of the parts concerning the orientation of the laser tracks are at an angle of α =180º and α=360º for the R0 strategy. It means that the parts must be rotated 90º or 270º anticlockwise around the Z axis from the position of part A as it is observed in Figure VI-45a, considering that the red ellipse(corresponding to the strain vectors of the workpiece in position A) is at an angle α=90º approximately, which represents the starting point. This aspect is of utmost importance as it represents the relative orientation of the crystals to the workpiece; therefore, it must be done carefully. For the R90 strategy(Figure VI-45b), the optimum orientation of the workpiece is when α=360º which represents that the workpiece must be rotated 270º anticlockwise. The same reasoning applies to strategy R67 (Figure VI-45c) where the part must be rotated 70º anticlockwise around the Z axis to obtain an optimal position regarding stiffness.

It is vitally important to bear in mind that the part rotations correspond to the rotation of the parts in the CAD, and the effect of the optimization in the Young modulus or any other property is achieved when the part is rotated without changing the orientation of the laser tracks relative to the base-plate reference system. The same effect is obtained if the orientation of the laser tracks is rotated around the Z-axis of the base plate but keeping the part in the initial position (position A). This can be better understood in section VI.2.4 and Figure VI-11.

The positions considered optimal in this section are not definitive, as they only represent the ones where Young's modulus increases concerning the orientation of the loads generated by the

machining. It is crucial to remember that these orientations are only optimal for the calculated strain vector fields, but the optimal orientation of the part to increase the stiffness may differ for different loads. Additionally, minimizing the cutting shear strength (through objective function F4(X)) is of a higher priority since the lack of stiffness of the part can be remedied with the use of stiffeners, as shown in the case of study II in section VI.3, while the cutting shear strength also affects tool wear.

Shear strength optimization for machining stability F4(X)

This section presents the steps to determine the design variables to minimize the cutting shear strength caused by the crystallographic effect. It is essential to remember that shear strength is a plastic deformation process in which, in addition to the crystallographic texture, there is also the effect of the grain boundary density and the dislocation density. The effect of crystallographic texture on the shear strength of an end-mill helical tool can be quantified through the Taylor factor with the model proposed in chapter IV. However, there are still no models to quantify the grain boundary density in the cutting planes generated by helical tools. Similarly, there are no models to predict the density of dislocations generated by the laser strategies used in manufacturing. Based on the above, the proposed methodology only aims to minimize the effect of texture on cutting shear strength. In addition, it is important to highlight that the higher the texture index, the more significant the effect of texture on shear strength is than the effect of grain boundary density, as in the case of monocrystalline materials in which, in theory, there are no significant grain boundaries or dislocation density. On this basis, it is possible to say that the quantification of shear strength through the Taylor factor is appropriate for textured polycrystals and single crystal-like materials.

Figure VI-47 shows the variation of the Taylor factor as a function of the rotation of the part (or of the laser tracks) employing the Euler angle $\varphi 1_p$ and the angle theta for strategies R0, R90, and R67. The angle θ is the angle of engagement of the tool, which represents the different orientations of the cutting planes generated by the action of the helix (see Figure VI-46a). It is essential to establish that the position of the tool relative to the workpiece is fixed, as shown in Figure VI-46b, and if the workpiece rotates, the tool rotates with the workpiece. The effect of the position of the tool relative to the workpiece and the effect of the engagement angle are explained in deep in chapter IV.
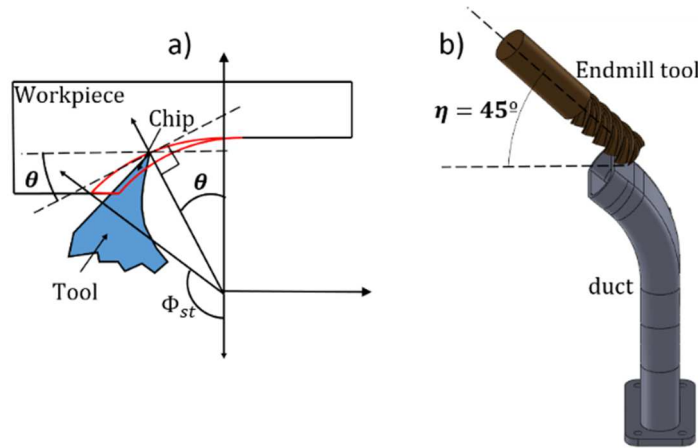
Figure VI-46. Tool position relative to workpiece and engagement angle. a) engagement angle θ, b) tool position angle relative to workpiece

The first row of Figure VI-47 shows the 3D Taylor maps for each strategy; however, in the 3D layout is challenging to determine the optimal position of the part.
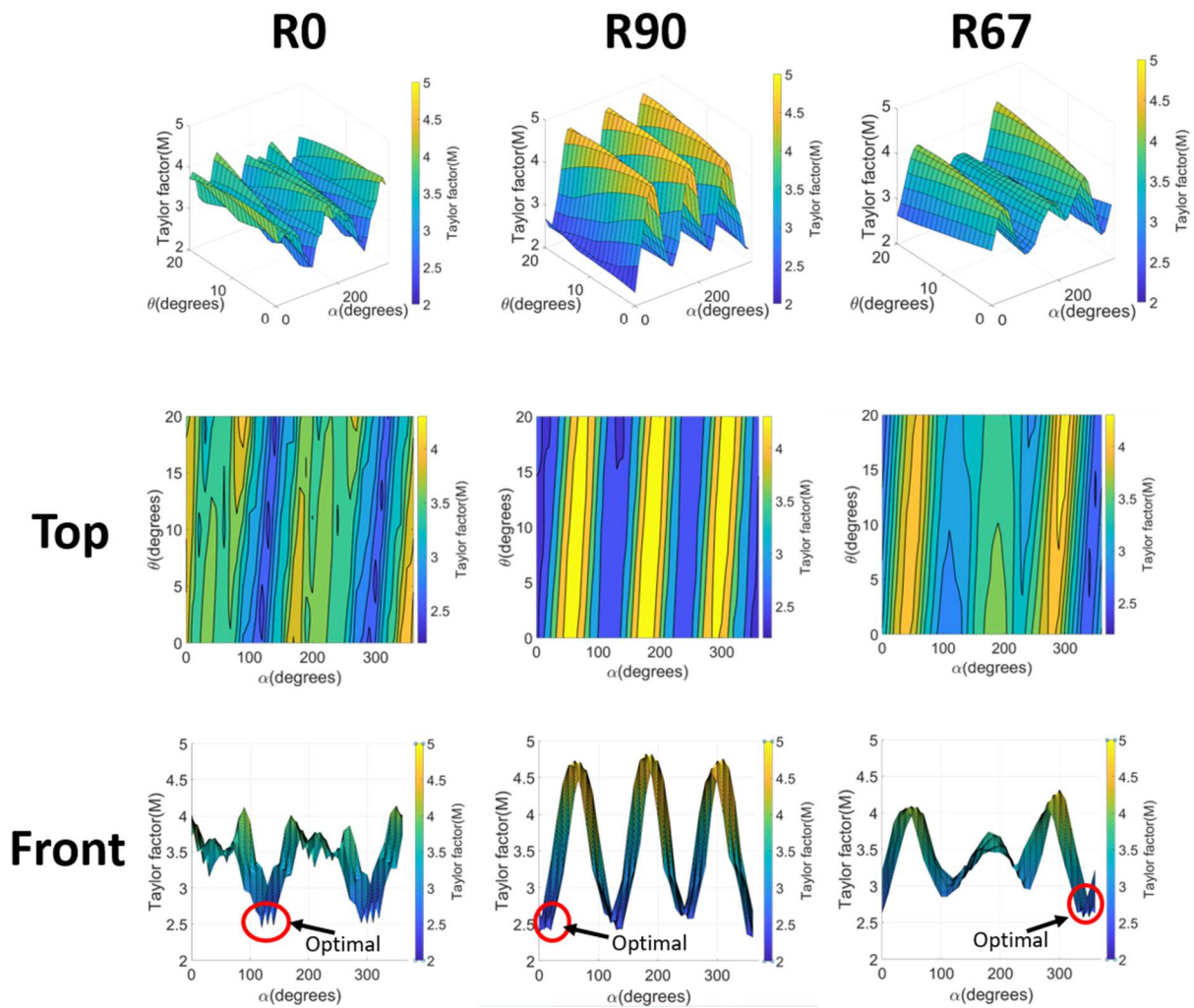
Figure VI-47. Oblique cutting shear strength Taylor maps by laser scanning strategy.

The second row shows the maps in a top view, where it is easier to observe the angle $\varphi 1_p$ where the Taylor factor is lower; additionally, the third row shows the same maps in a front view where the $\varphi 1_p$ angle that corresponds to the lower Taylor factor is even easier to observe. The figures in the third row show that the optimum zones for each strategy are enclosed in a red ellipse. This implies that the lowest texture shear strength is obtained with an angle α=120° for strategy RO , of α=0° for strategy R90 and α=360° for R67 strategy.

The curves in Figure VI-48 correspond to the lowest values of the Taylor factor of each strategy during the engagement (θ angle) of the tool. It is observed that strategy R90 presents the lowest shear strength. Considering that the shear strength is the variable with the most significance for the decision-making, the recommended position for manufacturing the parts is when the angle $\varphi 1_p$=0°.
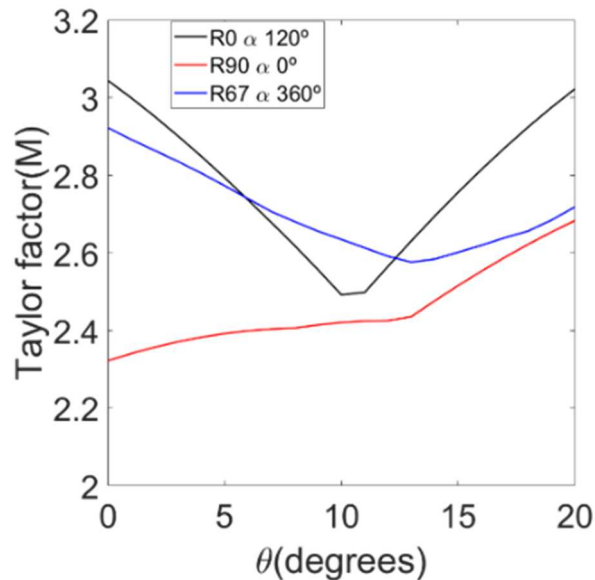
Figure VI-48. Comparison of optimal shear strength by Taylor factor by laser strategies

Figure VI-49 shows the equivalent stress distributions generated by the deformation fields of the vibration modes for the manufactured part in the unrotated position concerning the base-plate reference axis. ($\varphi 1_p = 0$). The results show that the stiffness of the parts under the three strategies is similar for mode 1; however, for modes 2 and 3, it is observed that strategy RO presents a 10% decrease in stiffness compared to strategies R67 and R90, which are very similar to each other. Based on these results, it is possible to establish that the R90 strategy with $\varphi 1_p = 0$ has a good balance between low shear strength and stiffness. It would therefore be the recommended design choice to improve machining stability.
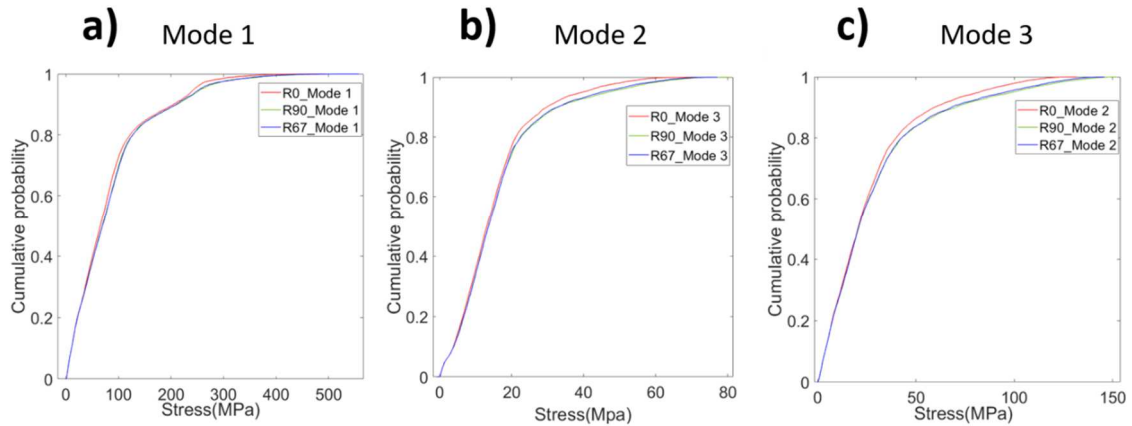
Figure VI-49. stress distributions in part (F2(X)) by vibration modes strain vector fields

Analytical Hierarchy Process(AHP)

Multi-objective optimization allows obtaining the combinations of design variables that allow obtaining optimal values of the objective functions; however, a final step is necessary to decide which design variables should be explicitly selected for the manufacture of the component. For this purpose, the AHP technique was used employing the Expert choice® software to quantify the hierarchy of the different alternatives on the maximization or minimization of the objective functions according to the need required for the design of the component.

Figure VI-50a shows the relative importance weights between the objective functions considered in the duct design. It was established that the Taylor factor is more important than the other objectives as it affects the machining stability and the tool wear. Young's modulus was considered second in the hierarchy because of its importance in machining stability. Additionally, nine different alternatives were analyzed corresponding to the three laser strategies evaluated (R0, R67, and R90) under three different workpiece orientations. ($\varphi1_p = 0, \varphi1_p = 120 \ and \ \varphi1_p = 350$). $\varphi1_p$ angles were selected based on the part orientations where the lowest shear strengths were predicted for each strategy in Figure VI-47.
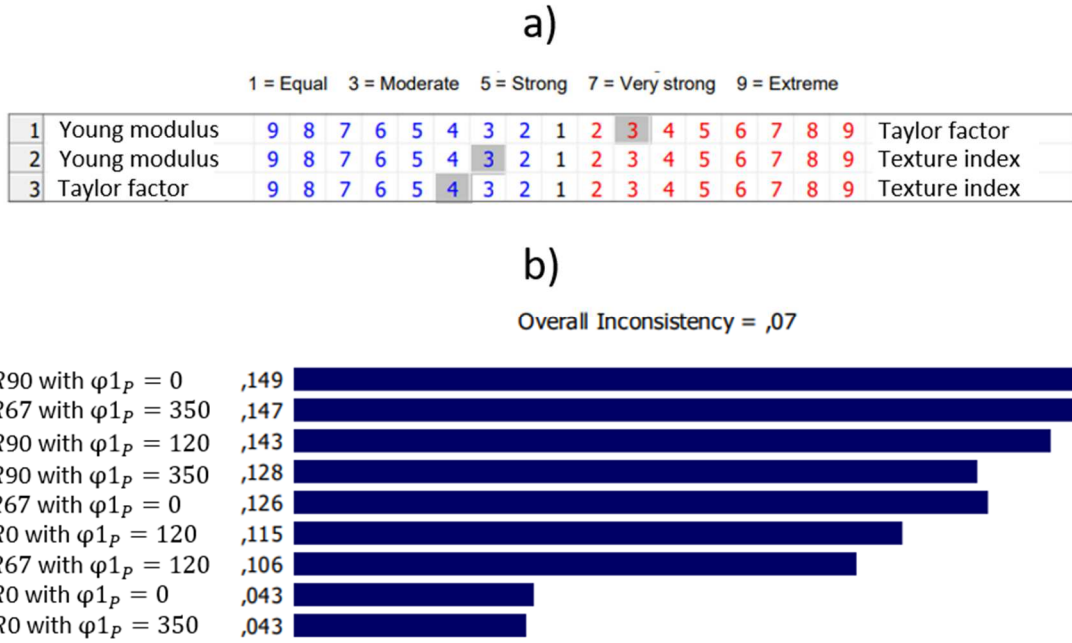
Figure VI-50. Analytical hierarchy process with an overall inconsistency of 0.07. a) relative importance between objective functions, b) hierarchy quantification of the evaluated alternatives

Figure VI-50b shows that the alternative R90 with $\varphi1_p = 0°$ had the highest rating in the design decision hierarchy, followed by the alternative R67 with $\varphi1_p = 350°$. Considering the similarity between $\varphi1_p = 0°$ and $\varphi1_p = 350°$ it is recommended to use $\varphi1_p = 0°$ to manufacture the ducts. In addition, the overall inconsistency of the design decision was 0.07 (lower than 0.1), which means that the decision is coherent.

VI.5.2. Manufacturing and verification

To evaluate the proposed methodology, six ducts were manufactured according to the design exposed in Figure VI-51a and the part orientation selected in section VI.5.1. The ducts were manufactured according to LPBF parameters of Set # 1 in Table VI-5. Three laser scanning strategies were used according to Figure VI-51. the ducts manufactured with the R0 strategy were laterally stiffened according to the stiffener design configuration recommended in the evaluation of case study I of section VI.3 for a second iteration. The red zone in ducts(see Figure VI-51b) is referred to as the zone to be machined for methodology analysis. In Figure VI-51, the orientations of the laser tracks of each strategy relative to the base-plate reference system are shown.
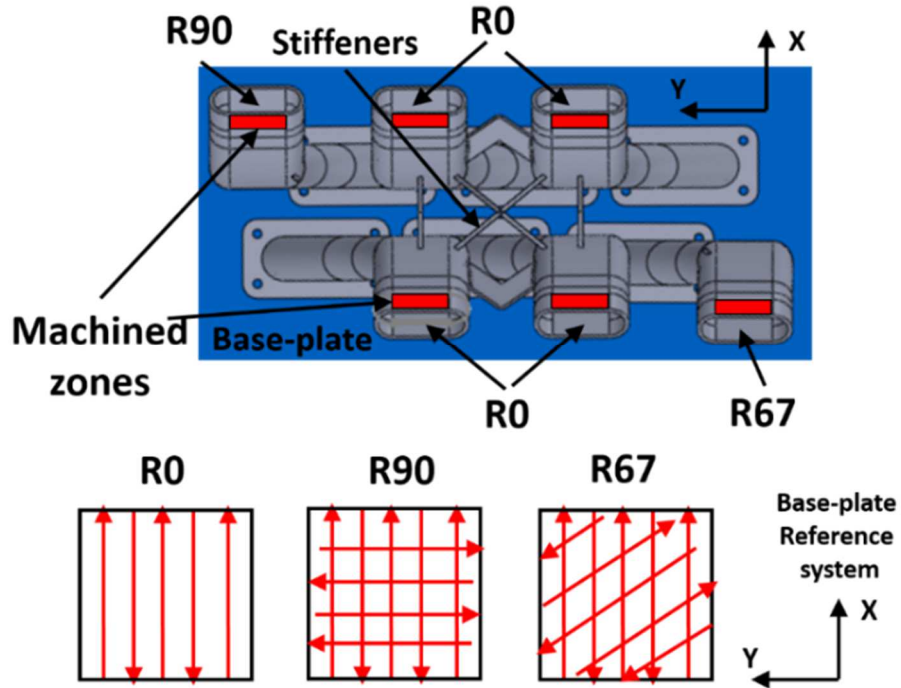
Figure VI-51. Workpiece geometry. a) ducts geometry, b) laser scanning strategies used in each duct

Figure VI-52a shows the set of ducts manufactured according to the established design. Figure VI-52b also shows the set-up for the machining of the parts.
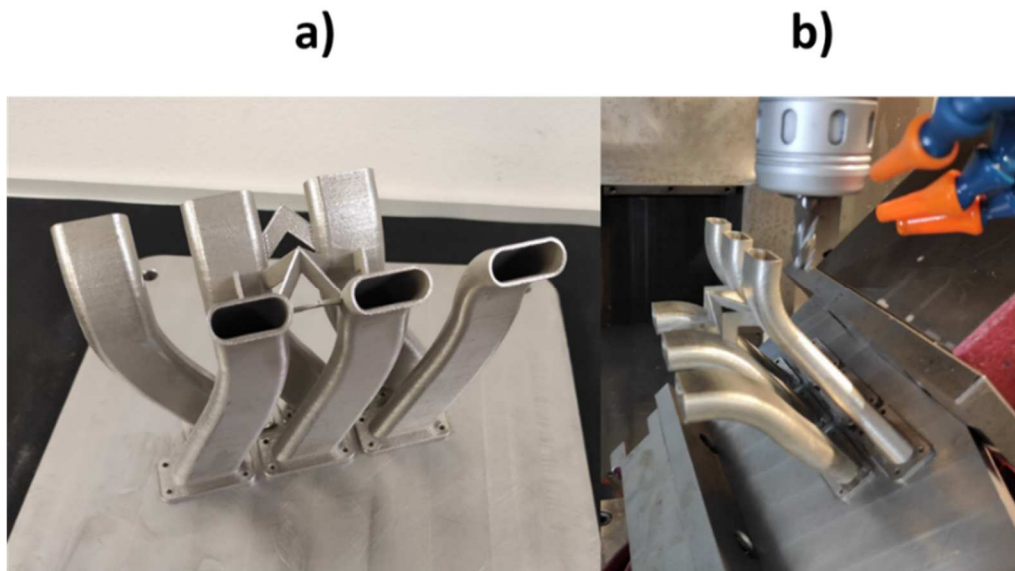
Figure VI-52. LPBF workpiece. a) as printed, b) set-up for milling

The stiffeners were designed with small holes in the base for easy removal after machining. (see Figure VI-53). The stiffeners can be removed manually with the use of a hand clamp.
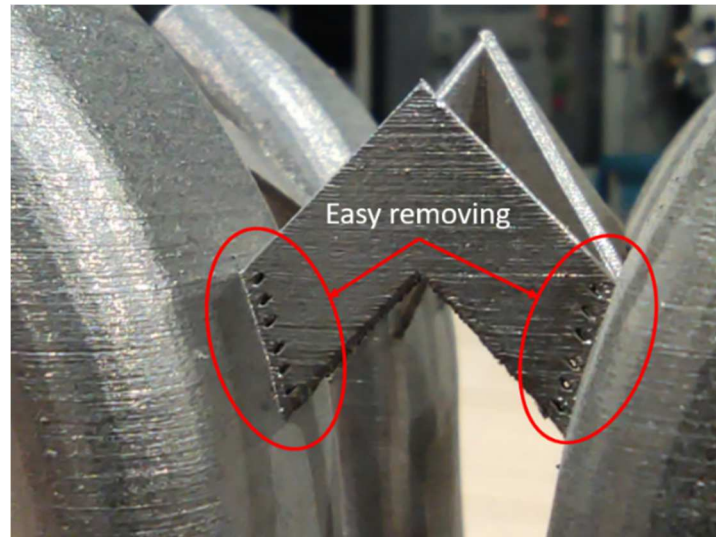
Figure VI-53. Easy removing system of stiffeners

The geometric mismatch of the manufactured part was verified using computed tomography(see Figure VI-54a). The analysis was conducted in a GE SEIFERT X-CUBE compact 195 KV with a minimum voxel size of 90 μm, and the obtained geometry was evaluated with GOM Inspect software, as can be observed in Figure VI-54b.
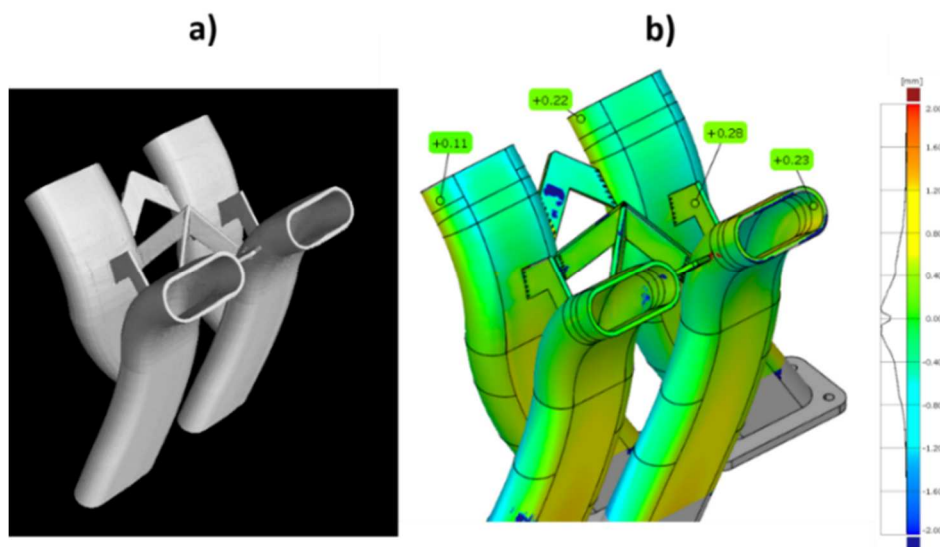
Figure VI-54. Geometric evaluation of ducts by computed tomography

The tomography results show that the dimensional deviations of the manufactured part relative to the CAD are around 0.3 mm. This is an indicator that the LPBF process is near net shape.

Figure VI-55 compares the static stiffness in the X and Y axes of the ducts manufactured by each strategy. It is important to clarify that for the stiffness measurement of the R0 duct, the

stiffeners that were in contact with the measured duct were previously removed, and the stiffness measurement of the ducts with stiffeners was performed before removing the stiffeners.
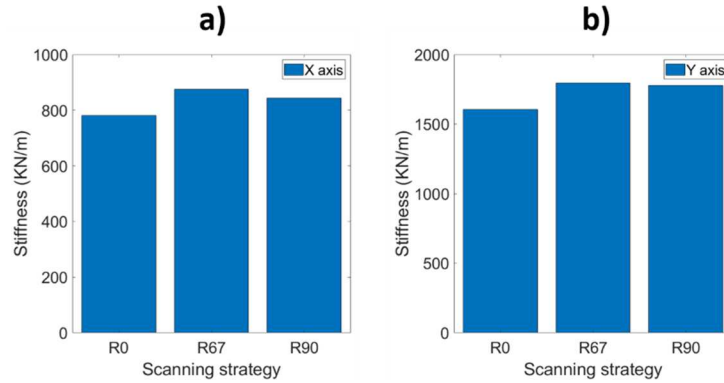
Figure VI-55. Static stiffness measurement. a) stiffness in the X-axis, b) stiffness in the Y axis

The static stiffness measurement results are similar to the simulation carried out in the design process (see Figure VI-49). The duct manufactured with the R0 strategy is 8% less stiff in the X direction than the duct manufactured with the R67 strategy, and 12% less stiff in the Y direction concerning the R67. Similarly, the stiffness of R67 and R90 ducts are similar, as shown in the previous simulation. Figure VI-56 compares the FRF of R90 and R67 non-stiffened ducts with R0 stiffened duct by hammer impact in the X and Y axis orientations.
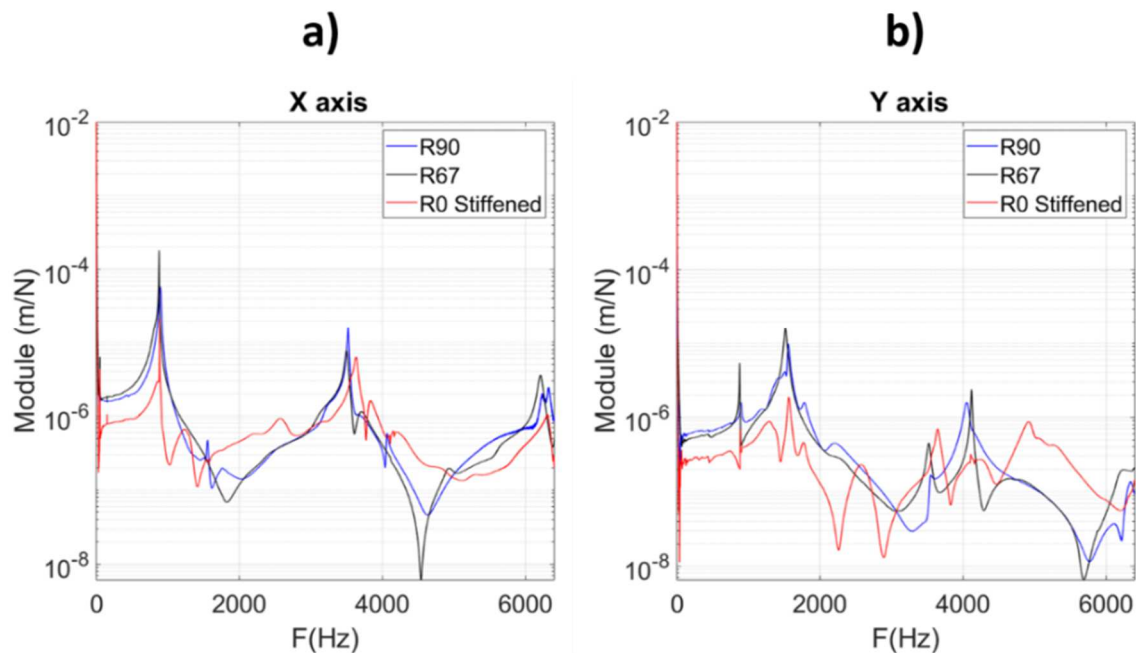
Figure VI-56. Semi logarithmic Frequency response function of ducts. a) X axis b) Y axis

The analysis of the FRF of the ducts shows that the amplitude of the vibration modes for the non-stiffened ducts R90 and R67 is similar, as is the frequency value. It confirms that both ducts' static and dynamic stiffness is similar, as observed in the design simulation in the previous section. On the other hand, the FRF of the R0 stiffened duct showed a significant reduction in the amplitude of the vibration modes and an increase in the vibration frequencies, which is proof of the increase of static and dynamic stiffness in the duct thanks to the stiffeners.

In addition to the stiffness check, the Peripheral milling experiments were performed on a Kondia A6 milling center with a Fagor 8070 CNC. An endmill of 10 mm of diameter with a helix angle of 30 degrees was used. A 60 m/min cutting speed and a 0.05 mm/tooth feed advance were applied. Figure VI-57 shows the comparative surface topography of the ducts after machining.
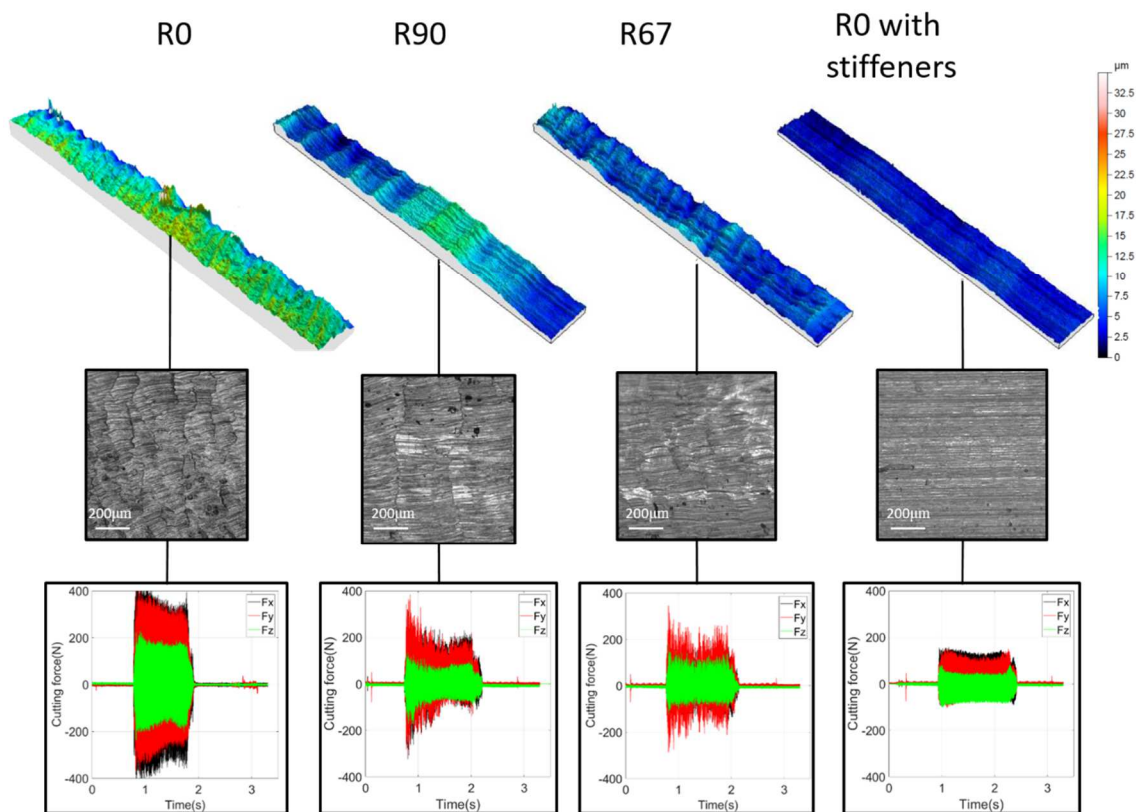
Figure VI-57. Comparison of surface topography of ducts after machining by strategies

It can be seen that the surface of duct R0 shows poor quality and the highest levels of cutting force. On the other hand, the surface quality of the ducts is slightly better in duct R90 than in the other ducts without stiffeners. Notably, the lowest values in shear strength were observed

in duct R90 as shown in section VI.5.1. The measurement of surface topography and roughness was done with LEICA DCM 3D equipment. The milling forces were measured using a Kistler 9255B dynamometer (16384 Hz). The surface quality of the RO stiffened duct was significantly higher than the other ducts, considering that the surface corrugations were lower than 5 microns.

Similarly, the cutting forces' magnitude was significantly lower than the other cases analyzed. Figure VI-58 compares the roughness levels Ra and Rz for the previously mentioned ducts. The roughness levels are aligned with the previous results, where it can be seen that the lowest roughness is obtained in the R0 stiffened duct, followed by the R90 non-stiffened duct.
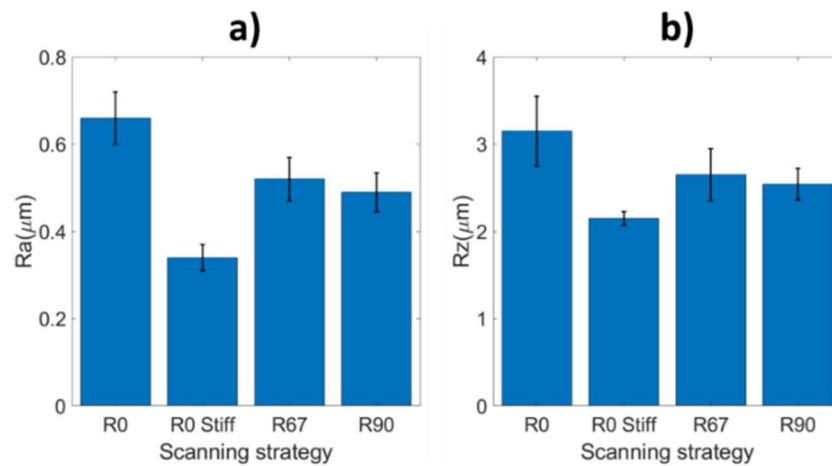
Figure VI-58. Roughness comparison of machined ducts

Figure VI-59 shows the Taylor maps for different laser strategies and shear angles(ϕ_c) as a function of tool inclination angles η and engagement angles θ (see Figure VI-46a,b). The red dash lines correspond to the values of the Taylor factor when the tool is tilted, as in Figure VI-46b (η=45°). The effect of shear angle ϕ_c on the Taylor factor is observed in the sequences of the figures, however the changes in Taylor distribution are not significant, which means that considering a range of ϕ_c between 30° and 45° is logical considering the angle of maximum shear stress.

Based on the above results, it is possible to establish that the selected design (R90 $\varphi1_p = 0$) allowed the best machining stability between the ducts without stiffeners. Although the surface quality is still not desired, the improvements obtained allow us to establish that anisotropy can be used as an optimization strategy to improve the manufacturing processes and even the mechanical properties of the components if a complete multi-objective optimization is carried

out. Additionally, it is essential to highlight that stiffeners allow a high level of stability in the machining process, which complements the improvements made by taking advantage of anisotropy.
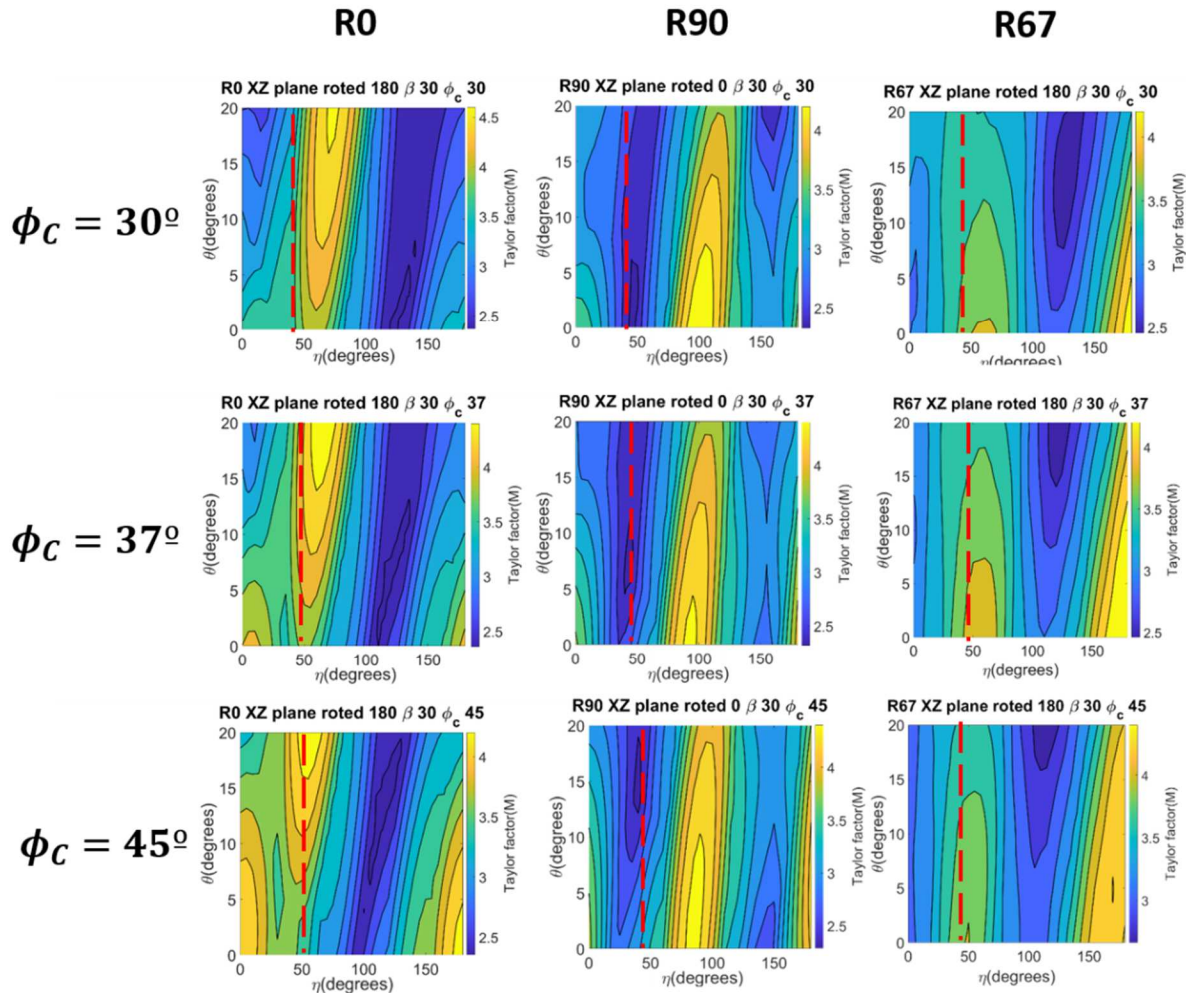
Figure VI-59. Shear strength Taylor maps for different shear angles and laser scanning strategies

Figure VI-60 shows the evolution of the Taylor factor as the tool's engagement progresses. It can be seen that for all the values of ϕ_c the shear strength is lower for the R90 strategy and higher for the R0 strategy. These results align with the experimental results of the strength, roughness, and surface quality measurements.
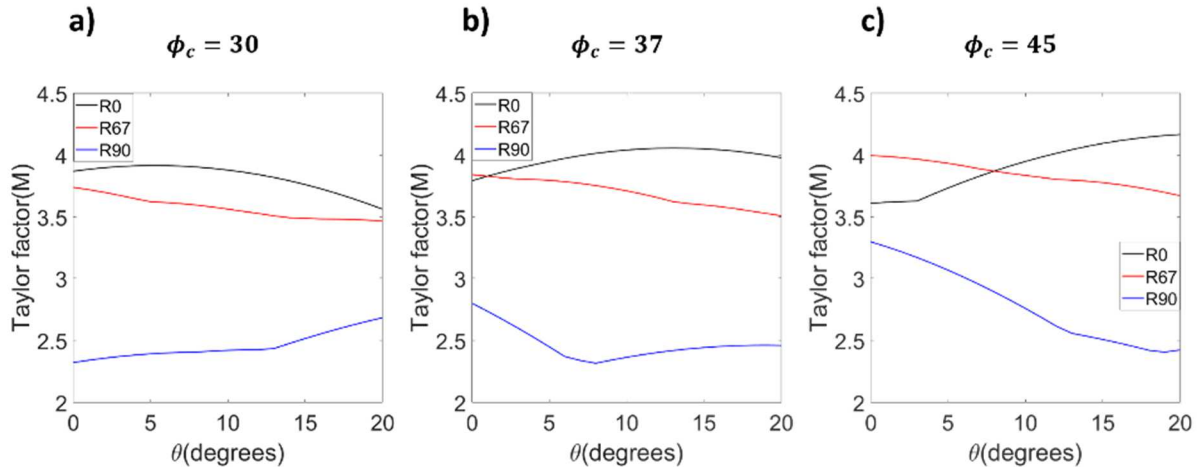
Figure VI-60. Evolution of Taylor factor during tool engagement for different laser strategies. a) ϕ_c=30°, b) ϕ_c=37°, c) ϕ_c=45°

VI.6. Conclusions

This chapter presents a holistic methodology for designing and manufacturing LPBF components, considering the variations in mechanical properties caused by texture-induced anisotropy and using these variations as a strategy to design LPBF parts with laser strategies and part orientation to align external loads with the strongest crystalline orientations. Three case studies are presented where much of the potential of this methodology is evaluated.

In case 1, a methodology for increasing the stiffness of components manufactured using LPBF was proposed in this case study. The cutting forces of the two Inconel 718 samples were characterized using different machining parameters. In addition, the crystalline texture of both samples and their respective elastic tensors were obtained to quantify the effect of anisotropy on Young's modulus. The steps established in the methodology were applied for the first iteration of the design process of the lateral stiffeners, which resulted in a significant improvement in the surface quality compared to a non-stiffened part.

The main results for case 1 are detailed below.

- The proposed methodology for increasing the stiffness of components manufactured by LPBF through the use of temporary lateral stiffeners can be a viable and low-cost alternative for finishing machining operations on this type of component. The machining

operations can be performed with the parts attached to the base plate without additional support fixturing.

- The simulation of the harmonic response of the component by FEM represents a quick way to obtain an initial approximation of the effect of the cutting force on the vibration amplitude. The iterative nature of the proposed methodology implies that the deviation between the actual vibration values and the values obtained via simulation becomes increasingly smaller because the information of the surface quality, cutting forces, and vibration magnitude during the previous iteration allows the design and location of the lateral stiffeners to be improved in the following phases of design iteration and optimization. Therefore, it is essential to develop specific methodologies for the design of lateral stiffeners based on component topology, geometry, and application.

- The similarity between the FEM and measured stiffness shows that the VOIGT-REUSS-HILL theory is an appropriate alternative to obtain the elasticity tensor and quantify the anisotropy in the mechanical properties. In the case evaluated, a 10% increase in Young's modulus was observed in the lt60 sample compared to the lt30 sample for the most extended area of the duct analyzed. In addition, the lt60 sample exhibited a less dense 001 ring-like texture relative to the lt30 sample, which was reflected in a lower level of elastic anisotropy in the lt60 sample compared to the lt30 sample.

- The significant difference in surface quality obtained in the first iteration allowed the establishment of temporary lateral stiffeners to be viable. The roughness profile showed an average maximum difference of 15 microns along the axial direction of the duct in the machined zone for the stiffened duct, whereas this difference increased to more than 90 µm in the unstiffened duct. Similarly, the cutting forces were almost five times higher in the unstiffened duct than in the stiffened duct.

- The analysis of the current stiffening configuration establishes that the stiffness of the ducts should be as homogeneous as possible along the duct perimeter. This implies that the stiffeners should cover the perimeter of the ducts as much as possible.

In the case of study II, the effect of 3 laser scanning strategies and two levels of VED on material physical parameters and mechanical properties are evaluated on IN718 LPBF samples. The main results are detailed below.

- A strong correlation is observed between the texture index J and the grain boundary density, which shows that LPBF configurations that allow obtaining a high texture index, such as R0 low VED or R90 high VED, allow obtaining components with a lower degree

of crystalline misorientation and a higher degree of anisotropy that can be used for the optimization of the mechanical properties.

- Samples with low texture index and high grain boundary density, as in the case of the R67 low VED sample, show better plastic properties than high texture index samples.

- The plates with inclined orientation (β=50º) showed higher stiffness for bending loads than the vertically fabricated plates (β=90º). The increase in stiffness of the inclined plates concerning the vertical plates was around 35-50%, which is significant and valuable in the design. Additionally, in the evaluation of modal parameters and FRF, it was observed that the bending mode frequency increased significantly due to the crystals' orientations relative to the parts' reference system for the vertically fabricated plates.

- The increase in the mechanical properties of the plastic range (YS and UTS) of the samples manufactured with inclined orientation (β=50º) can be explained by the higher level of grain boundary density of these samples to those manufactured with vertical orientation (β=90º).

In the case of study III, the multiobjective optimization methodology proposed in section VI.2.4 was carried out to select design variables that improve stability during machining. For this purpose, a duct with a complex shape requiring milling machining in the upper zone was proposed, and the objective functions, customer requirements, and process constraints were established. The most important results are presented below.

- The step-by-step optimization of the objective functions F2(X) and F4(X) is presented by obtaining Young's modulus and Taylor factor maps according to the different laser strategies used. In addition, it is shown graphically how to obtain orientations of the part that allow optimization of its stiffness for the strain vector field exerted by the first three vibration modes generated by the machining operation and by the position of the tool.

- For the last design stage, the AHP (analytical hierarchy process) technique was used to evaluate several optimal design variables to define the most recommendable manufacturing configuration according to the relative importance of each objective function.

- AHP analysis and multi-objective optimization showed that the fabrication of the ducts with LPBF R90 low VED configuration and with angle $\varphi 1_p = 0$ offered a good balance between low shear strength and stiffness.

- After the design stage, ducts were fabricated under the three strategies studied (R0, R67, and R90) with low VED and $\varphi 1_p = 0$. The R0 ducts were manufactured with easily removable stiffeners, and the ducts were subjected to milling to evaluate surface quality, roughness, and cutting forces. The results showed that R0 ducts with stiffeners showed optimal levels of surface quality, followed by R90 ducts without stiffeners, while ducts made with the R0 strategy without stiffeners had the worst surface quality. This indicates that the methodologies proposed in sections VI.2.4 and VI.2.5 are viable for the design of functional parts manufactured by LPBF.

Chapter VII. Contributions and future research lines

VII. Contributions and future research lines

This chapter summarizes the principal thesis contributions and future research lines associated with and derived from this work.

VII.1. Introduction

This work presents a new perspective for the fabrication of LPBF components in which the microstructural design flexibility of this technology is exploited beyond the geometrical flexibility of LPBF fabricated parts. In this way, the models and methodologies presented complement the traditional ways of designing LPBF components and manufacturing them.

VII.2. Thesis contributions

The most relevant results of this work are summarized in the following scientific contributions.

- A novel methodology is proposed to facilitate the prediction of the mechanical properties and microstructure of components manufactured by LPBF from the repeatability of the crystalline patterns that are associated with the different LPBF configurations.

- A methodology for linking the LPBF process to physical material parameters, mechanical properties, and machining post-processing.

- A methodology for the stiffening of components that require machining through the use of easily removable temporary lateral stiffeners.

- A model for quantifying crystallographic oblique cutting shear strength based on Taylor's theory of microplasticity.

- A model for obtaining instantaneous cutting shear coefficients that are proportional to shear strength and can be integrated with microstructure-based models.

- A model based on multi-objective functions and AHP for determining design variables to optimize mechanical properties and machining stability in a balanced way.

- Analysis and explanation of the effect of laser scanning strategies on the microstructure and crystallography of LPBF components.

- Present the anisotropy of LPBF materials as an opportunity for optimization rather than an obstacle to be avoided.

VII.3. Publications

During the period covered by this research activity, which has given rise to this doctoral thesis, the obtained results and knowledge spread across several scientific papers and a conference paper

VII.3.1. Indexed publications

- **On the Relationship between Cutting Forces and Anisotropy Features in the Milling of LPBF Inconel 718 for near Net Shape Parts.** Pérez-Ruiz, José David, Luis Norberto López de Lacalle, Gorka Urbikain, Octavio Pereira, Silvia Martínez, and Jorge Bris. 2021 *International Journal of Machine Tools and Manufacture* 170 (103801): https://doi.org/10.1016/J.IJMACHTOOLS.2021.103801.

- **Stiffening Near-Net-Shape Functional Parts of Inconel 718 LPBF Considering Material Anisotropy and Subsequent Machining Issues**. Pérez-Ruiz, José David, Felipe Marin, Silvia Martínez, Aitzol Lamikiz, Gorka Urbikain, and Luis Norberto López de Lacalle. 2022." *Mechanical Systems and Signal Processing* 168 (April): 108675. https://doi.org/10.1016/J.YMSSP.2021.108675.

- **Un Proceso Robusto Para El Acabado En Precisión De Piezas Fabricadas Por Impresión Metálica**. Perez Ruiz, Jose David, Silvia Martinez Rodriguez, Luis norberto Lopez de la calle Marcaide, Aitzol Lamikiz Mentxaka, Haizea Gonzalez barrio, and Octavio Pereira neto. 2020. *Dyna Ingenieria E Industria* 95 (1): 436–42. https://doi.org/10.6036/9382.

- (Pérez-Ruiz et al. 2022)

VII.3.2. National and international congresses

- **Deep Hole Finishing of Inconel 718 SLMed Features by Endmilling and Reaming**. Pérez, J D, P Fernandez, A Del Olmo, and L N López De Lacalle. 2021. *IOP Conference Series: Materials Science and Engineering* 1193 (1): 012006. https://doi.org/10.1088/1757-899X/1193/1/012006

VII.4. Future research lines

The presented dissertation opens new lines of interest for future research works, among which should be highlighted the following ones:

- Evaluation of crystalline repeatability patterns for different laser strategies under different geometrical topologies.

- The increased corrosion resistance of components manufactured by LPBF from developing high texture index components.

- Microstructural designs strategies of components for enhanced magnetic and electrical properties for e-mobility applications

- Development of new objective functions and design variables for developing multi-objective optimization software for intelligent design and manufacture of LPBF components.

- Optimization of the tool orientations and trajectories to improve surface integrity after machining of LPBF components.

Bibliography

Adetoro, O. B., and P. H. Wen. 2010. "Prediction of Mechanistic Cutting Force Coefficients Using ALE Formulation." *International Journal of Advanced Manufacturing Technology* 46 (1–4): 79–90. https://doi.org/10.1007/s00170-009-2079-7.

Agmell, Mathias, Volodymyr Bushlya, Rachid M'Saoubi, Oleksandr Gutnichenko, Oleg Zaporozhets, Sampsa Va Laakso, and Jan Eric Ståhl. 2020. "Investigation of Mechanical and Thermal Loads in PcBN Tooling during Machining of Inconel 718." *International Journal of Advanced Manufacturing Technology* 107 (3–4): 1451–62. https://doi.org/10.1007/S00170-020-05081-8/FIGURES/19.

Ahn, T. Y., K. F. Eman, and S. M. Wu. 1985. "Identification of the Transfer Function of Dynamic Cutting Processes — A Comparative Assessment." *International Journal of Machine Tool Design and Research* 25 (1): 75–90. https://doi.org/10.1016/0020-7357(85)90059-9.

Al-Rubaie, Kassim S., Saulo Melotti, Alexsandro Rabelo, José M. Paiva, Mohamed A. Elbestawi, and Stephen C. Veldhuis. 2020. "Machinability of SLM-Produced Ti6Al4V Titanium Alloy Parts." *Journal of Manufacturing Processes* 57 (September): 768–86. https://doi.org/10.1016/J.JMAPRO.2020.07.035.

Alexeev, V. P., A. V. Balyakin, and A. I. Khaimovich. 2017. "Influence of the Direction of Selective Laser Sintering on Machinability of Parts from 316L Steel." *IOP Conference Series: Materials Science and Engineering* 177 (1). https://doi.org/10.1088/1757-899X/177/1/012120.

Altintaş, Y., and E. Budak. 1995. "Analytical Prediction of Stability Lobes in Milling." *CIRP Annals* 44 (1): 357–62. https://doi.org/10.1016/S0007-8506(07)62342-7.

Altintas, Y., A. Spence, and J. Tlusty. 1991. "End Milling Force Algorithms for CAD Systems." *CIRP Annals - Manufacturing Technology* 40 (1): 31–34. https://doi.org/10.1016/S0007-8506(07)61927-1.

Altintas, Yusuf. 2011. *Manufacturing Automation*. *Manufacturing Automation*. Cambridge University Press. https://doi.org/10.1017/cbo9780511843723.

amirmahyar khorasani. 2018. " The Effect of Machining Parameters on Cutting Forces of SLM

Curved Component." In *International Conference of Additive Manufacturing*.

AMPower. 2021. "Metal Additive Manufacturing Market Valued at EUR 2.02 Billion in 2019."
2021. https://additive-manufacturing-report.com/additive-manufacturing-market/.

Amrita, M., and B. Kamesh. 2021. "Optimization of Graphene Based Minimum Quantity
Lubrication of Inconel718 Turning with Multiple Machining Performances." *Materials
Today: Proceedings* 39 (January): 1337–44.
https://doi.org/10.1016/J.MATPR.2020.04.568.

Andersson, Mats, and Jan-Eric Ståhl. 2007. "POLAR MACHINABILITY DIAGRAMS-A MODEL TO
PREDICT THE MACHINABILITY OF A WORK MATERIAL."

ASTM. 2022. "Additive Manufacturing — General Principles — Fundamentals and Vocabulary."
2022. https://www.astm.org/f3177-21.html.

Avdovic, Pajazit, Linhong Xu, Mats Andersson, and Jan Eric Ståhl. 2010. "Evaluating the
Machinability of Inconel 718 Using Polar Diagrams." *Proceedings of the ASME Turbo Expo*
1 (7): 987–96. https://doi.org/10.1115/GT2010-22695.

Baek, Jong Tae, Wan Sik Woo, and Choon Man Lee. 2018. "A Study on the Machining
Characteristics of Induction and Laser-Induction Assisted Machining of AISI 1045 Steel
and Inconel 718." *Journal of Manufacturing Processes* 34 (August): 513–22.
https://doi.org/10.1016/J.JMAPRO.2018.06.030.

Balsamo, Vittorio, Alessandra Caggiano, Krzysztof Jemielniak, Joanna Kossakowska, Miroslaw
Nejman, and Roberto Teti. 2016. "Multi Sensor Signal Processing for Catastrophic Tool
Failure Detection in Turning." *Procedia CIRP* 41 (January): 939–44.
https://doi.org/10.1016/J.PROCIR.2016.01.010.

Bartolomeis, Andrea de, Stephen T. Newman, Dirk Biermann, and Alborz Shokrani. 2021.
"State-of-the-Art Cooling and Lubrication for Machining Inconel 718." *Journal of
Manufacturing Science and Engineering, Transactions of the ASME* 143 (5).
https://doi.org/10.1115/1.4047842/1085360.

Bartolomeis, Andrea De, Stephen T. Newman, I. S. Jawahir, Dirk Biermann, and Alborz
Shokrani. 2021. "Future Research Directions in the Machining of Inconel 718." *Journal of
Materials Processing Technology* 297 (November): 117260.
https://doi.org/10.1016/J.JMATPROTEC.2021.117260.

Barz, A., T. Buer, and H. D. Haasis. 2016. "A Study on the Effects of Additive Manufacturing on the Structure of Supply Networks." *IFAC-PapersOnLine* 49 (2): 72–77. https://doi.org/10.1016/J.IFACOL.2016.03.013.

Basak, Amrita, and Suman Das. 2016. "Epitaxy and Microstructure Evolution in Metal Additive Manufacturing." *Annual Review of Materials Research* 46 (1): 125–49. https://doi.org/10.1146/annurev-matsci-070115-031728.

Bean, G. E., T. D. McLouth, D. B. Witkin, S. D. Sitzman, P. M. Adams, and R. J. Zaldivar. 2019a. "Build Orientation Effects on Texture and Mechanical Properties of Selective Laser Melting Inconel 718." *Journal of Materials Engineering and Performance* 28 (4): 1942–49. https://doi.org/10.1007/s11665-019-03980-w.

———. 2019b. "Build Orientation Effects on Texture and Mechanical Properties of Selective Laser Melting Inconel 718." *Journal of Materials Engineering and Performance* 28 (4): 1942–49. https://doi.org/10.1007/s11665-019-03980-w.

Beaucamp, Anthony, Yoshiharu Namba, and Phillip Charlton. 2015. "Process Mechanism in Shape Adaptive Grinding (SAG)." *CIRP Annals* 64 (1): 305–8. https://doi.org/10.1016/J.CIRP.2015.04.096.

Bittner, F., J. Thielsch, and W. G. Drossel. 2021. "Microstructure and Magnetic Properties of Nd-Fe-B Permanent Magnets Produced by Laser Powder Bed Fusion." *Scripta Materialia* 201 (August): 113921. https://doi.org/10.1016/J.SCRIPTAMAT.2021.113921.

Bonaiti, Giuseppe, Paolo Parenti, Massimiliano Annoni, and Shiv Kapoor. 2017. "Micro-Milling Machinability of DED Additive Titanium Ti-6Al-4V." *Procedia Manufacturing* 10 (January): 497–509. https://doi.org/10.1016/J.PROMFG.2017.07.104.

Bordin, A., S. Bruschi, A. Ghiotti, F. Bucciotti, and L. Facchini. 2014. "Comparison between Wrought and EBM Ti6Al4V Machinability Characteristics." *Key Engineering Materials* 611–612: 1186–93. https://doi.org/10.4028/WWW.SCIENTIFIC.NET/KEM.611-612.1186.

Bordin, A., S. Sartori, S. Bruschi, and A. Ghiotti. 2017. "Experimental Investigation on the Feasibility of Dry and Cryogenic Machining as Sustainable Strategies When Turning Ti6Al4V Produced by Additive Manufacturing." *Journal of Cleaner Production* 142 (January): 4142–51. https://doi.org/10.1016/J.JCLEPRO.2016.09.209.

Bouzid Saï, W., N. Ben Salah, and J. L. Lebrun. 2001. "Influence of Machining by Finishing

Milling on Surface Characteristics." *International Journal of Machine Tools and Manufacture* 41 (3): 443–50. https://doi.org/10.1016/S0890-6955(00)00069-9.

Boyer, R. R., J. D. Cotton, M. Mohaghegh, and R. E. Schafrik. 2015. "Materials Considerations for Aerospace Applications." *MRS Bulletin* 40 (12): 1055–65. https://doi.org/10.1557/MRS.2015.278/FIGURES/5.

Brown, D., C. Li, Z. Y. Liu, X. Y. Fang, and Y. B. Guo. 2018a. "Surface Integrity of Inconel 718 by Hybrid Selective Laser Melting and Milling." *Virtual and Physical Prototyping* 13 (1): 26–31. https://doi.org/10.1080/17452759.2017.1392681.

———. 2018b. "Surface Integrity of Inconel 718 by Hybrid Selective Laser Melting and Milling." *Virtual and Physical Prototyping* 13 (1): 26–31. https://doi.org/10.1080/17452759.2017.1392681.

Budak, E., Y. Altintaş, and E. J.A. Armarego. 1996. "Prediction of Milling Force Coefficients from Orthogonal Cutting Data." *Journal of Manufacturing Science and Engineering, Transactions of the ASME* 118 (2): 216–24. https://doi.org/10.1115/1.2831014.

Budak, Erhan. 1994. "Mechanics and Dynamics of Thin Walled Structures." University of British Columbia. https://doi.org/10.14288/1.0088030.

Bunge, H.-J. (Hans Joachim). 1993. *Texture Analysis in Materials Science : Mathematical Methods*. Cuvillier Verlag. https://books.google.com/books/about/Texture_Analysis_in_Materials_Science.html?hl=es&id=42UoOAAACAAJ.

C.N, Reid. 1973. *Deformation Geometry for Materials Scientists*. *Deformation Geometry for Materials Scientists*. Elsevier. https://doi.org/10.1016/C2013-0-02546-7.

Cai, Xiaojiang, Sheng Qin, Junli Li, Qinglong An, and Ming Chen. 2014. "EXPERIMENTAL INVESTIGATION ON SURFACE INTEGRITY OF END MILLING NICKEL-BASED ALLOY—INCONEL 718." *Http://Dx.Doi.Org/10.1080/10910344.2014.863627* 18 (1): 31–46. https://doi.org/10.1080/10910344.2014.863627.

Caiazzo, Fabrizia, Vittorio Alfieri, Gaetano Corrado, and Paolo Argenio. 2017. "Laser Powder-Bed Fusion of Inconel 718 to Manufacture Turbine Blades." *The International Journal of Advanced Manufacturing Technology 2017 93:9* 93 (9): 4023–31. https://doi.org/10.1007/S00170-017-0839-3.

Calleja, Amaia, Gorka Urbikain, Haizea González, Iker Cerrillo, Roberto Polvorosa, and Aitzol Lamikiz. 2018. "Inconel®718 Superalloy Machinability Evaluation after Laser Cladding Additive Manufacturing Process." *The International Journal of Advanced Manufacturing Technology 2018 97:5* 97 (5): 2873–85. https://doi.org/10.1007/S00170-018-2169-5.

Campa, F. J., L. N. López de Lacalle, A. Lamikiz, and J. A. Sánchez. 2007. "Selection of Cutting Conditions for a Stable Milling of Flexible Parts with Bull-Nose End Mills." *Journal of Materials Processing Technology* 191 (1–3): 279–82. https://doi.org/10.1016/j.jmatprotec.2007.03.023.

Campa, Francisco Javier, Luis Norberto de Lacalle, Gorka Urbicain, Aitzol Lamikiz, Sébastien Seguy, and Lionel Arnaud. 2011. "Critical Thickness and Dynamic Stiffness for Chatter Avoidance in Thin Floors Milling." In *High Speed Machining*, 188:116–21. Advanced Materials Research. Trans Tech Publications Ltd. https://doi.org/10.4028/www.scientific.net/AMR.188.116.

Campbell, Thomas A., and Olga S. Ivanova. 2013. "ADDITIVE MANUFACTURING AS A DISRUPTIVE TECHNOLOGY: IMPLICATIONS OF THREE-DIMENSIONAL PRINTING." *Technology & Innovation* 15 (1): 67–79. https://doi.org/10.3727/194982413X13608676060655.

Careri, Francesco, Domenico Umbrello, Khamis Essa, Moataz M. Attallah, and Stano Imbrogno. 2021. "The Effect of the Heat Treatments on the Tool Wear of Hybrid Additive Manufacturing of IN718." *Wear* 470–471 (April): 203617. https://doi.org/10.1016/J.WEAR.2021.203617.

Carlton, Holly D., Abdel Haboub, Gilbert F. Gallegos, Dilworth Y. Parkinson, and Alastair A. MacDowell. 2016. "Damage Evolution and Failure Mechanisms in Additively Manufactured Stainless Steel." *Materials Science and Engineering: A* 651 (January): 406–14. https://doi.org/10.1016/J.MSEA.2015.10.073.

Çelik, Ali, Melike Sert Alağaç, Servet Turan, Alpagut Kara, and Ferhat Kara. 2017. "Wear Behavior of Solid SiAlON Milling Tools during High Speed Milling of Inconel 718." *Wear* 378–379 (May): 58–67. https://doi.org/10.1016/J.WEAR.2017.02.025.

Chen, Liyong, Qingzhong Xu, Yan Liu, Gangjun Cai, and Jichen Liu. 2021. "Machinability of the Laser Additively Manufactured Inconel 718 Superalloy in Turning." *International Journal of Advanced Manufacturing Technology* 114 (3–4): 871–82.

https://doi.org/10.1007/S00170-021-06940-8/FIGURES/14.

Chen, Ni, Hao Nan Li, Jinming Wu, Zhenjun Li, Liang Li, Gongyu Liu, and Ning He. 2021.
"Advances in Micro Milling: From Tool Fabrication to Process Outcomes." *International
Journal of Machine Tools and Manufacture* 160 (January): 103670.
https://doi.org/10.1016/J.IJMACHTOOLS.2020.103670.

Chen, Niechen, Prashant Barnawal, and Matthew Charles Frank. 2018. "Automated Post
Machining Process Planning for a New Hybrid Manufacturing Method of Additive
Manufacturing and Rapid Machining." *Rapid Prototyping Journal* 24 (7): 1077–90.
https://doi.org/10.1108/RPJ-04-2017-0057.

Chen, Zhen, Shenggui Chen, Zhengying Wei, Lijuan Zhang, Pei Wei, Bingheng Lu, Shuzhe Zhang,
and Yu Xiang. 2018. "Anisotropy of Nickel-Based Superalloy K418 Fabricated by Selective
Laser Melting." *Progress in Natural Science: Materials International* 28 (4): 496–504.
https://doi.org/10.1016/j.pnsc.2018.07.001.

Chlebus, E., K. Gruber, B. Kuźnicka, J. Kurzac, and T. Kurzynowski. 2015. "Effect of Heat
Treatment on the Microstructure and Mechanical Properties of Inconel 718 Processed by
Selective Laser Melting." *Materials Science and Engineering A* 639 (July): 647–55.
https://doi.org/10.1016/j.msea.2015.05.035.

Cho, Jae-Hyung, A. D. Rollett, and K. H. Oh. 2004. "Determination of Volume Fractions of
Texture Components with Standard Distributions in Euler Space." *Metallurgical and
Materials Transactions A* 35 (3): 1075–86. https://doi.org/10.1007/s11661-004-0033-8.

Choudhury, I. A., and M. A. El-Baradie. 1999. "Machinability Assessment of Inconel 718 by
Factorial Design of Experiment Coupled with Response Surface Methodology." *Journal of
Materials Processing Technology* 95 (1–3): 30–39. https://doi.org/10.1016/S0924-
0136(99)00085-0.

Coen, Viktor, Louca Goossens, and Brecht Van Hooreweder. 2022. "Methodology and
Experimental Validation of Analytical Melt Pool Models for Laser Powder Bed Fusion."
Journal of Materials Processing Technology 304 (June): 117547.
https://doi.org/10.1016/J.JMATPROTEC.2022.117547.

Criales, Luis E., Yiğit M. Arısoy, Brandon Lane, Shawn Moylan, Alkan Donmez, and Tuğrul Özel.
2017a. "Laser Powder Bed Fusion of Nickel Alloy 625: Experimental Investigations of
Effects of Process Parameters on Melt Pool Size and Shape with Spatter Analysis."

International Journal of Machine Tools and Manufacture 121 (October): 22–36. https://doi.org/10.1016/j.ijmachtools.2017.03.004.

———. 2017b. "Laser Powder Bed Fusion of Nickel Alloy 625: Experimental Investigations of Effects of Process Parameters on Melt Pool Size and Shape with Spatter Analysis." *International Journal of Machine Tools and Manufacture* 121 (October): 22–36. https://doi.org/10.1016/J.IJMACHTOOLS.2017.03.004.

Cunningham, Ross, Cang Zhao, Niranjan Parab, Christopher Kantzos, Joseph Pauza, Kamel Fezzaa, Tao Sun, and Anthony D. Rollett. 2019. "Keyhole Threshold and Morphology in Laser Melting Revealed by Ultrahigh-Speed x-Ray Imaging." *Science* 363 (6429): 849–52. https://doi.org/10.1126/science.aav4687.

Dai, Chen Wei, Wen Feng Ding, Ye Jun Zhu, Jiu Hua Xu, and Hai Wu Yu. 2018. "Grinding Temperature and Power Consumption in High Speed Grinding of Inconel 718 Nickel-Based Superalloy with a Vitrified CBN Wheel." *Precision Engineering* 52 (April): 192–200. https://doi.org/10.1016/J.PRECISIONENG.2017.12.005.

Dai, Jichun, Mark A. Easton, Mingxing Zhang, Dong Qiu, Xiangyuan Xiong, Wencai Liu, and Guohua Wu. 2014. "Effects of Cooling Rate and Solute Content on the Grain Refinement of Mg-Gd-Y Alloys by Aluminum." *Metallurgical and Materials Transactions A: Physical Metallurgy and Materials Science* 45 (10): 4665–78. https://doi.org/10.1007/s11661-014-2390-2.

Das, M. K., and S. A. Tobias. 1967. "The Relation between the Static and the Dynamic Cutting of Metals." *International Journal of Machine Tool Design and Research* 7 (2): 63–89. https://doi.org/10.1016/0020-7357(67)90026-1.

DebRoy, T., H. L. Wei, J. S. Zuback, T. Mukherjee, J. W. Elmer, J. O. Milewski, A. M. Beese, A. Wilson-Heid, A. De, and W. Zhang. 2018a. "Additive Manufacturing of Metallic Components – Process, Structure and Properties." *Progress in Materials Science* 92 (March): 112–224. https://doi.org/10.1016/J.PMATSCI.2017.10.001.

———. 2018b. "Additive Manufacturing of Metallic Components – Process, Structure and Properties." *Progress in Materials Science*. Elsevier Ltd. https://doi.org/10.1016/j.pmatsci.2017.10.001.

Dere, E. Gözde, Hemant Sharma, Roumen H. Petrov, Jilt Sietsma, and S. Erik Offerman. 2013. "Effect of Niobium and Grain Boundary Density on the Fire Resistance of Fe–C–Mn Steel."

Scripta Materialia 68 (8): 651–54. https://doi.org/10.1016/J.SCRIPTAMAT.2012.12.030.

Didier, P., G. Le Coz, G. Robin, P. Lohmuller, B. Piotrowski, A. Moufki, and P. Laheurte. 2021. "Consideration of SLM Additive Manufacturing Supports on the Stability of Flexible Structures in Finish Milling." *Journal of Manufacturing Processes* 62 (February): 213–20. https://doi.org/10.1016/J.JMAPRO.2020.12.027.

Dilberoglu, Ugur M., Bahar Gharehpapagh, Ulas Yaman, and Melik Dolen. 2017. "The Role of Additive Manufacturing in the Era of Industry 4.0." *Procedia Manufacturing* 11 (January): 545–54. https://doi.org/10.1016/J.PROMFG.2017.07.148.

Dilip, J. J.S., Shanshan Zhang, Chong Teng, Kai Zeng, Chris Robinson, Deepankar Pal, and Brent Stucker. 2017. "Influence of Processing Parameters on the Evolution of Melt Pool, Porosity, and Microstructures in Ti-6Al-4V Alloy Parts Fabricated by Selective Laser Melting." *Progress in Additive Manufacturing* 2 (3): 157–67. https://doi.org/10.1007/s40964-017-0030-2.

Dinda, G. P., A. K. Dasgupta, and J. Mazumder. 2012. "Texture Control during Laser Deposition of Nickel-Based Superalloy." *Scripta Materialia* 67 (5): 503–6. https://doi.org/10.1016/j.scriptamat.2012.06.014.

Dippon, Joerg ;, Haikun ; Ren, Ben Foued, ; Amara, and Yusuf Altintas. 1999. "Orthogonal Cutting Mechanics of Medium Density Fiberboards." *Forest Products Journal* 50.

Du, Wei, Qian Bai, and Bi Zhang. 2016. "A Novel Method for Additive/Subtractive Hybrid Manufacturing of Metallic Parts." *Procedia Manufacturing* 5 (January): 1018–30. https://doi.org/10.1016/J.PROMFG.2016.08.067.

———. 2017. "Machining Characteristics of 18Ni-300 Steel in Additive/Subtractive Hybrid Manufacturing." *The International Journal of Advanced Manufacturing Technology 2017 95:5* 95 (5): 2509–19. https://doi.org/10.1007/S00170-017-1364-0.

Ducroux, Edouard, Guillaume Fromentin, Fabien Viprey, David Prat, and Alain D'Acunto. 2021a. "New Mechanistic Cutting Force Model for Milling Additive Manufactured Inconel 718 Considering Effects of Tool Wear Evolution and Actual Tool Geometry." *Journal of Manufacturing Processes* 64 (April): 67–80. https://doi.org/10.1016/J.JMAPRO.2020.12.042.

———. 2021b. "New Mechanistic Cutting Force Model for Milling Additive Manufactured

Inconel 718 Considering Effects of Tool Wear Evolution and Actual Tool Geometry."
Journal of Manufacturing Processes 64 (April): 67–80.
https://doi.org/10.1016/J.JMAPRO.2020.12.042.

Duocastella, Marti, and Craig B. Arnold. 2012. "Bessel and Annular Beams for Materials
Processing." *Laser & Photonics Reviews* 6 (5): 607–21.
https://doi.org/10.1002/LPOR.201100031.

DuPont, John N., John C. Lippold, and Samuel D. Kiser. 2011. *Introduction to Nickel and Nickel
Alloy Development*. *Welding Metallurgy and Weldability of Nickel-Base Alloys*. John Wiley
& Sons, Inc., Hoboken, New Jersey. https://www.wiley.com/en-
us/Welding+Metallurgy+and+Weldability+of+Nickel+Base+Alloys-p-9780470087145.

Easton, M. A., and D. H. StJohn. 2008. "Improved Prediction of the Grain Size of Aluminum
Alloys That Includes the Effect of Cooling Rate." *Materials Science and Engineering A* 486
(1–2): 8–13. https://doi.org/10.1016/j.msea.2007.11.009.

Ehmann, K. F., S. G. Kapoor, R. E. DeVor, and I. Lazoglu. 1997. "Machining Process Modeling: A
Review." *Journal of Manufacturing Science and Engineering* 119 (4B): 655–63.
https://doi.org/10.1115/1.2836805.

Eschey, C., S. Lutzmann, and M.F. Zaeh. 2009. "Examination of the Powder Spreading Effect in
Electron Beam Melting (EBM)," September. https://doi.org/10.26153/TSW/15110.

ETMM. 2019. "3D Printing a Rocket Engine." 2019. https://www.etmm-online.com/3d-
printing-a-rocket-engine-a-886960/.

Everton, Sarah K., Matthias Hirsch, Petros Stravroulakis, Richard K. Leach, and Adam T. Clare.
2016. "Review of In-Situ Process Monitoring and in-Situ Metrology for Metal Additive
Manufacturing." *Materials & Design* 95 (April): 431–45.
https://doi.org/10.1016/J.MATDES.2016.01.099.

Ezugwu, E. O., D. A. Fadare, J. Bonney, R. B. Da Silva, and W. F. Sales. 2005. "Modelling the
Correlation between Cutting and Process Parameters in High-Speed Machining of Inconel
718 Alloy Using an Artificial Neural Network." *International Journal of Machine Tools and
Manufacture* 45 (12–13): 1375–85.
https://doi.org/10.1016/J.IJMACHTOOLS.2005.02.004.

Fan, Yi Hang, Zhao Peng Hao, Min Li Zheng, Feng Lian Sun, and Shu Cai Yang. 2013. "Study of

Surface Quality in Machining Nickel-Based Alloy Inconel 718." *Int J Adv Manuf Technol* 69 (9–12): 2659–67. https://doi.org/10.1007/s00170-013-5225-1.

Fei, Jixiong, Guoliang Liu, Kaushalendra Patel, and Tuğrul Özel. 2019. "Cutting Force Investigation in Face Milling of Additively Fabricated Nickel Alloy 625 via Powder Bed Fusion." *International Journal of Mechatronics and Manufacturing Systems* 12 (3–4): 196–210. https://doi.org/10.1504/IJMMS.2019.103484.

Ferchow, Julian, Marvin Bühler, Marcel Schlüssel, Livia Zumofen, Christoph Klahn, Urs Hofmann, Andreas Kirchheim, and Mirko Meboldt. 2022. "Design and Validation of a Sheet Metal Clamping System for Additive Manufacturing and Post-Processing." *International Journal of Advanced Manufacturing Technology* 119 (11–12): 7947–67. https://doi.org/10.1007/S00170-022-08773-5/TABLES/7.

Fernandez-Zelaia, Patxi, Vinh Nguyen, Hayley Zhang, Arkadeep Kumar, and Shreyes N. Melkote. 2019. "The Effects of Material Anisotropy on Secondary Processing of Additively Manufactured CoCrMo." *Additive Manufacturing* 29 (October): 100764. https://doi.org/10.1016/j.addma.2019.06.015.

Ferreri, Nicholas C., Sven C. Vogel, and Marko Knezevic. 2020. "Determining Volume Fractions of γ, Γ', Γ", δ, and MC-Carbide Phases in Inconel 718 as a Function of Its Processing History Using an Advanced Neutron Diffraction Procedure." *Materials Science and Engineering: A* 781 (April): 139228. https://doi.org/10.1016/J.MSEA.2020.139228.

Finspång, Trollhättan. 2016. "Additive Manufacturing at Siemens Industrial Turbomachinery AB."

Flynn, Joseph M., Alborz Shokrani, Stephen T. Newman, and Vimal Dhokia. 2016. "Hybrid Additive and Subtractive Machine Tools – Research and Industrial Developments." *International Journal of Machine Tools and Manufacture* 101 (February): 79–101. https://doi.org/10.1016/J.IJMACHTOOLS.2015.11.007.

Ford, Simon, and Mélanie Despeisse. 2016. "Additive Manufacturing and Sustainability: An Exploratory Study of the Advantages and Challenges." *Journal of Cleaner Production* 137 (November): 1573–87. https://doi.org/10.1016/J.JCLEPRO.2016.04.150.

Foster, Jim, Crawford Cullen, Stephen Fitzpatrick, Grant Payne, Liza Hall, and James Marashi. 2019. "Remanufacture of Hot Forging Tools and Dies Using Laser Metal Deposition with Powder and a Hard-Facing Alloy Stellite 21®." *Journal of Remanufacturing* 9 (3): 189–203.

https://doi.org/10.1007/S13243-018-0063-9/FIGURES/13.

Fu, M. W., and J. L. Wang. 2021. "Size Effects in Multi-Scale Materials Processing and Manufacturing." *International Journal of Machine Tools and Manufacture* 167 (August): 103755. https://doi.org/10.1016/J.IJMACHTOOLS.2021.103755.

Furumoto, Tatsuaki, Satoshi Abe, Mitsugu Yamaguchi, and Akira Hosokawa. 2021. "Improving Surface Quality Using Laser Scanning and Machining Strategy Combining Powder Bed Fusion and Machining Processes." *International Journal of Advanced Manufacturing Technology* 117 (11–12): 3405–13. https://doi.org/10.1007/S00170-021-07880-Z/FIGURES/14.

Gaikwad, Aniruddha. n.d. "On Geometric Design Rules and In-Process Build Quality On Geometric Design Rules and In-Process Build Quality Monitoring of Thin-Wall Features Made Using Laser Powder Bed Monitoring of Thin-Wall Features Made Using Laser Powder Bed Fusion Additive Manufac." Accessed December 13, 2022. https://digitalcommons.unl.edu/mechengdiss.

Gajrani, Kishor Kumar. 2020. "Assessment of Cryo-MQL Environment for Machining of Ti-6Al-4V." *Journal of Manufacturing Processes* 60 (December): 494–502. https://doi.org/10.1016/J.JMAPRO.2020.10.038.

Gao, Wei, Yunbo Zhang, Devarajan Ramanujan, Karthik Ramani, Yong Chen, Christopher B. Williams, Charlie C.L. Wang, Yung C. Shin, Song Zhang, and Pablo D. Zavattieri. 2015. "The Status, Challenges, and Future of Additive Manufacturing in Engineering." *Computer-Aided Design* 69 (December): 65–89. https://doi.org/10.1016/J.CAD.2015.04.001.

Gao, Xiangxi, Chunhu Tao, Shengchuan Wu, Bingqing Chen, and Sujun Wu. 2022. "X-Ray Imaging of Defect Population and the Effect on High Cycle Fatigue Life of Laser Additive Manufactured Ti6Al4V Alloys." *International Journal of Fatigue* 162 (September). https://doi.org/10.1016/j.ijfatigue.2022.106979.

Garcés-Chávez, V., D. McGloin, H. Melville, W. Sibbett, and K. Dholakia. 2002. "Simultaneous Micromanipulation in Multiple Planes Using a Self-Reconstructing Light Beam." *Nature 2002 419:6903* 419 (6903): 145–47. https://doi.org/10.1038/nature01007.

Gargalis, Leonidas, Vincenzo Madonna, Paolo Giangrande, Roberto Rocca, Mark Hardy, Ian Ashcroft, Michael Galea, and Richard Hague. 2020. "Additive Manufacturing and Testing of a Soft Magnetic Rotor for a Switched Reluctance Motor." *IEEE Access* 8: 206982–91.

https://doi.org/10.1109/ACCESS.2020.3037190.

Gäumann, M., S. Henry, F. Cléton, J. D. Wagnière, and W. Kurz. 1999. "Epitaxial Laser Metal
Forming: Analysis of Microstructure Formation." *Materials Science and Engineering A* 271
(1–2): 232–41. https://doi.org/10.1016/s0921-5093(99)00202-6.

GE. 2022. "New Manufacturing Milestone: 30,000 Additive Fuel Nozzles | GE Additive." 2022.
https://www.ge.com/additive/stories/new-manufacturing-milestone-30000-additive-
fuel-nozzles.

Gebler, Malte, Anton J.M. Schoot Uiterkamp, and Cindy Visser. 2014. "A Global Sustainability
Perspective on 3D Printing Technologies." *Energy Policy* 74 (C): 158–67.
https://doi.org/10.1016/J.ENPOL.2014.08.033.

Geiger, Fabian, Karsten Kunze, and Thomas Etter. 2016. "Tailoring the Texture of IN738LC
Processed by Selective Laser Melting (SLM) by Specific Scanning Strategies." *Materials
Science and Engineering: A* 661 (April): 240–46.
https://doi.org/10.1016/J.MSEA.2016.03.036.

Godon, A., J. Creus, S. Cohendoz, E. Conforto, X. Feaugas, P. Girault, and C. Savall. 2010.
"Effects of Grain Orientation on the Hall-Petch Relationship in Electrodeposited Nickel
with Nanocrystalline Grains." *Scripta Materialia* 62 (6): 403–6.
https://doi.org/10.1016/j.scriptamat.2009.11.038.

Goel, B.S. 1976. "MEASUREMENT OF DYNAMIC CUTTING FORCE COEFFICIENTS."
https://macsphere.mcmaster.ca/handle/11375/8095.

Goh, G. D., Y. L. Yap, H. K.J. Tan, S. L. Sing, G. L. Goh, and W. Y. Yeong. 2019. "Process–
Structure–Properties in Polymer Additive Manufacturing via Material Extrusion: A
Review." *Https://Doi.Org/10.1080/10408436.2018.1549977* 45 (2): 113–33.
https://doi.org/10.1080/10408436.2018.1549977.

Gokcekaya, Ozkan, Takuya Ishimoto, Shinya Hibino, Jumpei Yasutomi, Takayuki Narushima, and
Takayoshi Nakano. 2021. "Unique Crystallographic Texture Formation in Inconel 718 by
Laser Powder Bed Fusion and Its Effect on Mechanical Anisotropy." *Acta Materialia* 212
(June): 116876. https://doi.org/10.1016/J.ACTAMAT.2021.116876.

Gokuldoss, Prashanth Konda, Sri Kolla, and Jürgen Eckert. 2017. "Additive Manufacturing
Processes: Selective Laser Melting, Electron Beam Melting and Binder Jetting—Selection

Guidelines." *Materials 2017, Vol. 10, Page 672* 10 (6): 672.
https://doi.org/10.3390/MA10060672.

Goldak, John A., and Mehdi Akhlaghi. 2005. *Computational Welding Mechanics*. *Computational Welding Mechanics*. Springer US. https://doi.org/10.1007/B101137/COVER.

Goli, Giacomo, Marco Fioravanti, Rémy Marchal, Luca Uzielli, and Simone Busoni. 2010. "Up-Milling and down-Milling Wood with Different Grain Orientations-the Cutting Forces Behaviour." *European Journal of Wood and Wood Products* 68 (4): 385–95. https://doi.org/10.1007/s00107-009-0374-5.

Gong, Haijun, Khalid Rafi, Hengfeng Gu, Thomas Starr, and Brent Stucker. 2014. "Analysis of Defect Generation in Ti-6Al-4V Parts Made Using Powder Bed Fusion Additive Manufacturing Processes." *Additive Manufacturing*. https://doi.org/10.1016/j.addma.2014.08.002.

Gong, Yadong, and Pengfei Li. 2019. "Analysis of Tool Wear Performance and Surface Quality in Post Milling of Additive Manufactured 316L Stainless Steel." *Journal of Mechanical Science and Technology 2019 33:5* 33 (5): 2387–95. https://doi.org/10.1007/S12206-019-0237-X.

Gonzalo, Oscar, Jokin Beristain, Haritz Jauregi, and Carmen Sanz. 2010a. "A Method for the Identification of the Specific Force Coefficients for Mechanistic Milling Simulation." *International Journal of Machine Tools and Manufacture* 50 (9): 765–74. https://doi.org/10.1016/J.IJMACHTOOLS.2010.05.009.

———. 2010b. "A Method for the Identification of the Specific Force Coefficients for Mechanistic Milling Simulation." *International Journal of Machine Tools and Manufacture* 50 (9): 765–74. https://doi.org/10.1016/J.IJMACHTOOLS.2010.05.009.

Gordon, S, and M T Hillery. 2003. "A Review of the Cutting of Composite Materials." *Proceedings of the Institution of Mechanical Engineers, Part L: Journal of Materials: Design and Applications* 217 (1): 35–45. https://doi.org/10.1177/146442070321700105.

Grigoriev, Sergey N., Andrey V. Gusarov, Alexander S. Metel, Tatiana V. Tarasova, Marina A. Volosova, Anna A. Okunkova, and Andrey S. Gusev. 2022. "Beam Shaping in Laser Powder Bed Fusion: PéClet Number and Dynamic Simulation." *Metals 2022, Vol. 12, Page 722* 12 (5): 722. https://doi.org/10.3390/MET12050722.

Großmann, Alexander, Julian Felger, Tilman Frölich, Julian Gosmann, and Christian Mittelstedt. 2019. "Melt Pool Controlled Laser Powder Bed Fusion for Customised Low-Density Lattice Structures." *Materials & Design* 181 (November): 108054. https://doi.org/10.1016/J.MATDES.2019.108054.

Grove, Thilo, Berend Denkena, Oliver Maiß, Alexander Krödel, Holger Schwab, and Uta Kühn. 2018. "Cutting Mechanism and Surface Integrity in Milling of Ti-5553 Processed by Selective Laser Melting." *Journal of Mechanical Science and Technology* 32 (10): 4883–92. https://doi.org/10.1007/s12206-018-0936-8.

Gruber, Konrad, Irina Smolina, Marcin Kasprowicz, and Tomasz Kurzynowski. 2021. "Evaluation of Inconel 718 Metallic Powder to Optimize the Reuse of Powder and to Improve the Performance and Sustainability of the Laser Powder Bed Fusion (LPBF) Process." *Materials 2021, Vol. 14, Page 1538* 14 (6): 1538. https://doi.org/10.3390/MA14061538.

Guo, Jiang, Ka Hing Au, Chen Nan Sun, Min Hao Goh, Chun Wai Kum, Kui Liu, Jun Wei, Hirofumi Suzuki, and Renke Kang. 2019. "Novel Rotating-Vibrating Magnetic Abrasive Polishing Method for Double-Layered Internal Surface Finishing." *Journal of Materials Processing Technology* 264 (February): 422–37. https://doi.org/10.1016/J.JMATPROTEC.2018.09.024.

Guo, Q. 2020. "In-Situ Full-Field Mapping of Melt Flow Dynamics in Laser Metal Additive Manufacturing." *Addit. Manuf.* 31: 100939.

Gusarov, A. V., and I. Smurov. 2010. "Modeling the Interaction of Laser Radiation with Powder Bed at Selective Laser Melting." *Physics Procedia* 5 (PART 2): 381–94. https://doi.org/10.1016/J.PHPRO.2010.08.065.

H Gong, K Rafi, H Gu, T Starr, B Stucker. 2014. "Analysis of Defect Generation in Ti-6Al-4V Parts Made Using Powder Bed Fusion Additive Manufacturing Processes." *Addit. Manuf.* 1: 87–98.

Hagihara, Koji, Takuya Ishimoto, Masahiro Suzuki, Ryosuke Ozasa, Aira Matsugaki, Pan Wang, and Takayoshi Nakano. 2021. "Factor Which Governs the Feature of Texture Developed during Additive Manufacturing; Clarified from the Study on Hexagonal C40-NbSi2." *Scripta Materialia* 203 (October): 114111. https://doi.org/10.1016/J.SCRIPTAMAT.2021.114111.

Hagihara, Koji, Takayoshi Nakano, Hideaki Maki, Yukichi Umakoshi, and Mitsuo Niinomi. 2016.

"Isotropic Plasticity of β-Type Ti-29Nb-13Ta-4.6Zr Alloy Single Crystals for the Development of Single Crystalline β-Ti Implants." *Scientific Reports 2016 6:1* 6 (1): 1–11. https://doi.org/10.1038/srep29779.

Hagihara, Koji, Takayoshi Nakano, Masahiro Suzuki, Takuya Ishimoto, Suyalatu, and Shi Hai Sun. 2017. "Successful Additive Manufacturing of MoSi2 Including Crystallographic Texture and Shape Control." *Journal of Alloys and Compounds* 696 (March): 67–72. https://doi.org/10.1016/J.JALLCOM.2016.11.191.

Hagihara, Koji, Masayoshi Okubo, Michiaki Yamasaki, and Takayoshi Nakano. 2016. "Crystal-Orientation-Dependent Corrosion Behaviour of Single Crystals of a Pure Mg and Mg-Al and Mg-Cu Solid Solutions." *Corrosion Science* 109 (August): 68–85. https://doi.org/10.1016/J.CORSCI.2016.03.019.

Hansal,W,Hansal,S.,Mann, R&Sandulache. 2019. Electropolishing method and system therefor, issued 2019.

Hansong ji,Munish kumar gupta, quinghua song,wentong cai, tao zheng,youle zhao,zhanquian liu, danil yu pimenov. 2021. "Microstructure and Machinability Evaluation in Micro Milling of Selective Laser Melted Inconel 718 Alloy." *Journal of Materials Research and Technology*.

Hassanin, Hany, Francesco Modica, Mahmoud Ahmed El-Sayed, Jian Liu, and Khamis Essa. 2016. "Manufacturing of Ti–6Al–4V Micro-Implantable Parts Using Hybrid Selective Laser Melting and Micro-Electrical Discharge Machining." *Advanced Engineering Materials* 18 (9): 1544–49. https://doi.org/10.1002/ADEM.201600172.

Herzog, Dirk, Vanessa Seyda, Eric Wycisk, and Claus Emmelmann. 2016. "Additive Manufacturing of Metals." *Acta Materialia* 117 (September): 371–92. https://doi.org/10.1016/j.actamat.2016.07.019.

Higashi, Masaya, and Tomomichi Ozaki. 2020. "Selective Laser Melting of Pure Molybdenum: Evolution of Defect and Crystallographic Texture with Process Parameters." *Materials and Design*. https://doi.org/10.1016/j.matdes.2020.108588.

Hintze, Wolfgang, Robert von Wenserski, Sebastian Junghans, and Carsten Möller. 2020. "Finish Machining of Ti6Al4V SLM Components under Consideration of Thin Walls and Support Structure Removal." *Procedia Manufacturing* 48 (January): 485–91. https://doi.org/10.1016/J.PROMFG.2020.05.072.

Hojati, F., A. Daneshi, B. Soltani, B. Azarhoushang, and D. Biermann. 2020. "Study on Machinability of Additively Manufactured and Conventional Titanium Alloys in Micro-Milling Process." *Precision Engineering* 62 (March): 1–9. https://doi.org/10.1016/J.PRECISIONENG.2019.11.002.

Holmberg, Jonas, Anders Wretland, Johan Berglund, and Tomas Beno. 2020a. "A Detailed Investigation of Residual Stresses after Milling Inconel 718 Using Typical Production Parameters for Assessment of Affected Depth." *Materials Today Communications* 24 (September): 100958. https://doi.org/10.1016/J.MTCOMM.2020.100958.

———. 2020b. "Selection of Milling Strategy Based on Surface Integrity Investigations of Highly Deformed Alloy 718 after Ceramic and Cemented Carbide Milling." *Journal of Manufacturing Processes* 58 (October): 193–207. https://doi.org/10.1016/J.JMAPRO.2020.08.010.

Hong, S. J., W. P. Chen, and T. W. Wang. 2001. "A Diffraction Study of the Γ″ Phase in INCONEL 718 Superalloy." *Metallurgical and Materials Transactions A 2001 32:8* 32 (8): 1887–1901. https://doi.org/10.1007/S11661-001-0002-4.

Hosford, William F. 1993. *The Mechanics of Crystals and Textured Polycrystals (Oxford Engineering Science Series).* Oxford University Press, USA. http://www.amazon.com/Mechanics-Crystals-Textured-Polycrystals-Engineering/dp/019507744X.

Hosseini, E., and V. A. Popovich. 2019. "A Review of Mechanical Properties of Additively Manufactured Inconel 718." *Additive Manufacturing*. Elsevier B.V. https://doi.org/10.1016/j.addma.2019.100877.

Hutchinson, B. 2015. "Critical Assessment 16: Anisotropy in Metals." *Materials Science and Technology* 31: 1393–1401. https://doi.org/10.1179/1743284715Y.0000000118.

Ion, John C. 2005. "Laser Processing of Engineering Materials: Principles, Procedure and Industrial Application." *Laser Processing of Engineering Materials*, 576. https://doi.org/0750660791.

Jambor, Michal, Otakar Bokůvka, František Nový, Libor Trško, and Juraj Belan. 2017. "Phase Transformations in Nickel Base Superalloy Inconel 718 during Cyclic Loading at High Temperature." *Production Engineering Archives* 15 (15): 15–18. https://doi.org/10.30657/PEA.2017.15.04.

Jean Willy, Habimana, Xinwei Li, Yong Hao Tan, Zhe Chen, Mehmet Cagirici, Ramadan Borayek, Tun Seng Herng, Chun Yee Aaron Ong, Chaojiang Li, and Jun Ding. 2020. "Overview of Finite Elements Simulation of Temperature Profile to Estimate Properties of Materials 3D-Printed by Laser Powder-Bed Fusion*." *Chinese Physics B* 29 (4): 048101. https://doi.org/10.1088/1674-1056/AB6D4E.

Ji, Xia, Yongfu Wang, and Steven Y. Liang. 2022. "Analytical Modeling of Temperature Evolution in Laser Powder Bed Fusion Considering the Size and Shape of the Build Part." *Journal of Materials Processing Technology* 301 (March): 117452. https://doi.org/10.1016/J.JMATPROTEC.2021.117452.

Ji, Yanzhou, Lei Chen, and Long Qing Chen. 2018. "Understanding Microstructure Evolution During Additive Manufacturing of Metallic Alloys Using Phase-Field Modeling." *Thermo-Mechanical Modeling of Additive Manufacturing*, January, 93–116. https://doi.org/10.1016/B978-0-12-811820-7.00008-2.

Jiménez, Amaia, Prveen Bidare, Hany Hassanin, Faris Tarlochan, Stefan Dimov, and Khamis Essa. 2021a. "Powder-Based Laser Hybrid Additive Manufacturing of Metals: A Review." *The International Journal of Advanced Manufacturing Technology 2021 114:1* 114 (1): 63–96. https://doi.org/10.1007/S00170-021-06855-4.

———. 2021b. "Powder-Based Laser Hybrid Additive Manufacturing of Metals: A Review." *The International Journal of Advanced Manufacturing Technology 2021 114:1* 114 (1): 63–96. https://doi.org/10.1007/S00170-021-06855-4.

Jing, Zehao, Teng Zhang, Peng Xiu, al -, Michael Munther, Tyler Martin, Ali Tajyar, et al. 2015. "Finishing of Additively Manufactured Titanium Alloy by Shape Adaptive Grinding (SAG)." *Surface Topography: Metrology and Properties* 3 (2): 024001. https://doi.org/10.1088/2051-672X/3/2/024001.

Johansson, J., H. Persson, J. E. Ståhl, J. M. Zhou, V. Bushlya, and F. Schultheiss. 2019. "Machinability Evaluation of Low-Lead Brass Alloys." *Procedia Manufacturing* 38 (January): 1723–30. https://doi.org/10.1016/J.PROMFG.2020.01.102.

JOHNSON, G.R., W.H. Cook, G Johnson, and W Cook. n.d. "A Constitutive Model and Data for Materials Subjected to Large Strains, High Strain Rates, and High Temperatures."

Joshi, Sunil C., and Abdullah A. Sheikh. 2015. "3D Printing in Aerospace and Its Long-Term Sustainability." *Virtual and Physical Prototyping* 10 (4): 175–85.

https://doi.org/10.1080/17452759.2015.1111519.

Kadivar, Mohammadali, Bahman Azarhoushang, Uta Klement, and Peter Krajnik. 2021. "The Role of Specific Energy in Micro-Grinding of Titanium Alloy." *Precision Engineering* 72 (November): 172–83. https://doi.org/10.1016/J.PRECISIONENG.2021.04.015.

Kamaya, Masayuki, Angus J. Wilkinson, and John M. Titchmarsh. 2005. "Measurement of Plastic Strain of Polycrystalline Material by Electron Backscatter Diffraction." *Nuclear Engineering and Design* 235 (6): 713–25. https://doi.org/10.1016/J.NUCENGDES.2004.11.006.

Kan, Wen Hao, Louis Ngai Sam Chiu, Chao Voon Samuel Lim, Yuman Zhu, Yang Tian, Derui Jiang, and Aijun Huang. 2022. "A Critical Review on the Effects of Process-Induced Porosity on the Mechanical Properties of Alloys Fabricated by Laser Powder Bed Fusion." *Journal of Materials Science 2022 57:21* 57 (21): 9818–65. https://doi.org/10.1007/S10853-022-06990-7.

Karayagiz, Kubra, Alaa Elwany, Gustavo Tapia, Brian Franco, Luke Johnson, Ji Ma, Ibrahim Karaman, and Raymundo Arróyave. 2018. "Numerical and Experimental Analysis of Heat Distribution in the Laser Powder Bed Fusion of Ti-6Al-4V." *Https://Doi.Org/10.1080/24725854.2018.1461964* 51 (2): 136–52. https://doi.org/10.1080/24725854.2018.1461964.

Karimi, P., T. Raza, J. Andersson, and L. E. Svensson. 2018. "Influence of Laser Exposure Time and Point Distance on 75-Mm-Thick Layer of Selective Laser Melted Alloy 718." *International Journal of Advanced Manufacturing Technology* 94 (5–8): 2199–2207. https://doi.org/10.1007/s00170-017-1019-1.

Karlsson, Joakim, Anders Snis, Håkan Engqvist, Jukka Lausmaa, Xiaoming Zhao, Jing Chen, Xin Lin, and Weidong Huang. 2013. "Characterization and Comparison of Materials Produced by Electron Beam Melting (EBM) of Two Different Ti–6Al–4V Powder Fractions." *Journal of Materials Processing Technology* 478 (1–2): 119–24. https://doi.org/10.1016/J.MSEA.2007.05.079.

Kaynak, Yusuf, and Ozhan Kitay. 2019. "The Effect of Post-Processing Operations on Surface Characteristics of 316L Stainless Steel Produced by Selective Laser Melting." *Additive Manufacturing* 26 (March): 84–93. https://doi.org/10.1016/J.ADDMA.2018.12.021.

Kaynak, Yusuf, and Emre Tascioglu. 2018. "Finish Machining-Induced Surface Roughness,

Microhardness and XRD Analysis of Selective Laser Melted Inconel 718 Alloy." *Procedia CIRP* 71 (January): 500–504. https://doi.org/10.1016/J.PROCIR.2018.05.013.

———. 2020. "Post-Processing Effects on the Surface Characteristics of Inconel 718 Alloy Fabricated by Selective Laser Melting Additive Manufacturing." *Progress in Additive Manufacturing* 5 (2): 221–34. https://doi.org/10.1007/S40964-019-00099-1/FIGURES/18.

Kegg, R. L. 1965. "Cutting Dynamics in Machine Tool Chatter: Contribution to Machine-Tool Chatter Research—3." *Journal of Engineering for Industry* 87 (4): 464–70. https://doi.org/10.1115/1.3670863.

Khanna, Navneet, Prassan Shah, Chetan Agrawal, Franci Pusavec, and Hussien Hegab. 2020. "Inconel 718 Machining Performance Evaluation Using Indigenously Developed Hybrid Machining Facilities: Experimental Investigation and Sustainability Assessment." *International Journal of Advanced Manufacturing Technology* 106 (11–12): 4987–99. https://doi.org/10.1007/S00170-020-04921-X/TABLES/7.

Kim, Dong Min, Eunju Park, Namhun Kim, and Hyung Wook Park. 2018a. "Experimental Investigation on Tool Wear during the Milling Processes for the Post-Processing of Selective Laser Melted Inconel 718 Alloys." In *ASME 2018 13th International Manufacturing Science and Engineering Conference, MSEC 2018*. Vol. 1. American Society of Mechanical Engineers (ASME). https://doi.org/10.1115/MSEC2018-6561.

———. 2018b. "Experimental Investigation on Tool Wear During the Milling Processes for the Post-Processing of Selective Laser Melted Inconel 718 Alloys." *ASME 2018 13th International Manufacturing Science and Engineering Conference, MSEC 2018* 1 (September). https://doi.org/10.1115/MSEC2018-6561.

Kim, Eun Jung, and Choon Man Lee. 2020. "Experimental Study on Power Consumption of Laser and Induction Assisted Machining with Inconel 718." *Journal of Manufacturing Processes* 59 (November): 411–20. https://doi.org/10.1016/J.JMAPRO.2020.09.064.

King, Wayne E., Holly D. Barth, Victor M. Castillo, Gilbert F. Gallegos, John W. Gibbs, Douglas E. Hahn, Chandrika Kamath, and Alexander M. Rubenchik. 2014a. "Observation of Keyhole-Mode Laser Melting in Laser Powder-Bed Fusion Additive Manufacturing." *J. Mater. Process. Technol.* 214 (12): 2915–25. https://doi.org/10.1016/j.jmatprotec.2014.06.005.

———. 2014b. "Observation of Keyhole-Mode Laser Melting in Laser Powder-Bed Fusion Additive Manufacturing." *Journal of Materials Processing Technology* 214 (12): 2915–25.

https://doi.org/10.1016/J.JMATPROTEC.2014.06.005.

Kirsch, Benjamin, Hendrik Hotz, Jörg Hartig, Sebastian Greco, Marco Zimmermann, and Jan C. Aurich. 2021. "Pendulum and Creep Feed Grinding of Additively Manufactured AISI 316L." *Procedia CIRP* 101 (January): 166–69. https://doi.org/10.1016/J.PROCIR.2020.03.156.

Klahn, Christoph, Bastian Leutenecker, and Mirko Meboldt. 2015. "Design Strategies for the Process of Additive Manufacturing." *Procedia CIRP* 36 (January): 230–35. https://doi.org/10.1016/J.PROCIR.2015.01.082.

Koenigsberger, F., and A. J.P. Sabberwal. 1961. "An Investigation into the Cutting Force Pulsations during Milling Operations." *International Journal of Machine Tool Design and Research* 1 (1–2): 15–33. https://doi.org/10.1016/0020-7357(61)90041-5.

Kok, Y., X. P. Tan, P. Wang, M. L.S. Nai, N. H. Loh, E. Liu, and S. B. Tor. 2018. "Anisotropy and Heterogeneity of Microstructure and Mechanical Properties in Metal Additive Manufacturing: A Critical Review." *Materials & Design* 139 (February): 565–86. https://doi.org/10.1016/J.MATDES.2017.11.021.

Komatsu, Takafumi, Tomoaki Yoshino, Takashi Matsumura, and Shiro Torizuka. 2012. "Effect of Crystal Grain Size in Stainless Steel on Cutting Process in Micromilling." *Procedia CIRP*. https://doi.org/10.1016/j.procir.2012.04.026.

Kromm, A., G. Bruno, T. Thiede, S. Cabeza, N Nadammal, and T. Mishurova. 2018. "Residual Stresses in Selective Laser Melted Samples of a Nickel Based Superalloy." In *Materials Research Proceedings*, 6:259–64. Materials Research Forum LLC. https://doi.org/10.21741/9781945291890-41.

Kurz, W., C. Bezençon, and M. Gäumann. 2001. "Columnar to Equiaxed Transition in Solidification Processing." *Science and Technology of Advanced Materials* 2 (1): 185–91. https://doi.org/10.1016/S1468-6996(01)00047-X.

Kuznetsov, Pavel, Anna Mozhayko, Ivan Shakirov, Vitaliy Bobyr, Mikhail Staritsyn, and Anton Zhukov. 2022. "Modeling of LPBF Scanning Strategy and Its Correlation with the Metallic 316 L, 321, and Alnico Magnets Samples Structure." *Advanced Additive Manufacturing [Working Title]*, May. https://doi.org/10.5772/INTECHOPEN.102073.

Labudovic, M., D. Hu, and R. Kovacevic. 2003. "A Three Dimensional Model for Direct Laser

Metal Powder Deposition and Rapid Prototyping." *Journal of Materials Science 2003 38:1* 38 (1): 35–49. https://doi.org/10.1023/A:1021153513925.

Lamikiz, A., L. N.López De Lacalle, J. A. Sánchez, and M. A. Salgado. 2004. "Cutting Force Estimation in Sculptured Surface Milling." *International Journal of Machine Tools and Manufacture* 44 (14): 1511–26. https://doi.org/10.1016/j.ijmachtools.2004.05.004.

Lamikiz, A., L. N. Lopez De Lacalle, J. A. Sanchez, and U. Bravo. 2005. "Calculation of the Specific Cutting Coefficients and Geometrical Aspects in Sculptured Surface Machining." *Machining Science and Technology* 9 (3): 411–36. https://doi.org/10.1080/15321790500226614.

Langston, Lee S. 2015. "Each Blade a Single Crystal." *American Scientist* 103 (1): 30–33. https://doi.org/10.1511/2015.112.30.

Lawley, A. 2001. "Atomization." *Encyclopedia of Materials: Science and Technology*, January, 387–92. https://doi.org/10.1016/B0-08-043152-6/00077-2.

Layegh K, S. Ehsan, and Ismail Lazoglu. 2014. "A New Identification Method of Specific Cutting Coefficients for Ball End Milling." *Procedia CIRP* 14 (January): 182–87. https://doi.org/10.1016/J.PROCIR.2014.03.059.

Lee, Kang Hyun, and Gun Jin Yun. 2020. "A Novel Heat Source Model for Analysis of Melt Pool Evolution in Selective Laser Melting Process." *Additive Manufacturing* 36 (December): 101497. https://doi.org/10.1016/j.addma.2020.101497.

Lee, Sang Hoon, Koji Hagihara, and Takayoshi Nakano. 2012. "Microstructural and Orientation Dependence of the Plastic Deformation Behavior in SS-Type Ti-15Mo-5Zr-3Al Alloy Single Crystals." *Metallurgical and Materials Transactions A: Physical Metallurgy and Materials Science* 43 (5): 1588–97. https://doi.org/10.1007/S11661-011-0986-3/FIGURES/11.

Lee, W. B., C. F. Cheung, and S. To. 2002. "A Microplasticity Analysis of Micro-Cutting Force Variation in Ultra-Precision Diamond Turning." *Journal of Manufacturing Science and Engineering* 124 (2): 170–77. https://doi.org/10.1115/1.1454108.

Lee, W. B., S. To, Y. K. Sze, and C. F. Cheung. 2003. "Effect of Material Anisotropy on Shear Angle Prediction in Metal Cutting - A Mesoplasticity Approach." In *International Journal of Mechanical Sciences*, 45:1739–49. Pergamon. https://doi.org/10.1016/j.ijmecsci.2003.09.024.

Lee, W. B., and M. Zhou. 1993. "A Theoretical Analysis of the Effect of Crystallographic
Orientation on Chip Formation in Micromachining." *International Journal of Machine
Tools and Manufacture* 33 (3): 439–47. https://doi.org/10.1016/0890-6955(93)90050-5.

Lei, Zhenglong, Jiang Bi, Yanbin Chen, Xi Chen, Xikun Qin, and Ze Tian. 2019. "Effect of Energy
Density on Formability, Microstructure and Micro-Hardness of Selective Laser Melted Sc-
and Zr- Modified 7075 Aluminum Alloy." *Powder Technology* 356 (November): 594–606.
https://doi.org/10.1016/j.powtec.2019.08.082.

Letenneur, Morgan, Alena Kreitcberg, and Vladimir Brailovski. 2019. "Optimization of Laser
Powder Bed Fusion Processing Using a Combination of Melt Pool Modeling and Design of
Experiment Approaches: Density Control." *Journal of Manufacturing and Materials
Processing 2019, Vol. 3, Page 21* 3 (1): 21. https://doi.org/10.3390/JMMP3010021.

Leung, Chu Lun Alex, Sebastian Marussi, Robert C. Atwood, Michael Towrie, Philip J. Withers,
and Peter D. Lee. 2018. "In Situ X-Ray Imaging of Defect and Molten Pool Dynamics in
Laser Additive Manufacturing." *Nat. Commun.* 9 (1). https://doi.org/10.1038/s41467-018-
03734-7.

Lewandowski, John J., and Mohsen Seifi. 2016. "Metal Additive Manufacturing: A Review of
Mechanical Properties." *Http://Dx.Doi.Org/10.1146/Annurev-Matsci-070115-032024* 46
(July): 151–86. https://doi.org/10.1146/ANNUREV-MATSCI-070115-032024.

Li, P., D. H. Warner, A. Fatemi, and N. Phan. 2016. "Critical Assessment of the Fatigue
Performance of Additively Manufactured Ti–6Al–4V and Perspective for Future
Research." *International Journal of Fatigue* 85 (April): 130–43.
https://doi.org/10.1016/J.IJFATIGUE.2015.12.003.

Li, X. P., A. Y.C. Nee, Y. S. Wong, and H. Q. Zheng. 1999. "Theoretical Modelling and Simulation
of Milling Forces." *Journal of Materials Processing Technology* 89–90 (May): 266–72.
https://doi.org/10.1016/S0924-0136(99)00076-X.

Liang, Xiaoliang, Zhanqiang Liu, and Bing Wang. 2019. "State-of-the-Art of Surface Integrity
Induced by Tool Wear Effects in Machining Process of Titanium and Nickel Alloys: A
Review." *Measurement* 132 (January): 150–81.
https://doi.org/10.1016/J.MEASUREMENT.2018.09.045.

Liao, Yunn Shiuan, Chin Hsi Liao, and Hsien Mou Lin. 2017. "Study of Oil-Water Ratio and Flow
Rate of MQL Fluid in High Speed Milling of Inconel 718." *International Journal of Precision*

Engineering and Manufacturing 2017 18:2 18 (2): 257–62.
https://doi.org/10.1007/S12541-017-0033-4.

Lin, Chi-Jen, Yu-Ting Lui, Yu-Fu Lin, Hsian-Bing Wang, Steven Y. Liang, and Jiunn-Jyh Junz Wang.
2021. "Prediction of Shearing and Ploughing Constants in Milling of Inconel 718." *Journal
of Manufacturing and Materials Processing 2021, Vol. 5, Page 8* 5 (1): 8.
https://doi.org/10.3390/JMMP5010008.

Lindgren, Lars Erik. 2001. "Finite Element Modeling and Simulation of Welding. Part 2:
Improved Material Modeling." *Journal of Thermal Stresses* 24 (3): 195–231.
https://doi.org/10.1080/014957301300006380.

Liou, Frank, Kevin Slattery, Mary Kinsella, Joseph Newkirk, Hsin Nan Chou, and Robert Landers.
2007. "Applications of a Hybrid Manufacturing Process for Fabrication of Metallic
Structures." *Rapid Prototyping Journal* 13 (4): 236–44.
https://doi.org/10.1108/13552540710776188/FULL/PDF.

Liu, Chang, Chengzu Ren, Guofeng Wang, Yinwei Yang, and Lu Zhang. 2015. "Study on Surface
Defects in Milling Inconel 718 Super Alloy." *Journal of Mechanical Science and Technology
2015 29:4* 29 (4): 1723–30. https://doi.org/10.1007/S12206-015-0345-1.

Liu, Jian, and Albert C. To. 2017. "Quantitative Texture Prediction of Epitaxial Columnar Grains
in Additive Manufacturing Using Selective Laser Melting." *Additive Manufacturing* 16
(August): 58–64. https://doi.org/10.1016/j.addma.2017.05.005.

Liu, Jinge, and Peng Wen. 2022. "Metal Vaporization and Its Influence during Laser Powder Bed
Fusion Process." *Materials & Design* 215 (March): 110505.
https://doi.org/10.1016/J.MATDES.2022.110505.

Liu, S. Y., H. Q. Li, C. X. Qin, R. Zong, and X. Y. Fang. 2020. "The Effect of Energy Density on
Texture and Mechanical Anisotropy in Selective Laser Melted Inconel 718." *Materials and
Design* 191 (June): 108642. https://doi.org/10.1016/j.matdes.2020.108642.

Liu, Zhaoyang, and Huan Qi. 2015a. "Effects of Processing Parameters on Crystal Growth and
Microstructure Formation in Laser Powder Deposition of Single-Crystal Superalloy."
Journal of Materials Processing Technology 216 (February): 19–27.
https://doi.org/10.1016/J.JMATPROTEC.2014.08.025.

———. 2015b. "Effects of Substrate Crystallographic Orientations on Crystal Growth and

Microstructure Formation in Laser Powder Deposition of Nickel-Based Superalloy." *Acta Materialia* 87 (April): 248–58. https://doi.org/10.1016/J.ACTAMAT.2014.12.046.

———. 2015c. "Effects of Substrate Crystallographic Orientations on Crystal Growth and Microstructure Formation in Laser Powder Deposition of Nickel-Based Superalloy." *Acta Materialia* 87 (April): 248–58. https://doi.org/10.1016/j.actamat.2014.12.046.

Lizzul, Lucia, Marco Sorgato, Rachele Bertolini, Andrea Ghiotti, and Stefania Bruschi. 2020. "Influence of Additive Manufacturing-Induced Anisotropy on Tool Wear in End Milling of Ti6Al4V." *Tribology International* 146 (June): 106200. https://doi.org/10.1016/J.TRIBOINT.2020.106200.

———. 2021. "Anisotropy Effect of Additively Manufactured Ti6Al4V Titanium Alloy on Surface Quality after Milling." *Precision Engineering* 67 (January): 301–10. https://doi.org/10.1016/J.PRECISIONENG.2020.10.003.

López-Castro, J. D., A. Marchal, L. González, and J. Botana. 2017. "Topological Optimization and Manufacturing by Direct Metal Laser Sintering of an Aeronautical Part in 15-5PH Stainless Steel." *Procedia Manufacturing* 13 (January): 818–24. https://doi.org/10.1016/J.PROMFG.2017.09.121.

Lott, Philipp, Henrich Schleifenbaum, Wilhelm Meiners, Konrad Wissenbach, Christian Hinke, and Jan Bültmann. 2011. "Design of an Optical System for the In Situ Process Monitoring of Selective Laser Melting (SLM)." *Physics Procedia* 12 (January): 683–90. https://doi.org/10.1016/J.PHPRO.2011.03.085.

Ma, Jian wei, Fu ji Wang, Zhen yuan Jia, Qiang Xu, and Yan yu Yang. 2014. "Study of Machining Parameter Optimization in High Speed Milling of Inconel 718 Curved Surface Based on Cutting Force." *The International Journal of Advanced Manufacturing Technology 2014 75:1* 75 (1): 269–77. https://doi.org/10.1007/S00170-014-6115-X.

Ma, Mingming, Zemin Wang, and Xiaoyan Zeng. 2017. "A Comparison on Metallurgical Behaviors of 316L Stainless Steel by Selective Laser Melting and Laser Cladding Deposition." *Materials Science and Engineering A* 685 (February): 265–73. https://doi.org/10.1016/j.msea.2016.12.112.

Mahesh, Kore, Jibin T. Philip, S. N. Joshi, and Basil Kuriachen. 2021. "Machinability of Inconel 718: A Critical Review on the Impact of Cutting Temperatures." *Https://Doi.Org/10.1080/10426914.2020.1843671* 36 (7): 753–91.

https://doi.org/10.1080/10426914.2020.1843671.

Make. 2012. "Single Crystal Superalloys - Make:" 2012.
https://makezine.com/article/science/single-crystal-superalloys/.

Malakizadi, Amir, Tina Hajali, Fiona Schulz, Stefan Cedergren, Joakim Ålgårdh, Rachid
M'Saoubi, Eduard Hryha, and Peter Krajnik. 2021. "The Role of Microstructural
Characteristics of Additively Manufactured Alloy 718 on Tool Wear in Machining."
International Journal of Machine Tools and Manufacture 171 (December): 103814.
https://doi.org/10.1016/J.IJMACHTOOLS.2021.103814.

Mali, Rahul, M. T. Telsang, and T. V.K. Gupta. 2017. "Real Time Tool Wear Condition
Monitoring in Hard Turning of Inconel 718 Using Sensor Fusion System." *Materials Today:
Proceedings* 4 (8): 8605–12. https://doi.org/10.1016/J.MATPR.2017.07.208.

Mallipeddi, D., T. Hajali, L. E. Rännar, A. Bergström, S. Hernandez, E. Strandh, L. Nyborg, and P.
Krajnik. 2020. "Surface Integrity of Machined Electron Beam Melted Ti6Al4V Alloy
Manufactured with Different Contour Settings and Heat Treatment." *Procedia CIRP* 87
(January): 327–32. https://doi.org/10.1016/J.PROCIR.2020.02.091.

Mani, Mahesh, Haeseong Jee, and Paul Witherell. 2017. "Design Rules for Additive
Manufacturing: A Categorization." In *Proceedings of the ASME Design Engineering
Technical Conference*. Vol. 1. https://doi.org/10.1115/DETC2017-68446.

Manogharan, Guha, Richard A Wysk, and Ola L.A. Harrysson. 2015. "Additive Manufacturing–
Integrated Hybrid Manufacturing and Subtractive Processes: Economic Model and
Analysis." *International Journal of Computer Integrated Manufacturing* 29 (5): 473–88.
https://doi.org/10.1080/0951192X.2015.1067920.

Manogharan, Guhaprasanna. 2014. "Hybrid Manufacturing: Analysis of Integrating Additive
and Subtractive Methods." https://repository.lib.ncsu.edu/handle/1840.16/9663.

Manvatkar, V., A. De, and T. Debroy. 2014. "Heat Transfer and Material Flow during Laser
Assisted Multi-Layer Additive Manufacturing." *Journal of Applied Physics* 116 (12):
124905. https://doi.org/10.1063/1.4896751.

Manvatkar, V., A. De, and T. DebRoy. 2014. "Spatial Variation of Melt Pool Geometry, Peak
Temperature and Solidification Parameters during Laser Assisted Additive Manufacturing
Process." *Https://Doi.Org/10.1179/1743284714Y.0000000701* 31 (8): 924–30.

https://doi.org/10.1179/1743284714Y.0000000701.

Mao, Zhongquan, Zhenhui He, Dihu Chen, W. Y. Cheung, and S. P. Wong. 2007. "Crystal Orientation Dependence of Ferromagnetism in Fe-Implanted MgO Single Crystals." *Solid State Communications* 142 (6): 329–32. https://doi.org/10.1016/J.SSC.2007.02.038.

Marattukalam, Jithin James, Dennis Karlsson, Victor Pacheco, Přemysl Beran, Urban Wiklund, Ulf Jansson, Björgvin Hjörvarsson, and Martin Sahlberg. 2020. "The Effect of Laser Scanning Strategies on Texture, Mechanical Properties, and Site-Specific Grain Orientation in Selective Laser Melted 316L SS." *Materials & Design* 193 (August): 108852. https://doi.org/10.1016/J.MATDES.2020.108852.

Marketresearchfuture. 2022. "Aerospace Additive Manufacturing Market - Global Forecast 2027 | MRFR." 2022. https://www.marketresearchfuture.com/reports/aerospace-additive-manufacturing-market-1551.

Martukanitz, Richard, Pan Michaleris, Todd Palmer, Tarasankar DebRoy, Zi Kui Liu, Richard Otis, Tae Wook Heo, and Long Qing Chen. 2014. "Toward an Integrated Computational System for Describing the Additive Manufacturing Process for Metallic Materials." *Additive Manufacturing* 1–4 (October): 52–63. https://doi.org/10.1016/J.ADDMA.2014.09.002.

Matthews, M. J., T. T. Roehling, S. A. Khairallah, T. U. Tumkur, G. Guss, R. Shi, J. D. Roehling, et al. 2020. "Controlling Melt Pool Shape, Microstructure and Residual Stress in Additively Manufactured Metals Using Modified Laser Beam Profiles." *Procedia CIRP* 94 (January): 200–204. https://doi.org/10.1016/J.PROCIR.2020.09.038.

Mehmeti, Aldi, Pavel Penchev, Donal Lynch, Denis Vincent, Nathalie Maillol, Johannes Maurath, Julien Bajolet, David Ian Wimpenny, Khamis Essa, and Stefan Dimov. 2020. "Mechanical Behaviour and Interface Evaluation of Hybrid MIM/PBF Stainless Steel Components." *Rapid Prototyping Journal* 26 (10): 1809–25. https://doi.org/10.1108/RPJ-10-2019-0256/FULL/PDF.

Mendoza, Michael Y., Peyman Samimi, David A. Brice, Iman Ghamarian, Matt Rolchigo, Richard LeSar, and Peter C. Collins. 2019. "On the Role of Composition and Processing Parameters on the Microstructure Evolution of Ti-XMo Alloys." *BMC Chemistry* 13 (3): 1–8. https://doi.org/10.1186/s13065-019-0529-3.

Merchant, M. Eugene. 1944. "Basic Mechanics of the Metal-Cutting Process." *Journal of Applied Mechanics* 11 (3): A168–75. https://doi.org/10.1115/1.4009380.

Milton, Samuel, Arnaud Duchosal, Florent Chalon, René Leroy, and Antoine Morandeau. 2019. "Thermal Study during Milling of Ti6Al4V Produced by Electron Beam Melting (EBM) Process." *Journal of Manufacturing Processes* 38 (February): 256–65. https://doi.org/10.1016/J.JMAPRO.2018.12.027.

Milton, Samuel, Antoine Morandeau, Florent Chalon, and Rene Leroy. 2016. "Influence of Finish Machining on the Surface Integrity of Ti6Al4V Produced by Selective Laser Melting." *Procedia CIRP* 45 (January): 127–30. https://doi.org/10.1016/J.PROCIR.2016.02.340.

Milton, Samuel, Olivier Rigo, Sebastien LeCorre, Antoine Morandeau, Raveendra Siriki, Philippe Bocher, and René Leroy. 2021. "Microstructure Effects on the Machinability Behaviour of Ti6Al4V Produced by Selective Laser Melting and Electron Beam Melting Process." *Materials Science and Engineering: A* 823 (August): 141773. https://doi.org/10.1016/J.MSEA.2021.141773.

Mishra, Sarvesh Kumar, Gaizka Gómez-Escudero, Haizea González-Barrio, Amaia Calleja-Ochoa, Silvia Martinez, Michale Barton, and Luis Norberto Lopez de Lacalle. 2022. "Machining-Induced Characteristics of Microstructure-Supported LPBF-IN718 Curved Thin Walls." *Procedia CIRP* 108 (January): 176–81. https://doi.org/10.1016/J.PROCIR.2022.03.031.

Mishurova, Tatiana, Sandra Cabeza, Tobias Thiede, Naresh Nadammal, Arne Kromm, Manuela Klaus, Christoph Genzel, Christoph Haberland, and Giovanni Bruno. 2018. "The Influence of the Support Structure on Residual Stress and Distortion in SLM Inconel 718 Parts." *Metallurgical and Materials Transactions A* 49 (7): 3038–46. https://doi.org/10.1007/s11661-018-4653-9.

Monaca, Andrea la, James W. Murray, Zhirong Liao, Alistair Speidel, Jose A. Robles-Linares, Dragos A. Axinte, Mark C. Hardy, and Adam T. Clare. 2021. "Surface Integrity in Metal Machining - Part II: Functional Performance." *International Journal of Machine Tools and Manufacture* 164 (May): 103718. https://doi.org/10.1016/J.IJMACHTOOLS.2021.103718.

Mosier, Charles, and Larry Taube. 1985. "The Facets of Group Technology and Their Impacts on Implementation—A State-of-the-Art Survey." *Omega* 13 (5): 381–91. https://doi.org/10.1016/0305-0483(85)90066-0.

Moufki, A., G. Le Coz, and D. Dudzinski. 2017. "End-Milling of Inconel 718 Superalloy-An Analytical Modelling." In *Procedia CIRP*, 58:358–63. Elsevier B.V.

https://doi.org/10.1016/j.procir.2017.03.330.

Mouritz, Adrian. 2012. "Strengthening of Metal Alloys." In *Introduction to Aerospace Materials*, 57–90. Woodhead Publishing. https://doi.org/10.1533/9780857095152.57.

Moussa, C., M. Bernacki, R. Besnard, and N. Bozzolo. 2017. "Statistical Analysis of Dislocations and Dislocation Boundaries from EBSD Data." *Ultramicroscopy* 179 (August): 63–72. https://doi.org/10.1016/j.ultramic.2017.04.005.

Moussaoui, K., W. Rubio, M. Mousseigne, T. Sultan, and F. Rezai. 2018. "Effects of Selective Laser Melting Additive Manufacturing Parameters of Inconel 718 on Porosity, Microstructure and Mechanical Properties." *Materials Science and Engineering A* 735 (September): 182–90. https://doi.org/10.1016/j.msea.2018.08.037.

Mullin, R., M. Farhadmanesh, A. Ahmadian, and K. Ahmadi. 2020. "Modeling and Identification of Cutting Forces in Milling of Carbon Fibre Reinforced Polymers." *Journal of Materials Processing Technology* 280 (June): 116595. https://doi.org/10.1016/j.jmatprotec.2020.116595.

Mumtaz, K. A., and N. Hopkinson. 2010. "Selective Laser Melting of Thin Wall Parts Using Pulse Shaping." *Journal of Materials Processing Technology* 210 (2): 279–87. https://doi.org/10.1016/J.JMATPROTEC.2009.09.011.

Nadammal, Naresh, Sandra Cabeza, Tatiana Mishurova, Tobias Thiede, Arne Kromm, Christoph Seyfert, Lena Farahbod, et al. 2017. "Effect of Hatch Length on the Development of Microstructure, Texture and Residual Stresses in Selective Laser Melted Superalloy Inconel 718." *Materials and Design* 134 (November): 139–50. https://doi.org/10.1016/j.matdes.2017.08.049.

Nafar Dastgerdi, Jairan, Omid Jaberi, and Heikki Remes. 2022. "Influence of Internal and Surface Defects on the Fatigue Performance of Additively Manufactured Stainless Steel 316L." *International Journal of Fatigue* 163 (October): 107025. https://doi.org/10.1016/j.ijfatigue.2022.107025.

Nagalingam, Arun Prasanth, Hemanth Kumar Yuvaraj, and S. H. Yeo. 2020. "Synergistic Effects in Hydrodynamic Cavitation Abrasive Finishing for Internal Surface-Finish Enhancement of Additive-Manufactured Components." *Additive Manufacturing* 33 (May): 101110. https://doi.org/10.1016/J.ADDMA.2020.101110.

Neikov, Oleg D. 2009. "Atomization and Granulation." *Handbook of Non-Ferrous Metal Powders*, January, 102–42. https://doi.org/10.1016/B978-1-85617-422-0.00005-7.

Ni, Chenbing, Lida Zhu, Zhongpeng Zheng, Jiayi Zhang, Yun Yang, Jin Yang, Yuchao Bai, Can Weng, Wen Feng Lu, and Hao Wang. 2020. "Effect of Material Anisotropy on Ultra-Precision Machining of Ti-6Al-4V Alloy Fabricated by Selective Laser Melting." *Journal of Alloys and Compounds* 848 (December): 156457. https://doi.org/10.1016/j.jallcom.2020.156457.

Ni, Mang, Chao Chen, Xiaojun Wang, Pengwei Wang, Ruidi Li, Xiaoyong Zhang, and Kechao Zhou. 2017a. "Anisotropic Tensile Behavior of in Situ Precipitation Strengthened Inconel 718 Fabricated by Additive Manufacturing." *Materials Science and Engineering A* 701 (July): 344–51. https://doi.org/10.1016/j.msea.2017.06.098.

———. 2017b. "Anisotropic Tensile Behavior of in Situ Precipitation Strengthened Inconel 718 Fabricated by Additive Manufacturing." *Materials Science and Engineering: A* 701 (July): 344–51. https://doi.org/10.1016/J.MSEA.2017.06.098.

Nieh, T. G., L. M. Hsiung, J. Wadsworth, and R. Kaibyshev. 1998. "High Strain Rate Superplasticity in a Continuously Recrystallized Al–6%Mg–0.3%Sc Alloy." *Acta Materialia* 46 (8): 2789–2800. https://doi.org/10.1016/S1359-6454(97)00452-7.

NIST. 2020. "Qualification for Additive Manufacturing Materials, Processes, and Parts | NIST." 2020. https://www.nist.gov/programs-projects/qualification-additive-manufacturing-materials-processes-and-parts.

Oliveira, Amanda Rossi de, and Erik Gustavo Del Conte. 2021. "Concurrent Improvement of Surface Roughness and Residual Stress of As-Built and Aged Additively Manufactured Maraging Steel Post-Processed by Milling." *International Journal of Advanced Manufacturing Technology* 116 (7–8): 2309–23. https://doi.org/10.1007/S00170-021-07527-Z/FIGURES/15.

Oliveira Campos, Fábio de, Anna Carla Araujo, André Luiz Jardini Munhoz, and Shiv Gopal Kapoor. 2020. "The Influence of Additive Manufacturing on the Micromilling Machinability of Ti6Al4V: A Comparison of SLM and Commercial Workpieces." *Journal of Manufacturing Processes* 60 (December): 299–307. https://doi.org/10.1016/J.JMAPRO.2020.10.006.

Olleak, Alaa, and Zhimin Xi. 2020. "Efficient LPBF Process Simulation Using Finite Element

Modeling with Adaptive Remeshing for Distortions and Residual Stresses Prediction."
Manufacturing Letters 24 (April): 140–44.
https://doi.org/10.1016/J.MFGLET.2020.05.002.

Olovsjö, Stefan, Peter Hammersberg, Pajazit Avdovic, Jan Eric Ståhl, and Lars Nyborg. 2011.
"Methodology for Evaluating Effects of Material Characteristics on Machinability—Theory
and Statistics-Based Modelling Applied on Alloy 718." *The International Journal of
Advanced Manufacturing Technology 2011 59:1* 59 (1): 55–66.
https://doi.org/10.1007/S00170-011-3503-3.

Olvera, D., A. Elías-Zúñiga, O. Martínez-Romero, L. N. López de Lacalle, H. Martínez-Alfaro, H.
R. Siller, and M. W. Pineda. 2016. "Improved Predictions of the Stability Lobes for Milling
Cutting Operations of Thin-Wall Components by Considering Ultra-Miniature
Accelerometer Mass Effects." *International Journal of Advanced Manufacturing
Technology* 86 (5–8): 2139–46. https://doi.org/10.1007/s00170-015-8287-4.

optics.org. 2016. "SLM-Based Prototyping Speeds Turbine Blade Design." 2016.
https://optics.org/news/7/7/17.

Ostra, Txomin, Unai Alonso, Fernando Veiga, Mikel Ortiz, Pedro Ramiro, and Amaia Alberdi.
2019. "Analysis of the Machining Process of Inconel 718 Parts Manufactured by Laser
Metal Deposition." *Materials 2019, Vol. 12, Page 2159* 12 (13): 2159.
https://doi.org/10.3390/MA12132159.

Oxley, P. L. B. (Peter Louis Brennan). 1989. *The Mechanics of Machining : An Analytical
Approach to Assessing Machinability*. E. Horwood.

Oxley, P. L.B. 1961. "A Strain-Hardening Solution for the 'Shear Angle' in Orthogonal Metal
Cutting." *International Journal of Mechanical Sciences* 3 (1–2): 68–79.
https://doi.org/10.1016/0020-7403(61)90039-X.

Oyelola, Olusola, Pete Crawforth, Rachid M'Saoubi, and Adam T. Clare. 2018. "On the
Machinability of Directed Energy Deposited Ti6Al4V." *Additive Manufacturing* 19
(January): 39–50. https://doi.org/10.1016/J.ADDMA.2017.11.005.

Papanikolaou, Michail, and Konstantinos Salonitis. 2021. "Grain Size Effects on Nanocutting
Behaviour Modelling Based on Molecular Dynamics Simulations." *Applied Surface Science*
540 (February): 148291. https://doi.org/10.1016/J.APSUSC.2020.148291.

Parimi, Lakshmi L., G. Ravi, Daniel Clark, and Moataz M. Attallah. 2014. "Microstructural and Texture Development in Direct Laser Fabricated IN718." *Materials Characterization* 89 (March): 102–11. https://doi.org/10.1016/j.matchar.2013.12.012.

Park, Eunju, Dong Min Kim, Hyung Wook Park, Young Bin Park, and Namhun Kim. 2020. "Evaluation of Tool Life in the Dry Machining of Inconel 718 Parts from Additive Manufacturing (AM)." *International Journal of Precision Engineering and Manufacturing* 21 (1): 57–65. https://doi.org/10.1007/S12541-019-00275-X/FIGURES/9.

Patel, Kaushalendra, Jixiong Fei, Guoliang Liu, and Tuğrul Özel. 2019. "Milling Investigations and Yield Strength Calculations for Nickel Alloy Inconel 625 Manufactured with Laser Powder Bed Fusion Process." *Production Engineering* 13 (6): 693–702. https://doi.org/10.1007/S11740-019-00922-2/FIGURES/10.

Pelayo, Gorka Urbikain. 2019. "Modelling of Static and Dynamic Milling Forces in Inclined Operations with Circle-Segment End Mills." *Precision Engineering* 56 (March): 123–35. https://doi.org/10.1016/J.PRECISIONENG.2018.11.007.

Penchev, Pavel, Debajyoti Bhaduri, Luke Carter, Aldi Mehmeti, Khamis Essa, Stefan Dimov, Nicholas J.E. Adkins, et al. 2019. "System-Level Integration Tools for Laser-Based Powder Bed Fusion Enabled Process Chains." *Journal of Manufacturing Systems* 50 (January): 87–102. https://doi.org/10.1016/J.JMSY.2018.12.003.

Pereira, O., G. Urbikain, A. Rodríguez, A. Fernández-Valdivielso, A. Calleja, I. Ayesta, and L. N.López de Lacalle. 2017. "Internal Cryolubrication Approach for Inconel 718 Milling." *Procedia Manufacturing* 13 (January): 89–93. https://doi.org/10.1016/J.PROMFG.2017.09.013.

Pereira, Octavio, Ainhoa Celaya, Gorka Urbikaín, Adrián Rodríguez, Asier Fernández-Valdivielso, and L. Noberto López de Lacalle. 2020. "CO2 Cryogenic Milling of Inconel 718: Cutting Forces and Tool Wear." *Journal of Materials Research and Technology* 9 (4): 8459–68. https://doi.org/10.1016/J.JMRT.2020.05.118.

Pérez-Ruiz, José David, Luis Norberto López de Lacalle, Gorka Urbikain, Octavio Pereira, Silvia Martínez, and Jorge Bris. 2021. "On the Relationship between Cutting Forces and Anisotropy Features in the Milling of LPBF Inconel 718 for near Net Shape Parts." *International Journal of Machine Tools and Manufacture* 170 (103801). https://doi.org/10.1016/J.IJMACHTOOLS.2021.103801.

Pérez-Ruiz, José David, Felipe Marin, Silvia Martínez, Aitzol Lamikiz, Gorka Urbikain, and Luis Norberto López de Lacalle. 2022. "Stiffening Near-Net-Shape Functional Parts of Inconel 718 LPBF Considering Material Anisotropy and Subsequent Machining Issues." *Mechanical Systems and Signal Processing* 168 (April): 108675. https://doi.org/10.1016/J.YMSSP.2021.108675.

Pérez, J D, P Fernandez, A Del Olmo, and L N López De Lacalle. 2021. "Deep Hole Finishing of Inconel 718 SLMed Features by Endmilling and Reaming." *IOP Conference Series: Materials Science and Engineering* 1193 (1): 012006. https://doi.org/10.1088/1757-899X/1193/1/012006.

Pérez, José David, Heriberto Maury, Jorge Bris, and Marianella Ojeda. 2020. "Thermomechanical Modeling of a Sleeve Rehabilitation System for Pressure Pipes." *Journal of Pressure Vessel Technology* 142 (6). https://doi.org/10.1115/1.4047443.

Perez Ruiz, Jose David, Silvia Martinez Rodriguez, Luis norberto Lopez de la calle Marcaide, Aitzol Lamikiz Mentxaka, Haizea Gonzalez barrio, and Octavio Pereira neto. 2020. "Un Proceso Robusto Para El Acabado En Precisión De Piezas Fabricadas Por Impresión Metálica." *Dyna Ingenieria E Industria* 95 (1): 436–42. https://doi.org/10.6036/9382.

Periane, S., A. Duchosal, S. Vaudreuil, H. Chibane, A. Morandeau, M. Anthony Xavior, and R. Leroy. 2020. "Selection of Machining Condition on Surface Integrity of Additive and Conventional Inconel 718." *Procedia CIRP* 87 (January): 333–38. https://doi.org/10.1016/J.PROCIR.2020.02.092.

Peters, Jacques, Paul Vanherck, and Hendrik Van Brussel. 1971. "The Measurement of the Dynamic Cutting Coefficient." *CIRP Annals-Manufacturing Technology*. https://lirias.kuleuven.be/1746594.

Pham, Minh Son, Bogdan Dovgyy, Paul A. Hooper, Christopher M. Gourlay, and Alessandro Piglione. 2020a. "The Role of Side-Branching in Microstructure Development in Laser Powder-Bed Fusion." *Nature Communications* 11 (1): 1–12. https://doi.org/10.1038/s41467-020-14453-3.

———. 2020b. "The Role of Side-Branching in Microstructure Development in Laser Powder-Bed Fusion." *Nature Communications* 11 (1): 1–12. https://doi.org/10.1038/s41467-020-14453-3.

Piqué, Alberto, James M. Fitz-Gerald, Philip D. Rack, Bradley Ringeisen, Daniel Young, Rohit

Modi, Ray Auyeung, and Huey-Daw Wu. 2002. "Chapter 17 – Matrix Assisted Pulsed Laser Evaporation-Direct Write (Maple-Dw): A New Method to Rapidly Prototype Organic and Inorganic Materials." *Direct-Write Technologies for Rapid Prototyping*, 517–53.

Polák, J. 2016. "Cyclic Deformation, Crack Initiation, and Low-Cycle Fatigue." In *Reference Module in Materials Science and Materials Engineering*. Elsevier. https://doi.org/10.1016/B978-0-12-803581-8.00890-0.

Przybyla, Craig. 2005. "Methodology for Determining the Variance of the Taylor Factor: Application in Fe-3%Si." *Theses and Dissertations*. https://scholarsarchive.byu.edu/etd/687.

Qu, Minglei, Qilin Guo, Luis I. Escano, Ali Nabaa, S. Mohammad H. Hojjatzadeh, Zachary A. Young, and Lianyi Chen. 2022. "Controlling Process Instability for Defect Lean Metal Additive Manufacturing." *Nature Communications 2022 13:1* 13 (1): 1–8. https://doi.org/10.1038/s41467-022-28649-2.

Rahim Abadi, Seyyed Mohammad Ali Noori, Yongcui Mi, Fredrik Sikström, and Isabelle Choquet. 2020. "Influence of Laser Beam Shaping on Melt Pool Thermocapillary Flow." *Proceedings of the World Congress on Mechanical, Chemical, and Material Engineering*, 1–9. https://doi.org/10.11159/HTFF20.125.

Rahman, M., W. K.H. Seah, and T. T. Teo. 1997. "The Machinability of Inconel 718." *Journal of Materials Processing Technology* 63 (1–3): 199–204. https://doi.org/10.1016/S0924-0136(96)02624-6.

Ramoni, Monsuru, Ragavanantham Shanmugam, Nimel Sworna Ross, and Munish Kumar Gupta. 2021. "An Experimental Investigation of Hybrid Manufactured SLM Based Al-Si10-Mg Alloy under Mist Cooling Conditions." *Journal of Manufacturing Processes* 70 (October): 225–35. https://doi.org/10.1016/J.JMAPRO.2021.08.045.

Rappaz, M., S. A. David, J. M. Vitek, and L. A. Boatner. 1989. "Development of Microstructures in Fe-15Ni-15Cr Single Crystal Electron Beam Welds." *Metallurgical Transactions A* 20 (6): 1125–38. https://doi.org/10.1007/BF02650147.

Rappaz, M., and Ch A. Gandin. 1993. "Probabilistic Modelling of Microstructure Formation in Solidification Processes." *Acta Metallurgica et Materialia* 41 (2): 345–60. https://doi.org/10.1016/0956-7151(93)90065-Z.

Razavykia, Abbas, Eugenio Brusa, Cristiana Delprete, and Reza Yavari. 2020. "An Overview of Additive Manufacturing Technologies—A Review to Technical Synthesis in Numerical Study of Selective Laser Melting." *Materials 2020, Vol. 13, Page 3895* 13 (17): 3895. https://doi.org/10.3390/MA13173895.

Rolls-Royce. 2022. "Rolls-Royce Plc | Flickr." 2022. https://www.flickr.com/photos/rolls-royceplc/with/14150915649/.

Russell, Richard, Douglas Wells, Jess Waller, Behrang Poorganji, Eric Ott, Tsuyoshi Nakagawa, Hector Sandoval, Nima Shamsaei, and Mohsen Seifi. 2019. "Qualification and Certification of Metal Additive Manufactured Hardware for Aerospace Applications." *Additive Manufacturing for the Aerospace Industry*, January, 33–66. https://doi.org/10.1016/B978-0-12-814062-8.00003-0.

Sabberwal, A. J.P. 1962. "Cutting Forces in down Milling." *International Journal of Machine Tool Design and Research* 2 (1): 27–41. https://doi.org/10.1016/0020-7357(62)90025-2.

Sames, W. J., F. A. List, S. Pannala, R. R. Dehoff, and S. S. Babu. 2016. "The Metallurgy and Processing Science of Metal Additive Manufacturing." *Http://Dx.Doi.Org/10.1080/09506608.2015.1116649* 61 (5): 315–60. https://doi.org/10.1080/09506608.2015.1116649.

Sanchez, Salomé, Peter Smith, Zhengkai Xu, Gabriele Gaspard, Christopher J. Hyde, Wessel W. Wits, Ian A. Ashcroft, Hao Chen, and Adam T. Clare. 2021. "Powder Bed Fusion of Nickel-Based Superalloys: A Review." *International Journal of Machine Tools and Manufacture* 165 (June): 103729. https://doi.org/10.1016/J.IJMACHTOOLS.2021.103729.

Santomaso, A., P. Lazzaro, and P. Canu. 2003. "Powder Flowability and Density Ratios: The Impact of Granules Packing." *Chemical Engineering Science* 58 (13): 2857–74. https://doi.org/10.1016/S0009-2509(03)00137-4.

Sartori, S., L. Moro, A. Ghiotti, and S. Bruschi. 2017. "On the Tool Wear Mechanisms in Dry and Cryogenic Turning Additive Manufactured Titanium Alloys." *Tribology International* 105 (January): 264–73. https://doi.org/10.1016/J.TRIBOINT.2016.09.034.

Sartori, Stefano, Alberto Bordin, Andrea Ghiotti, and Stefania Bruschi. 2016. "Analysis of the Surface Integrity in Cryogenic Turning of Ti6Al4 V Produced by Direct Melting Laser Sintering." *Procedia CIRP* 45 (January): 123–26. https://doi.org/10.1016/J.PROCIR.2016.02.328.

Sato, Mototaro, Yoshio Kato, Shoichi Aoki, and Atsushi Ikoma. 1983. "Effects of Crystal Orientation on the Cutting Mechanism of the Aluminum Single Crystal : 2nd Report : On the (111) Plane and the (112) End Cutting." *Bulletin of JSME* 26 (215): 890–96. https://doi.org/10.1299/jsme1958.26.890.

Sato, Mototaro, Yoshio Kato, Kazuhiro Tsutiya, and Shoichi Aoki. 1981. "Effects of Crystal Orientation on the Cutting Mechanism of Aluninum Single Crystal." *Bulletin of JSME* 24 (196): 1864–70. https://doi.org/10.1299/jsme1958.24.1864.

Saunders, Marc. 2017. "Meeting the Machining Challenges of Additive Manufacturing | Modern Machine Shop." 2017. https://www.mmsonline.com/articles/meeting-the-machining-challenges-of-additive-manufacturing.

Scime, Luke, and Jack Beuth. 2018. "Anomaly Detection and Classification in a Laser Powder Bed Additive Manufacturing Process Using a Trained Computer Vision Algorithm." *Additive Manufacturing* 19 (January): 114–26. https://doi.org/10.1016/J.ADDMA.2017.11.009.

Scipioni Bertoli, Umberto, Alexander J. Wolfer, Manyalibo J. Matthews, Jean Pierre R. Delplanque, and Julie M. Schoenung. 2017. "On the Limitations of Volumetric Energy Density as a Design Parameter for Selective Laser Melting." *Materials and Design* 113 (January): 331–40. https://doi.org/10.1016/j.matdes.2016.10.037.

Scott-Emuakpor, Onome, Tommy George, Brian Runyon, Casey Holycross, Bryan Langley, Luke Sheridan, Ryan O'Hara, Phil Johnson, and Joseph Beck. 2018. "Investigating Damping Performance of Laser Powder Bed Fused Components With Unique Internal Structures." In *Turbo Expo: Power for Land, Sea and Air*. American Society of Mechanical Engineers Digital Collection. https://doi.org/10.1115/GT2018-75977.

Segerstark, Andreas, Joel Andersson, Lars Erik Svensson, and Olanrewaju Ojo. 2018. "Effect of Process Parameters on the Crack Formation in Laser Metal Powder Deposition of Alloy 718." *Metallurgical and Materials Transactions A: Physical Metallurgy and Materials Science* 49 (10): 5042–50. https://doi.org/10.1007/S11661-018-4767-0/FIGURES/12.

Segreto, Tiziana, Alessandro Simeone, and Roberto Teti. 2012. "Sensor Fusion for Tool State Classification in Nickel Superalloy High Performance Cutting." *Procedia CIRP* 1 (January): 593–98. https://doi.org/10.1016/J.PROCIR.2012.05.005.

Seifi, Mohsen, Michael Gorelik, Jess Waller, Nik Hrabe, Nima Shamsaei, Steve Daniewicz, and

John J. Lewandowski. 2017. "Progress Towards Metal Additive Manufacturing Standardization to Support Qualification and Certification." *JOM* 69 (3): 439–55. https://doi.org/10.1007/S11837-017-2265-2/FIGURES/7.

Seifi, Mohsen, Ayman Salem, Jack Beuth, Ola Harrysson, and John J. Lewandowski. 2016. "Overview of Materials Qualification Needs for Metal Additive Manufacturing." *JOM* 68 (3): 747–64. https://doi.org/10.1007/S11837-015-1810-0/FIGURES/14.

Serrano-Munoz, Itziar, Tobias Fritsch, Tatiana Mishurova, Anton Trofimov, Daniel Apel, Alexander Ulbricht, Arne Kromm, René Hesse, Alexander Evans, and Giovanni Bruno. 2021. "On the Interplay of Microstructure and Residual Stress in LPBF IN718." *Journal of Materials Science* 56 (9): 5845–67. https://doi.org/10.1007/S10853-020-05553-Y/FIGURES/14.

Serrano-Munoz, Itziar, Tatiana Mishurova, Tobias Thiede, Maximilian Sprengel, Arne Kromm, Naresh Nadammal, Gert Nolze, Romeo Saliwan-Neumann, Alexander Evans, and Giovanni Bruno. 2020a. "The Residual Stress in As-Built Laser Powder Bed Fusion IN718 Alloy as a Consequence of the Scanning Strategy Induced Microstructure." *Scientific Reports 2020 10:1* 10 (1): 1–15. https://doi.org/10.1038/s41598-020-71112-9.

———. 2020b. "The Residual Stress in As-Built Laser Powder Bed Fusion IN718 Alloy as a Consequence of the Scanning Strategy Induced Microstructure." *Scientific Reports 2020 10:1* 10 (1): 1–15. https://doi.org/10.1038/s41598-020-71112-9.

SHI, Guanghui, Chengqi GUAN, Dongliang QUAN, Dongtao WU, Lei TANG, and Tong GAO. 2020. "An Aerospace Bracket Designed by Thermo-Elastic Topology Optimization and Manufactured by Additive Manufacturing." *Chinese Journal of Aeronautics* 33 (4): 1252–59. https://doi.org/10.1016/J.CJA.2019.09.006.

Shin, Yung C., and Andrew J. Waters. 1997. "A New Procedure to Determine Instantaneous Cutting Force Coefficients for Machining Force Prediction." *International Journal of Machine Tools and Manufacture* 37 (9): 1337–51. https://doi.org/10.1016/S0890-6955(96)00093-4.

Shokrani, Alborz, Vimal Dhokia, and Stephen T. Newman. 2017. "Hybrid Cooling and Lubricating Technology for CNC Milling of Inconel 718 Nickel Alloy." *Procedia Manufacturing* 11 (January): 625–32. https://doi.org/10.1016/J.PROMFG.2017.07.160.

Shrestha, Subin, and Kevin Chou. 2022. "Formation of Keyhole and Lack of Fusion Pores during

the Laser Powder Bed Fusion Process." *Manufacturing Letters* 32 (April): 19–23. https://doi.org/10.1016/J.MFGLET.2022.01.005.

Shunmugavel, Manikandakumar, Ashwin Polishetty, Moshe Goldberg, Rajkumar Singh, and Guy Littlefair. 2017. "A Comparative Study of Mechanical Properties and Machinability of Wrought and Additive Manufactured (Selective Laser Melting) Titanium Alloy - Ti-6Al-4V." *Rapid Prototyping Journal* 23 (6): 1051–56. https://doi.org/10.1108/RPJ-08-2015-0105/FULL/PDF.

Shvedov, Vladlen G., Andrei V. Rode, Yana V. Izdebskaya, Anton S. Desyatnikov, Wieslaw Krolikowski, and Yuri S. Kivshar. 2010. "Giant Optical Manipulation." *Physical Review Letters* 105 (11): 118103. https://doi.org/10.1103/PHYSREVLETT.105.118103/FIGURES/4/MEDIUM.

SLM. 2022. "Additive Manufacturing - Aviation and Aeronautics | SLM Solutions." 2022. https://www.slm-solutions.com/industries/aerospace-and-defense/.

Slotwinski, J. A., E. J. Garboczi, P. E. Stutzman, C. F. Ferraris, S. S. Watson, and M. A. Peltz. 2014. "Characterization of Metal Powders Used for Additive Manufacturing." *Journal of Research of the National Institute of Standards and Technology* 119: 460. https://doi.org/10.6028/JRES.119.018.

Smith, Jacob, Wei Xiong, Wentao Yan, Stephen Lin, Puikei Cheng, Orion L. Kafka, Gregory J. Wagner, Jian Cao, and Wing Kam Liu. 2016. "Linking Process, Structure, Property, and Performance for Metal-Based Additive Manufacturing: Computational Approaches with Experimental Support." *Computational Mechanics* 57 (4): 583–610. https://doi.org/10.1007/S00466-015-1240-4/FIGURES/15.

Song, Chunlei, and Xiaoliang Jin. 2020. "Shearing-Buckling Mechanism in Orthogonal Cutting of Unidirectional Carbon Fiber Reinforced Polymer." *Journal of Materials Processing Technology* 280 (June): 116612. https://doi.org/10.1016/j.jmatprotec.2020.116612.

Souza, Adriano Fagali de, Kassim S. Al-Rubaie, Sabrina Marques, Bruno Zluhan, and Edson Costa Santos. 2019. "Effect of Laser Speed, Layer Thickness, and Part Position on the Mechanical Properties of Maraging 300 Parts Manufactured by Selective Laser Melting." *Materials Science and Engineering A* 767 (November): 138425. https://doi.org/10.1016/j.msea.2019.138425.

Spierings, A. B., T. L. Starr, and K. Wegener. 2013. "Fatigue Performance of Additive

Manufactured Metallic Parts." *Rapid Prototyping Journal* 19 (2): 88–94. https://doi.org/10.1108/13552541311302932/FULL/PDF.

Sprouster, David J., W. Streit Cunningham, Gary P. Halada, Hanfei Yan, Ajith Pattammattel, Xiaojing Huang, Daniel Olds, et al. 2021. "Dislocation Microstructure and Its Influence on Corrosion Behavior in Laser Additively Manufactured 316L Stainless Steel." *Additive Manufacturing* 47 (November): 102263. https://doi.org/10.1016/J.ADDMA.2021.102263.

Ståhl, Jan-Eric. 2012. *Metal Cutting — Theories and Models*. Suède (Lund University, Box 118, 221 00 Lund, Sweden) : Division of Production and Materials Engineering, cop.2012. https://search.ebscohost.com/login.aspx?direct=true&AuthType=shib&db=cat02894a&AN=hig.14878414&lang=sv&site=eds-live&custid=s3912055.

Subhas, B. K., R. Bhat, K. Ramachandra, and H. K. Balakrishna. 2000. "Dimensional Instability Studies in Machining of Inconel 718 Nickel Based Superalloy as Applied to Aerogas Turbine Components." *Journal of Engineering for Gas Turbines and Power* 122 (1): 55–61. https://doi.org/10.1115/1.483175.

Subrahmanyam, K. V.R., Wong Yoke San, Hong Geok Soon, and Huang Sheng. 2010. "Cutting Force Prediction for Ball Nose Milling of Inclined Surface." *International Journal of Advanced Manufacturing Technology* 48 (1–4): 23–32. https://doi.org/10.1007/s00170-009-2275-5.

Sun, Shi Hai, Koji Hagihara, and Takayoshi Nakano. 2018a. "Effect of Scanning Strategy on Texture Formation in Ni-25 at.%Mo Alloys Fabricated by Selective Laser Melting." *Materials & Design* 140 (February): 307–16. https://doi.org/10.1016/J.MATDES.2017.11.060.

———. 2018b. "Effect of Scanning Strategy on Texture Formation in Ni-25 at.%Mo Alloys Fabricated by Selective Laser Melting." *Materials and Design* 140 (February): 307–16. https://doi.org/10.1016/j.matdes.2017.11.060.

Suwas, Satyam, and Ranjit Kumar Ray. 2014. "Texture Evolution During Solidification and Solid-State Transformation." In , 73–93. Springer, London. https://doi.org/10.1007/978-1-4471-6314-5_4.

Suzuki, Norikazu, Risa Enmei, Yohei Hashimoto, Eiji Shamoto, and Yuki Hatano. 2014. "Tool Failure Mechanism in   High-Speed Milling of Inconel 718 by Use of Ceramic Tools." *International Journal of Automation Technology* 8 (6): 837–46.

https://doi.org/10.20965/IJAT.2014.P0837.

Tane, M., S. Akita, T. Nakano, K. Hagihara, Y. Umakoshi, M. Niinomi, and H. Nakajima. 2008. "Peculiar Elastic Behavior of Ti–Nb–Ta–Zr Single Crystals." *Acta Materialia* 56 (12): 2856–63. https://doi.org/10.1016/J.ACTAMAT.2008.02.017.

Tang, H. P., M. Qian, N. Liu, X. Z. Zhang, G. Y. Yang, and J. Wang. 2015. "Effect of Powder Reuse Times on Additive Manufacturing of Ti-6Al-4V by Selective Electron Beam Melting." *JOM* 67 (3): 555–63. https://doi.org/10.1007/S11837-015-1300-4/TABLES/6.

Teich, Heiko, Clemens Maucher, and Hans Christian Möhring. 2021. "Influence of LPBF Parameters and Strategies on Fine Machining of Pre-Built Bores." *Journal of Machine Engineering* Vol. 21, N (2): 91–101. https://doi.org/10.36897/JME/133344.

Tekumalla, Sravya, Jian Eng Chew, Sui Wei Tan, Manickavasagam Krishnan, and Matteo Seita. 2022. "Towards 3-D Texture Control in a β Titanium Alloy via Laser Powder Bed Fusion and Its Implications on Mechanical Properties." *Additive Manufacturing* 59 (November). https://doi.org/10.1016/j.addma.2022.103111.

Thakur, A., and S. Gangopadhyay. 2016. "State-of-the-Art in Surface Integrity in Machining of Nickel-Based Super Alloys." *International Journal of Machine Tools and Manufacture* 100 (January): 25–54. https://doi.org/10.1016/J.IJMACHTOOLS.2015.10.001.

Thakur, D. G., B. Ramamoorthy, and L. Vijayaraghavan. 2009a. "Machinability Investigation of Inconel 718 in High-Speed Turning." *The International Journal of Advanced Manufacturing Technology 2009 45:5* 45 (5): 421–29. https://doi.org/10.1007/S00170-009-1987-X.

———. 2009b. "Study on the Machinability Characteristics of Superalloy Inconel 718 during High Speed Turning." *Materials & Design* 30 (5): 1718–25. https://doi.org/10.1016/J.MATDES.2008.07.011.

Thijs, Lore, Maria Luz Montero Sistiaga, Ruben Wauthle, Qingge Xie, Jean Pierre Kruth, and Jan Van Humbeeck. 2013. "Strong Morphological and Crystallographic Texture and Resulting Yield Strength Anisotropy in Selective Laser Melted Tantalum." *Acta Materialia* 61 (12): 4657–68. https://doi.org/10.1016/j.actamat.2013.04.036.

Thijs, Lore, Frederik Verhaeghe, Tom Craeghs, Jan Van Humbeeck, and Jean Pierre Kruth. 2010. "A Study of the Microstructural Evolution during Selective Laser Melting of Ti-6Al-4V."

Acta Materialia. https://doi.org/10.1016/j.actamat.2010.02.004.

Thompson, Mary Kathryn, Giovanni Moroni, Tom Vaneker, Georges Fadel, R. Ian Campbell, Ian Gibson, Alain Bernard, et al. 2016. "Design for Additive Manufacturing: Trends, Opportunities, Considerations, and Constraints." *CIRP Annals* 65 (2): 737–60. https://doi.org/10.1016/J.CIRP.2016.05.004.

Thorsson, Lena, Mattias Unosson, María Teresa Pérez-Prado, Xueze Jin, Paola Tiberto, Gabriele Barrera, Bastian Adam, et al. 2022. "Selective Laser Melting of a Fe-Si-Cr-B-C-Based Complex-Shaped Amorphous Soft-Magnetic Electric Motor Rotor with Record Dimensions." *Materials & Design* 215 (March): 110483. https://doi.org/10.1016/J.MATDES.2022.110483.

Tobias, S. A., and W. Fishwick. 1958. "The Chatter of Lathe Tools Under Orthogonal Cutting Conditions." *Journal of Fluids Engineering* 80 (5): 1079–87. https://doi.org/10.1115/1.4012609.

Tofail, Syed A.M., Elias P. Koumoulos, Amit Bandyopadhyay, Susmita Bose, Lisa O'Donoghue, and Costas Charitidis. 2018. "Additive Manufacturing: Scientific and Technological Challenges, Market Uptake and Opportunities." *Materials Today* 21 (1): 22–37. https://doi.org/10.1016/J.MATTOD.2017.07.001.

Toyserkani, Ehsan, Dyuti Sarker, Osezua Obehi Ibhadode, Farzad Liravi, Paola Russo, Katayoon Taherkhani, and John Wiley & Sons. 2021. *Metal Additive Manufacturing*. Wiley.

Tsai, Jhy-Cherng, Chung-Yu Kuo, Zing-Ping Liu, and Kelvin Hsi-Hung Hsiao. 2018. "An Investigation on the Cutting Force of Milling Inconel 718." *MATEC Web of Conferences* 169 (May): 01039. https://doi.org/10.1051/MATECCONF/201816901039.

Tucho, Wakshum M., Priscille Cuvillier, Atle Sjolyst-Kverneland, and Vidar Hansen. 2017. "Microstructure and Hardness Studies of Inconel 718 Manufactured by Selective Laser Melting before and after Solution Heat Treatment." *Materials Science and Engineering A* 689 (March): 220–32. https://doi.org/10.1016/j.msea.2017.02.062.

Tumkur, Thejaswi U., Thomas Voisin, Rongpei Shi, Philip J. Depond, Tien T. Roehling, Sheldon Wu, Michael F. Crumb, et al. 2021. "Nondiffractive Beam Shaping for Enhanced Optothermal Control in Metal Additive Manufacturing." *Science Advances* 7 (38): 9358–73. https://doi.org/10.1126/SCIADV.ABG9358/SUPPL_FILE/SCIADV.ABG9358_MOVIES_S1_A

ND_S2.ZIP.

Ucun, irfan, Kubilay Aslantas, and Fevzi Bedir. 2013. "An Experimental Investigation of the Effect of Coating Material on Tool Wear in Micro Milling of Inconel 718 Super Alloy." *Wear* 300 (1–2): 8–19. https://doi.org/10.1016/J.WEAR.2013.01.103.

Umbrello, Domenico. 2013. "Investigation of Surface Integrity in Dry Machining of Inconel 718." *Int J Adv Manuf Technol* 69 (9–12): 2183–90. https://doi.org/10.1007/s00170-013-5198-0.

Urbikain Pelayo, G., and D. Olvera Trejo. 2020. "Model-Based Phase Shift Optimization of Serrated End Mills: Minimizing Forces and Surface Location Error." *Mechanical Systems and Signal Processing* 144 (October): 106860. https://doi.org/10.1016/J.YMSSP.2020.106860.

Veiga, Fernando, Alain Gil Del Val, Alfredo Suárez, and Unai Alonso. 2020. "Analysis of the Machining Process of Titanium Ti6Al-4V Parts Manufactured by Wire Arc Additive Manufacturing (WAAM)." *Materials 2020, Vol. 13, Page 766* 13 (3): 766. https://doi.org/10.3390/MA13030766.

Wan, H. Y., Z. J. Zhou, C. P. Li, G. F. Chen, and G. P. Zhang. 2018. "Effect of Scanning Strategy on Grain Structure and Crystallographic Texture of Inconel 718 Processed by Selective Laser Melting." *Journal of Materials Science and Technology* 34 (10): 1799–1804. https://doi.org/10.1016/j.jmst.2018.02.002.

Wan, M., W. H. Zhang, G. H. Qin, and G. Tan. 2007. "Efficient Calibration of Instantaneous Cutting Force Coefficients and Runout Parameters for General End Mills." *International Journal of Machine Tools and Manufacture* 47 (11): 1767–76. https://doi.org/10.1016/j.ijmachtools.2006.06.012.

Wang, Bing, Zhanqiang Liu, Qinghua Song, Yi Wan, and Xiaoping Ren. 2020. "An Approach for Reducing Cutting Energy Consumption with Ultra-High Speed Machining of Super Alloy Inconel 718." *International Journal of Precision Engineering and Manufacturing - Green Technology* 7 (1): 35–51. https://doi.org/10.1007/S40684-019-00125-1/FIGURES/16.

Wang, Di, Shibiao Wu, Fan Fu, Shuzhen Mai, Yongqiang Yang, Yang Liu, and Changhui Song. 2017. "Mechanisms and Characteristics of Spatter Generation in SLM Processing and Its Effect on the Properties." *Mater. Des.* 117 (March): 121–30. https://doi.org/10.1016/j.matdes.2016.12.060.

Wang, Dianzheng, Chenfan Yu, Jing Ma, Wei Liu, and Zhijian Shen. 2017. "Densification and Crack Suppression in Selective Laser Melting of Pure Molybdenum." *Materials and Design* 129 (September): 44–52. https://doi.org/10.1016/j.matdes.2017.04.094.

Wang, Xingyu, Chunlin Ma, Weiping Zhou, and Weishi Tan. 2022. "Crystalline Orientation-Dependent Ferromagnetism in N+-Implanted MgO Single Crystal." *Materials* 15 (20). https://doi.org/10.3390/MA15207274.

Wang, Yachao, Jing Shi, and Yang Liu. 2019. "Competitive Grain Growth and Dendrite Morphology Evolution in Selective Laser Melting of Inconel 718 Superalloy." *Journal of Crystal Growth* 521 (September): 15–29. https://doi.org/10.1016/j.jcrysgro.2019.05.027.

Webster, Samantha, Hui Lin, Fred M. Carter, Kornel Ehmann, and Jian Cao. 2021. "Physical Mechanisms in Hybrid Additive Manufacturing: A Process Design Framework." *Journal of Materials Processing Technology* 291 (May): 117048. https://doi.org/10.1016/J.JMATPROTEC.2021.117048.

Wei, H. L., J. W. Elmer, and T. Debroy. 2016. "Origin of Grain Orientation during Solidification of an Aluminum Alloy." *Acta Materialia* 115 (August): 123–31. https://doi.org/10.1016/j.actamat.2016.05.057.

Wei, H. L., J. Mazumder, and T. DebRoy. 2015. "Evolution of Solidification Texture during Additive Manufacturing." *Scientific Reports* 5 (1): 1–7. https://doi.org/10.1038/srep16446.

Wei, H. L., T. Mukherjee, and T. DebRoy. 2016. "Grain Growth Modeling for Additive Manufacturing of Nickel Based Superalloys." In *Proceedings of the 6th International Conference on Recrystallization and Grain Growth, ReX and GG 2016*, 265–69. Springer International Publishing AG. https://doi.org/10.1007/978-3-319-48770-0_39.

Woo, Wan Sik, Eun Jung Kim, Ho In Jeong, and Choon Man Lee. 2020. "Laser-Assisted Machining of Ti-6Al-4V Fabricated by DED Additive Manufacturing." *International Journal of Precision Engineering and Manufacturing - Green Technology* 7 (3): 559–72. https://doi.org/10.1007/S40684-020-00221-7/FIGURES/19.

Wu, Baohai, Xue Yan, Ming Luo, and Ge Gao. 2013. "Cutting Force Prediction for Circular End Milling Process." *Chinese Journal of Aeronautics* 26 (4): 1057–63. https://doi.org/10.1016/j.cja.2013.04.003.

Wu, D. W., and C. R. Liu. 1985. "An Analytical Model of Cutting Dynamics. Part 1: Model Building." *Journal of Engineering for Industry* 107 (2): 107–11. https://doi.org/10.1115/1.3185972.

Wu, Zhengkai, Shengchuan Wu, Jianguang Bao, Weijian Qian, Suleyman Karabal, Wei Sun, and Philip J. Withers. 2021. "The Effect of Defect Population on the Anisotropic Fatigue Resistance of AlSi10Mg Alloy Fabricated by Laser Powder Bed Fusion." *International Journal of Fatigue* 151 (October): 106317. https://doi.org/10.1016/J.IJFATIGUE.2021.106317.

Xavior, M. Anthony, Mahesh Patil, Abheek Maiti, Mrinal Raj, and Nitesh Lohia. 2016. "Machinability Studies on INCONEL 718." *IOP Conference Series: Materials Science and Engineering* 149 (1): 012019. https://doi.org/10.1088/1757-899X/149/1/012019.

Xia, Mujian, Dongdong Gu, Guanqun Yu, Donghua Dai, Hongyu Chen, and Qimin Shi. 2016. "Influence of Hatch Spacing on Heat and Mass Transfer, Thermodynamics and Laser Processability during Additive Manufacturing of Inconel 718 Alloy." *International Journal of Machine Tools and Manufacture* 109 (October): 147–57. https://doi.org/10.1016/J.IJMACHTOOLS.2016.07.010.

xian Wu, Liang li, Chengjiao Yao, Meng Zhao. 2016. "Influence of the Cutting Edge Radius and the Material Grain Size on the Cutting Force in Micro Cutting." *Precision Engineering* 45: 359–64.

Xu, Linhong, Fredrik Schultheiss, Mats Andersson, and Jan Eric Stahl. 2013. "General Conception of Polar Diagrams for the Evaluation of the Potential Machinability of Workpiece Materials." *International Journal of Machining and Machinability of Materials* 14 (1): 24–44. https://doi.org/10.1504/IJMMM.2013.055119.

Yadollahi, A., M. J. Mahtabi, A. Khalili, H. R. Doude, and J. C. Newman. 2018. "Fatigue Life Prediction of Additively Manufactured Material: Effects of Surface Roughness, Defect Size, and Shape." *Fatigue and Fracture of Engineering Materials and Structures* 41 (7): 1602–14. https://doi.org/10.1111/FFE.12799.

Yamazaki, Taku. 2016. "Development of A Hybrid Multi-Tasking Machine Tool: Integration of Additive Manufacturing Technology with CNC Machining." *Procedia CIRP* 42 (January): 81–86. https://doi.org/10.1016/J.PROCIR.2016.02.193.

Yang, Lihang, Kaushalendra V. Patel, Krzysztof Jarosz, and Tuğrul Özel. 2020. "Surface Integrity

Induced in Machining Additively Fabricated Nickel Alloy Inconel 625." *Procedia CIRP* 87 (January): 351–54. https://doi.org/10.1016/J.PROCIR.2020.02.104.

Yang, Yun, Wei Hong Zhang, and Min Wan. 2011. "Effect of Cutter Runout on Process Geometry and Forces in Peripheral Milling of Curved Surfaces with Variable Curvature." *International Journal of Machine Tools and Manufacture* 51 (5): 420–27. https://doi.org/10.1016/j.ijmachtools.2011.01.005.

Yang, Yuying, Yadong Gong, Shuoshuo Qu, Yulong Rong, Yao Sun, and Ming Cai. 2018. "Densification, Surface Morphology, Microstructure and Mechanical Properties of 316L Fabricated by Hybrid Manufacturing." *The International Journal of Advanced Manufacturing Technology 2018 97:5* 97 (5): 2687–96. https://doi.org/10.1007/S00170-018-2144-1.

Yap, C. Y., C. K. Chua, Z. L. Dong, Z. H. Liu, D. Q. Zhang, L. E. Loh, and S. L. Sing. 2015. "Review of Selective Laser Melting: Materials and Applications." *Applied Physics Reviews* 2 (4): 041101. https://doi.org/10.1063/1.4935926.

Yi, J. H., J. W. Kang, T. J. Wang, X. Wang, Y. Y. Hu, T. Feng, Y. L. Feng, and P. Y. Wu. 2019. "Effect of Laser Energy Density on the Microstructure, Mechanical Properties, and Deformation of Inconel 718 Samples Fabricated by Selective Laser Melting." *Journal of Alloys and Compounds* 786 (May): 481–88. https://doi.org/10.1016/j.jallcom.2019.01.377.

Yin, Qingan, Zhanqiang Liu, Bing Wang, Qinghua Song, and Yukui Cai. 2020. "Recent Progress of Machinability and Surface Integrity for Mechanical Machining Inconel 718: A Review." *International Journal of Advanced Manufacturing Technology* 109 (1–2): 215–45. https://doi.org/10.1007/S00170-020-05665-4/FIGURES/38.

Yoon, M. C., and Y. G. Kim. 2004. "Cutting Dynamic Force Modelling of Endmilling Operation." *Journal of Materials Processing Technology* 155–156 (1–3): 1383–89. https://doi.org/10.1016/j.jmatprotec.2004.04.218.

Young, Hong Tsu, P. Mathew, and P. L.B. Oxley. 1994. "Predicting Cutting Forces in Face Milling." *International Journal of Machine Tools and Manufacture* 34 (6): 771–83. https://doi.org/10.1016/0890-6955(94)90058-2.

Yücesan, G., and Y. Altintaş. 1994. "Improved Modelling of Cutting Force Coefficients in Peripheral Milling." *International Journal of Machine Tools and Manufacture* 34 (4): 473–87. https://doi.org/10.1016/0890-6955(94)90079-5.

Yuchao Bai, Cuiling Zhao, Yu Zhang, Jie Chen, Hao Wang. 2021. "Additively Manufactured CuCrZr Alloy: Microstructure, Mechanical Properties and Machinability." *Materias Science and Engineering* 819.

Zerilli, Frank J., and Ronald W. Armstrong. 1987. "Dislocation-Mechanics-Based Constitutive Relations for Material Dynamics Calculations." *Journal of Applied Physics* 61 (5): 1816–25. https://doi.org/10.1063/1.338024.

———. 2008. "Constitutive Relations for the Plastic Deformation of Metals." In *AIP Conference Proceedings*, 309:989–92. AIP Publishing. https://doi.org/10.1063/1.46201.

Zhang, Dongyun, Wen Niu, Xuanyang Cao, and Zhen Liu. 2015. "Effect of Standard Heat Treatment on the Microstructure and Mechanical Properties of Selective Laser Melting Manufactured Inconel 718 Superalloy." *Materials Science and Engineering A* 644 (September): 32–40. https://doi.org/10.1016/j.msea.2015.06.021.

Zhang, Jiong, Akshay Chaudhari, and Hao Wang. 2019. "Surface Quality and Material Removal in Magnetic Abrasive Finishing of Selective Laser Melted 316L Stainless Steel." *Journal of Manufacturing Processes* 45 (September): 710–19. https://doi.org/10.1016/J.JMAPRO.2019.07.044.

Zhang, R. Y., H. L. Qin, Z. N. Bi, J. Li, S. Paul, T. L. Lee, S. Y. Zhang, J. Zhang, and H. B. Dong. 2020. "Evolution of Lattice Spacing of Gamma Double Prime Precipitates During Aging of Polycrystalline Ni-Base Superalloys: An In Situ Investigation." *Metallurgical and Materials Transactions A: Physical Metallurgy and Materials Science* 51 (2): 574–85. https://doi.org/10.1007/S11661-019-05536-Y/TABLES/3.

Zhang, Zhao, Zepeng Liang, Ming Luo, Baohai Wu, and Dinghua Zhang. 2021. "A General Method for Calibration of Milling Force Coefficients and Cutter Runout Parameters Simultaneously for Helical End Milling." *The International Journal of Advanced Manufacturing Technology 2021*, July, 1–9. https://doi.org/10.1007/S00170-021-07657-4.

Zhao, Chenhao, Ningsong Qu, and Xiaochuan Tang. 2021. "Removal of Adhesive Powders from Additive-Manufactured Internal Surface via Electrochemical Machining with Flexible Cathode." *Precision Engineering* 67 (January): 438–52. https://doi.org/10.1016/J.PRECISIONENG.2020.11.003.

Zhao, Ji Cheng, and Jack H. Westbrook. 2003. "Ultrahigh-Temperature Materials for Jet

Engines." *MRS Bulletin* 28 (9): 622–27. https://doi.org/10.1557/MRS2003.189.

Zhao, Xiaoming, Jing Chen, Xin Lin, and Weidong Huang. 2008. "Study on Microstructure and Mechanical Properties of Laser Rapid Forming Inconel 718." *Materials Science and Engineering: A* 478 (1–2): 119–24. https://doi.org/10.1016/J.MSEA.2007.05.079.

Zhou, Jinming, Volodymyr Bushlya, Pajazit Avdovic, and Jan Eric Ståhl. 2011. "Study of Surface Quality in High Speed Turning of Inconel 718 with Uncoated and Coated CBN Tools." *The International Journal of Advanced Manufacturing Technology 2011 58:1* 58 (1): 141–51. https://doi.org/10.1007/S00170-011-3374-7.

Zhou, M, and B K A Ngoi. 2001. "Effect of Tool and Workpiece Anisotropy on Microcutting Processes." *Proceedings of the Institution of Mechanical Engineers, Part B: Journal of Engineering Manufacture* 215 (1): 13–19. https://doi.org/10.1243/0954405011515091.

Zou, Tianchun, Yao Ou, He Zhu, and Jiaxu Qin. 2020. "Microstructure and Mechanical Properties of Selective Laser Melted AlSi7Mg Alloy." *Cailiao Daobao/Materials Reports* 34 (5): 10098–102. https://doi.org/10.11896/CLDB.19040019.